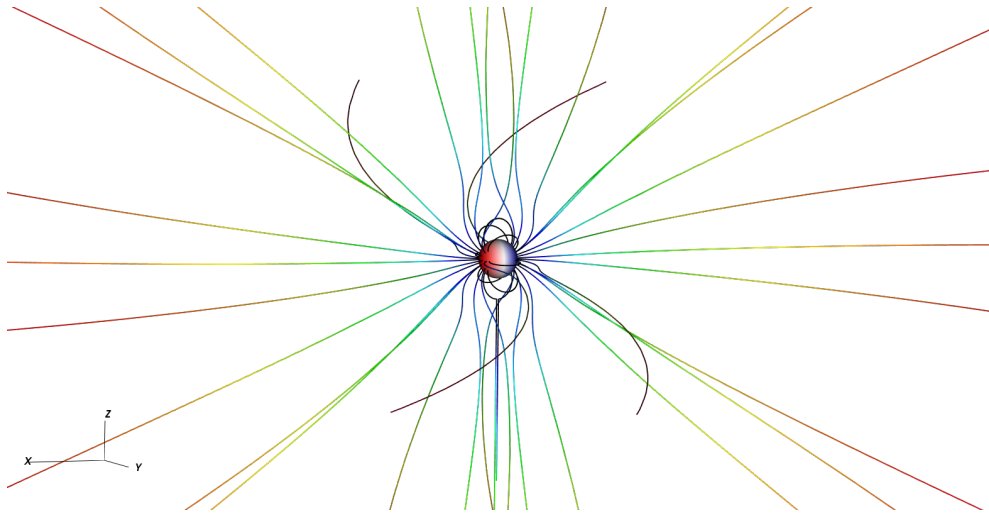


# CONSTRAINING THE ANGULAR MOMENTUM-LOSS RATES OF THE SUN AND OTHER SUN-LIKE STARS

Adam Finley



Submitted by Adam Finley to the University of Exeter as a thesis for the degree of Doctor of Philosophy in Physics, April 2020.

This thesis is available for Library use on the understanding that it is copyright material and that no quotation from the thesis may be published without proper acknowledgement.

I certify that all material in this thesis which is not my own work has been identified and that no material has previously been submitted and approved for the award of a degree by this or any other University.

Signed: .....

Adam Finley

Date: 14th May 2020

## Abstract

1st Supervisor: Prof. Sean P. Matt      2nd Supervisor: Prof. Matthew Browning

Stellar rotation, convection, and magnetism are intricately linked in low-mass stars like the Sun. In their outer convective envelopes, the interplay of rotation and convection form a magnetic dynamo capable of sustaining both large and small scale magnetic fields. The strength of these magnetic fields are observed to grow with increasing rotation rate. The coronae of low-mass stars are heated by these magnetic fields (the exact mechanism of which remains under debate), such that the thermal pressure drives a quasi-steady outflow of plasma, referred to as a stellar wind. Due to the interaction of the large-scale magnetic field with the outflowing plasma, stellar winds are able to efficiently remove angular momentum from these stars. Therefore, the evolution of rotation for low-mass stars (on the the main sequence) is governed by their stellar winds, and by interrelation, the evolution of their magnetic activity and stellar wind output. In this thesis I attempt to better constrain the angular momentum-loss rates of the Sun and other Sun-like stars through the use of magnetohydrodynamic simulations combined with a broad range of observations. Though I do not find a concrete value for the solar case, I reduce the uncertainty in its value to within a factor of a few by locating key factors/quantities which limit our predictions, and further highlight the importance of understanding the solar angular momentum-loss rate in an astrophysical context. For the other Sun-like stars, I find the simulation results largely under-predict the angular momentum-loss rates implied by current rotation-evolution models. The reason(s) for this are uncertain, but likely involve uncertainties in both the observed magnetic field strengths and mass-loss rates of these stars, along with the under-prediction of how much of the surface magnetic field is “opened” by the stellar wind.

Copyright 2016-2020 Adam J. Finley.

---

# Contents

<b>1</b>	<b>Introduction and Background</b>	<b>1</b>
1.1	Motivation . . . . .	1
1.2	Stellar Structure . . . . .	2
1.3	Convection, Magnetism, and Rotation of Low-mass Stars . . . . .	6
1.3.1	Observations of Magnetic Activity . . . . .	6
1.3.2	The Dynamo Mechanism . . . . .	11
1.3.3	Rotation Period Evolution . . . . .	14
1.4	Anatomy of an Astrosphere . . . . .	18
1.4.1	The Quasi-steady Wind . . . . .	19
1.4.2	Transient Mass Ejections . . . . .	24
1.4.3	Encounter with the Interstellar Medium . . . . .	27
<b>2</b>	<b>Stellar Wind Physics and Modelling</b>	<b>29</b>
2.1	The Physics of Plasmas . . . . .	29
2.2	Ideal Magnetohydrodynamic Equations . . . . .	38
2.2.1	Magnetohydrodynamic Waves . . . . .	42
2.3	Summary of the Ideal Magnetohydrodynamic Equations . . . . .	45
2.4	The Solar Wind . . . . .	45
2.4.1	First Mathematical Description of the Solar Wind - Parker (1958) . . . . .	46
2.4.2	The “Polytropic Approximation” . . . . .	48
2.4.3	Heating the Corona . . . . .	50
2.5	Magnetised Stellar Winds . . . . .	52
2.5.1	Parker Spiral Magnetic Field . . . . .	53

2.5.2	Angular Momentum Loss in Stellar Winds - Weber & Davis (1987)	55
2.5.3	Current Models of Solar and Stellar Winds . . . . .	63
2.5.4	1D Semi-analytic Theory . . . . .	64
2.5.5	Conserved Quantities in Stationary Ideal Magnetohydrodynamic Flows . . . . .	71
2.6	Thesis Outline . . . . .	72
<b>3</b>	<b>The Effect of Combined Magnetic Geometries on Thermally Driven Winds</b>	<b>74</b>
3.1	Introduction . . . . .	74
3.2	The PLUTO Magnetohydrodynamic Code . . . . .	75
3.3	Published Article: “I. Interaction of Dipolar and Quadrupolar Fields” . . . . .	80
3.4	Published Article: “II. Dipolar, Quadrupolar, and Octupolar Topologies” . . . . .	98
3.5	Additional Information . . . . .	117
3.5.1	Steady-state and Time-varying Solutions . . . . .	117
3.5.2	Errors in Omega Effective . . . . .	117
3.5.3	Comparison with Other Works . . . . .	120
3.6	Summary . . . . .	121
<b>4</b>	<b>The Effect of Magnetic Variability on Stellar Angular Momentum Loss</b>	<b>123</b>
4.1	Introduction . . . . .	123
4.2	Observations of Solar Magnetism and the Solar Wind . . . . .	124
4.2.1	Remote-sensing Observations . . . . .	124
4.2.2	In-situ Measurements . . . . .	129
4.3	Published Article: “I. The Solar Wind Torque during Sunspot Cycles 23 and 24”	131
4.4	Observations of Stellar Magnetism and Winds . . . . .	146
4.4.1	The Zeeman-Doppler Imaging Technique . . . . .	146
4.4.2	Mass-loss Rates from Astrospheric Lym- $\alpha$ Absorption . . . . .	149
4.5	Published Article: “II. The Sun, 61 Cygni A, $\epsilon$ Eridani, $\xi$ Bootis A, and $\tau$ Bootis A” . . . . .	151
4.6	Additional Information . . . . .	166
4.6.1	Empirical Correction to the Surface Field Formulation . . . . .	166
4.6.2	Transient Mechanisms of Angular Momentum-Loss . . . . .	168

4.6.3	Application to Rotation Period Evolution . . . . .	170
4.7	Summary . . . . .	172
<b>5</b>	<b>Solar Angular Momentum-Loss Over the Past Several Millennia</b>	<b>174</b>
5.1	Introduction . . . . .	174
5.2	Observations of the Solar Wind During the Space-age . . . . .	175
5.3	Reconstructions of Solar Activity from Centuries to Millennia . . . . .	177
5.3.1	Geomagnetic Indices . . . . .	177
5.3.2	Sunspot Number Records . . . . .	178
5.3.3	Cosmogenic Radionuclides . . . . .	180
5.4	Published Article: “ <i>Solar Angular Momentum Loss Over the Past Several Millennia</i> ” . . . . .	181
5.5	Additional Information . . . . .	191
5.5.1	Improving the Solar Mass-loss Rate Prediction . . . . .	191
5.6	Summary . . . . .	191
<b>6</b>	<b>Attempts to Directly Measure the Solar Angular Momentum-Loss Rate</b>	<b>194</b>
6.1	Introduction . . . . .	194
6.2	Review of In-situ Spacecraft Capabilities . . . . .	195
6.2.1	Instrumentation Overview . . . . .	196
6.2.2	Examples of Past and Present Spacecraft Observations . . . . .	198
6.3	Latitudinal Distribution of Mass and Angular Momentum Flux from Simulations . . . . .	201
6.4	Published Article: “ <i>Direct Detection of Solar Angular Momentum Loss with the Wind Spacecraft</i> ” . . . . .	201
6.5	Additional Information . . . . .	209
6.5.1	Latitudinal Angular Momentum Flux Distribution with Ulysses . . . . .	209
6.5.2	Results from the Parker Solar Probe . . . . .	210
6.5.3	Future work with Solar Orbiter . . . . .	211
6.6	Summary . . . . .	212
<b>7</b>	<b>Modelling Non-axisymmetric Stellar Winds</b>	<b>215</b>
7.1	Introduction . . . . .	215

7.2	Article in Preparation: “ <i>The Influence of Magnetic Field Inclination on Angular Momentum Loss from Thermally Driven Winds</i> ” . . . . .	215
7.3	Summary . . . . .	228
<b>8</b>	<b>The Conclusion</b>	<b>229</b>
8.1	Concluding Remarks . . . . .	229
8.2	Further Work . . . . .	231
	<b>The Appendices</b>	<b>233</b>
<b>A</b>	<b>Stellar Magnetic Field Modelling</b>	<b>234</b>
A.1	Potential Magnetic Fields . . . . .	234
A.2	Non-potential Magnetic Fields . . . . .	237
A.3	Potential Field Source Surface (PFSS) Model . . . . .	239
A.4	Visualising Magnetic Field Lines . . . . .	241
A.4.1	Contours of the Magnetic Stream Function $\Psi$ . . . . .	242
<b>B</b>	<b>Derivation of Conserved Quantities</b>	<b>245</b>
<b>C</b>	<b>Numerical Methods</b>	<b>249</b>
C.1	Newton-Raphson Solver . . . . .	249
C.1.1	Application to Isothermal Parker Wind . . . . .	250
C.1.2	Application to Polytropic Parker Wind . . . . .	250
C.2	Basics of Computational Fluid Dynamics . . . . .	252
<b>D</b>	<b>Other Publications</b>	<b>257</b>
	<b>Bibliography</b>	<b>261</b>
	<b>Index</b>	<b>309</b>

# List of Figures

1.1	Gaia Hertzsprung-Russell Diagram . . . . .	3
1.2	Kippenhahn Diagram for Low-mass Stars . . . . .	4
1.3	Image of a Sunspot from the Swedish Solar Telescope . . . . .	6
1.4	Comparison of Modern and Historical Sunspot Observations . . . . .	7
1.5	Activity Cycles Measured Using Ca II H & K Emission . . . . .	8
1.6	Comparison of Chromospheric Activity Cycle Periods and Rotation Periods . . . . .	9
1.7	X-ray Activity Versus Rossby Number for Low-mass Stars . . . . .	11
1.8	Schematic of Dynamo-Action in Low-mass Stars . . . . .	12
1.9	Butterfly Diagram for the Sun using SOHO/MDI and SDO/HMI Magnetogram Observations . . . . .	14
1.10	Rotation Period Versus Stellar Mass Diagrams for Star-forming Regions and Open Clusters . . . . .	15
1.11	Rotation Periods of Sun-like Stars Versus Stellar Age . . . . .	17
1.12	Solar Wind Encountered by Parker Solar Probe . . . . .	19
1.13	Schematic of a Solar Wind Stream Interaction . . . . .	20
1.14	Schematic of Planetary Magnetospheres . . . . .	21
1.15	Simulations of Star-Planet Interactions for Close-in Exoplanets . . . . .	23
1.16	Coronagraph Image and Schematic of a Coronal Mass Ejection . . . . .	25
1.17	Schematic of the Heliosphere . . . . .	26
2.1	Different Kinds of Plasmas Separated by Temperature and Density . . . . .	31
2.2	The Motion of Charged Particles in Electromagnetic Fields . . . . .	34
2.3	Schematic of Charged Particle Motion in the Earth's Magnetosphere . . . . .	35

2.4	Isothermal Parker Wind Solutions . . . . .	47
2.5	Temperature of the Solar Atmosphere Versus Height . . . . .	50
2.6	Combined Eclipse Image from 2019 . . . . .	52
2.7	Parker Spiral Magnetic Field Model Using Data from Parker Solar Probe and the <i>Wind</i> Spacecraft . . . . .	53
2.8	Weber-Davis Wind Solutions . . . . .	58
2.9	Angular Momentum Flux Distribution Between Protons and Magnetic Field Stress . . . . .	60
2.10	Schematic Representation of the 1D Semi-analytic Model . . . . .	65
2.11	The Effect of Magnetic Topology on Magnetic Braking . . . . .	67
2.12	The Effect of Stellar Rotation on Magnetic Braking . . . . .	68
2.13	The Effect of Wind Acceleration on Magnetic Braking . . . . .	70
3.1	Solar Cycle Variation in the Solar Wind Topology . . . . .	75
3.2	Schematic of Finite Volume Discretisation . . . . .	77
3.3	Example Riemann Problem . . . . .	79
3.4	Omega Effective for a Dipole, Quadrupole, and Octupole Stellar Wind So- lution . . . . .	118
3.5	Omega Effective for Mixed Magnetic Geometry Stellar Wind Solutions . .	119
3.6	Alfvén Radius Comparison with Other Works . . . . .	120
4.1	Comparison of Solar Magnetograms . . . . .	125
4.2	Spherical Harmonic Components of the Sun’s Magnetic Field . . . . .	126
4.3	Variation of the Solar Magnetic Field . . . . .	128
4.4	Variation of the Solar Wind Mass Flux and Magnetic Field Strength . . . .	130
4.5	Magnetic Properties of Low-mass Stars Revealed with Zeeman-Doppler Imaging . . . . .	148
4.6	ZDI Observations of 61 Cyg A . . . . .	149
4.7	Schematic of Lym- $\alpha$ Absorption . . . . .	150
4.8	Schematic Representation of the Important Radii in Stellar Winds . . . . .	167
4.9	Correction Factor for the Semi-analytic Formula . . . . .	169
4.10	Application of Semi-analytic Correction to the Result from Section 4.3 . .	169



4.11	Application of Semi-analytic Torques to Spin-evolution Modelling . . . . .	173
5.1	Open Magnetic Flux in the Heliosphere During the Space-age . . . . .	175
5.2	Open Magnetic Flux Reconstructed from Geomagnetic Indices and Sunspot Number Records . . . . .	177
5.3	Open Magnetic Flux Reconstructed from Cosmogenic Radionuclide Records	180
5.4	Experiment in Predicting Mass-loss Rate from Open Magnetic Flux . . . . .	192
6.1	Examples of Past and Present Spacecraft Immersed in the Solar Wind . . . . .	195
6.2	Image of the Parker Solar Probe Instrument Suite . . . . .	196
6.3	Angular Momentum Flux Measurement with Helios A and B Spacecraft . . . . .	198
6.4	Measurements of Tangential Solar Wind Speed with the Ulysses Spacecraft . . . . .	199
6.5	Latitudinal Distribution of Mass-flux and Angular Momentum-flux from a 2.5D PLUTO Wind Model . . . . .	200
6.6	Latitudinal Distribution of Magnetic Stresses as Measured by the Ulysses Spacecraft . . . . .	210
6.7	Angular Momentum Flux as Measured by the Parker Solar Probe . . . . .	213
6.8	Comparison of Trajectories for Parker Solar Probe and Solar Orbiter . . . . .	214
A.1	Potential Field Source Surface Models . . . . .	240
A.2	Example of 2.5D PLUTO Wind Simulation Using Contours of the Stream Function to Show Field Lines . . . . .	244
C.1	Discretisation of a One-dimensional Domain in Space and Time . . . . .	252

## Declaration

I declare that all the research presented in this thesis, unless stated below, was performed by myself in collaboration with my PhD supervisor Sean P. Matt. All the numerical simulations presented in this work were computed using the PLUTO code, developed by Andrea Mignone and his collaborators at the University of Torino. In this thesis:

- Chapter 3 contains two first author papers published in *The Astrophysical Journal* (ApJ 845.1 (2017): 46, and ApJ 854.2 (2018): 78).
- Chapter 4 contains two first author papers published in *The Astrophysical Journal* (ApJ 864.2 (2018): 125, and ApJ 876.1 (2019): 44), the work for which involved collaboration with Victor See (University of Exeter).
- Chapter 5 contains one first author paper published in *The Astrophysical Journal* (ApJ 883.1 (2019): 67), the work for which was carried out by myself and Siddhant Deshmukh (supervised summer student, 2018), with collaboration from Mathew Owens (University of Reading), and Chi-Ju Wu (MPI für Sonnensystemforschung).
- Chapter 6 contains one first author paper published in *The Astrophysical Journal Letters* (ApJL 885 (2019): L30), the work for which was carried out by myself and Amy Hewitt (supervised summer student, 2019) with collaboration from Mathew Owens, Rui Pinto (IRAP, Université Toulouse), and Victor Réville (IRAP, Université Toulouse).
- Chapter 6 contains data from the Parker Solar Probe mission, for which credit is given to the instrument teams; most notably the FIELDS and SWEAP teams.

- Chapter 7 contains one first author paper intended for publication in *The Astrophysical Journal* during 2020, the work for which involved collaboration with Claudio Zanni (University of Torino).
- Appendix D contains summaries of collaborative works for which I am not first author. My level of input is noted with each summary.

# Acknowledgements

In loving memory of my father, Mark, who sadly passed away during the final year of my PhD. My father always encouraged me to follow my dreams, despite often not understanding what I wanted to do. In my heart I know that he would be very proud of this accomplishment, I only wish that he could have been here to share it with me.

I could not have completed my PhD without the love and support I have received from my family; my mother Claire, and my siblings, Rebecca, Mathew, Jessica, and Abigail. My family have provided a stable and loving foundation for me to build my life upon. They each have inspired me to work hard and pursue my academic career. Claire, specifically, has nurtured my interests in maths and science from as far back as I can remember. The completion of this PhD thesis is fuelled by her belief that I could succeed in whatever I wanted to do.

I thank my supervisor Sean Matt for his guidance, and encouragement during the last four years. As soon as I arrived in Exeter, Sean made me feel at home and has since provided me with a happy, and fruitful environment to grow as an academic. For contributing to this environment, I must also thank the entire Exeter Astrophysics group, past and present. This includes Sean's AWESoMeStars ERC group who I have shared many an adventure with, from working in cafes around Exeter to travelling across Chile to see a total solar eclipse. Here I must show my extreme gratitude to one of these individuals, Victor See. Throughout my PhD, Victor has been a strong role model for me to follow, always happy to chat about the small things and provide support/advice whenever I asked. In the same vein, I sincerely thank the individuals who have shared office space with me during this time, most notably the members of G27; Aarynn, Brendan, Mark, and Tom. I blame the antics of G27 wholeheartedly for many lapses in productivity during the last

four years. Though these interruptions have helped me to maintain my sanity during difficult times, for which I am incredibly grateful. During my time in Exeter, I have made many friends through my love of kayaking with the Exeter University Canoe Club. I thank all the people who have spent time kayaking with me over the years, especially those from my undergraduate days in Lancaster who continue to be firm friends. The support network that this community has provided me with during my PhD is immense and I am extremely thankful for it.

I thank my PhD examiners Rony Keppens, and Nathan Mayne, for diligently reading through my thesis during such a difficult time for so many people. They both provided insightful comments and corrections which helped improved the quality of this thesis.

I dedicate this thesis to all the people I mentioned above, and others who I did not have time to acknowledge. In future, I hope that I can pay forward the time and energy that has been invested in my success.

Adam J. Finley

Exeter, U.K.

14<sup>rd</sup> May 2020

# Chapter 1

## Introduction and Background

*“It is not knowledge, but the act of learning, not possession but the act of getting there, which grants the greatest enjoyment.”*

— *Carl Friedrich Gauss*

### 1.1 Motivation

Low-mass stars are observed to possess dynamo-driven magnetic fields which heat their outer atmospheres to millions of degrees. The resulting thermal pressure drives a quasi-steady wind of magnetised plasma away from the stellar surface, through interplanetary space, and into the interstellar medium. With the exception of the solar wind, the stellar winds of low-mass stars cannot be directly observed due to their tenuous nature and so are poorly quantified. However, their potential interactions with planetary bodies leaves many open questions surrounding the habitability of exoplanets. In the Solar System, for example, the surface of Mars is inhospitable to life despite the planet possessing an orbit within the “habitable zone” (as defined by temperature). This is likely a result of exposure to the solar wind as, unlike Earth, Mars lacks a global magnetic field sufficient to protect its surface, leading to the erosion of liquid water/volatiles. Additionally, the strength of a stellar wind evolves during the star’s lifetime, i.e. the solar wind was likely stronger during the Sun’s youth. An example of this appears in the apparent contradiction between

the appearance of liquid water on the Earth's surface and the supposed luminosity of the Sun during its younger-years ( $\sim 4.5$  billion years ago). One explanation for this could be that the Sun's mass changed drastically during the early stages of its life, due to an enhanced mass-loss rate in the solar wind. Such an increase in the mass-loss rates of young Sun-like stars would likely have a significant impact on our definition of planetary habitability (note this is not the only proposed resolution to the discrepancy, others include an increased greenhouse effect or astrophysical interactions). To gain insight on the past, current, and future environments of planets orbiting the Sun and other Sun-like stars, it is important to understand the physics of stellar winds. Given the difficulties of studying stellar winds directly, in this work I focus on the indirect effect of stellar winds in governing the rotational evolution of low-mass stars. Though only a small fraction of a star's mass is lost during the main sequence to its stellar wind, the torque exerted by the wind on the star is significant due to its interaction with the stellar magnetic field. Typically the rotation period of a Sun-like star grows from a few days to around a month during its lifetime on the main sequence. By better understanding the angular momentum-loss rates of stellar winds, the observed rotation period evolution of low-mass stars can be used to provide information on the global properties of winds and infer the plasma environments experienced by exoplanets.

## 1.2 Stellar Structure

Stellar winds are ubiquitous in astrophysics, appearing in many different places across the Hertzsprung-Russell (HR) diagram (see Figure 1.1 for examples). There are many different mechanisms that power them, from radiation pressure acting on dust grains to complex magnetohydrodynamic (MHD) processes in protostellar disks, however they all share the tendency to transport mass and angular momentum around a system. Stellar winds in particular, either line-driven (e.g. Castor et al. 1975), dust-driven (e.g. Sedlmayr and Dominik 1995), or coronal (e.g. thermally-driven like those in this thesis), are responsible for many significant changes in the lifetime of a star. For example, hot stars (types O, B and A) lose a significant amount of their Zero Age Main Sequence (ZAMS) mass through

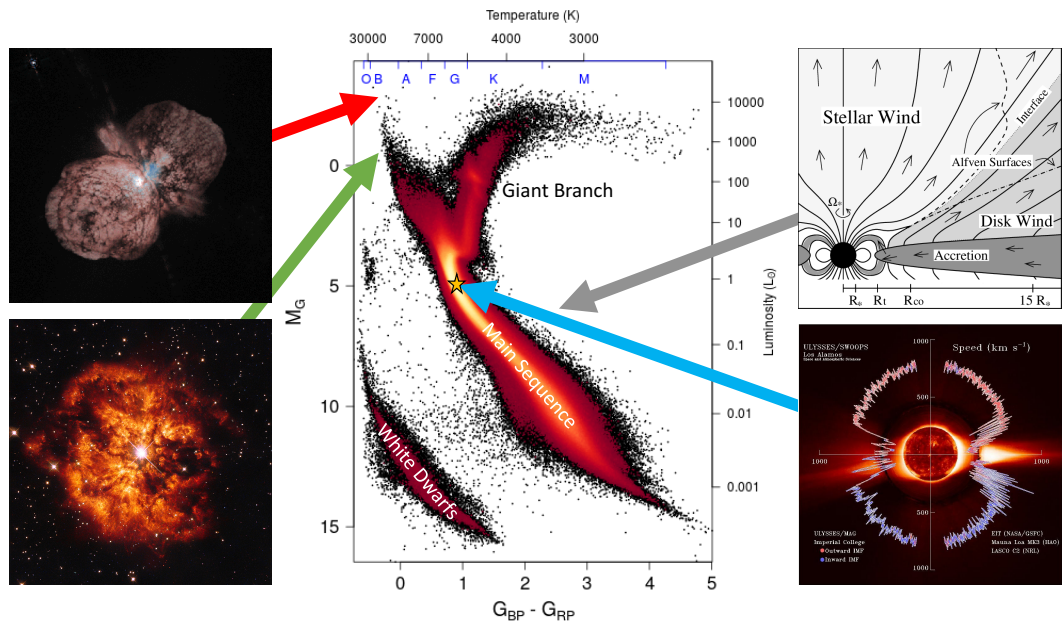


**Figure 1.1:** The Hertzsprung-Russell diagram produced from Gaia DR2, taken from Babusiaux et al. (2018). Effective temperature is shown against luminosity which sorts different populations of stars. On the left, examples of dust driven-winds from eta Carinae and a Wolf-Rayet star (image credits: Hubble Legacy Archive, NASA, ESA). On the right, examples of coronal-winds from T-Tauri stars (Matt and Pudritz 2008) and low-mass main sequence stars like the Sun (McComas et al. 2013).

strong line-driven winds, with mass-loss rates as high as  $\sim 10^{-5} M_{\odot}/\text{yr}$ , that impact their evolution during the Main Sequence (MS) (Pauldrach et al. 1986). Cool stars (otherwise referred to as low-mass stars) which host coronal-winds (driven by high temperatures and MHD processes) typically have much lower mass-loss rates, around  $10^{-14} M_{\odot}/\text{yr}$  for the Sun. However their winds have a much stronger influence over their rotational evolution during the MS (see review of Bouvier et al. 2014). These different regimes are a direct consequence of stellar mass, which governs the internal structure of stars.

Stars form through the gravitational collapse of large molecular ( $H_2$ ) clouds in the interstellar medium (Larson 2003). A fragmented cloud collapses down to form a proto-star (along with an accretion disk), where the stellar contraction is slowed by an increase in the thermal energy of the now mostly ionised Hydrogen. Due to the conservation of angular momentum, proto-stars are generally thought to be born rotating rapidly (Hartmann and MacGregor 1982). During the formation of a low-mass star ( $M_* < 1.3 M_{\odot}$ ), the proto-star interacts with its accretion disk via its magnetic field, exchanging angular momentum and mass (Tinker et al. 2002; Matt and Pudritz 2004). Therefore the rotation period of the proto-star after the disk has been evaporated is strongly connected to the physics of stellar



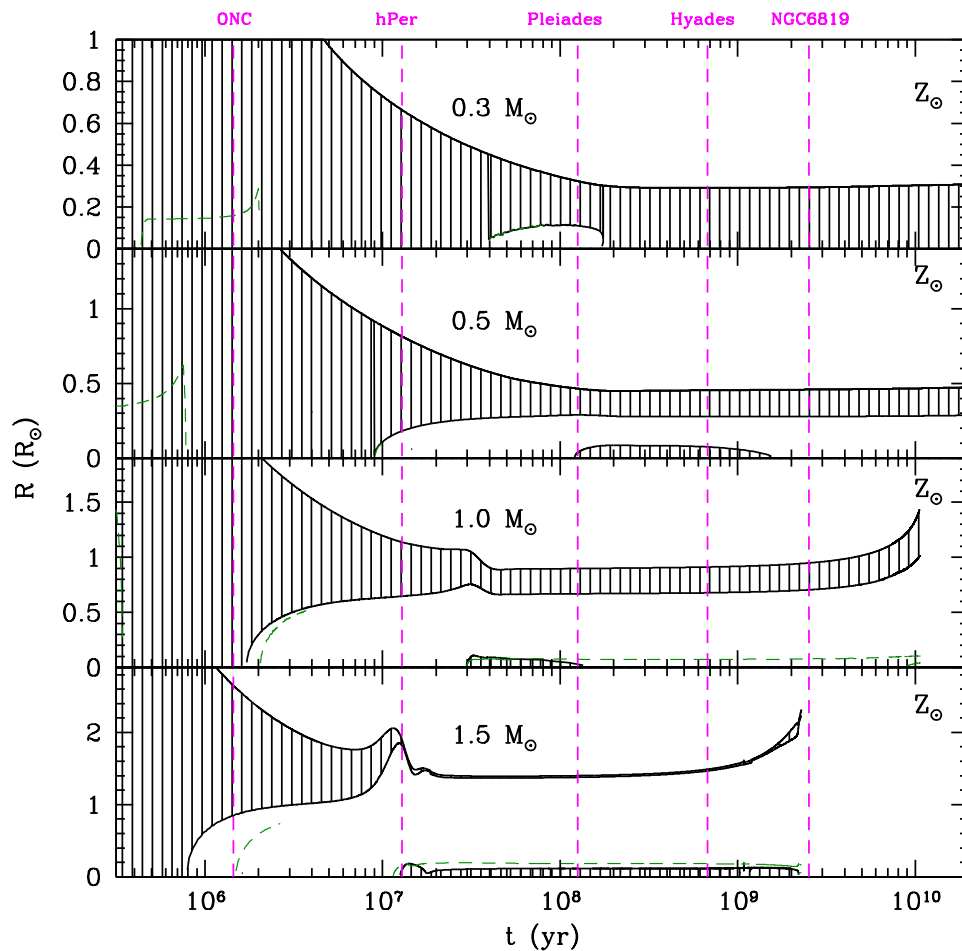
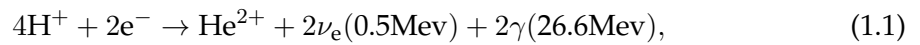


**Figure 1.2:** Kippenhahn diagram showing the internal structure-evolution for different stellar masses. The upper line represents the surface of the star, below which a shaded area represents the extent of the surface convection zone. The surface convection diminishes in size with increasing mass. Areas without shading are radiative. These models are non-rotating with solar metallicity. The ages of a few well-known open clusters are indicated by magenta lines. Taken from Amard et al. (2019).

winds, accretion, and other MHD processes (Suttner and Yorke 2001; Matt and Pudritz 2008; Zanni and Ferreira 2009). This phase of a low-mass star's life, before the ignition of nuclear fusion, is referred to as the Pre Main Sequence (PMS) (Stahler et al. 1986; Siess et al. 2002). Nuclear fusion begins once the proto-star has collapsed to the point that the pressure within the core is large enough to fuse Hydrogen/Deuterium, moving the star onto the MS. All stars are powered by nuclear fusion, which takes place in, and sometimes around the Hydrogen burning core (see the models of Baraffe et al. 2015). The dominant nuclear reaction for low-mass stars is the proton-proton chain reaction (pp-chain), whose

overall reaction is described as,



where energy is released from the binding energy of Helium, and the annihilation of positrons that are produced in the reaction (Bethe 1939; Filippone 1986). The neutrinos escape from the core, unaffected by the overlying mass of the star, allowing the nuclear reaction rate to be probed (e.g. Bahcall et al. 2003). Another common nuclear reaction, the Carbon-Nitrogen-Oxygen cycle (CNO-cycle), has the same overall reaction and becomes important towards the end of a low-mass stars lifetime (when the temperatures in the core become hotter). Though it involves many more nuclear reactions than the pp-chain, through the proton capture of Carbon to Nitrogen to Oxygen etc. The CNO-cycle is thought to dominate the energy production of stars with masses greater than  $1.5M_{\odot}$ . For completeness, I also mention the triple- $\alpha$  process, which converts three Helium nuclei into Carbon. This final process occurs in stars where there is a high abundance of Helium and a high enough temperature. This is therefore likely to be after the MS when Hydrogen burning has been exhausted in the core (e.g. Dotter and Paxton 2009).

The burning of Hydrogen in the core releases energy in the form of thermal motion and  $\gamma$ -rays, which balances the star from further gravitational collapse during its entire MS lifetime. The transport of energy from the core to the surface takes a few different forms, that are said to either be radiative, i.e. radiative diffusion and thermal conduction are the dominant forms of energy transport, or convective, i.e. convective motions are the most dominant form of energy transport (Hansen et al. 2012). Convection zones form inside a star when the vertical temperature gradients become very steep, such that a rising parcel of fluid remains hotter than its surroundings and therefore continues to rise due to buoyancy (Spiegel 1971). Figure 1.2 shows the evolution of stellar structure for four different mass stars;  $0.3M_{\odot}$  (fully-convective star),  $0.5M_{\odot}$  (Sun-like star),  $1.0M_{\odot}$  (partly-convective star), and  $1.5M_{\odot}$  (upper-limit of stars with outer convection zones), from Amard et al. (2019). As stellar mass increases, it is clear that the outer convective envelope diminishes, which leads to the properties of these stars being different.

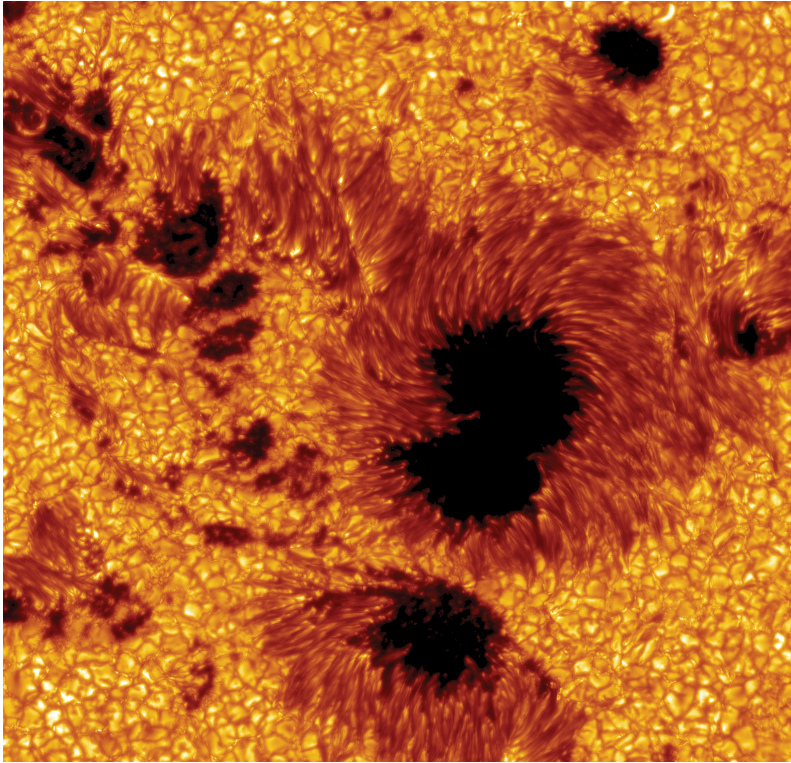


**Figure 1.3:** High resolution image of a sunspot embedded in the solar photosphere taken with the Swedish Solar Telescope. Granulation surrounds the sunspot, whose structure is revealed as a central umbra (the darkest part) with a surrounding penumbra (a slightly lighter colour). Credit: The Royal Swedish Academy of Sciences/The Institute for Solar Physics.

### 1.3 Convection, Magnetism, and Rotation of Low-mass Stars

For low-mass stars, the presence of an outer convective envelope is strongly connected to the evolution of their rotation periods, and magnetic activity. In this Section I will discuss the observations that show this, and how their magnetism links to their observed rotation period distributions.

#### 1.3.1 Observations of Magnetic Activity

Magnetism is commonly observed for low-mass stars, so much so, that magnetic fields are thought to be ubiquitous for all masses less than  $\approx 1.5M_{\odot}$  (see review of Reiners 2012). The most well-documented and studied example of a stellar magnetic field is that of the Sun's (see review of Charbonneau 2010). The Sun's surface is covered with small-scale granulation, i.e. convective motions, which are organised on the large-scale into supergranulation. Sunspots appear as dark features in comparison to the granulation

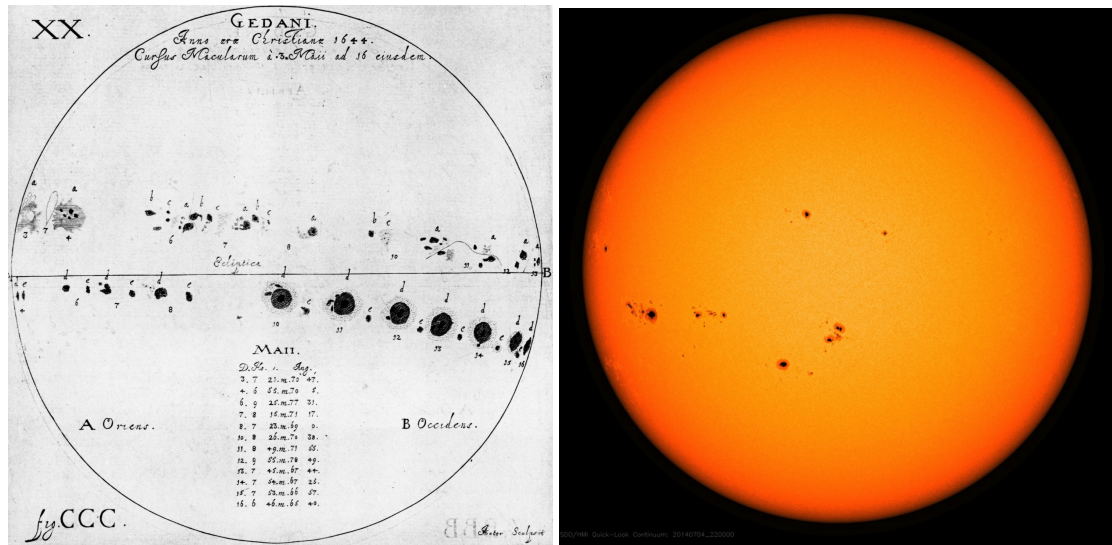


**Figure 1.4:** Comparison of a hand-drawn recording of sunspots moving across the solar disk, with a modern image of the Sun. Taken from Johannes Hevelius (1647) and the Helioseismic and Magnetic Imager (HMI) onboard the Solar Dynamics Observatory (July, 2014).

of the photosphere (see Figure 1.3), having a lower temperature of  $\sim 4500\text{K}$ , compared to the average temperature in the photosphere of  $\sim 5800\text{K}$ . Hale (1908) discovered that these sunspots have intense kG magnetic fields, which are ultimately responsible for the suppression of convection and their relatively “cool” temperatures. Following this, it was noted that sunspots tend to emerge in pairs and have bipolar magnetic fields which have opposite east-west polarity from the other (northern or southern) hemisphere (Hale and Nicholson 1925). Intriguingly, sunspot pairs also tend to be tilted towards the equator i.e. the leading spot is closer to the equator than the following spot (Zirin 1988). The number of sunspots on the Sun is observed to vary with an  $\sim 11$  year period, which is referred to as the sunspot cycle (see review by Hathaway 2015). Sunspots are observed to emerge at around  $\pm 30$  degrees in latitude at the start of the cycle (solar minimum), this emergence latitude progresses down toward the equator as the number of sunspots increases (towards solar maximum). The number of sunspots then decreases to a new minimum at the end of the  $\sim 11$  year period. Each cycle is slightly different to the one that came before, with the length and peak number of sunspots for each cycle varying significantly (Hathaway et al. 1994). Sunspots have been recorded for hundreds of years, including some early observations from Galileo Galilei (e.g. Galilei 1957). One such recording is shown in Figure 1.4, made by Johannes Hevelius in 1647. This historical recording is compared to a modern observation of the Sun from July 2014, and will be further discussed in Section 5.3.

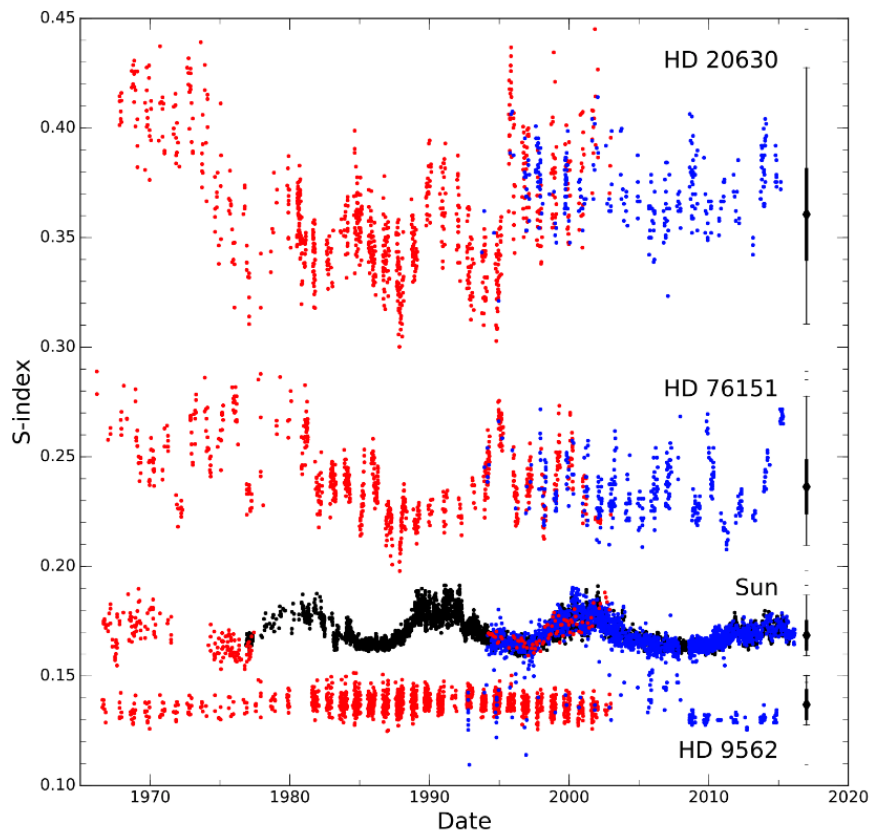


**Figure 1.5:** Temporal evolution of the emission in Ca II H & K lines, a proxy for magnetic activity. A subset of example stars from Baliunas et al. (1995), Hall et al. (2007), and Egeland et al. (2017), which show the variety of observed activity. For example, HD 20630 (kappa Ceti) has roughly the same mass as the Sun, but is likely to be much younger and have a faster rotation rate. Taken from Egeland (2018) (<https://www2.hao.ucar.edu/news/2019-may/ricky-egeland-developed-sunstardb>).

Along with sunspots, bright features called faculae appear on the Sun’s surface. Though they are less visually obvious than sunspots, they contribute strongly to the variation in the Sun’s brightness during the sunspot cycle (Shapiro et al. 2016).

For other low-mass stars, faculae may even be the dominant component of the brightness variations (Shapiro et al. 2014). Furthermore, the transition between dark spots and bright faculae controlling the brightness variations of a star may remove our ability to detect stellar rotation periods (see Reinhold et al. 2019, and Section 1.3.3). Another indicator, linked with faculae, is the increased emission in the Ca II H & K lines. This is observed for the Sun as being correlated directly with the deposition of magnetic energy into the chromosphere. Increased emission in Ca II is also found for other stars, and so by analogy is linked to heating processes in the stellar chromosphere (Eberhard and Schwarzschild 1913; Noyes et al. 1984; Testa et al. 2015). Ca II H & K emission is observed

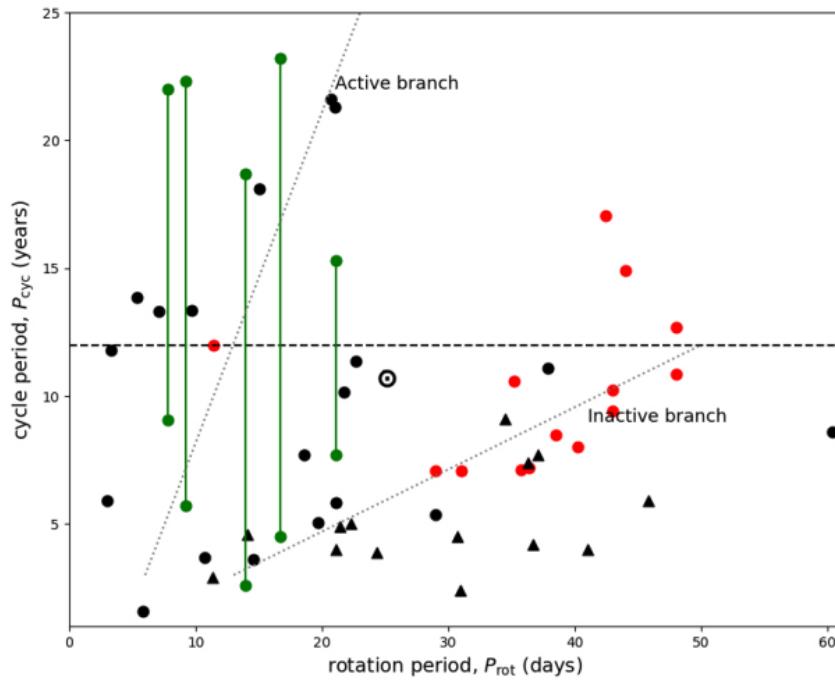


**Figure 1.6:** Chromospheric activity cycle versus rotation period for low-mass stars with periodic Ca II H & K emission. Proposed active and inactive branches are shown with dashed lines. Stars with multiple cycle periods are shown in green. The Sun is shown with a hollow circle. Taken from Saikia et al. (2018b).

to vary during the sunspot cycle (Schrijver et al. 1989), similar to the number of sunspots. The “S-index” is a common measure of magnetic activity, derived from observations of Ca II emission. It has been calculated for many stars using the results of multi-decadal observations taken at the Mount Wilson Observatory and a few other locations (Wilson 1978; Baliunas et al. 1995; Hall et al. 2007; Egeland et al. 2017). Figure 1.5 shows the S-index of the Sun during the last four decades, compared with that from other Sun-like stars. This represents a subset of stars with S-index observations, but it clearly shows the variety of observed magnetic activity. Some stars have stronger emission than the Sun, with a similar periodic/variable magnetic activity. Whilst the weakest star shows little to no discernible temporal evolution at all. From such datasets it is possible to evaluate the magnetic cycle periods for stars that present with clear cycles, these can be then compared with the Sun’s activity cycle.

The Sun has a magnetic cycle of  $\sim 22$  years, over which time the polarity of the Sun’s large-scale magnetic field reverses once, and then again, returning to the original polarity (DeRosa et al. 2012). However, in activity indicators such as Ca II and sunspot number, the

Sun has an  $\sim 11$  year activity cycle, where its activity is low then increases to a maximum, and then back down to low. It is therefore important to be clear when discussing magnetic cycles, whether it is the chromospheric activity cycle (typical) or magnetic cycle that is being compared. In an attempt to better understand the magnetic fields of other stars, when clear periodic cycles are detected, their periods are often plotted against rotation period (see Figure 1.6). When first plotted this way, it was noticed that activity cycles appeared to follow two distinct branches, labelled “active” and “inactive” (Brandenburg et al. 1998; Saar and Brandenburg 1999). This was further developed by Böhm-Vitense (2007) who suggested each branch was related to a distinct magnetic field generation mechanism within stars. This received some support with the appearance of stars with multiple cycle periods (e.g. Metcalfe et al. 2013), though it left the Sun (arguably the most reliable data point) in between the two branches. This led to the idea of the Sun being “in transition” between the branches (see Metcalfe et al. 2016). However, subsequent work has shown that with an increased sample size, and better definitions of cyclic activity, the branches are likely to be caused by selection bias (see Saikia et al. 2018b) and therefore not representative of the physics of magnetic field generation.

One of the most fascinating discoveries regarding the magnetic fields of low-mass stars comes from observations of their x-ray activity. Figure 1.7 shows the x-ray luminosity of stars, normalised by their bolometric luminosity, against Rossby number  $R_o = P/\tau_{cz}$ . Here  $R_o$  is the stellar rotation period normalised by the convective turnover timescale in the convection zone  $\tau_{cz}$  (which is thought to remove any mass-dependence). What appears is arguably the clearest diagnostic of the magnetic field generation in low-mass stars, whereby stars with large rotation period (high  $R_o$ ) have the weakest magnetic activity (x-ray activity), and as their rotation periods increase (towards low  $R_o$ ) magnetic activity increases as well, until saturation at  $R_o = 0.1 - 0.2$ . In Figure 1.7, the grey circles represent the x-ray activity of stars above the fully-convective limit ( $> 0.35M_\odot$ ) which are partly convective (see Figure 1.2), and red circles show stars that are fully convective ( $< 0.35M_\odot$ ). Regardless of interior structure, the magnetic activity of low-mass stars appears to be a strong function of  $R_o$ . Other diagnostics of stellar magnetic fields exist, such as techniques that rely on the Zeeman effect (Zeeman 1897), which will be discussed in Section 4.4.

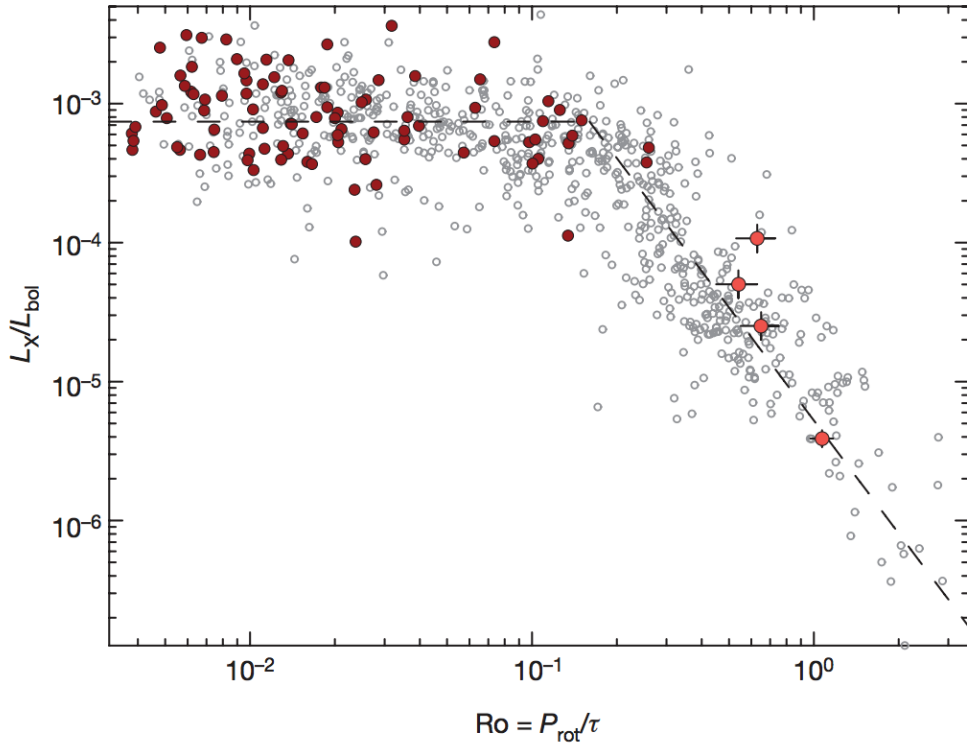


**Figure 1.7:** Rotation-activity relation for partly-convective stars (grey circles) and full-convective stars (red circles). Fractional x-ray luminosity (of Bolometric luminosity) versus Rossby number  $R_o$ . Regardless of stellar structure, the x-ray activity of low-mass stars appears to follow the same relationship versus  $R_o$ . The best fit relation is shown with dashed black lines. Taken from Wright and Drake (2016).

### 1.3.2 The Dynamo Mechanism

The magnetic activity cycles of stars, and the structure of x-ray activity versus rotation rate (or  $R_o$ ), are thought to be explained by the magnetic dynamos that govern the generation of magnetic fields in low-mass stars (see review of Brun and Browning 2017). In this Section I will provide some background to magnetic field generation through dynamo-action. This process revolves around the induction equation (note the induction equation is simply stated here, with the MHD equations being further discussed in Chapter 2),

$$\frac{\partial \mathbf{B}}{\partial t} = \underbrace{\nabla \times (\mathbf{V} \times \mathbf{B})}_{\text{induction}} + \underbrace{R_m^{-1} \nabla^2 \mathbf{B}}_{\text{diffusion}}, \quad (1.2)$$

which describes the evolution of a magnetic field  $\mathbf{B}$  embedded in a plasma with uniform magnetic diffusivity  $\eta$  and flow velocity  $\mathbf{V}$ . Note this equation is written in its non-dimensional form, where  $R_m = UL/\eta$  is the magnetic Reynolds number,  $U$  is the char-



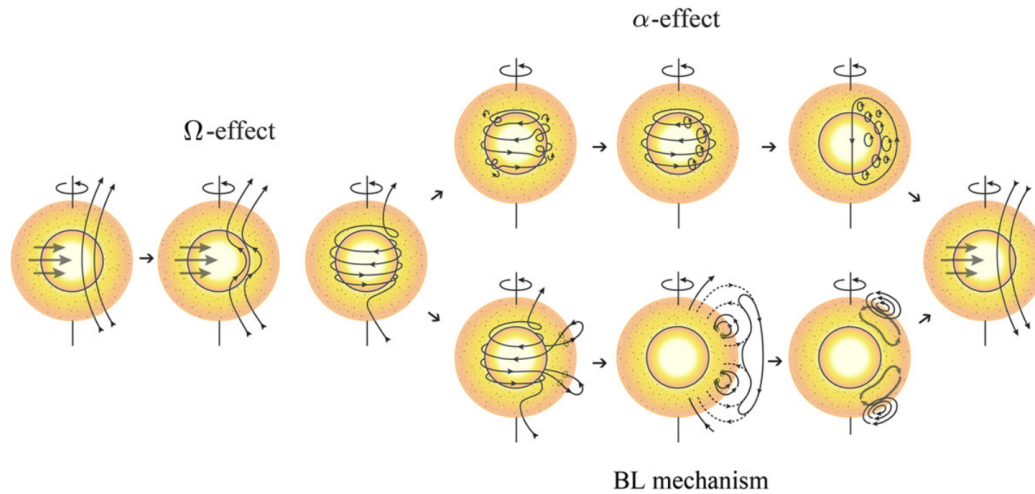


**Figure 1.8:** Schematic of dynamo-action, whereby differential rotation takes an initially poloidal field and converts it into toroidal magnetic field deep inside the star, which is then converted back to poloidal field via the  $\alpha$ -effect or the Babcock-Leighton mechanism. Taken from Sanchez et al. (2013).

characteristic speed, and  $L$  is the characteristic length scale. In plasmas with  $R_m \gg 1$ , the induction term dominates (the plasma is said to be “ideal”, further discussed in Section 2.2) and the diffusive term can be ignored. In this regime the magnetic field is advected with fluid motions, and vice versa. Alternatively, magnetic fields with  $R_m \ll 1$  will decay away due to the diffusive term, this is the case for magnetic fields generated in laboratory settings. Given the MS lifetime of low-mass stars, and the comparatively short diffusion timescale of the magnetic field (when using the characteristic scales and diffusivity coefficient for stellar plasma), any magnetism present from a star’s formation will be dissipated during its lifetime. Therefore, the magnetism of low-mass stars must be dynamically generated through the induction term.

To show this, here I detail a simple Mean Field Theory (MFT) approach to modelling stellar magnetism (see Moffatt 1978). This requires separating the plasma flow and magnetic field vectors into their mean and time-varying components,

$$\mathbf{B} = \langle \mathbf{B} \rangle + \mathbf{b}, \quad (1.3)$$

$$\mathbf{V} = \langle \mathbf{V} \rangle + \mathbf{v}. \quad (1.4)$$

Upon substitution to the induction equation (allowing for a non-uniform  $\eta$ ), it is possible

to show,

$$\frac{\partial \mathbf{B}}{\partial t} = \nabla \times (\mathbf{V} \times \mathbf{B} - \eta \nabla \times \mathbf{B}), \quad (1.5)$$

$$\frac{\partial \langle \mathbf{B} \rangle}{\partial t} = \nabla \times (\langle \mathbf{V} \rangle \times \langle \mathbf{B} \rangle + \langle \mathbf{v} \times \mathbf{b} \rangle - \eta \nabla \times \langle \mathbf{B} \rangle), \quad (1.6)$$

where the time-averages of the fluctuating components satisfy  $\langle \mathbf{b} \rangle = 0$ , and  $\langle \mathbf{v} \rangle = 0$ . From this I denote  $\langle \mathbf{E} \rangle = \langle \mathbf{v} \times \mathbf{b} \rangle$  as the “turbulent electromotive force” which is associated with the magnetic field induced by the fluctuating components. A closure equation must be found for  $\langle \mathbf{E} \rangle$  in order to solve the mean field induction equation above. For this, it is possible to perform a Taylor expansion around  $\langle \mathbf{B} \rangle$ , e.g.  $\langle \mathbf{E} \rangle = \alpha \langle \mathbf{B} \rangle - \beta \nabla \times \langle \mathbf{B} \rangle$  (where  $\alpha$  and  $\beta$  are numerical coefficients), which when substituted into equation (1.6) gives,

$$\frac{\partial \langle \mathbf{B} \rangle}{\partial t} = \nabla \times (\langle \mathbf{V} \rangle \times \langle \mathbf{B} \rangle + \alpha \langle \mathbf{B} \rangle - (\eta + \beta) \nabla \times \langle \mathbf{B} \rangle). \quad (1.7)$$

Therefore, there are three terms that govern the evolution of the mean field  $\langle \mathbf{B} \rangle$ ; 1) the large-scale flows, 2) turbulence i.e.  $\nabla \times (\alpha \langle \mathbf{B} \rangle)$ , and 3) magnetic diffusion. From this equation the  $\alpha - \Omega$  dynamo is proposed, where the large-scale flows, associated with rotation, twist poloidal magnetic field into toroidal magnetic field at the base of the convection zone, and then helical turbulence from the  $\alpha$  term within the convection zone regenerates the poloidal magnetic field (Parker 1955). This process is shown in the top row of Figure 1.8. From this simple model it is clear that stellar dynamos generate stronger magnetic fields with increased rotation i.e. enhanced  $\Omega$ -effect, which is necessary to explain the observations in Figure 1.7. More recently, flux transport dynamos have been developed which explain the regeneration of poloidal field through the Backcock-Leighton effect i.e. bipolar magnetic field regions appear (on the Sun) with tilt angles, such that a large-scale meridional circulation will transport opposite polarity flux poleward (Babcock 1961; Leighton 1964). This is shown on the bottom row of Figure 1.8, and is favoured currently in the literature (Brun and Browning 2017).

For the Sun, I plot the latitudinally-averaged magnetic field strength in the photosphere for the last  $\sim 20$  years in Figure 1.9. From this, the so called butterfly-diagram ap-

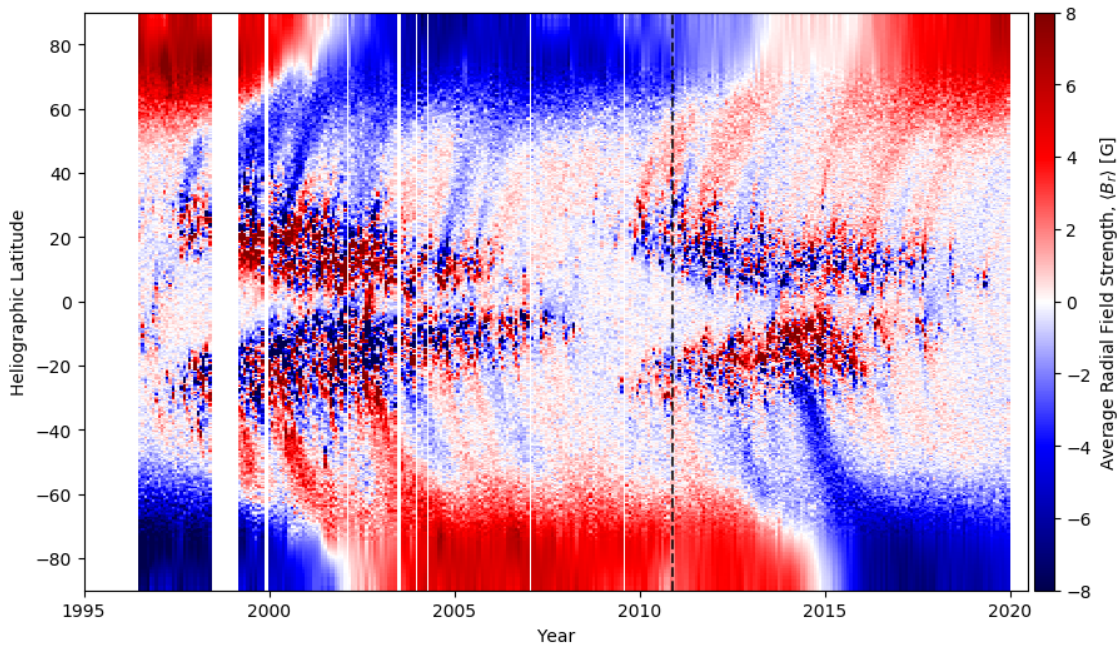


**Figure 1.9:** Magnetic butterfly diagram for the Sun, using magnetograms from the Michelson Doppler Imager (MDI) onboard the Solar and Heliospheric Observatory (SOHO), and the Helioseismic and Magnetic Imager (HMI) onboard the Solar Dynamics Observatory (SDO). The magnetic field of the Sun is averaged latitudinally over a Carrington rotation ( $\sim 27$  days), and  $\sim 20$  years of data is then stacked together to reveal the large-scale polarity reversals and active latitudes of the Sun. Observations span sunspot cycle 23 and 24. The dashed line indicates when SDO/HMI takes over from SOHO/MDI.

pears which shows the emergence latitude of bipolar active regions migrating towards the equator during the solar cycle. The polar magnetic field also appears to be advected via the Backcock-Leighton effect from the break-up of active regions. The generation of toroidal magnetic field is thought to be based in the tachocline, i.e. the interface between the radiative and convective regions within the Sun. However, stars that are fully-convective lack somewhere with differential rotation/shear flow to generate the  $\Omega$ -effect. This has led to the development of other types of dynamo (e.g.  $\alpha^2$ ,  $\alpha^2 - \Omega$ , etc). Such that the importance of a tachocline in generating the magnetic fields of stars is under debate (Guerrero et al. 2016). It is likely not a fundamental requirement for dynamo-action, though it may play a role in shaping the morphology of magnetic field that forms.

### 1.3.3 Rotation Period Evolution

The photospheres of low-mass stars are thought to be similar to that of the Sun, bearing large-scale imperfections (i.e. spots and faculae) that produce time-varying signals

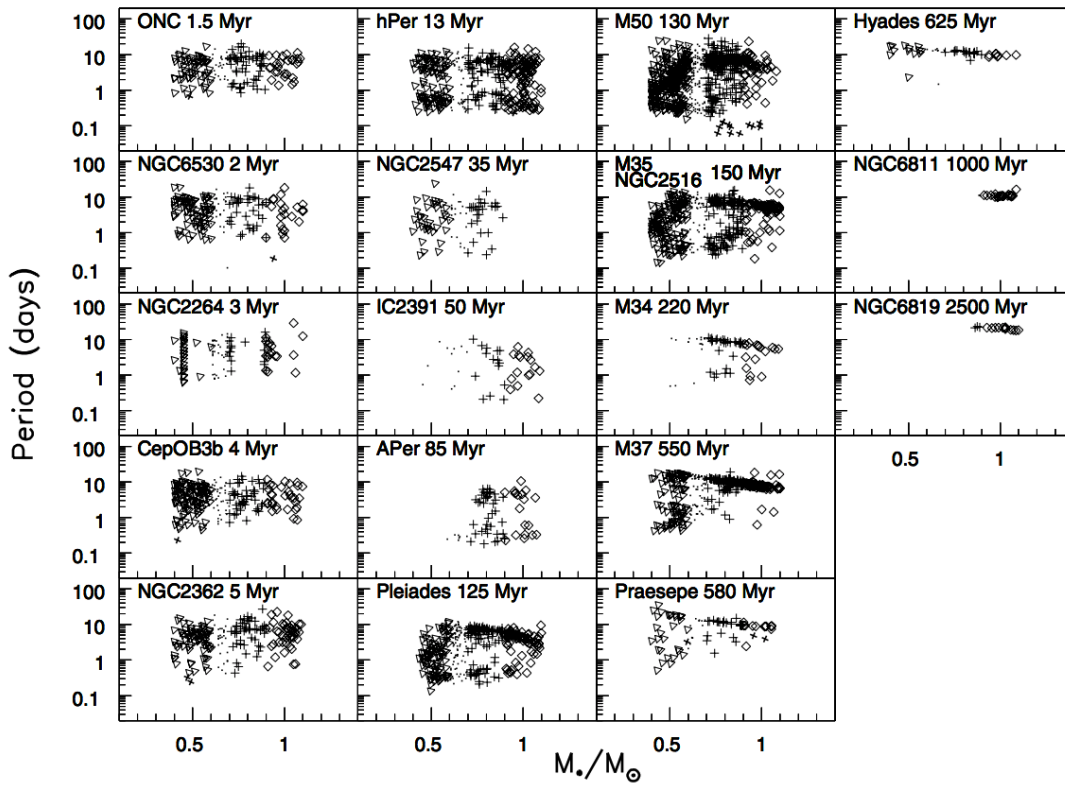


**Figure 1.10:** Rotation periods versus stellar mass for observed star-forming and open clusters, with varying ages. Stars with masses of  $0.4\text{-}0.6$ ,  $0.7\text{-}0.9$ , and  $0.9\text{-}1.1M_{\odot}$  are indicated with triangles, crosses and squares respectively. Initially stars have a broad rotation period distribution across all masses. As time progresses, the rotation periods of stars appear to converge from the higher-masses. Taken from Gallet and Bouvier (2015).

when observed in white-light (Foukal and Lean 1986). So called light-curves, whereby the brightness of a target star is plotted against time, provide information about the star's rotation rate through Fourier-analysis. By passing the light-curve through a periodogram (such as the Lomb-Scargle; Press and Rybicki 1989), the power in different periods can be assessed, and a likely rotation period inferred. Of course this is complicated by surface differential rotation (Reinhold et al. 2013), for example dark and bright features on the Sun appear at different active latitudes (and vary during the solar cycle), thus it is the rotation period of those active latitudes that would be recovered by periodogram analysis (Hempelmann 2003). The evolution of a low-mass star's rotation period is, on average, expected to be much larger than the effect of differential rotation and so this is generally ignored (especially given our imperfect knowledge of magnetic dynamos).

By gathering a large sample of rotation periods, as done by McQuillan et al. (2013) using the Kepler field stars, it is clear that (for low-mass stars) there is structure in the mass-period diagram. This can be further examined by plotting stars with a similar age,

as shown in Figure 1.10 for many different star forming clusters and open clusters (Gallet and Bouvier 2015). Viewed in this way, like snapshots in time, the evolution of a star through this diagram becomes apparent. Initially proto-stars become visible with their accretion disks, here they have a wide range of rotation periods (with perhaps a slight mass-dependence). Their disks exchange angular momentum such that their rotation periods remain roughly constant (Gallet et al. 2019) until the disk is lost, a phase often referred to as disk-locking (Matt and Pudritz 2004). For the next few million years, the proto-stars contract, causing their rotation periods to decrease as the stars spin-up as they leave the PMS. Once stars are on the MS, their rotation periods begin to increase in a mass-dependent way (Matt et al. 2015), such that at late-ages stars have converged onto a tight mass-rotation sequence. The discovery of stellar spin-down on the MS is accredited to Skumanich (1972), who compared the rotation period of the Sun, to stars in the Pleiades, Ursa Major, and Hyades clusters, showing that they appeared to spin-down with the square-root of age (see also Soderblom 1983). Since this discovery, empirical relationships have been derived in order to infer the ages of low-mass stars, given their rotation period and mass (or B-V), a technique called Gyrochronology (Barnes 2003, 2007). As rotation is connection to magnetic activity (Section 1.3.2), a similar technique has been developed using their magnetic properties known as Magnetochronology (Vidotto et al. 2014a).

As the number of rotation period observations has grown (e.g. Agüeros et al. 2011; McQuillan et al. 2013; Núñez et al. 2015; Covey et al. 2016; Rebull et al. 2016; Douglas et al. 2017; Agüeros 2017), models that describe the physical processes of rotation period evolution have become increasingly detailed (e.g. Bouvier et al. 1997; Matt et al. 2015; Sadeghi Ardestani et al. 2017; See et al. 2017b; Garraffo et al. 2018). These models generally evolve the angular momentum equation,

$$\frac{d\Omega_*}{dt} = \frac{\tau}{I_*} - \frac{\Omega_*}{I_*} \frac{dI_*}{dt}, \quad (1.8)$$

where the rotation rate of stars  $\Omega_* = 2\pi/P_{rot}$  evolves due to an applied torque  $\tau$  and changes to the moment of inertia  $I_*$ . There also exist a wide range of models which account for the internal transport of angular momentum within stars themselves (e.g. Kepens et al. 1995; Solanki et al. 1997; Gallet and Bouvier 2013, 2015; Amard et al. 2019). A

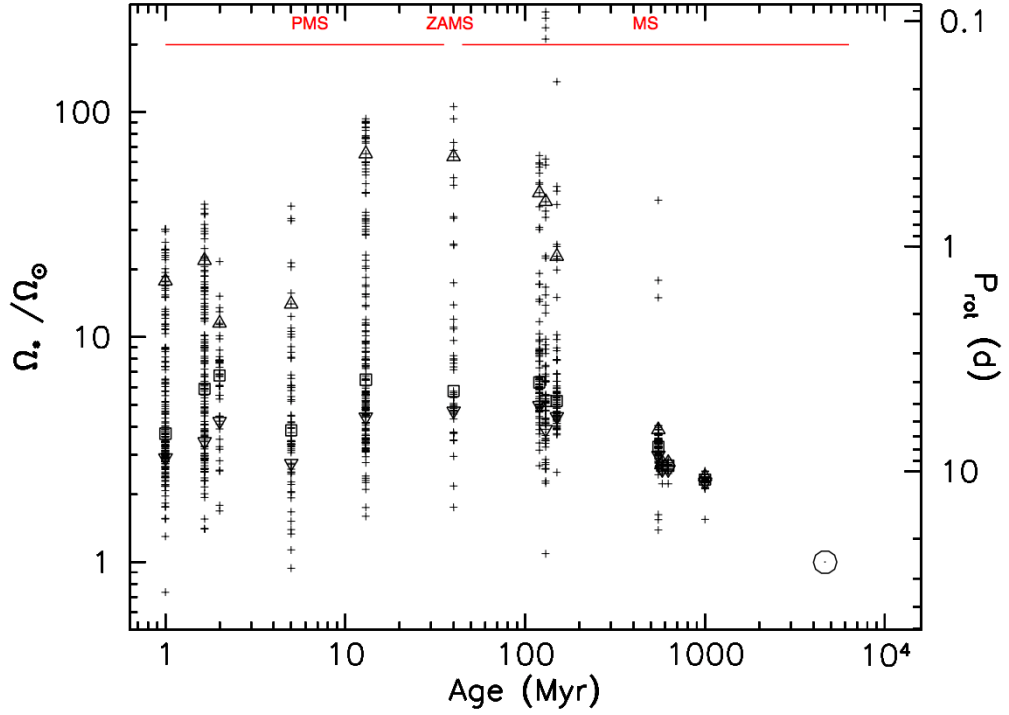


**Figure 1.11:** Rotation period observations for Sun-like stars in clusters with known ages. Triangles (direct and inverted), and squares, indicate the 90th, 25th percentiles and median rotators from each cluster, respectively. Rotation period observations span the Pre Main Sequence (PMS) into the Main Sequence (MS), where a clear structure emerges from the initially broad distribution. The rotation period and age of the Sun are indicated by a large circle. Taken from Gallet and Bouvier (2013).

popular paradigm for this is core-envelope decoupling, in which the convective envelope and radiative core are allowed to rotate at different rates and have a timescale for transporting angular momentum between them. The angular momentum equation can then be written as a set of coupled equations,

$$\frac{d\Omega_{conv}}{dt} = \frac{\tau_{ce}}{I_{conv}} - \frac{2R_{rad}^2}{3I_{conv}}\Omega_{conv}\frac{dM_{rad}}{dt} - \frac{\tau_{wind}}{I_{conv}} - \frac{\Omega_{conv}}{I_{conv}}\frac{dI_{conv}}{dt}, \quad (1.9)$$

$$\frac{d\Omega_{rad}}{dt} = -\frac{\tau_{ce}}{I_{rad}} + \frac{2R_{rad}^2}{3I_{rad}}\Omega_{conv}\frac{dM_{rad}}{dt} - \frac{\Omega_{rad}}{I_{rad}}\frac{dI_{rad}}{dt}, \quad (1.10)$$

where quantities corresponding to the radiative core and convective envelope and denoted with the subscripts “rad” and “conv”, respectively. The rotation-evolution of the envelope is governed the applied torque of the stellar wind  $\tau_{wind}$ , the exchange of angular momentum with the radiative core  $\tau_{ce}$ , plus terms resulting from changes to the size of the envelope/core, and the moment of inertia of the envelope. Similarly, the rotation of the core is controlled by the corresponding exchange of angular momentum from the enve-

loped, and its own structural changes. Importantly, the radiative core does not experience the stellar wind torque directly and acts like a reservoir of angular momentum, coupled by  $\tau_{ce}$ .

It should now be clear that there exists a complex relationship between stellar mass (convection), rotation, and magnetic activity which is fundamentally intertwined with the stellar wind outflow. For the rotation periods of low-mass stars to change drastically during the MS, they must lose angular momentum very efficiently to their stellar wind. Additionally, stars that rotate the fastest should lose angular momentum at a higher rate than the slower rotators, for their rotation periods to converge. Given the relatively weak mass-loss rates of low-mass stars, the stellar magnetic field must play a key role in increasing the efficiency of angular momentum lost through stellar winds on the MS (Weber and Davis 1967; Mestel 1968). This increased efficiency is referred to as magnetic braking, and is the focus of this thesis.

Better observations have also begun to show features of rotation-evolution which have yet to be completely explained, i.e. weakened braking (van-Saders et al. 2016), stalled braking (Curtis et al. 2019), the gap in intermediate rotation periods (Davenport and Covey 2018; Reinhold et al. 2019), and others. In this thesis I focus on Sun-like stars, therefore in Figure 1.11 I show the rotation-evolution of stars from  $0.9 - 1.1 M_{\odot}$  from the clusters in Figure 1.10. The MS is very sparsely sampled, with the Sun used as a constraint within most models (even those attempting to explain the van-Saders et al. 2016 asteroseismic stars), therefore independently evaluating the Sun's angular momentum-loss rate is a valuable test of any theory explaining the rotation-evolution of low-mass stars.

## 1.4 Anatomy of an Astrosphere

In this Section, I briefly describe the general features of the area surrounding a star, where its stellar wind is the dominant form of plasma. Chapter 2 is dedicated to a more in-depth overview of the physical processes and mathematical framework which describes the winds of the Sun and other Sun-like stars.

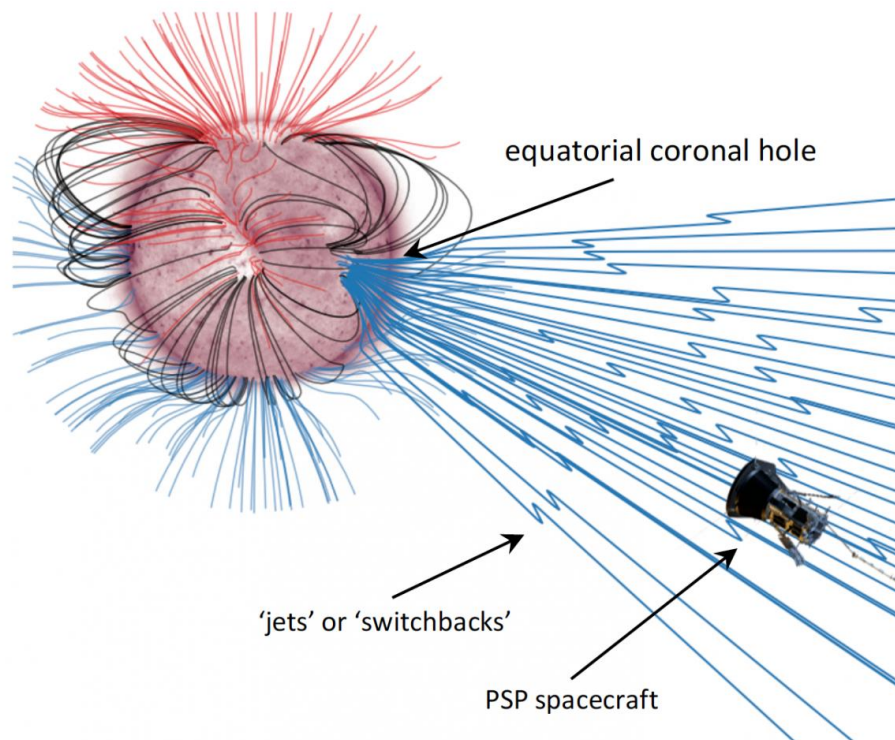


**Figure 1.12:** Schematic of the Sun’s magnetic field, from a Potential Field Source Surface model (see Appendix A), showing the connectivity of the solar wind to the Parker Solar Probe spacecraft during its first close encounter with the Sun. Credit UC Berkeley; spacecraft image courtesy of NASA/Johns Hopkins APL.

### 1.4.1 The Quasi-steady Wind

As with our understanding of stellar magnetism, the winds of other stars are often described by analogy with the solar wind. The solar wind is highly structured and shaped by the Sun’s surface magnetic field, an example of this is shown in Figure 1.12. “Fast” wind emerges from coronal holes, these are regions on the solar surface where the magnetic field has been pushed open by thermal pressure. Coronal holes are often characterised by a lack of emission in Ultraviolet radiation (e.g. Lowder et al. 2014). Fast wind tends to have a speed of around 750km/s and carries with it Alfvénic fluctuations which are evidence of its heating mechanism (Tu 1988; Bavassano et al. 2000). “Slow” solar wind appears above closed magnetic features on the Sun, such as the heliospheric current sheet/streamer belts. The slow wind (speed of 300-400km/s) is observed to be denser and contains stronger magnetic fields than the fast wind (Ebert et al. 2009). There is also evidence that the slow wind sometimes contains Alfvénic fluctuations (often found in very-slow wind) like the fast wind (D’Amicis and Bruno 2015), suggesting a common driving mechanism between



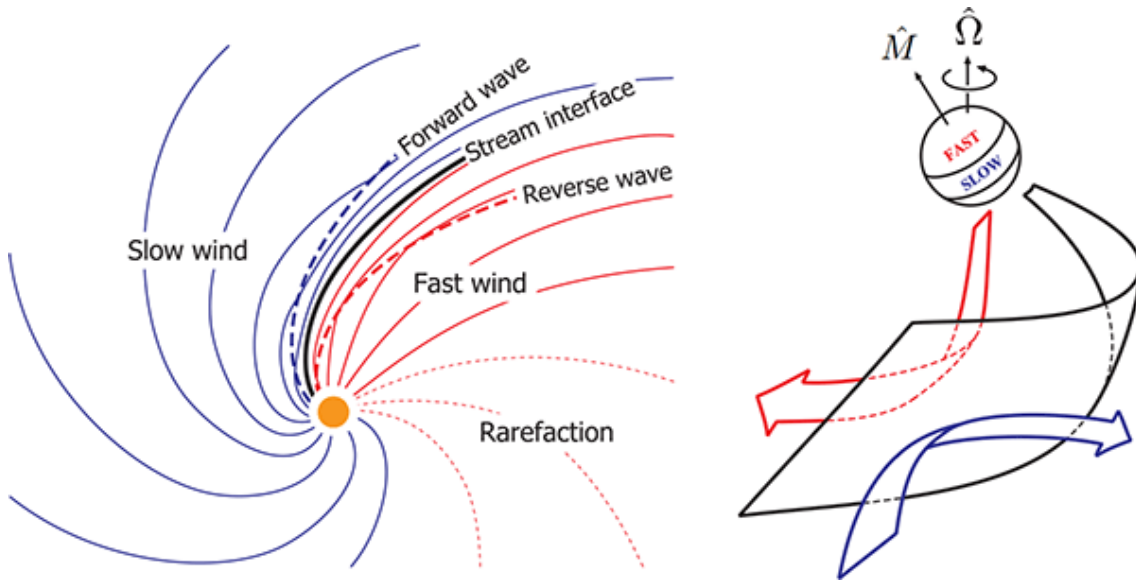


**Figure 1.13:** Schematic depiction of a wind stream interaction. The star’s rotation axis is denoted by  $\hat{\Omega}$ , its magnetic moment is denoted by  $\hat{M}$ . Fast wind is shown in red, slow in blue. Taken from Owens and Forsyth (2013).

the very-slow and fast wind streams (Sanchez-Diaz et al. 2016). Differences between the two likely originate from a larger expansion of the magnetic field (flux tubes) that contains the very-slow wind. The mechanism(s) that produce the slow wind are less understood, ranging from interchange reconnection on the open-closed field boundary to bursty reconnection at the top of closed field loops (Fisk et al. 1998).

Like the solar wind, the wind emerging from a low-mass star’s hot corona will also have a variety of speeds. As the wind travels through interplanetary space, the rotation of the star will cause wind streams with different speeds to collide/interact (see Figure 1.13). This leads to an increased wind density at the interface of different speed streams, with fast wind (typically catching up to slow wind) being deflected away from the interaction. In the solar wind these are referred to as Stream Interaction Regions (SIRs), and have an effect on the magnetic field structure in the solar wind (Jones et al. 1998). Generally, as the large-scale coronal magnetic field doesn’t evolve much during a solar rotation, these features are often found to corotate with the Sun (Gosling and Pizzo 1999). Therefore they form persistent features in the wind that orbiting (exo)planets will periodically experience.

Planets in orbit around low-mass stars experience the plasma environment produced by the stellar wind directly. In the Solar System, all of the planets, from Mercury to

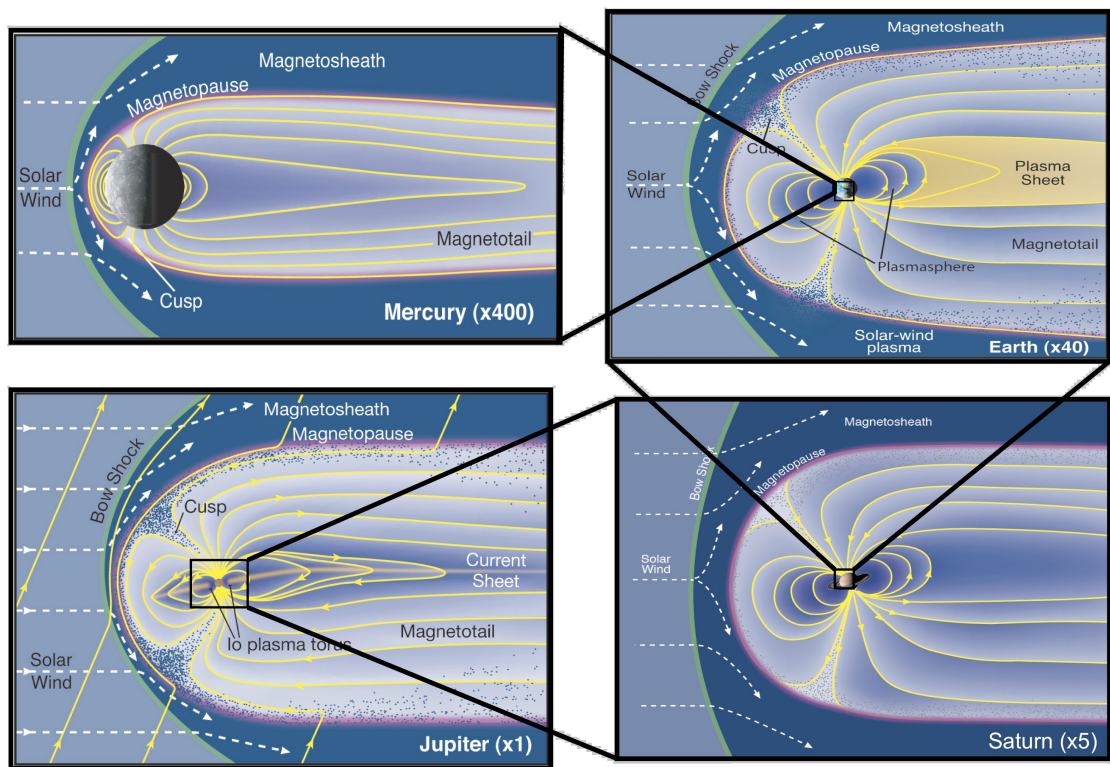


**Figure 1.14:** Variety of magnetospheres found in the Solar System, with their relative sizes indicated. Mercury’s magnetic field likely contains a component induced by the solar wind, and is weak enough to become nearly fully open to the solar wind. The Earth’s magnetosphere is the most studied, and is dominated by the Dungey cycle. Jupiter and Saturn both have magnetospheres which contain plasma from their moons (Io and Enceladus, respectively), this changes the response of their magnetospheric standoff distances to changes in solar wind pressure. Jupiter’s magnetosphere is dominated by the Vasyliunas-cycle, whereas Saturn most-likely has components of both Vasyliunas and Dungey-cycles (Badman and Cowley 2007). Credit: Fran Bagenal and Steve Bartlett.

Neptune, are located in super-Alfvénic wind. This means that any disturbances caused by the planet interacting with the wind cannot be transmitted back to the host star. For planets with no magnetic field (induced or dynamo-driven), the plasma in the wind directly impinges onto the atmosphere (and/or surface) leading to the erosion of atmosphere and any volatile elements (Zendejas et al. 2010). This is likely the reason why Mars has no atmosphere or surface volatiles, despite evidence for liquid water on the surface in the past (Martin-Torres et al. 2015). Most planets in the Solar System however, host large-scale magnetic fields (typically dipolar) which control the plasma environment surrounding them (see Figure 1.14). The physics of their magnetospheres is a subject for another thesis entirely, though they have some common features. The strength of a planet’s magnetic field sets the magnetopause standoff distance, where the magnetic pressure of the magne-

tosphere balances the wind ram pressure. For example, Jupiter has the strongest magnetic field and therefore has a magnetopause distance of around 45 Jupiter radii (Chané et al. 2017), whereas the Earth has a standoff distance of 10 earth radii (McFadden et al. 2006).

The solar wind interacts with the planetary magnetospheres in a number of ways, one of the most significant is through dayside reconnection when the magnetic field in the wind and planetary magnetosphere are oppositely directed (times of negative  $B_z$  for Earth). This strips the magnetic field from the dayside, which is subsequently advected by the solar wind into the nightside magnetotail (Hoshino and Nishida 1983; Borovsky et al. 2008). The release of stored magnetic energy in the magnetotail via further reconnection (known as a substorm), causes magnetotail plasma to flow along magnetic field lines connected to the auroral oval (initiating the aurora). In Earth's magnetosphere the nightside flux is then transported back to the dayside for the process to start again, this is referred to as the Dungey cycle (Dungey 1965). For the giant planets, their rapid rotation rates play a significant role in governing the circulation of magnetospheric plasmas when compared to the Dungey-cycle (e.g. the Vasyliunas-cycle, see Delamere 2015, for a review). Auroral emission is observed from most of the planets in the Solar System (Badman et al. 2015). Along with emission from the auroral oval, the plasma spiralling down the magnetic field lines produces the synchrotron emission of radio waves. Jupiter's magnetosphere, when viewed in radio, is one of the largest objects in the night's sky (De Pater 1990). The detection of auroral radio emission from exoplanets would provide a valuable diagnostic of their stellar wind environment, given that the auroral power scales as the stellar wind power incident on the magnetosphere (Zarka 2007). However as of yet, there have been no detections, which may be linked to the radio photosphere of the stellar wind plasma obscuring the radio emission (Kavanagh et al. 2019; Vidotto et al. 2019). More promisingly, the magnetospheres of transiting exoplanets have been shown to function as "wind-ometers" to measure the properties of stellar winds around other stars (Vidotto and Bourrier 2017).

For exoplanets that are close enough to their host star to experience sub-Alfvénic wind, there exist a wide range of Star-Planet Interactions (SPIs) that could feasibly occur. Information from the interaction of the planet with the stellar wind can now be transmitted

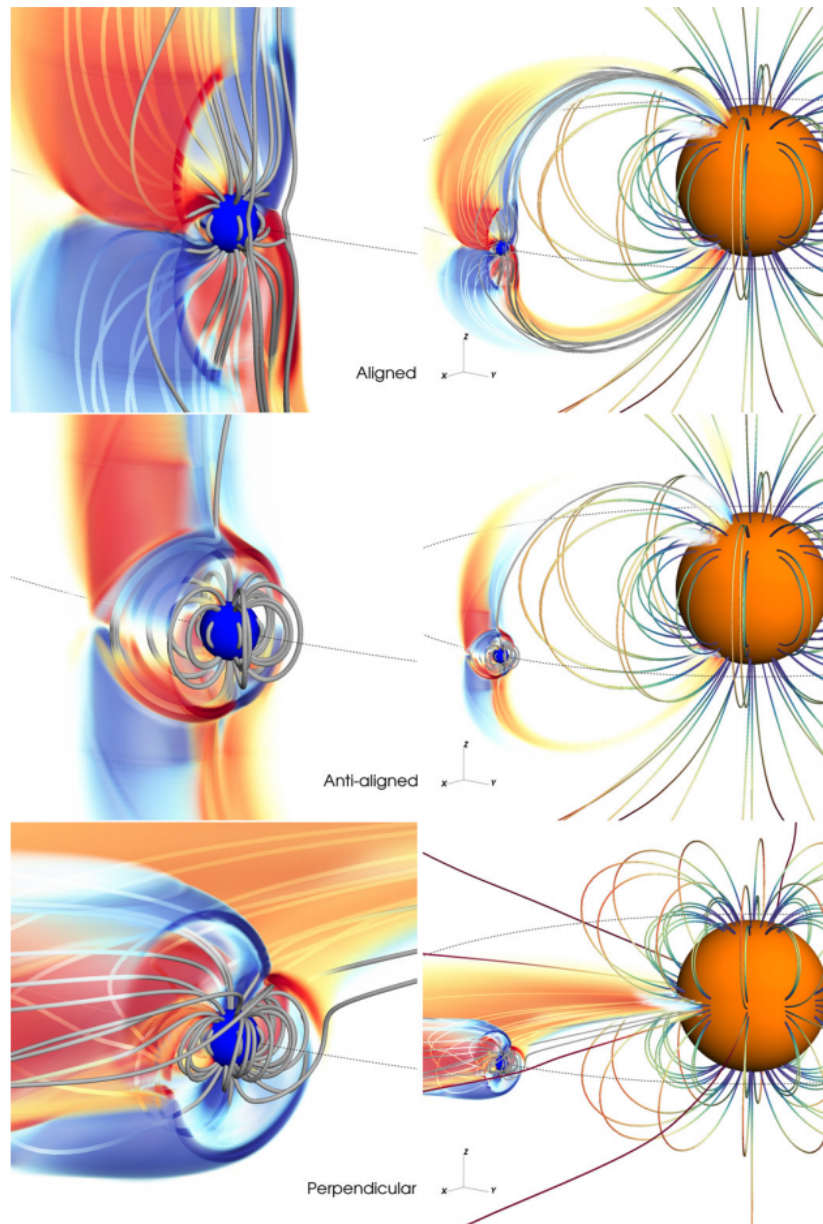


**Figure 1.15:** Examples of Star-Planet Interactions (SPI) from numerical simulations. Top has the magnetic field of the star and planet aligned such that the field lines from each hemisphere can connect. The middle scenario has anti-aligned field between the star and planet, thus the interaction is limited. The bottom scenario shows a more complicated quadrupolar stellar magnetic field, which is perpendicular to the planet’s magnetic field in the equator. Taken from Strugarek et al. (2015).

back to the surface of the star by MHD waves, which for example, could lead to induced features on the surface (e.g. Shkolnik et al. 2003). A few different SPIs from Strugarek et al. (2015) are shown in Figure 1.15. The star and planet can now interact through magnetic torques, which may cause the planet to migrate towards or away from the star (Strugarek et al. 2014b). The degree to which SPIs are important varies with the topology of the stellar magnetic field, planetary magnetic field, and orbital parameters.

### 1.4.2 Transient Mass Ejections

Along with the quasi-steady wind, there exist transient features that appear stochastically in stellar winds. The most iconic are Coronal Mass Ejections (CMEs), an example is shown on the left of Figure 1.16 for the Sun. CMEs occur when massive amounts of magnetic energy are released in the solar atmosphere, they are sometimes accompanied by flaring (Zhang et al. 2001). The build-up of magnetic energy is usually facilitated by an active region, whose large kG field strengths and magnetic foot point twisting-motions produce non-potential structures in the solar atmosphere (Georgoulis et al. 2019). Stellar CMEs are largely unconstrained (Crosley and Osten 2018) unlike stellar flares, which have been extensively studied due to the data produced by the Kepler and Transiting Exoplanet Survey Satellite (TESS) missions (Davenport 2016). Stellar CMEs have been numerically simulated in order to understand their behaviour for more active stars than the Sun. Simply assuming a correlation of CME energy with flare energy (as often shown for Sun) leads to unbounded CME energies which are likely unphysical. In reality, it is likely that strong overlying large-scale magnetic fields suppress the eruption of such CMEs (e.g. Alvarado-Gómez et al. 2018).

For the Sun, the number of CMEs, or Interplanetary CMEs (ICMEs) when detected by in-situ spacecraft, varies through the solar cycle. During times of high solar activity CMEs occur around five times a day, whilst during solar minima CMEs occur on average once every few days (Webb et al. 2017). CMEs are observed to have a three-part structure, 1) a bright shock front, 2) a dark cavity, and 3) a bright core, which expands with distance from the Sun (see left of Figure 1.16). As the CME travels through interplanetary space, it disturbs the background wind creating a shock front and turbulent boundary layer around itself (see right of Figure 1.16). Within the ICME there is often a structured flux rope, which is observed as a clear rotation of the magnetic field vector by in-situ measurements (Cane and Richardson 2003). The flux rope is likely a remnant from the original CME structure, which are often highly twisted flux ropes in the corona (Amari et al. 1999). ICMEs (along with SIRs) are a large driver of space weather on Earth (Schwenn 2006), causing changes to the ionosphere (i.e. reduced radio propagation, and scintillation), damaging spacecraft (i.e. spacecraft charging, increasing atmospheric drag, etc), and inducing currents along

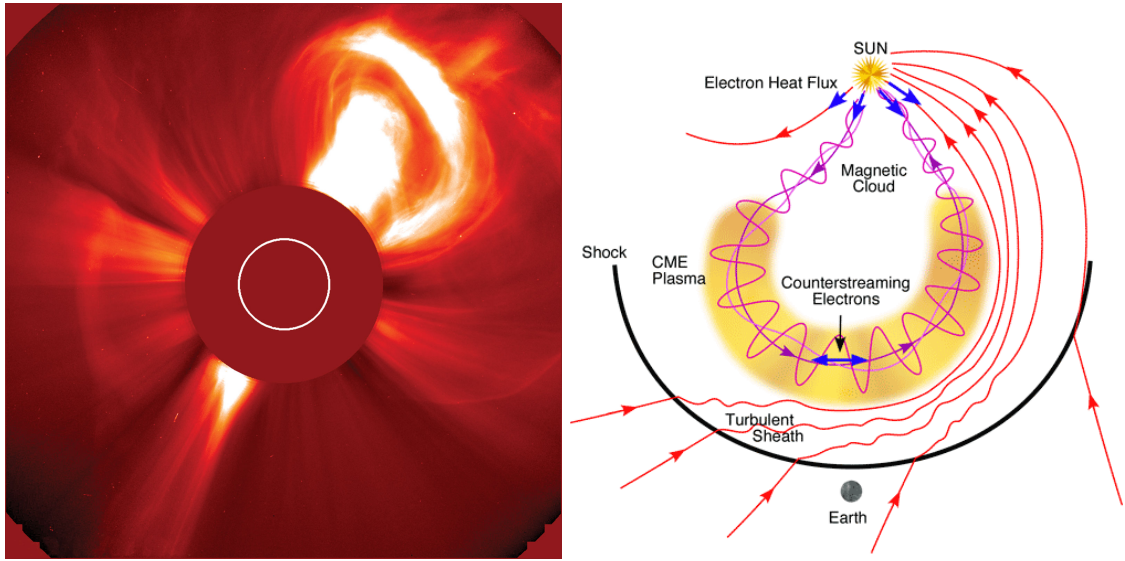


**Figure 1.16:** Left: Scatter light image of a Coronal Mass Ejection (CME). Right: Schematic depiction of the main features of an Interplanetary CME (ICME). Image from the Large Angle and Spectrometric Coronagraph (LASCO) onboard the Solar and Heliospheric Observatory (SOHO), and schematic taken from Zurbuchen and Richardson (2006).

man-made structures on the ground (i.e. cables and pipes) (see review of Pulkkinen 2007). For more active stars, CMEs are also likely to contribute to atmospheric erosion, and so are also important in constraining exoplanet habitability (Khodachenko et al. 2007).

A transient feature that has gained more interest recently, is that of “slingshot” prominences. Prominence on the Sun are observed as absorption features as they transit the solar disk (also known as filaments), then in emission once they move past the limb of the Sun. Solar prominences contain cool, dense material which is supported by magnetic pressure (Xia and Keppens 2016), which typically either drain back down to the photosphere or erupt off the Sun as CMEs (Parenti 2014). Slingshot prominences on the other hand, are typically detected in rapidly rotating stars (Collier Cameron and Robinson 1989a, 1989b), for which plasma has accumulated at the top of closed field loops with large radial extent. These prominences are supported against the centrifugal force by magnetic forces, and are mass-loaded by the stellar wind (e.g. Stauffer et al. 2017). These prominences are observed as an absorption feature as they transit the stellar disk (Collier Cameron 1999), and are ejected when the mass of the prominence surpasses the amount which can be sustained in equilibrium (Jardine et al. 2001; Villarreal D’Angelo et al. 2018). For low-mass stars, these prominences are fed by a supersonic wind, such that the stellar surface does not respond to the growing mass of the prominence at the

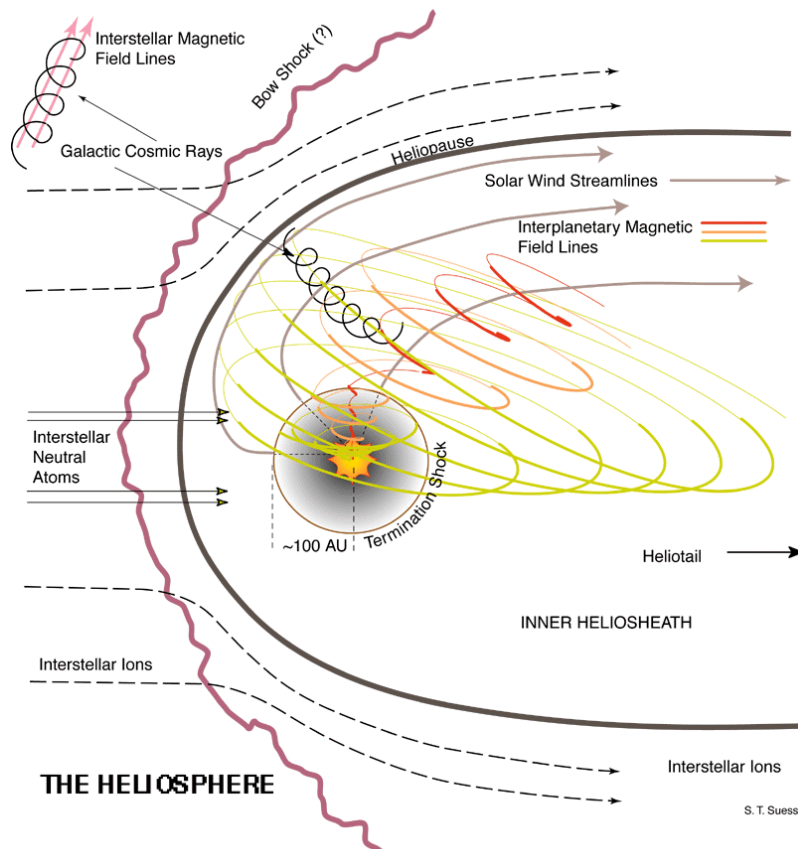


**Figure 1.17:** Diagram of the heliosphere, showing the termination shock, heliosheath, and heliopause. The material in the heliosphere presents a barrier for cosmic ray particles and interstellar material. Credit: Jet Propulsion Laboratory, Steven T. Suess.

top of the closed loop. This mass is ejected, and the process begins again with a repeating timescale that can be calculated from observations. Once the maximum supported mass of a loop is calculated, the ejection timescale can be used to produce an estimate of the mass-loss rate for the underlying stellar wind (Jardine and Collier Cameron 2019). Therefore, slingshot prominences provide a valuable measurement of the mass-loss rates from magnetically-active, rapidly rotating low-mass stars. Further work has shown that the properties of these prominences change during the lifetime of a low-mass star, with median to fast rotators predicted to host slingshot prominences for a considerable part of their lives (Villarreal D'Angelo et al. 2019).

### 1.4.3 Encounter with the Interstellar Medium

Stellar winds ultimately travel away from their host star and encounter the Interstellar Medium (ISM). Much like the planetary magnetospheres previously discussed, the ram pressure of the wind and that of the ISM govern the size of this “astrosphere” (the region of influence of stellar wind plasma). For the Sun, the edge of the heliosphere (in the Sun’s relative direction of motion with the ISM) was found to be around 100au by both Voyager spacecraft (Stone et al. 2008). As the Sun is moving with respect to the ISM, the heliosphere is not spherical and instead has a tail-like structure in its wake (see Figure 1.17). Given the scale of the heliosphere, and the tenuous nature of solar wind plasma, little is known about it. The termination shock, the point where the solar wind become subsonic due to its interaction with the ISM was crossed by Voyager 1 in 2004 and Voyager 2 in 2007. The two spacecraft crossed this shock at different distances from the Sun, indicating that the heliosphere may be irregular in shape (Stone et al. 2008), or is strongly time varying (Washimi et al. 2017). Beyond the termination shock lies the heliosheath which is a layer of compressed and turbulent plasma. Voyager 1 detected a region within the heliosheath where the solar wind speed slowed to near-zero, at which point an increased number of high-energy particles from outside the heliosphere began to be detected (Burlaga and Ness 2012). The heliopause, the location where both solar wind and ISM pressures are equal was crossed by Voyager 1 in August 2012. Voyager 1 then sampled the ISM magnetic field for the first time in human history, with data suggesting the local galactic magnetic field is aligned with the Sun’s magnetic field (Burlaga and Ness 2014).

Like the Sun, the stellar winds of other stars carve out their own regions of the ISM (see review by Wood 2004). Interestingly, neutral Hydrogen from the ISM was first thought to pass through the heliosphere/astrosphere unaffected by its structure, as collisional interactions for neutrals are much smaller than for charged plasma. However it was subsequently realised that neutrals could be important due to charge exchange interactions (Holzer 1972; Wallis 1975), which was further supported by detections of Ly $\alpha$  emission from neutral Hydrogen surrounding the heliosphere and other astrospheres. The detection of this “Hydrogen wall” has allowed for a hand-full of close low-mass stars, to have their mass-loss rates constrained based on the expected neutral Hydrogen abun-



dances from hydrodynamic models (Wood et al. [2002](#), [2005](#)). This is further discussed in Section [4.4.2](#).

## Chapter 2

# Stellar Wind Physics and Modelling

This Chapter contains information and relevant equations pertinent to the future Chapters of the thesis. Similar material is presented in the introductions of the published papers throughout this thesis.

### 2.1 The Physics of Plasmas

A *plasma* is generally defined as being a quasi-neutral gas of charged particles (which can also include neutrals), that exhibit a collective behaviour. Collective behaviour is described as when the motion of particles in the gas are not only dependent on the local collisions, but are also influenced by changes to the gas in remote regions, i.e. charged particles in the plasma produce electric fields and currents which affect the motions of other charged particles at distance. This collective behaviour leads to some interesting properties, such as the plasma frequency and the Debye length.

Consider a quasi-neutral plasma of electrons and ions, upon a small displacement  $\delta x$  of a “slab” of electrons the electric field ( $E = -4\pi n_e e \delta x$ ) created (considering the charge density which develops on the leading face of the slab) acts as a restoring force on the electrons,

$$m_e \frac{d^2 \delta x}{dt^2} = eE = -4\pi n_e e^2 \delta x. \quad (2.1)$$

This causes the electrons to oscillate with the frequency,

$$\omega_p^2 = \frac{4\pi n_e e^2}{m_e}, \quad (2.2)$$

where  $n_e$  is the electron number density,  $e$  is the charge of an electron, and  $m_e$  is the mass of an electron. Note these oscillations have a group velocity of zero, and so do not transport energy or information around the plasma. Equally the ions also have an associated plasma frequency, though this is usually at a much lower frequency than the electrons, and so is less important. A useful relationship for the plasma frequency is,

$$f_p = 9 \times 10^3 \text{Hz} \sqrt{n_e [\text{cm}^{-3}]}, \quad (2.3)$$

so for example, the solar wind with  $n_e = 10^2 \text{cm}^{-3}$  has an electron plasma frequency of  $9 \times 10^4 \text{Hz}$ .

Now consider applying an electric field  $E$  to the same quasi-neutral plasma. In this case, the charged particles in the plasma move in such a way as to “shield” the rest of the plasma from the applied field. This shielding is dielectric in nature, i.e. the plasma become polarised such that the redistribution of charges prevents the applied electric field from penetrating further into the plasma. The length-scale for this effect is called the Debye length (and the overall effect is often referred to as Debye screening), which is given by,

$$\lambda_D = \sqrt{\frac{k_B T_e}{4\pi n_e e^2}}, \quad (2.4)$$

where  $k_B$  is the Boltzmann constant, and  $T_e$  is the temperature of the electrons. Debye screening will only occur if the number of charged particles within a Debye length is significant i.e.

$$N_D = n_e \frac{4}{3} \pi \lambda_D^3 \gg 1, \quad (2.5)$$

where  $N_D$  is the average number of electrons in a Debye length of one another in the plasma.

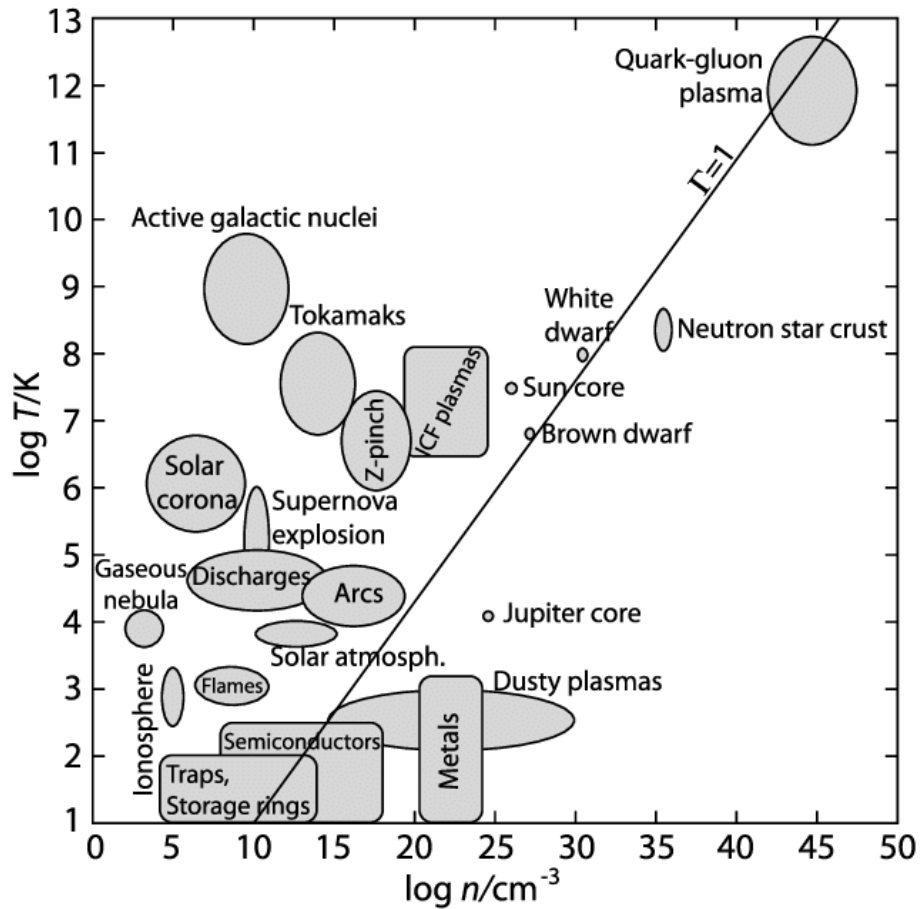


**Figure 2.1:** A variety of plasmas depicted in the temperature  $\log(T)$  - number density  $\log(n)$  plane. Hot, low density plasmas are generally termed collisionless, as electromagnetic forces are primarily responsible for the interactions of individual charged particles, this is the case for the solar corona.  $\Gamma$  is the ratio of the mean potential energy per particle to the mean kinetic energy per particle. This ratio measures the degree to which many-body interactions affect the particle dynamics. When  $\Gamma \ll 1$  (left of  $\Gamma = 1$  line), the system is weakly coupled. When  $\Gamma \gg 1$  (right of line), the interactions between particles strongly influence the particle dynamics and so the system is strongly coupled. Credit: Donkó, Hartmann, and Kalman.

Therefore for an ionised gas to be truly considered a plasma, it must satisfy; 1) quasi-neutrality, by having a Debye length much smaller than the size of the system  $\lambda_D \ll L$ , 2) collective behaviour, by having a high enough density of charged particles to allow for Debye screening to occur, and in general 3) the motions of particles in the gas are primarily influenced by electromagnetic forces. The varying degree to which collisions are important within the plasma gives rise to two main types, non-collisional and collisional. In the collisional case, the particles in the plasma collide regularly enough to achieve a thermodynamic equilibrium, which is not typically the case in a non-collisional plasma. The plasma in the solar corona is generally “collisionless” due to its high temperature and low density. One way to quantify the degree of collisionality in a plasma is through the

ratio of the plasma frequency to the collision frequency  $\nu$ ,

$$\frac{\omega_p}{\nu} \propto \sqrt{\frac{T^3}{n}}, \quad (2.6)$$

which is related to the plasma temperature  $T$  and density  $n$ . Therefore, colder and denser plasmas are more likely to be collisional e.g. neutron star atmospheres. Figure 2.1 shows the broad range of plasmas that are often studied in the temperature-density plane. It should be noted that the different plasmas in the Sun, from the Sun's core to its atmosphere and corona, span a wide range in this parameter space and so they require different approximations to model.

Taking a closer look at individual charged particles in the plasma, other than collisions with other particles, their motions are governed by the Lorentz force,

$$F = q \left( \mathbf{E} + \frac{\mathbf{v}}{c} \times \mathbf{B} \right), \quad (2.7)$$

where the particle's charge is  $q$ , and velocity is  $\mathbf{v}$ . The background electromagnetic field is characterised by the electric field  $\mathbf{E}$  and magnetic field  $\mathbf{B}$ . The effect of an applied electric field has already been discussed, let's instead consider applying a magnetic field  $\mathbf{B}$  perpendicular to the initial direction of particle motion. It can be shown that by solving the equation of motion including the Lorentz force, charged particles in this uniform magnetic field perform a gyration motion (in the plane perpendicular to  $\mathbf{B}$ ) with a constant speed  $v_{\perp}$ . The radius of the circle traversed by this motion is given by,

$$r_B = \frac{m v_{\perp}}{q B}, \quad (2.8)$$

with a gyro-frequency of,

$$\omega_{gyro} = \frac{v_{\perp}}{r_B} = \frac{q B}{m c}. \quad (2.9)$$

This motion is displayed in Figure 2.2 (top row). Given the form of the Lorentz force, different charged particles gyrate in opposite directions. It can also be quickly deduced that

the ion gyro-radius is much larger than the electron gyro-radius, for a given  $v_{\perp}$ . The centre of gyration is generally referred to as the guiding centre, as the motion of charged particles subject to electromagnetic fields can be described by a superposition of the gyro-motion and a drift motion due to additional forces. The simplest example of this is the famous  $\mathbf{E} \times \mathbf{B}$  drift. For the same gyro-motion, when an electric field is applied perpendicular to the magnetic field, the particles have to work against an additional force during their orbit around the guiding centre which changes  $v_{\perp}$  during the orbit. The effect this has on the shape of the gyration is shown in the second row of Figure 2.2, and more generally for an applied force  $\mathbf{F}$  in the third row. The speed at which the guiding centres of the particles drift is given by,

$$\mathbf{v}_{\text{drift}} = \frac{\mathbf{F} \times \mathbf{B}}{qB^2}, \quad (2.10)$$

which for  $\mathbf{E} \times \mathbf{B}$  drift becomes,

$$\mathbf{v}_{\mathbf{E} \times \mathbf{B}} = \frac{\mathbf{E} \times \mathbf{B}}{B^2}. \quad (2.11)$$

It is important to note that in the case of  $\mathbf{E} \times \mathbf{B}$  drift, differently charged particles drift in the same direction and at the same speed  $\mathbf{v}_{\mathbf{E} \times \mathbf{B}}$ , such that charge neutrality is maintained and no currents are established. In the case of an applied force, like the gradients in (or curvature of) the magnetic field, the drift velocities are opposite for different charges and so act to create currents (one example is the ring current in the Earth's magnetosphere).

The Earth's magnetosphere is an illustrative example of some of the general motions that charged particles can undertake (see Figure 2.3). Consider plasma trapped along closed dipolar magnetic field lines, then there are three principle motions that describe how these particles move. Firstly the gyro-motion around the guiding centre magnetic field, secondly the particle drifts due to the gradient and curvature of the magnetic field, and thirdly bounce motion which is described as follows. For a particle gyrating around its guiding centre, it can have a component of its velocity parallel to the magnetic field. In the case of a uniform magnetic field this component  $v_{\parallel}$  is unperturbed, however particles travelling along closed magnetic field lines experience the magnetic field strength increasing as they travel towards one of the field foot points. The magnetic moment (first

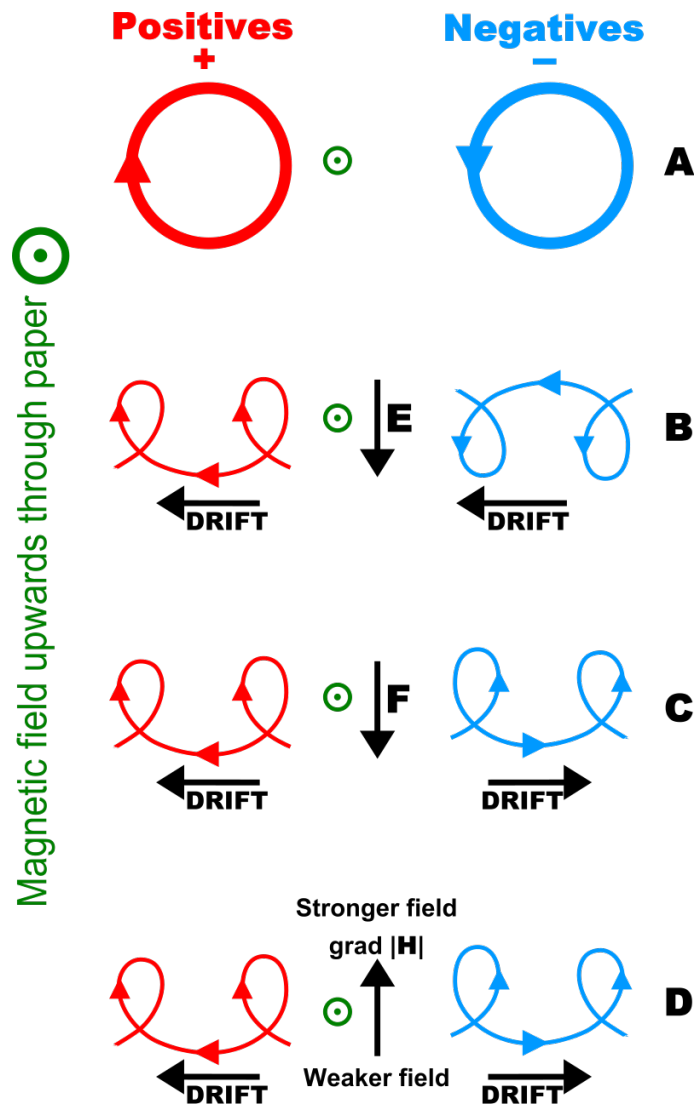


**Figure 2.2:** The motion of positive and negative charged particles in a magnetic field. A: motion of particles in a uniform perpendicular magnetic field. B: gyro-motion from A, with the addition of an electric field. C: a general force  $F$  in place of the electric field from B. D: the force  $F$  is due to the gradient of the magnetic field ( $H$ ). Figure based on Hannes Alfvén's, *Cosmical Electrodynamics* (1950); Redesigned by Ian Tresman.

adiabatic invariant) of the gyrating particle must be conserved i.e.,

$$\mu = \frac{1}{2} \frac{mv_{\perp}^2}{B}, \quad (2.12)$$

and so as the field strength  $B$  increases, the particle's perpendicular speed  $v_{\perp}$  must also increase (for  $\mu$  to be a constant). For the particle to conserve kinetic energy, the parallel motion  $v_{\parallel}$  must decrease to compensate for the increase in  $v_{\perp}$ , until the parallel velocity is zero. From here a small kick in  $v_{\parallel}$  in the opposite direction (from an atmospheric collision,

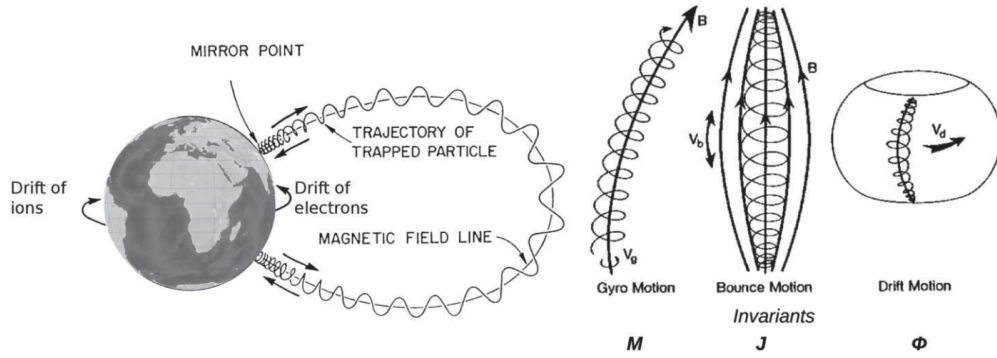


**Figure 2.3:** Overview of particle motions in the Earth's inner magnetosphere. Particles gyrate around magnetic field lines, undertake bounce motion between mirroring points, and drift around in opposing directions (given their charge) causing the ring current. Taken from Regi (2016).

etc) will cause the inverse process to occur, with the particle accelerating back along the magnetic field line. The particles therefore “bounce” between mirroring points (locations of speed reversal), with closed magnetic field lines acting like magnetic bottles. Of these three motions, gyration is the highest frequency (fraction of a milli second), followed by bounce-motion ( $\sim$ second), and then drift-motion (10-20 minutes, to go around the Earth).

Now examining the plasma as a whole, it is a very good electrical conductor given that it consists of many charged particles with a low-frequency of collisions. To understand the importance of this, let's consider how the motions of the plasma influence the electromagnetic fields. From Ohm's law, the current density is given by,

$$\mathbf{j} = \sigma \left( \mathbf{E} + \frac{\mathbf{v} \times \mathbf{B}}{c} \right), \quad (2.13)$$

where  $\sigma$  is the conductivity of the plasma. This can be rearranged and substituted into Faraday's law,

$$\frac{\partial \mathbf{B}}{\partial t} = -c \nabla \times \mathbf{E}, \quad (2.14)$$

$$\frac{\partial \mathbf{B}}{\partial t} = -c \nabla \times \left( -\frac{\mathbf{v} \times \mathbf{B}}{c} + \frac{\mathbf{j}}{\sigma} \right), \quad (2.15)$$

which after using Ampère's law,

$$\mathbf{j} = \frac{c}{4\pi} \nabla \times \mathbf{B}, \quad (2.16)$$



and the zero divergence of the magnetic field,

$$\nabla \cdot \mathbf{B} = 0, \quad (2.17)$$

produces the induction equation,

$$\frac{\partial \mathbf{B}}{\partial t} = \nabla \times (\mathbf{v} \times \mathbf{B}) + \frac{c^2}{4\pi\sigma} \nabla^2 \mathbf{B}, \quad (2.18)$$

where  $\mu = c^2/4\pi\sigma$  is the magnetic diffusivity of the plasma. This equation describes how the bulk motion of the plasma  $\mathbf{v}$  can generate magnetic field in opposition to its diffusion (previously discussed in Section 1.3.2). As the plasma in the solar (or stellar) wind is classically regarded as collisionless, its electrical conductivity can be treated as being infinite (or the diffusivity equal to zero). This is often quantified using the magnetic Reynolds number  $R_m = UL/\mu$  (characteristic length  $L$  and velocity  $U$ ), for which the advection of the magnetic field dominates its diffusion when  $R_m \gg 1$ . In this case, the induction equation simplifies to the idealised form,

$$\frac{\partial \mathbf{B}}{\partial t} = \nabla \times (\mathbf{v} \times \mathbf{B}), \quad (2.19)$$

which has interesting implications for how the plasma behaves. Consider the magnetic flux  $\Phi$  threading a closed surface  $S(t)$  which is being advected by the fluid (this thought experiment is referred to as Alfvén's frozen-flux theorem). The evolution of  $\Phi$  is described by changes to  $\mathbf{B}$  at  $S(t)$  and the divergence of flux through the surface swept out by the movement of  $S$  in time (Clarke et al. 2007),

$$\frac{d\Phi}{dt} = \int_{S(t)} \frac{\partial \mathbf{B}}{\partial t} \cdot d\mathbf{S} - \int_C (\mathbf{v} \times \mathbf{B}) \cdot d\mathbf{l}, \quad (2.20)$$

where  $C$  is a contour enclosing  $S(t)$ . Using Stokes' theorem this is equivalent to,

$$\frac{d\Phi}{dt} = \int_{S(t)} \left[ \frac{\partial \mathbf{B}}{\partial t} - \nabla \times (\mathbf{v} \times \mathbf{B}) \right] \cdot d\mathbf{S}. \quad (2.21)$$

The integrand of this equation can be replaced using the induction equation to show that,

$$\frac{d\Phi}{dt} = \int_{S(t)} \mu \nabla^2 \mathbf{B} \cdot d\mathbf{S}, \quad (2.22)$$

i.e., the magnetic flux enclosed by a co-moving surface only changes as a result of the diffusion term in the induction equation. Therefore in the idealised case of infinite conductivity,

$$\frac{d\Phi}{dt} = 0, \quad (2.23)$$

which implies that the plasma and magnetic field move together, or that the charged particles in the plasma are fixed to the magnetic field line that they gyrate around. The magnetic field is said to be “frozen-in” into the plasma. This is typically the case for most space plasmas, from the Earth’s magnetosphere to the solar/stellar wind. However diffusion is still important in governing fundamental processes like reconnection, ohmic heating, and mixing of different plasmas. To investigate this, let’s consider the electron momentum equation (in the absence of gravity),

$$\rho_e \frac{\partial \mathbf{v}_e}{\partial t} + \rho_e (\mathbf{v} \cdot \nabla) \mathbf{v}_e = -en_e \left( \mathbf{E} + \frac{\mathbf{v}_e \times \mathbf{B}}{c} \right) - \nabla \cdot \mathbf{p}_e + \mathbf{P}_{ie}, \quad (2.24)$$

where the motions of the electrons  $\mathbf{v}_e$  in a plasma are described in the form of the Navier-Stokes fluid equation.  $\mathbf{p}_e$  is the electron pressure tensor, and  $\mathbf{P}_{ie}$  represents the momentum exchanged between ions and electrons in the form of collisions. From this the generalised Ohm’s law can be derived,

$$\mathbf{E} + \frac{\mathbf{v} \times \mathbf{B}}{c} = \mu \mathbf{j} + \frac{\mathbf{j} \times \mathbf{B}}{en_e c} - \frac{\nabla \cdot \mathbf{p}_e}{n_e e c} + \frac{m_e}{n_e e^2} \frac{d\mathbf{j}}{dt}, \quad (2.25)$$

from which ignoring the last three terms on the right hand side returns us to the classical Ohm’s law of equation (2.13). Further to this, assuming infinite conductivity ( $\mu = 0$ ) takes us back to the idealised Ohm’s law. From left to right the additional three terms are, the Hall effect, the electron pressure, and the electron inertia. So the frozen-in condition can be broken by finite  $\mu$  (ohmic dissipation/Joule heating), the decoupling of the electrons

and ions (Hall), divergence in the electron pressure (ambipolar diffusion), and changes to the electron inertia ( $d\mathbf{v}_e/dt$ ). The Hall effect is specifically quite interesting, where (in the absence of diffusivity  $\mu$ ) the magnetic field becomes frozen-in to the electrons rather than the bulk plasma, leading to the creation of dispersive whistler waves which are observed in many space plasma environments, from the Earth's magnetosphere to the solar corona. These terms introduce physics at very small scales, for example the Hall and electron pressure terms become important at the ion inertial length,

$$d_i = \frac{c}{\omega_{pi}} = \sqrt{\frac{c^2 m_i}{4\pi n_i q^2}}, \quad (2.26)$$

and the electron inertia enters at the electron inertial length,

$$d_e = \frac{c}{\omega_p} = \sqrt{\frac{c^2 m_e}{4\pi n_e e^2}}, \quad (2.27)$$

where by inertial length, I mean the characteristic length scale for ions and electrons to be affected by electromagnetic forces. Typically the ion inertial length is much larger than the electrons, some examples include; the solar corona ( $d_i \approx 7\text{m}$ ;  $d_e \approx 20\text{cm}$ ), and the solar wind at 1au ( $d_i \approx 70\text{km}$ ;  $d_e \approx 2\text{km}$ ). Given these scales are relatively short in comparison with the large-scale dynamics of stellar wind physics, they are set aside throughout this thesis.

## 2.2 Ideal Magnetohydrodynamic Equations

Here I describe the generalised set of equations that govern a single-fluid MHD plasma at a macroscopic level (further details can be found in Clarke et al. 2007; Priest 2014; Goedbloed et al. 2019). To arrive at these equations a few assumptions are required, most notably the simplification of charged particle motions into a macroscopic fluid description, i.e. that the local thermodynamic properties of the plasma can be meaningfully defined. These equations account for fluid motions that have length and temporal scales much larger than the gyro/kinetic plasma scales, and so by construction do not recover oscillations in

the plasma at high frequencies (like the plasma frequency). The number density  $n$  is said to be of equal parts, positive and negative charges (satisfying charge neutrality), such that for a fully-ionised Hydrogen plasma the conditions,

$$n \approx n_e + n_p = 2n_e, \quad (2.28)$$

$$n_p - n_e \ll n, \quad (2.29)$$

describe the plasma everywhere. There are said to be no charge imbalances  $\rho^* = (n_p - n_e)e$  in the plasma, therefore the electric field  $\mathbf{E}$  has zero divergence as given by,

$$\nabla \cdot \mathbf{E} = 4\pi\rho^* = 0. \quad (2.30)$$

The mass density of this overall neutrally-charged plasma is given by  $\rho = nm$ , where  $m$  is the average particle mass, which is  $0.5m_p$  for the fully-ionised hydrogen plasma. The conservation of the mass density is maintained by,

$$\frac{\partial \rho}{\partial t} + \nabla \cdot (\rho \mathbf{v}) = 0, \quad (2.31)$$

where  $\mathbf{v}$  is the bulk fluid velocity. Ohm's law describes the current density  $\mathbf{j}$  in the plasma due to the total electric field (in a frame of reference with the plasma), which as previously stated, in the ideal case provides a relation between the electric field  $\mathbf{E}$  and the magnetic field  $\mathbf{B}$ ,

$$\mathbf{E} = -\frac{\mathbf{v} \times \mathbf{B}}{c}. \quad (2.32)$$

The evolution of the magnetic field is given by the idealised induction equation,

$$\frac{\partial \mathbf{B}}{\partial t} = \nabla \times (\mathbf{v} \times \mathbf{B}), \quad (2.33)$$

which must also maintain zero divergence,

$$\nabla \cdot \mathbf{B} = 0. \quad (2.34)$$

The gas pressure  $p$  is given by the equation of state, which is often taken as the ideal gas law,

$$p = \frac{k_B}{m} \rho T. \quad (2.35)$$

For an adiabatic process, pressure and density are connected by,

$$p \propto \rho^\gamma, \quad (2.36)$$

where  $\gamma$  is the ratio of specific heats and has a value of  $5/3$  for a monoatomic ideal gas. The Lagrangian form of the energy equation is then given by,

$$\frac{p^\gamma}{\gamma - 1} \frac{d}{dt} \left( \frac{p}{\rho^\gamma} \right) = -\mathcal{L}, \quad (2.37)$$

which utilises the conservation of entropy ( $S = p/\rho^\gamma$ ). This includes the energy loss function  $\mathcal{L}$ , which can incorporate different heating and cooling processes into the conservation of energy equation. Some examples include; thermal conduction, radiative cooling (or absorption), ohmic dissipation, or even nuclear heating (i.e. in the star's core). More generally this equation is written in the Eulerian form (as previously done for the conservation of mass and momentum equations),

$$\frac{\partial \rho \varepsilon}{\partial t} + \nabla \cdot (\rho \varepsilon \mathbf{v}) = -p_T \nabla \cdot \mathbf{v} - \mathcal{L}, \quad (2.38)$$

where  $\varepsilon$  is the energy density of the plasma, the total pressure is  $p_T = p + \mathbf{B}^2/8\pi$ , the total energy is  $E = \rho \varepsilon + \rho \mathbf{v}^2/2 + \mathbf{B}^2/8\pi$ , and  $\mathcal{L} = 0$  in the idealised case. Note pressure and energy include a contribution from the magnetic field  $\mathbf{B}$ . The magnetic field also influences the plasma through the  $\mathbf{j} \times \mathbf{B}$  force which enters into the momentum equation as,

$$\rho \frac{\partial \mathbf{v}}{\partial t} + \rho (\mathbf{v} \cdot \nabla) \mathbf{v} = \rho \mathbf{g} + \frac{\mathbf{j} \times \mathbf{B}}{c} - \nabla p. \quad (2.39)$$

This equation describes the time-evolution of the bulk plasma motion  $\mathbf{v}$ , which is subject to a gravitational acceleration  $\mathbf{g}$ , the  $\mathbf{j} \times \mathbf{B}$  force, and forces due to pressure gradients within the plasma itself. The  $\mathbf{j} \times \mathbf{B}$  force can be broken down into the magnetic tension

and pressure components,

$$\begin{aligned} \frac{\mathbf{j} \times \mathbf{B}}{c} &= \frac{(\nabla \times \mathbf{B}) \times \mathbf{B}}{4\pi}, \\ &= \frac{\mathbf{B} \cdot \nabla \mathbf{B}}{4\pi} - \nabla \left( \frac{B^2}{8\pi} \right). \end{aligned} \quad (2.40)$$

The magnetic tension acts a restoring force to curvature in the magnetic field, and allows for Alfvén waves to propagate along magnetic field lines (see Section 2.2.1). Though the  $\mathbf{j} \times \mathbf{B}$  force must be orthogonal to  $\mathbf{B}$ , the tension and pressure terms can have components parallel to  $\mathbf{B}$ , which cancel each other. The magnetic tension force can be rewritten in terms of the curvature vector  $\boldsymbol{\xi}$  as follows. First define a unit vector in the direction of the magnetic field  $\hat{\mathbf{B}} = \mathbf{B}/|\mathbf{B}|$ . Then  $\boldsymbol{\xi}$  points towards the centre of curvature, given by,

$$\boldsymbol{\xi} = \hat{\mathbf{B}} \cdot \nabla \hat{\mathbf{B}} = -\frac{\mathbf{R}_c}{R_c^2}, \quad (2.41)$$

where  $\mathbf{R}_c$  is a vector pointing out from the centre of curvature. The product rule can then be used to rewrite the  $\mathbf{j} \times \mathbf{B}$  force using,

$$\frac{\mathbf{B} \cdot \nabla \mathbf{B}}{4\pi} = \frac{B \hat{\mathbf{B}} \cdot \nabla (B \hat{\mathbf{B}})}{4\pi} = \frac{\hat{\mathbf{B}} (\hat{\mathbf{B}} \cdot \nabla) B^2}{8\pi} + \frac{B^2 \hat{\mathbf{B}} \cdot \nabla \hat{\mathbf{B}}}{4\pi}, \quad (2.42)$$

as,

$$\frac{\mathbf{j} \times \mathbf{B}}{c} = \boldsymbol{\xi} \frac{B^2}{4\pi} - \nabla_{\perp} \left( \frac{B^2}{8\pi} \right). \quad (2.43)$$

The operator  $\nabla_{\perp}$  is now defined as,

$$\nabla_{\perp} = \nabla - \hat{\mathbf{B}} (\hat{\mathbf{B}} \cdot \nabla), \quad (2.44)$$

which keeps only the derivatives that are orthogonal to  $\mathbf{B}$ . The ratio of the magnetic pressure term and the thermal pressure is often used to infer the behaviour of the plasma i.e.,

$$\beta = \frac{p}{B^2/8\pi} = \frac{8\pi p}{B^2}. \quad (2.45)$$

For high- $\beta$  plasma ( $\beta \gg 1$ ), the gas pressure is large compared to the magnetic pressure which is the case in the solar photosphere. For low- $\beta$  plasma ( $\beta \ll 1$ ), the magnetic pressure dominates and so the thermal pressure can be ignored, as is the case of the low-corona where the dynamics are said to be dominated by the large-scale magnetic field (see Appendix A where coronal magnetic field models are discussed).

It is illustrative to consider different, but equivalent, forms of the MHD equations. For example the time-evolution of the kinetic energy density can be found by taking the scalar product of  $\mathbf{v}$  with the momentum equation,

$$\frac{d}{dt} \left( \frac{1}{2} \rho \mathbf{v}^2 \right) = -\mathbf{v} \cdot \nabla p + \mathbf{v} \cdot \mathbf{j} \times \mathbf{B} + \rho \mathbf{v} \cdot \mathbf{g}. \quad (2.46)$$

This shows that changes in the mechanical energy of the plasma are due to the work done by pressure, gravitation and the  $\mathbf{j} \times \mathbf{B}$  force.

### 2.2.1 Magnetohydrodynamic Waves

The ideal MHD equations allow for a variety of waves to propagate through the plasma. Typically wave solutions are found by considering a small perturbation (denoted by  $'$ ) to a uniform background plasma (denoted by  $_0$ ). For a static and uniform plasma, the MHD equations, simplified to first-order, become,

$$\frac{\partial \rho'}{\partial t} + \rho_0 (\nabla \cdot \mathbf{v}') = 0, \quad (2.47)$$

$$\rho_0 \frac{\partial \mathbf{v}'}{\partial t} = -\frac{1}{4\pi} \mathbf{B}_0 \times (\nabla \times \mathbf{B}') - \nabla p', \quad (2.48)$$

$$\frac{\partial \mathbf{B}'}{\partial t} = \nabla \times (\mathbf{v}' \times \mathbf{B}_0). \quad (2.49)$$

Taking the time-derivative of the first-order perturbed momentum equation, substituting the relation for  $\nabla p = \sqrt{\gamma p/\rho} \nabla \rho$ , and the other time-derivatives produces,

$$\frac{\partial^2 \mathbf{v}'}{\partial t^2} + \frac{\mathbf{B}_0}{4\pi\rho_0} \times \left( \nabla \times \frac{\partial \mathbf{B}'}{\partial t} \right) - \frac{\gamma p_0}{\rho_0^2} \nabla \left( \frac{\partial \rho'}{\partial t} \right) = 0, \quad (2.50)$$

$$\frac{\partial^2 \mathbf{v}'}{\partial t^2} + \mathbf{v}_A \times \nabla \times [\nabla \times (\mathbf{v}' \times \mathbf{v}_A)] - c_s^2 \nabla (\nabla \cdot \mathbf{v}') = 0, \quad (2.51)$$

where the sound speed,

$$c_s = \sqrt{\frac{\gamma p_0}{\rho_0}}, \quad (2.52)$$

and Alfvén speed,

$$\mathbf{v}_A = \frac{\mathbf{B}_0}{\sqrt{4\pi\rho_0}}, \quad (2.53)$$

have now been defined. The sound speed  $c_s$  controls how fast perturbations in pressure and density can travel through the plasma. The Alfvén speed  $\mathbf{v}_A$  defines how fast transverse oscillations in the magnetic field can propagate (this is analogous to a wave traveling along a string, with magnetic tension acting as the restoring force).

Introducing perturbations, with wave vector  $\mathbf{k}$  and frequency  $\omega$ , of the form,

$$\mathbf{v} = \mathbf{v}' \exp[i(\mathbf{k} \cdot \mathbf{r} - \omega t)], \quad (2.54)$$

the linearised equations above can be used to construct a dispersion relation i.e.,

$$-\omega^2 \mathbf{v}' + (c_s^2 + \mathbf{v}_A^2)(\mathbf{k} \cdot \mathbf{v}')\mathbf{k} + (\mathbf{v}_A \cdot \mathbf{k})[(\mathbf{v}_A \cdot \mathbf{k})\mathbf{v}' - (\mathbf{v}_A \cdot \mathbf{v}')\mathbf{k} - (\mathbf{k} \cdot \mathbf{v}')\mathbf{v}_A] = 0. \quad (2.55)$$

If  $\mathbf{k}$  is perpendicular to  $\mathbf{v}_A$  this equation simplifies to,

$$-\omega^2 \mathbf{v}' + (c_s^2 + \mathbf{v}_A^2)(\mathbf{k} \cdot \mathbf{v}')\mathbf{k} = 0, \quad (2.56)$$

$$\omega = \pm k \sqrt{c_s^2 + \mathbf{v}_A^2}, \quad (2.57)$$

whose solution is a longitudinal magnetosonic wave with phase velocity  $\sqrt{c_s^2 + \mathbf{v}_A^2}$ . The restoring pressure force is now a sum of the gas pressure and magnetic pressure, i.e. suc-



cessive compressions and rarefactions in the gas pressure are accompanied by the bunching and separating of magnetic field lines (as the magnetic field is frozen-in to the plasma). In the case that  $\mathbf{k}$  is parallel to  $\mathbf{v}_A$ , equation (2.55) becomes,

$$(\mathbf{k}^2 \mathbf{v}_A^2 - \omega^2) \mathbf{v}' + \left( \frac{c_s^2}{\mathbf{v}_A^2} - 1 \right) \mathbf{k}^2 (\mathbf{v}_A \cdot \mathbf{v}') \mathbf{v}_A = 0. \quad (2.58)$$

There are two types of wave motion which satisfy this relation; 1) ordinary longitudinal wave which travels at  $c_s$  and 2) the transverse Alfvén wave which travels at  $\mathbf{v}_A$ . For the more general case, where the angle between the wave vector  $\mathbf{k}$  and the magnetic field vector  $\mathbf{B}_0$  (or  $\mathbf{v}_A$ ) is  $\Theta$ , the dispersion relation can be written,

$$\omega(\omega^2 - k^2 v_A^2 \cos^2 \Theta) [\omega^4 - \omega^2 k^2 (c_s^2 + v_A^2) + c_s^2 v_A^2 k^4 \cos^2 \Theta] = 0. \quad (2.59)$$

From this, transverse Alfvén waves have the dispersion relation,

$$\omega = \pm (v_A \cos \Theta) k, \quad (2.60)$$

and the fast (+) and slow (-) magnetosonic waves follow,

$$\omega = \pm k \sqrt{\frac{1}{2} (c_s^2 + v_A^2) \pm \frac{1}{2} \sqrt{(c_s^2 + v_A^2)^2 - 4c_s^2 v_A^2 \cos^2 \Theta}}. \quad (2.61)$$

Along with the trivial entropy wave solution ( $\omega = 0$ ), an initial disturbance to the plasma will create backwards/forwards waves for each of the slow-magnetosonic, fast-magnetosonic, and Alfvén waves (totalling 7 waves). As will be shown in the following Section, the flow of stellar wind plasma accelerates from sub-sonic (and sub-Alfvénic) speeds, passing through critical points where the flow speed matches the MHD wave speeds. At each of the critical points, information about features up-stream of that critical point can no longer be transmitted back to the base of the stellar wind by the corresponding MHD wave. A final useful relation is given by the ratio of the isothermal sound speed and the Alfvén speed,

$$\beta = \frac{2c_s^2}{v_A^2} = \frac{2p/\rho}{B^2/4\pi\rho} = \frac{8\pi p}{B^2}, \quad (2.62)$$

which relates back to the plasma  $\beta$  parameter.

## 2.3 Summary of the Ideal Magnetohydrodynamic Equations

The equations used to describe stellar wind plasma throughout this thesis are as follows,

$$\text{mass conservation: } \frac{\partial \rho}{\partial t} + \nabla \cdot (\rho \mathbf{v}) = 0, \quad (2.63)$$

$$\text{momentum conservation: } \rho \frac{\partial \mathbf{v}}{\partial t} + \rho (\mathbf{v} \cdot \nabla) \mathbf{v} = \rho \mathbf{g} + \frac{\mathbf{j} \times \mathbf{B}}{c} - \nabla p, \quad (2.64)$$

$$\text{magnetic flux conservation: } \frac{\partial \mathbf{B}}{\partial t} = \nabla \times (\mathbf{v} \times \mathbf{B}), \quad (2.65)$$

$$\text{energy conservation: } \frac{\partial \rho \varepsilon}{\partial t} + \nabla \cdot (\rho \varepsilon \mathbf{v}) = -p_T \nabla \cdot \mathbf{v}. \quad (2.66)$$

These equations completely describe the motion of an idealised single-fluid plasma with density  $\rho$ , pressure  $p$ , velocity  $\mathbf{v}$  and magnetic field  $\mathbf{B}$  (note that the electric field  $\mathbf{E}$  and current density  $\mathbf{j}$  are not required).

## 2.4 The Solar Wind

Geomagnetic substorms were first observed in the 19th century, and were found to occur a few days after large solar flares (Carrington 1859). The link between the two phenomena was not established until Chapman (1929), who reasoned that the geomagnetic disturbances were caused by streams of particles that were ejected from solar flares and travelled through the vacuum of space to Earth. This was motivated by the work of Birkeland (1908), who performed laboratory experiments using charged particles and strong magnetic fields in order to reproduce the aurora. In explaining the deflection of cometary tails, Biermann (1951) also provided evidence for a stream of particles leaving the Sun, however these seemed to be more continuous than previously suggested by Chapman (1929). The first mathematical description of the Sun's corona was produced by Chapman and Zirin (1957), who imagined it to be in hydrostatic equilibrium, reaching out beyond the Earth

and into the ISM. Hydrostatic equilibrium is given by simplifying the radial momentum equation to,

$$\frac{dp}{dr} + \frac{GM_*\rho}{r^2} = 0, \quad (2.67)$$

where  $G$  is Newton's gravitational constant,  $M_*$  is the Sun's mass, and  $r$  is the radial distance from the Sun centred on  $r = 0$  with a radius of  $r = R_*$ . By integrating the hydrostatic equilibrium, using the ideal gas law from equation (2.35) the pressure in the corona becomes,

$$p = p_0 \exp\left(-\int_{r_0}^r \frac{GM_*p_0T_0}{\rho_0r^2T(r)}dr\right), \quad (2.68)$$

for any temperature profile  $T(r)$ , with  $p_0 = p(r_0)$ ,  $T_0 = T(r_0)$  and  $\rho_0 = \rho(r_0)$ . For an isothermal corona ( $T = \text{constant}$ ) the pressure becomes,

$$p = p_0 \exp\left[-\frac{GM_*p_0}{\rho_0}\left(\frac{1}{r_0} - \frac{1}{r}\right)\right], \quad (2.69)$$

which as  $r \rightarrow \infty$ ,  $p$  tends to a constant i.e.  $p_\infty = p_0 \exp(-GM_*p_0/\rho_0r_0)$ . However, in Chapman's model the pressure of the ISM required to balance a hydrostatic corona exceeds any reasonable value (the ISM pressure is thought to be around  $10^{-15}\text{Pa}$ ). Additionally, models for which the temperature  $T$  decreased with distance produced infinitely large  $\rho$  at large distances i.e.  $\rho \sim p/T$  so as  $T \rightarrow 0$ ,  $\rho \rightarrow \infty$ . These inconsistencies were amended by allowing the corona to be continuously expanding outward from the Sun.

### 2.4.1 First Mathematical Description of the Solar Wind - Parker (1958)

In 1957, Eugene Parker laid down the first model of the solar wind as it is known today. Parker realised that the thermal pressure of the million degree corona was enough to overcome gravity, and drive a supersonic outflow of plasma. As gravity weakens with distance, Parker suggested that the solar wind was in fact similar to the "de Laval nozzle" (De Laval and Fagerstroem 1911), which incites a transition from subsonic to supersonic flow. Parker's work was submitted to *The Astrophysical Journal*, where it received heavy criticism and was rejected by two referees before being published by the editor Subrahmanyan

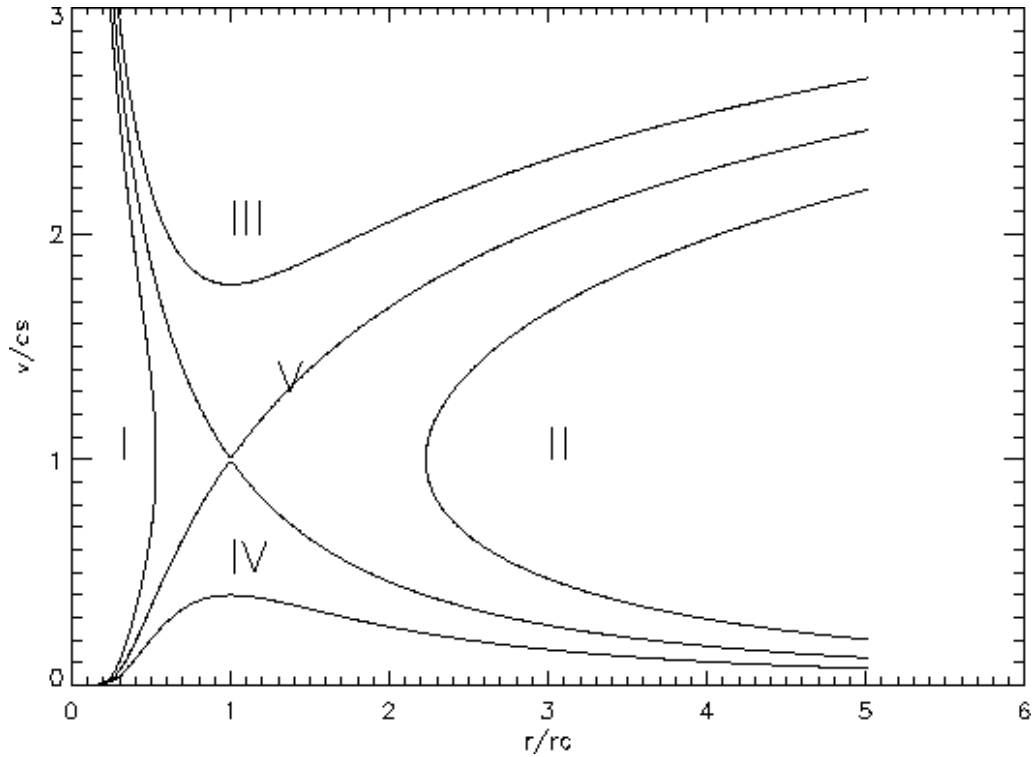


**Figure 2.4:** Wind speed versus radial distance for the five different types of solution produced by the isothermal Parker wind model. Solution V is the most physical solution, starting at the base of the corona as a subsonic flow which transitions through the critical point  $r_c$  to become supersonic. Credit: Alan Hood.

Chandrasekhar who worked in the same building as Parker at the time. The results from Parker (1958) are as follows.

Consider a spherically-symmetric outflow of an isothermal plasma with a radial velocity of  $v_r$ . The conservation of mass requires,

$$4\pi r^2 \rho v_r = \text{constant}. \quad (2.70)$$

Then the momentum equation, considering only the forces of gravity and pressure (from the hot corona) is used to find  $v_r$ ,

$$v_r \frac{dv_r}{dr} + \frac{1}{\rho} \frac{dp}{dr} + \frac{GM_*}{r^2} = 0, \quad (2.71)$$

where  $p$  is the thermal pressure of the plasma/gas, which is assumed to be ideal. As the  $T$  is isothermal,  $\rho$  can be eliminated and the momentum equation can be re-written in terms of the isothermal sound speed  $c_s = \sqrt{p/\rho}$ , and the critical radius  $r_c = GM_*/(2c_s^2)$  (sonic

point),

$$\left(v_r - \frac{c_s^2}{v_r}\right) \frac{dv_r}{dr} + \frac{2c_s^2}{r^2}(r_c - r) = 0. \quad (2.72)$$

In this form, the equation can be integrated analytically,

$$\left(\frac{v_r}{c_s}\right)^2 - 2 \ln\left(\frac{v_r}{c_s}\right) - 4 \ln\left(\frac{r}{r_c}\right) - \frac{4r_c}{r} = C, \quad (2.73)$$

where  $C$  is a constant of integration. This equation can be solved numerically through the implementation of the Newton-Raphson technique (see Appendix C.1). Different values of  $C$  produce a variety of solutions in a plane where the critical point  $r_c$  is a saddle point, see Figure 2.4. Solutions I and II are unphysical as they are double valued, and fail to connect regions close to the Sun with those further away. Solution III have supersonic speeds everywhere, including down to the solar surface, which is not observed. Solution IV is referred to as the solar breeze, and remains subsonic everywhere. This solution tends to a constant pressure at large distances, as found with the hydrostatic model. This leaves solution V, which is the Parker wind solution (given by  $C = -3$ ). The solar wind begins subsonic and transitions through the critical point  $r_c$  to become supersonic. At large distances the velocity follows  $v_r \sim 2c_s(\ln r/r_c)^{1/2}$ , while the density falls off as  $\rho \sim r^{-2}(\ln r)^{-1/2}$ . This means that  $p \rightarrow 0$  and  $r \rightarrow \infty$  as required.

## 2.4.2 The ‘‘Polytropic Approximation’’

A common addition to Parker’s model is the inclusion of a polytropic equation of state i.e. using the adiabatic relation  $p \propto \rho^\gamma$ , for which  $\gamma$  is the ratio of specific heats and has a value of 5/3. In the polytropic approximation the value of  $\gamma$  can be artificially lowered to mimic the plasma heating as it expands, without the need for an energy equation to be solved (e.g. Lamers and Cassinelli 1999). The polytropic sound speed is now  $c_s = \sqrt{\gamma p/\rho}$ , and is no longer constant due to the variation of  $T \propto \rho^{\gamma-1} \propto (v_r r^2)^{1-\gamma}$  with distance. The resulting wind equations, found by manipulating equation (2.71), are,

$$\left(\frac{v_r}{v_c}\right)^{\gamma+1} - \left(\frac{v_r}{v_c}\right)^{\gamma-1} \left[ \frac{4r_c}{r} + \left(\frac{5-3\gamma}{\gamma-1}\right) \right] + \frac{2}{\gamma-1} \left(\frac{r}{r_c}\right)^{2-2\gamma} = 0, \quad (2.74)$$

and,

$$\frac{R_*}{r_c} - \frac{\gamma - 1}{5 - 3\gamma} \left( \frac{v_{esc}}{2c_{s,*}} \right)^{\frac{4}{\gamma-1}} \left( \frac{R_*}{r_c} \right)^{\frac{5-3\gamma}{\gamma-1}} - \frac{2}{5 - 3\gamma} \left( \frac{2c_{s,*}}{v_{esc}} \right)^2 + 4 \frac{\gamma - 1}{5 - 3\gamma} = 0, \quad (2.75)$$

where equation (2.74) describes the radial velocity  $v_r$ , with the location of  $r_c$  being solved for using equation (2.75). The wind speed at  $r_c$  is  $v_c = \sqrt{GM_*/(2r_c)} = c_s(r_c)$ . The radial profile of  $p$  (or equally  $T$ ) is then related to  $\rho$  by  $p(r) = c_{s,*}^2 \rho_*^{1-\gamma} \rho(r)^\gamma / \gamma$ , where  $\rho(r)$  is given by mass conservation from the surface value  $\rho_*$  (equation (2.70)).

Mathematically, the value of  $\gamma$  (otherwise referred to as the polytropic index) can range from 1 to 5/3, with the case of 5/3 representing an adiabatic expansion. Typically the value of  $\gamma$  is lowered to around  $1 < \gamma < 1.1$  (as done in this thesis), which reproduces the approximately isothermal nature of the solar wind (see examples from Parker 1965; Kopp and Holzer 1976; Washimi and Shibata 1993; Washimi and Sakurai 1993; Keppens and Goedbloed 1999; Matt et al. 2012; Vidotto et al. 2014b; Réville et al. 2015a; Pantolmos and Matt 2017). Further to this, some models involve a spatially varying polytropic index which allows for the locations of energy deposition into the wind to be tuned (see Cohen et al. 2006).

When used in Chapter 3 as an initial condition for the MHD wind simulations, the control parameter  $c_{s,*}/v_{esc}$  i.e. the ratio of sound speed at the base of the wind to surface escape speed  $v_{esc} = \sqrt{2GM_*/R_*}$ , is used frequently. This can be transformed into a coronal base temperature via,

$$T_* = \left( \frac{c_{s,*}}{v_{esc}} \right)^2 \left( \frac{2GM_* m}{R_* k_B} \right). \quad (2.76)$$

The Parker wind models, both isothermal and polytropic, require extremely large coronal temperatures in order to approach the terminal speed of the fast solar wind ( $\sim 700\text{km/s}$ ), which are not observed. It is understood that the heating and acceleration of coronal plasma is more complex than Parker's original model, although the Parker wind provides a good basis to build from.

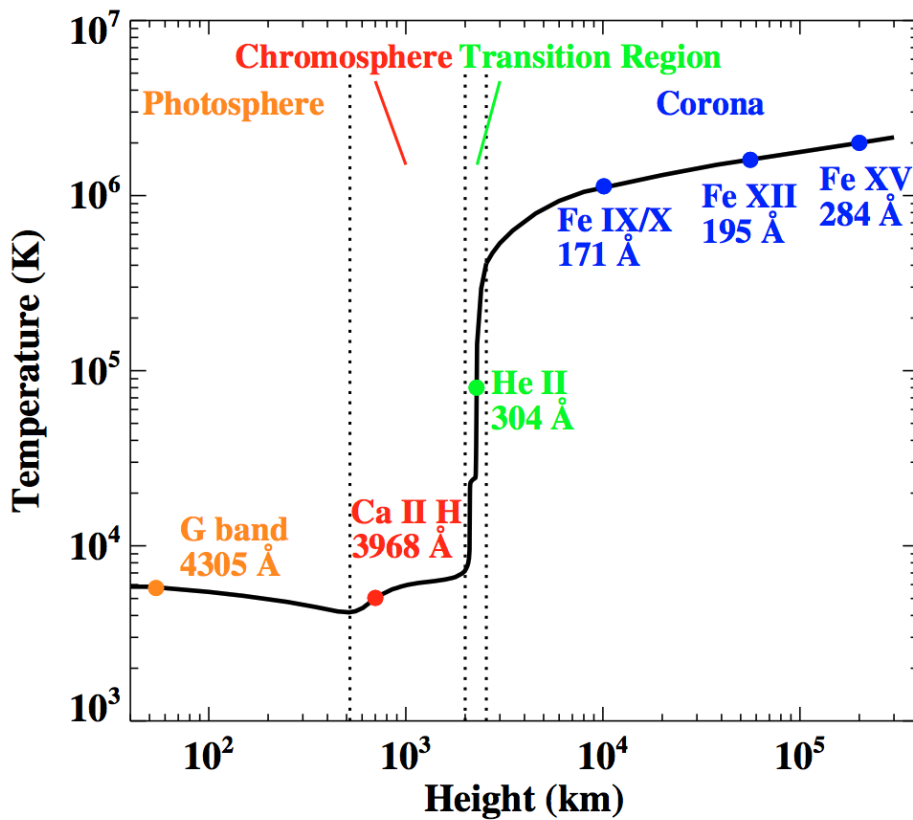


Figure 2.5: Temperature variation of the solar atmosphere with height. Named regions are highlighted, along with the source regions of some frequently used emission lines. Taken from Yang et al. (2009).

### 2.4.3 Heating the Corona

The heating of the corona (and solar wind) continues to be a pervasive issue in solar physics, with a variety of proposed mechanisms that operate under a range of different conditions. These include shock dissipation, Alfvén waves (resonant absorption, mode coupling, turbulent heating, Landau damping, etc), and small-scale reconnection (i.e. nanoflares). It is expected that current in-situ measurements from Parker Solar Probe (Fox et al. 2016) and Solar Orbiter (Mueller et al. 2013) will shed light on this by studying the Sun’s atmosphere up close. The polytropic Parker wind model is able to approximate the extended heating of the wind, but without connection to a physical mechanism. This is acceptable for the purposes of this thesis, as the exact mechanisms which cause the wind acceleration do not need to be parameterised. Instead the polytropic approximation allows for a wide range of potential wind solutions to be experimented upon, with the results feeding back into one-dimensional theory (see Section 2.5.4). In this Section I briefly

review the heating of the corona for completeness (for more details, see the reviews of Klimchuk 2006; Parnell and De Moortel 2012; Priest 2014).

The temperature structure of the solar atmosphere is shown in Figure 2.5. Though the surface temperature of the Sun is only  $\sim 5800\text{K}$ , the corona above this has a temperature of  $\sim 1\text{MK}$ . These high temperatures are responsible for driving the solar wind, as described by Parker (1958), however they defy our natural expectation that temperature decreases with distance from the heating source (i.e. nuclear fusion in this case). The deposition of energy and momentum into the solar atmosphere is particularly challenging, given the variety of temperatures, densities and magnetic field structures that it contains. This is coupled with mass and energy being transported around the different regions of the solar atmosphere; the photosphere, the chromosphere, the transition region, and the corona (see Figure 2.5). Before the space-age, the only way to view the Sun's atmosphere was through solar eclipse observations, see an example in Figure 2.6.

Energy in the corona is likely input by the Sun's magnetic field, evidence for this comes from the observations of the hottest coronal loops which tend to have stronger magnetic fields than others (Fisher et al. 1998). This can be described in terms of the Poynting flux (energy flux of the electromagnetic field) as,

$$\int \frac{\mathbf{E} \times \mathbf{B}}{4\pi} \cdot d\mathbf{S} = \int \left[ \frac{j^2}{\sigma} + \mathbf{v} \cdot \mathbf{j} \times \mathbf{B} + \frac{\partial}{\partial t} \left( \frac{B^2}{8\pi} \right) \right] dV, \quad (2.77)$$

where the input energy through a surface  $\mathbf{S}$  can do three things, heat the plasma via Ohmic dissipation, accelerate the plasma via the  $\mathbf{j} \times \mathbf{B}$  force, or increase the magnetic energy in the corona. Energy flux is driven from the photosphere by the motion (due to convective motions) of magnetic field lines embedded there. These motions are then thought to fuel MHD waves (see Section 2.2) or magnetic reconnection in the solar atmosphere, which dissipate their energy higher up in the corona. The difficulty in describing the heating of the corona comes from both of these processes likely playing significant roles. For example in the low corona, reconnection is observed directly to heat the corona (i.e. flares, jets, spicules, microflares, etc.) (Hudson 1991). Whereas the solar wind is observed to contain Alfvénic waves, which are the “smoking gun” of Alfvén-wave heating (Hollweg 1986;





**Figure 2.6:** Solar eclipse from July 2019. Imaged by both ESO’s La Silla Observatory and the Large Angle and Spectrometric Coronagraph (LASCO) onboard the Solar and Heliospheric Observatory (SOHO) spacecraft. These observations are combined to provide a detailed image of the Sun’s corona structure. Credit: ESO/P. Horálek/SOHO (ESA & NASA).

Goldstein et al. 1995). As well as heating the wind, MHD waves are proposed to also help accelerate the wind (e.g. Suzuki 2011). This helps to resolve the need for unphysically large thermal temperatures in the corona to drive the fast solar wind in Parker’s model.

## 2.5 Magnetised Stellar Winds

In the context of rotation period evolution, it is clear from observations that the stellar magnetic field is important. Not only for heating the corona (and accelerating the wind), but for increasing the effectiveness of angular momentum transfer to the stellar wind.

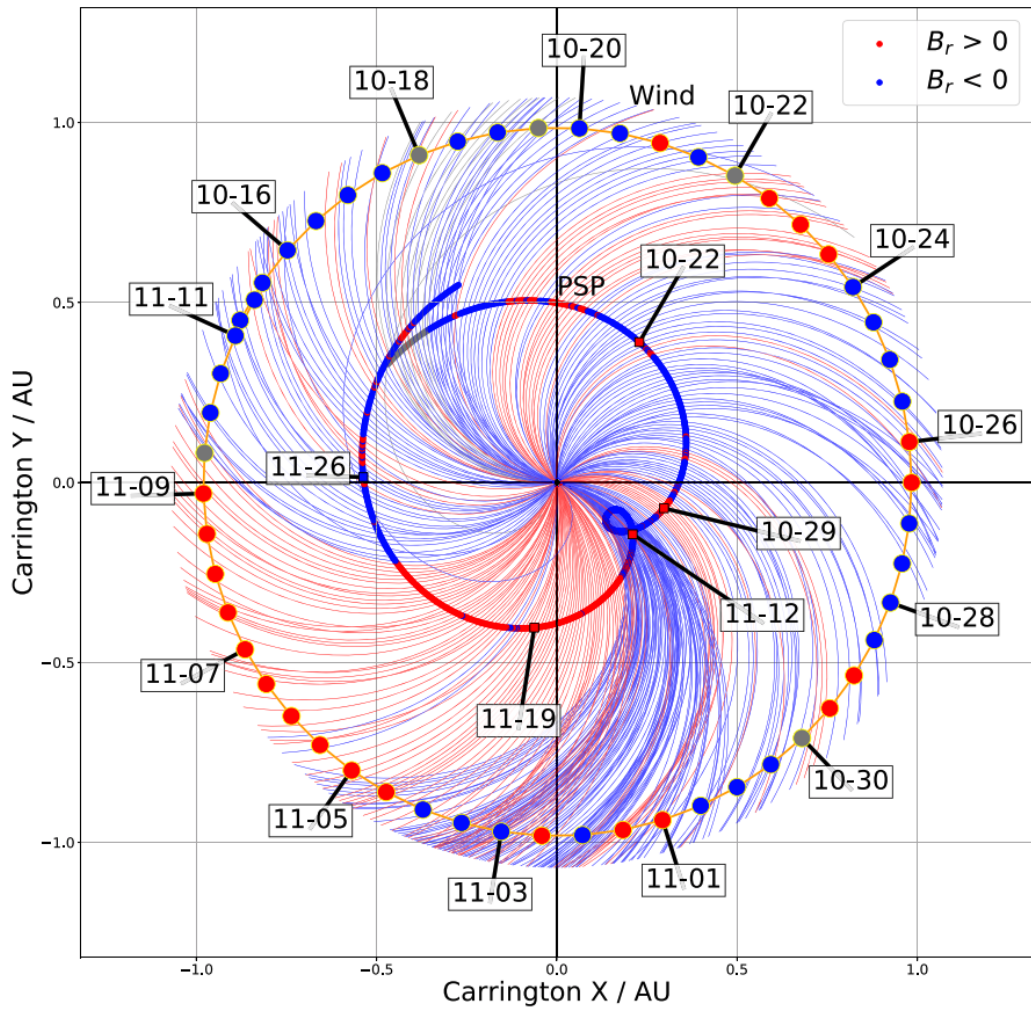


**Figure 2.7:** Parker spiral magnetic field using the polarity of the magnetic field observed by the Parker Solar Probe (PSP) during its first perihelion pass of the Sun (shown in the rotating frame). The average measured field polarity from PSP colours its orbit. Similarly, the average field polarity for the *Wind* spacecraft at  $\sim 1$  au is shown around the edge with coloured circles that represent 12-hour averages. The Parker spirals follow equation (2.84) and appear to reproduce the heliospheric magnetic field structure well. Taken from Badman et al. (2020).

### 2.5.1 Parker Spiral Magnetic Field

First, there is still more to learn from Parker (1958). Parker further explained, along with the solar wind, the structure of the solar wind magnetic field. Consider a rotating frame of reference, that contains a spherically-symmetric purely radial wind  $v_r$ , the azimuthal wind velocity is then given by,

$$v_\phi = -\Omega_*(r - R_*) \sin \theta. \quad (2.78)$$

This non-radial component of velocity comes directly from the transformation into the rotating frame. Then the path followed by a magnetic field line anchored into the stellar surface is,

$$\frac{1}{r} \frac{dr}{d\phi} = \frac{v_r}{v_\phi} = -\frac{v_r}{\Omega_*(r - R_*) \sin \theta}, \quad (2.79)$$

which is the streamline of velocity (see Appendix A). It follows that the magnetic field itself is described by,

$$B_r(r, \theta, \phi) = B_*(\theta, \phi) \left( \frac{r}{R_*} \right)^{-2}, \quad (2.80)$$

$$B_\theta(r, \theta, \phi) = 0, \quad (2.81)$$

$$B_\phi(r, \theta, \phi) = -B_*(\theta, \phi) \frac{\Omega_* R_*^2 \sin \theta}{v_r r}, \quad (2.82)$$

where  $B_\theta$  is zero due to the flow being purely radial, and the  $B_r$  term decays following the conservation of magnetic flux i.e.  $\nabla \cdot \mathbf{B} = 0$ .  $B_*(\theta, \phi)$  corresponds to the surface magnetic field, however this surface does not have to be the stellar/solar surface (and isn't usually). The magnetic field described by these equations predicts that the flow at various latitudes  $\theta$  is essentially wrapped around the surface of a cone, the winding of which is less-severe with proximity to the rotation poles. This predicts that the angle of the solar wind (in the equator  $\theta = 90^\circ$ ), upon arrival at Earth should be,

$$\psi = \tan^{-1} \left( \frac{\Omega_*(r - R_*)}{v_r} \right), \quad (2.83)$$

which for  $\Omega_* = 2.6 \times 10^{-6} \text{rad/s}$ ,  $r = 1.5 \times 10^8 \text{km}$ , and  $v_r \approx 400 \text{km/s}$ , gives a value of  $\psi \approx 44^\circ$ . More generally, the longitude of an equatorial magnetic field line is given by,

$$\phi(r) = \phi_* - \frac{\Omega_*}{v_r} (r - R_*), \quad (2.84)$$

where  $\phi_*$  is the longitude where the field line begins. After Parker proposed the ‘‘spiral’’ model, spacecraft observations soon supported the idea, measuring the solar wind magnetic field to lay in the equatorial plane with an average angle that matched the spiral

prediction (Coleman et al. 1962; Ness and Wilcox 1964). A relatively recent implementation of the Parker spiral can be found in Figure 2.7, again with good agreement to the available data.

### 2.5.2 Angular Momentum Loss in Stellar Winds - Weber & Davis (1987)

One of the most fundamental results concerning the angular momentum-loss of low-mass stars comes from Weber and Davis (1967). This thesis relies heavily on the mathematical framework established in this work. First, let's consider a wind with rotation but without a magnetic field. It can be shown simply from the azimuthal momentum equation that, for a surface rotation rate of  $\Omega_*$ , the azimuthal wind speed is,

$$v_\phi = \frac{\Lambda}{r} = \frac{\Omega_* R_*^2}{r}, \quad (2.85)$$

where (in this case)  $\Lambda$  is the specific angular momentum of the plasma. This represents the conservation of angular momentum. Now let's add magnetic fields. Consider a wind with velocity,

$$\mathbf{v} = v_r \hat{r} + v_\phi \hat{\phi}, \quad (2.86)$$

and magnetic field,

$$\mathbf{B} = B_r \hat{r} + B_\phi \hat{\phi}, \quad (2.87)$$

that describe an equatorial flow, i.e.  $r$  is the cylindrical radius. A few conditions arise naturally, such as the conservation of magnetic flux,

$$r^2 B_r = \text{constant}, \quad (2.88)$$

and the flow  $\mathbf{v}$  being parallel to  $\mathbf{B}$  in the rotating frame of reference with the star,

$$r(v_r B_\phi - v_\phi B_r) = \text{constant} = -\Omega_* r^2 B_r. \quad (2.89)$$

The radial momentum equation for the wind plasma (in the rotating frame) is,

$$v_r \frac{\partial v_r}{\partial r} + \rho \frac{\partial p}{\partial r} + \frac{GM_*}{r^2} + \frac{1}{4\pi r \rho} B_\phi \frac{d}{dr}(rB_\phi) + \frac{v_\phi^2}{r} = 0, \quad (2.90)$$

which now includes the Lorentz force  $(\mathbf{j} \times \mathbf{B})_r/c$ , and the centrifugal force  $[\rho \boldsymbol{\Omega}_* \times (\boldsymbol{\Omega}_* \times \mathbf{r})]_r$ . Using a polytropic equation of state  $p \propto \rho^\gamma$ , the radial momentum equation can be rewritten as,

$$\frac{d}{dr} \left\{ \frac{1}{2} v_r^2 + \frac{\gamma}{\gamma - 1} \frac{p_*}{\rho_*} \left( \frac{\rho}{\rho_*} \right)^{\gamma-1} - \frac{GM_*}{r} \right\} = \frac{v_\phi^2}{r} - \frac{1}{8\pi r^2 \rho} \frac{d}{dr} (rB_\phi)^2. \quad (2.91)$$

In this expression the pressure gradient was rearranged as follows,

$$\frac{1}{\rho} \frac{dp}{dr} = \frac{1}{\rho} \frac{d}{dr} \left[ p_* \left( \frac{\rho}{\rho_*} \right)^\gamma \right], \quad (2.92)$$

$$= \frac{\gamma \rho^{\gamma-1} d\rho}{\rho} \left( \frac{p_*}{\rho_*^\gamma} \right), \quad (2.93)$$

$$= \frac{\gamma}{\gamma - 1} \frac{d\rho^{\gamma-1}}{dr} \left( \frac{p_*}{\rho_*^\gamma} \right), \quad (2.94)$$

$$= \frac{d}{dr} \left\{ \frac{\gamma}{\gamma - 1} \frac{p_*}{\rho_*} \left( \frac{\rho}{\rho_*} \right)^{\gamma-1} \right\}. \quad (2.95)$$

Notice, if the terms on the right hand-side of equation (2.91) are set to zero, i.e. removing the influence of the magnetic field and stellar rotation, the term on the left hand-side is the Parker wind solution from the previous Section. In order to find solutions to equation (2.91),  $v_\phi$  and  $B_\phi$  must first be solved for.

Given this flow is axisymmetric, the azimuthal momentum equation involves only the magnetic force,

$$\frac{v_r}{r} \frac{d}{dr} (rv_\phi) = \frac{1}{\rho c} (\mathbf{j} \times \mathbf{B})_\phi = \frac{B_r}{4\pi r \rho} \frac{d}{dr} (rB_\phi). \quad (2.96)$$

Then it can be shown that

$$\frac{d}{dr} \left\{ rv_\phi - \frac{B_r}{4\pi \rho v_r} rB_\phi \right\} = 0, \quad (2.97)$$

i.e.,

$$rv_\phi - \frac{B_r}{4\pi\rho v_r} r B_\phi = \text{constant} = \Lambda, \quad (2.98)$$

because,

$$\frac{B_r r^2}{4\pi\rho v_r r^2} = \text{constant}, \quad (2.99)$$

from the conservation of flux and mass equations. As written above,  $\Lambda$  is the poloidal vorticity-current stream function (see Goedbloed et al. 2019, for more details), and is often mislabelled in the literature as being the specific angular momentum flux (this misnomer is also unfortunately present throughout this thesis). Recall the value of  $\Lambda$  for the case without a magnetic field in equation (2.85), this corresponds to the specific angular momentum which is a mechanical flux in the plasma. This term is also found in equation (2.98), along with a second term that corresponds to the transport of angular momentum via stresses/torques in the magnetic field. The Alfvénic Mach number is defined as,

$$M_A^2 = \left(\frac{v_r}{v_A}\right)^2 = \frac{4\pi\rho v_r^2}{B_r^2}. \quad (2.100)$$

From equation (2.89), the azimuthal velocity can then be written,

$$rv_r \left\{ (rv_\phi - \Lambda) \frac{4\pi\rho v_r}{r B_r} \right\} - rv_\phi B_r = -\Omega_* r^2 B_r, \quad (2.101)$$

$$B_r M_A^2 (rv_\phi - \Lambda) - rv_\phi B_r = -\Omega_* r^2 B_r, \quad (2.102)$$

$$rv_\phi (M_A^2 - 1) - \Lambda M_A^2 = -\Omega_* r^2, \quad (2.103)$$

$$v_\phi = \Omega_* r \frac{\Lambda M_A^2 r^{-2} \Omega_*^{-1} - 1}{M_A^2 - 1}. \quad (2.104)$$

From this a new critical point is defined, the Alfvén radius  $R_A$ , where  $M_A^2 - 1 = 0$ . At this point the denominator of the azimuthal velocity equations goes to zero, and so to keep the expression finite the numerator must also vanish producing the condition,

$$\Lambda = \Omega R_A^2. \quad (2.105)$$

The azimuthal velocity equation can be reduced by considering the conservation of mag-

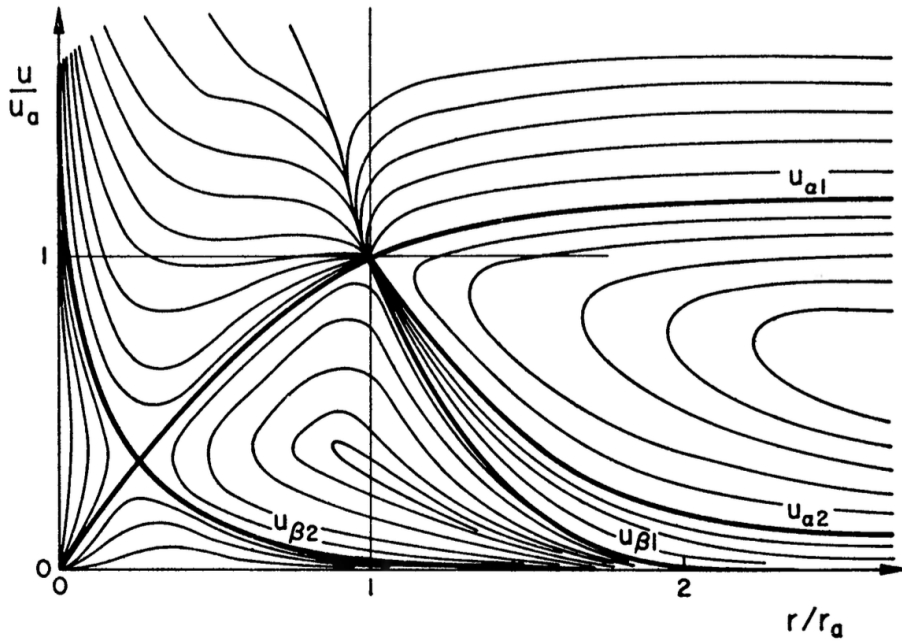


**Figure 2.8:** Wind speed versus radial distance for the different solutions produced by the Weber-Davis wind model. The wind speed  $v_r$  is normalised by the Alfvén velocity  $v_A$ , and the radius  $r$  is normalised by the Alfvén radius  $R_A$ . There are two critical points, the sonic point and the Alfvén point (highlighted with straight lines). The physical solution traverse both critical points from subsonic to super-Alfvénic. Taken from Weber and Davis (1967).

netic flux and mass,

$$\frac{M_A^2}{v_r r^2} = \frac{4\pi\rho v_r}{B_r r^2} = \text{constant}, \quad (2.106)$$

such that,

$$v_\phi = \frac{\Omega_* r v_A - v_r}{v_A (1 - M_A^2)}. \quad (2.107)$$

From this the azimuthal magnetic field is,

$$B_\phi = -\frac{B_r}{v_r}(\Omega_* r - v_\phi), \quad (2.108)$$

$$B_\phi = -B_r \frac{\Omega_* r}{v_A} \frac{R_A^2 - r^2}{R_A^2 (1 - M_A^2)}, \quad (2.109)$$

where again the fact that  $M_A^2/v_r r^2 = \text{constant}$  has been used.

Returning to the radial momentum equation, it is now possible to numerically solve,

$$\begin{aligned} \frac{dv_r}{dr} = \frac{v_r}{r} \left\{ \left( \frac{2\gamma p_A}{\rho_A M_A^{2(\gamma-1)}} - \frac{GM_*}{r} \right) (M_A^2 - 1)^3 + \Omega_*^2 r^2 \left( \frac{v_r}{v_A} - 1 \right) \left[ (M_A^2 + 1) \frac{v_r}{v_A} \right. \right. \\ \left. \left. - 3M_A^2 + 1 \right] \right\} \times \left[ \left( v_r^2 - \frac{\gamma p_A}{\rho_A M_A^{2(\gamma-1)}} \right) (M_A^2 - 1)^3 - \Omega_*^2 r^2 M_A^2 \left( \frac{R_A^2}{r^2} - 1 \right) \right]^{-1}, \end{aligned} \quad (2.110)$$

as done previously for the Parker wind solutions. The solutions to this are shown in Figure 2.8. A similar structure can be found to the Parker wind solution in Figure 2.4, but now with two critical points; the slow and fast magnetosonic points. As done for the Parker wind, we adopt the solution that begins subsonic and traverses both critical points to become supersonic and super-Alfvénic. The radial momentum equation can be integrated in order to evaluate the energy flux per steradian in the wind as follows,

$$F = \rho v_r r^2 \left\{ \frac{v_r^2}{2} + \frac{v_\phi^2}{2} + \frac{\gamma}{\gamma-1} \frac{p_A}{\rho_A} M_A^{-2(\gamma-1)} - \frac{GM_*}{r} - \frac{B_\phi B_r \Omega_* r}{4\partial\rho v_r} \right\}, \quad (2.111)$$

which shows the kinetic energy flux in both the radial and azimuthal velocity, the flux of thermal energy, gravitational energy, and the Poynting energy flux. The total energy flux is a constant.

The angular momentum-loss rate of the wind is given by,

$$\tau = \int_A \Lambda \rho \mathbf{v} \cdot \mathbf{dA} = \int_A \left( r \rho v_r v_\phi - \frac{B_r}{4\pi} r B_\phi \right) r^2 \sin \theta dr d\theta d\phi, \quad (2.112)$$

where the poloidal vorticity-current stream function  $\Lambda$  is multiplied by the mass flux in the wind and integrated over (in this case) a spherical closed surface. Given the result of equation (2.105), the angular momentum-loss rate can also be written,

$$\tau = \int_A \Omega_* r_A^2 \rho v_r r^2 \sin \theta dr d\theta d\phi, \quad (2.113)$$

note that  $R_A$  is the cylindrical radius such that we insert a factor of  $\sin \theta$ , to integrate over



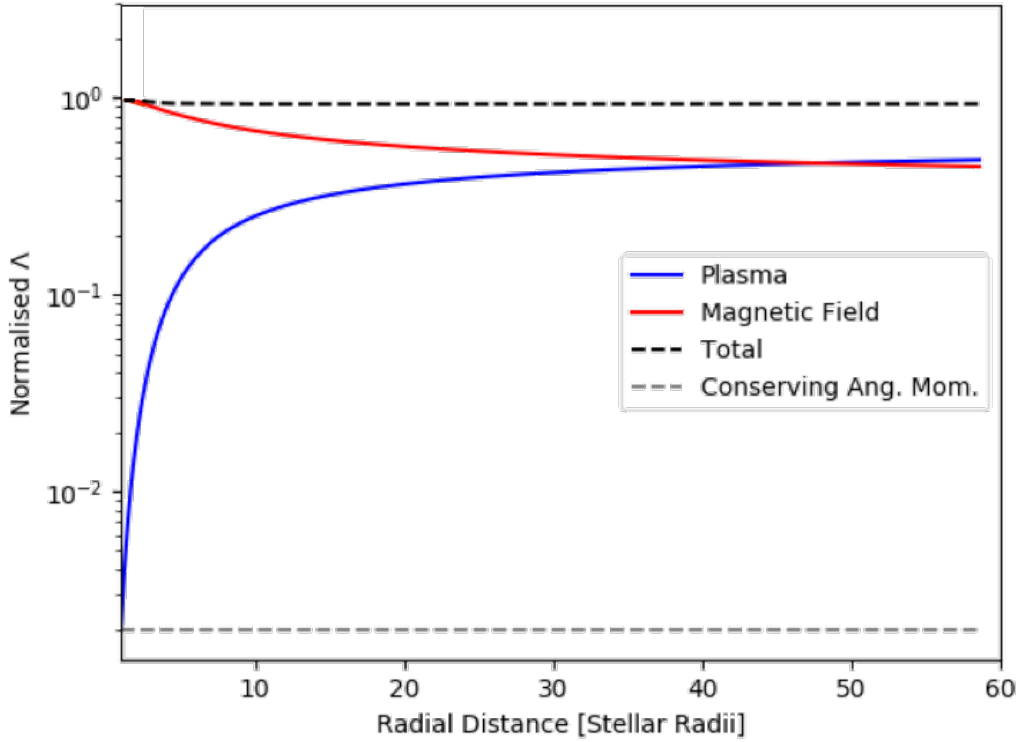


**Figure 2.9:** Distribution of specific angular momentum  $\Lambda$  between the plasma and magnetic field stresses along a magnetic field line. Values are taken from one of the wind simulations in Chapter 3. Note that this is just one example, and the lines may cross earlier, later or not at all depending on the simulation parameters.

a sphere with the same radius  $r_A = R_A \sin \theta$ ,

$$\tau = \int_A \Omega_* (R_A \sin \theta)^2 \rho v_r r^2 \sin \theta dr d\theta d\phi = \frac{2}{3} \Omega_* R_A^2 (4\pi r^2 \rho v_r) = \frac{2}{3} \Omega_* R_A^2 \dot{M}. \quad (2.114)$$

This shows that the Alfvén radius  $R_A$  is the key factor in determining the effectiveness of the angular momentum lost through the stellar wind mass-loss  $\dot{M}$ . Recall the non-magnetised case from equation (2.85), upon calculating the resulting angular momentum-loss rate,

$$\tau = \int_A \Omega_* (R_* \sin \theta)^2 \rho v_r r^2 \sin \theta dr d\theta d\phi = \frac{2}{3} \Omega_* R_*^2 \dot{M}, \quad (2.115)$$

it can be seen that  $R_A$  analytically acts “like” a surface of rigid rotation for the wind (as the stellar surface does for the un-magnetised case). In this thesis, I endeavour to characterise the effectiveness of magnetic braking due to stellar winds by evaluating the  $R_A$  from MHD wind simulations with various magnetic properties. This is also combined with relation-

ships from one-dimensional theory, see Section 2.5.4. Note however, that in reality the wind does not rigidly-rotate out to  $R_A$ , instead the stellar wind contains both an angular momentum flux in the plasma (protons)  $F_{AM,p}$ , and magnetic field stresses  $F_{AM,B}$ , which vary with radial distance. The stresses in the magnetic field transfer angular momentum to the protons with distance, which when integrated is mathematically equivalent to rigid rotation at  $R_A$ . The radial profiles of  $\Lambda$  shown in Figure 2.9 are not fixed, and so vary with the strength of the magnetic field, temperature of the wind, etc, with the magnetic field or plasma terms dominating in different parts of the parameter space, following,

$$\Lambda_p = r \sin \theta v_\phi = \Omega_* (r \sin \theta)^2 \frac{M_A^2 \frac{R_A^2}{r^2} - 1}{M_A^2 - 1}, \quad (2.116)$$

$$\Lambda_B = -r \sin \theta B_\phi \frac{B_r}{4\pi \rho v_r} = -\Omega_* (r \sin \theta)^2 \frac{\frac{R_A^2}{r^2} - 1}{M_A^2 - 1}. \quad (2.117)$$

This makes the ratio of the angular momentum flux and magnetic field stresses  $F_{AM,p}/F_{AM,B}$  a useful diagnostic of the stellar wind, especially when comparing observations of the solar wind. From here I consider the mechanical angular momentum flux in the protons  $F_{AM,p}$  and the angular momentum transported by magnetic field stresses  $F_{AM,B}$  at various limits in the Weber and Davis (1967) model (see Marsch and Richter 1984a, for more details). These are defined as,

$$F_{AM,p} = \rho v_r \Lambda_p = \rho v_r \Omega_* (r \sin \theta)^2 \frac{M_A^2 \frac{R_A^2}{r^2} - 1}{M_A^2 - 1}, \quad (2.118)$$

$$F_{AM,B} = \rho v_r \Lambda_B = -\rho v_r \Omega_* (r \sin \theta)^2 \frac{\frac{R_A^2}{r^2} - 1}{M_A^2 - 1}, \quad (2.119)$$

for which  $r$  is now the spherical radius. These terms often appear normalised by  $r^2$ , which better represents the angular momentum-loss rate (see Section 6.4). As  $r \rightarrow 0$ , these terms

become,

$$F_{AM,p}|_{r \rightarrow 0} \approx \Omega_* (r \sin \theta)^2 \rho v_r = 0, \quad (2.120)$$

$$F_{AM,B}|_{r \rightarrow 0} \approx \Omega_* (R_A \sin \theta)^2 \rho v_r, \quad (2.121)$$

such that their ratio,

$$\frac{F_{AM,p}}{F_{AM,B}} \Big|_{r \rightarrow 0} \approx 0. \quad (2.122)$$

Similarly for  $M_A^2 \gg 1$  and  $r \gg R_A$ ,

$$F_{AM,p}|_{r \rightarrow \infty} \approx \rho \sin^2 \theta \Omega_* R_A^2 (v_r - v_r(R_A)), \quad (2.123)$$

$$F_{AM,B}|_{r \rightarrow \infty} \approx \rho \sin^2 \theta \Omega_* R_A^2 v_r(R_A), \quad (2.124)$$

so,

$$\frac{F_{AM,p}}{F_{AM,B}} \Big|_{r \rightarrow \infty} \approx \frac{v_r}{v_r(R_A)} - 1. \quad (2.125)$$

From this analysis it is clear that the ratio  $F_{AM,p}/F_{AM,B}$  varies considerably with distance, and also has some useful features. This implies that if the radial wind speed at larger distances is less than twice the wind speed at the Alfvén radius, the angular momentum-loss will mainly be governed by the magnetic stresses. If the radial wind speed is higher, then the angular momentum will be principally carried by the plasma in the wind. One interesting result derived in Marsch and Richter (1984a) is that,

$$R_A^2 = \frac{\Lambda_B}{\Omega_* (1 + F_{AM,p}/F_{AM,B})}, \quad (2.126)$$

and so observational constraints on the distribution of angular momentum in the wind can be used to infer the location of the Alfvén radius. Fundamentally, this implies that winds which have more angular momentum carried in magnetic stresses have larger  $R_A$ . Measurements of  $F_{AM,p}/F_{AM,B}$  are further discussed in Section 6.4.

### 2.5.3 Current Models of Solar and Stellar Winds

In the literature, models of the solar wind have typically diverged away from the models that are now frequently used to model stellar winds. Here I discuss the kinds of models that exist and their applications. Given the wealth of observations of the Sun's magnetism and solar wind, the models that are used to explain the solar wind have become increasingly complex. This links to Section 2.4.3, in which the heating of the corona was discussed. Alfvén wave-driven solar wind models have been able to reproduce the properties of flows emerging from coronal holes, along open magnetic field lines (Suzuki 2011, Shoda et al. Submitted). These models must span a huge range of density and temperature scales from the photosphere to the corona, and so are normally one-dimensional (following the expansion of a flux tube). Alfvén waves dissipate heat and momentum into the corona through wave reflection and other processes, which all must be captured self-consistently in these models. When the same physics is applied to multi-dimensional MHD simulations, these physical effects are parameterised, see for example the Alfvén Wave Solar Model (AWSoM) by van-der-Holst et al. (2014). These global solar wind models do a reasonable job of reproducing observations (Usmanov et al. 2018; Réville et al. 2020). However some authors have liberally applied solar wind models to the winds of other Sun-like stars (e.g. Garraffo et al. 2017; Alvarado-Gómez et al. 2019), where it is unclear if the prescribed heating functions are valid given the reconstructed magnetic fields of these stars are likely missing significant amounts of their small scale flux (See et al. 2019b). Another branch of solar wind models exist, primarily for space weather forecasting (Wang and Sheeley Jr 1990; Odstrcil et al. 2002; Riley et al. 2011; Parsons et al. 2011). These models are semi-empirical, relying on trends in past data to predict the arrival times of ICMEs at Earth, or the severity of SIRs.

Previous MHD stellar wind simulations have opted for a simple approach, developing polytropic Parker-type winds that span a wide range of the parameter space (see Matt et al. 2012; Réville et al. 2015a; Pantolmos and Matt 2017). The advantage of this is that the fundamental connections between properties can be understood, i.e. increased heating, stronger magnetic field strengths, etc. However, the mass-loss rates in these simulations are not informed by realistic physics, with the wind emerging from the low-corona at a

given speed and density. Because of this, the models have been used to construct semi-analytic prescriptions for the angular momentum-loss rates of stars, given the mass-loss rate and stellar properties. This means that for the semi-analytic relations to be used, the mass-loss rates of stars need to also be prescribed such as through the model of Cranmer and Saar (2011). Recently, the one-dimensional Alfvén wave-driven models have been applied to the wind of other Sun-like stars, revealing the dependence of the mass-loss rate on various physical parameters (Shoda et al. Submitted). The model of Shoda et al. Submitted (see Appendix D), also shows good agreement with the angular momentum-loss scalings of previous MHD polytropic wind models.

#### 2.5.4 1D Semi-analytic Theory

Following the work of Weber and Davis (1967), when evaluating results from MHD wind simulations (such as those presented in this thesis) the general aim is to find scaling relations which explain the dependencies of  $R_A$  on the input parameters. To accomplish this, many previous works have turned to one-dimensional analysis, which has been shown to yield useful results (e.g. Matt et al. 2012; Réville et al. 2015a; Pantolmos and Matt 2017). Consider a steady one-dimensional ideal MHD flow, that travels along a magnetic flux tube. Let's assume that this flow is representative of the entire wind i.e. the wind is spherically-symmetric and depends only on radial distance. The magnetic field is approximated by two regions, a potential inner region and a magnetically-open outer region,

$$B_r = \begin{cases} B_* \left( \frac{R_*}{r} \right)^{l+2}, & \text{for } r < R_o, \\ B_o \left( \frac{R_o}{r} \right)^2, & \text{for } r \geq R_o, \end{cases} \quad (2.127)$$

where  $R_o$  is the radius at which the wind pressure opens the magnetic field to become purely radial, and  $B_o$  is the field strength at  $R_o$  (this is depicted in Figure 2.10). Henceforth quantities denoted with "A" are measured at  $r = R_A$ , "\*" at  $r = R_*$ , and "o" at  $r = R_o$ . The order of the magnetic field  $l$  increases with complexity i.e. dipole  $l = 1$ , quadrupole  $l = 2$ , octupole  $l = 3$ , etc. From this, a relationship for  $R_A$  can be produced that depends

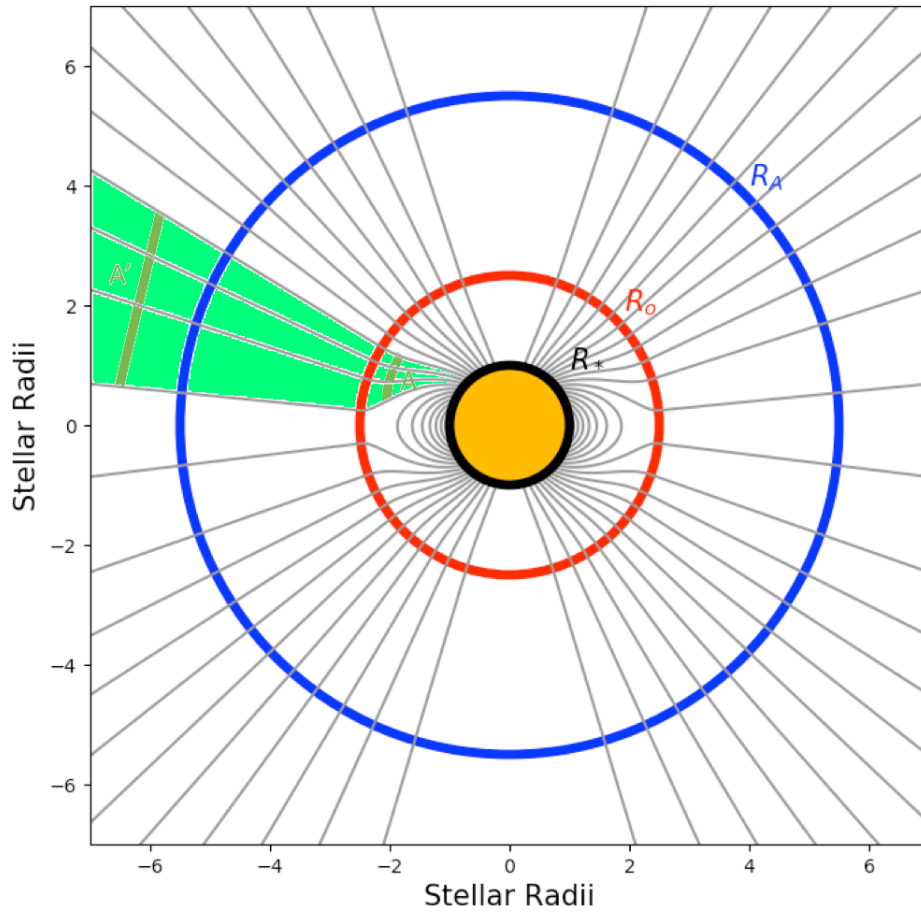


**Figure 2.10:** Schematic of a dipolar magnetic field in the framework of the 1D semi-analytic theory. The opening radius  $R_o$  is shown in red, the Alfvén radius  $R_A$  is shown in blue. The behaviour of a flux tube area  $A$  with radial distance is depicted in green. Importantly this figure shows the difficulty in capturing the dynamics of multidimensional flows with a one-dimensional relationship. In reality, and for the MHD models explored throughout this thesis, the Alfvén surface is not spherical and so the best “spherical” value for a given surface must be found numerically.

on either; 1) the surface magnetic field strength, or 2) the open magnetic flux in the wind.

From previous simulation results,  $R_A$  is generally located in the open-field region, so here it is assumed that  $R_A > R_o$ . The field strength at the Alfvén radius  $B_A$  is then given by,

$$B_A = B_o \left( \frac{R_o}{R_A} \right)^2 = B_* \left( \frac{R_*}{R_o} \right)^{l+2} \left( \frac{R_o}{R_A} \right)^2. \quad (2.128)$$

As the flow is ideal, the magnetic flux  $\Phi$  and mass-loss rate  $\dot{M}$ , are conserved quantities

along the magnetic flux tube (stellar wind),

$$\Phi_A = 4\pi R_A^2 B_A = 4\pi R_o^2 B_o = \Phi_{open}, \quad (2.129)$$

$$\dot{M} = \rho v_r A = \begin{cases} \rho v_r 4\pi R_o^2 \left(\frac{r}{R_o}\right)^{l+2}, & \text{for } r < R_o, \\ \rho v_r 4\pi r^2, & \text{for } r \geq R_o. \end{cases} \quad (2.130)$$

To derive a relationship for  $R_A$  based on the surface field strength  $B_*$ , I begin with the Alfvén speed  $v_A$  squared, and substitute the relation for  $B_A$  in terms of the surface field strength  $B_*$ ,

$$v_A^2 = \frac{B_A^2}{4\pi\rho_A} = \frac{\left[B_* \left(\frac{R_*}{R_o}\right)^{l+2} \left(\frac{R_o}{R_A}\right)^2\right]^2}{4\pi\rho_A}. \quad (2.131)$$

This relation is then rearranged, and  $\dot{M} = \rho_A v_A 4\pi R_A^2$  is substituted into the denominator,

$$\begin{aligned} v_A &= \frac{B_*^2 \left(\frac{R_*}{R_o}\right)^{2l+4} \left(\frac{R_o}{R_A}\right)^4}{4\pi\rho_A v_A} = \frac{B_*^2 \left(\frac{R_*}{R_o}\right)^{2l+2} \left(\frac{R_o}{R_A}\right)^2 \left(\frac{R_*}{R_A}\right)^2}{\dot{M}/R_A^2} \\ &= \frac{B_*^2 R_*^2 \left(\frac{R_*}{R_o}\right)^{2l+2} \left(\frac{R_o}{R_A}\right)^2}{\dot{M}}. \end{aligned} \quad (2.132)$$

Further rearranging for  $R_A$ ,

$$\left(\frac{R_A}{R_*}\right)^2 \left(\frac{R_o}{R_*}\right)^{2l} = \left(\frac{R_A}{R_*}\right)^2 \left(\frac{R_A}{R_o}\right)^{2l} \left(\frac{R_o}{R_*}\right)^{2l} = \frac{B_*^2 R_*^2}{\dot{M} v_A}, \quad (2.133)$$

and defining the wind magnetisation  $\Upsilon = B_*^2 R_*^2 / (\dot{M} v_{esc})$ , where  $v_{esc} = \sqrt{2GM_*/R_*}$  is the surface escape speed, leads to,

$$\left(\frac{R_A}{R_*}\right)^{2l+2} \left(\frac{R_o}{R_A}\right)^{2l} = \Upsilon \frac{v_{esc}}{v_A}. \quad (2.134)$$

This final equation relates  $R_A$  to  $\Upsilon$ , but there are some unknowns i.e. the ratio of  $R_o/R_A$ , and the flow speed at  $R_A$ . Typically,  $R_o/R_A$  is assumed to be constant (or has a dependence

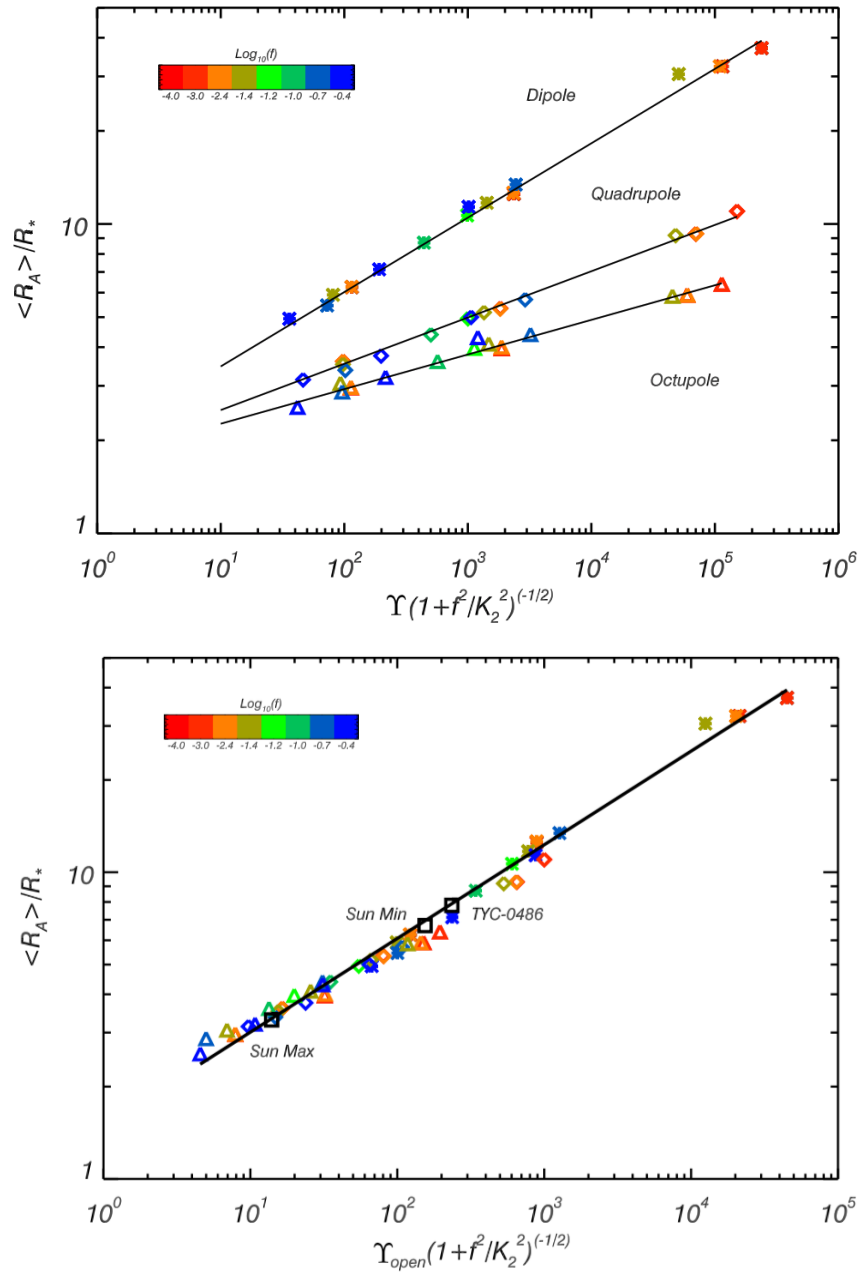


**Figure 2.11:** Top: Alfvén radius  $R_A$  versus wind magnetisation  $\Upsilon$  for stellar winds with dipolar, quadrupolar and octupolar magnetic fields. Coloured symbols represent the rotation rate of the stars (using the fraction of break-up speed  $f$ ), which are accounted for with the additional term  $(1 + f^2 / K_2^2)^{-1/2}$ . For a given surface magnetic field strength and mass-loss rate, increasing the complexity of the field reduces the size of  $R_A$  i.e. weakens the strength of magnetic braking. Bottom: Alfvén radius  $R_A$  versus open-flux wind magnetisation  $\Upsilon_{open}$  for the stellar winds in the top panel. There is still a slight spread in values, which is likely caused by variation in the wind acceleration profiles between the different magnetic topologies, see Section 3.4. Taken from Réville et al. (2015a).

on  $\Upsilon$  that can be accounted for), and  $v_A$  is parameterised as,

$$\frac{v_A}{v_{esc}} \propto \left( \frac{R_A}{R_*} \right)^q. \quad (2.135)$$



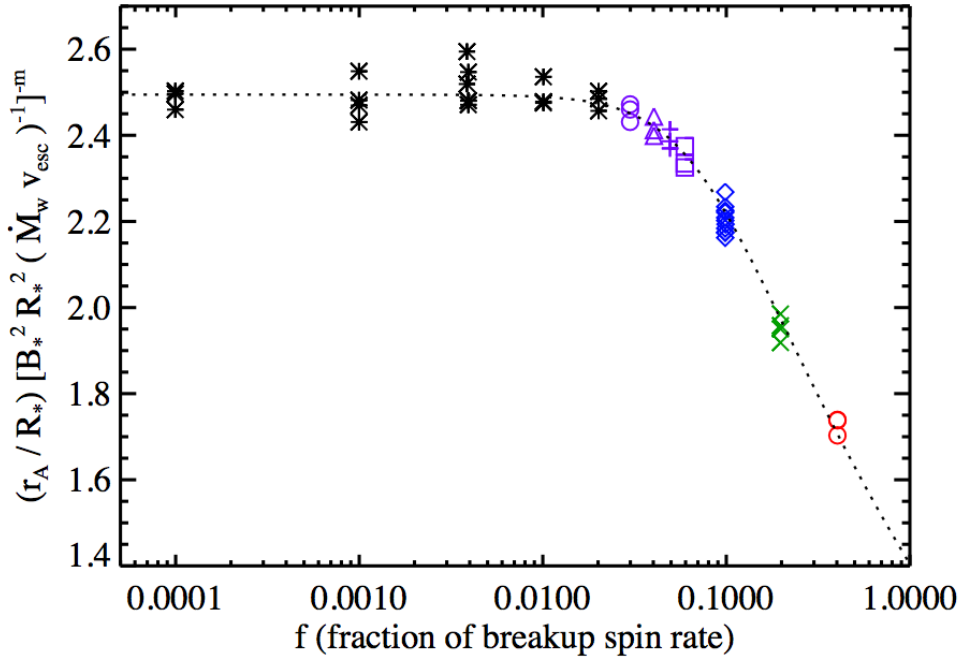


**Figure 2.12:** Alfvén radius divided by  $\Upsilon^{1/(2l+2)}$ , versus increasing rotation rate (in units of the break-up speed  $f$ ). Neglecting rotation, the residual of this division should be  $(v_{esc}/v_A)^{1/(2l+2)}$ , however centrifugal forces change this relation to  $(v_{esc}(1 + f^2/K^2)^{-1/2}/v_A)^{1/(2l+2)}$ , which is plotted with a dashed line. The difference from this and the previous relationship are negligible up to around  $f = 0.03$ . Taken from Matt et al. (2012).

This relation is further discussed in the Appendix of the published paper in Section 3.3.

Using these assumptions, equation (2.134) can be written as,

$$\frac{R_A}{R_*} \propto \left( \Upsilon \frac{v_{esc}}{v_A} \right)^{1/(2l+2)} \propto \Upsilon^{1/(2l+2+q)}, \quad (2.136)$$

which is the relation typically used to parameterise simulation results (see Réville et al. 2015a; Pantolmos and Matt 2017). The fit proportionality constants contain information about the multi-dimensional nature of the flow, and so deviate slightly from what would be expected analytically. The scaling of  $R_A$  versus  $\Upsilon$  for stellar winds with dipolar, quadrupolar and octupolar magnetic fields are shown in the top panel of Figure 2.11. Notice that the simulations in Figure 2.11 use a variety of rotation rates, which modify the scaling due to the magnetocentrifugal effect. Matt et al. (2012) parameterised this by changing the wind speed used in the denominator of the wind magnetisation,

$$v_{new}^2 = v_{esc}^2 + \frac{2\Omega_*^2 R_*^2}{K^2} = v_{esc}^2 (1 + f^2/K^2), \quad (2.137)$$

where  $f = \Omega_* R_* / \sqrt{GM_* / R_*}$  is the fraction of break-up velocity, and  $K$  is a fit parameter to the wind simulations (Réville et al. 2015a). This factor is already incorporated into Figure 2.11. Centrifugal forces only become significant at the strongest rotation rates (i.e.  $f > 0.03$ ), see Figure 2.12 where the functional form of equation (2.137) is shown with a dashed line (in good agreement with the simulation results).

A similar scaling relation can be derived in terms of the open magnetic flux  $\Phi_{open}$ , which is independent of the complexity of the coronal magnetic field  $l$ . However, it is less applicable to the study of other stars, where the open magnetic flux cannot be evaluated. Starting again with substituting the field strength at  $R_A$  in the relation for  $v_A^2$ ,

$$v_A^2 = \frac{B_A^2}{4\pi\rho_A} = \frac{\left[ B_o \left( \frac{R_o}{R_A} \right)^2 \right]^2}{4\pi\rho_A}, \quad (2.138)$$

which is rearranged,

$$v_A^2 = \frac{1}{(4\pi)^2} \frac{(4\pi)^2 B_o^2 R_o^4 / R_*^2 \left( \frac{R_*}{R_A} \right)^2}{4\pi\rho_A R_A^2}, \quad (2.139)$$

such that the open magnetic flux  $\Phi_{open} = 4\pi B_o R_o^2$  can be substituted, along with  $\dot{M}$ ,

$$v_A = \frac{1}{(4\pi)^2} \frac{\Phi_{open}^2 / R_*^2 \left( \frac{R_*}{R_A} \right)^2}{\dot{M}}. \quad (2.140)$$

Finally, by defining the open-flux wind magnetisation as  $\Upsilon_{open} = \Phi_{open}^2 / R_*^2 / (\dot{M} v_{esc})$ , a relation for  $R_A$  is produced,

$$\left( \frac{R_A}{R_*} \right)^2 = \frac{1}{(4\pi)^2} \frac{\Phi_{open}^2 / R_*^2}{\dot{M} v_A} = \frac{1}{(4\pi)^2} \Upsilon_{open} \frac{v_{esc}}{v_A}. \quad (2.141)$$

As with the surface field strength formulation, by using equation (2.135), the scaling of  $R_A$  in terms of  $\Upsilon_{open}$  is given by,

$$\frac{R_A}{R_*} \propto \left( \Upsilon_{open} \frac{v_{esc}}{v_A} \right)^{1/2} \propto \Upsilon_{open}^{1/(2+q)}. \quad (2.142)$$

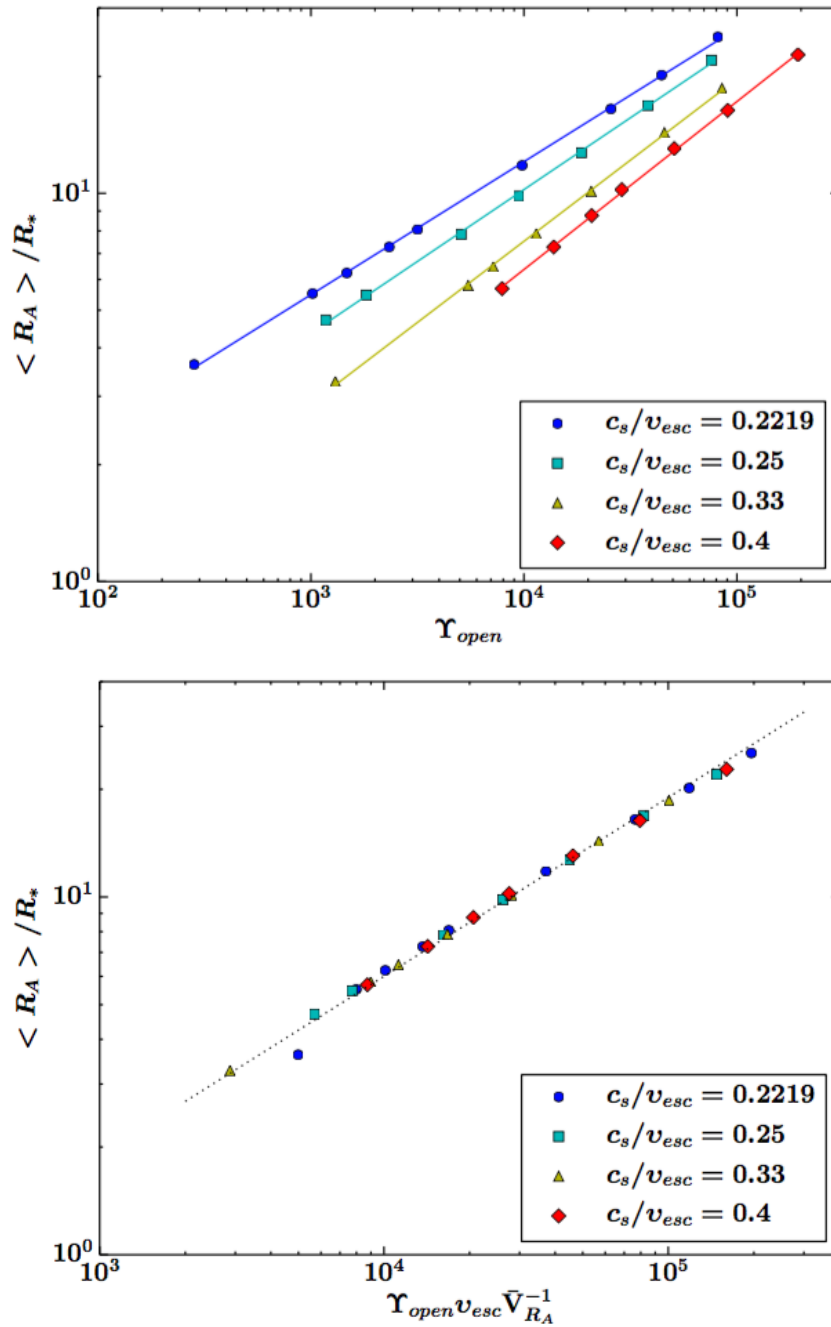


**Figure 2.13:** Top: Alfvén radius  $R_A$  versus open-flux wind magnetisation  $\Upsilon_{open}$  for stellar winds with different wind-driving temperatures. All simulations use a dipolar magnetic field configuration. For a given open magnetic flux and mass-loss rate, increasing the temperature of the wind reduces the size of  $R_A$ . Bottom: Alfvén radius  $R_A$  versus open-flux wind magnetisation  $\Upsilon_{open}$  including the average wind speed at the Alfvén radius  $\langle v_A \rangle$ , calculated from the simulations. This additional factor collapses all the wind simulations onto a single scaling relation. Therefore the open magnetic flux, mass-loss rate, and stellar wind acceleration are significant factors that affect the efficiency of magnetic braking in low-mass stars. Taken from Pantolmos and Matt (2017).

For the wind simulations shown in Figure 2.11, this relation collapses the data points onto a relatively tight sequence (see bottom panel). However, the simulations from Réville et al. (2015a) are all driven by the same thermal wind temperature, unlike the simulations from

Pantolmos and Matt (2017) which are shown in the top panel of Figure 2.13. Changes to the thermal driving consequently affects the value of  $v_A$ , and so changes the fit parameters needed to explain the wind simulations. By evaluating the average wind speed at the Alfvén radius  $\langle v_A \rangle$ , Pantolmos and Matt (2017) were able to show that equation (2.142) is able to describe all of their simulation results (see bottom panel of Figure 2.13).

One-dimensional semi-analytic theory is able to explain the results of MHD wind simulations that include different pure magnetic geometries, differing rotation rates and a variety of thermal wind driving temperatures. It is likely that these results are also true in combination, i.e. the scaling of an octupole stellar wind with a range of thermal-driving will be adequately described by the mathematics of this Section. However, the magnetic fields of low-mass stars are not simply one magnetic geometry, instead containing multiple magnetic components. In this case, which component produces the dominant scaling? Where would a mixed geometry magnetic field be located in Figures 2.11 and 2.13?

### 2.5.5 Conserved Quantities in Stationary Ideal Magnetohydrodynamic Flows

For the idealised simulations conducted in this work, through Chapter 3 and 7, there are some fundamental quantities that are conserved along magnetic field lines. This means they satisfy,

$$\mathbf{B} \cdot \nabla \alpha = 0, \quad (2.143)$$

where  $\alpha$  is the conserved quantity. These quantities are as follows,

$$\kappa = \rho \frac{v_p}{B_p}, \quad (2.144)$$

$$\Lambda = r \sin \theta \left( v_\phi - \frac{B_\phi}{4\pi\kappa} \right), \quad (2.145)$$

$$\Omega_{eff} = \frac{1}{r \sin \theta} \left( v_\phi - \frac{\kappa B_\phi}{\rho} \right), \quad (2.146)$$

$$E_T = \frac{v^2}{2} + \frac{\gamma}{\gamma - 1} \frac{p}{\rho} - \frac{GM_*}{r} + r \sin \theta \Omega_{eff} \frac{\rho B_\phi}{\kappa}, \quad (2.147)$$

$$S = p \rho^{-\gamma}, \quad (2.148)$$

where  $\kappa$  is the mass flux per field strength,  $\Lambda$  is the specific angular momentum flux,  $\Omega_{eff}$  is the effective rotation rate of the flow,  $E_T$  is the Bernoulli's equation for energy, and  $S$  is the entropy of the plasma. These quantities are derived in Appendix B.

## 2.6 Thesis Outline

In this thesis, I develop magnetohydrodynamic models of stellar winds that include more complex magnetic geometries than previous works, which favoured single magnetic geometries. These are then used to develop semi-analytic prescriptions for stellar angular momentum-loss rates, referred to as “braking laws” (Chapter 3). I apply my semi-analytic braking laws to a variety of observationally motivated cases in order to examine the effect of variable magnetic activity on angular momentum-loss rates. Using both remote sensing observations of the Sun’s photospheric magnetic field and in-situ measurements of the solar wind, I calculate the braking torque due to the solar wind over  $\sim 20$  years (Chapter 4). Additionally, 61 Cyg A,  $\epsilon$  Eri,  $\xi$  Boo A and  $\tau$  Boo A have all been observed with the Zeeman-Doppler imaging technique over multiple epochs such that the variation of their large scale magnetic fields has been mapped. This is combined with estimated mass-loss rates from astrospheric Lym- $\alpha$  observations, for all but tau Boo A, such that their time-varying angular momentum-loss rates can be calculated (Chapter 4). For the Sun and these four stars, I find a discrepancy between my semi-analytic braking law and the angular momentum-loss rates expected by current rotational evolution models (mine being a factor of 2-30 smaller). To begin ruling out further temporal variability as the cause of this discrepancy, I calculate the solar angular momentum-loss rate using reconstructions of solar activity from cosmogenic radioisotopes records (which span around 9000 years), and show no evidence for an increased angular momentum-loss rate over this timescale (Chapter 5). An attempt is made to directly measure the angular momentum content of the solar wind using in-situ measurements from the *Wind* spacecraft, which appears to support the result from my braking law (Chapter 6). This work continues and is the focus of current and future collaborations with Parker Solar Probe and Solar Orbiter, two spacecraft that will venture closer to the Sun than any other man-made objects, collecting in-situ

---

measurements of the solar wind which may shed light on the true angular momentum-loss rate. Finally, the braking laws are revised to include the effect of non-axisymmetric magnetic geometries, for which I perform some 3D magnetohydrodynamic simulations (Chapter 7).

## Chapter 3

# The Effect of Combined Magnetic Geometries on Thermally Driven Winds

### 3.1 Introduction

From Section 2.5.4, the angular momentum-loss rates of thermally-driven winds that contain a single magnetic geometry (i.e. dipole, quadrupole, etc) with a known wind acceleration profile are well described by semi-analytic theory. However some open questions remain, e.g. the effect of more realistic magnetic geometries. As an example, the Sun's photospheric magnetic field is observed to be far more complex than just a dipole, with small scale active regions in addition to an organised large-scale field that evolves during the 11-year solar activity cycle (DeRosa et al. 2012; Vidotto et al. 2018). This is reflected in the large-scale morphology of the solar wind seen through coronagraph images (see Figure 3.1, Michels et al. 1988; Lamy et al. 2019), or during total solar eclipses (e.g. Mikić et al. 2018). The magnetic fields of other Sun-like stars have also been studied through the Zeeman-Doppler imaging technique (ZDI, discussed further in Chapter 4), which resolves their large-scale magnetic fields, and shows that their surface magnetic fields contain a variety of geometries that evolve in time (Petit et al. 2009; Morgenthaler et al. 2012;

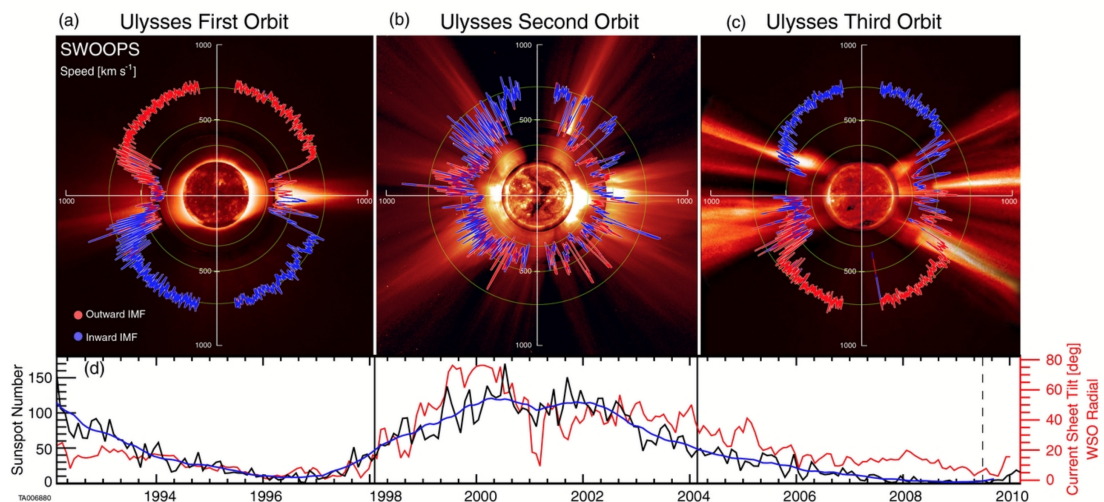


**Figure 3.1:** Variation of the large-scale solar wind during the Ulysses mission. Top panel shows the average wind speed and magnetic field polarity versus latitude for each orbit, over the top of coronagraph images of the Sun taken by the Large Angle and Spectrometric Coronagraph (LASCO) onboard the Solar and Heliospheric Observatory (SOHO) spacecraft during the corresponding time periods. Bottom panel shows the solar activity cycle in sunspot number and the inclination of the Heliospheric Current Sheet. Taken from McComas et al. (2013).

Jeffers et al. 2014; Saikia et al. 2016; Jeffers et al. 2017, 2018; Saikia et al. 2018a). In order to apply semi-analytic theory to these observed magnetic fields, it is first important to understand how combinations of the simplest large-scale magnetic field geometries (dipole, quadrupole, and octupole) modify the relationships gained from studying isolated magnetic geometries. In this Chapter, I begin with an overview of the PLUTO MHD code which I use to simulate stellar winds with a variety of combined magnetic fields. The results from which, appear as they were published in *The Astrophysical Journal*. Following this, I present some additional details/figures that were left out of the papers, and finally I summarise the results from this Chapter in the context of the overall thesis.

## 3.2 The PLUTO Magnetohydrodynamic Code

PLUTO is a versatile shock capturing code, written in *c* (Mignone et al. 2007; Mignone 2009), designed to evolve the HD or MHD equations (including their relativistic extensions) on a static or adaptive grid. For readers that are not well-versed in computational fluid dynamics, Appendix C.2 contains some introductory examples of finite difference methods that illustrate the general concepts that will be discussed in this Section. The



PLUTO code is highly modular in structure, meaning pieces of code can be included (or excluded) to suit the system under study. PLUTO exploits a finite volume formalism to evolve the HD or MHD equations in conservative form i.e.,

$$\frac{\partial U}{\partial t} + \nabla \cdot F = S, \quad (3.1)$$

where  $U$ ,  $F$ , and  $S$  represent conserved quantities, flux variables and source terms respectively. For this Chapter, PLUTO is used to solve the ideal MHD equations (see Section 2.2 for more information), which correspond to,

$$U = \begin{bmatrix} \rho \\ \rho \mathbf{v} \\ E \\ \mathbf{B} \end{bmatrix}, \quad F = \begin{bmatrix} \rho \mathbf{v} \\ \rho \mathbf{v} \mathbf{v} - \mathbf{B} \mathbf{B} + \mathbf{I} p_T \\ (E + p_T) \mathbf{v} - \mathbf{B} (\mathbf{v} \cdot \mathbf{B}) \\ \mathbf{v} \mathbf{B} - \mathbf{B} \mathbf{v} \end{bmatrix}^T, \quad S = \begin{bmatrix} 0 \\ \rho \mathbf{g} \\ \rho \mathbf{v} \cdot \mathbf{g} \\ 0 \end{bmatrix}, \quad (3.2)$$

where  $\rho$  is the mass density,  $\mathbf{v}$  is the velocity field,  $\mathbf{g}$  is the gravitational acceleration,  $\mathbf{B}$  is the magnetic field<sup>1</sup>,  $p_T = p + B^2/2$  is the combined thermal and magnetic pressure,  $\mathbf{I}$  is the identity matrix, and  $E = \rho \epsilon + \rho \mathbf{v}^2/2 + \mathbf{B}^2/2$  is the total energy density, with  $\epsilon$  representing the internal energy per unit mass of the fluid. Note the MHD equations require a closing equation of state (EoS), which here is taken to be the ideal gas law i.e.  $\rho \epsilon = p/(\gamma - 1)$ , where  $\gamma$  represents the ratio of specific heats.

In a finite volume discretisation, the domain is decomposed into control volumes (or grid cells) whose properties are known only as a volume-average i.e.,

$$\langle U \rangle_i^n = \frac{1}{\Delta x} \int_{x_{i-\frac{1}{2}}}^{x_{i+\frac{1}{2}}} U(x, t^n) dx, \quad (3.3)$$

where the control volume (in one dimension) denoted  $i$  has cell faces at  $i - 1/2$  and  $i + 1/2$ , see Figure 3.2. These volume-averages are evolved by considering the fluxes through each cell interface. This can be derived mathematically by considering first the differential form

1. The PLUTO code operates with a factor of  $1/\sqrt{4\pi}$  absorbed into the normalisation of  $\mathbf{B}$ .

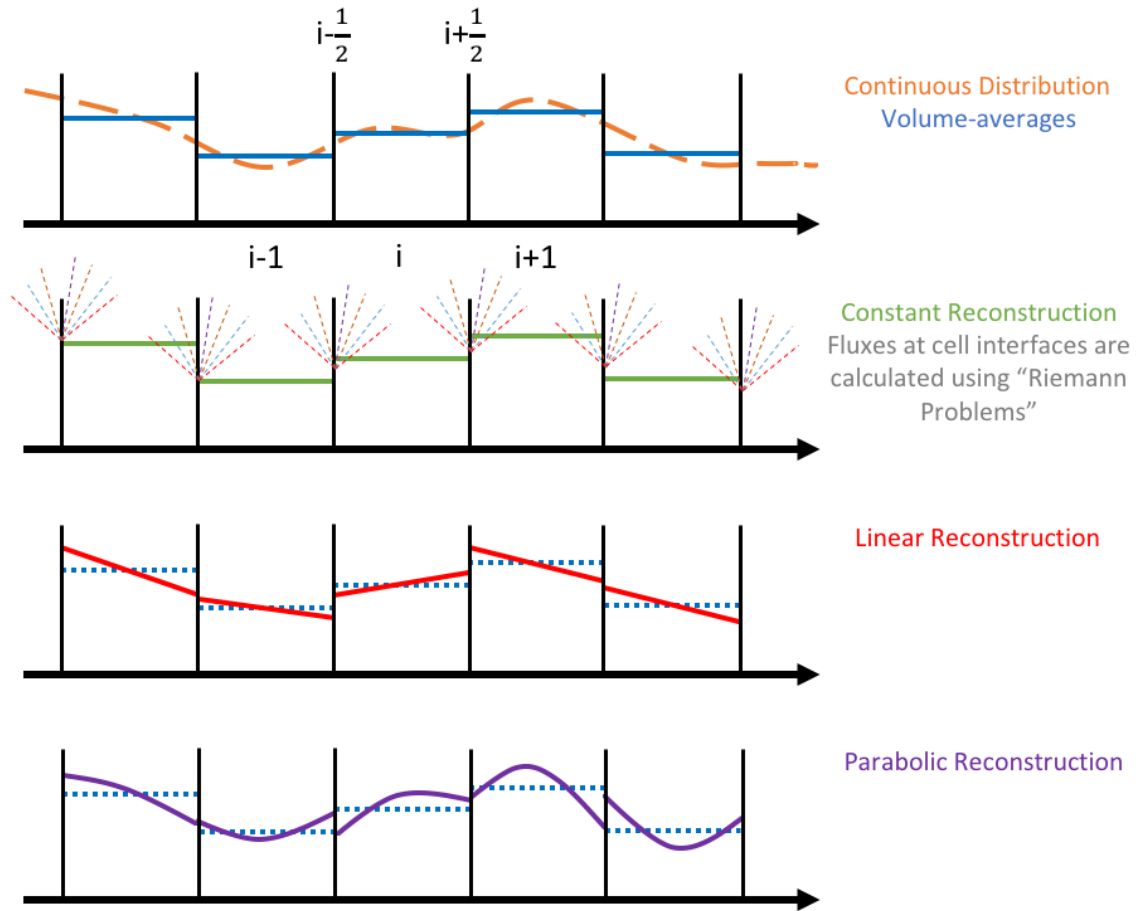


**Figure 3.2:** Finite volume discretisation of the orange dashed function, volume averages are shown at the top of the Figure (solid blue lines). In order to compute the fluxes through the cell faces, Riemann problems are solved at the cell interfaces. This requires knowledge that is removed by averaging over each cell volume. The bottom three examples show different reconstructions from the volume-averaged value, located at the cell centre.

of equation (3.1) in one dimension (ignoring source terms),

$$\frac{\partial U}{\partial t} + \frac{\partial F}{\partial x} = 0 \quad \Longrightarrow \quad \int_{t_n}^{t^{n+1}} \int_{x_{i-\frac{1}{2}}}^{x_{i+\frac{1}{2}}} \left( \frac{\partial U}{\partial t} + \frac{\partial F}{\partial x} \right) dx dt = 0, \quad (3.4)$$

when integrated over a time interval of  $\Delta t = t^{n+1} - t^n$  and a cell size of  $\Delta x = x_{i+\frac{1}{2}} - x_{i-\frac{1}{2}}$  this gives an integral form of discretisation,

$$\langle U \rangle_i^{n+1} = \langle U \rangle_i^n - \frac{\Delta t}{\Delta x} \left( \tilde{F}_{i+\frac{1}{2}}^n - \tilde{F}_{i-\frac{1}{2}}^n \right), \quad (3.5)$$

where,

$$\tilde{F}_{i+\frac{1}{2}}^n = \frac{1}{\Delta t} \int_{t_n}^{t^{n+1}} F(x_{i+\frac{1}{2}}, t) dt, \quad (3.6)$$

is the integrated flux through the  $i + 1/2$  cell interface. This method exactly evolves the

volume-averages of  $U$ , however the fluxes between cells are unknown. To find these fluxes, the PLUTO code solves “Riemann problems” at every cell interface, i.e. the temporal evolution of an initial discontinuity separating two constant states. The Riemann problem is defined by the initial condition,

$$U(x, 0) = \begin{cases} U_L, & \text{for } x < x_{i+\frac{1}{2}}, \\ U_R, & \text{for } x > x_{i+\frac{1}{2}}, \end{cases} \quad (3.7)$$

where the value of  $U(x_{i+\frac{1}{2}}, t > 0)$  is to be found. The evolution of this problem is exactly known for the HD case and is approximated by Riemann solvers for MHD. This is shown schematically in Figure 3.3, the initial discontinuity evolves into shocks and rarefactions which travel at the characteristic speeds of the system. In the HD case, this corresponds to a forwards and backwards propagating sound wave and an entropy wave. In ideal MHD this problem is more complex, with the solution of the Riemann problem following a 7 wave pattern (for the entropy wave plus the forward/backward propagating slow-magnetosonic, Alfvén, and fast-magnetosonic waves), see the diagram on the right of Figure 3.3. The flux through the cell interface is evaluated on the discontinuity between the initial states. For the wind simulations in this Chapter, the Harten, Lax, and van Leer (HLL) solver (Einfeldt 1988) is used to solve the Riemann problems at cell interfaces. Though this scheme is more numerically diffusive than others, it was found that this diffusivity acts to stabilise some of the numerically challenging features of stellar winds, such as the open-closed magnetic field boundary.

To evolve the MHD equations accurately, the Riemann problems must be provided with the left and right states, however the finite volume method only evolves volume-averaged quantities which reside at the cell centres. Therefore, error in this scheme follows from uncertainty in reconstructing the spatial variation of the function inside each control volume from its volume-averaged value. The simplest method to acquire left and right states at the cell faces, is to assume the volume-averaged value is representative of the whole control volume and use that (green lines in Figure 3.2). A slightly more sophisticated method would be to reconstruct the variation over the cell with a linear or even parabolic function, in order to more accurately portray the continuous distribution in each volume.

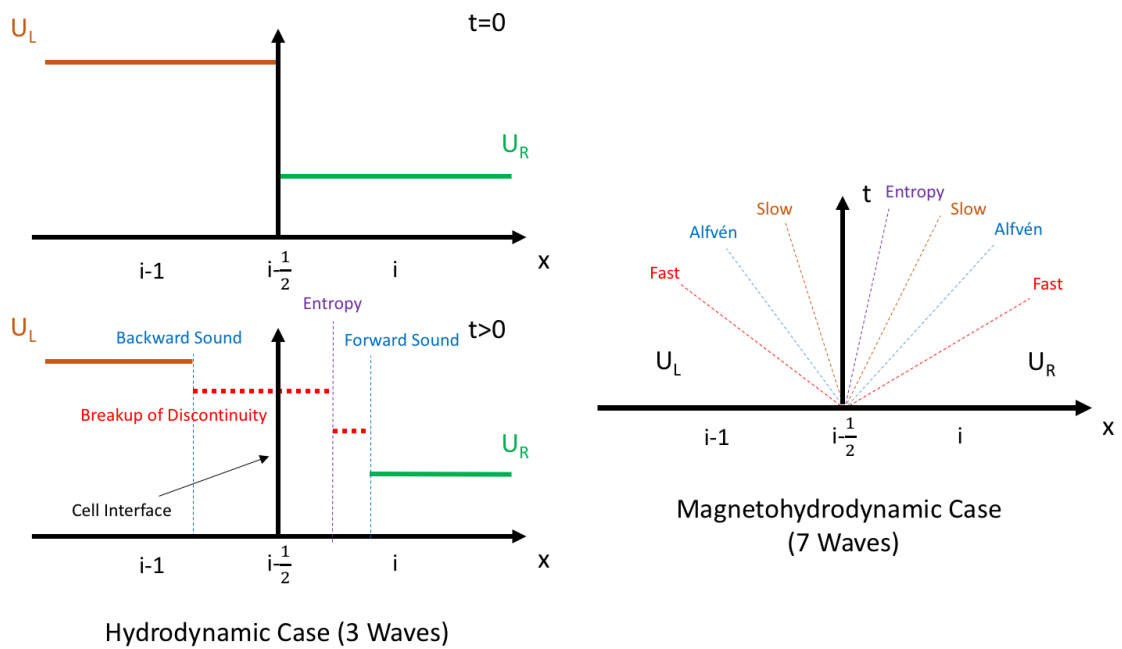


**Figure 3.3:** Left: Example of a hydrodynamic Riemann problem. Right: Schematic of the 7 waves from the magnetohydrodynamic Riemann problems evolving in time.

Linear and parabolic reconstructions are shown in the lower half of Figure 3.2. It is easy to see that these reconstructions could create slopes that are too steep and that give spurious negative values for quantities at the cell faces. To resolve this, PLUTO uses slope limiters which restrict the gradient of the reconstructions inside each cell to prevent unphysical or anomalous values at the interfaces which may leave to numerical errors or oscillatory solutions. The system of MHD equations is evolved in time using a Runge Kutta (2 or 3 step) time stepping, where the time step  $\Delta t^n$  is calculated using the Courant-Friedrichs-Lewy (CFL) number (supplied by the user) and information available in the previous time step.

For MHD cases, another constraint is produced as the magnetic field must maintain  $\nabla \cdot \mathbf{B} = 0$ , which is not automatically done by the numerical methods above. The PLUTO code has multiple schemes to enforce zero divergence of the magnetic field, two of which are used in this thesis: Hyperbolic Divergence Cleaning (Div Cleaning) (Dedner et al. 2002), and Constrained Transport (CT) (see Tóth 2000, for discussion). In Div Cleaning, the divergence free constraint is maintained by solving a modified set of the induction equation and solenoidal constraint which allow for the creation of magnetic monopoles. These monopoles are advected out of the simulation domain at the fastest admissible

speed and are also subjected to a damping throughout their time in the domain. In CT, two versions of the magnetic field are created, one at the cell-centre ( $\mathbf{B}$ ) and another staggered onto the cell faces ( $\mathbf{b}$ ), which is an area-weighted average. The electromotive force ( $\boldsymbol{\varepsilon} = -\mathbf{v} \times \mathbf{B}$ ) is calculated at the corners of the control volumes and is used to evolve the staggered magnetic field using,

$$\int \left( \frac{\partial \mathbf{b}}{\partial t} + \nabla \times \boldsymbol{\varepsilon} \right) \cdot d\mathbf{A} = 0 \quad \implies \quad \frac{db_x}{dt} + \frac{1}{A} \oint \boldsymbol{\varepsilon} \cdot d\boldsymbol{\ell} = 0, \quad (3.8)$$

where  $\mathbf{A}$  is the area of the cell interface in the  $x$  direction, and  $\boldsymbol{\ell}$  is the edge surrounding the area  $\mathbf{A}$ . This method conserves the divergence of the magnetic field at machine accuracy (which means that any initial error will propagate into the solution!). I find the CT method in PLUTO is generally more accurate than the Div Cleaning method, especially for studying time-dependent flows or instabilities. The work in this Chapter uses CT, though the work in Chapter 7 uses Div Cleaning as the current implementation of CT in PLUTO does not work with a three dimensional spherical grid geometry. Additionally, in this thesis the magnetic field used in PLUTO is split into a background component  $\mathbf{B}_0$  and a deviation  $\mathbf{B}_1$  such that the total magnetic field satisfies  $\mathbf{B} = \mathbf{B}_0 + \mathbf{B}_1$ . The background field is stationary, curl-free and satisfies the divergence constraint. The MHD equations can then be reduced in terms of  $\mathbf{B}_0$  and  $\mathbf{B}_1$ , which is computationally useful. The stellar wind solutions in this work are initialised with a potential large-scale magnetic field  $\mathbf{B}_0$  which is acted upon by the stellar wind thus creating  $\mathbf{B}_1$ .



# The Effect of Combined Magnetic Geometries on Thermally Driven Winds. I. Interaction of Dipolar and Quadrupolar Fields

Adam J. Finley  and Sean P. Matt 

University of Exeter (UK), Department of Physics & Astronomy, Stoker Road, Devon, Exeter, EX4 4QL, UK; af472@exeter.ac.uk  
Received 2017 May 18; revised 2017 July 11; accepted 2017 July 11; published 2017 August 10

## Abstract

Cool stars with outer convective envelopes are observed to have magnetic fields with a variety of geometries, which on large scales are dominated by a combination of the lowest-order fields such as the dipole, quadrupole, and octupole modes. Magnetized stellar wind outflows are primarily responsible for the loss of angular momentum from these objects during the main sequence. Previous works have shown the reduced effectiveness of the stellar wind braking mechanism with increasingly complex but singular magnetic field geometries. In this paper, we quantify the impact of mixed dipolar and quadrupolar fields on the spin-down torque using 50 MHD simulations with mixed fields, along with 10 each of the pure geometries. The simulated winds include a wide range of magnetic field strength and reside in the slow-rotator regime. We find that the stellar wind braking torque from our combined geometry cases is well described by a broken power-law behavior, where the torque scaling with field strength can be predicted by the dipole component alone or the quadrupolar scaling utilizing the total field strength. The simulation results can be scaled and apply to all main-sequence cool stars. For solar parameters, the lowest-order component of the field (dipole in this paper) is the most significant in determining the angular momentum loss.

*Key words:* magnetohydrodynamics (MHD) – stars: evolution – stars: low-mass – stars: magnetic field – stars: rotation – stars: winds, outflows

## 1. Introduction

The spin down of cool stars ( $M_* \lesssim 1.3 M_\odot$ ) is a complex function of mass and age, as shown by the increasing number of rotation-period measurements for large stellar populations (Barnes 2003, 2010; Irwin & Bouvier 2009; Agüeros et al. 2011; Meibom et al. 2011; McQuillan et al. 2013; Bouvier et al. 2014; Stauffer et al. 2016; Davenport 2017). The observed properties of these stars show a wide range of mass-loss rates, coronal temperatures, field strengths, and geometries, which all connect with stellar rotation to control the loss of angular momentum (Reiners & Mohanty 2012; Gallet & Bouvier 2013; Van Saders & Pinsonneault 2013; Brown 2014; Gallet & Bouvier 2015; Matt et al. 2015; Amard et al. 2016; Blackman & Owen 2016). Despite the wide range of interlinking stellar properties, an overall trend of spin down with an approximately Skumanich law is observed at late ages:  $\Omega_* \propto \tau^{-0.5}$  (Skumanich 1972; Soderblom 1983).

For Sun-like stars on the main sequence, the spin-down process is governed primarily by their magnetized stellar winds, which remove angular momentum over the star's lifetime. Parker (1958) originally posited that stellar winds must exist due to the thermodynamic pressure gradient between the high-temperature corona and interplanetary space. Continued solar observations have constrained theoretical models for the solar wind to a high degree of accuracy (Usmanov et al. 2014; van der Holst et al. 2014; Oran et al. 2015). Recent models of the solar wind are beginning to accurately reproduce the energetics within the corona and explain the steady outflow of plasma into the heliosphere (e.g., Grappin et al. 1983; Van der Holst et al. 2010; Pinto et al. 2016). The wind driving is now known to be much more complex than a thermal pressure gradient, with authors typically heating the wind through the dissipation of Alfvén waves in the corona. Other cool stars are observed with X-ray emissions indicating hot stellar

coronae like that of the Sun (Rosner et al. 1985; Wright et al. 2004; Wolk et al. 2005; Hall et al. 2007). Similar stellar winds and wind heating mechanisms are therefore expected to exist across a range of Sun-like stars. Assuming equivalent mass-loss mechanisms, results from the solar wind are incorporated into more general stellar wind modeling efforts (e.g., Cohen & Drake 2014; Alvarado-Gómez et al. 2016).

Detailed studies of wind-driving physics remain computationally expensive to run and so are usually applied on a case-by-case basis. How applicable the heating physics gained from modeling the solar wind is to other stars is still in question. With the reliability of such results even for the global properties of a given star in question, large-parameter studies with simpler physics remain useful. A more general method can allow for parameterizations that are more appropriate to the variety of stellar masses and rotation periods found in observed stellar populations. Parker-type solutions remain useful for this due to their simplicity and versatility (Parker 1965; Mestel 1968; Sakurai 1990; Keppens & Goedbloed 1999). In these solutions, wind plasma is accelerated from the stellar surface and becomes transonic at the sonic surface. With the addition of magnetic fields, the wind also becomes trans-Alfvénic, i.e., faster than the Alfvén speed, at the Alfvén surface. Weber & Davis (1967) showed for a one-dimensional magnetized wind that the Alfvén radius represented a lever arm for the spin-down torque. Since the introduction of this result, many researchers have produced scaling laws for the Alfvén radius (Mestel 1984; Kawaler 1988; Matt & Pudritz 2008; Ud-Doula et al. 2009; Pinto et al. 2011; Matt et al. 2012; Réville et al. 2015a), all of which highlight the importance of the magnetic field strength and mass-loss rate in correctly parameterizing a power-law dependence. In such formulations, the mass-loss rate is incorporated as a free parameter, as the physical mechanisms that determine it are not yet completely

understood. Measuring the mass-loss rate from Sun-like stars is particularly difficult due to the wind's tenuous nature and poor emission. Wood (2004) used  $\text{Ly}\alpha$  absorption from the interaction of stellar winds and their local interstellar medium to measure mass-loss rates, but the method is model-dependent and only available for a few stars. Theoretical work from Cranmer & Saar (2011) predicts the mass-loss rates from Sun-like stars, but it is uncertain if the physics used within the model scales correctly between stars. Therefore, parameter studies where the mass-loss rate is an unknown parameter are needed.

In addition to the mass-loss rate, the angular momentum loss rate is strongly linked with the magnetic properties of a given star. Frequently, researchers assume the dipole component of the field to be the most significant in governing the global wind dynamics (e.g., Ustyugova et al. 2006; Zanni & Ferreira 2009; Gallet & Bouvier 2013; Cohen & Drake 2014; Gallet & Bouvier 2015; Johnstone et al. 2015; Matt et al. 2015). Zeeman Doppler imaging (ZDI) studies (e.g., Morin et al. 2008; Petit et al. 2008; Fares et al. 2009; Jeffers et al. 2014; Vidotto et al. 2014a; See et al. 2015, 2016, 2017; Folsom et al. 2016; Hébrard et al. 2016) provide information on the large-scale surface magnetic fields of active stars. Observations have shown stellar magnetic fields to be much more complex than simple dipoles, containing combinations of many different field modes. ZDI is a topographic technique that typically decomposes the field at the stellar surface into individual spherical harmonic modes. The 3D field geometry can then be recovered with field extrapolation techniques using the ZDI map as an inner boundary. Several studies have considered how these observed fields affect the global wind properties. Typically used to determine an initial 3D field solution, a magnetohydrodynamics (MHD) code then evolves this initial state in time until a steady-state solution for the wind and magnetic field geometry is attained (e.g., Cohen et al. 2011; Vidotto et al. 2011; Alvarado-Gómez et al. 2016; do Nascimento et al. 2016; Garraffo et al. 2016a; Nicholson et al. 2016; Réville et al. 2016). These works are less conducive to the production of semianalytical formulations, as the principal drivers of the spin-down process are hidden within complex field geometries, rotation, and wind-heating physics.

A few studies show systematically how previous torque formulations depend on magnetic geometry using single modes. Réville et al. (2015a) explored thermally driven stellar winds with dipolar, quadrupolar, and octupolar field geometries. They concluded that higher-order field modes produce a weaker torque for the same field strength and mass loss, which is supported by results from Garraffo et al. (2016b). Despite these studies and works like them, only one study has systematically scaled the mass-loss rate for a mixed geometry field (Strugarek et al. 2014a). However, the aforementioned studies of the angular momentum loss from Sun-like stars have yet to address the systematic addition of individual spherical harmonic field modes.

Mixed geometry fields are observed within our closest star, the Sun, which undergoes an 11 yr cycle oscillating between dipolar and quadrupolar field modes from cycle minimum to maximum, respectively (DeRosa et al. 2012). Observed Sun-like stars also exhibit a range of spherical harmonic field combinations. Simple magnetic cycles are observed using ZDI. Both HD 201091 (Saikia et al. 2016) and HD 78366 (Morgenthaler et al. 2012) show combinations of the dipole,

quadrupole, and octupole field modes oscillating similarly to the solar field. Other cool stars exist with seemingly stochastic changing field combinations (Petit et al. 2009; Morgenthaler et al. 2011). The observed magnetic geometries all contain combinations of different spherical harmonic modes with a continuous range of mixtures; it is unclear what impact this will have on the braking torque.

In this study, we investigate the significance of the dipole field when combined with a quadrupolar mode. We focus on these two field geometries, which are thought to contribute in antiphase to the solar cycle and perhaps more generally to stellar cycles in cool stars. Section 2 covers the numerical setup with a small discussion of the magnetic geometries for which we develop stellar wind solutions. Section 3 presents the main simulation results, including discussion of the qualitative wind properties and field structure, along with quantitative parameterizations for the stellar wind torque. We also highlight the dipole's importance in the braking and introduce an approximate scaling relation for the torque. Finally, in Section 4, we focus on the magnetic field in the stellar wind, first with a discussion of the overall evolution of the flux, then with a discussion of the open flux and opening radius within our simulations. Conclusions and thoughts for further work can be found in Section 5. The Appendix contains a short note on the wind acceleration profiles of our wind solutions.

## 2. Simulation Method

### 2.1. Numerical Setup

This work uses the MHD code PLUTO (Mignone et al. 2007; Mignone 2009), a finite-volume code that solves Riemann problems at cell boundaries in order to calculate the flux of conserved quantities through each cell. PLUTO is modular by design, capable of interchanging solvers and physics during setup. The present work uses a diffusive numerical scheme, the solver of Harten, Lax, and van Leer (HLL; Einfeldt 1988), which allows for greater numerical stability in the higher-strength magnetic field cases. The magnetic field solenoidality condition ( $\nabla \cdot \mathbf{B} = 0$ ) is maintained using the constrained transport method (See Tóth 2000 for discussion).

The MHD equations are solved in a conservative form, with each equation relating to the conservation of mass, momentum, and energy, plus the induction equation for the magnetic field:

$$\frac{\partial \rho}{\partial t} + \nabla \cdot \rho \mathbf{v} = 0, \quad (1)$$

$$\frac{\partial \mathbf{m}}{\partial t} + \nabla \cdot (\mathbf{m} \mathbf{v} - \mathbf{B} \mathbf{B} + \mathbf{I} p_T) = \rho \mathbf{a}, \quad (2)$$

$$\frac{\partial E}{\partial t} + \nabla \cdot ((E + p_T) \mathbf{v} - \mathbf{B}(\mathbf{v} \cdot \mathbf{B})) = \mathbf{m} \cdot \mathbf{a}, \quad (3)$$

$$\frac{\partial \mathbf{B}}{\partial t} + \nabla \cdot (\mathbf{v} \mathbf{B} - \mathbf{B} \mathbf{v}) = 0. \quad (4)$$

Here  $\rho$  is the mass density,  $\mathbf{v}$  is the velocity field,  $\mathbf{a}$  is the gravitational acceleration,  $\mathbf{B}$  is the magnetic field<sup>1</sup>,  $p_T = p + \mathbf{B}^2/2$  is the combined thermal and magnetic pressure, and  $\mathbf{m} = \rho \mathbf{v}$  is the momentum density. The total energy density is written as  $E = \rho \epsilon + \mathbf{m}^2/(2\rho) + \mathbf{B}^2/2$ , with  $\epsilon$  representing the internal energy per

<sup>1</sup> The PLUTO code operates with a factor of  $1/\sqrt{4\pi}$  absorbed into the normalization of  $\mathbf{B}$ . Tabulated parameters are given in cgs units with this factor incorporated.

**Table 1**  
Input Parameters and Results from the 70 Simulations

Case	$\mathcal{R}_{\text{dip}}$	$V_A/v_{\text{esc}}$	$\langle R_A \rangle / R_*$	$\Upsilon$	$R_O / R_*$	$\Upsilon_{\text{open}}$	$\langle v(R_A) \rangle / v_{\text{esc}}$	Case	$\mathcal{R}_{\text{dip}}$	$V_A/v_{\text{esc}}$	$\langle R_A \rangle / R_*$	$\Upsilon$	$R_O / R_*$	$\Upsilon_{\text{open}}$	$\langle v(R_A) \rangle / v_{\text{esc}}$
1	1	0.1	3.06	11.1	1.31	294	0.123	36	0.3	2	5.66	2930	2.61	2040	0.242
2	1	0.3	4.19	73.2	1.88	819	0.183	37	0.3	3	6.76	6850	3.01	3460	0.283
3	1	0.5	5.05	192	2.33	1450	0.221	38	0.3	6	9.41	31200	3.8	8840	0.360
4	1	1	6.88	773	2.95	3550	0.287	39	0.3	12	13	137000	5.05	21600	0.432
5	1	1.5	8.56	1880	3.41	6530	0.334	40	0.3	24	15.7	360000	6.18	37300	0.476
6	1	2	10	3660	3.8	9970	0.367	41	0.2	0.1	2.43	10.7	1.2	120	0.078
7	1	3	12.6	9280	4.54	18100	0.414	42	0.2	0.3	2.96	72.4	1.54	245	0.109
8	1	6	18.2	43900	6.07	47000	0.463	43	0.2	0.5	3.33	190	1.76	368	0.129
9	1	12	25.1	178000	8	109000	0.544	44	0.2	1	4.04	729	2.1	701	0.163
10	1	24	29.6	452000	9.75	180000	0.543	45	0.2	1.5	4.61	1630	2.39	1070	0.187
11	0.8	0.1	2.51	11.2	1.2	245	0.114	46	0.2	2	5.09	2930	2.56	1480	0.205
12	0.8	0.3	3.89	73.5	1.76	651	0.168	47	0.2	3	5.92	6840	2.9	2390	0.240
13	0.8	0.5	4.64	192	2.1	1120	0.203	48	0.2	6	7.93	31600	3.58	5890	0.301
14	0.8	1	6.19	751	2.73	2620	0.261	49	0.2	12	10.4	129000	4.54	13500	0.392
15	0.8	1.5	7.6	1780	3.12	4690	0.305	50	0.2	24	12.6	359000	5.56	24500	0.439
16	0.8	2	8.88	3390	3.46	7210	0.339	51	0.1	0.1	2.44	10.5	1.2	121	0.079
17	0.8	3	11.1	8660	4.14	13100	0.386	52	0.1	0.3	2.95	71.3	1.54	243	0.110
18	0.8	6	16.3	41700	5.67	35000	0.463	53	0.1	0.5	3.29	188	1.76	358	0.129
19	0.8	12	22.9	183000	7.77	84500	0.531	54	0.1	1	3.92	722	2.16	652	0.164
20	0.8	24	27.9	475000	9.07	147000	0.560	55	0.1	1.5	4.41	1620	2.44	964	0.190
21	0.5	0.1	2.63	11.4	1.14	168	0.095	56	0.1	2	4.81	2890	2.61	1290	0.208
22	0.5	0.3	3.38	74.1	1.54	407	0.140	57	0.1	3	5.53	6840	2.9	2050	0.244
23	0.5	0.5	3.94	191	1.82	674	0.169	58	0.1	6	7.13	33900	3.52	4850	0.317
24	0.5	1	5.11	736	2.33	1500	0.223	59	0.1	12	8.96	149000	4.31	10300	0.376
25	0.5	1.5	6.11	1660	2.67	2510	0.259	60	0.1	24	10.5	452000	5.16	17700	0.408
26	0.5	2	7.03	3050	2.95	3740	0.289	61	0	0.1	2.47	10.2	1.2	127	0.081
27	0.5	3	8.65	7500	3.46	6670	0.334	62	0	0.3	2.98	70.3	1.59	256	0.113
28	0.5	6	12.6	36600	4.6	17900	0.407	63	0	0.5	3.33	185	1.82	377	0.134
29	0.5	12	18.3	172000	6.3	46000	0.464	64	0	1	3.96	715	2.22	682	0.168
30	0.5	24	23	485000	7.49	83300	0.519	65	0	1.5	4.44	1600	2.5	1010	0.196
31	0.3	0.1	2.46	11	1.14	124	0.077	66	0	2	4.83	2890	2.67	1350	0.214
32	0.3	0.3	3.04	73.4	1.48	268	0.109	67	0	3	5.54	6950	2.95	2150	0.252
33	0.3	0.5	3.46	191	1.71	420	0.130	68	0	6	6.98	34900	3.63	4910	0.326
34	0.3	1	4.3	733	2.1	870	0.171	69	0	12	8.46	158000	4.43	9970	0.390
35	0.3	1.5	5.03	1630	2.39	1420	0.215	70	0	24	9.65	584000	5.16	16400	0.421



unit mass of the fluid. In addition,  $\mathbf{I}$  is the identity matrix. A polytropic wind is used for this study, such that the closing equation of state takes the form  $\rho\epsilon = p/(\gamma - 1)$ , where  $\gamma$  represents the polytropic index.

We assume the wind profiles to be axisymmetric and solve the MHD equations using a spherical geometry in 2.5D; i.e., our domain contains two spatial dimensions ( $r, \theta$ ) but allows for 3D axisymmetric solutions for the fluid flow and magnetic field using three vector components ( $r, \theta, \phi$ ). The domain extends from one stellar radius ( $R_*$ ) out to  $60 R_*$  with a uniform grid spacing in  $\theta$  and a geometrically stretched grid in  $r$ , which grows from an initial spacing of 0.01 to  $1.08 R_*$  at the outer boundary. The computational mesh contains  $N_r \times N_\theta = 256 \times 512$  grid cells. These choices allow for the highest resolution near the star, where we set the boundary conditions that govern the wind profile in the rest of the domain.

Initially, a polytropic Parker wind (Parker 1965; Keppens & Goedbloed 1999) with  $\gamma = 1.05$  fills the domain, along with a superimposed background field corresponding to our chosen magnetic geometry and strength. During the time evolution, the plasma pressure, density, and poloidal components of the magnetic field ( $B_r, B_\theta$ ) are held fixed at the stellar surface, while the poloidal components of the velocity ( $v_r, v_\theta$ ) are allowed to evolve in response to the magnetic field (the boundary is held with  $dv_r/dr = 0$  and  $dv_\theta/dr = 0$ ). We then enforce the flow at the surface to be parallel to the magnetic field ( $\mathbf{v} \parallel \mathbf{B}$ ). The star rotates as a solid body, with  $B_\phi$  linearly extrapolated into the boundary and  $v_\phi$  set using the stellar rotation rate  $\Omega_*$ ,

$$v_\phi = \Omega_* r \sin \theta + \frac{v_p \cdot \mathbf{B}_p}{|\mathbf{B}_p|^2} B_\phi, \quad (5)$$

where the subscript ‘‘p’’ denotes the poloidal components ( $r, \theta$ ) of a given vector. This condition enforces an effective rotation rate for the field lines that, in steady-state ideal MHD, should be equal to the stellar rotation rate and conserved along field lines (Zanni & Ferreira 2009; Réville et al. 2015a). This ensures that the footpoints of the stellar magnetic field are correctly anchored into the surface of the star. The final boundary conditions are applied to the outer edges of the simulation. A simple outflow (zero derivative) is set at  $60 R_*$  allowing for the outward transfer of mass, momenta, and magnetic field, along with an axisymmetric condition along the rotation axis ( $\theta = 0$  and  $\pi$ ). Due to the supersonic flow properties at the outer boundary and its large radial extent compared with the location of the fast magnetosonic surface, any artifacts from the outer boundary cannot propagate upwind into the domain.

The code is run, following the MHD equations above, until a steady-state solution is found. The magnetic fields modify the wind dynamics compared to the spherically symmetric initial state, with regions of high magnetic pressure shutting off the radial outflow. In this way, the applied boundary conditions allow for closed and open regions of flow to form (e.g., Washimi & Shibata 1993; Keppens & Goedbloed 2000), as observed within the solar wind. In some cases of strong magnetic field, small reconnection events are seen, caused by the numerical diffusivity of our chosen numerical scheme. Reconnection events are also seen in G. Pantolmos & S. Matt (2017, in preparation) and discussed in their Appendix. We adopt a similar method for deriving flow quantities in cases

exhibiting periodic reconnection events. In such cases, once a quasi-steady state is established, a temporal average of quantities such as torque and mass loss are used.

Inputs for the simulations are given as ratios of characteristic speeds that control key parameters such as the wind temperature ( $c_s/v_{\text{esc}}$ ), field strength ( $v_A/v_{\text{esc}}$ ), and rotation rate ( $v_{\text{rot}}/v_{\text{kep}}$ ). Where  $c_s = \sqrt{\gamma p/\rho}$  is the sound speed at the surface,  $v_A = B_*/\sqrt{4\pi\rho}$  is the Alfvén speed at the north pole,  $v_{\text{rot}}$  is the rotation speed at the equator,  $v_{\text{esc}} = \sqrt{2GM_*/R_*}$  is the surface escape speed, and  $v_{\text{kep}} = \sqrt{GM_*/R_*}$  is the Keplerian speed at the equator. In this way, all simulations represent a family of solutions for stars with a range of gravities. As this work focuses on the systematic addition of dipolar and quadrupolar geometries, we fix the rotation rate for all of our simulations. Matt et al. (2012) showed that the nonlinear effects of rotation on their torque scaling can be neglected for slow rotators. They defined velocities as a fraction of the breakup speed,

$$f = \frac{v_{\text{rot}}}{v_{\text{kep}}} \bigg|_{r=R_*, \theta=\pi/2} = \frac{\Omega_* R_*^{3/2}}{(GM_*)^{1/2}}. \quad (6)$$

The Alfvén radius remains independent of the stellar spin rate until  $f \approx 0.03$ , after which the effects of fast rotation start to be important. For this study, a solar rotation rate is chosen ( $f = 4.46 \times 10^{-3}$ ) that is well within the slow-rotator regime. We set the temperature of the wind with  $c_s/v_{\text{esc}} = 0.25$ , higher than the  $c_s/v_{\text{esc}} = 0.222$  used in Réville et al. (2015a). This choice of higher sound speed drives the wind to slightly higher terminal speeds, which are more consistent with observed solar wind speeds. Each geometry is studied with 10 different field strengths controlled by the input parameter  $v_A/v_{\text{esc}}$ , which is defined here with the Alfvén speed on the stellar north pole (see next section). Table 1 lists all of our variations of  $v_A/v_{\text{esc}}$  for each geometry.

Due to the use of characteristic speeds as simulation inputs, our results can be scaled to any stellar parameter. For example, using solar parameters, the wind is driven by a coronal temperature of  $\approx 1.4$  MK, and our parameter space covers a range of stellar magnetic field strengths from 0.9 to 87 G over the pole. Changing these normalizations will modify this range.

## 2.2. Magnetic Field Configuration

Within this work, we consider magnetic field geometries that encompass a range of dipole and quadrupole combinations with different relative strengths. We represent the mixed fields using the ratio,  $\mathcal{R}_{\text{dip}}$ , of the dipolar field to the total combined field strength.

In this study, the magnetic fields of the dipole and quadrupole are described in the formalism of Gregory et al. (2010) using polar field strengths:

$$B_{r,\text{dip}}(r, \theta) = B_*^{l=1} \left( \frac{R_*}{r} \right)^3 \cos \theta, \quad (7)$$

$$B_{\theta,\text{dip}}(r, \theta) = \frac{1}{2} B_*^{l=1} \left( \frac{R_*}{r} \right)^3 \sin \theta, \quad (8)$$

$$B_{r,\text{quad}}(r, \theta) = \frac{1}{2} B_*^{l=2} \left( \frac{R_*}{r} \right)^4 (3 \cos^2 \theta - 1), \quad (9)$$

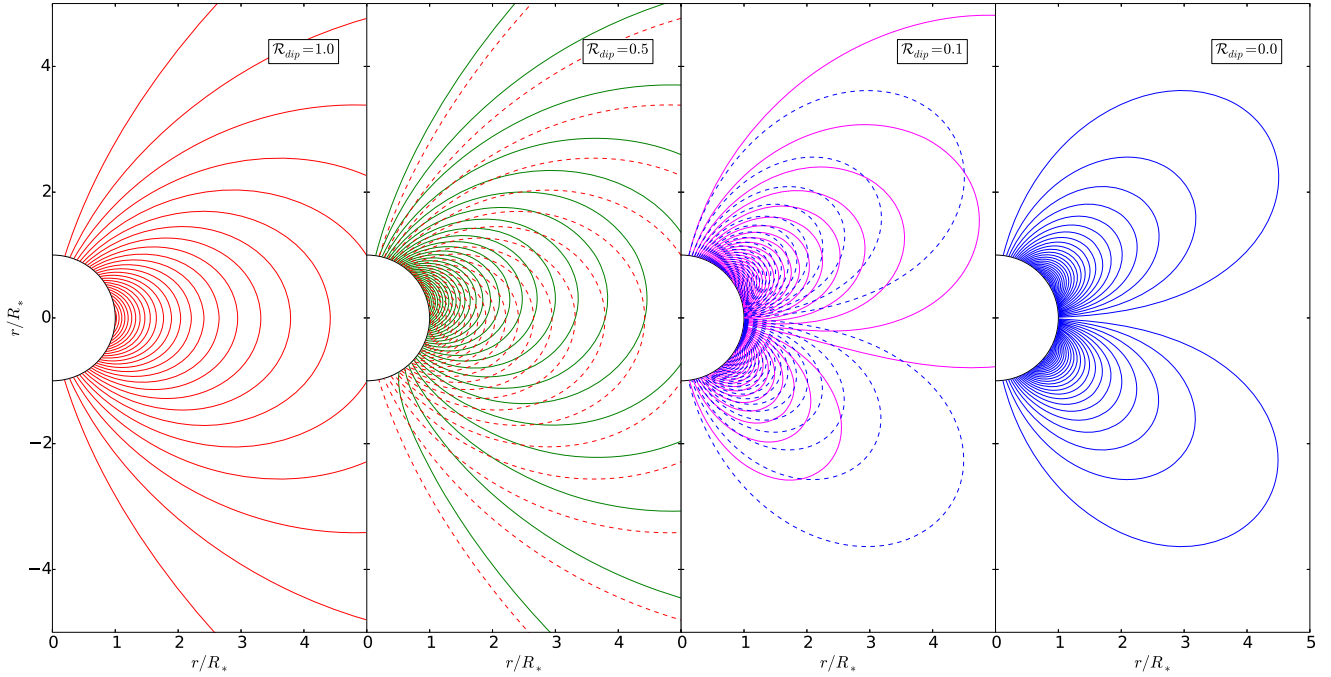


**Figure 1.** Initial magnetic configurations for a dipolar field, quadrupolar field, and two mixed cases (red, green, magenta, and blue for the dipole fractions of 100%, 50%, 10%, and purely quadrupole, respectively). Mixed cases have the dominant pure field geometry overplotted with dashed colored lines. The combined fields add in the northern hemisphere and subtract in the southern hemisphere because they belong to opposite field symmetry families. With as much as half the field strength in the quadrupole, shown in green, the topology of the field is still dominated by the dipole field.

$$B_{\theta, \text{quad}}(r, \theta) = B_*^{l=2} \left( \frac{R_*}{r} \right)^4 \cos \theta \sin \theta. \quad (10)$$

The total field, comprised of the sum of the two geometries,

$$\mathbf{B}(r, \theta) = \mathbf{B}_{\text{dip}}(r, \theta) + \mathbf{B}_{\text{quad}}(r, \theta), \quad (11)$$

where the total polar field,  $B_* = B_*^{l=1} + B_*^{l=2}$ , is controlled by the  $\mathcal{R}_{\text{dip}}$  parameter,

$$\mathcal{R}_{\text{dip}} = \frac{B_{r, \text{dip}}}{B_{r, \text{dip}} + B_{r, \text{quad}}} \Big|_{r=R_*, \theta=0} = \frac{B_*^{l=1}}{B_*}. \quad (12)$$

This work considers aligned magnetic moments such that  $\mathcal{R}_{\text{dip}}$  ranges from 1 to 0, corresponding to all the field strengths in the dipolar or quadrupolar mode, respectively. As with  $v_A/v_{\text{esc}}$ ,  $\mathcal{R}_{\text{dip}}$  is calculated at the north pole. This sets the relative strengths of the dipole and quadrupole fields,

$$B_*^{l=1} = \mathcal{R}_{\text{dip}} B_*, \quad B_*^{l=2} = (1 - \mathcal{R}_{\text{dip}}) B_*, \quad (13)$$

Alternative parameterizations are commonly used in the analysis of ZDI observations and dynamo modeling. These communities use the surface-averaged field strengths,  $\langle |B| \rangle$ , or the ratio of magnetic energy density ( $E_m \propto B^2$ ) stored within each of the dipole and quadrupole field modes at the stellar surface. During the solar magnetic cycle, values of  $B_{\text{quad}}^2/B_{\text{dip}}^2$  can range from  $\approx 10$ – $100$  at solar maximum to  $\approx 10^{-2}$  at solar minimum (DeRosa et al. 2012). A transformation from our parameter to the ratio of energies is simply given by

$$\frac{B_{\text{quad}}^2}{B_{\text{dip}}^2} = \frac{2(1 - \mathcal{R}_{\text{dip}})^2}{3\mathcal{R}_{\text{dip}}}, \quad (14)$$

where the numerical prefactor accounts for the integration of magnetic energy in each mode over the stellar surface.

Initial field configurations are displayed in Figure 1. The pure dipolar and quadrupolar cases are shown in comparison to two mixed cases ( $\mathcal{R}_{\text{dip}} = 0.5, 0.1$ ). These combined geometry fields add in one hemisphere and subtract in the other. This effect is due to the different symmetry families each geometry belongs to, with the dipole’s polarity reversing over the equator, unlike the equatorially symmetric quadrupole. Continuing the use of “primary” and “secondary” families as in McFadden et al. (1991) and DeRosa et al. (2012), we refer to the dipole as primary and quadrupole as secondary. The fields are chosen such that they align in polarity in the northern hemisphere. This choice has no impact on the derived torque or mass-loss rate due to the symmetry of the quadrupole about the equator. Either aligned or antialigned, these fields will always create one additive hemisphere and one subtracting; swapping their relative orientations simply switches the respective hemispheres. This is in contrast to combining dipole and octupole fields, where the aligned and antialigned cases cause subtraction at the equator or poles, respectively (Gregory et al. 2016; A. Finley & S. Matt 2017, in preparation).

Figure 1 indicates that even with equal quadrupole and dipole polar field strengths,  $\mathcal{R}_{\text{dip}} = 0.5$ , the overall dipole topology will remain. In this case, the magnetic energy density in the dipolar mode is 1.5 times greater than that in the quadrupolar mode coupled with the more rapid radial decay of the quadrupolar field; this explains the overall dipolar topology. A higher fraction of quadrupole is required to produce a noticeable deviation from this configuration, which is shown at  $\mathcal{R}_{\text{dip}} = 0.1$ . More than half of the parameter space that we explore lies in the range where the energy density of the quadrupole mode is greater than that of the dipole ( $B_{\text{quad}}^2/B_{\text{dip}}^2 > 1.0$ ). For this study, the pure dipolar and quadrupolar fields are used as controls (both of which were studied in detail within Réville et al. 2015a), and five mixed

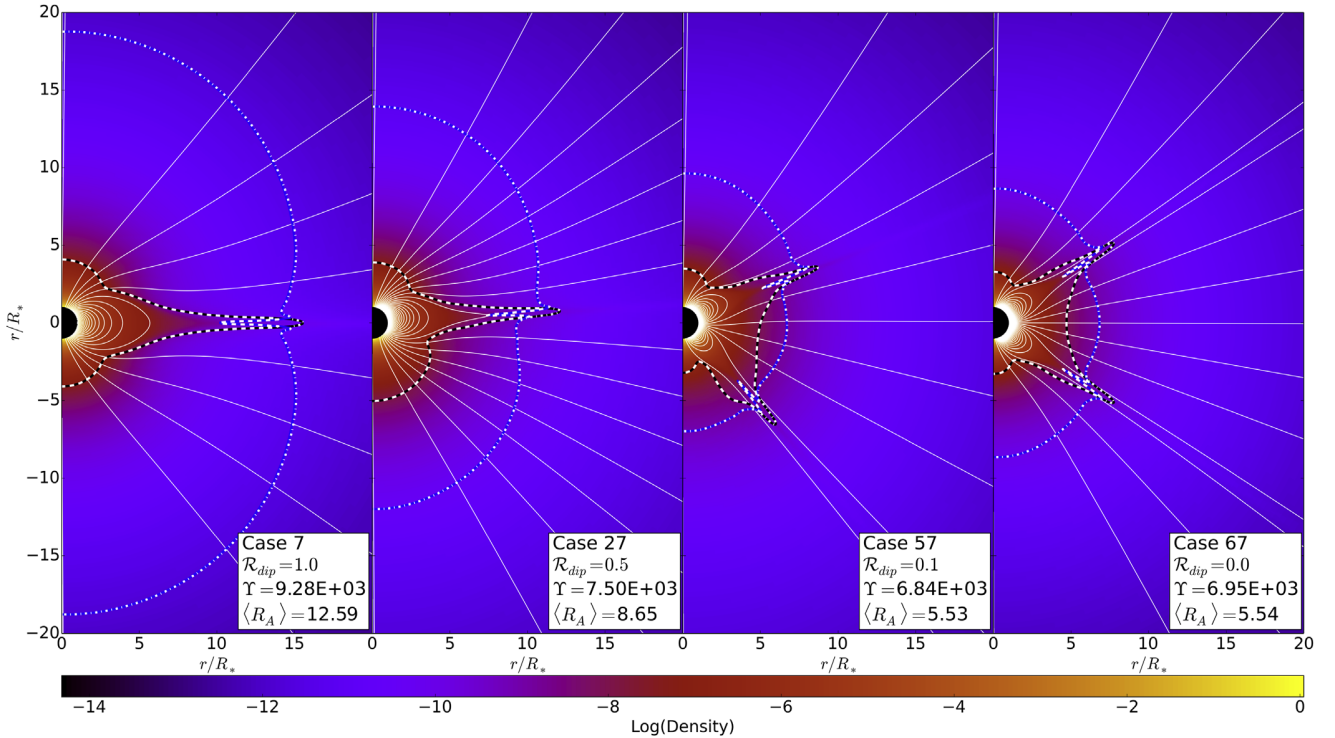


**Figure 2.** Logarithm of density normalized by the surface value for dipolar, quadrupolar, and mixed magnetic fields for cases 7, 27, 57, and 67 (see Table 1). The winds are initialized using the same initial polytropic Parker wind solution with  $\gamma = 1.05$  and  $c_s/v_{\text{esc}} = 0.25$ . Stellar rotation rate and magnetic field strength are set with  $f = 4.46 \times 10^{-3}$  and  $v_A/v_{\text{esc}} = 3.0$ . The Alfvén and sonic Mach surfaces are shown in blue and black, respectively; in addition, the fast and slow magnetosonic surfaces are indicated with dot-dashed and dashed white lines. A transition from one to two streamers is seen with increasing quadrupolar field (decreasing  $\mathcal{R}_{\text{dip}}$ ), and the two combined field cases exhibit asymmetric field topologies about the equator due to the field addition and subtraction between the antisymmetric dipole and symmetric quadrupole.

cases are parameterized by  $\mathcal{R}_{\text{dip}}$  values ( $\mathcal{R}_{\text{dip}} = 0.8, 0.5, 0.3, 0.2, 0.1$ ). We include  $\mathcal{R}_{\text{dip}} = 0.8$  to demonstrate the dominance of the dipole at higher values. Each  $\mathcal{R}_{\text{dip}}$  value is given a unique identifying color that is maintained in all figures throughout this paper. Table 1 contains a complete list of parameters for all cases, which are numbered by increasing  $v_A/v_{\text{esc}}$  and quadrupole fraction.

### 3. Simulation Results

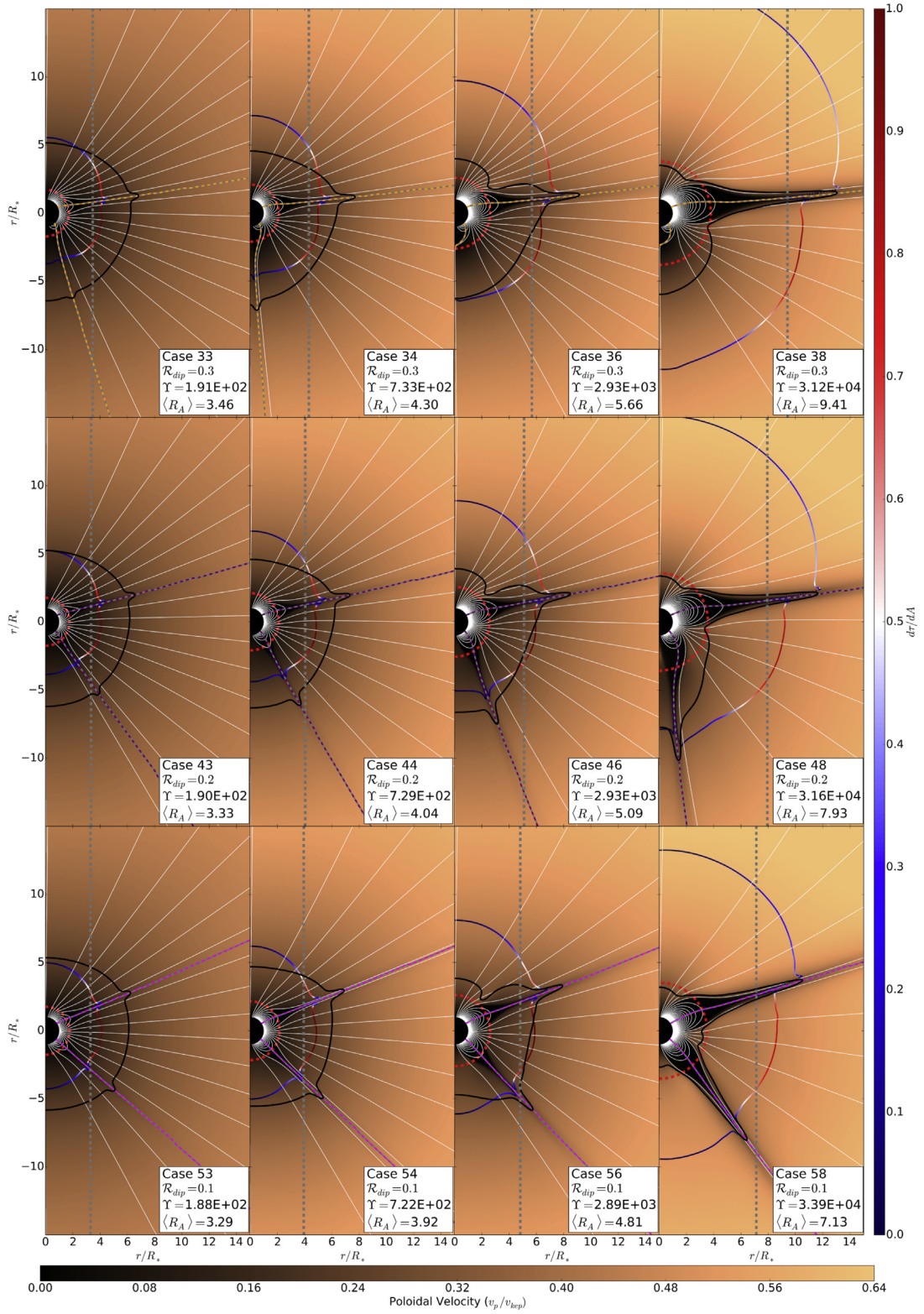
#### 3.1. Morphology of the Field and Wind Outflow

Figure 1 shows the topological changes in field structure from the addition of dipole and quadrupole fields. It is evident in these initial magnetic field configurations that the global magnetic field becomes asymmetric about the equator for mixed cases, as does the magnetic boundary condition that is maintained fixed at the stellar surface. It is not immediately clear how this will impact the torque scaling from Réville et al. (2015a), who studied only single geometries.

Results for these field configurations using our PLUTO simulations are displayed in Figure 2. The dipole and quadrupole cases are shown in conjunction with the mixed field cases  $\mathcal{R}_{\text{dip}} = 0.5, 0.1$ . The figure displays the different sizes of Alfvén surface that are produced for a comparable value of polar magnetic field strength. The mixed magnetic geometries modify the size and morphology of the Alfvén and sonic surfaces. Due to the slow rotation, the fast and slow magnetosonic surfaces are colocated with the sonic and Alfvén surfaces (the fast magnetosonic surface always being the larger of the two surfaces).

The field geometry is found to imprint itself onto the stellar wind velocity with regions of closed magnetic field confining the flow and creating areas of corotating plasma, referred to as dead zones (Mestel 1968). Steady-state wind solutions typically have regions of open field where a faster wind and most of the torque is contained, along with these dead zone(s), around which a slower wind is produced. Similar to the solar wind, slower wind can be found on the open field lines near the boundary of the closed field (Fisk et al. 1998; Feldman et al. 2005; Riley et al. 2006). Observations of the Sun reveal the fast wind component emerging from deep within coronal holes, typically over the poles, and the slow wind component originating from the boundary between the coronal holes and closed field regions. Due to the polytropic wind used here, we do not capture the different heating and acceleration mechanisms required to create a true fast and slow solar-like wind (as seen with the *Ulysses* spacecraft; e.g., McComas et al. 2000; Ebert et al. 2009). Our models produce an overall wind speed consistent with a slow solar wind component, which we assume to represent the average global flow. More complex wind-driving and coronal-heating physics are required to recover a multispeed wind, as observed from the Sun (Cranmer et al. 2007; Pinto et al. 2016).

Figure 3 displays a grid of simulations with a range of magnetic field strengths and  $\mathcal{R}_{\text{dip}} = 0.3, 0.2, 0.1$  values ( $B_{\text{quad}}^2/B_{\text{dip}}^2$  ranges from 3.6 to 54, values consistent with the solar cycle maximum), where the mixing of the fields plays a clear role in the changing dynamics of the flow. Regions of closed magnetic field cause significant changes to the morphology of the wind. A single dead zone is established on the equator by the dipole geometry,



**Figure 3.** Simulation results for the lowest  $\mathcal{R}_{dip}$  values 0.3, 0.2, and 0.1 (top, middle, and bottom, respectively), colored by poloidal wind speed, with field lines in white. The current sheets are indicated by dashed lines, whose color corresponds to their  $\mathcal{R}_{dip}$  value in future figures. The streamer configuration is modified by changes to both the field strength and mixing ratio. Increased field strength or  $\mathcal{R}_{dip}$  value tends to revolve the southern hemisphere streamer toward the south pole. The Alfvén surfaces have been colored to show the flux of angular momentum normal to the surface (units normalized by  $8 \times 10^{-6} \rho_* v_{kep} R_*$ ). The average Alfvén radius,  $\langle R_A \rangle$ , from Equation (19) is shown by dashed gray lines. The sonic surface and opening radius are shown by solid black and dashed red lines, respectively. The morphology and properties of the lower field cases are nearly indistinguishable, with only slight differences in the streamer locations. The reduction in torque with increasing quadrupolar fraction can be visually seen by moving along the grid. The most dipolar field is in the top right panel, and the most quadrupolar is in the bottom left; these models are chosen to emphasize the transition in field dominance.

whereas the quadrupole creates two over the midlatitudes. Mixed cases have intermediate states between the pure regimes. Within our simulations, the dead zones are accompanied by streamers that form above the closed field regions and drive a slower-speed wind than that from the open field regions. The dynamics of these streamers and their location and size are an interesting result of the changing topology of the flow.

The dashed colored lines in Figure 3 show where the field polarity reverses using  $B_r = 0$ , which traces the location of the streamers. The motion of the streamers through the grid of simulations is then observed. With increasing quadrupole field, the single dipolar streamer moves into the northern hemisphere, and, with continued quadrupole addition, a second streamer appears from the southern pole and travels toward the northern hemisphere until the quadrupolar streamers are recovered, both sitting at midlatitudes. This motion can also be seen for fixed  $\mathcal{R}_{\text{dip}}$  cases as the magnetic field strength is decreased. For a given  $\mathcal{R}_{\text{dip}}$  value, the current sheets sweep toward the southern hemisphere with increased polar field strength, in some cases (36 and 38) moving onto the axis of rotation. This is the opposite behavior to decreasing the  $\mathcal{R}_{\text{dip}}$  value; i.e., the streamer configuration is seen to take a more dipolar morphology as the field strength is increased. Additionally in Figure 3, for low field strengths, each  $\mathcal{R}_{\text{dip}}$  produces a comparable Alfvén surface with very similar morphology, all dominated by the quadrupolar mode.

### 3.2. Global Flow Quantities

Our simulations produce steady-state solutions for the density, velocity, and magnetic field structure. To compute the wind torque on the star, we calculate  $\Lambda$ , a quantity related directly to the angular momentum flux  $\mathbf{F}_{\text{AM}} = \Lambda \rho \mathbf{v}$  (Keppens & Goedbloed 2000),

$$\Lambda(r, \theta) = r \sin \theta \left( v_\phi - \frac{B_\phi}{\rho} \frac{|\mathbf{B}_p|^2}{\mathbf{v}_p \cdot \mathbf{B}_p} \right). \quad (15)$$

Within axisymmetric steady-state ideal MHD,  $\Lambda$  is conserved along any given field line. However, we find variations from this along the open-closed field boundary due to numerical diffusion across the sharp transition in quantities found there. The spin-down torque,  $\tau$ , due to the transfer of angular momentum in the wind is then given by the area integral,

$$\tau = \int_A \Lambda \rho \mathbf{v} \cdot d\mathbf{A}, \quad (16)$$

where  $A$  is the area of any surface enclosing the star. For illustrative purposes, Figure 3 shows the Alfvén surface colored by angular momentum flux (thick multicolored lines), which is seen to be strongly focused around the equatorial region. The angular momentum flux is calculated normal to the Alfvén surface,

$$\frac{d\tau}{dA} = \Lambda \rho \mathbf{v} \cdot \hat{\mathbf{A}} = \mathbf{F}_{\text{AM}} \cdot \hat{\mathbf{A}}, \quad (17)$$

where  $\hat{\mathbf{A}}$  is the normal unit vector to the Alfvén surface. The mass-loss rate from our wind solutions is calculated similarly to the torque,

$$\dot{M} = \int_A \rho \mathbf{v} \cdot d\mathbf{A}. \quad (18)$$

Both expressions for the mass loss and torque are evaluated using spherical shells of area  $A$  that are outside the closed field regions. This allows for the calculation of an average Alfvén radius (which is cylindrical from the rotation axis) in terms of the torque, mass flux, and rotation rate,

$$\langle R_A \rangle = \sqrt{\frac{\tau}{\dot{M} \Omega_*}}. \quad (19)$$

Throughout this work,  $\langle R_A \rangle$  is used as a normalized torque that accounts for the mass-loss rates that we do not control. Values of the average Alfvén radius are tabulated in Table 1, and  $\langle R_A \rangle$  is shown in Figure 3 using dashed gray lines. For each case, the cylindrical Alfvén radius is offset inward of the maximum Alfvén radius from the simulation, a geometrical effect, as this corresponds to the average cylindrical  $R_A$  and includes variations in flow quantities as well. Exploring Figure 3, the motion of the dead zones/current sheets has little impact on the overall torque. For example, no abrupt increase in the Alfvén radius is seen from cases 34 to 36 (where the southern streamer is forced onto the rotation axis) compared to cases 44 and 46. The torque is instead governed by the magnetic field strength in the wind that controls the location of the Alfvén surface.

We parameterize the magnetic and mass-loss properties using the “wind magnetization” defined by

$$\Upsilon = \frac{B_*^2 R_*^2}{\dot{M} v_{\text{esc}}}, \quad (20)$$

where  $B_*$  is the combined field strength at the pole. Previous studies that used this parameter defined it with the equatorial field strength (e.g., Matt & Pudritz 2008; Matt et al. 2012; Réville et al. 2015a; G. Pantolmos & S. Matt 2017, in preparation). We use polar values, unlike previous authors, due to the additive property of the radial field at the pole for aligned axisymmetric fields. Note that selecting one value of the field on the surface will not always produce a value that describes the field as a whole. The polar strength works for these aligned fields but will easily break down for unaligned fields and antialigned axisymmetric odd  $l$  fields; thus, it suits the present study, but a move away from this parameter in future is warranted.

During analysis, the wind magnetization,  $\Upsilon$ , is treated as an independent parameter that determines the Alfvén radius  $\langle R_A \rangle$  and thus the torque  $\tau$ . We increase  $\Upsilon$  by setting a larger  $v_A/v_{\text{esc}}$ , creating a stronger global magnetic field. Table 1 displays all the input values of  $\mathcal{R}_{\text{dip}}$  and  $v_A/v_{\text{esc}}$ , as well as the resulting global outflow properties from our steady-state solutions, which are used to formulate the torque scaling relations within this study. Figure 4 displays all 70 simulations in  $\Upsilon$ - $\mathcal{R}_{\text{dip}}$  space. Cases are color-coded by their  $\mathcal{R}_{\text{dip}}$  value, a convention that is continued throughout this work.

### 3.3. Single-mode Torque Scalings

The efficiency of the magnetic braking mechanism is known to be dependent on the magnetic field geometry. This has been previously shown for single-mode geometries (e.g., Réville et al. 2015a; Garraffo et al. 2016b). We first consider two pure geometries, dipole and quadrupole, using the formulation from

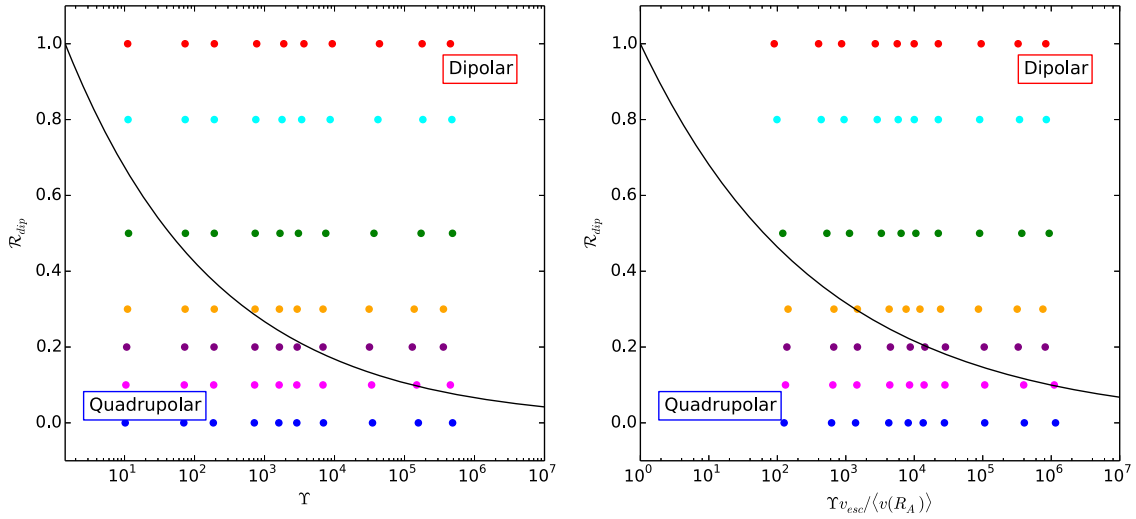


**Figure 4.** Parameter space explored in terms of  $\Upsilon$ ,  $\Upsilon v_{\text{esc}} / \langle v(R_A) \rangle$ , and  $\mathcal{R}_{\text{dip}}$ . Five mixed geometries are explored, along with pure cases of both dipole and quadrupole geometries. Colors for each  $\mathcal{R}_{\text{dip}}$  value are used throughout this work. The black line indicates  $\Upsilon_{\text{crit}}$  (Equation (27)). The formula for predicting the torque exhibits a quadrupolar scaling for  $\Upsilon$  and  $\mathcal{R}_{\text{dip}}$  values below the line and dipolar above (see Section 3.4).

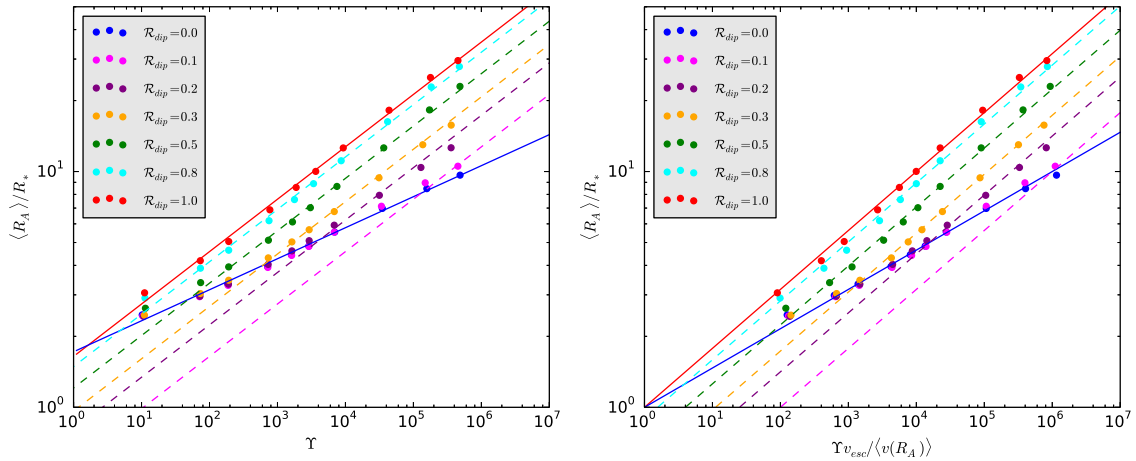


**Figure 5.** Average Alfvén radius vs. wind magnetization for all cases. Simulations are marked with color-coded circles indicating their  $\mathcal{R}_{\text{dip}}$  value. Left: solid lines show the fit of dipole (red) and quadrupole (blue) to Equation (21). Dashed lines show the dipolar component fit (Equation (24)). Right: solid lines show the analytic solution of dipole (red) and quadrupole (blue) to Equation (22) with  $K_l = 1$ . Dashed lines show the dipolar component fit from Equation (25), dependent only on the value of the field order  $l$ , unlike in the  $\Upsilon$  space.

Matt & Pudritz (2008),

$$\frac{\langle R_A \rangle}{R_*} = K_s \Upsilon^{m_s}, \quad (21)$$

where  $K_s$  and  $m_s$  are fitting parameters for the pure dipole and quadrupole cases using the surface field strength. Here we empirically fit  $m_s$ ; the interpretation of  $m_s$  is discussed in Matt & Pudritz (2008), Réville et al. (2015a), and G. Pantolmos & S. Matt (2017, in preparation), where it is determined to be dependent on magnetic geometry and the wind acceleration profile. The Appendix contains further discussion of the wind acceleration profile and its impact on this power-law relationship.

The left panel of Figure 5 shows the Alfvén radii versus the wind magnetizations for all cases (color-coded with their  $\mathcal{R}_{\text{dip}}$  value). The solid lines show the scaling relations for dipolar (red) and quadrupolar (blue) geometries, as first shown in Réville et al. (2015a). We calculate best-fit values for  $K_s$  and  $m_s$  for the dipole and quadrupole, tabulated in Table 2. Values here differ due to our hotter wind ( $c_s/v_{\text{esc}} = 0.25$  versus their

$c_s/v_{\text{esc}} = 0.222$ ) using polar  $B_*$ , and we do not account for our low rotation rate. As previously shown, the dipole field is far more efficient at transferring angular momentum than the quadrupole. In this study, we consider the effect of combined geometries; within Figure 5, these cases lie between the dipole and quadrupole slopes, with no single power law of this form to describe them.

G. Pantolmos & S. Matt (2017, in preparation) have shown the role of the velocity profile in the power-law dependence of the torque. In our simulations, the acceleration of the flow from the base wind velocity to its terminal speed is primarily governed by the thermal pressure gradient; however, magnetic topologies can all modify the radial velocity profile (as can changes in wind temperature,  $\gamma$ , and rapid rotation, not included in our study). Effects on the torque formulations due to these differences in acceleration can be removed via the multiplication of  $\Upsilon$  with  $v_{\text{esc}} / \langle v(R_A) \rangle$ . In their work, the authors determined the theoretical power-law dependence,  $m_{l,\text{th}} = 1/(2l + 2)$ , from one-dimensional analysis. In this formulation, the slope of the power

**Table 2**  
Best-fit Parameters to Equations (21) and (22)

Topology ( $l$ )	$K_s$	$m_s$	$K_l$	$m_l$	$m_{l,\text{th}}(l)$
Dipole (1)	$1.49 \pm 0.03$	$0.231 \pm 0.003$	$0.92 \pm 0.04$	$0.258 \pm 0.005$	0.250
Quadrupole (2)	$1.72 \pm 0.03$	$0.132 \pm 0.003$	$1.11 \pm 0.04$	$0.156 \pm 0.004$	0.167

law is controlled only by the order of the magnetic geometry,  $l$ , which is  $l = 1$  and  $l = 2$  for the dipole and quadrupole, respectively,

$$\frac{\langle R_A \rangle}{R_*} = K_l \left[ \Upsilon \frac{v_{\text{esc}}}{\langle v(R_A) \rangle} \right]^{m_l}, \quad (22)$$

where  $K_l$  and  $m_l$  are fit parameters to our wind solutions, tabulated in Table 2. The value of  $\langle v(R_A) \rangle$  is calculated as an average of the velocity at all points on the Alfvén surface in the meridional plane.<sup>2</sup>

Equation (22) is able to accurately predict the power-law dependence for the two pure modes using the order of the spherical harmonic field,  $l$ . We show this in the right panel of Figure 5, where the Alfvén radii are plotted against the new parameter,  $\Upsilon_{\text{esc}}/\langle v(R_A) \rangle$ . A similar qualitative behavior is shown in the scaling with  $\Upsilon$  in the left panel. Using the theoretical power-law dependencies, the dipolar (red) and quadrupolar (blue) slopes are plotted with  $m_{l,\text{th}} = 1/4$  and  $1/6$ , respectively. Using a single-fit constant  $K_l = 1$  for both slopes within this figure shows good agreement with the simulation results.

More accurate values of  $K_l$  and  $m_l$  are fit for each mode independently. These values produce a better fit and are compared with the theoretical values in Table 2. The mixed simulations show a similar qualitative behavior to the plot against  $\Upsilon$ .

Obvious trends are seen within the mixed-case scatter. A saturation to quadrupolar Alfvén radii values for lower  $\Upsilon$  and  $\mathcal{R}_{\text{dip}}$  values is observed, along with a power-law trend with a dipolar gradient for higher  $\Upsilon$  and  $\mathcal{R}_{\text{dip}}$  values. This indicates that both geometries play a role in governing the lever arm, with the dipole dominating the braking process at higher wind magnetizations.

### 3.4. Broken Power-law Scaling for Mixed Field Cases

Observationally, the field geometries of cool stars are, at large scales, dominated by the dipole mode, with higher-order  $l$  modes playing smaller roles in shaping the global field. It is the global field that controls the spin-down torque in the magnetic braking process. Higher-order modes (such as the quadrupole) radially decay much faster than the dipole, and as such they have a reduced contribution to setting the Alfvén speed at distances larger than a few stellar radii.

We calculate  $\Upsilon_{\text{dip}}$ , which only takes into account the dipole’s field strength,

$$\Upsilon_{\text{dip}} = \left( \frac{B_*^{l=1}}{B_*} \right)^2 \frac{B_*^2 R_*^2}{M v_{\text{esc}}} = \mathcal{R}_{\text{dip}}^2 \Upsilon. \quad (23)$$

Taking as a hypothesis that the field controlling the location of the Alfvén radius is the dipole component, a power-law scaling

<sup>2</sup> It could be argued that this should be weighted by the total area of the Alfvén surface, but, for simplicity, we calculate the unweighted average.

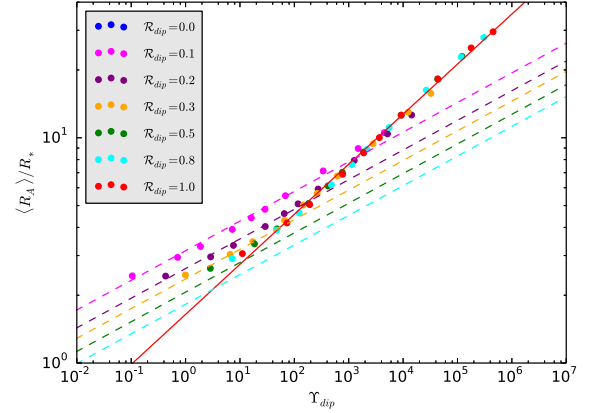


**Figure 6.** Average Alfvén radius vs. the dipolar wind magnetization. Considering only the dipolar field strength, we produce a single power law for the Alfvén radius (Equation (24)). Our wind solutions are shown to agree well with the dipole prediction in most cases. Disagreements at low  $\Upsilon_{\text{dip}}$  and  $\mathcal{R}_{\text{dip}}$  values are explained by the quadrupolar slopes, shown by colored dashed lines.

using  $\Upsilon_{\text{dip}}$  can be constructed in the same form as that of Matt & Pudritz (2008),

$$\frac{\langle R_A \rangle}{R_*} = K_{s,\text{dip}} [\Upsilon_{\text{dip}}]^{m_{s,\text{dip}}} = K_{s,\text{dip}} [\mathcal{R}_{\text{dip}}^2 \Upsilon]^{m_{s,\text{dip}}}. \quad (24)$$

Substitution of the dipole component into Equation (22) similarly gives

$$\frac{\langle R_A \rangle}{R_*} = K_{l,\text{dip}} \left[ \mathcal{R}_{\text{dip}}^2 \Upsilon \frac{v_{\text{esc}}}{\langle v(R_A) \rangle} \right]^{m_{l,\text{dip}}}, \quad (25)$$

where  $K_{s,\text{dip}}$ ,  $m_{s,\text{dip}}$ ,  $K_{l,\text{dip}}$ , and  $m_{l,\text{dip}}$  will be parameters fit to simulations.

A comparison of these approximations can be seen in Figure 5, where Equations (24) (left panel) and (25) (right panel) are plotted with dashed lines for all the  $\mathcal{R}_{\text{dip}}$  values used in our simulations. Mixed cases that lie above the quadrupolar slope are shown to agree with the dashed lines in both forms. Such cases are dominated by the dipole component of the field only, irrespective of the quadrupolar component.

The role of the dipole is even more clear in Figure 6, where only the dipole component of  $\Upsilon$  is plotted for each simulation. The solid red line in Figure 6, given by Equation (24), shows agreement at a given  $\mathcal{R}_{\text{dip}}$ , with deviation from this caused by a regime change onto the quadrupolar slope (shown by colored dashed lines).

The behavior of our simulated winds, despite using a combination of field geometries, simply follows existing scaling relations with this modification. In general, the dipole ( $\Upsilon_{\text{dip}}$ ) prediction shows good agreement with the simulated wind models, except in cases where the Alfvén surface is close to the star. In these cases, the quadrupole mode still has a magnetic field strength able to control the location of the Alfvén surface. Interestingly, and in contrast to the

dipole-dominated regime, the quadrupole-dominated regime behaves as if all the field strength is within the quadrupolar mode. This is visible in Figure 5 for low values of  $\Upsilon$  and  $\mathcal{R}_{\text{dip}}$ .

The mixed field ( $R_A$ ) scaling can be described as a broken power law, set by the maximum of either the dipole component or the pure quadrupolar relation. With the break in the power law given by  $\Upsilon_{\text{crit}}$ ,

$$\frac{\langle R_A \rangle}{R_*} = \begin{cases} K_{s,\text{dip}} [\mathcal{R}_{\text{dip}}^2 \Upsilon]^{m_{s,\text{dip}}}, & \text{if } \Upsilon > \Upsilon_{\text{crit}}(\mathcal{R}_{\text{dip}}), \\ K_{s,\text{quad}} [\Upsilon]^{m_{s,\text{quad}}}, & \text{if } \Upsilon \leq \Upsilon_{\text{crit}}(\mathcal{R}_{\text{dip}}), \end{cases} \quad (26)$$

where  $\Upsilon_{\text{crit}}$  is the location of the intercept for the dipole component and pure quadrupole scalings,

$$\Upsilon_{\text{crit}}(\mathcal{R}_{\text{dip}}) = \left[ \frac{K_{s,\text{dip}}}{K_{s,\text{quad}}} \mathcal{R}_{\text{dip}}^{2m_{s,\text{dip}}} \right]^{\frac{1}{m_{s,\text{quad}} - m_{s,\text{dip}}}}. \quad (27)$$

The solid lines in Figure 4 show the value of  $\Upsilon_{\text{crit}}$  (Equation (27)), dividing the two regimes. Specifically, the solutions above the black line behave as if only the dipole component ( $\Upsilon_{\text{dip}}$ ) is governing the Alfvén radius.

Transitioning from regimes is not perfectly abrupt. Therefore, producing an analytical solution for the mixed cases that includes this behavior would increase the accuracy for stars near the regime change. For example, we have formulated a slightly better fit using a relationship based on the quadrature addition of different regions of field. However, it provides no reduction in the error on this simpler form and is not easily generalized to higher topologies. For practical purposes, the scaling of Equations (26) and (27) accurately predicts the simulation torque with increasing magnetic field strength for a variety of dipole fractions. We therefore present the simplest available solution, leaving the generalized form to be developed in future work.

#### 4. The Impact of Geometry on the Magnetic Flux in the Wind

##### 4.1. Evolution of the Flux

The magnetic flux in the wind is a useful diagnostic tool. The rate of the stellar flux decay with distance is controlled by the overall magnetic geometry. We calculate the magnetic flux as a function of radial distance by evaluating the integral of the magnetic field threading closed spherical shells, where we take the absolute value of the flux to avoid field polarity cancellations,

$$\Phi(r) = \oint_r |\mathbf{B} \cdot d\mathbf{A}|. \quad (28)$$

Considering the initial potential fields of the two pure modes, this is simply a power law in field order  $l$ ,

$$\Phi(r)_P = \Phi_* \left( \frac{R_*}{r} \right)^l, \quad (29)$$

where  $l = 1$  dipole and  $l = 2$  quadrupole, and we denote the flux with  $P$  for the potential field. Figure 7 displays the flux decay of all values of  $v_A/v_{\text{esc}}$  for each  $\mathcal{R}_{\text{dip}}$  value (gray lines). The behavior is qualitatively identical to that observed in previous works (e.g., Schrijver et al. 2003; Johnstone et al. 2010; Vidotto et al. 2014b; Réville et al. 2015a), where the field decays as the potential field does until the pressure of the

wind forces the field into a purely radial configuration with a constant magnetic flux, referred to as the open flux. The power-law dependence of Equation (29) indicates that, for higher  $l$  mode magnetic fields, the decay will be faster. We therefore expect the more quadrupolar-dominated fields studied in this work to have less open flux.

In the case of mixed geometries, a simple power law is not available for the initial potential configurations; instead, we evaluate the flux using Equation (28), where  $\mathbf{B}$  is the initial potential field for each mixed geometry. This allows us to calculate the radial evolution of the flux for a given  $\mathcal{R}_{\text{dip}}$ , which we compare to the simulated cases. Figure 7 shows the flux normalized by the surface flux versus radial distance from the star. For each  $\mathcal{R}_{\text{dip}}$  value, the magnetic flux decay of the potential field (black line) is shown with the different-strength  $v_A/v_{\text{esc}}$  simulations (gray lines). A comparison of the flux decay for all potential magnetic geometries is given in the bottom right panel, showing, as expected, the increasingly quadrupolar fields decaying faster.

In this study, we control  $v_A/v_{\text{esc}}$ , which, for a given surface density, sets the polar magnetic field strength for our simulations. The stellar flux for different topologies and the same  $B_*$  will differ and must be taken into account in order to describe the dipole and quadrupolar components (dashed red and blue lines) in Figure 7. We plot the magnetic flux of the potential field quadrupole component alone with a dashed blue line for each  $\mathcal{R}_{\text{dip}}$  value,

$$\Phi(r)_{P,\text{quad}} = (1 - \mathcal{R}_{\text{dip}}) \Phi_{*,\text{quad}} \left( \frac{R_*}{r} \right)^2, \quad (30)$$

and, similarly, the potential field dipole component of the magnetic flux,

$$\Phi(r)_{P,\text{dip}} = \mathcal{R}_{\text{dip}} \Phi_{*,\text{dip}} \left( \frac{R_*}{r} \right), \quad (31)$$

where in both equations the surface flux of a pure dipole/quadrupole ( $\Phi_{*,\text{dip}}$ ,  $\Phi_{*,\text{quad}}$ ) field is required to match our normalized flux representation.

Due to the rapid decay of the quadrupolar mode, the flux at large radial distances for all simulations containing the dipole mode is described by the dipolar component. The quadrupole component decay sits below and parallel to the potential field prediction for small radii, becoming indistinguishable for the lowest  $\mathcal{R}_{\text{dip}}$  values as the flux stored in the dipole is decreased. Importantly for small radii, simulations containing a quadrupolar component are dominated by the quadrupolar decay following an  $l = 2$  power-law decay, which can be seen by shifting the blue dashed line upward to intercept  $\Phi/\Phi_* = 1$  at the stellar surface.

This result for the flux decay is reminiscent of the broken power-law description for the Alfvén radius in Section 3.4. The field acts as a quadrupole, using the total field for small radii and the dipole component only for large radii. There is a transition between these two regimes that is not described by either approximation. But it is shown by the potential solution (black lines).

##### 4.2. Topology-independent Open Flux Formulation

The magnetic flux within the wind decays following the potential field solution closely until the magnetic field geometry is opened by the pressures of the stellar wind and



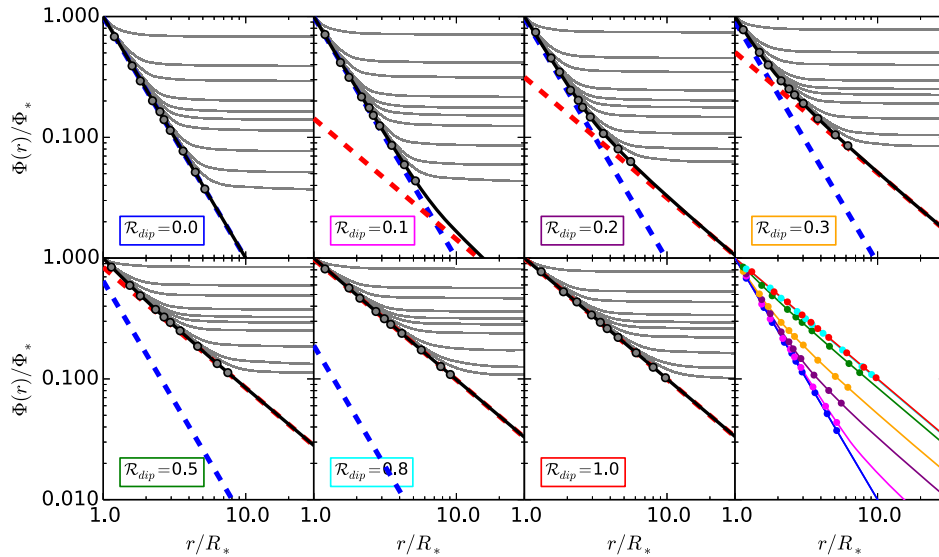


**Figure 7.** Magnetic flux vs. radial distance for all cases studied in this work compared with analytical predictions. Gray lines show the 10 simulation fields for each field geometry. Solutions of Equation (28) for the potential field magnetic flux are shown by black lines for each  $\mathcal{R}_{\text{dip}}$  value. In each case, the flux of the dipole and quadrupole components using a potential field are plotted with dashed red and blue lines, respectively (Equations (30) and (31)). Each simulation matches the potential field flux until the wind pressures open the field to a constant flux. The open flux radii are displayed as gray circles. The bottom right panel shows a comparison of each potential field flux decay along with the opening radii for each case (i.e., the black lines and gray circles from the other panels), color-coded to the value of  $\mathcal{R}_{\text{dip}}$ .

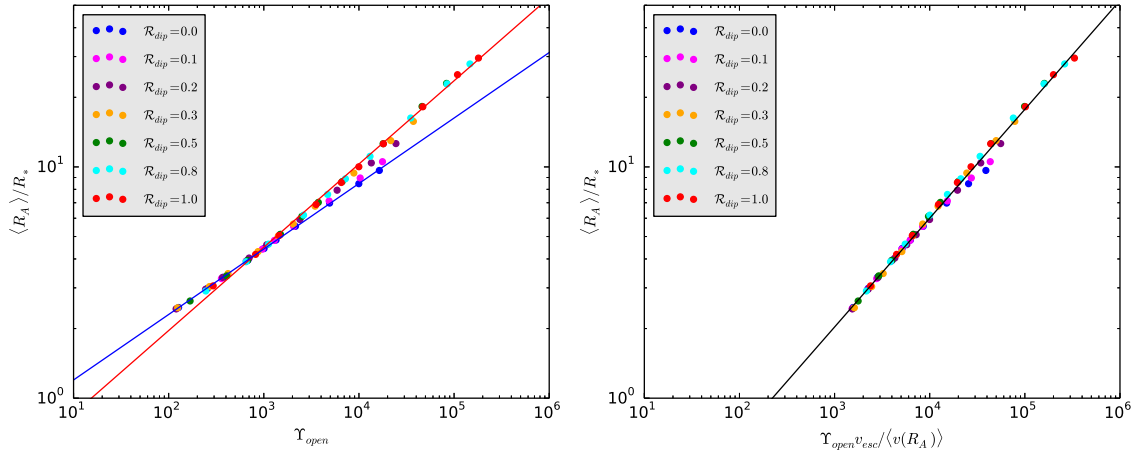


**Figure 8.** Left: average Alfvén radius vs. open flux magnetization for all cases. Fits to Equation (33) are shown for the dipole ( $\mathcal{R}_{\text{dip}} = 1$ ) and quadrupole ( $\mathcal{R}_{\text{dip}} = 0$ ) fields. The geometry of the field is shown to influence the scaling relation due to differences in the wind acceleration. Right: average Alfvén radius vs. open flux magnetization accounting for the acceleration profile using work done by G. Pantolmos & S. Matt (2017, in preparation). The fit of Equation (34) is shown to reduce the scatter for all simulations. A systematic discrepancy is still seen from the single power law with changing geometry.

the field lines are forced into a nearly radial configuration with constant flux, shown in Figure 7 for all simulations. The importance of this open flux is discussed by Réville et al. (2015a). These authors showed a single power-law dependence for the Alfvén radius, independent of magnetic geometry, when parameterized in terms of the open flux,  $\Phi_{\text{open}}$ ,

$$\Upsilon_{\text{open}} = \frac{\Phi_{\text{open}}^2 / R_*^2}{\dot{M} v_{\text{esc}}}, \quad (32)$$

which, ignoring the effects of rapid rotation, can be fit with

$$\frac{\langle R_A \rangle}{R_*} = K_o [\Upsilon_{\text{open}}]^{m_o}, \quad (33)$$

where  $m_o$  and  $K_o$  are fitting parameters for the open flux formulation.

Using the open flux parameter, Figure 8 shows a collapse toward a single power-law dependence as in Réville et al. (2015a). However, our wind solutions show a systematic difference in power-law dependence from dipole to quadrupole. On careful inspection of the result from Figure 6 of Réville et al. (2015a), the same systematic trend between their topologies and the fit scaling is seen.<sup>3</sup> We calculate the best fits for each pure mode separately, i.e., the dipole and quadrupole, tabulated in Table 3.

G. Pantolmos & S. Matt (2017, in preparation) find solutions for thermally driven winds with different coronal temperatures. From these, they find that the wind acceleration profiles of a given wind very significantly alter the slope in  $R_A$ - $\Upsilon_{\text{open}}$  space.

<sup>3</sup> A choice in our parameter space may have made this clearer in Figure 8, due to the increased heating and therefore larger range of acceleration allowing the topology to impact the velocity profile.

**Table 3**  
Open Flux Best-fit Parameters to Equations (33) and (34)

Topology ( $l$ )	$K_o$	$m_o$		
Dipole (1)	$0.37 \pm 0.05$	$0.360 \pm 0.006$		
Quadrupole (2)	$0.62 \pm 0.01$	$0.283 \pm 0.002$		
	$K_c$	$K_{c,th}$	$m_c$	$m_{c,th}$
Topology-independent	$0.08 \pm 0.03$	0.0796	$0.471 \pm 0.003$	0.500

From this work, our trend with geometry indicates that each geometry must have a slightly different wind acceleration profile. This is most likely due to differences in the superradial expansion of the flux tubes for each geometry, which is not taken into account with Equation (33). The field geometry is imprinted onto the wind as it accelerates out to the Alfvén surface. As such, this scaling relation is not entirely independent of topology. Further details on the wind acceleration profile in our study are available in the Appendix. G. Pantolmos (2017, in preparation) are able to include the effects of acceleration in their scaling through multiplication of  $\Upsilon_{\text{open}}$  with  $v_{\text{esc}}/\langle v(R_A) \rangle$ . The expected semianalytical solution from G. Pantolmos & S. Matt (2017, in preparation) is given as

$$\frac{\langle R_A \rangle}{R_*} = K_c \left[ \Upsilon_{\text{open}} \frac{v_{\text{esc}}}{\langle v(R_A) \rangle} \right]^{m_c}, \quad (34)$$

where the fit parameters are derived from 1D theory as constants,  $K_{c,th} = 1/4\pi$  and  $m_{c,th} = 1/2$ .

We are able to reproduce this power-law fit of  $\Upsilon_{\text{open}}$ , with the wind acceleration effects removed, in the right panel of Figure 8. Including all simulations in the fit, we arrive at values of  $K_c = 1.01K_{c,th} \pm 0.07$  and  $m_c = 0.942m_{c,th} \pm 0.009$  for the constants of proportionality and power-law dependence. However, a systematic difference is still seen from one  $\mathcal{R}_{\text{dip}}$  value to another. More precise fits can be found for each geometry independently, but the systematic difference appearing in the right panel implies that a modification to our semianalytical formulations is required to describe the torque fully in terms of the open flux.

Here we show that the scaling law from Réville et al. (2015a) is improved with the modification from G. Pantolmos (2017, in preparation). This formulation is able to describe the Alfvén radius scaling with changing open flux and mass loss. However, with the open flux remaining an unknown from observations and difficult to predict, scaling laws that incorporate known parameters (such as those of Equations (26) and (27)) are still needed for rotational evolution calculations.

#### 4.3. The Relationship between the Opening and Alfvén Radii

The location of the field opening is an important distance. It is critical both for determining the torque and for comparison to potential field source surface (PFSS) models (Altschuler & Newkirk 1969), which set the open flux with a tunable free parameter  $R_{ss}$ . The opening radius,  $R_o$ , we define as the radial distance at which the potential flux reaches the value of the open flux ( $\Phi_P(R_o) = \Phi_{\text{open}}$ ). This definition is chosen because it relates to the 1D analysis employed to describe the power-law dependences of our torque scaling relations. Specifically, a known value of  $R_o$  allows for a precise calculation of the open flux (a priori from the potential field equations), which then

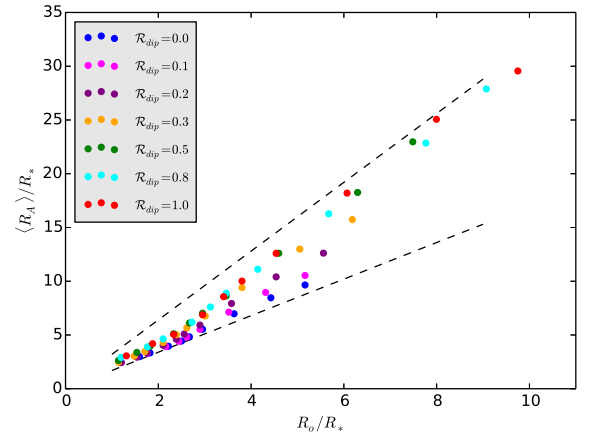


**Figure 9.** Alfvén radii vs. opening radii for all simulated cases. Dashed lines represent  $R_A/R_o = 3.2$  and 1.7. Different geometries have a changing relationship between the torque lever arm and the opening radius of the field.

gives the torque on the star within our simulations. The physical opening of the simulation field takes place at slightly larger radii than this, with the field becoming nonpotential due to its interaction with the wind (which explains why the closed field regions seen in Figure 3 typically extend slightly beyond  $R_o$ ). A similar smooth transition is produced with PFSS modeling.

In Figure 7,  $R_o$  is marked for each simulation and for comparative purposes in the bottom right panel. It is clear that smaller opening radii are found for lower  $\mathcal{R}_{\text{dip}}$  cases. Due to their more rapidly decaying flux, they tend to have a smaller fraction of the stellar flux remaining in the open flux. From the radial decay of the magnetic field, the open flux and opening radii are observed to be dependent on the available stellar flux and topology. G. Pantolmos & S. Matt (2017, in preparation) have recently shown these to also be dependent on the wind acceleration profile. This complex dependence makes it difficult to predict the open flux for a given system.

Our simulations produce values for the average Alfvén radius,  $\langle R_A \rangle$ , and the opening radius,  $R_o$ , for the seven different geometries studied. It is interesting to consider the relative size of these radii, as they both characterize key dynamic properties for each stellar wind solution. For all cases shown in Figure 3, the opening radii are plotted with dashed red lines, allowing for the relative size to be compared with the cylindrical Alfvén radius, shown with dashed gray lines. With increasing magnetic field strength ( $\Upsilon$ ), both radii are seen to grow from case to case; however, with increasing  $\mathcal{R}_{\text{dip}}$ , the cylindrical Alfvén radius generally grows faster than the opening radius. To quantify this, Figure 9 shows a plot of the Alfvén radii versus the opening radii for all cases. Linear trends of  $R_A/R_o = 3.2$  and 1.7 are indicated with dashed lines. For each  $\mathcal{R}_{\text{dip}}$  value, the relationship between the Alfvén and opening radius ( $\langle R_A \rangle/R_o$ ) is seen to systematically decrease with increasing higher-order field component. In all cases, for small radii, a shallower slope is observed, which then steepens with increasing radial extent.

The dependence of the Alfvén radius and opening radius on field geometry and magnetization is a constraint on PFSS models, which are readily used with ZDI observations as a less computationally expensive alternative to MHD modeling (Jardine et al. 1999, 2002; Dunstone et al. 2008; Cohen et al. 2010; Johnstone et al. 2010; Réville et al. 2015b; Rosén et al. 2015). PFSS models are a useful tool; however, they require

the source surface radius,  $R_{ss}$ , as an input. Authors often set a source surface and change the geometry and strength of the field freely (Fares et al. 2010; See et al. 2015, 2017). We find, however, that for a given  $\mathcal{R}_{\text{dip}}$  value there exists a differing relation for the opening radius, as we define it here, to the Alfvén radius and magnetization. These trends are observed to continue for higher  $l$  mode fields (A. Finley & S. Matt 2017, in preparation), with  $\langle R_A \rangle / R_o$  decreasing overall with increased field complexity. As such, our results confirm that the opening radius should not remain fixed when changing geometries or increasing the wind magnetization. We find that the relationship of  $\langle R_A \rangle / R_o$  changes in both cases. With fixed magnetization, the opening radius should move toward the star for higher-order fields to maintain a constant thermal driving. Maintaining the opening radius while increasing the field complexity infers that the wind has a reduced acceleration. Similarly, with increased wind magnetization, the opening radius should move further from the star. The value of  $R_o$  as we have defined it is directly related to the source surface radius, and, for a given magnetic geometry, the two should scale approximately together. For example, for a dipole field, comparing our definition of  $R_o$  to the PFSS model shows that  $R_{ss}$  equals an approximately constant value of  $3/2 R_o$ . Thus, conclusions made about the opening radii are constraints on future PFSS modeling.

A method for predicting  $R_o$  within our simulations remains unknown; however, it is understood that  $R_o$  is key to predicting the torque from our simulated winds. We do, however, find the ratio of  $\langle R_A \rangle / R_o$  to be roughly constant for a given geometry, deviations from which may be numerical or suggest additional physics that we do not explore here.

## 5. Conclusion

We undertake a systematic study of the two simplest magnetic geometries, dipolar and quadrupolar, and, for the first time, their combinations with varying relative strengths. We parameterize the study using the ratio,  $\mathcal{R}_{\text{dip}}$ , of dipolar to total combined field strength, which is shown to be a key variable in our new torque formulation.

We have shown that a large proportion of the magnetic field energy needs to be in the quadrupole for any significant morphology changes to be seen in the wind. All cases above the 50% dipole field show a single streamer and are dominated by dipolar behavior. Even in cases of small  $\mathcal{R}_{\text{dip}}$ , we observe the dipole field to be the key parameter controlling the morphology of the flow, with the quadrupolar field rapidly decaying away for most cases, leaving the dipole component behind. For smaller field strengths, the Alfvén radii appear close to the star, where the quadrupolar field is still dominant, and thus a quadrupolar morphology is established. Increasing the fraction of quadrupolar field strength allows this behavior to continue for larger Alfvén radii.

The morphology of the wind can be considered in the context of star–planet or disk interactions. Our findings suggest that the connectivity, polarity, and strength of the field within the orbital plane depend in a simple way on the relative combination of the dipole and quadrupole fields. Different combinations of these two field modes change the location of the current sheet(s) and the relative orientation of the stellar wind magnetic field with respect to any planetary or disk magnetic field. Asymmetries such as these can modify the Poynting flux exchange for close-in planets (Strugarek et al. 2014b) or the

strength of magnetospheric driving and geomagnetic storms on Earth-like exoplanets. Cohen et al. (2014) used observed magnetic fields to simulate the stellar wind environment surrounding the planet-hosting star EV Lac. They calculated the magnetospheric joule heating on the exoplanets orbiting the M dwarf, finding significant changes to atmospheric properties such as thickness and temperature. Additionally, transient phenomena in the solar wind, such as coronal mass ejections, are shown to deflect toward streamer belts (Kay et al. 2013). This has been applied to mass ejections around M dwarf stars (Kay & Opher 2014) and could similarly be applied here using the knowledge of the streamer locations from our model grid.

If the host star magnetic field can be observed and decomposed into constituent field modes containing dominant dipole and quadrupole components, a qualitative assessment of the stellar wind environment can be made. We find that the addition of these primary and secondary fields creates an asymmetry that may shift potentially habitable exoplanets in and out of volatile wind streams. Observed planet-hosting stars such as  $\tau$  Bootis have already been shown to have global magnetic fields that are dominated by combinations of these low-order field geometries (Donati et al. 2008). With further investigation, it is possible to qualitatively approximate the conditions for planets in the orbits of such stars. For dipole- and quadrupole-dominated host stars with a given magnetic field strength, our grid of models provide an estimate of the location of the streamers and open field regions.

In this work, we build on the scaling relations from Matt et al. (2012), Réville et al. (2015a), and G. Pantolmos & S. Matt (2017, in preparation). We confirm existing scaling laws and explore a new mixed field parameter space with similar methods. From our wind solutions, we fit the variables  $K_{s,\text{dip}}$ ,  $m_{s,\text{dip}}$ ,  $K_{s,\text{quad}}$ , and  $m_{s,\text{quad}}$  (see Table 2), which describe the torque scaling for the pure dipole and quadrupole modes. From the 50 mixed-case simulations, we produce an approximate scaling relation that takes the form of a broken power law, as a single power-law fit is not available for the mixed geometry cases in  $\Upsilon$  space.

For low  $\Upsilon$  and dipole fractions, the Alfvén radius behaves like a pure quadrupole,

$$\tau = K_{s,\text{quad}} \dot{M} \Omega_* R_*^2 [\Upsilon]^{2m_{s,\text{quad}}}, \quad (35)$$

$$= K_{s,\text{quad}} \dot{M}^{1-2m_{s,\text{quad}}} \Omega_* R_*^{2+4m_{s,\text{quad}}} \left[ \frac{(B_*)^2}{v_{\text{esc}}} \right]^{2m_{s,\text{quad}}}. \quad (36)$$

At higher  $\Upsilon$  and dipole fractions, the torque is only dependent on the dipolar component of the field,

$$\tau = K_{s,\text{dip}} \dot{M} \Omega_* R_*^2 [\Upsilon_{\text{dip}}]^{2m_{s,\text{dip}}}, \quad (37)$$

$$= K_{s,\text{dip}} \dot{M}^{1-2m_{s,\text{dip}}} \Omega_* R_*^{2+4m_{s,\text{dip}}} \left[ \frac{(B_*^{l=1})^2}{v_{\text{esc}}} \right]^{2m_{s,\text{dip}}}. \quad (38)$$

The later formulation is used when the Alfvén radius of a given dipole and quadrupole mixed field is greater than the pure quadrupole case for the same  $\Upsilon$ , i.e., the maximum of our new formula or the pure quadrupole. We define  $\Upsilon_{\text{crit}}$  to separate the two regimes (see Figure 4).

The importance of the relative radial decay of both modes and the location of the opening and Alfvén radii appear to play a key role and deserve further follow-up investigation. This work analytically fits the decay of the magnetic flux, but a

**Table 4**  
Predicting  $m_s$  and  $m_o$  Using  $q = 0.8 \pm 0.1$

Topology ( $l$ )	$m_s$	$m_{s,\text{th}}(l, q)$	$m_o$	$m_{o,\text{th}}(q)$
Dipole (1)	$0.231 \pm 0.003$	$0.21 \pm 0.01$	$0.360 \pm 0.006$	$0.36 \pm 0.02$
Quadrupole (2)	$0.132 \pm 0.003$	$0.15 \pm 0.01$	$0.283 \pm 0.002$	$0.36 \pm 0.02$

parametric relationship for the field opening remains uncertain. The relation of the relative sizes of the Alfvén and opening radii are found to be dependent on geometry, which can be used to inform PFSS modeling, where by the source surface must be specified when changing the field geometry.

Paper II includes the addition of octupolar field geometries, another primary symmetry family that introduces an additional complication in the relative orientation of the octupole to the dipole. It is shown, however, that the mixing of any two axisymmetric geometries will follow a similar behavior, especially if each belongs to a different symmetry family (A. Finley & S. Matt 2017, in preparation). The lowest-order mode largely dominates the dynamics of the torque until the Alfvén and opening radii are sufficiently close to the star for the higher-order modes to impact the field strength.

Thanks for helpful discussions and technical advice from Georgios Pantolmos, Victor See, Victor Réville, Sasha Brun, and Claudio Zanni. This project has received funding from the European Research Council (ERC) under the European Union’s Horizon 2020 research and innovation program (grant agreement No. 682393). We thank Andrea Mignone and others for the development and maintenance of the PLUTO code. Figures in this work are produced using the python package matplotlib (Hunter 2007).

### Appendix Wind Acceleration

The creation of a semianalytical formulation for the Alfvén radius for a variety of stellar parameters has been the goal of many studies proceeding this one (e.g., Matt & Pudritz 2008; Matt et al. 2012; Réville et al. 2015a; G. Pantolmos & S. Matt 2017, in preparation). Using a 1D approximation based on work by Kawaler (1988), previous studies aimed to predict the power-law dependence,  $m$ , of the torque formulations used in this work.

Using the 1D framework, the field strength is assumed to decay as a power law  $B(r) = B_*(R_*/r)^{l+2}$ , which in this study is only valid for the pure cases. G. Pantolmos & S. Matt (2017, in preparation) show that the effect of wind acceleration can be removed from the torque scaling relations through the multiplication of  $\Upsilon$  and  $\Upsilon_{\text{open}}$  with  $v_{\text{esc}}/\langle v(R_A) \rangle$ . The power-law dependence then becomes

$$m_{l,\text{th}} = 1/(2l + 2), \quad (39)$$

and, similarly,

$$m_{c,\text{th}} = 1/2. \quad (40)$$

The modified dependent parameter,  $\Upsilon_{v_{\text{esc}}}/\langle v(R_A) \rangle$ , is used throughout this work (see Figures 5 and 8), and the analytic predictions for the power-law slopes are shown to have good agreement with our simulations. This dependent variable, however, requires additional information about the wind speed at the Alfvén surface that is often unavailable.

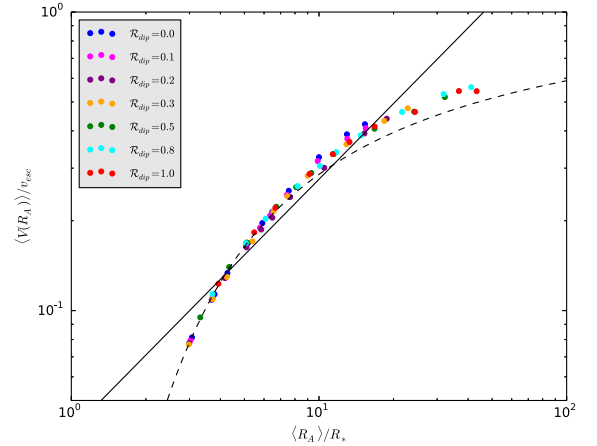


**Figure 10.** Scatter of the average Alfvén speed at the Alfvén surface as a function of the average Alfvén radius. The dashed line shows a hydrodynamic Parker wind with  $c_s/v_{\text{esc}} = 0.25$ , and the solid line shows a fit to all of our simulation data. Variation is seen between the dipolar and quadrupolar data toward the extreme values of the Alfvén radius. The combined average wind acceleration profile (black) gives  $q = 0.84$ . The winds in our simulations are set with a higher coronal temperature than that of Réville et al. (2015a) and thus show a larger acceleration (they produce  $q \approx 0.7$ ).

Typically, rotational evolution models use the available stellar surface parameters, e.g.,  $\Upsilon$ . Therefore, knowledge of the flow speed at the Alfvén radius,  $v(R_A)$ , is required for the semianalytical formulations. G. Pantolmos & S. Matt (2017, in preparation) and Réville et al. (2015a) show that  $v(R_A)$  shares a similar profile to a 1D thermal wind,  $v(r)$ . Figure 10 displays the average Alfvén speed versus the Alfvén radius for all 70 simulations (colored circles). The Parker wind solution (Parker 1965) used in the initial condition is displayed for comparison (dashed line). Nearly all simulations follow the hydrodynamic solution, with a behavior mostly independent of  $\mathcal{R}_{\text{dip}}$ . Toward higher values of the Alfvén radius, a noticeable separation starts to develop between geometries. This range is accessed less by the higher  $l$  order geometries as the range of Alfvén radii is much smaller than that for the pure dipole mode.

In order to include the effects of wind acceleration in the simplified 1D analysis to explain the simulation scalings between  $R_A$  and  $\Upsilon$ , Réville et al. (2015a) introduced a parameterization for the acceleration of the wind to the Alfvén radius with a power-law dependence in radial distance using  $q$ ,

$$v(R_A)/v_{\text{esc}} = (R_A/R_*)^q. \quad (41)$$

A single power law with  $q = 0.84$  is fit to the simulation data. This power law is chosen for simplicity within the 1D formalism. The use of this  $q$  parameter is approximate if  $v(R_A)$  is a power law in  $R_A$ , which we show over the parameter space has a significant deviation. Using the semianalytical theory, Réville et al. (2015a) then derived the power-law dependence for the  $\Upsilon$  scaling (Equation (21)),

$$m_{s,\text{th}} = 1/(2l + 2 + q), \quad (42)$$

which includes geometric and wind acceleration parameters in the form of  $l$  and  $q$ , respectively. Using this result,  $m_{s,\text{th}}$  is computed for both the dipole ( $l=1$ ) and quadrupole ( $l=2$ ) geometries in Table 4 and compared to the simulation results with good agreement.

G. Pantolmos & S. Matt (2017, in preparation) explain the power-law dependence, so long as  $R_o/R_A$  remains constant and the wind acceleration profile is known. Reiners & Mohanty (2012), Réville et al. (2015a), and G. Pantolmos & S. Matt (2017, in preparation) all analytically described the power-law dependence of the open flux formulation (Equation (33)) using the power-law dependence  $q$ ,


$$m_{o,\text{th}} = 1/(2 + q). \quad (43)$$

The result is independent of geometry,  $l$ . As before, the  $q$  parameter approximates the wind driving as a power law in radius, which is fit with a single power law for both geometries such that  $m_{o,\text{th}}$  should be the same for both the dipole and quadrupole. This prediction is tabulated in Table 4; however, the simulation slopes are shown to no longer agree with the result. It is suggested that the open flux slope is much more sensitive to the wind acceleration than the  $\Upsilon$  formulation; therefore, slight changes in flow acceleration modify the result. Slightly different slopes can be fit for the dipole and quadrupole cases that can recover the different  $m_o$  values; however, this is seemingly just a symptom of the power-law approximation breaking down.

We conclude that the approximate power law of Equation (41) gives a reasonable adjustment to the torque prediction for known wind velocity profiles, despite the badness of fit to the simulation points. Even though the power-law approximation to the wind velocity profile (Equation (41)) is not a precise fit to the data in Figure 10, the value of  $q$  does provide a way to approximately include the contribution of the wind acceleration to the fit power-law exponents  $m_o$  and  $m_s$ . A more precise formulation could be derived based on a Parker-like wind profile without the use of a power law; however, the torque scaling with  $\Upsilon$  is relatively insensitive to the chosen approximate velocity profile.

### ORCID iDs

Adam J. Finley  <https://orcid.org/0000-0002-3020-9409>

Sean P. Matt  <https://orcid.org/0000-0001-9590-2274>

### References

- Agüeros, M. A., Covey, K. R., Lomonias, J. J., et al. 2011, *ApJ*, 740, 110  
 Altschuler, M. D., & Newkirk, G. 1969, *SoPh*, 9, 131  
 Alvarado-Gómez, J., Hussain, G., Cohen, O., et al. 2016, *A&A*, 594, A95  
 Amard, L., Palacios, A., Charbonnel, C., Gallet, F., & Bouvier, J. 2016, *A&A*, 587, A105  
 Barnes, S. A. 2003, *ApJ*, 586, 464  
 Barnes, S. A. 2010, *ApJ*, 722, 222  
 Blackman, E. G., & Owen, J. E. 2016, *MNRAS*, 458, 1548  
 Bouvier, J., Matt, S. P., Mohanty, S., et al. 2014, in *Protostars and Planets VI*, ed. H. Beuther et al. (Tucson, AZ: Univ. Arizona Press), 433  
 Brown, T. M. 2014, *ApJ*, 789, 101  
 Cohen, O., Drake, J., Glocer, A., et al. 2014, *ApJ*, 790, 57  
 Cohen, O., Drake, J., Kashyap, V., Hussain, G., & Gombosi, T. 2010, *ApJ*, 721, 80  
 Cohen, O., & Drake, J. J. 2014, *ApJ*, 783, 55  
 Cohen, O., Kashyap, V., Drake, J., et al. 2011, *ApJ*, 733, 67  
 Cranmer, S. R., & Saar, S. H. 2011, *ApJ*, 741, 54  
 Cranmer, S. R., Van Ballegooijen, A. A., & Edgar, R. J. 2007, *ApJS*, 171, 520  
 Davenport, J. R. A. 2017, *ApJ*, 835, 16  
 DeRosa, M., Brun, A., & Hoeksema, J. 2012, *ApJ*, 757, 96  
 do Nascimento, J.-D., Jr, Vidotto, A., Petit, P., et al. 2016, *ApJL*, 820, L15  
 Donati, J.-F., Moutou, C., Fares, R., et al. 2008, *MNRAS*, 385, 1179  
 Dunstone, N., Hussain, G., Collier Cameron, A., et al. 2008, *MNRAS*, 387, 481  
 Ebert, R., McComas, D., Elliott, H., Forsyth, R., & Gosling, J. 2009, *JGRA*, 114, A01109  
 Einfeldt, B. 1988, *SJNA*, 25, 294  
 Fares, R., Donati, J.-F., Moutou, C., et al. 2009, *MNRAS*, 398, 1383  
 Fares, R., Donati, J.-F., Moutou, C., et al. 2010, *MNRAS*, 406, 409  
 Feldman, U., Landi, E., & Schwadron, N. 2005, *JGRA*, 110, A07109  
 Fisk, L., Schwadron, N., & Zurbuchen, T. 1998, *SSRv*, 86, 51  
 Folsom, C. P., Petit, P., Bouvier, J., et al. 2016, *MNRAS*, 457, 580  
 Gallet, F., & Bouvier, J. 2013, *A&A*, 556, A36  
 Gallet, F., & Bouvier, J. 2015, *A&A*, 577, A98  
 Garraffo, C., Drake, J. J., & Cohen, O. 2016a, *ApJL*, 833, L4  
 Garraffo, C., Drake, J. J., & Cohen, O. 2016b, *A&A*, 595, A110  
 Grappin, R., Leorat, J., & Pouquet, A. 1983, *A&A*, 126, 51  
 Gregory, S., Jardine, M., Gray, C., & Donati, J. 2010, *RPPH*, 73, 126901  
 Gregory, S. G., Donati, J.-F., & Hussain, G. A. 2016, *arXiv:1609.00273*  
 Hall, J. C., Lockwood, G., & Skiff, B. A. 2007, *AJ*, 133, 862  
 Hébrard, É., Donati, J.-F., Delfosse, X., et al. 2016, *MNRAS*, 461, 1465  
 Hunter, J. D. 2007, *CSE*, 9, 90  
 Irwin, J., & Bouvier, J. 2009, in *IAU Symp. 258, The Age of Stars* (Cambridge: Cambridge Univ. Press), 363  
 Jardine, M., Barnes, J. R., Donati, J.-F., & Cameron, A. C. 1999, *MNRAS*, 305, L35  
 Jardine, M., Collier Cameron, A., & Donati, J.-F. 2002, *MNRAS*, 333, 339  
 Jeffers, S., Petit, P., Marsden, S., et al. 2014, *A&A*, 569, A79  
 Johnstone, C., Güdel, M., Lüftinger, T., Toth, G., & Brott, I. 2015, *A&A*, 577, A27  
 Johnstone, C., Jardine, M., & Mackay, D. 2010, *MNRAS*, 404, 101  
 Kawaler, S. D. 1988, *ApJ*, 333, 236  
 Kay, C., & Opher, M. 2014, in *AAS Meeting 224 Abstract*, 120.24  
 Kay, C., Opher, M., & Evans, R. M. 2013, *ApJ*, 775, 5  
 Keppens, R., & Goedbloed, J. 1999, *A&A*, 343, 251  
 Keppens, R., & Goedbloed, J. 2000, *ApJ*, 530, 1036  
 Matt, S., & Pudritz, R. E. 2008, *ApJ*, 678, 1109  
 Matt, S. P., Brun, A. S., Baraffe, I., Bouvier, J., & Chabrier, G. 2015, *ApJL*, 799, L23  
 Matt, S. P., MacGregor, K. B., Pinsonneault, M. H., & Greene, T. P. 2012, *ApJL*, 754, L26  
 McComas, D., Barraclough, B., Funsten, H., et al. 2000, *JGRA*, 105, 10419  
 McFadden, P., Merrill, R., McElhinny, M., & Lee, S. 1991, *JGRB*, 96, 3923  
 McQuillan, A., Aigrain, S., & Mazeh, T. 2013, *MNRAS*, 432, 1203  
 Meibom, S., Mathieu, R. D., Stassun, K. G., Liebesny, P., & Saar, S. H. 2011, *ApJ*, 733, 115  
 Mestel, L. 1968, *MNRAS*, 138, 359  
 Mestel, L. 1984, *Cool Stars, Stellar Systems, and the Sun* (Berlin: Springer), 49  
 Mignone, A. 2009, *MSAIS*, 13, 67  
 Mignone, A., Bodo, G., Massaglia, S., et al. 2007, *ApJS*, 170, 228  
 Morgenthaler, A., Petit, P., Morin, J., et al. 2011, *AN*, 332, 866  
 Morgenthaler, A., Petit, P., Saar, S., et al. 2012, *A&A*, 540, A138  
 Morin, J., Donati, J.-F., Petit, P., et al. 2008, *MNRAS*, 390, 567  
 Nicholson, B., Vidotto, A., Mengel, M., et al. 2016, *MNRAS*, 459, 1907  
 Oran, R., Landi, E., van der Holst, B., et al. 2015, *ApJ*, 806, 55  
 Parker, E. 1965, *SSRv*, 4, 666  
 Parker, E. N. 1958, *ApJ*, 128, 664  
 Petit, P., Dintrans, B., Morgenthaler, A., et al. 2009, *A&A*, 508, L9  
 Petit, P., Dintrans, B., Solanki, S., et al. 2008, *MNRAS*, 388, 80  
 Pinto, R., Brun, A., & Rouillard, A. 2016, *A&A*, 592, A65  
 Pinto, R. F., Brun, A. S., Jouve, L., & Grappin, R. 2011, *ApJ*, 737, 72  
 Reiners, A., & Mohanty, S. 2012, *ApJ*, 746, 43  
 Réville, V., Brun, A. S., Matt, S. P., Strugarek, A., & Pinto, R. F. 2015a, *ApJ*, 798, 116  
 Réville, V., Brun, A. S., Strugarek, A., et al. 2015b, *ApJ*, 814, 99  
 Réville, V., Folsom, C. P., Strugarek, A., & Brun, A. S. 2016, *ApJ*, 832, 145  
 Riley, P., Linker, J., Mikić, Z., et al. 2006, *ApJ*, 653, 1510  
 Rosén, L., Kochukhov, O., & Wade, G. A. 2015, *ApJ*, 805, 169  
 Rosner, R., Golub, L., & Vaiana, G. 1985, *ARA&A*, 23, 413  
 Saikia, S. B., Jeffers, S., Morin, J., et al. 2016, *A&A*, 594, A29  
 Sakurai, T. 1990, *CoPhR*, 12, 247  
 Schrijver, C. J., DeRosa, M. L., et al. 2003, *ApJ*, 590, 493

- See, V., Jardine, M., Vidotto, A., et al. 2015, *MNRAS*, 453, 4301
- See, V., Jardine, M., Vidotto, A., et al. 2016, *MNRAS*, 462, 4442
- See, V., Jardine, M., Vidotto, A., et al. 2017, *MNRAS*, 466, 1542
- Skumanich, A. 1972, *ApJ*, 171, 565
- Soderblom, D. 1983, *ApJS*, 53, 1
- Stauffer, J., Rebull, L., Bouvier, J., et al. 2016, *AJ*, 152, 115
- Strugarek, A., Brun, A., Matt, S., et al. 2014a, in *SF2A-2014a: Proc. Annual Meeting of the French Society of Astronomy and Astrophysics*, ed. J. Ballet et al., 279
- Strugarek, A., Brun, A. S., Matt, S. P., & Réville, V. 2014b, *ApJ*, 795, 86
- Tóth, G. 2000, *JCoPh*, 161, 605
- Ud-Doula, A., Owocki, S. P., & Townsend, R. H. 2009, *MNRAS*, 392, 1022
- Usmanov, A. V., Goldstein, M. L., & Matthaeus, W. H. 2014, *ApJ*, 788, 43
- Ustyugova, G., Koldoba, A., Romanova, M., & Lovelace, R. 2006, *ApJ*, 646, 304
- Van der Holst, B., Manchester, W., IV, Frazin, R., et al. 2010, *ApJ*, 725, 1373
- van der Holst, B., Sokolov, I. V., Meng, X., et al. 2014, *ApJ*, 782, 81
- Van Saders, J. L., & Pinsonneault, M. H. 2013, *ApJ*, 776, 67
- Vidotto, A., Gregory, S., Jardine, M., et al. 2014a, *MNRAS*, 441, 2361
- Vidotto, A., Jardine, M., Morin, J., et al. 2014b, *MNRAS*, 438, 1162
- Vidotto, A., Jardine, M., Opher, M., Donati, J., & Gombosi, T. 2011, in *ASP Conf. Ser. 448, 16th Cambridge Workshop on Cool Stars, Stellar Systems, and the Sun*, ed. C. M. Johns-Krull, M. K. Browning, & A. A. West (San Francisco, CA: ASP), 1293
- Washimi, H., & Shibata, S. 1993, *MNRAS*, 262, 936
- Weber, E. J., & Davis, L. 1967, *ApJ*, 148, 217
- Wolk, S., Harnden, F., Jr, Flaccomio, E., et al. 2005, *ApJS*, 160, 423
- Wood, B. E. 2004, *LRSP*, 1, 1
- Wright, J. T., Marcy, G. W., Butler, R. P., & Vogt, S. S. 2004, *ApJS*, 152, 261
- Zanni, C., & Ferreira, J. 2009, *A&A*, 508, 1117



# The Effect of Combined Magnetic Geometries on Thermally Driven Winds. II. Dipolar, Quadrupolar, and Octupolar Topologies

Adam J. Finley and Sean P. Matt

University of Exeter, Department of Physics & Astronomy, Stoker Road, Devon, Exeter, EX4 4QL, UK; [af472@exeter.ac.uk](mailto:af472@exeter.ac.uk)  
Received 2017 November 21; revised 2018 January 18; accepted 2018 January 23; published 2018 February 15

## Abstract

During the lifetime of Sun-like or low-mass stars a significant amount of angular momentum is removed through magnetized stellar winds. This process is often assumed to be governed by the dipolar component of the magnetic field. However, observed magnetic fields can host strong quadrupolar and/or octupolar components, which may influence the resulting spin-down torque on the star. In Paper I, we used the MHD code PLUTO to compute steady-state solutions for stellar winds containing a mixture of dipole and quadrupole geometries. We showed the combined winds to be more complex than a simple sum of winds with these individual components. This work follows the same method as Paper I, including the octupole geometry, which not only increases the field complexity but also, more fundamentally, looks for the first time at combining the same symmetry family of fields, with the field polarity of the dipole and octupole geometries reversing over the equator (unlike the symmetric quadrupole). We show, as in Paper I, that the lowest-order component typically dominates the spin-down torque. Specifically, the dipole component is the most significant in governing the spin-down torque for mixed geometries and under most conditions for real stars. We present a general torque formulation that includes the effects of complex, mixed fields, which predicts the torque for all the simulations to within 20% precision, and the majority to within  $\approx 5\%$ . This can be used as an input for rotational evolution calculations in cases where the individual magnetic components are known.

*Key words:* magnetohydrodynamics (MHD) – stars: low-mass – stars: magnetic field – stars: rotation – stars: winds, outflows

*Supporting material:* machine-readable table

## 1. Introduction

Cool stars are observed to host global magnetic fields that are embedded within their outer convection zones (Reiners 2012). Stellar magnetism is driven by an internal dynamo that is controlled by the convection and stellar rotation rate, the exact physics of which is still not fully understood (see review by Brun & Browning 2017). As observed for the Sun, plasma escapes the stellar surface, interacting with this magnetic field and forming a magnetized stellar wind that permeates the environment surrounding the star (Cranmer et al. 2017). Young main-sequence stars show a large spread in rotation rates for a given mass. As a given star ages on the main sequence, their stellar wind removes angular momentum, slowing the rotation of the star (Schatzman 1962; Weber & Davis 1967; Mestel 1968). This in turn reduces the strength of the magnetic dynamo process, feeding back into the strength of the applied stellar wind torque. This relationship leads to a convergence of the spin rates toward a tight mass–rotation relationship at late ages, as stars with faster rotation incur larger spin-down torques and vice versa for slow rotators. This is observed to produce a simple relation between rotation period and stellar age ( $\Omega_* \propto t^{-0.5}$ ; Skumanich 1972), which is approximately followed, on average (Soderblom 1983), over long timescales.

With the growing number of observed rotation periods (Irwin & Bouvier 2009; Agüeros et al. 2011; Meibom et al. 2011; McQuillan et al. 2013; Bouvier et al. 2014; Stauffer et al. 2016; Davenport 2017), an increased effort has been channeled into correctly modeling the spin-down process (e.g., Reiners & Mohanty 2012; Gallet & Bouvier 2013; Van Saders & Pinsonneault 2013; Brown 2014; Gallet & Bouvier 2015; Matt et al. 2015; Amard et al. 2016; Blackman &

Owen 2016; See et al. 2017a), as it is able to test our understanding of basic stellar physics and also date observed stellar populations.

The process of generating stellar ages from rotation is referred to as gyrochronology, whereby a cluster’s age can be estimated from the distribution of observed rotation periods (Barnes 2003; Meibom et al. 2009; Barnes 2010; Delorme et al. 2011; Van Saders & Pinsonneault 2013). This requires an accurate prescription of the spin-down torques experienced by stars as a result of their stellar wind, along with their internal structure and properties of the stellar dynamo. Based on results from magnetohydrodynamic (MHD) simulations, parameterized relations for the stellar wind torque are formulated using the stellar magnetic field strength, mass-loss rate, and basic stellar parameters (Mestel 1984; Kawaler 1988; Matt & Pudritz 2008; Ud-Doula et al. 2009; Pinto et al. 2011; Matt et al. 2012; Réville et al. 2015). The present work focuses on improving the modeled torque on these stars due to their magnetized stellar winds, by including the effects of combined magnetic geometries.

Magnetic field detections from stars, other than the Sun, were reported over 30 yr ago via Zeeman broadening observations (Robinson et al. 1980; Gray 1984; Marcy 1984), a technique that has since been used on a multitude of stars (e.g., Saar 1990; Johns-Krull & Valenti 2000). This technique, however, only allows for an average line-of-sight estimate of the unsigned magnetic flux and provides no information about the geometry of the stellar magnetic field (see review by Reiners 2012). More recently, the use of Zeeman Doppler Imaging (ZDI), a tomographic technique capable of providing information about the photospheric magnetic field of a given

star, enables the observed field to be broken down into individual spherical harmonic contributions (e.g., Hussain et al. 2002; Donati et al. 2006, 2008; Morin et al. 2008a, 2008b; Petit et al. 2008; Fares et al. 2009; Morgenthaler et al. 2011; Jeffers et al. 2014; Vidotto et al. 2014; See et al. 2015, 2016, 2017b; Folsom et al. 2016; Hébrard et al. 2016; Saikia et al. 2016; Kochukhov et al. 2017). This allows the 3D magnetic geometry to be recovered, typically using a combination of field extrapolation and MHD modeling (e.g., Cohen et al. 2011; Vidotto et al. 2011; Alvarado-Gómez et al. 2016; do Nascimento et al. 2016; Garraffo et al. 2016b; Nicholson et al. 2016; Réville et al. 2016).

Pre-main-sequence stars, observed with ZDI, show a variety of multipolar components, typically dependent on the internal structure of the host star (Gregory et al. 2012; Hussain & Alecian 2013). Many of these objects show an overall dipolar geometry with an accompanying octupole component (e.g., Donati et al. 2007; Gregory et al. 2012). The addition of dipole and octupole fields has been explored analytically, for these stars, and is shown to impact the disk truncation radius along with the topology and field strength of accretion funnels (Gregory & Donati 2011; Gregory et al. 2016). For main-sequence stellar winds, the behavior of combined magnetic geometries has yet to be systematically explored. Our closest star, the Sun, hosts a significant quadrupolar contribution during the solar activity cycle maximum that dominates the large-scale magnetic field geometry along with a small dipole component (DeRosa et al. 2012; Brun et al. 2013). The impact of these mixed geometry fields on the spin-down torque generated from magnetized stellar winds remains uncertain.

It is known that the magnetic field stored in the lowest-order geometries, e.g., dipole, quadrupole, and octupole, has the slowest radial decay and therefore governs the strength of the magnetic field at the Alfvén surface (and thus its size and shape). With the cylindrical extent of the Alfvén surface being directly related to the efficiency of the magnetic braking mechanism, it is this global field strength and geometry that are required to compute accurate braking torques in MHD simulations (Réville et al. 2015, 2016). However, the effect of the higher-order components on the acceleration of the wind close in to the star may not be non-negligible (Cranmer & Van Ballegoijen 2005; Cohen et al. 2009). Additionally, the small-scale surface features described by these higher-order geometries (e.g., starspots and active regions) will play a vital role in modulating the chromospheric activity (e.g., Testa et al. 2004; Aschwanden 2006; Güdel 2007; Garraffo et al. 2013), which is often assumed to be decoupled from the open-field regions producing the stellar wind. Models such as the AWESOM (van der Holst et al. 2014) include this energy dissipation in the lower corona and are able to match observed solar parameters well. Work by Pantolmos & Matt (2017) shows how this additional acceleration can be accounted for globally within their semianalytic formulations.

Previous works have aimed to understand the impact of more complex magnetic geometries on the rotational evolution of Sun-like stars. Holzwarth (2005) examined the effect of nonuniform flux distributions on the magnetic braking torque, investigating the latitudinal dependence of the stellar wind produced within their MHD simulations. Similarly, Garraffo et al. (2016a) included magnetic spots at differing latitudes and examined the resulting changes to mass-loss rate and spin-down torque. The effectiveness of the magnetic braking

from a stellar wind is found to be reduced for higher-order magnetic geometries (Garraffo et al. 2015). This is explained in Réville et al. (2015) as a reduction to the average Alfvén radius, which acts mathematically as a lever arm for the applied braking torque. Finley & Matt (2017, hereafter Paper I) continue this work by discussing the morphology and braking torque generated from combined dipolar and quadrupolar field geometries using ideal MHD simulations of thermally driven stellar winds. In this current work, we continue this mixed-field investigation by including combinations with an octupole component.

Section 2 introduces the simulations and the numerical methods used, along with our parameterization of the magnetic field geometries and derived simulation properties. Section 3 explores the resulting relationship of the average Alfvén radius with increasing magnetic field strength for pure fields, as well as generic combinations of axisymmetric dipole, quadrupole, or octupole geometries. Section 4 uses the decay of the unsigned magnetic flux with distance to explain observed behaviors in our Alfvén radii relations; analysis of the open magnetic flux in our wind solutions follows with a singular relation for predicting the average Alfvén radius based on the open flux. Conclusions and thoughts for future work can be found in Section 5.

## 2. Simulation Method and Numerical Setup

As in Paper I, we use the PLUTO MHD code (Mignone et al. 2007; Mignone 2009) with a spherical geometry to compute 2.5D (two dimensions,  $r$ ,  $\theta$ , and three vector components,  $r$ ,  $\theta$ , and  $\phi$ ) steady-state wind solutions for a range of magnetic geometries.

The full set of ideal MHD equations are solved, including the energy equation and a closing equation of state. The internal energy density  $\epsilon$  is given by  $\rho\epsilon = p/(\gamma - 1)$ , where  $\gamma$  is the ratio of specific heats. This general set of equations is capable of capturing nonadiabatic processes, such as shocks; however, the solutions found for our steady-state winds generally do not contain these. For a gas composed of protons and electrons  $\gamma$  should take a value of 5/3; however, we decrease this value to 1.05 in order to reproduce the observed near-isothermal nature of the solar corona (Steinolfson & Hundhausen 1988) and a terminal speed consistent with the solar wind. This is done, such that on large scales the wind follows the polytropic approximation, i.e., the wind pressure and density are related as  $p \propto \rho^\gamma$  (Parker 1965; Keppens & Goedbloed 1999). The reduced value of  $\gamma$  has the effect of artificially heating the wind as it expands, without an explicit heating term in our equations.

We adopt the numerics used in Paper I, except that we modify the radial discretization of the computational mesh. Instead of a geometrically stretched radial grid as before, we now employ a stepping ( $dr$ ) that grows logarithmically. The domain extent remains unchanged, from one stellar radius ( $R_*$ ) to  $60 R_*$ , containing  $N_r \times N_\theta = 256 \times 512$  grid cells. This modification produces a more consistent aspect ratio between  $dr$  and  $r d\theta$  over the whole domain, which marginally increases our numerical accuracy and stability.

Characteristic speeds such as the surface escape speed and Keplerian speed,  $v_{\text{esc}}$  and  $v_{\text{kep}}$ , and the equatorial rotation speed,  $v_{\text{rot}}$ , along with the surface adiabatic sound speed,  $c_s$ ,



**Table 1**  
Fixed Simulation Parameters

Parameter	Value	Description
$\gamma$	1.05	Polytropic index
$c_s/v_{\text{esc}}$	0.25	Surface sound speed/escape speed
$f$	4.46E-03	Fraction of breakup rotation

and Alfvén speed,  $v_A$ , are given as follows:

$$v_{\text{esc}} = \sqrt{\frac{2GM_*}{R_*}} = \sqrt{2} v_{\text{kep}}, \quad (1)$$

where  $G$  is the gravitational constant,  $R_*$  is the stellar radius, and  $M_*$  is the stellar mass;

$$v_{\text{rot}} = \Omega_* R_*, \quad (2)$$

where  $\Omega_*$  is the angular stellar rotation rate (which is assumed to be in solid-body rotation);

$$c_s = \sqrt{\frac{\gamma p_*}{\rho_*}}, \quad (3)$$

where  $\gamma$  is the polytropic index and  $p_*$  and  $\rho_*$  are the gas pressure and mass density at the stellar surface, respectively; and

$$v_A = \frac{B_*}{\sqrt{4\pi\rho_*}}, \quad (4)$$

where  $B_*$  is the characteristic polar magnetic field strength (see Section 2.1).

We set an initial wind speed within the domain using a spherically symmetric Parker wind solution (Parker 1965), with the ratio of the surface sound speed to the escape speed  $c_s/v_{\text{esc}}$  setting the base wind temperature in such a way as to represent a group of solutions for differing gravitational field strengths. The same normalization is applied to the surface magnetic field strength with  $v_A/v_{\text{esc}}$ , and the surface rotation rate using  $f = v_{\text{rot}}/v_{\text{kep}}$ , such that each wind solution represents a family of solutions that can be applied to a range of stellar masses. The same system of input parameters is used by many previous authors (e.g., Matt & Pudritz 2008; Matt et al. 2012; Réville et al. 2015; Pantolmos & Matt 2017). For this study we fix the wind temperature and stellar rotation at the values tabulated in Table 1.

A background field corresponding to our chosen potential magnetic field configuration (see Section 2.1) is imposed over the initial wind solution, and then all quantities are evolved to a steady-state solution by the PLUTO code. The boundary conditions are enforced, as in Paper I, at the inner radial boundary (stellar surface), which are appropriate to give a self-consistent wind solution for a rotating magnetized star. A fixed surface magnetic geometry is therefore maintained along with solid-body rotation.

The use of a polytropic wind produces solutions that are far more isotropic than observed for the Sun (Vidotto et al. 2009). The velocity structure of the solar wind is known to be largely bimodal, having a slow and fast component that originate under different circumstances (Fisk et al. 1998; Feldman et al. 2005; Riley et al. 2006). This work and previous studies using a polytropic assumption aim to model the globally averaged wind, which can be more generally applied to the variety of

observed stellar masses and rotation periods. More complex wind driving and heating physics are needed in order to reproduce the observed velocity structure of the solar wind; however, they are far harder to generalize for other stars (Cranmer et al. 2007; Pinto et al. 2016).

## 2.1. Magnetic Field Configurations

The magnetic geometries considered in this work include dipole, quadrupole, and octupole combinations, with different field strengths and in some cases relative orientations. As in Paper I, we describe the mixing of different field geometries using the ratio of the polar field strength in a given component to the total field strength. Care is taken to parameterize the field combinations due to the behavior of the two equatorially antisymmetric components, dipole and octupole, at the poles.

We generalize the ratio defined within Paper I for each component such that

$$\mathcal{R}_x = \frac{B_*^{l=x}}{|B_*^{l=1}| + |B_*^{l=2}| + |B_*^{l=3}|} = \frac{B_*^{l=x}}{B_*}, \quad (5)$$

where in this work  $l$  is the principle spherical harmonic number and  $x$  can be 1, 2, or 3 for dipole, quadrupole, or octupole fields. The polar field strength of a given component is written as  $B_*^{l=x}$ , and the  $B_* = |B_*^{l=1}| + |B_*^{l=2}| + |B_*^{l=3}|$  is a characteristic field strength. The polar field strengths in the denominator are given with absolute values because we are interested in the characteristic strength of the combined components, which are the same for aligned and anti-aligned fields. Therefore, summing the absolute value of the ratios produces unity,

$$\sum_{l=1}^3 |\mathcal{R}_l| = 1, \quad (6)$$

which allows the individual values of  $\mathcal{R}_{\text{dip}}$ ,  $\mathcal{R}_{\text{quad}}$ , and  $\mathcal{R}_{\text{oct}}$  ( $\equiv \mathcal{R}_1$ ,  $\mathcal{R}_2$  and  $\mathcal{R}_3$ ) to range from 1 to  $-1$  (north pole positive or negative), with the absolute total remaining constant. We define the magnetic field components using these ratios and the Legendre polynomials  $P_{lm}$ , which for the axisymmetric ( $m=0$ ) field components can be written as

$$B_r(r, \theta) = B_* \sum_{l=1}^3 \mathcal{R}_l P_{l0}(\cos \theta) \left( \frac{R_*}{r} \right)^{l+2}, \quad (7)$$

$$B_\theta(r, \theta) = B_* \sum_{l=1}^3 \frac{1}{l+1} \mathcal{R}_l P_{l1}(\cos \theta) \left( \frac{R_*}{r} \right)^{l+2}. \quad (8)$$

The northern polar magnetic field strengths for each component are given by

$$B_*^{l=1} = \mathcal{R}_{\text{dip}} B_*, \quad B_*^{l=2} = \mathcal{R}_{\text{quad}} B_*, \quad B_*^{l=3} = \mathcal{R}_{\text{oct}} B_*, \quad (9)$$

The relative orientation of the magnetic components is controlled throughout this work by setting the dipole and quadrupole fields ( $B_*^{l=1}$  and  $B_*^{l=2}$ ) to be positive at the northern stellar pole. The octupole component ( $B_*^{l=3}$ ) is then combined with the dipolar and quadrupolar components using either a positive or negative strength on the north pole, which we define as the aligned and anti-aligned cases, respectively.

The addition of dipole and quadrupole components was explored in Paper I. We showed the fields to add in one hemisphere and subtract in the other. Similar to the dipole, the octupole component belongs in the “primary” symmetry

family, having antisymmetric field polarity about the equator (McFadden et al. 1991). The addition of any primary geometries with any “secondary” family quadrupole (equatorially symmetric) would be expected to behave qualitatively similarly. A different behavior is expected from the addition of the two primary geometries (dipole–octupole). Here the field addition and subtraction are primarily governed by the relative orientations of the field with respect to one another. Aligned fields will combine constructively over the pole and subtract from one another in the equatorial region. Anti-aligned primary fields, conversely, will subtract on the pole and add over the equator.

Including the results from Paper I, this work includes combinations of all the possible permutations of the axisymmetric dipole, quadrupole, and octupole magnetic geometries. Table 2 contains a complete list of stellar parameters for the cases computed within this work. Parameters for the dipole–quadrupole combined field cases are available in Table 1 of Paper I. It is noted that in the course of the current work the pure dipolar and quadrupole cases are resimulated; see Table 2.

## 2.2. Derived Stellar Wind Properties

The simulations produce steady-state solutions for density,  $\rho$ , pressure,  $p$ , velocity,  $\mathbf{v}$ , and magnetic field strength,  $\mathbf{B}$ , for each stellar wind case. From these results, the behavior of the spin-down torque is ascertained. The torque on the star,  $\tau$ , due to the loss of angular momentum in the stellar wind is calculated as

$$\tau = \int_A \Lambda \rho \mathbf{v} \cdot d\mathbf{A}, \quad (10)$$

where the angular momentum flux, given by  $\mathbf{F}_{AM} = \Lambda \rho \mathbf{v}$  (Keppens & Goedbloed 2000), is integrated over spherical shells of area  $A$  (outside the closed-field regions).  $\Lambda$  is given by

$$\Lambda(r, \theta) = r \sin \theta \left( v_\phi - \frac{B_\phi}{\rho} \frac{|\mathbf{B}_p|^2}{\mathbf{v}_p \cdot \mathbf{B}_p} \right). \quad (11)$$

Similarly, the mass-loss rate from our wind solutions is calculated as

$$\dot{M} = \int_A \rho \mathbf{v} \cdot d\mathbf{A}. \quad (12)$$

An average Alfvén radius is then defined, in terms of the torque, mass-loss rate  $\dot{M}$ , and rotation rate  $\Omega_*$ :

$$\langle R_A \rangle \equiv \sqrt{\frac{\tau}{\dot{M} \Omega_*}}, \quad (13)$$

In this formulation,  $\langle R_A \rangle / R_*$  is defined as a dimensionless efficiency factor, by which the magnetized wind carries angular momentum from the star, i.e., a larger average Alfvén radius produces a larger torque for a fixed rotation rate and mass-loss rate,

$$\tau = \dot{M} \Omega_* R_*^2 \left( \frac{\langle R_A \rangle}{R_*} \right)^2. \quad (14)$$

In ideal MHD,  $\langle R_A \rangle$  is associated with a cylindrical Alfvén radius, which acts like a “lever arm” for the spin-down torque on the star.

The methodology of this work follows closely that of Paper I, in which we produce semianalytic formulations for  $\langle R_A \rangle$  in terms of the wind magnetization,  $\Upsilon$ , as defined in

previous works (Matt & Pudritz 2008; Matt et al. 2012; Réville et al. 2015; Pantolmos & Matt 2017),

$$\Upsilon = \frac{B_*^2 R_*^2}{\dot{M} v_{\text{esc}}}, \quad (15)$$

where  $B_*$  is now the characteristic polar field, which is split among the different geometries using the ratios  $\mathcal{R}_{\text{dip}}$ ,  $\mathcal{R}_{\text{quad}}$ , and  $\mathcal{R}_{\text{oct}}$ . The values of  $\Upsilon$  produced from the steady-state solutions are indirectly controlled by increasing the value of  $v_A/v_{\text{esc}}$ . This increases the polar magnetic field strength for a given density normalization. The mass-loss rate is similarly uncontrolled and evolves to steady state, depending mostly on our choice of Parker wind parameters, but is also adjusted self-consistently by the magnetic field. The values of  $\Upsilon$  are tabulated in Table 2, along with  $\mathcal{R}_l$  values, magnetic field strengths given by  $v_A/v_{\text{esc}}$ , and the average Alfvén radii for each case simulated. Results for combined dipole–quadrupole cases are available in Table 1 of Paper I. Figure 1 shows the parameter space of simulations with their value of  $\Upsilon$  against the different ratios for either quadrupole–octupole or dipole–octupole cases, with the lower-order geometry ratio labeling the cases ( $\mathcal{R}_{\text{quad}}$  and  $\mathcal{R}_{\text{dip}}$ , respectively).

## 3. Wind Solutions and $\langle R_A \rangle$ Scaling Relations

### 3.1. Single Geometry Winds

For single magnetic geometries, increasing the complexity of the field decreases the effectiveness of the magnetic braking process by reducing the average Alfvén radius (braking lever arm) for a given field strength (Garraffo et al. 2015). The impact of changing field geometries on the scaling of the Alfvén radius for thermally driven winds was shown by Réville et al. (2015) for the dipole, quadrupole, and octupole geometries. We repeat the result of Réville et al. (2015) for a slightly hotter coronal temperature wind,  $c_s = 0.25$  in our cases, compared to  $c_s = 0.222$ . This temperature more reasonably approximates the solar wind terminal velocity, typically resulting in a wind speed of  $\approx 500 \text{ km s}^{-1}$  at 1 au for solar parameters. For each magnetic geometry, we simulate eight different field strengths, changing the input value of  $v_A/v_{\text{esc}}$  as tabulated in Table 2 (cases 1–24).

Each wind solution gives a value for the Alfvén radius,  $\langle R_A \rangle$ , and the wind magnetization,  $\Upsilon$ . These values are represented in Figure 2 as colored circles, and their scaling can be described using the Alfvén radius relation from Matt & Pudritz (2008), with three precise power-law relations for the different magnetic geometries, as found previously in the work of Réville et al. (2015):

$$\frac{\langle R_A \rangle}{R_*} = K_s \Upsilon^{m_s}, \quad (16)$$

where  $K_s$  and  $m_s$  are fit parameters for this relation, which utilizes the surface field strength. Best-fit parameters for each geometry are tabulated in Table 3.

With increasing  $l$  values, the higher-order geometries produce increasingly shallow slopes with wind magnetization, such that they approach a purely hydrodynamical lever arm, i.e., the wind carries away angular momentum corresponding to the surface rotation alone, with the torque efficiency equal to the average cylindrical radius of the stellar surface from the

**Table 2**  
Input Parameters and Results from Simulations with One and Two Magnetic Components

Case	$\mathcal{R}_{\text{dip}}/\mathcal{R}_{\text{quad}}/\mathcal{R}_{\text{oct}}$	$v_A/v_{\text{esc}}$	$\langle R_A \rangle/R_*$	$\Upsilon$	$\Upsilon_{\text{open}}$	$\langle v(R_A) \rangle/v_{\text{esc}}$	Case	$\mathcal{R}_{\text{dip}}/\mathcal{R}_{\text{quad}}/\mathcal{R}_{\text{oct}}$	$v_A/v_{\text{esc}}$	$\langle R_A \rangle/R_*$	$\Upsilon$	$\Upsilon_{\text{open}}$	$\langle v(R_A) \rangle/v_{\text{esc}}$
1	1.0 0.0 0.0	0.5	5.0	185	1460	0.22	65	0.5 0.0 0.5	0.5	3.8	203	648	0.17
2	1.0 0.0 0.0	1.0	6.9	735	3540	0.29	66	0.5 0.0 0.5	1.0	4.9	705	1380	0.22
3	1.0 0.0 0.0	1.5	8.5	1790	6440	0.34	67	0.5 0.0 0.5	1.5	5.8	1580	2300	0.26
4	1.0 0.0 0.0	2.0	9.9	3380	9710	0.37	68	0.5 0.0 0.5	2.0	6.7	2860	3420	0.29
5	1.0 0.0 0.0	3.0	12.3	8330	17100	0.42	69	0.5 0.0 0.5	3.0	8.3	6830	6300	0.34
6	1.0 0.0 0.0	6.0	17.5	36500	43200	0.49	70	0.5 0.0 0.5	6.0	11.7	29800	16200	0.42
7	1.0 0.0 0.0	12.0	22.6	134000	85300	0.54	71	0.5 0.0 0.5	12.0	15.1	110000	33800	0.49
8	1.0 0.0 0.0	20.0	28.1	353000	156000	0.60	72	0.5 0.0 0.5	20.0	18.7	299000	61000	0.50
9	0.0 1.0 0.0	0.5	3.4	179	409	0.14	73	0.3 0.0 0.7	0.5	3.4	159	451	0.12
10	0.0 1.0 0.0	1.0	4.0	689	733	0.18	74	0.3 0.0 0.7	1.0	4.3	607	977	0.20

(This table is available in its entirety in machine-readable form.)

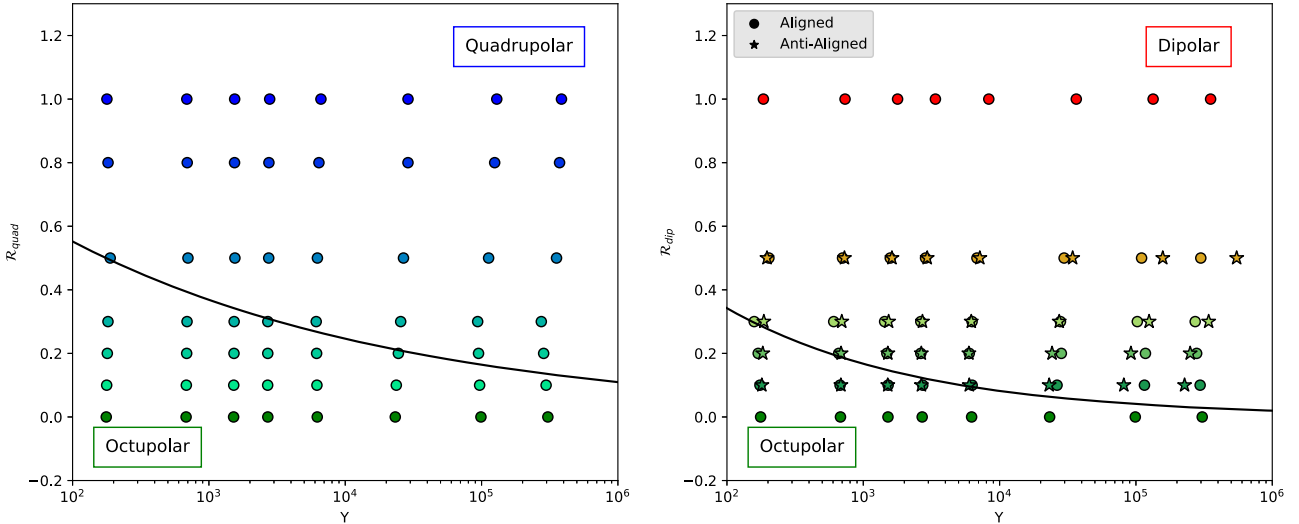


**Figure 1.** The two parameter spaces first examined in this work, quadrupole–octupole (left) and dipole–octupole (right), shown in terms of  $\Upsilon$  and either  $\mathcal{R}_{\text{quad}}$  or  $\mathcal{R}_{\text{dip}}$  (Equation (5)), respectively. Each point represents a simulation using the PLUTO code, with the color of each point labeling them throughout this work, depending on their relative combination of field components. The black solid lines represent  $\Upsilon_{\text{crit}}$  for each combination, where the break in the Alfvén radius scaling is found (see equation (19)). In both two component parameter spaces, the average Alfvén radius scales as a pure octupole (bottom left) for low wind magnetisations and high octupole fraction. Then scales with the lowest-order component, either dipole or quadrupole (upper right).

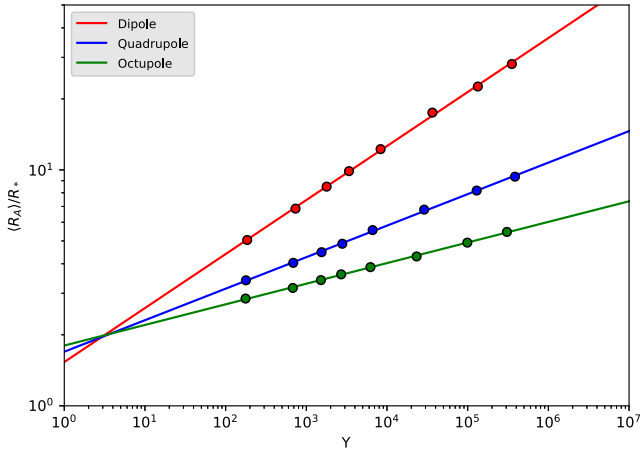


**Figure 2.** Average Alfvén radius vs. the wind magnetization,  $\Upsilon$  (Equation (15)), in our simulations with single geometries (circles). Different scaling relations are shown for each pure geometry (solid lines). Higher  $l$  order geometries produce a smaller Alfvén radius and thus smaller spin-down torque for a given polar field strength and mass-loss rate. A similar result was first shown by Réville et al. (2015).

rotation axis,  $\langle R_A \rangle / R_* = (2/3)^{1/2}$  (Mestel 1968). Any significant magnetic braking in Sun-like stars will therefore be predominantly mediated by the lowest-order components.

### 3.2. Combined Magnetic Geometries

Based on work performed in Paper I, we anticipate the behavior of the average Alfvén radius for magnetic field geometries that contain, dipole, quadrupole, and octupole components. The dipole component, having the slowest radial decay, is expected to govern the field strength at large distances, then the field should scale like the quadrupole at intermediate distances, and finally, close to the star, the field should scale like the octupole geometry. The Alfvén radius formulation therefore takes the form of a twice-broken power

**Table 3**  
Single Component Fit Parameters to Equation (16)

Topology ( $l$ )	$K_s$	$m_s$
Dipole (1)	$1.53 \pm 0.03$	$0.229 \pm 0.002$
Quadrupole (2)	$1.70 \pm 0.02$	$0.134 \pm 0.002$
Octupole (3)	$1.80 \pm 0.01$	$0.087 \pm 0.001$

**Note.** Fit values deviate slightly from those presented in Paper I owing to the more accurate numerical results found with logarithmic grid spacing, used here.

law,

$$\frac{\langle R_A \rangle}{R_*} = \max \begin{cases} K_{s,\text{dip}} [\mathcal{R}_{\text{dip}}^2 \Upsilon]^{m_{s,\text{dip}}}, \\ K_{s,\text{quad}} [(|\mathcal{R}_{\text{dip}}| + |\mathcal{R}_{\text{quad}}|)^2 \Upsilon]^{m_{s,\text{quad}}}, \\ K_{s,\text{oct}} [(|\mathcal{R}_{\text{dip}}| + |\mathcal{R}_{\text{quad}}| + |\mathcal{R}_{\text{oct}}|)^2 \Upsilon]^{m_{s,\text{oct}}}, \end{cases} \quad (17)$$

which approximates the simulated values of the average Alfvén radius. Note that  $|\mathcal{R}_{\text{dip}}| + |\mathcal{R}_{\text{quad}}| + |\mathcal{R}_{\text{oct}}| = 1$ , such that the final scaling depends purely on the total  $\Upsilon$ .

Here we present simulation results from combinations of each field, sampling a range of mixing fractions and field strengths. These are used to validate this semianalytic prescription for predicting the spin-down torque on a star, due to a given combination of axisymmetric magnetic fields.

#### 3.2.1. Dipole Combined with Quadrupole

The regime of dipole and quadrupole combined geometries is presented in Paper I. We briefly reiterate the results here, displaying values from that study in Figure 3.

These fields belong to different symmetry families, primary and secondary. As such, their addition creates a globally asymmetric field about the equator, with the north pole in this case being stronger than the south. The relative fraction of the two components alters the location of the current

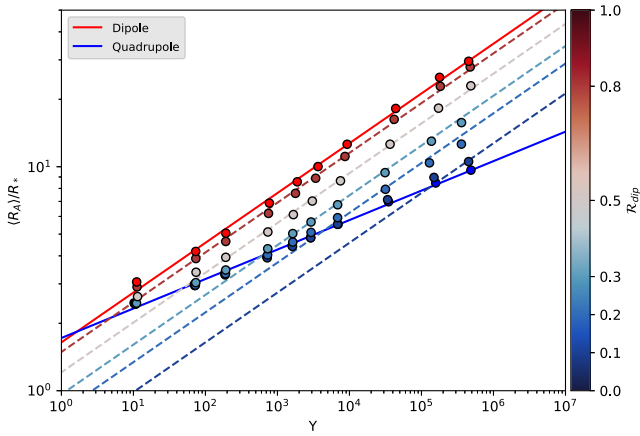


**Figure 3.** Average Alfvén radius scaling with wind magnetization,  $\Upsilon$ , for the different combinations of dipole and quadrupole, from the study in Paper I (circles). Solid lines show scaling for pure dipole and quadrupole. The deviation from single power laws shows how the combination of dipole and quadrupole fields modifies the Alfvén radius scaling, compared to single geometries. The scaling predicted by only considering the fractional dipole component is plotted with multiple dashed colored lines corresponding to the different  $\mathcal{R}_{dip}$  values. This shows that  $\langle R_A \rangle / R_*$  scales with the dipole component only, unless the quadrupole is dominant at a distance of  $\approx R_A$ .

sheet/streamers, which appear to resemble the dominant global geometry.

It is shown in Paper I that the quadrupole component has a faster radial decay than the dipole, and therefore at large distances only the dipole component of the field influences the location of the Alfvén radius. Closer to the star, the total field decays radially like the quadrupole, with the dipole component adding its strength, so near to the star the Alfvén radius scaling depends on the total field strength. Therefore, we developed a broken power law to describe the behavior of the average Alfvén radius scaling with wind magnetization, which uses the maximum of either the quadrupole slope using the total field strength, as if the combined field decays like a quadrupole (solid blue line), or the dipolar slope using only the dipole component (shown in color-coded dashed lines). The dipole component of the wind magnetization is formulated as

$$\Upsilon_{dip} = \left( \frac{B_*^{l=1}}{B_*} \right)^2 \frac{B_*^2 R_*^2}{\dot{M} v_{esc}} = \mathcal{R}_{dip}^2 \Upsilon. \quad (18)$$

Mathematically, Equation (17) becomes the broken power law from Paper I when  $\mathcal{R}_{oct} = 0$ ,

$$\frac{\langle R_A \rangle}{R_*} = \begin{cases} K_{s,dip} [\mathcal{R}_{dip}^2 \Upsilon]^{m_{s,dip}}, & \text{if } \Upsilon > \Upsilon_{crit}(\mathcal{R}_{dip}), \\ K_{s,quad} [\Upsilon]^{m_{s,quad}}, & \text{if } \Upsilon \leq \Upsilon_{crit}(\mathcal{R}_{dip}), \end{cases} \quad (19)$$

where the octupolar relation is ignored, and  $|\mathcal{R}_{dip}| + |\mathcal{R}_{quad}| = 1$ . Here  $\Upsilon_{crit}$  describes the intercept of the dipole component and quadrupole slopes,

$$\Upsilon_{crit}(\mathcal{R}_{dip}) = \left[ \frac{K_{s,dip} \mathcal{R}_{dip}^{2m_{s,dip}}}{K_{s,quad}} \right]^{m_{s,quad}^{-1} - m_{s,dip}}. \quad (20)$$

Equation (17) further expands the reasoning above to include any field combination of the axisymmetric dipole, quadrupole, and octupole. The following sections test this formulation against simulated combined geometry winds.

### 3.2.2. Quadrupole Combined with Octupole

Stellar magnetic fields containing both a quadrupole and octupole field component present another example of primary and secondary family fields in combination. As with the axisymmetric dipole–quadrupole addition, the relative orientation of the two components simply determines which regions of magnetic field experience addition and subtraction about the equator, so that the torque and mass-loss rate do not depend on their relative orientation. Compared with the dipole component, both fields are less effective in generating a magnetic lever arm to brake rotation at a given value of  $\Upsilon$ .

We test the validity of Equation (17), setting  $\mathcal{R}_{dip} = 0$  and systematically varying the value of  $\mathcal{R}_{quad}$ , with the octupole fraction composing the remaining field,  $\mathcal{R}_{oct} = 1 - \mathcal{R}_{quad}$ . Five mixed case values are selected ( $\mathcal{R}_{quad} = 0.8, 0.5, 0.3, 0.2, 0.1$ ) that parameterize the mixing of the two geometries. Steady-state wind solutions are displayed in Figure 4, showing, as with dipole–quadrupole addition, the equatorially asymmetric fields produced. With increasing polar field strength, the streamers are observed to shift toward the lowest-order geometry morphology (quadrupolar in this case), as was shown for the dipole in Paper I.

The average Alfvén radii and wind magnetization are shown in Figure 5. The behavior of  $\langle R_A \rangle$  is quantitatively similar to that of the dipole–quadrupole addition, where combined field cases are scattered between the two pure geometry scaling relations. The range of available  $\langle R_A \rangle$  values between the pure quadrupole and octupole scaling relations (solid blue and green, respectively) is reduced compared to the previous dipole–quadrupole, due to the weaker dependence of the Alfvén radius with wind magnetization.

As required by Equation (17), with no dipolar component, we introduce the quadrupole component of  $\Upsilon$  as

$$\Upsilon_{quad} = \left( \frac{B_*^{l=2}}{B_*} \right)^2 \frac{B_*^2 R_*^2}{\dot{M} v_{esc}} = \mathcal{R}_{quad}^2 \Upsilon, \quad (21)$$

and the second relation in Equation (17) takes the form

$$\frac{\langle R_A \rangle}{R_*} = K_{s,quad} [\Upsilon_{quad}]^{m_{s,quad}}, \quad (22)$$

where  $K_{s,quad}$  and  $m_{s,quad}$  are determined from the pure geometry scaling (see Table 3).

The quadrupole component of the wind magnetization is plotted for different  $\mathcal{R}_{quad}$  values in Figure 5, showing an identical behavior to the dipole component in the dipole–quadrupole combined fields. The  $\Upsilon_{quad}$  formulation is shown in Figure 6, with the solid blue line described by Equation (22). This agrees with a large proportion of the wind solutions, with deviations due to a switch of regime onto the octupole relation, the third relation in Equation (17),

$$\frac{\langle R_A \rangle}{R_*} = K_{s,oct} [\Upsilon]^{m_{s,oct}} = \frac{K_{s,oct}}{\mathcal{R}_{quad}^{2m_{s,oct}}} [\Upsilon_{quad}]^{m_{s,oct}}, \quad (23)$$

shown with a solid green line in Figure 5 and dashed color-coded lines in Figure 6. As with the dipole–quadrupole addition, a broken power law can be formulated taking the maximum of either the octupole scaling or the quadrupole component scaling, for a given  $\mathcal{R}_{quad}$  value. For the cases simulated, we find a deviation from this broken power

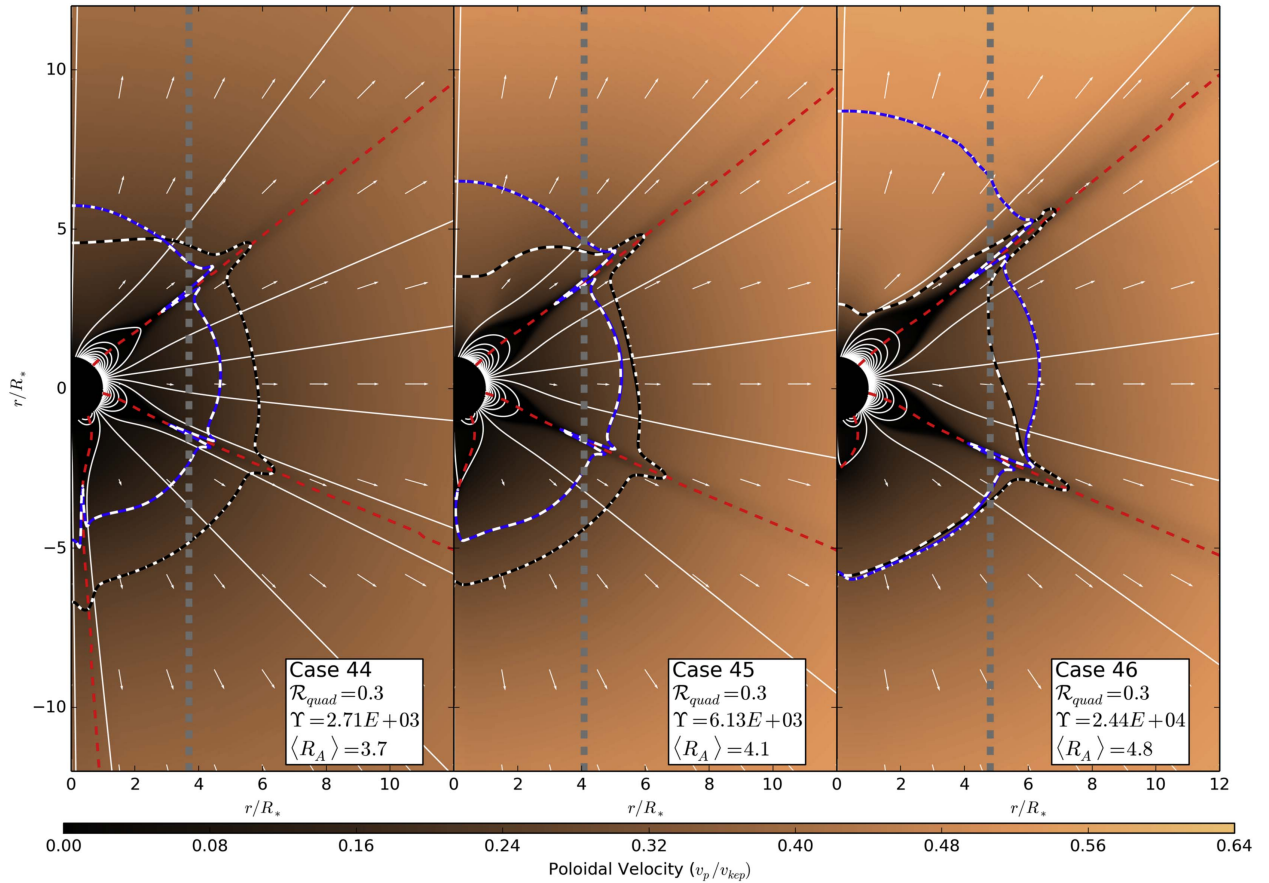


**Figure 4.** Steady-state solutions for the quadrupole–octupole combined geometry cases 44, 45, and 46, showing a progression from weaker to stronger magnetization ( $\Upsilon$ ) from left to right. The color background represents the poloidal speed normalized by the Keplerian speed (e.g.,  $\approx 400 \text{ km s}^{-1}$  for solar parameters). Dead zones are therefore in black. Thin white lines trace the magnetic field, with red dashed lines highlighting the field polarity reversals (i.e., where  $B_r = 0$ ). Alfvén and sonic surfaces are indicated with thick blue and black lines, respectively, with the fast and slow magnetosonic surfaces represented as dot-dashed and dashed white lines. Vertical gray dashed lines show the average Alfvén radius  $\langle R_A \rangle$  (Equation (13)), representing the torque efficiency, scales with the size of the Alfvén surface. The asymmetry of the global magnetic field about the equator is shown, with a qualitatively similar behavior to the dipole–quadrupole simulations in Paper I.

law of no greater than 5%, with most cases showing a closer agreement.

### 3.2.3. Dipole Combined with Octupole

Unlike the previous field combinations, both the dipole and octupole belong to the primary symmetry family, and thus their addition produces two distinct field topologies for aligned or anti-aligned fields. Again, we test Equation (17), now with  $\mathcal{R}_{quad} = 0$ . The field combinations are parameterized using the ratio of dipolar field to total field strength,  $\mathcal{R}_{dip}$ , with the remaining field in the octupolar component  $\mathcal{R}_{oct} = 1 - \mathcal{R}_{dip}$ . The ratio of dipolar field is varied ( $\mathcal{R}_{dip} = 0.5, 0.3, 0.2, 0.1$ ). Additionally, we repeat these ratios for both aligned and anti-aligned fields. This produces eight distinct field geometries that cover a range of mixed dipole–octupole fields.

Figure 7 displays the behavior of both aligned and anti-aligned cases with increasing field strength. The combination of dipolar and octupolar fields produces a complex field topology that is alignment dependent and impacts the local flow properties of the stellar wind. The symmetric property of the global field is maintained about the equator. Aligned combinations have magnetic field addition over the poles, which increases the Alfvén speed, producing a larger Alfvén radius over the poles. However, the fields subtract over the

equator, which reduces the size of the Alfvén radius over the equator; see the top panel of Figure 4. The bottom panel shows anti-aligned mixed cases to exhibit the opposite behavior, with a larger equatorial Alfvén radius and a reduction to the size of the Alfvén surface at higher latitudes. The torque-averaged Alfvén radius is shown by the gray dashed lines in each case, representing the cylindrical Alfvén radius  $\langle R_A \rangle$ . For the simulations in this work, the anti-aligned cases produce a larger lever arm compared with their aligned counterparts, with a few exceptions. In general, the increased Alfvén radius at the equator for the anti-aligned fields is more effective at increasing the torque-averaged Alfvén radius compared with the larger high-latitude Alfvén radius in the aligned field cases.

The locations of the current sheets are shown in Figure 7 using red dashed lines. As noted with the dipole–quadrupole addition in Paper I, the global dipolar geometry is restored with increasing fractions of the dipole component or increased field strength for a given mixed geometry. The latter is shown in Figure 7 for both aligned and anti-aligned cases. With increased field strength, a single dipolar streamer begins to be recovered over the equator. A key difference between the two field alignments is the asymptotic location of the three streamers. In the case of an aligned octupole component, increasing the total field strength for a given ratio forces the streamers toward the equator, at which point they begin to

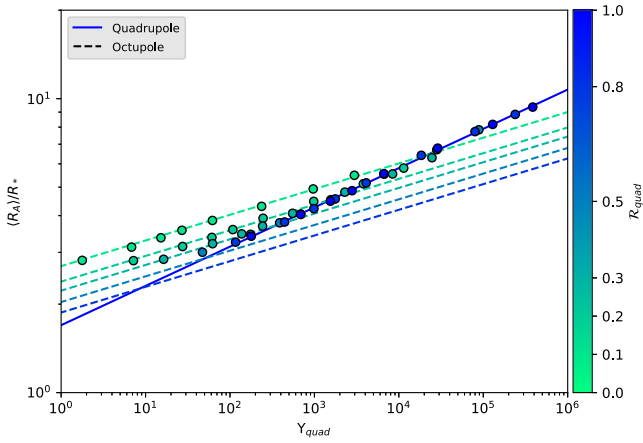


**Figure 5.** Average Alfvén radius vs. wind magnetization,  $\Upsilon$ , for the different combinations of quadrupole and octupole, in a similar format to Figure 3. Color-coded dashed lines relate to the prediction considering only the quadrupolar component of the field for each  $\mathcal{R}_{quad}$ . The combinations shown here behave in a similar manner to dipole–quadrupole combined fields, in a sense that the lower-order field (with the lowest  $l$ ) governs the Alfvén radius for large wind magnetizations,  $\Upsilon$ , and the higher-order field (large  $l$ ) controlling the low magnetization scaling.

merge into the dipolar streamer. With an anti-aligned octupole component, the opposite is found, with the high-latitude streamers forced toward the poles and onto the rotation axis. It is unclear whether this effect is significant itself in influencing the global torque.

Using Equation (17), with no quadrupolar component, we anticipate that the dipolar component (first relation) will be the most significant in governing the global torque. Figures 8 and 9 show the dipole–octupole cases following the expected behavior, as observed for dipole–quadrupole and quadrupole–octupole combinations. We see that the average Alfvén radius follows either the dipole component scaling ( $\Upsilon_{dip}$ ) or the octupole scaling relation,

$$\frac{\langle R_A \rangle}{R_*} = K_{s,oct} [\Upsilon]^{m_{s,oct}} = \frac{K_{s,oct}}{\mathcal{R}_{dip}^{2m_{s,oct}}} [\Upsilon_{dip}]^{m_{s,oct}}. \quad (24)$$

However, as evident in both figures, there is a deviation from this scaling, with the strongest variations belonging to low- $\mathcal{R}_{dip}$  cases. Anti-aligned cases follow the behavior expected from Paper I with a much higher precision than the anti-aligned cases. Figure 9 shows the dipole scaling to overpredict the aligned cases compared with the anti-aligned cases. This occurs because Equation (17) is a simplified picture of the actual dynamics within our simulations, and as such, it does not encapsulate all of the physical effects. The trends are still obvious for both aligned and anti-aligned cases, and the scatter simply represents a reduction to the precision of our formulation.

Despite this deviation from predicted values, Figure 9 shows the dipole component again to be the most significant in governing the global torque. With a more complex (higher  $l$ ) secondary component, the dipole dominates the Alfvén radius scaling at a much lower wind magnetization, when compared with the dipole–quadrupole combinations. For the dipole–octupole cases simulated, the dipole component dominates the majority of the simulated cases. For our dipole and octupole mixed fields the transition between regimes occurs at

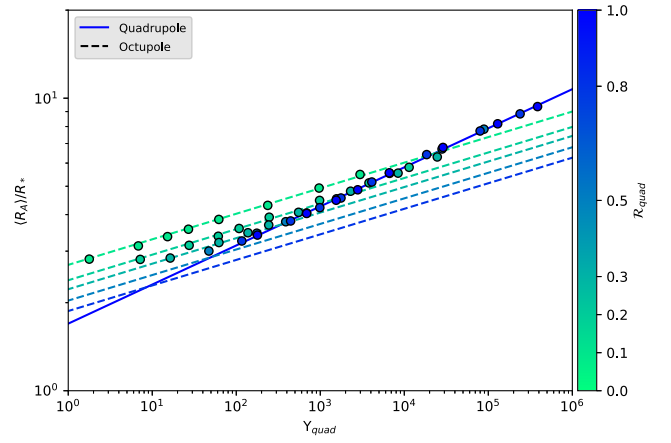


**Figure 6.** Average Alfvén radius vs. the quadrupolar component of the wind magnetization,  $\Upsilon_{quad}$ , for cases with mixed quadrupole and octupole components (circles). The solid blue line shows the prediction based on the quadrupole component only (Equation (22)). The dashed lines show the octupolar scaling (Equation (23)). A broken power law composed of the quadrupole component and the octupolar scaling ( $\mathcal{R}_{quad}$  dependent) can be constructed similarly to work done in Paper I. The quadrupolar geometry dominates the scaling, for all of the  $\mathcal{R}_{quad}$  values simulated here, at  $\langle R_A \rangle / R_* \approx 9$ . The point at which the quadrupolar geometry dominates for a given  $\mathcal{R}_{quad}$  value can be approximated by considering the strength of the two fields at the Alfvén radii, i.e., the radial distance when the strength of the quadrupole matches or exceeds that of the octupole  $B_{quad}/B_{oct} = \mathcal{R}_{quad}/(1 - \mathcal{R}_{quad})(r/R_*)$ .

$\Upsilon_{dip} \approx 100$ , such that the  $\langle R_A \rangle$  for fields with  $\mathcal{R}_{dip} = 0.1$ , or higher, and a physically realistic wind magnetization will all be governed by the dipole component.

### 3.2.4. Combined Dipole, Quadrupole, and Octupole Fields

In addition to the quadrupole–octupole and dipole–octupole combinations presented previously, we also perform a small set of simulations containing all three components. Their stellar wind parameters and results are tabulated in Table 4. We select a regime where the dipole does not dominate ( $\mathcal{R}_{dip} = 0.1$ ), to observe the interplay of the additional quadrupole and octupole components. We also utilize cases 89–96 and 121–128 from this work and cases 51–60 from Paper I, all of which sample varying fractions of quadrupole and octupole with a fixed  $\mathcal{R}_{dip} = 0.1$ . These are compared against the three-component cases, 129–160.

Equation (17) is adopted, now using all three components, such that the results from these simulations are expected to scale in magnetization like a twice-broken power law. As noted with the dipole–octupole addition, the inclusion of an octupolar component introduces behaviors that will not be accounted for by this formulation, i.e., Equation (17) is independent of field alignments, etc. We aim to characterize this unaccounted-for physics in terms of an available precision on the use of Equation (17). The simulated Alfvén radii are compared against their predicted values in Figure 10, along with the other simulations from this work (shown in white). The three-component field combinations have a small dipolar component; therefore, the dipolar scaling of the average Alfvén radius is rarely the dominant term in Equation (17). The different values of quadrupolar and octupolar field that compose the remaining field strength govern the average Alfvén radius scaling for the majority of this parameter space. From Figure 10, the approximate

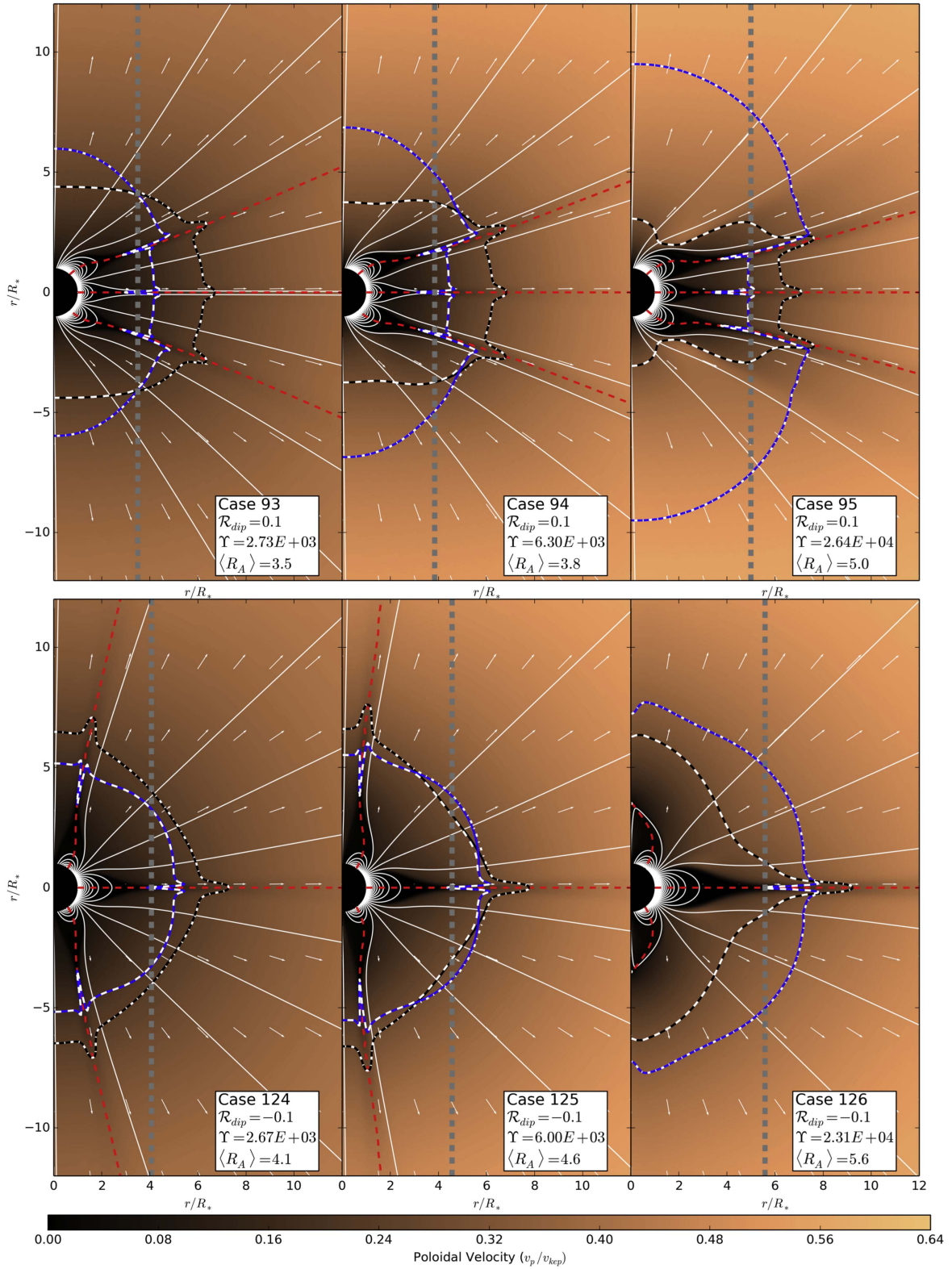


**Figure 7.** Steady-state solutions for the dipole–octupole combined geometries with aligned fields (top row; cases 93, 94, and 95) and anti-aligned fields (bottom row; cases 124, 125, and 126). The format and lines are the same as in Figure 4. The aligned cases have field adding near the poles and subtracting near the equator, where the opposite is true for the anti-aligned cases. The difference in how these two cases combine results in a different shape of the Alfvén surface. Also, for the same magnetization ( $\Upsilon$ ), the anti-aligned cases, in general, systematically produce a larger torque efficiency ( $\langle R_A \rangle$ ; vertical dashed gray lines). This is due to these cases having a stronger field at low latitudes, where the angular momentum loss is more efficient.



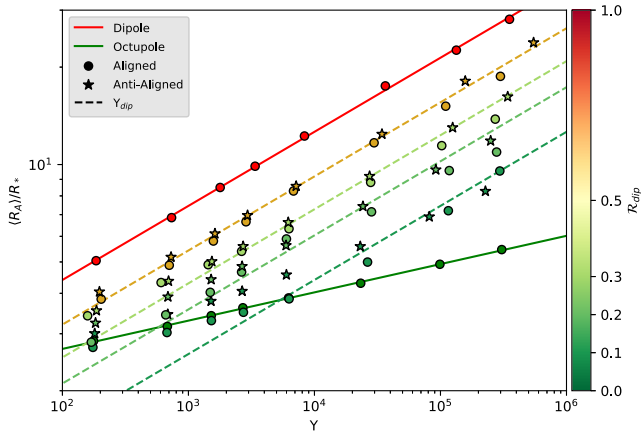


**Figure 8.** Average Alfvén radius scaling with wind magnetization,  $\Upsilon$ , for the different combinations of dipole and octupole. The fields are either added aligned at the poles (circles) or anti-aligned (stars). Dashed lines show the dipole component scaling, color-coded to match the simulated values of  $\mathcal{R}_{\text{dip}}$ . The overall behavior here is similar to the previous mixed combined fields, with the lower-order field governing the Alfvén radius for large wind magnetizations. However, the different field alignments appear to scatter around the  $\Upsilon_{\text{dip}}$  approximation, with the anti-aligned cases typically having larger  $R_A$  than the aligned cases, for the same  $\Upsilon$ .

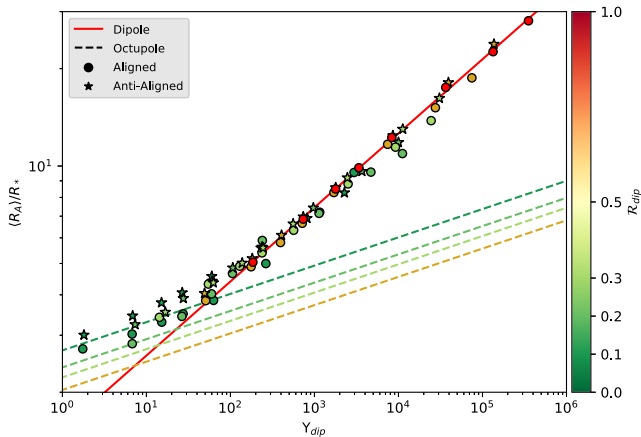


**Figure 9.** Average Alfvén radius scaling with only the dipolar component of the wind magnetization,  $\Upsilon_{\text{dip}}$ , for cases with combined dipole and octupole components. Aligned field are shown with circles, anti-aligned with stars. The parameter space investigated here is well approximated by the dipole component scaling relation (solid red line). Generally the aligned field cases are shown to undershoot the dipole component approximation, while the anti-aligned cases match the power law with similar agreement to the previous combined geometries. The qualitative behavior is again similar to the previous combined cases; however, due to the larger difference in radial decay of the field, i.e.,  $B_{\text{dip}}/B_{\text{oct}} = \mathcal{R}_{\text{dip}}/(1 - \mathcal{R}_{\text{dip}})(r/R_*)^2$ , the dipole dominates at much smaller  $R_A \approx 3$ .

formulation agrees well with the simulated values, with the largest discrepancies emerging at smaller radii and for anti-aligned cases; see the residual plot below. A 10% divergence from our prediction (dashed lines in both the top and bottom panels of Figure 10) is shown to roughly approximate the effects not taken into account by the simple scaling, with the largest deviation to 18.3%.

Equation (17) is observed to have increasing accuracy as the Alfvén radii become larger in Figure 10; this is due to the increasing dominance of the dipolar component at large distances. Quantifying the scatter in our residual, we approximate the distribution of deviations as Gaussian and

calculate a standard deviation of 5.1%, when evaluating all 160 of our simulated cases. Considering the 32 three-component cases, the standard deviation remains of the same order of 5.2%, indicating that the formulation maintains precision with the inclusion of all three antisymmetric components. The largest deviations from the predicted values belong to the dipole–octupole simulations, and these are observed within Figures 8 and 9. In both figures, as well as the residual, the predicted values are shown to underestimate the simulated values, for small average Alfvén radii, but with increasing field strength they begin to overpredict. The trends in the residual represent physics not incorporated into our approximate formula and can be explained. The underestimation at first is due to the sharpness of the regime transition from the broken-power-law representation; in reality, there is a smoother transition that is always larger than the break in power laws. This significantly impacts the dipole–octupole simulations, as they most often probe this regime, as can be seen within Figure 9. For the dipole–octupole combinations, we propose that this transition must be much broader to match the deviations in the residual of Figure 10.

Equation (17) represents an approximation to the impact of mixed geometry fields on the prediction of the average Alfvén radius. Our mixed cases are found to be well behaved and can all be predicted by this formulation within  $\approx \pm 20\%$  accuracy for the most deviant; the majority lie within  $\approx \pm 5\%$  accuracy.

### 3.3. Analysis of Previous Mixed Fields

Réville et al. (2015) presented mixed-field simulations containing axisymmetric dipole, quadrupole, and octupole components, based on observations of the Sun, at maximum and minimum of magnetic activity, along with a solar-like star TYC-0486. To further test our formulation, we use input parameters and results from Table 3 of Réville et al. (2015) and predict values for the average Alfvén radii of the mixed cases produced in their work. We use Equation (17) with the fit constants from their lower-temperature wind ( $c_s/v_{\text{esc}} = 0.222$ ) and manipulate the given field strengths into suitable  $\mathcal{R}_l$  values. Results can be found in Table 5 and are shown in Figure 10 with red squares. The predicted values for the Alfvén radii agree to better than 10% precision. The largest deviation,  $\approx 8\%$ , is for TYC-0486, which we credit to the location of the predicted Alfvén radius falling in between regimes, at the break in the power law (almost governed by the dipole component only), where the broken-power-law approximation has the biggest error.

Recent work by Réville & Brun (2017) presented 13 thermally driven wind simulations, in 3D, for the solar wind, using Wilcox Solar Observatory magnetograms, spanning the years 1989–2001. These simulations use the spherical harmonic coefficients derived from the magnetograms, up to  $l = 15$ , including the nonaxisymmetric modes. We predict the values of the average Alfvén radii using Equation (17), allowing the strength of any nonaxisymmetric component to be added in quadrature with the axisymmetric component to produce representative strengths for the dipole, quadrupole, and octupole components. For example, the dipole field strength is computed as

$$B_*^{l=1} = \sqrt{(B_{m=-1}^{l=1})^2 + (B_{m=0}^{l=1})^2 + (B_{m=1}^{l=1})^2}. \quad (25)$$

**Table 4**  
Input Parameters and Results from Simulations with Three Magnetic Components

Case	$\mathcal{R}_{\text{dip}} \mathcal{R}_{\text{quad}} \mathcal{R}_{\text{oct}}$	$v_A/v_{\text{esc}}$	$\langle R_A \rangle/R_*$	$\Upsilon$	$\Upsilon_{\text{open}}$	$\langle v(R_A) \rangle/v_{\text{esc}}$
129	0.1 0.6 0.3	0.5	3.1	181	289	1.09
130	0.1 0.6 0.3	1.0	3.6	698	502	1.33
131	0.1 0.6 0.3	1.5	4.0	1550	709	1.49
132	0.1 0.6 0.3	2.0	4.4	2760	923	1.61
133	0.1 0.6 0.3	3.0	4.9	6320	1400	1.81
134	0.1 0.6 0.3	6.0	6.3	27100	3030	2.17
135	0.1 0.6 0.3	12.0	7.9	111000	6430	2.65
136	0.1 0.6 0.3	20.0	9.3	308000	11200	3.09
137	0.1 0.6 0.6	0.5	2.7	182	194	0.97
138	0.1 0.3 0.6	1.0	3.1	702	326	1.17
139	0.1 0.3 0.6	1.5	3.4	1560	451	1.29
140	0.1 0.3 0.6	2.0	3.7	2760	585	1.37
141	0.1 0.3 0.6	3.0	4.2	6230	903	1.53
142	0.1 0.3 0.6	6.0	5.5	25600	2180	1.85
143	0.1 0.3 0.6	12.0	7.2	97000	4850	2.25
144	0.1 0.3 0.6	20.0	8.6	246000	8560	2.61
145	0.1 0.6  - 0.3	0.5	3.2	34	312	1.13
146	0.1 0.6  - 0.3	1.0	3.7	119	533	1.37
147	0.1 0.6  - 0.3	1.5	4.1	258	765	1.53
148	0.1 0.6  - 0.3	2.0	4.5	451	1000	1.65
149	0.1 0.6  - 0.3	3.0	5.1	1020	1500	1.85
150	0.1 0.6  - 0.3	6.0	6.5	4450	3400	2.21
151	0.1 0.6  - 0.3	12.0	8.2	18600	7260	2.69
152	0.1 0.6  - 0.3	20.0	10.1	55300	13200	3.17
153	0.1 0.3  - 0.6	0.5	3.0	4	254	1.05
154	0.1 0.3  - 0.6	1.0	3.5	21	430	1.25
155	0.1 0.3  - 0.6	1.5	3.9	49	607	1.37
156	0.1 0.3  - 0.6	2.0	4.2	91	782	1.49
157	0.1 0.3  - 0.6	3.0	4.7	214	1160	1.65
158	0.1 0.3  - 0.6	6.0	5.9	916	2440	2.01
159	0.1 0.3  - 0.6	12.0	7.5	3770	5360	2.41
160	0.1 0.3  - 0.6	20.0	9.3	11300	10200	2.85

We obtained the field strengths for the dipole, quadrupole, and octupole components of the magnetograms used in the simulations of Réville & Brun (2017), ignoring the higher-order field components (V. Réville 2017, private communication). The results from this are shown in Figure 10 with magenta squares and show a good agreement in most cases to the simulated values. However, we note that the Alfvén radii tabulated within Réville & Brun (2017) are geometrically averaged rather than torque averaged, as used in this work (both scale with wind magnetization in a similar manner). These values thus represent the average spherical radius for the Alfvén surface in their 3D simulations. The base wind temperature for their simulations is also cooler ( $c_s/v_{\text{esc}} \approx 0.234$ ) than in our simulations. Nevertheless, Figure 10 shows good agreement with the predicted values; we calculate a standard deviation of 8.4%. If we apply an approximate correction to the spherical radii with a factor of  $2/3$  (due to the angular momentum lever arm being proportional to  $r \sin \theta$ ) and use torque scaling coefficients fit to the lower-temperature wind from Pantolmos & Matt (2017), we find that all the magenta simulations fit within the 10% precision, despite the inclusion of the nonaxisymmetric components. This suggests that Equation (17) can be used in cases with nonaxisymmetric geometries in combination, but further study is required to test more fully.

## 4. Analysis Based on Open Flux

### 4.1. Magnetic Flux Profiles

The behavior of the stellar wind torque, quantified in the previous sections, is similar to the results found in Paper I. Lower-order magnetic components decay more slowly with radius than higher-order components. Thus, the lower-order component typically dominates the dynamics of the global torque. The higher-order component can usually be ignored, unless it has a comparable field strength to the lower-order component at the Alfvén radius, which requires the higher-order field to dominate at the surface.

The radial dependence of the magnetic field is best described by the unsigned magnetic flux. To calculate this, we evaluate an integral of the magnetic field threading closed spherical shells with area  $A$ ; this produces the unsigned magnetic flux as a function of radial distance,

$$\Phi(r) = \oint_r |\mathbf{B} \cdot d\mathbf{A}|. \quad (26)$$

For a potential field, as used in the initial conditions, the magnetic flux decays as a simple power law,

$$\Phi(r) = \Phi_* \left( \frac{R_*}{r} \right)^l, \quad (27)$$

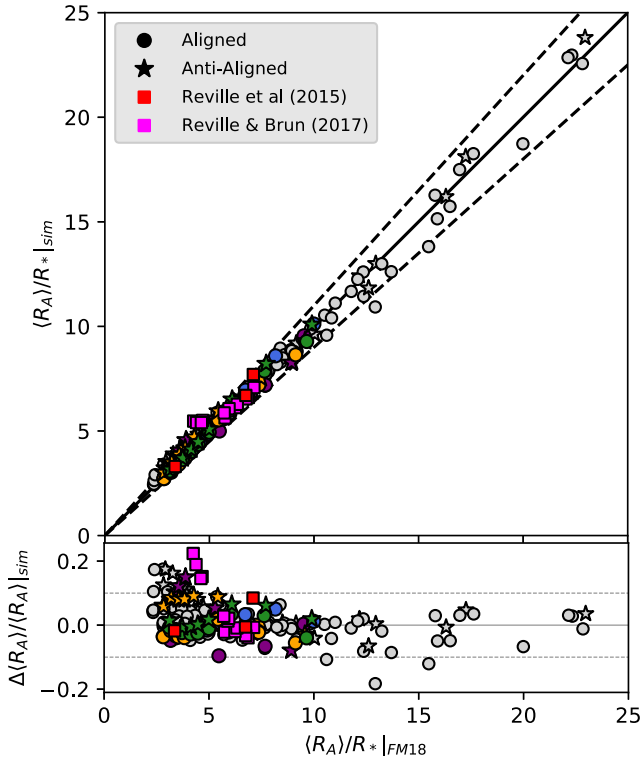


**Figure 10.** Top panel: comparison of the simulated Alfvén radii vs. the predicted Alfvén radii using Equation (17). The line of agreement is shown with a solid black line, and the bounds of 10% deviation from the predicted value are shown with black dashed lines. The bottom panel shows the residual,  $(\langle R_A \rangle_{\text{sim}} - \langle R_A \rangle_{\text{FM18}}) / \langle R_A \rangle_{\text{sim}}$ , and the 10% deviation with dashed lines. Cases 129–135 and 145–152 are colored purple, and cases 137–144 and 153–160 are colored orange, different from the color scheme of previous figures. The quadrupole- and octupole-dominated cases with  $\mathcal{R}_{\text{dip}} = 0.1$  are shown with their original coloring (blue and green, respectively). All other simulations from this work and Paper I are shown in gray. Three red squares represent axisymmetric mixed-field simulations from Réville et al. (2015). Thirteen magenta squares represent 3D nonaxisymmetric simulations with  $l_{\text{max}} = 15$  from Réville & Brun (2017) (the average Alfvén radius is computed differently than Equation (13)).

**Table 5**

Comparison of Results,  $R_A/R_{*|\text{sim}}$ , from Cases of Réville et al. (2015) to the Prediction of Equation (17),  $R_A/R_{*|\text{FM18}}$

Object	$\mathcal{R}_{\text{dip}} \mathcal{R}_{\text{quad}} \mathcal{R}_{\text{oct}}$	$\Upsilon$	$R_A/R_{* \text{sim}}$	$R_A/R_{* \text{FM18}}$
Sun Min	−0.47 0.03  −0.50	812	6.7	6.74
Sun Max	0.13 0.73 0.14	130	3.3	3.36
TYC-0486	−0.10 0.79  −0.11	17600	7.7	7.10

where  $\Phi_*$  is the surface magnetic flux and  $l$  represents the magnetic order of the field, increasing for more complex fields. Thus, higher-order fields decay radially faster.

The radial profiles of the flux in our steady-state solutions are shown with thin gray lines in Figures 11–13. Each ratio ( $\mathcal{R}_l$ ) represents a different combined field geometry, with each gray line having a different field strength. In each figure we include the potential field solution for the flux with a solid black line, produced by Equation (26), showing the initial magnetic field configuration. No longer is a single power law produced; instead, the components interact and produce a varying radial decay. In magnetized winds, the magnetic forces balance the thermal and ram pressures close to the star. Therefore, the

unsigned flux approximately follows the potential solution. Farther from the star the pressure of the wind forces the magnetic field into a nearly radial configuration, beyond which the unsigned flux becomes constant. This constant value is referred to as the open flux,  $\Phi_{\text{open}}$  (typically larger field strength produces a smaller fraction of open flux to surface flux).

In the cases with quadrupole–octupole mixed fields (Figure 11), the individual potential field quadrupole and octupole components are indicated with thick dashed blue and green lines, respectively. As with the previous dipole and quadrupole addition, the broken-power-law behavior shown in the Alfvén radius formulation is visible. The quadrupole component often represents the most significant contribution to the total flux, as the dipole did within Paper I. The bottom right panel of Figure 11 shows the relative decay of all the potential fields.

Figure 12 shows the radial magnetic flux evolution for the dipole–octupole combinations in a similar format to Figure 11. A quantitatively similar behavior to the dipole–quadrupole and quadrupole–octupole combinations is shown with the anti-aligned field geometries, seen in the bottom row. This explains why previously the anti-aligned cases provided a better fit to the broken-power-law approximation than the aligned cases. For the cases with an aligned octupole component, the profile of the flux decay is distinctly different. The smooth transition between the two regimes of the broken power law is replaced with a deviation from the dipole that passes below the dipole component at first and then asymptotes back. This is caused by the subtraction of the dipole and octupole fields over the equator, which reduces the unsigned flux and has the largest impact at the radial distance where the two components have the equal and opposite field strength.

For these two-component simulations, the approximate formulation, Equation (17), mathematically approximates the radial decay of the magnetic field with two regimes, an octupolar decay close in to the star followed by a sharp transition to the lower-order geometry (dipole or quadrupole), which ignores any influence of the octupolar field. The formulation works well when this is a good approximation, which is typically the case for the dipole–quadrupole, quadrupole–octupole, and anti-aligned dipole–octupole cases. The inflection of the magnetic flux for aligned cases creates a discrepancy between our simplification and the physics in the simulation; therefore, we observe a scatter in our results between the aligned and anti-aligned cases. Our formulation is least precise when the inflection occurs near the Alfvén radius, causing the formula to overpredict the average Alfvén radius. However, in Section 3.2.4 we show this to be a systematic and measurable effect that does not impact the validity of Equation (17).

For the three-component simulations, the behavior of the dipole–octupolar component alignment is shown to oppose the previous dipole–octupole addition. Equation (17) more accurately approximates the mixed-field cases with an aligned octupole component than with an anti-aligned component. To explore this, we show the radial evolution of the magnetic flux in Figure 13. The top panel displays the aligned cases with increasing octupolar component and decreasing quadrupolar component, moving to the right. The reduction of flux, or inflection in the flux profile, due to the dipole and octupole addition is only seen to be significant for one case, where the octupole fraction is maximized. In the remaining cases the

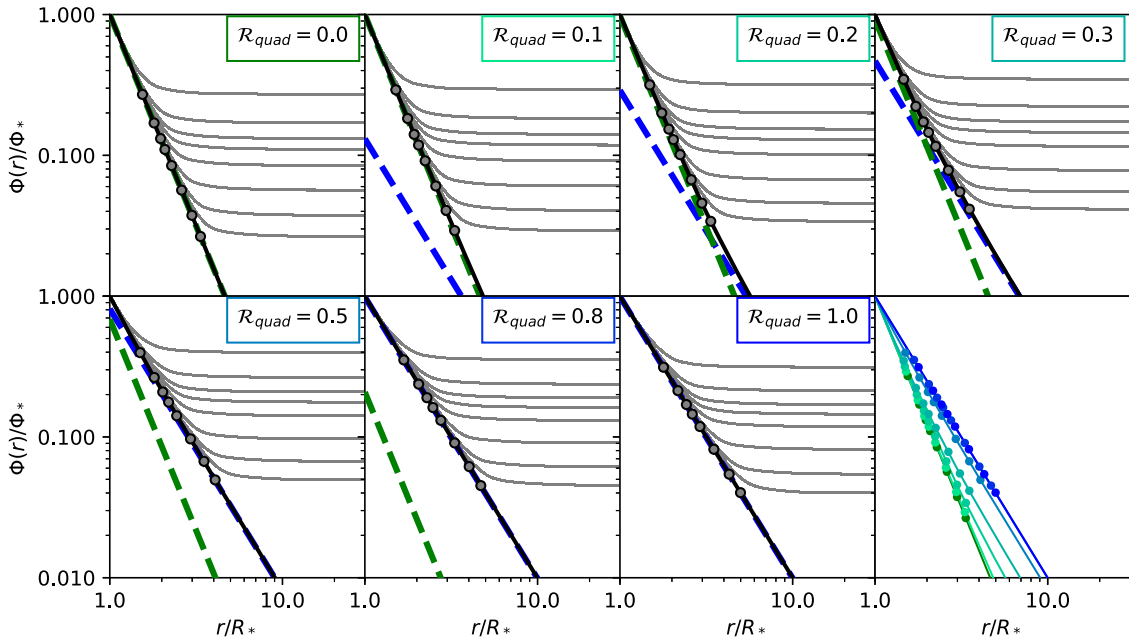


**Figure 11.** Unsigned magnetic flux vs. radial distance (gray lines) for all the cases with combined quadrupole and octupole components (labeled  $\mathcal{R}_{quad} = 0.1 - 0.8$ , along with the pure quadrupole and octupole cases (labeled  $\mathcal{R}_{quad} = 0.0$  and  $1.0$ ). Thick dashed blue and green lines show the value for a potential field for the quadrupole and octupole components, respectively, on their own. The total potential field flux, used as the initial condition, Equation (26), is shown in solid black. Thin gray lines in each panel show the magnetic flux in a single steady-state solution, for different field strengths of a given geometry. The flux within the simulations follows the potential field solution closely until the magnetic field is opened into a radial configuration with constant flux. Gray circles indicate the location of the field opening radii  $R_o$ , as we define it in this work. The mixed field geometries decay with an octupolar dependence until reaching the quadrupolar component, at which point the quadrupole controls the decay. This explains why the broken-power-law approximation is a good fit to the data in most cases. For comparison, the final panel shows all of the potential (initial) field geometries and their opening radii, colored according to their  $\mathcal{R}_{quad}$  value.

octupolar fraction is too small to produce a strong reduction in the equatorial flux with the dipole, hence the well-behaved relation between the simulated aligned cases and the predicted average Alfvén radii in Figure 10. The poorest-fitting cases to Equation (17) are the anti-aligned mixed cases shown in Figure 13 with purple and orange stars. The potential field solutions, shown with solid black lines, sit above the dashed component slopes (most significant for cases 153–160, in orange) showing an increased field strength due to the complex addition of the three components in combination. This is unlike most of the previous combined field cases, which are typically described by either one component or the other; hence, the predicted values differ for these cases.

This behavior is difficult to parameterize within our Alfvén radius approximation, as it requires knowledge about the magnetic field evolution in the wind. For this work, we simply show why the simulations deviate from Equation (17) and suggest that care be taken when using such formulations with dipolar and octupolar components.

#### 4.2. Open Flux Torque Relation

The open flux,  $\Phi_{open}$ , remains a key parameter in describing the torque scaling for any magnetic geometry. Réville et al. (2015) construct a semianalytic formulation for the average Alfvén radius using the open flux wind magnetization,

$$\Upsilon_{open} = \frac{\Phi_{open}^2 / R_*^2}{\dot{M} v_{esc}}. \quad (28)$$

The dependence of the average Alfvén radius on  $\Upsilon_{open}$  is then parameterized:

$$\frac{\langle R_A \rangle}{R_*} = K_o [\Upsilon_{open}]^{m_o}, \quad (29)$$

where  $K_o$  and  $m_o$  represent fit parameters to our simulations using this open flux formulation. In Paper I, we show the dependence of these fit parameters on magnetic geometry. We show this again within the left panel of Figure 14. The scatter in average Alfvén radius values for different field geometries is reduced compared with that seen in the  $\Upsilon$  parameter spaces (Figures 3, 5, and 8), such that a single power-law fit is viable, shown with a solid black line. However, better fits are obtained when considering each pure geometry independently, tabulated in Table 6.

Work by Pantolmos & Matt (2017) showed how differing wind acceleration affects the scaling relation by using different base wind temperatures to accelerate their winds. Different magnetic topologies produce slightly different wind acceleration from the stellar surface out to the Alfvén radius, due to the varying degree of super-radial expansion of the magnetic field lines (Velli 2010; Riley & Luhmann 2012; Réville et al. 2016). Thus, this causes the distinctly different scaling relations in the left panel of Figure 14. Using the averaged Alfvén speed  $\langle v(R_A) \rangle$  at the Alfvén surface, this difference in wind acceleration can be removed (see Pantolmos & Matt 2017), and the result is shown in the right panel of Figure 14.

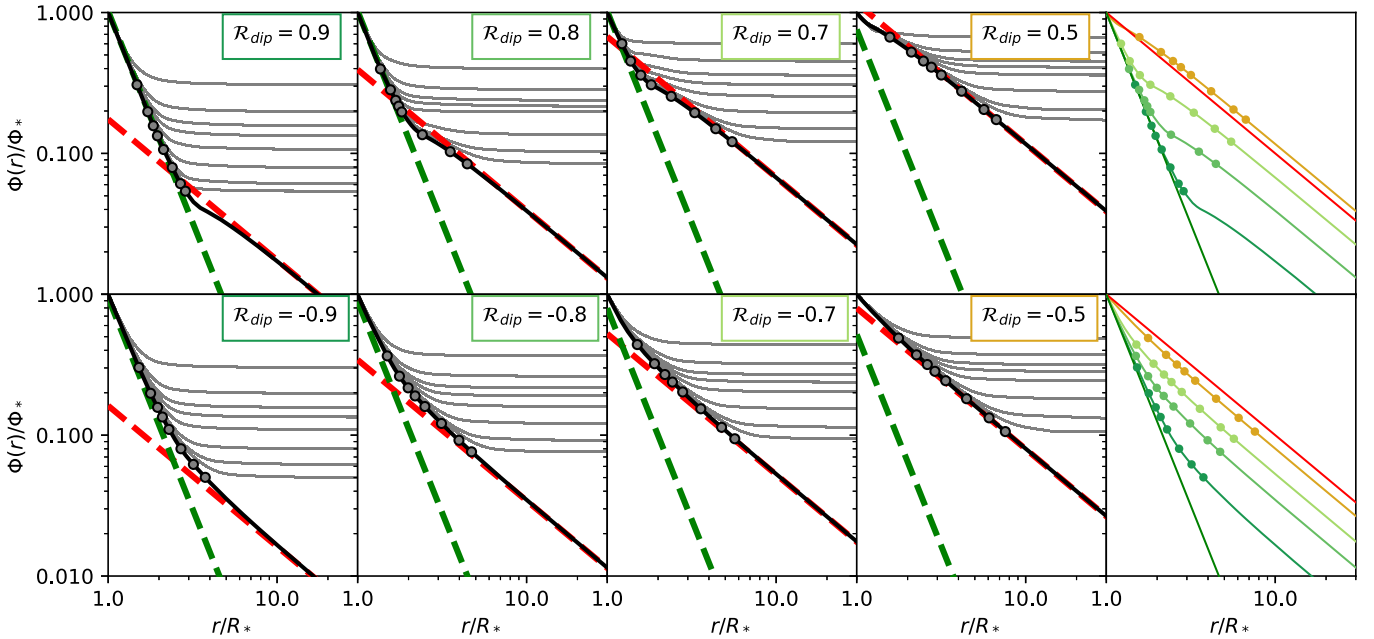


**Figure 12.** Unsigned magnetic flux vs. radial distance for all the cases with combined dipole and octupole components (labeled  $\mathcal{R}_{dip} = \pm 0.5-0.9$ ), both aligned (top row) and anti-aligned (bottom row), in a similar format to Figure 11. Thick dashed red and green lines show the value for a potential field for the dipole and octupole components, respectively, on their own. The aligned cases have a qualitatively different behavior from the dipole–quadrupole, quadrupole–octupole, and anti-aligned dipole–octupole cases, in that the former show a subtle inflection in their flux vs. radius (most apparent in the solid black lines for large  $\mathcal{R}_{dip}$  values, the three top left panels). This is caused by the subtraction of the two fields in the equatorial region, which has a maximum effect at the radius where the two components have the same magnitude. The net effect of this inflection in the magnetic flux is subtle, and thus our scaling relation (which does not treat the aligned and anti-aligned cases differently) remains an acceptable approximation to all simulations. For comparison, the rightmost panel shows all of the potential (initial) field geometries and their opening radii, colored according to their  $\mathcal{R}_{dip}$  value, for the aligned and anti-aligned cases, respectively.

The semianalytic solution from Pantolmos & Matt (2017) is given by

$$\frac{\langle R_A \rangle}{R_*} = K_c \left[ \Upsilon_{\text{open}} \frac{v_{\text{esc}}}{\langle v(R_A) \rangle} \right]^{m_c}, \quad (30)$$

where  $K_c$  and  $m_c$  are fit parameters to this formulation. The fit relationship from Pantolmos & Matt (2017) and a fit to our simulation data (Table 6) are shown with all our simulated cases (both Paper I and this paper) in the right panel of Figure 14.

A small geometry-dependent scatter remains in the right panel, which is noted in Paper I. The cause of this is an unanswered question but may relate to systematic numerical errors due to modeling small-scale complex field geometries. Our fit agrees well with that from Pantolmos & Matt (2017), with a shallower slope due to the inclusion of the higher-order geometries that show this systematic deviation from the dipole simulations.

### 4.3. Field Opening Radius

As in previous works (e.g., Pantolmos & Matt 2017; Paper I), we define an opening radius  $R_o$  using the value of the open flux. The opening radius is defined as the radial distance at which the potential field for a given geometry matches the value of the open flux, i.e.,  $\Phi(R_o) = \Phi_{\text{open}}$ . In this way, given the surface magnetic field geometry and the value of  $R_o$ , the open flux in the wind is recovered, and thus the torque can be predicted. However, producing a single relation

for predicting the opening radius, and thus the open flux, for our simulations remains an unsolved problem.

In Figures 11–13, the opening radii for all simulations are marked with gray circles and compared in the final panel (colored to match the respective  $\mathcal{R}_l$  value). With increasing field strength, the simulations produce a larger average Alfvén radius and a larger dead zone/opening radius. The Alfvén and opening radii roughly grow together with increasing wind magnetization, but their actual behavior is more complex. The field complexity also has an affect on this relationship, with more complex geometries producing smaller opening radii, as the wind pressure is able to open the magnetic field closer to the star.

We compare the average Alfvén radii and opening radii within Figure 15. The simulations containing an octupolar component, in general, show a shallower dependence, which continues the trend from dipole to quadrupole presented in Paper I. Interestingly, the aligned dipole–octupole fields are shown to have reduced values of  $R_o$  for the Alfvén radii they produce, compared to the aligned cases, which is a consequence of the reduced flux from the field subtraction over the equator. For these cases the wind pressure is able to open the field much closer to the star, compared to the anti-aligned cases.

The relationship between the opening radius and the lever arm for magnetic braking torque in our wind simulations is evidently complex and interrelated with magnetic geometry, field strength, and mass-loss rate. The opening radius, as we define it here, is algebraically related to the source surface radius,  $r_{ss}$ , used within the potential field source surface (PFSS) models. As such, the  $R_o$  scales with  $r_{ss}$  for a given field

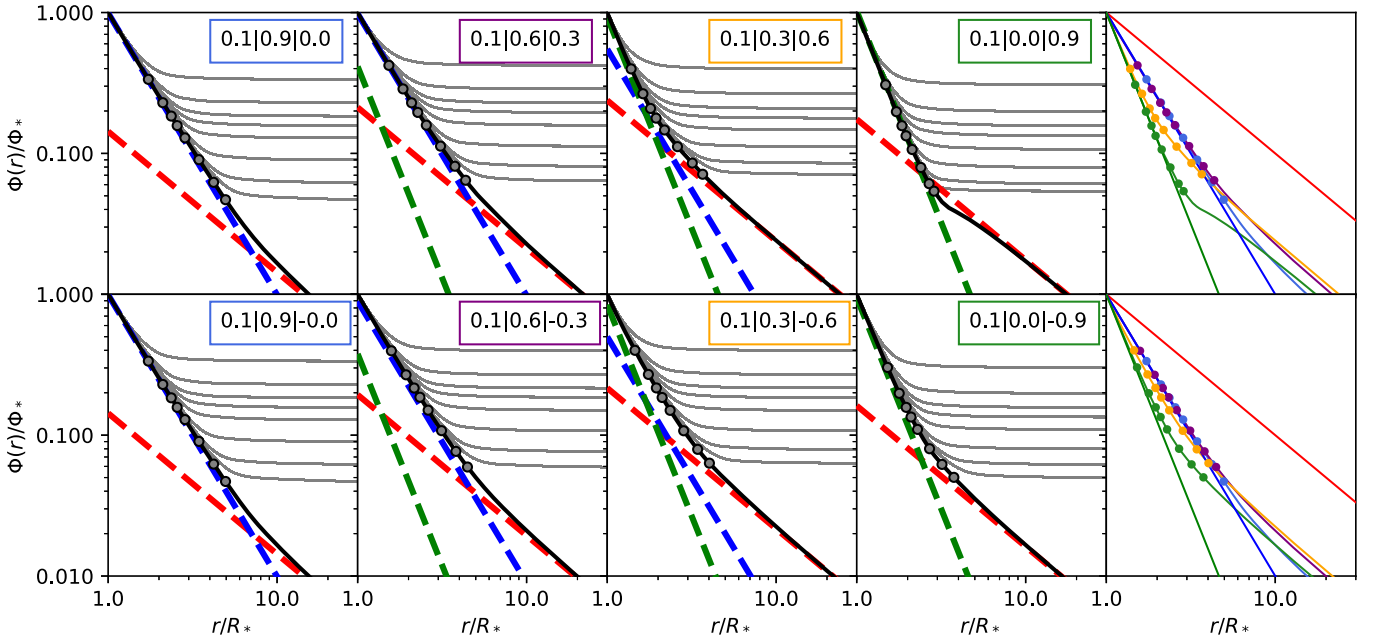


**Figure 13.** Unsigned magnetic flux vs. radial distance for the sample of mixed dipole, quadrupole, and octupole cases in the same format as Figure 11. All cases shown have 10% in the dipole component. Then, from left to right, the fraction in the octupole increases from 0% to 90% (with the remaining fraction in the quadrupole component). The top row has aligned dipole–octupole; the bottom has anti-aligned.

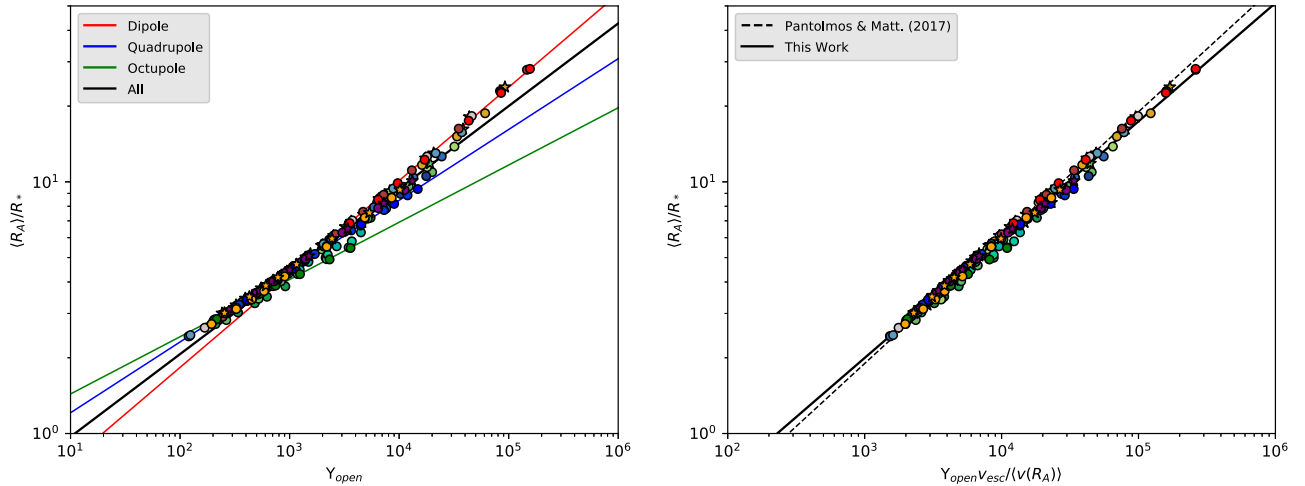


**Figure 14.** Average Alfvén radius vs. the open flux magnetization,  $\Upsilon_{open}$ , Equation (28). All simulations from this study and Paper I are shown, color-coded as in the previous figures. Left: different scaling relations (Equation (29), Table 6) are shown for each pure geometry and a combined fit. Right: open flux magnetization divided by the average speed at the Alfvén surface ( $v(R_A)$ ). The scatter is reduced, indicating that the different scalings in the left panel are primarily due to the effect of magnetic geometry on the wind acceleration (as discussed in Paper I). However, there remains a small systematic trend, in that the higher-order geometry winds sit lower for a given magnetization (seen in Paper I), which may be due to systematic numerical effects. The solid black line represents the fit to all data (see Table 6); the dashed line represents the result from dipole wind simulations with different base wind temperatures from Pantolmos & Matt (2017).

geometry, and its behavior with increasing field strength should be accounted for within future PFSS models.

## 5. Conclusions

This work presents results from 160 new MHD simulations and 50 previously discussed simulations from Paper I, which we use to disentangle the impacts of complex magnetic field geometries on the spin-down torque produced by magnetized stellar winds. Axisymmetric dipole, quadrupole, and octupole fields are used to construct differing combined field geometries.

We systematically vary the ratios,  $\mathcal{R}_{dip}$ ,  $\mathcal{R}_{quad}$ , and  $\mathcal{R}_{oct}$ , of each field geometry with a range of total field strengths. Here we reinforce results from Paper I. With simple estimates using realistic magnetic field topologies (obtained from ZDI observations) and representative field strengths and mass-loss rates for main-sequence stars, the dipole component dominates the spin-down process, irrespective of the higher-order components (A. Finley et al. 2018, in preparation). The original formulation from Matt et al. (2012) remains robust in most cases even for significantly nondipolar fields. Combined with the work from Pantolmos & Matt (2017), these formulations represent a strong

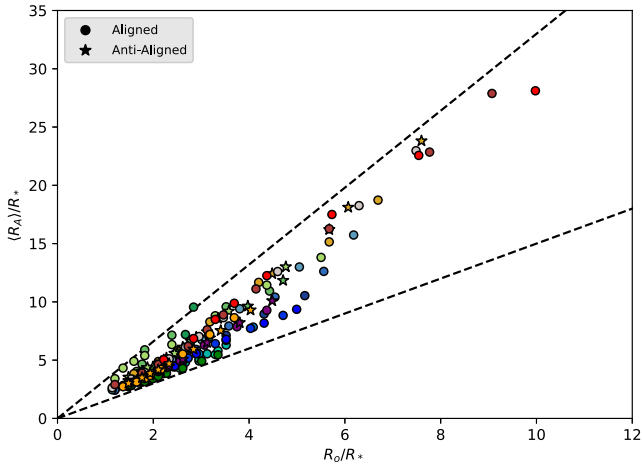


**Figure 15.** Average Alfvén radius vs. opening radius for all cases. Black dashed lines represent  $R_A/R_o = 3.3$  and  $1.5$ , which bound all cases. The simulations show a similar behavior to that discussed in Paper I, namely, a geometry-dependent separation, with the octupole geometries having the shallowest slope.

foundation for predicting the stellar wind torques from a variety of cool stars with differing properties.

We show the distinctly different changes to topology from our combined primary (dipole, octupole) and secondary (quadrupole) symmetry family fields, “primary” being anti-symmetric about the equator and “secondary” symmetric about the equator (McFadden et al. 1991; DeRosa et al. 2012). The addition of primary and secondary fields produces an asymmetric field about the stellar equator, in contrast to the combination of two primary fields, which maintains equatorial symmetry. However, the latter case breaks the degeneracy of the field alignment, producing two different topologies dependent on the relative orientation of the combined geometries. This is not the case for primary and secondary field addition, i.e., dipole–quadrupole and quadrupole–octupole, which produces the same global field reflected about the equator.

The magnetic braking torque is shown, as in Paper I, to be largely dependent on the dominant lowest-order field component. For observed field geometries this is, in general, dipolar in nature. We parameterize the torque from our mixed-field simulations based on the decay of the magnetic field. The average Alfvén radius,  $\langle R_A \rangle$ , is defined to represent a lever arm, or efficiency factor, for the torque, Equation (14). From our simulated cases we produce an approximate formulation for the average Alfvén radius, Equation (17), where both  $K_s$  and  $m_s$  have tabulated values from our simulations in Table 3. These values are temperature dependent, e.g.,  $\approx 1.7$  MK for a  $1 M_\odot$  star. In this formulation, the octupole geometry dominates the magnetic field close to the star; then it decays radially, leaving the quadrupole governing the radial decay of the field; and finally the quadrupole decays, leaving only the dipole component of the field. In each regime the strength of the field includes any component that is yet to decay away.

Using this formula, we are able to predict the torque in all of our simulations to  $\approx 20\%$  accuracy, with the majority predicted to within  $\approx 5\%$ . This is then extended to mixed-field simulations presented in Réville et al. (2015) and Réville & Brun (2017). The formulation presented within this work remains an approximation, with a smoother transition from each regime observed with the simulations. This work

**Table 6**  
Open Flux Fit Parameters to Equations (29) and (30)

Topology( $l$ )	$K_c$	$m_c$
Dipole (1)	$0.33 \pm 0.03$	$0.371 \pm 0.003$
Quadrupole (2)	$0.63 \pm 0.02$	$0.281 \pm 0.003$
Octupole (3)	$0.85 \pm 0.03$	$0.227 \pm 0.004$
All simulations	$0.46 \pm 0.03$	$0.329 \pm 0.004$
	$K_c$	$m_c$
Topology independent	$0.08 \pm 0.04$	$0.470 \pm 0.004$

represents a modification to existing torque formulations, which accounts for combined field geometries in a very general way. A key finding remains that the dipole component is able to account for the majority of the magnetic braking torque, in most cases. Thus, previous works based on the assumption of the dipolar component being representative of the global field are validated. It is noted here, however, that it is the dipole component of the field and not the total field strength that enters in the torque formulation; therefore, it is important to decompose any observed field correctly to avoid miscalculation.

In this study, as in the previous one, we do not include the effects of rapid rotation or varying coronal temperatures. Prescriptions for rotational effects on the three pure geometries studied here are available (Matt et al. 2012; Réville et al. 2015), along with differing coronal temperatures for dipolar geometries (Pantolmos & Matt 2017). In general, differences in wind-driving parameters and physics will introduce more deviation from Equation (17); however, it is expected to remain valid.

Work remains in modeling the behavior of nonaxisymmetric components on the stellar wind environments surrounding Sun-like and low-mass stars and the associated spin-down torques. Observed fields are shown to host a varied amount of nonaxisymmetry (e.g., See et al. 2015). Works including more complex coronal magnetic fields, such as the inclusion of magnetic spots (e.g., Cohen et al. 2009; Garraffo et al. 2015), tilted magnetospheres (e.g., Vidotto et al. 2010), and using ZDI observations (e.g., Vidotto et al. 2011, 2014; Alvarado-Gómez et al. 2016; Garraffo et al. 2016b; Nicholson et al. 2016; Réville et al. 2016), have shown the impact of specific cases but have yet to fully parameterize the variety of potential magnetic geometries. The relative orientations of some field combinations shown in this work have produced differences in the braking lever arm; therefore, we expect the same to be true for nonaxisymmetric geometries in combination. Since Equation (17) predicts the Alfvén radii from Réville & Brun (2017) (Section 3.3), this suggests that our approximate formulation holds for nonaxisymmetric components (using a quadrature addition of  $\pm l$  components), but this remains to be validated.

Thanks for helpful discussions and technical advice from Georgios Pantolmos, Victor See, Victor Réville, Sasha Brun, and Claudio Zanni. This project has received funding from the European Research Council (ERC) under the European Unions Horizon 2020 research and innovation program (grant agreement no. 682393). We thank Andrea Mignone and others for the development and maintenance of the PLUTO code. Figures within this work are produced using the python package matplotlib (Hunter 2007).

*Software:* matplotlib (Hunter 2007), PLUTO (Mignone et al. 2007; Mignone 2009).

## ORCID iDs

Adam J. Finley  <https://orcid.org/0000-0002-3020-9409>

Sean P. Matt  <https://orcid.org/0000-0001-9590-2274>

## References

- Agüeros, M. A., Covey, K. R., Lomonias, J. J., et al. 2011, *ApJ*, 740, 110
- Alvarado-Gómez, J., Hussain, G., Cohen, O., et al. 2016, *A&A*, 594, A95
- Amard, L., Palacios, A., Charbonnel, C., Gallet, F., & Bouvier, J. 2016, *A&A*, 587, A105
- Aschwanden, M. 2006, *Physics of the Solar Corona: An Introduction with Problems and Solutions* (2nd ed.; Berlin: Springer)
- Barnes, S. A. 2003, *ApJ*, 586, 464
- Barnes, S. A. 2010, *ApJ*, 722, 222
- Blackman, E. G., & Owen, J. E. 2016, *MNRAS*, 458, 1548
- Bouvier, J., Matt, S. P., Mohanty, S., et al. 2014, in *Protostars and Planets VI*, ed. H. Beuther et al. (Tucson, AZ: Univ. Arizona Press), 433
- Brown, T. M. 2014, *ApJ*, 789, 101
- Brun, A. S., & Browning, M. K. 2017, *LRSP*, 14, 4
- Brun, A. S., Petit, P., Jardine, M., & Spruit, H. C. 2013, in *IAU Symp. 302, Magnetic Fields throughout Stellar Evolution*, ed. P. Petit et al. (Cambridge: Cambridge Univ. Press), 114
- Cohen, O., Drake, J., Kashyap, V., & Gombosi, T. 2009, *ApJ*, 699, 1501
- Cohen, O., Kashyap, V., Drake, J., et al. 2011, *ApJ*, 733, 67
- Cranmer, S., & Van Ballegoijen, A. 2005, *ApJS*, 156, 265
- Cranmer, S. R., Gibson, S. E., & Riley, P. 2017, *SSRv*, 212, 1345
- Cranmer, S. R., Van Ballegoijen, A. A., & Edgar, R. J. 2007, *ApJS*, 171, 520
- Davenport, J. R. A. 2017, *ApJ*, 835, 16
- Delorme, P., Cameron, A. C., Hebb, L., et al. 2011, *MNRAS*, 413, 2218
- DeRosa, M., Brun, A., & Hoeksema, J. 2012, *ApJ*, 757, 96
- do Nascimento, J.-D., Jr, Vidotto, A., Petit, P., et al. 2016, *ApJL*, 820, L15
- Donati, J.-F., Forveille, T., Cameron, A. C., et al. 2006, *Sci*, 311, 633
- Donati, J.-F., Jardine, M., Gregory, S., et al. 2007, *MNRAS*, 380, 1297
- Donati, J.-F., Moutou, C., Fares, R., et al. 2008, *MNRAS*, 385, 1179
- Fares, R., Donati, J.-F., Moutou, C., et al. 2009, *MNRAS*, 398, 1383
- Feldman, U., Landi, E., & Schwadron, N. 2005, *JGRA*, 110, A07109
- Finley, A. J., & Matt, S. P. 2017, *ApJ*, 845, 46
- Fisk, L., Schwadron, N., & Zurbuchen, T. 1998, *SSRv*, 86, 51
- Folsom, C. P., Petit, P., Bouvier, J., et al. 2016, *MNRAS*, 457, 580
- Gallet, F., & Bouvier, J. 2013, *A&A*, 556, A36
- Gallet, F., & Bouvier, J. 2015, *A&A*, 577, A98
- Garraffo, C., Cohen, O., Drake, J., & Downs, C. 2013, *ApJ*, 764, 32
- Garraffo, C., Drake, J. J., & Cohen, O. 2015, *ApJ*, 813, 40
- Garraffo, C., Drake, J. J., & Cohen, O. 2016a, *A&A*, 595, A110
- Garraffo, C., Drake, J. J., & Cohen, O. 2016b, *ApJL*, 833, L4
- Gray, D. 1984, *ApJ*, 277, 640
- Gregory, S., Donati, J.-F., Morin, J., et al. 2012, *ApJ*, 755, 97
- Gregory, S. G., & Donati, J.-F. 2011, *AN*, 332, 1027
- Gregory, S. G., Donati, J.-F., & Hussain, G. A. 2016, arXiv:1609.00273
- Güdel, M. 2007, *LRSP*, 4, 3
- Hébrard, É., Donati, J.-F., Delfosse, X., et al. 2016, *MNRAS*, 461, 1465
- Holzwarth, V. 2005, *A&A*, 440, 411
- Hunter, J. D. 2007, *CSE*, 9, 90
- Hussain, G. A., & Alecian, E. 2013, in *IAU Symp. 302, Magnetic Fields throughout Stellar Evolution*, ed. P. Petit (Cambridge: Cambridge Univ. Press), 25
- Hussain, G. A., Van Ballegoijen, A., Jardine, M., & Cameron, A. C. 2002, *ApJ*, 575, 1078
- Irwin, J., & Bouvier, J. 2009, in *IAU Symp. 258, The Ages of Stars*, ed. D. R. Soderblom & E. E. Mamajek (Cambridge: Cambridge Univ. Press), 363
- Jeffers, S., Petit, P., Marsden, S., et al. 2014, *A&A*, 569, A79
- Johns-Krull, C. M., & Valenti, J. A. 2000, in *ASP Conf. Ser. 198, Stellar Clusters and Associations: Convection, Rotation, and Dynamics*, ed. R. Pallavicini, G. Micela, & S. Sciortino (San Francisco, CA: ASP), 371
- Kawaler, S. D. 1988, *ApJ*, 333, 236
- Keppens, R., & Goedbloed, J. 1999, *A&A*, 343, 251
- Keppens, R., & Goedbloed, J. 2000, *ApJ*, 530, 1036
- Kochukhov, O., Petit, P., Strassmeier, K., et al. 2017, *AN*, 338, 428
- Marcy, G. 1984, *ApJ*, 276, 286
- Matt, S., & Pudritz, R. E. 2008, *ApJ*, 678, 1109
- Matt, S. P., Brun, A. S., Baraffe, I., Bouvier, J., & Chabrier, G. 2015, *ApJL*, 799, L23
- Matt, S. P., MacGregor, K. B., Pinsonneault, M. H., & Greene, T. P. 2012, *ApJL*, 754, L26
- McFadden, P., Merrill, R., McElhinny, M., & Lee, S. 1991, *JGR*, 96, 3923
- McQuillan, A., Aigrain, S., & Mazeh, T. 2013, *MNRAS*, 432, 1203
- Meibom, S., Mathieu, R. D., & Stassun, K. G. 2009, *ApJ*, 695, 679
- Meibom, S., Mathieu, R. D., Stassun, K. G., Liebesny, P., & Saar, S. H. 2011, *ApJ*, 733, 115
- Mestel, L. 1968, *MNRAS*, 138, 359
- Mestel, L. 1984, in *Cool Stars, Stellar Systems, and the Sun*, ed. S. L. Baliunas & L. Hartmann (Berlin: Springer), 49
- Mignone, A. 2009, *MSAIS*, 13, 67
- Mignone, A., Bodo, G., Massaglia, S., et al. 2007, *ApJS*, 170, 228
- Morgenthaler, A., Petit, P., Morin, J., et al. 2011, *AN*, 332, 866
- Morin, J., Donati, J.-F., Forveille, T., et al. 2008a, *MNRAS*, 384, 77
- Morin, J., Donati, J.-F., Petit, P., et al. 2008b, *MNRAS*, 390, 567
- Nicholson, B., Vidotto, A., Mengel, M., et al. 2016, *MNRAS*, 459, 1907
- Pantolmos, G., & Matt, S. P. 2017, *ApJ*, 849, 83
- Parker, E. 1965, *SSRv*, 4, 666
- Petit, P., Dintrans, B., Solanki, S., et al. 2008, *MNRAS*, 388, 80
- Pinto, R., Brun, A., & Rouillard, A. 2016, *A&A*, 592, A65
- Pinto, R. F., Brun, A. S., Jouve, L., & Grappin, R. 2011, *ApJ*, 737, 72
- Reiners, A. 2012, *LRSP*, 9, 1
- Reiners, A., & Mohanty, S. 2012, *ApJ*, 746, 43
- Réville, V., & Brun, A. S. 2017, *ApJ*, 850, 45
- Réville, V., Brun, A. S., Matt, S. P., Strugarek, A., & Pinto, R. F. 2015, *ApJ*, 798, 116
- Réville, V., Folsom, C. P., Strugarek, A., & Brun, A. S. 2016, *ApJ*, 832, 145
- Riley, P., Linker, J., Mikić, Z., et al. 2006, *ApJ*, 653, 1510
- Riley, P., & Luhmann, J. 2012, *SoPh*, 277, 355
- Robinson, R., Worden, S., & Harvey, J. 1980, *ApJL*, 236, L155
- Saar, S. 1990, in *IAU Symp. 138, The Solar Photosphere: Structure, Convection, and Magnetic Fields*, ed. J. O. Stenflo (Cambridge: Cambridge Univ. Press), 427
- Saikia, S. B., Jeffers, S., Morin, J., et al. 2016, *A&A*, 594, A29
- Schatzman, E. 1962, *AnAp*, 25, 18
- See, V., Jardine, M., Vidotto, A., et al. 2015, *MNRAS*, 453, 4301
- See, V., Jardine, M., Vidotto, A., et al. 2016, *MNRAS*, 462, 4442
- See, V., Jardine, M., Vidotto, A., et al. 2017a, *MNRAS*, 466, 1542
- See, V., Jardine, M., Vidotto, A., et al. 2017b, *MNRAS*, 474, 536
- Skumanich, A. 1972, *ApJ*, 171, 565
- Soderblom, D. 1983, *ApJS*, 53, 1
- Stauffer, J., Rebull, L., Bouvier, J., et al. 2016, *AJ*, 152, 115
- Steinolfson, R., & Hundhausen, A. 1988, *JGR*, 93, 14269
- Testa, P., Drake, J. J., & Peres, G. 2004, *ApJ*, 617, 508
- Ud-Doula, A., Owocki, S. P., & Townsend, R. H. 2009, *MNRAS*, 392, 1022
- van der Holst, B., Sokolov, I. V., Meng, X., et al. 2014, *ApJ*, 782, 81
- Van Saders, J. L., & Pinsonneault, M. H. 2013, *ApJ*, 776, 67
- Velli, M. 2010, in *AIP Conf. Proc. 1216, Twelfth International Solar Wind Conference*, ed. M. Maksimovic et al. (Melville, NY: AIP), 14
- Vidotto, A., Gregory, S., Jardine, M., et al. 2014, *MNRAS*, 441, 2361
- Vidotto, A., Jardine, M., Opher, M., Donati, J., & Gombosi, T. 2011, in *ASP Conf. Ser. 448, 16th Cambridge Workshop on Cool Stars, Stellar Systems, and the Sun*, ed. C. M. Johns-Krull, M. K. Browning, & A. A. West (San Francisco, CA: ASP), 1293
- Vidotto, A., Opher, M., Jatenco-Pereira, V., & Gombosi, T. 2009, *ApJ*, 699, 441
- Vidotto, A., Opher, M., Jatenco-Pereira, V., & Gombosi, T. 2010, *ApJ*, 720, 1262
- Weber, E. J., & Davis, L. 1967, *ApJ*, 148, 217





## Erratum “The Effect of Combined Magnetic Geometries on Thermally Driven Winds. II. Dipolar, Quadrupolar, and Octupolar Topologies” (2018, ApJ, 854, 78)

Adam J. Finley and Sean P. Matt

University of Exeter, Department of Physics & Astronomy, Stoker Road, Devon, Exeter, EX4 4QL, UK; [af472@exeter.ac.uk](mailto:af472@exeter.ac.uk)

Received 2018 March 28; revised 2018 April 2; published 2018 April 25

In the original manuscript, Figure 5 was incorrectly printed as a copy of Figure 6. This erratum shows Figure 5 as it was intended. All tabulated data and scientific results of the paper remain unaffected.

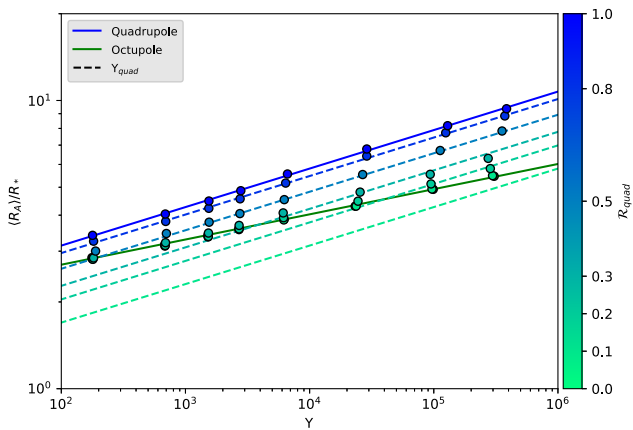


**Figure 5.** Average Alfvén radius vs. wind magnetization,  $\Upsilon$ , for the different combinations of quadrupole and octupole, in a similar format as Figure 3. Color-coded dashed lines relate to the prediction considering only the quadrupolar component of the field for each  $\mathcal{R}_{\text{quad}}$ . The combinations shown here behave in a similar manner to dipole–quadrupole combined fields, in a sense that the lower order field (with the lowest  $l$ ) governs the Alfvén radius for large wind magnetizations,  $\Upsilon$ , and the higher order (large  $l$ ) controlling the low magnetization scaling.

## 3.5 Additional Information

Details regarding the methodology of simulating stellar winds with PLUTO are given in the published papers (3.3 & 3.4), however here I would like to highlight a few points of interest.

### 3.5.1 Steady-state and Time-varying Solutions

In Sections 3.3 and 3.4 the 2.5D simulations are said to reach a steady-state, however no condition is given to explain this. Throughout this work steady-states are evaluated by monitoring the time-evolution of  $\dot{M}$ ,  $\tau$ , and  $\phi_{open}$ , which are calculated on spherical shells for each radial grid step from the stellar surface to the outer boundary. In the magnetically “open” wind, all three variables should be constant in time and with radial distance. Thus, for a steady-state to be declared these variables must show numerical stability on timescales much longer than it takes waves to propagate across the domain.

Three simulations (which each have very strong magnetic fields) reach quasi-steady states whereby the closed field regions experience a periodic reconnection due to numerical diffusion. Similar solutions are studied in Appendix A of Pantolmos and Matt (2017), where it is shown that they have a well behaved oscillatory behaviour. For simulations in this quasi-steady state, sufficient time-averages are taken when comparing values (like  $\Upsilon$ ,  $\langle R_A \rangle$ , etc) from these simulations with the other steady-state solutions.

### 3.5.2 Errors in Omega Effective

To quantify any departure from ideal MHD, due to numerical error, I inspect the effective rotation rate of magnetic field lines. This is a conserved quantity in ideal MHD given by,

$$\Omega_{eff} = \frac{1}{r \sin \theta} \left( v_\phi - B_\phi \frac{\mathbf{v}_p \cdot \mathbf{B}_p}{|\mathbf{B}_p|^2} \right), \quad (3.9)$$

where the subscript  $p$  denotes the poloidal component ( $r$  and  $\theta$ ) of each vector. Given the simulations presented in this Chapter, which all use solid body rotation, it is expected

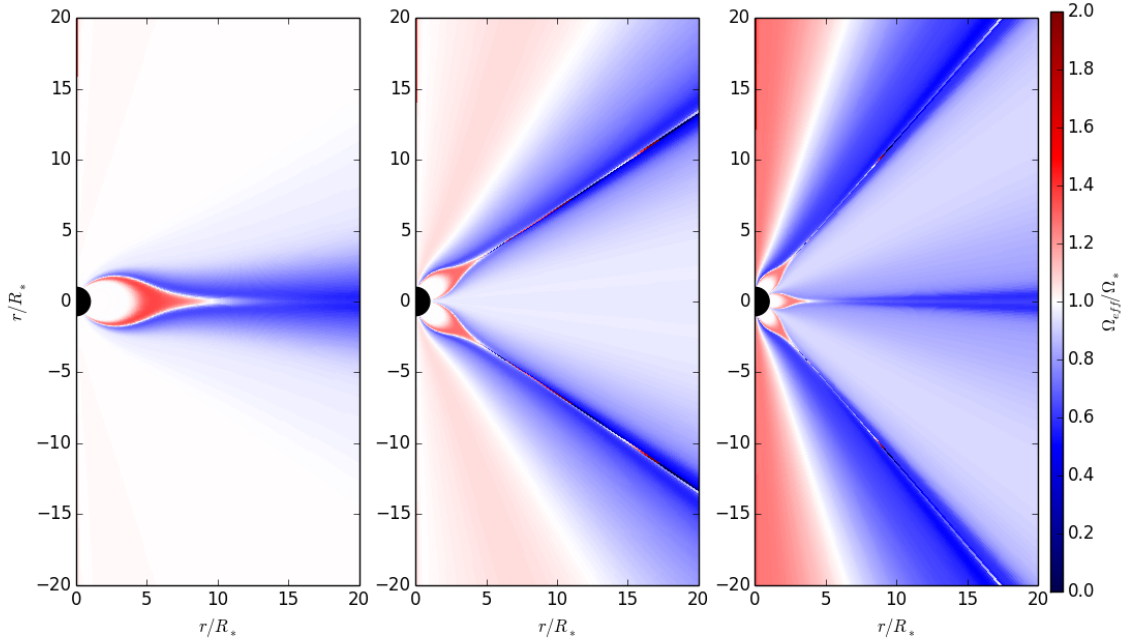


**Figure 3.4:** Left to right: Omega effective for a typical dipole, quadrupole, and octupole stellar wind solution. A perfect ideal MHD solution would have the value of unity (white) everywhere in the simulation domain. Flows that are blue are sub-rotating and flows that are red are super-rotating, relative to the true ideal MHD solution.

that the ratio of  $\Omega_{eff}$  to the surface rotation rate  $\Omega_*$  should equal unity everywhere in the simulation domain. In Figure 3.4 I show  $\Omega_{eff}/\Omega_*$  for a typical dipole, quadrupole, and octupole wind simulation. Similarly in Figure 3.5 I show a mixed field case, where I have zoomed into the region closest to the star.

From these Figures it is clear that the largest deviations from unity are found along field lines that lie near the boundary between closed and open magnetic field. Generally, the largest closed field loops are super-rotating relative to the expected ideal MHD result, and the flow surrounding the open-closed field line boundary is sub-rotating. Furthermore the axisymmetric boundary condition on the rotation axis appears to instigate a super-rotation in the field lines closest to it. Open magnetic field lines generally have a much better conservation of the effective rotation rate. However, the area that the open magnetic field lines occupy at the stellar surface decreases with increasing magnetic complexity, and so each of the errors mentioned previously increase in severity from dipole to octupole. The errors surrounding the open-closed magnetic field boundary are likely caused by numerical diffusion, i.e. magnetic field lines slipping forwards or backwards

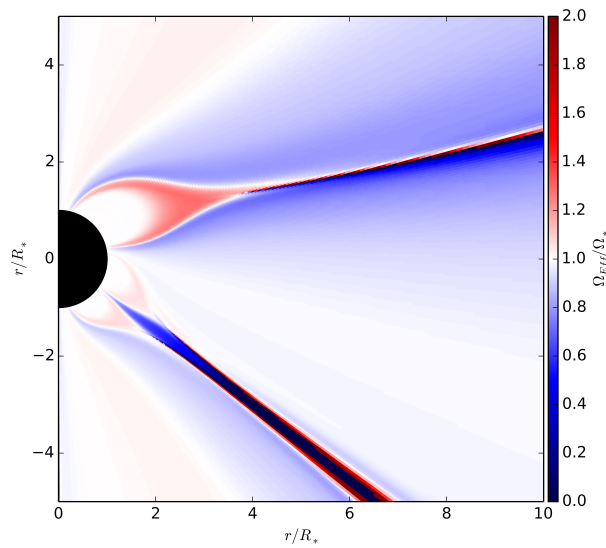


**Figure 3.5:** Zoomed example of error in the effective rotation rate of magnetic field lines in a mixed magnetic geometry stellar wind solution. Typically strong sub-rotation is found near a super-rotating flow, or vice versa. The strongest errors are located in the streamers.

with respect to each other. By using a less diffusive Riemann solver, like the roe solver (Roe 1981), the error in  $\Omega_{eff}$  can be reduced at the cost of the numerical scheme becoming less stable.

Fortunately, errors in  $\Omega_{eff}$  appear to oppose themselves, i.e. whenever a field line strongly sub-rotates, there is often a super-rotating magnetic field line nearby. This is likely an effect of angular momentum conservation in the PLUTO code. The impact these errors have on the angular momentum-loss rate is not easily quantified, however it is known that along a magnetic field line,

$$\frac{R_A}{R_*} = \sqrt{\frac{\Lambda}{\Omega_{eff} R_*^2}}, \quad (3.10)$$

where  $\Lambda$  is the specific angular momentum flux, and  $\Omega_{eff}$  resides in the denominator such that sub-rotating flows produce a larger  $R_A$  than the ideal MHD case and super-rotating flows produce a smaller  $R_A$ . As the error in  $\Omega_{eff}$  grows with increasing complexity and generally favours sub-rotation (see Figure 3.4), this implies that the scaling relations for  $\langle R_A \rangle$  are likely over-predicting compared with simulations that correctly satisfy ideal MHD everywhere. In this case, the size of this shift will be larger for more complex magnetic geometries, like the octupole. Additionally, as the  $\Omega_{eff}$  errors also grow with increasing  $\Upsilon$  (or field strength), this implies that the power law slopes of  $\langle R_A \rangle - \Upsilon$  are

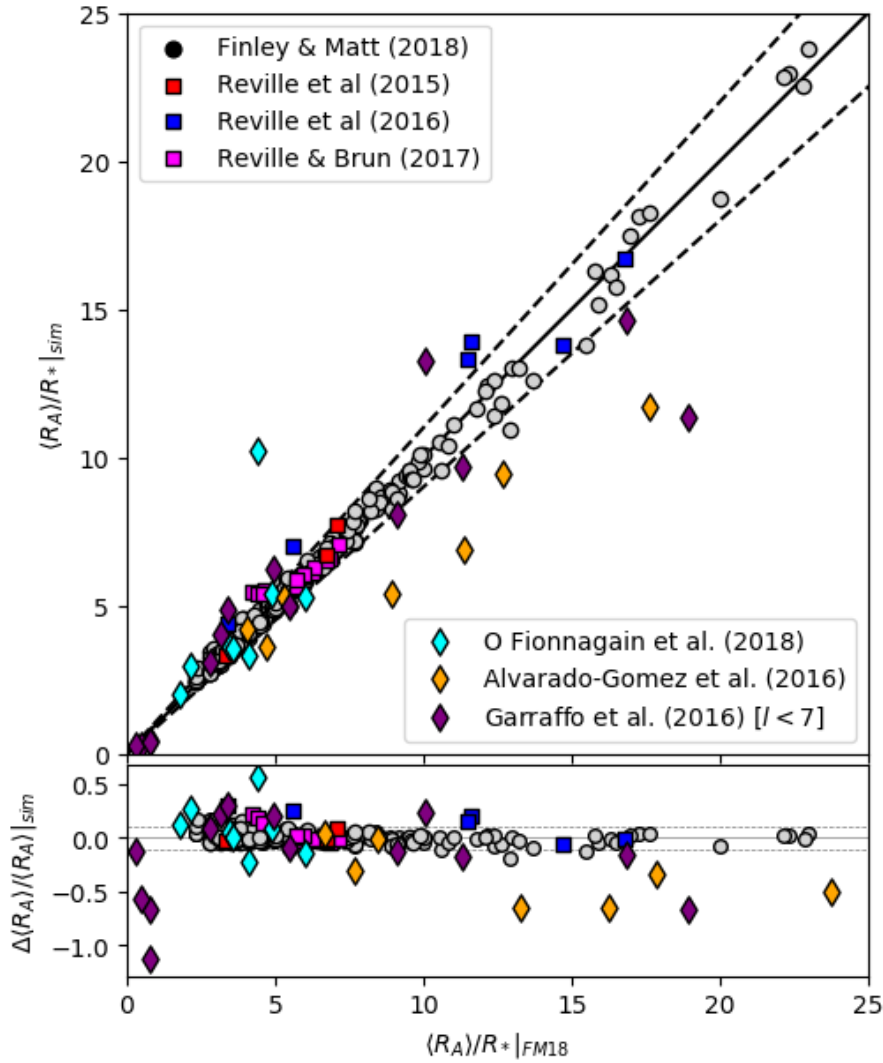


**Figure 3.6:** Copy of Figure 10 from the published paper in Section 3.4. Predicted Alfvén radii from the semi-analytic formulae of Chapter 3 versus the values from other publications. Squares use the surface field formulation  $\Upsilon$ , diamonds use the open flux formulation  $\Upsilon_{open}$ . All use the fit values from the 2.5D MHD simulations in Chapter 3, apart from the Alvarado-Gómez et al. (2016) simulations for which I adopt a hotter thermal-driving temperature from Pantolmos and Matt (2017) of  $c_s/v_{esc} = 0.4$ .

likely steeper than the ideal MHD case, again this effect will be larger for the more complex fields. Given that the values of  $\langle R_A \rangle$  generally coincide with the cylindrical extent of the simulated 2D Alfvén surfaces, this effect is likely small and isn't expected to change any of the findings from this Chapter.

### 3.5.3 Comparison with Other Works

Many other authors have produced MHD simulations of stellar winds, most using slightly different methodologies. The results from these simulations are often presented in dif-

ferent ways, which makes them difficult to compare. In Figure 3.6 I have plotted the prediction of my semi-analytic formulae versus the results from Réville et al. (2015a), Réville et al. (2016), Alvarado-Gómez et al. (2016), Garraffo et al. (2016a), Réville and Brun (2017), and Ó Fionnagáin et al. (2019). Without adjustment the semi-analytic work agrees with the majority of the parameter space explored in other works, some exceptions include the extremely small  $R_A$  of Garraffo et al. (2016a), and the simulations of Alvarado-Gómez et al. (2016) for which I had to use a hotter wind driving temperature ( $c_s/v_{esc} = 0.4$ ) to match their results. Such “tuning” is to be expected, as each of these works uses different numerics and wind-driving physics. In future, it would be interesting to do a more thorough comparison.

### 3.6 Summary

In this Chapter I have presented hundreds of 2.5D MHD wind simulations computed using the PLUTO code. These stellar winds contain various combinations of axisymmetric dipole, quadrupole, and octupole magnetic geometries, for which I calculate the angular momentum-loss rates. For pure magnetic geometries, increasing the complexity of the magnetic field reduces the effectiveness of the angular momentum process; for a given polar magnetic field strength (as shown by Réville et al. 2015a). When in combination, the magnetic geometries compete to control the scaling of the angular momentum-loss rate as a function of wind magnetisation. If the magnetic field becomes “open” close to the star, the higher order magnetic field components typically govern the angular momentum-loss rate. If the magnetic field is opened further away from the star, where the higher order components have decayed away, the dipole component sets the scaling of the angular momentum-loss rate. This is due to the strong link between open magnetic flux and the angular momentum-loss rate. The radial decay of the magnetic field and the location where the magnetic field becomes open govern how much open magnetic flux is created, and therefore the angular momentum-loss rate. I approximate the behaviour of  $\langle R_A \rangle - \Upsilon$  with a broken power law, which is applied to a variety of problems in this thesis (see Chapters 4, 5, 6, and Appendix D).

Generally, the acceleration of stellar wind plasma is similar across all the simulations in this Chapter, as the coronal (driving) temperature is fixed. Slight deviations in the wind acceleration occur due to differences in how magnetic flux tubes expand with radial distance. These small differences in acceleration are shown to affect the  $\langle R_A \rangle - \Upsilon_{open}$  scaling but can be removed (as shown by Pantolmos and Matt 2017) by considering the wind speed at the Alfvén surface. Additionally the relationship between the radius at which the magnetic field becomes open and the Alfvén radius is explored for different wind topologies. These quantities are interlinked and so represent an interesting diagnostic to compare wind simulations in future.

This Chapter ignores the effect of non-axisymmetric magnetic fields, and the relation between magnetic field topology and coronal heating. In Chapter 7 I address the effect of non-axisymmetric magnetic fields on the results from this Chapter. Though it is left for future works to explore the more complex relationship between heating, topology and angular momentum-loss.

## Chapter 4

# The Effect of Magnetic Variability on Stellar Angular Momentum Loss

### 4.1 Introduction

In the previous Chapter, based on 2.5D MHD thermally-driven wind models, I developed two semi-analytic formulae for the angular momentum-loss rates of low-mass stars (also referred to as “braking laws”). This Chapter focuses on the application of these braking laws, both require the mass-loss rate in the wind, but they each need different quantities to describe the stellar magnetic field. The first formula requires the surface magnetic field strengths of the dipole, quadrupole and octupole components (parameterised with  $\Upsilon$ ), the second requires the value of the open magnetic flux in the stellar wind ( $\Upsilon_{open}$ ). Given that all of these quantities are difficult to evaluate (even for our closest star), the number of candidates available to study is small. In the first part of this Chapter, I focus on the Sun for which there are remote sensing observations of its surface magnetic field, along with in-situ observations of the solar wind mass flux and magnetic field. By using the in-situ measurements to approximate the global mass-loss rate and open magnetic flux, the Sun represents a chance to test both braking laws. Additionally, the Sun is a middle-aged star, and so its angular momentum-loss rate is also predicted by models of stellar rotation evolution (e.g. Matt et al. 2015), which I also compare to the two braking laws.



In total I present three separate estimates of the solar wind angular momentum-loss rate, which appear as they were published in *The Astrophysical Journal*. For the second part of this Chapter, I focus on stars which have been repeatedly monitored by Zeeman-Doppler imaging (ZDI) these are: 61 Cyg A,  $\epsilon$  Eri,  $\xi$  Boo A and  $\tau$  Boo A. This means the strength of their surface magnetic fields (dipole, quadrupole and octupole components) have been evaluated. Additionally, 61 Cyg A,  $\epsilon$  Eri and  $\xi$  Boo A all have mass-loss rates estimated using observations of astrospheric Lym- $\alpha$  absorption (Wood and Linsky 1998; Wood et al. 2002, 2005). Therefore, I can apply the first braking law to these stars and assess how their time-varying magnetic fields affect their angular momentum-loss rates. Again the results appear as they were published in *The Astrophysical Journal*. Following this, I present some additional details/figures that were left out of the papers, and finally I summarise the results from this Chapter in the context of the overall thesis.

## 4.2 Observations of Solar Magnetism and the Solar Wind

### 4.2.1 Remote-sensing Observations

Magnetographs are a general class of instrument which are used to measure the Zeeman effect (in one form or another e.g. splitting or polarisation) in spectral lines from the Sun (e.g. Beckers 1968). When these instruments are designed, choices in the wavelength of observation change the results in a number of ways, from the sensitivity and saturation of the Zeeman signal, to the height in the solar atmosphere that is being probed. There is also a variety in resolutions, with some magnetographs located in space and some on the ground. Those on the ground, in principle, should provide higher resolution images as they are less limited in the size of the telescope. However they suffer from atmospheric effects that reduce their resolution to that of smaller space-based instruments (see Figure 4.1). Given the different sensitivities of current instruments and their different resolutions, an absolute calibration of magnetic field strengths is a true challenge (see for example Riley et al. 2014).

Additionally, most magnetographs are located on, or in orbit of, Earth and so a

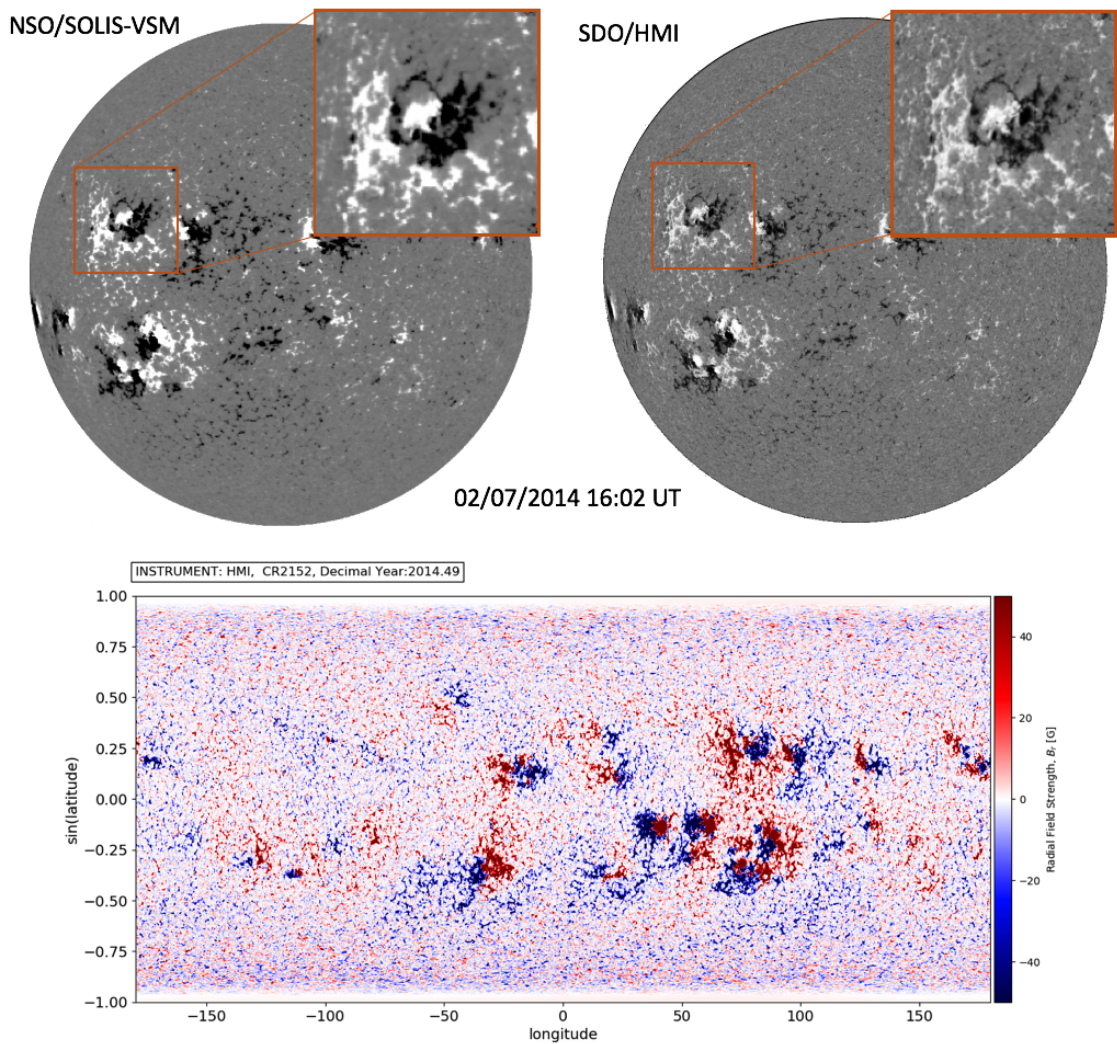


**Figure 4.1:** Top: Comparison of full-disk magnetograms from: Left) the Synoptic Optical Long-term Investigations of the Sun (SOLIS) instrument built by the National Solar Observatory (NSO). Right) The Helioseismic and Magnetic Imager (HMI) onboard the Solar Dynamics Observatory (SDO), on the 2nd July 2014 (during solar maximum). Differences appear in the recovered field strengths between magnetograms (in general) due to each instrument using different spectral lines to study the Zeeman effect. Additionally, space-based observations mitigate atmospheric effects (and clouds), and so have a better resolving power than typical ground based instruments (see the zoomed panels). Bottom: Synoptic magnetogram constructed from observations by HMI on SDO during the same time period at the full-disk images above (Carrington Rotation 2152). The zoomed feature from the top panel is located between 50 and 100 degrees in longitude, and  $\sin(\text{latitude})$  around 0.25.

global view of the Sun's surface magnetic field cannot be produced<sup>1</sup>. To get around this, it has been common practice to stitch full-disk magnetogram images together over the course of the Sun's rotation period (more specifically a Carrington Rotation,  $\sim 27$  days), and build-up maps of the Sun's surface magnetic field known as synoptic magnetograms. One such synoptic magnetogram is shown in Figure 4.1 for Carrington Rotation 2152 (which

1. Note, though the two Solar Terrestrial Relations Observatory (STEREO) spacecraft did not carry magnetographs, in February 2011 they were located 180 degrees apart from each other (around Earth's orbit), such that the entire Sun could be observed simultaneously in the EUV.

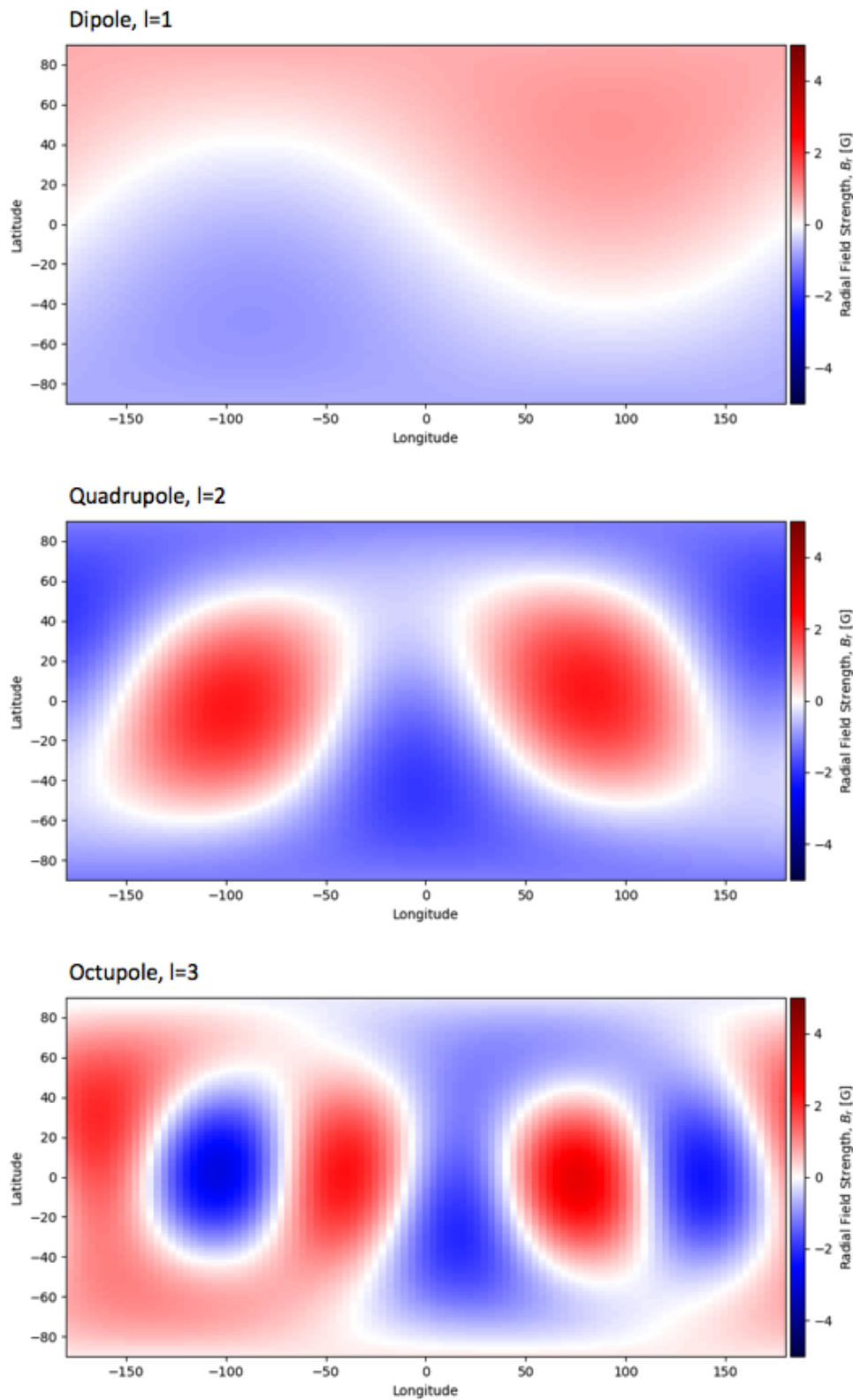


**Figure 4.2:** Dipole, quadrupole, and octupole components of the synoptic magnetogram shown in Figure 4.1. During solar maximum, the dipole component of the Sun's photospheric magnetic field is weakened, with more energy being stored in the higher order magnetic field geometries.

is during solar activity maximum of Solar Cycle 24).

Magnetographs measure the line-of-sight magnetic field component, and so care must also be taken in transforming this into the radial magnetic field at the solar surface. This issue is strongest towards the rotation poles of the Sun, for which our vantage point in the ecliptic means there is a large amount of noise due to projection effects. For the synoptic magnetograms taken by the Michelson Doppler Imager (MDI) onboard the Solar and Heliospheric Observatory (SOHO), and the Helioseismic and Magnetic Imager (HMI) onboard the Solar Dynamics Observatory (SDO), this has been mitigated by applying a polar field correction (e.g. Sun et al. 2011), which uses smoothed north and south pole observations along with a simple flux transport model to interpolate the polar field strengths for the final output synoptic magnetograms. Provided the Sun’s magnetic field doesn’t evolve faster than the  $\sim 27$  day timescale, synoptic magnetograms produce reasonably reliable results. For the purposes of this work, synoptic maps track the large-scale magnetic field components that are required (see DeRosa et al. 2012; Obridko et al. 2020). However, current operational whole-sun magnetograms (used for forecasting space weather) now tend to favour data assimilation techniques as active regions can emerge or evolve significantly on timescales shorter than this (see ADAPT magnetograms in Hickmann et al. 2015).

Interestingly, there is another (more recent) form of synoptic magnetogram, which provides information on the vector components of the Sun’s magnetic field. These are produced by the conversion of full-disk magnetograms taken by the Synoptic Optical Long-term Investigations of the Sun (SOLIS) Vector Spectromagnetograph (VSM), into synoptic magnetograms (see Gosain et al. 2013). This development has allowed for the Sun’s photospheric magnetic field to be studied in new ways (see Vidotto 2016; Vidotto et al. 2018), including its temporal evolution. These will be further discussed in Section 4.4.

Using the synoptic magnetograms from SOHO/MDI and SDO/HMI, which together cover 20+ years, it is possible to study the evolution of the large-scale magnetic field of the Sun. Each magnetogram is decomposed into spherical harmonics  $Y_{lm}(\theta, \phi)$  which have weightings  $\alpha_{lm}$ , where  $l$  is the spherical harmonic order ( $l = 1$  the dipole,  $l = 2$  the quadrupole,  $l = 3$  the octupole, etc), and  $m$  is the spherical harmonic degree

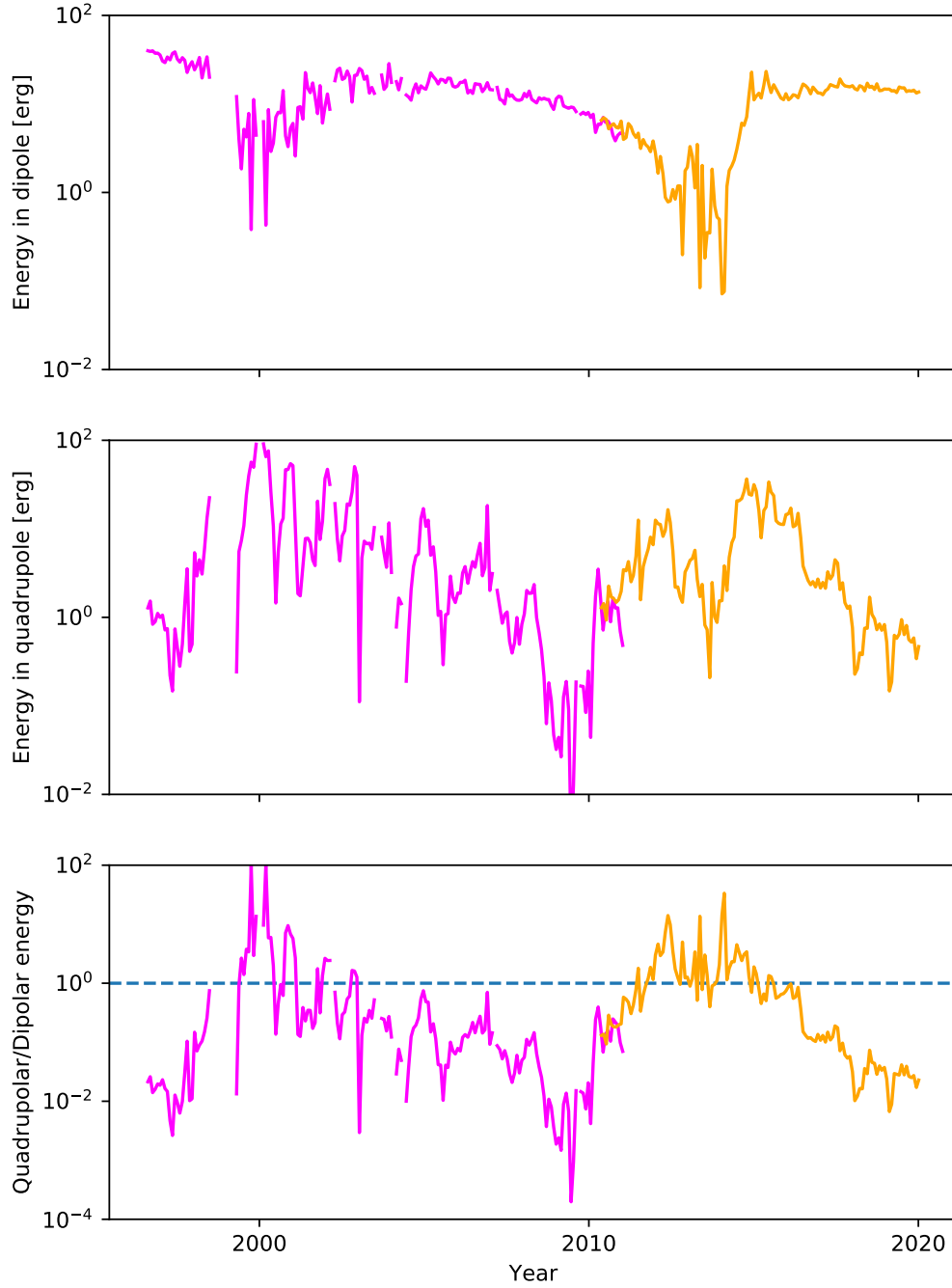


**Figure 4.3:** Magnetic energy found in the dipole and quadrupole component of the Sun’s surface magnetic field (top panels), plus the ratio of the two energies (bottom panel). Data is taken from the Michelson Doppler Imager (MDI) onboard the Solar and Heliospheric Observatory (SOHO), shown in magenta, and the Helioseismic and Magnetic Imager (HMI) onboard the Solar Dynamics Observatory (SDO), shown in yellow. Synoptic magnetograms from both instruments are decomposed into their spherical harmonic components, from which the dipole and quadrupole magnetic field strengths and energies are derived. The bottom panel clearly shows the solar cycle variation in dipole to quadrupole energies, which was shown originally by DeRosa et al. (2012). The dipole dominates during solar minima and the quadrupole dominates during solar maxima.

( $-l \leq m \leq l$ ), following,

$$B_r(\theta, \phi) = \sum_{l=0}^{\infty} \sum_{m=-l}^l \alpha_{lm} Y_{lm}(\theta, \phi). \quad (4.1)$$

Here  $\theta$  is heliographic latitude and  $\phi$  is Carrington longitude. Further information about spherical harmonics is available in Appendix A. This decomposition includes the  $l = 0$  monopole component as synoptic magnetograms contain divergent field due to the stitching process (the monopole component is subsequently ignored). An example of this decomposition is shown in Figure 4.2, where the SDO/HMI synoptic magnetogram from Figure 4.1 is decomposed into its dipole, quadrupole, and octupole components.

The  $\alpha_{lm}$  coefficients quantify the strength of each spherical harmonic, which can be translated into magnetic energy as,

$$E_l = \sum_{m=-l}^l (c_{lm}\alpha_{lm})^2, \quad (4.2)$$

where  $c_{lm}$  is the normalisation for each spherical harmonic component (see equation (A.14) in Appendix A). The magnetic energy in the dipole ( $E_1$ ) and quadrupole ( $E_2$ ), during solar cycle 23 and 24, is shown in Figure 4.3 along with the ratio of their energies  $E_2/E_1$ . Through the solar cycle, it is observed that the dipole and quadrupole energies fluctuate, with the ratio of quadrupole to dipole energy being strongest during solar maxima and weakest during solar minima (see also DeRosa et al. 2012).

## 4.2.2 In-situ Measurements

In-situ observations (i.e., data from particle detectors, magnetometers, etc, which are immersed in the solar wind) are available from a number of spacecraft. In this Chapter I use measurements from:

1. Advanced Composition Explorer (ACE) - In orbit around the  $L_1$  Lagrangian point between the Sun and Earth, which is approximately 1.5 million km from Earth, since December 1997. ACE's primary mission is to provide real-time early warning data for space weather forecasting<sup>2</sup>. I use data from the Solar Wind Electron, Proton and Alpha Monitor (SWEPAM), and Magnetometer (MAG) instruments.

---

2. ACE was joined at  $L_1$  by the Deep Space Climate Observatory (DSCOVR) in February 2015 as its successor for space weather monitoring, however since June 2019 DSCOVR has been in safe mode after an anomaly occurred in the laser gyroscope. Hopefully a software patch will allow DSCOVR to return to duty during 2020.

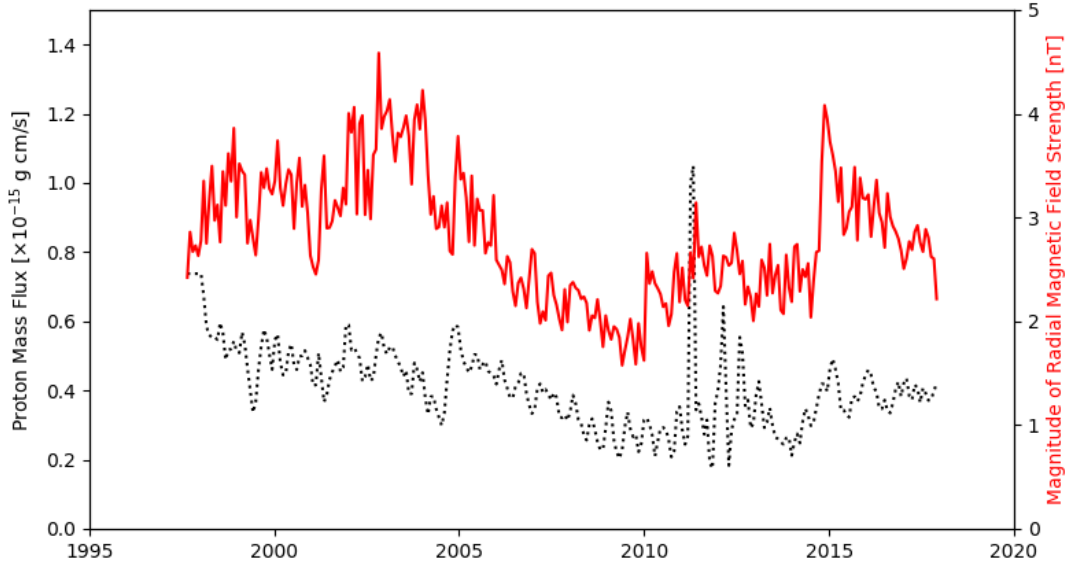


**Figure 4.4:** 27 day averages of the proton mass flux (black dotted line) and radial magnetic field (red solid line) measured by the Advanced Composition Explorer (ACE) spacecraft during 1997-2017. The interplanetary magnetic field strength varies with solar cycle, stronger at activity maxima than minima. The mass flux has little correlation with solar activity. Note these averages make no attempt to remove Interplanetary Coronal Mass Ejections (ICMEs), which are shown to affect the result by a few percent.

2. Ulysses - Launched in 1990, was a (polar) solar orbiter which completed three “fast latitude scans” during its lifetime, ending in June 2009. Ulysses used a gravity assist from Jupiter in 1992 to modify its orbit out of the ecliptic by 80 degrees, but its perihelion was limited to  $\sim 1$  au. I use data from the SWOOPS (Solar Wind Observations Over the Poles of the Sun), and Vector Helium Magnetometer / Flux Gate Magnetometer (VHM/FGM) instruments.

Both of these spacecraft are/were capable of detecting the radial velocity of the solar wind  $v_r$ , the proton density  $\rho$ , and the vector magnetic field  $\mathbf{B}$  (for which we only consider  $B_r$  in this Chapter). A more detailed review of in-situ spacecraft capabilities can be found in Section 6.2.

Examples of the mass flux ( $\rho v_r$ ) and radial magnetic field strength ( $|B_r|$ ) are shown in Figure 4.4. These values have been averaged on a 27 day timescale (in line with Carrington rotations) in an attempt to remove longitudinal features in the solar wind, i.e. each data point represents the average equatorial value of that quantity. It is known that the solar wind is highly structured (see Chapter 2), so this is a necessary step to average spu-

rious features such as fast wind from equatorial coronal holes, or slow wind around the Heliospheric Current Sheet (HCS), which are not individually representative of the equatorial wind as a whole. Given these 27 day averages, and assuming that the magnetic flux in the solar wind is distributed evenly versus latitude (at large distances from the Sun), and similarly for the mass flux, then these values can be used to estimate global quantities. A few issues arise from this approach however, which are discussed in the following published paper, namely the effect of transient features and our ignorance of the structure of the solar wind.

Assuming that the evolution of fast/slow wind streams is captured in the 27 day averaging process, the main contribution to transients in the in-situ observations is that of ICMEs. These are discussed in Chapter 2, but in general, are observed as discontinuous features in the in-situ measurements. It is possible to remove most (not all) of these events from near-Earth observations through the use of ICME catalogues (e.g. Cane and Richardson 2003), or by setting thresholds on solar wind properties (such as strong increases in magnetic field strength and proton density). In the following published paper, the ACE dataset is used as the primary source of data, given its temporal coverage and consistent distance to the Sun. However the Ulysses data provides a strong constrain on the variation of the mass and magnetic flux versus heliographic latitude, which strengthens the case for approximating the solar wind as isotropic.





# The Effect of Magnetic Variability on Stellar Angular Momentum Loss. I. The Solar Wind Torque during Sunspot Cycles 23 and 24

Adam J. Finley , Sean P. Matt , and Victor See

University of Exeter, Department of Physics & Astronomy, Stoker Road, Devon, Exeter, EX4 4QL, UK; [af472@exeter.ac.uk](mailto:af472@exeter.ac.uk)  
Received 2018 May 23; revised 2018 July 29; accepted 2018 July 31; published 2018 September 7

## Abstract

The rotational evolution of cool stars is governed by magnetized stellar winds that slow the stellar rotation during their main sequence lifetimes. Magnetic variability is commonly observed in Sun-like stars, and the changing strength and topology of the global field is expected to affect the torque exerted by the stellar wind. We present three different methods for computing the angular momentum loss in the solar wind. Two are based on MHD simulations from Finley & Matt (2018), with one using the open flux measured in the solar wind, and the other using remotely observed surface magnetograms. Both methods agree in the variation of the solar torque seen through the solar cycle and show a 30%–40% decrease from cycles 23 to 24. The two methods calculate different average values,  $2.9 \times 10^{30}$  erg (open flux) and  $0.35 \times 10^{30}$  erg (surface field). This discrepancy results from the already well-known difficulty of reconciling the magnetograms with the observed open flux, which is currently not understood, leading to an inability to discriminate between these two calculated torques. The third method is based on the observed spin rates of Sun-like stars, which decrease with age, directly probing the average angular momentum loss. This method gives  $6.2 \times 10^{30}$  erg for the solar torque, larger than the other methods. This may be indicative of further variability in the solar torque on timescales much longer than the magnetic cycle. We discuss the implications for applying the formula to other Sun-like stars, where only surface field measurements are available, and where the magnetic variations are ill-constrained.

*Key words:* magnetohydrodynamics (MHD) – solar wind – stars: low-mass – stars: magnetic field – stars: rotation – stars: winds, outflows

## 1. Introduction

Angular momentum loss through stellar winds explains the rotational evolution of low-mass stars ( $M_* \leq 1.3 M_\odot$ ) on the main sequence. These stars are shown to have outer convection zones (Marcy 1984; Donati et al. 2006, 2008; Morin et al. 2008; Petit et al. 2008; Morgenthaler et al. 2011; Gregory et al. 2012; Reiners 2012; Folsom et al. 2016, 2017) that are able to support magnetic fields through the interplay of rotation and convection, forming a dynamo (Brun & Browning 2017). The magnetic field generation of such dynamos is linked with rotation (Browning 2008; Reiners et al. 2009; Reiners & Basri 2010; Vidotto et al. 2014; See et al. 2015; Shulyak et al. 2017) such that a faster rotator will, in general, produce a larger field strength. Stellar winds are found to be more effective at slowing rotation in the presence of these large-scale magnetic fields (Weber & Davis 1967; Mestel 1968; Keppens & Goedbloed 2000; Matt et al. 2012; Garraffo et al. 2015; Réville et al. 2015a). Therefore, the relation of stellar rotation, magnetism, and angular momentum loss leads to the convergence of rotation periods at late ages (Skumanich 1972; Soderblom 1983; Barnes 2003, 2010; Delorme et al. 2011; Van Saders & Pinsonneault 2013; Bouvier et al. 2014).

Observations of the rotation rates of stars at different ages, and our knowledge of stellar structure, also give us direct constraints on the total external torque on the star. This value is independent from any knowledge of the physical mechanism for that angular momentum loss, but it probes only a long-time average torque (i.e., only on timescales smaller than the spin-down time, which can be in the range of tens to hundreds of Myr for main sequence stars). With the increasing number of accurate rotation period measurements available for comparison with model results (e.g., Agüeros et al. 2011; McQuillan

et al. 2013; Núñez et al. 2015; Rebull et al. 2016; Covey et al. 2016; Agüeros 2017; Douglas et al. 2017), we are able to examine the physical mechanisms of stellar wind braking in greater detail (Irwin & Bouvier 2009; Bouvier et al. 2014). A variety of spin evolution models have been developed to date (e.g., Gallet & Bouvier 2013; Van Saders & Pinsonneault 2013; Gallet & Bouvier 2015; Johnstone et al. 2015; Matt et al. 2015; Amard et al. 2016; Sadeghi Ardestani et al. 2017; See et al. 2018) that relate basic stellar properties; mass, radius, rotation period, field strength, and mass loss rate, with results from analytic or numerical models for the spin-down torque applied to the star, and the subsequent redistribution of internal angular momentum.

Stellar mass and radius remain essentially constant throughout the main sequence. However, in addition to the long-time secular changes of the magnetic field due to rotation, magnetic activity is also observed to vary significantly over timescales of years to decades (Baliunas et al. 1995; Azizi & Mirtorabi 2018). This is routinely observed for the Sun, which is known to have a magnetic activity cycle (Babcock 1961; Wilcox & Scherrer 1972; Willson & Hudson 1991; Guedel et al. 1997; Güdel 2007; Schrijver & Liu 2008), moving from an activity maximum through minimum and back to maximum in roughly 11 years. The Sun's cyclic behavior is apparent in changes to the large-scale magnetic field (DeRosa et al. 2012), which significantly modifies the solar wind structure and outflow properties (Smith & Balogh 1995; McComas et al. 2000; Wang et al. 2000; Tokumaru et al. 2010). Activity cycles on other stars are quantified using activity proxies such as the long-term monitoring of Ca II HK emission (Baliunas et al. 1995; Egeland et al. 2017), observed light curve modulation due to star spots (Lockwood et al. 2007), X-ray activity (Hempelmann

et al. 1996), and more recently Zeeman Doppler Imaging, ZDI (Donati et al. 1989; Semel 1989; Brown et al. 1991; Donati & Brown 1997). The mass loss rate of the Sun is shown to vary with the magnetic cycle (McComas et al. 2013) and is fundamentally connected with magnetic activity (Cranmer et al. 2007). This behavior is expected to be similar for other low-mass stars.

Previous theoretical studies have shown the variation in angular momentum loss over magnetic cycles (Pinto et al. 2011; Garraffo et al. 2015; Réville et al. 2015b; Alvarado-Gómez et al. 2016; Réville & Brun 2017). However, they require costly MHD simulations that attempt to simultaneously fit the mass loss rate and magnetic field strengths for single epochs. By contrast, using the stellar wind braking formulations from Réville et al. (2015a), Finley & Matt (2017), Pantolmos & Matt (2017) and Finley & Matt (2018), hereafter FM18, one can easily predict the torque for any known mass loss rate and magnetic field strength/geometry, without the need for new simulations. This allows, for the first time, a more continuous calculation of the angular momentum loss rate.

Using the multitude of current observations of the Sun (this work), and multi-epoch studies of other stars from the ZDI community (Paper II), we can now evaluate the variation of stellar wind torques over decadal timescales. We briefly reiterate the angular momentum loss prescriptions from FM18 in Section 2, collate solar observations in Section 3, and implement them in Section 4 to produce the most up-to-date determination of the solar braking torque, using methods based on the surface magnetogram data obtained from *SOHO*/MDI and *SDO*/HMI, and evaluating the open magnetic flux from the *Ulysses* and *Advanced Composition Explorer* (ACE) spacecraft, along with an estimate based on the rotational behavior of other Sun-like stars. In Section 5 we then discuss our results and address the observed discrepancy between surface field and open flux methods, along with the differences between our torque value and the derived long-time average result.

## 2. Semi-analytic Torque Formulations

FM18 provides semi-analytic prescriptions for the angular momentum loss rate based on over 160 stellar wind simulations using the PLUTO magnetohydrodynamics (MHD) code (Mignone et al. 2007; Mignone 2009). The simulations in FM18 use a polytropic equation of state, which equates to a thermally driven wind with a coronal temperature of 1.7MK for the Sun, and a polytropic index of  $\gamma = 1.05$ , which is nearly isothermal. The use of a nearly isothermal wind leads to some discrepancy with the observed multi-speed solar wind, which is known to be bimodal in nature (Ebert et al. 2009). Nevertheless, work by Pantolmos & Matt (2017) has shown that changes to this assumed global wind acceleration can be understood within these models, and have a well described impact on our result.

As discussed in Pantolmos & Matt (2017), variations in the chosen wind speed, i.e., a wind comprised of all slow or all fast wind, differ by a factor of  $\sim 2$  in the predicted torque. In reality the solar wind is comprised of both components, with the relative fraction of slow and fast wind changing with magnetic activity, which means that the true torque is between these two extremes. For this work, we adopt the parameters derived originally in FM18, with a temperature between the extremes (see Pantolmos & Matt 2017), and accept the

potential discrepancies in the wind acceleration over the solar cycle.

The simulations of FM18 are axisymmetric, so derived torques neglect 3D effects as observed in the simulations of Réville & Brun (2017). The advantage of these formulations is that calculations can be performed much faster than MHD simulations. This allows us to use all the available data to produce the most coherent picture of solar angular momentum loss over the last 22 years.

The torque,  $\tau$ , due to the solar wind is then given by

$$\tau = \dot{M} \Omega_* R_*^2 \left( \frac{\langle R_A \rangle}{R_*} \right)^2, \quad (1)$$

where,  $\dot{M}$  is the solar wind mass loss rate, the stellar rotation rate is assumed to be solid body (no differential rotation) with  $\Omega_* = \Omega_\odot = 2.6 \times 10^{-6} \text{ rad s}^{-1}$ , and  $R_*$  is the stellar radius for which we adopt  $R_* = R_\odot = 6.96 \times 10^{10} \text{ cm}$ . As with previous torque formulations, Equation (1) defines the average Alfvén radius,  $\langle R_A \rangle$ , to behave as a lever arm, or efficiency factor for the stellar wind in braking the stellar rotation (Weber & Davis 1967; Mestel 1968).

### 2.1. Formulation Using Surface Magnetic Field

In Equation (1) the torque depends on the average Alfvén radius. Simulations of FM18 showed that  $\langle R_A \rangle$  can be predicted using the wind magnetization parameter,

$$\Upsilon = \frac{B_*^2 R_*^2}{\dot{M} v_{\text{esc}}}, \quad (2)$$

where the total axisymmetric field strength is evaluated using the polar field strengths from the lowest order modes  $B_* = |B_*^{l=1}| + |B_*^{l=2}| + |B_*^{l=3}|$  ( $l$  is the magnetic order, for which 1, 2, and 3 correspond to the dipole, quadrupole, and octupole modes, respectively), and the escape velocity is given by  $v_{\text{esc}} = \sqrt{2GM_*/R_*}$ , for which we adopt  $M_* = M_\odot = 1.99 \times 10^{33} \text{ g}$ .

For mixed geometry axisymmetric fields, the average simulated Alfvén radius is found to behave as a broken power law of the form

$$\frac{\langle R_A \rangle}{R_*} = \max \begin{cases} K_{\text{dip}} [\mathcal{R}_{\text{dip}}^2 \Upsilon]^{m_{\text{dip}}}, \\ K_{\text{quad}} [(|\mathcal{R}_{\text{dip}}| + |\mathcal{R}_{\text{quad}}|)^2 \Upsilon]^{m_{\text{quad}}}, \\ K_{\text{oct}} [(|\mathcal{R}_{\text{dip}}| + |\mathcal{R}_{\text{quad}}| + |\mathcal{R}_{\text{oct}}|)^2 \Upsilon]^{m_{\text{oct}}}, \end{cases} \quad (3)$$

which approximates the stellar wind solutions from FM18, using  $K_{\text{dip}} = 1.53$ ,  $K_{\text{quad}} = 1.70$ ,  $K_{\text{oct}} = 1.80$ ,  $m_{\text{dip}} = 0.229$ ,  $m_{\text{quad}} = 0.134$ , and  $m_{\text{oct}} = 0.087$ . The variables describing the field geometry,  $\mathcal{R}_{\text{dip}}$ ,  $\mathcal{R}_{\text{quad}}$ , and  $\mathcal{R}_{\text{oct}}$  are defined as the ratios of the polar strengths of each mode over the total; i.e.,  $\mathcal{R}_{\text{dip}} = B_*^{l=1}/B_*$ , etc. The scaling of Equation (3) is such that for most field strengths, in the solar case, we find that the dipole-only term dominates the angular momentum loss (i.e., the dipole-only formulation of Matt et al. 2012 holds).

### 2.2. Formulation Using Open Magnetic Flux

Réville et al. (2015a) show that by parameterizing the relationship for the average Alfvén radius in terms of the open magnetic flux,  $\phi_{\text{open}}$ , a scaling behavior independent of

magnetic geometry can be formulated. Such a general formula for the torque is very useful. However, the open magnetic flux cannot be observed for other stars than the Sun. We define the unsigned open flux as

$$\phi_{\text{open}} = \oint_A |\mathbf{B} \cdot d\mathbf{A}|, \quad (4)$$

where  $A$  is a closed spherical surface located outside of the last closed field loop, i.e., in the magnetically open wind. The wind can then be parameterized with the open flux wind magnetization,

$$\Upsilon_{\text{open}} = \frac{\phi_{\text{open}}^2 / R_*^2}{\dot{M} v_{\text{esc}}}, \quad (5)$$

and the average Alfvén radius given by

$$\frac{\langle R_A \rangle}{R_*} = K_o [\Upsilon_{\text{open}}]^{m_o}, \quad (6)$$

where, from FM18,  $K_o = 0.33$  and  $m_o = 0.371$ . Here we assume the dipolar coefficient as the dipolar fraction of the total field  $\mathcal{R}_{\text{dip}}$  remains significant throughout the solar cycle, with few exceptions.

The simplicity of the semi-analytic derivation for the open flux torque formulation (see Pantolmos & Matt 2017) suggests that this method produces the most reliable torque for a given estimate of the open flux. This method is insensitive to surface geometry and any details of how the field is opened. The only factors that cause the angular momentum to deviate from this formulation is the wind acceleration and the 3D structure of the mass flux.

### 3. Observed Solar Wind Parameters

Information regarding the magnetic properties of the Sun are used here in two forms. First, we use the synoptic magnetograms of the surface magnetic field produced by both the Michelson Doppler Imager on board the *Solar and Heliospheric Observatory* (SOHO/MDI), and the Helioseismic and Magnetic Imager on board the *Solar Dynamic Observatory* (SDO/HMI), from which we calculate time-varying magnetic field strengths for the dipole, quadrupole, and octupole field components. Second, measurements of the interplanetary magnetic field (IMF) strength are taken in situ by the *Ulysses* and *ACE* spacecraft, which we use to produce an estimate of the time-varying solar open flux. Measurements of the solar wind speed and density are also made in situ by multiple spacecraft, but here we focus on results from *Ulysses* and *ACE*.

During the calculation of our solar wind quantities, we perform 27 day averages to remove any longitudinal variation and produce more representative values for the global wind. In doing this we have removed information of any temporal or spatial variation on smaller scales than this, which has been shown by previous authors (e.g., DeForest et al. 2014).

An additional complication arises from Coronal Mass Ejections (CMEs), or Interplanetary CMEs (ICMEs), as they arrive at the spacecraft detectors. ICMEs are observed in the data as impulsive increases in the in situ solar wind properties. CMEs occur on average up to five times a day at solar maximum and 1 every 2–3 days at solar minimum (Webb et al. 2017). Some authors have removed these events from their data sets (e.g., Cohen 2011) using CME catalogs (e.g., Cane & Richardson 2003) and by identifying anomalous

spikes. CMEs carry only a few percent of the total mass loss rate that is mainly located near the maximum of activity, and due to the distribution of their ejection trajectories into the Heliosphere, a reduced fraction of these events are recorded at the in situ detectors.

In order to gauge the impact of the enhanced magnetic field strengths and densities carried by ICMEs, we re-ran the analysis, removing periods when the wind density and field strength are greater than  $10 \text{ cm}^{-3}$  and  $10 \text{ nT}$ , respectively, from the hourly spacecraft data (as done for *Ulysses* by Cohen 2011). This results in  $\sim 3\%$  of the hourly data being cut in each 27 day average at solar maximum, and  $\sim 0\%$  at the minimum. During the 22 years this averages to removing  $\sim 1\%$  of the data from each 27 day bin. We find by removing the ICMEs, the average open flux and mass loss rates we derive are reduced by  $\sim 4\%$ . However, as CMEs should have a contribution to the total torque we prefer to include these events in our derived mass loss rate and open flux, even though there is not yet a model to show how their angular momentum loss per mass loss rate may be different than that of a steady global wind (see, e.g., Aarnio et al. 2012). As such, the results presented in the remainder of this work use the full, unclipped data set.

#### 3.1. Surface Magnetic Variability from SOHO/MDI and SDO/HMI

Using synoptic magnetograms taken from MDI and HMI,<sup>1</sup> the complete radial surface magnetic field strength,  $B_r$ , is recorded over the past 22 years for each Carrington rotation (CR)<sup>2</sup> from 1996 July (CR 1910) to the present. Both instrument teams provide polar field corrected data sets (Sun et al. 2011; Sun 2018), accounting for projection effects on the line of sight magnetic field measurements that result in a large amount of noise at the poles, along with other effects such as the Sun's tilt angle that periodically hides these areas from view. The two instruments observed the Sun over different time periods with an overlap from the beginning of HMI in 2010 May (CR 2097) until the end of MDI in 2010 December (CR 2104). Therefore, the data sets have been calibrated to produce consistent results. For this work, we apply a multiplicative factor to the HMI field strengths of 1.2, as suggested by Liu et al. (2012).

We use a total of 282 synoptic magnetograms that cover the entirety of sunspot cycle 23 (1996 August–2008 December, CR 1913–CR 2078), and cycle 24 up to 2018 January (CR 2199). These magnetograms are decomposed into their spherical harmonic components using the pySHTOOLS code (Wieczorek 2011). The magnetograms require remapping from the sine-latitude format of the observations onto an equal sampled grid that the code can use. Each map is then decomposed into a set of spherical harmonic modes  $Y_m^l$ , which have the order  $l = 1, 2, 3, \dots, l_{\text{max}}$  (a truncation limit placed at  $l_{\text{max}} = 150$ ) and degree  $-l \leq m \leq l$ . This process produces complex coefficients  $\alpha_m^l$  that weight each of the spherical harmonic modes,

$$B_r(\theta, \phi) = \sum_{l=0}^{l_{\text{max}}} \sum_{m=-l}^{m=l} \alpha_m^l Y_m^l(\theta, \phi), \quad (7)$$

where  $\theta$  and  $\phi$  represent the co-latitude and longitude of the magnetograms, respectively.

<sup>1</sup> <http://hmi.stanford.edu/data/synoptic.html>

<sup>2</sup> There are some Carrington rotations within the SOHO/MDI sample that have missing data and as such they are excluded from our analysis.

This method was performed by DeRosa et al. (2012) on 36 years of observations from the Wilcox Solar Observatory and, similarly to this work, the MDI data set. The results from our decomposition agree strongly with the results presented in DeRosa et al. (2012) for the MDI observations. Appendix A contains a full breakdown of the dipole, quadrupole, and octupole components that we calculate.

For the calculation of the solar wind torque based on the surface field, we require the dipole ( $l = 1$ ), quadrupole ( $l = 2$ ), and octupole ( $l = 3$ ) component strengths. The pySHTOOLS code produces a strength for the axisymmetric component ( $m = 0$ ) and the subsequent non-axisymmetric components ( $0 < |m| \leq l$ ) for each harmonic order  $l$ . The formulation from FM18 is produced using axisymmetric simulations only, here we produce a combined field strength including all  $m$ , rather than neglecting the non-axisymmetric components ( $m > 0$ ). We adopt the quadrature addition of field components,

$$B_*^l = \sqrt{\sum_{m=-l}^l (B_m^l)^2}, \quad (8)$$

where  $B_m^l = \alpha_m^l \max(|Y_m^l(\theta, \phi)|)$  characterizes the polar field strength of each mode. This results in  $B_*^l$  representing a combined dipole strength using all the spherical harmonic components with  $l = 1$  and,  $m = \{-1, 0, 1\}$ . Similarly this is done for the quadrupole ( $B_*^{l=2}$ ) and octupole ( $B_*^{l=3}$ ) modes. The left 3 panels of Figure 1 show how these combined dipole, quadrupole, and octupole field strengths (solid lines) vary as a function of time over 22 years of magnetogram observations.

### 3.2. Mass Loss Rates and Magnetic Open Flux Variability from ACE/Ulysses

Along with the magnetic properties of the Sun, the mass loss rate is required to calculate the loss of angular momentum in the solar wind. The ACE spacecraft<sup>3</sup> has been performing in situ monitoring of the fundamental solar wind properties since its arrival at the  $L_1$  Lagrangian point (on the Sun–Earth line, approximately 1.5 million km from Earth) in 1996 December. A global mass loss rate is constructed from the 27 day average<sup>4</sup> over the spacecraft data, assuming the observed solar wind flux to be characteristic of the total wind (i.e., the wind is isotropically the value observed by ACE),

$$\dot{M} = 4\pi \langle R^2 v_r(R) \rho(R) \rangle_{27\text{day}}, \quad (9)$$

where  $\dot{M}$  is the observed mass loss rate,  $R$  is the radial distance from the Sun of a given observation,  $v_r$  is the radial wind speed, and  $\rho$  is the mass density of the wind.

The mass loss rate produced from ACE data is shown in the top right panel of Figure 1 using a solid black line. The estimated mass loss rate varies between  $0.43$  and  $2.72 \times 10^{12} \text{ g s}^{-1}$ , with an average value of  $1.14 \times 10^{12} \text{ g s}^{-1}$ , which is consistent with previous works (Wang 1998; Cranmer 2008; Cranmer et al. 2017).

The same calculation is performed on the data available from the Ulysses spacecraft<sup>5</sup> shown in light gray. Ulysses again made in situ observations of the solar wind. However, it took a

polar orbit around the Sun with perihelion at  $\approx 1.35$  au and aphelion at  $\approx 5.4$  au. The spacecraft was launched in late 1990 and received a gravity assist from Jupiter in 1992 that modified the inclination of the orbit to around  $80^\circ$ . Notably, the Ulysses spacecraft made three fast latitude scans of the solar wind, each passing from the north pole to the south pole in approximately a year. These passes occurred between 1994 August–1995 July, 2000 November–2001 September, and 2007 February–2008 January, which corresponds to periods of minimum, maximum, and minimum solar activity, respectively. These time periods are highlighted in Figure 1 in magenta.

Both sets of spacecraft observations produce the same  $\dot{M}$  magnitude and variation with the cycle phase, although they do differ on a point-by-point basis, most notably when Ulysses was furthest from the Sun. The ACE data is concurrent with the 22 years of magnetogram observations, and as such we use this value of the mass loss rate in future calculations.

Both spacecraft are also capable of sampling the magnetic properties of the wind, i.e., the field direction and magnitude. Since the heliospheric magnetic field at the orbital distances of both spacecraft is thought to be predominantly open (Riley 2007; Owens et al. 2011, 2017), these measurements allow us to make an estimate of the total unsigned solar open flux,

$$\phi_{\text{open}} = 4\pi \langle R^2 |B_r(R)| \rangle_{|l| \text{ hr}}, \quad (10)$$

where  $\phi_{\text{open}}$  is the unsigned open flux, and  $B_r$  is the radial magnetic field strength observed by the spacecraft. The use of averaged 27 day radial field measurements, again assuming isotropy, to estimate the open flux is shown to be a good approximation, as the normalized value of the radial field,  $R^2 |B_r(R)|$ , is independent of heliographic latitude (Smith & Balogh 1995). The solar wind is found to redistribute significant magnetic flux variations due to the latitudinally directed magnetic pressure gradients formed from non-isotropy (Wang & Sheeley 1995; Lockwood et al. 2004; Pinto & Rouillard 2017). Thus, a single point measurement can be used to form a reasonable approximation of the total solar flux (Owens et al. 2008).

For the magnetic field observations taken with Ulysses, it is understood that the noise on the radial component  $B_r$  will grow with distance from the Sun, such that the prediction of Equation (10) will become discrepant to near-Earth measurements around 2 au (Owens et al. 2008). Therefore, we limit the open flux data used from Ulysses to include only the fast latitude scans, at which time the spacecraft was within 2 au of the Sun. ACE, located at  $L_1$ , is well within this cut off distance, therefore a complete open flux estimate is produced for the time of its observations. The solar open flux is evaluated using Equation (10) and shown in the second right panel of Figure 1 with a solid gray line. It is found to vary over the 22 years of observations between  $(2.02\text{--}13.2) \times 10^{22} \text{ Mx}$ , with an average value of  $7.98 \times 10^{22} \text{ Mx}$ . The estimated open flux is maximum around the solar activity maximum for each sunspot cycle, as with the mass loss rate.

## 4. Evaluating the Solar Wind Angular Momentum Loss Rate

Here we consider three methods for determining the angular momentum loss in the solar wind. The first uses the surface magnetic field strength  $B_r$  (FM18, Equation (3)),

<sup>3</sup> <http://www.srl.caltech.edu/ACE/ASC/level2/>

<sup>4</sup> An averaging period of 27 days is chosen to match the average synodic period of a Carrington rotation.

<sup>5</sup> <http://ufa.esac.esa.int/ufa/>

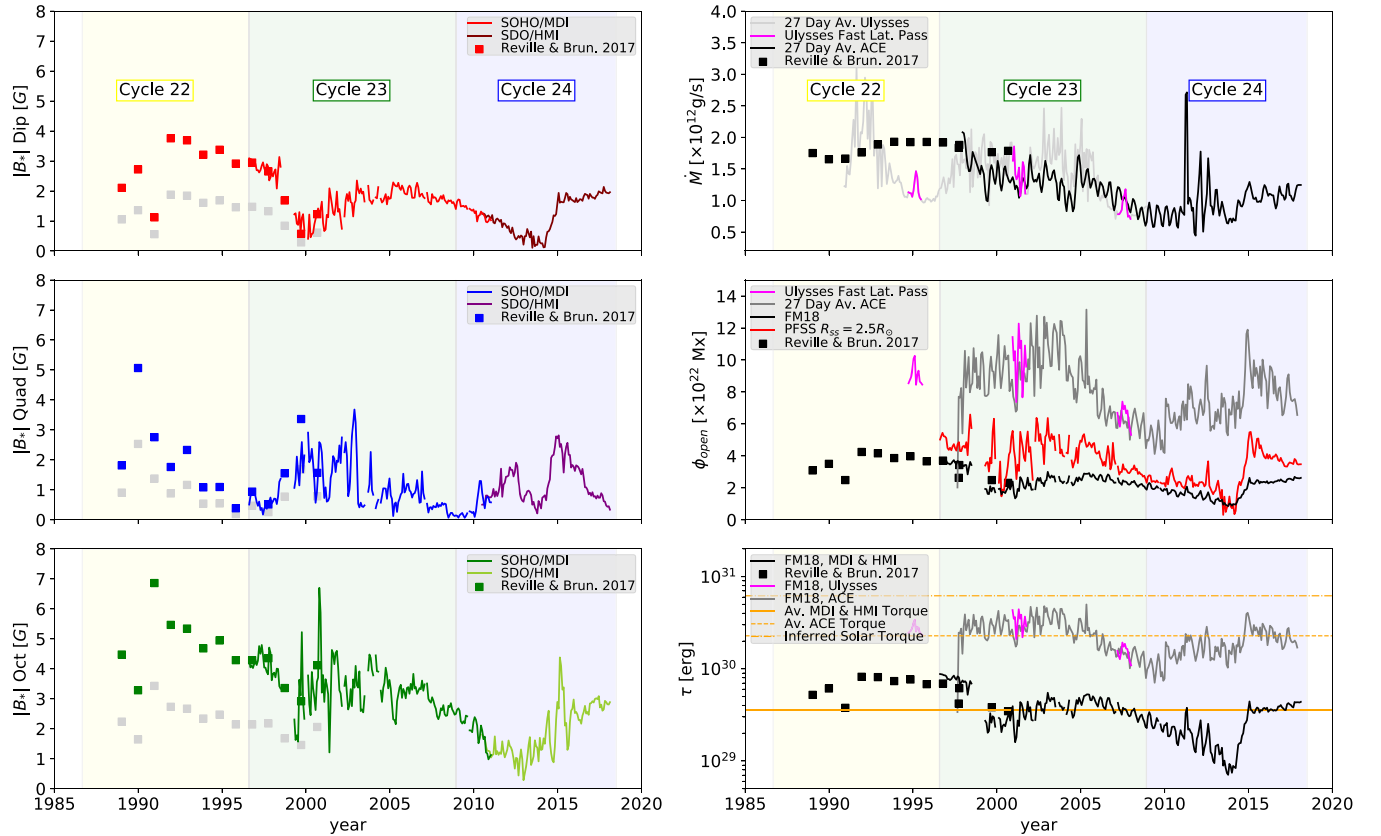


**Figure 1.** Calculation of the angular momentum loss rate,  $\tau$ , in the solar wind over the last 22 years, through various observations and utilizing the torque formulations presented in FM18. Left: three panels presenting the lowest order spherical harmonic components, dipole, quadrupole, and octupole, from the *SOHO*/MDI and *SDO*/HMI instruments along with the Carrington rotations used in Réville & Brun (2017) (gray squares are derived from the WSO maps directly, whereas the colored squares include a scale factor to bring the observations in line with MDI and HMI). Right: the top panel shows the mass loss rate using Equation (9) for the *ACE* data with a black line, all *Ulysses* data with a light gray line, the fast latitude scans indicated in magenta, and the models from Réville & Brun (2017) with black squares. The middle panel shows the open magnetic flux using Equation (10) for the *ACE* data with a dark gray line, *Ulysses* fast latitude scans in magenta, the results of using a potential field source surface model and the associated open flux from the FM18 model on the MDI and HMI magnetograms in red and black, respectively, and the models from Réville & Brun (2017) with black squares. The bottom panel shows the angular momentum loss rate, with the surface field method using MDI and HMI magnetograms along with the mass loss rate from the *ACE* spacecraft shown with a black line, and the open flux method using *ACE* data and *Ulysses* data in gray and magenta, respectively. The average torque for each method along with the value derived in Equation (13) are highlighted in solid, dashed, and dot-dashed lines, respectively. The torques from Réville & Brun (2017) are indicated with black squares.

the second uses the open magnetic flux  $\phi_{\text{open}}$  (FM18, Equation (6)), and the third calculates the expected torque on the Sun based on empirical trends in the observed rotation periods of other stars, i.e.,  $\tau \propto \Omega_*^3$ . We aim to characterize any difference between these torque predictions, and attempt to determine the most accurate estimate of the solar wind torque and its variability.

#### 4.1. Torque Predictions from Surface Field Measurements

Using the decomposed surface magnetograms from *SOHO* and *SDO*, along with mass loss rate measurements from the *ACE* spacecraft, we evaluate the solar wind torque using work from FM18. As previously discussed, Equation (3) applies for axisymmetric combinations of dipole, quadrupole, and octupole fields only. Despite this, we assume this relation holds for the non-axisymmetric field components also, and describes a single field strength for each harmonic mode  $l$  using Equation (8). This assumption is discussed in Section 5.1.

The predicted torques based on magnetograms from MDI and HMI are displayed in the bottom right panel of Figure 1 with a solid black line. The average torque predicted over the 22 years of data using this method is  $3.51 \times 10^{29}$  erg. Splitting

this time period into separate sunspot cycles<sup>6</sup> we produce a histogram of the torque and average Alfvén radii (top panels of Figure 2). The average angular momentum loss for cycle 23 is  $4.27 \times 10^{29}$  erg, whereas cycle 24 currently has an average of  $2.51 \times 10^{29}$  erg, 41% lower. The Alfvén radii predicted by Equation (3) are also shown to be distinctly different for each cycle.

#### 4.2. Torque Predictions from Open Flux Measurements

The angular momentum loss rates calculated using Equation (6) with the open flux and mass loss rate observations from *Ulysses* and *ACE* are displayed in the bottom right panel of Figure 1 in magenta and gray, respectively. Notably, both sets of observations agree well, and indicate that the solar maximum coincides with the maximum braking torque in the solar wind. The average torque predicted using the open flux method is  $2.28 \times 10^{30}$  erg, which is 3.26 times greater than the surface field method in the previous section. The sunspot cycles

<sup>6</sup> The first reversed polarity sunspot of cycle 24 occurred in 2008 January, but we adopt the time of the minimum smoothed monthly sunspot number that occurred in 2008 December.

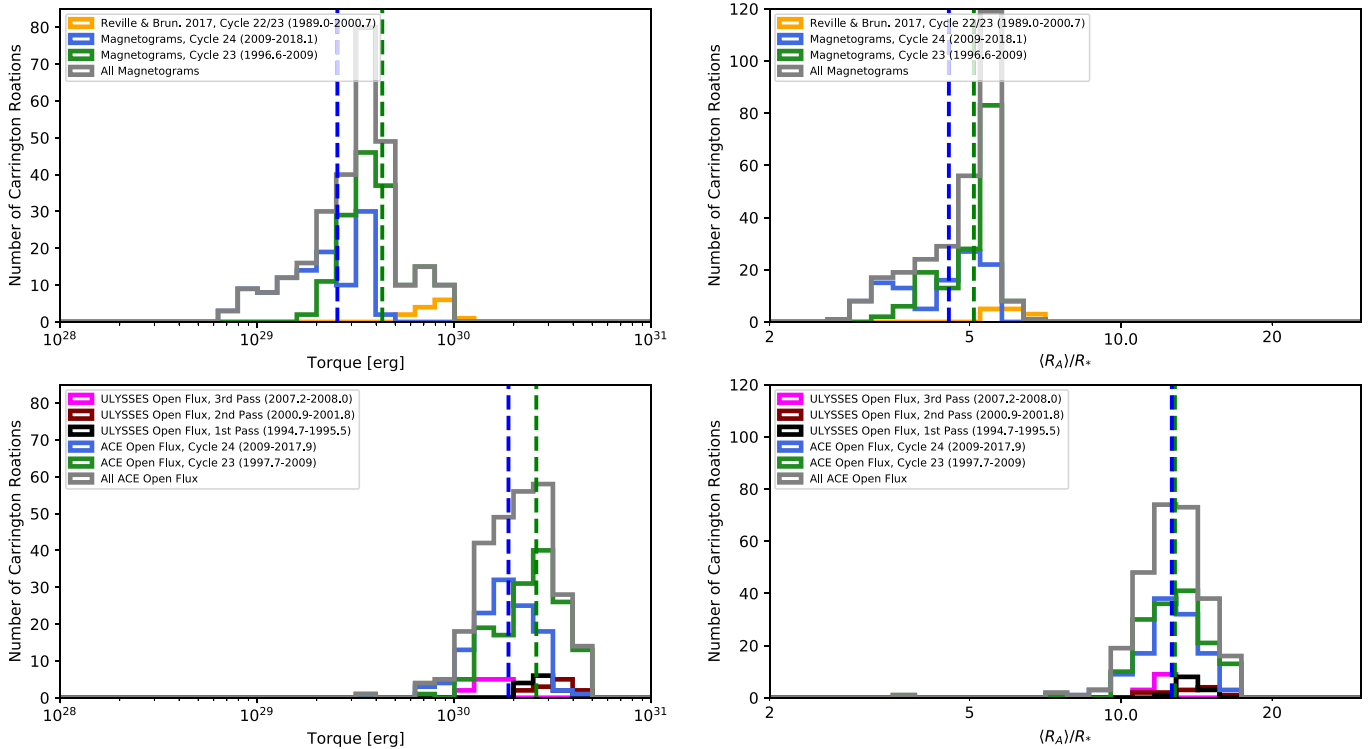


**Figure 2.** Histograms of the predicted torque and average Alfvén radii (right) for the magnetogram method in Section 4.1 (top), and the open flux method in Section 4.2 (bottom). Data is binned in Carrington rotations (27 day intervals), and colored either green or blue for cycle 23 and 24, respectively. Cycle 23 has complete coverage, whereas cycle 24 is still in its declining phase. Additionally, results from Réville & Brun (2017) (yellow) are compared with the magnetogram results in the top panels. The distributions appear approximately log-normal for each cycle. In both methods the torque distribution produced is lower in the current cycle (irrespective of the incomplete data) than cycle 23 (and note the averages for the current cycle are expected to decrease as the cycle moves into an activity minimum), indicating significant variability between cycles.

can again be distinguished. The torque and Alfvén radii predicted by Equation (6) are shown in the bottom panels of Figure 2. The average angular momentum loss for cycle 23 is  $2.60 \times 10^{30}$  erg, whereas cycle 24 currently has an average of  $1.88 \times 10^{30}$  erg, 28% lower. Similar to the torque predicted from the surface field measurements, we find a decreasing value of the solar torque, however the difference in the average Alfvén radii from cycle to cycle is far smaller for the open flux method.

Figure 3 displays the ACE derived torque along with the monthly averaged sunspot number; roughly, the angular momentum loss rate rises in accordance with the sunspot number with a hint that it lags behind in the declining phase of the sunspot cycle (see Section 5.4 for further discussion).

### 4.3. Solar Torque Inferred from Observed Stellar Rotation Rates

At the start of the main sequence phase, stars with nearly a solar mass exhibit a wide distribution of rotation rates, which is observed to converge toward a narrow distribution of rotation rates by an age of a few hundred Myr (e.g., Bouvier et al. 2014). The distribution of spin rates continues to narrow, as the average spin rate decreases in time. The narrowing distribution and common evolution of spin rates suggests that the stellar wind torques for all (or most) solar-mass stars approach a single relationship that depends simply on stellar parameters and spin rate, and which becomes independent of

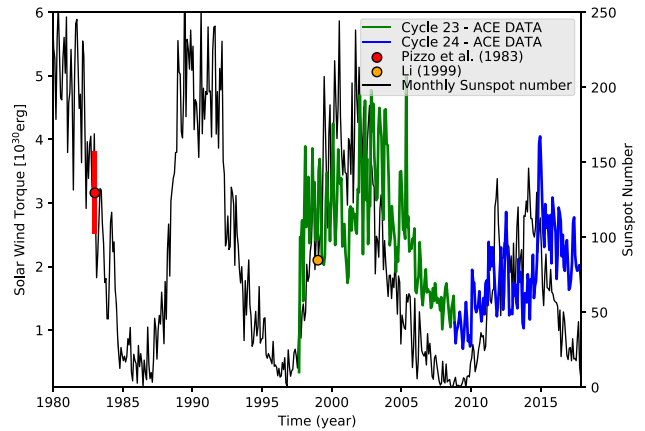


**Figure 3.** Solar angular momentum loss calculated using data from the ACE spacecraft and the open flux torque formulation from FM18 vs. time (colored line), along with the sunspot number (black line) and previous estimates of the angular momentum loss rate. Data from Cycle 23 is colored green and the current Cycle 24 is blue. Cycle 24 is weaker in both activity and the predicted torque. This could explain the larger value from Pizzo et al. (1983), which was measured during a stronger magnetic cycle.

the “initial” conditions (e.g., independent of whether the star was a fast or slow rotator at the start of the main sequence phase).

For this late-time, the asymptotic behavior of the observed stellar spin rates gives us constraints on the external torques,

completely independent from any knowledge of the physics of stellar winds. To derive such a constraint for solar-mass stars older than a few hundred Myr (following Schatzman 1962; Durney 1985; Kawaler 1988; Matt et al. 2015), we first approximate that the external torque depends simply on the rotation rate as a power law,

$$\tau_{\text{rot}} = \langle \tau_{\odot} \rangle_{\text{rot}} \left( \frac{\Omega}{\Omega_{\odot}} \right)^{p+1}, \quad (11)$$

where  $\langle \tau_{\odot} \rangle_{\text{rot}}$  is the current long-time-average torque of the Sun,  $\Omega$  is the stellar rotation rate,  $\Omega_{\odot}$  is the solar rotation rate, and  $p$  will be constrained by observations and theory. Next, if we assume that the moment of inertia of stars is constant during the main sequence phase and that the stars rotate as solid bodies, we can integrate the angular momentum equation analytically. This analysis shows that, for any value of  $p > 0$ , and independent of any reasonable “initial” spin rate (at young ages), the rotation rates will converge toward the relationship

$$\frac{\Omega}{\Omega_{\odot}} = \left( \frac{I_{\odot} \Omega_{\odot}}{p \langle \tau_{\odot} \rangle_{\text{rot}} t} \right)^{\frac{1}{p}} \quad (12)$$

where  $I_{\odot}$  is the solar moment of inertia and  $t$  is the current age of the star. From the age of a few hundred Myr to that of the Sun, it has been long known that the average spin rates of Sun-like stars decreases as approximately the inverse square root of the age (Skumanich 1972; Soderblom 1983; Barnes 2003), which implies  $p \approx 2$ .

Using solar parameters, Equation (12) predicts the present-day average torque, which is required to explain observed spin rates of Sun-like stars,

$$\langle \tau_{\odot} \rangle_{\text{rot}} = 6.2 \times 10^{30} \text{ erg} \left( \frac{I_{\odot}}{6.90 \times 10^{53} \text{ g cm}^2} \right) \times \left( \frac{\Omega_{\odot}}{2.6 \times 10^{-6} \text{ rad s}^{-1}} \right) \left( \frac{4.55 \text{ Gyr}}{t_{\odot}} \right) \left( \frac{2}{p} \right), \quad (13)$$

where we input fiducial values for the solar moment of inertia (Baraffe et al. 2015), representative rotation rate (Snodgrass & Ulrich 1990), age (Guenther 1989), and  $p$ . Appendix B discusses the validity and uncertainties associated with the prediction of Equation (13).

Using observed stellar rotation rates to probe the torque is only sensitive to torques averaged over a timescale that is much shorter than the spin-down time, but larger than magnetic cycle timescales. For ages near the Sun’s, this means that Equation (13) estimates the torque as averaged over a timescale of  $\sim 100$  Myr. Although the converging of stellar spin rates at late times suggest that the torques are “well-behaved” and predictable, the observations do not rule out that stellar wind torques could (and apparently do) vary quite substantially on short timescales.

#### 4.4. Comparison to Previous Calculations of the Solar Torque

A large number of solar wind models exist in the literature, many of which produce estimates for the solar-mass loss and angular momentum loss rates (Usmanov et al. 2000; Riley et al. 2001; Pinto et al. 2011; Alvarado-Gómez et al. 2016; Garraffo et al. 2016; Réville & Brun 2017; Pognan et al. 2018). The

**Table 1**  
Solar Angular Momentum Loss Rates from This Work and Others

$\langle \tau \rangle$ ( $\times 10^{30}$ erg)	Citation
0.35	This Work, Magnetograms/Equation (3)
2.28	This Work, Open Flux/Equation (6)
6.20	This Work, Observed Spins/Equation (13)
<hr/>	
2.51–3.77	Pizzo et al. (1983)
2.1	Li (1999)
2.18	Pinto et al. (2011)
0.9–2.3	Pantolmos & Matt (2017)
0.80	Réville & Brun (2017)

reported values have a wide range due to the large differences in input physics, such as the use of polytropic winds or the inclusion of a specific coronal heating function. As the mass loss rate is typically evolved self consistently in these models, differences in the modeled torque value is often due to discrepant mass loss rates when compared to observations (as this is a challenging problem). With the correct adjustments to recover the observed solar-mass loss rate, most models produce a comparable value to the present work. Unlike the works above, the parametrization of FM18 allows for the impact mass loss and the magnetic field to be decoupled such that we can produce a semi-analytic result which matches the observed solar values.

In this section we focus on a few theoretical models that consider the effects of magnetic variability over the solar cycle, plus data driven models of the solar wind. This includes the dynamo driven wind simulations of Pinto et al. (2011), the recent 3D wind simulations of Réville & Brun (2017), and estimates for the torque using observed values such as Pizzo et al. (1983) using the *HELIOS* spacecraft, and Li (1999) who further supported this value with data from *Ulysses*. From these authors, only Pinto et al. (2011) and Réville & Brun (2017) consider the variability of the Sun. Table 1 collects previous estimates of the solar torque and compares them to this work.

Estimates made of the solar wind torque from Pizzo et al. (1983) and Li (1999) both agree in magnitude with the open flux estimate performed in Section 4.2. Pizzo et al. (1983) made a direct measurement of the solar angular momentum flow, which should be the most accurate method, however they required very significant assumed spacecraft pointing corrections. Therefore, it is not clear how robust the measurement is. Based on our observed variability of the sunspot cycle it is expected that the estimate made for the torque using the *HELIOS* spacecraft should be higher than our current average, as the Sun was more active during cycle 21, which is calculated to be in the range of  $(2.55\text{--}3.77) \times 10^{30}$  erg by Pizzo et al. (1983) (see Figure 3). The average value of the solar wind torque during cycles 23 and 24 is  $\sim 30\%$  lower than this, which is potentially evidence for continued variability on longer timescales than those considered within this work.

Pinto et al. (2011) used a solar-like kinematic dynamo model to drive an axisymmetric MHD wind simulation. The results did not intend to model the actual Sun, but this was the first work to include the effect of magnetic variability in the calculation of the angular momentum loss rate. Results from this work agree with the average Alfvén radii predicted by Equation (3) from FM18, apart from at their minimum of activity, in which the axisymmetric dipole decreases without a

rise in the equatorial dipole component to maintain the size of the Alfvén radius. Due to this, the torque predicted is strongly anti-correlated with the solar activity cycle. This highlights the need to include the equatorial component to produce a smoothly varying torque, as seen in the open flux method. Their average torque agrees with previous works but requires a mass loss rate that is twice as large as the observed solar value.

Réville & Brun (2017) compute 13 3D MHD simulations of the solar wind, stretching between cycles 22 and 23, which we compare to our results in Figure 1 (shown in filled squares). Surface magnetic field data is gathered from the Solar Wilcox Observatory (WSO, Scherrer et al. 1977) synoptic maps (Réville 2018, private communication), which display similar trends to the MDI and HMI data used in this work, see the top three panels (gray squares). The WSO observations are known to be less sensitive and underrepresent the strength of the field when compared with MDI and HMI results (DeRosa et al. 2012; Riley et al. 2014). A multiplicative factor has been used to scale the strengths (colored squares); note that this was not done for the values used within Réville & Brun (2017), only for completeness here. The PLUTO code is used to construct 3D wind solutions for each WSO magnetogram. This produces global values for the mass loss rate and open magnetic flux (V. Réville 2018, private communication), which are used to generate a torque in the bottom panel of Figure 1. The mass loss rates match the observed average, with slight variation due to differences in the expansion of the field lines for the changing magnetic topologies (also discussed in Réville et al. 2016 and Finley & Matt 2017). However, the factor of  $\sim 2$  variation in the mass loss rate with the magnetic cycle phase is not reproduced, shown in both the observations from *ACE* and *Ulysses*. As discussed by Réville & Brun (2017), this occurs due to the lack of additional wind driving physics that should correlate with the surface magnetic field energy, such as energy deposition through Alfvén wave heating (e.g., Cranmer et al. 2007; Pinto et al. 2016).

Interestingly, these 3D simulations contain the non-axisymmetric components of the magnetic field ( $l_{\max} = 15$ ). Since the resulting torques from these simulations and our use of Equation (3) appear to agree, it strengthens our previous assumption for including the non-axisymmetric components in our calculation. The results for the Alfvén radii also show good agreement, as shown in FM18. The methods used in the MHD wind simulation of Réville & Brun (2017) are similar to that of FM18, using a polytropic wind acceleration profile. Therefore, the torque estimate is similar to the magnetogram-based calculation from Section 4.1.

## 5. Discussion

Using the torque formulations from FM18, the value of the solar wind torque is shown to be lower than the empirical estimate based on the rotation of other Sun-like stars. We also find a disagreement between the two predictions from FM18, using either the surface or open flux method for calculating the torque. Both methods show the angular momentum loss rate to be variable in time, seemingly linked with the strength of magnetic activity on the Sun. Differences in the dynamical torque estimates for the current Sun and the long-time-average value may then be due to magnetic variation on longer timescales than the 22 year magnetic cycle. Here we discuss such factors that may be responsible for the discrepancies in our predicted torques, and also the implications for using the

work of FM18 on other Sun-like stars, for which we can only obtain basic information about their surface magnetic field. Knowing that the open flux method is perhaps the most reliable, how can we reconcile our results for future use of the surface field method?

### 5.1. The Impact of Non-axisymmetric Magnetic Components

In our calculation of the solar torque, based on surface magnetogram observations, we include the strength of the non-axisymmetric components through Equation (8) that adds the components in quadrature to produce a combined strength for each mode  $l$ . This is done because the non-axisymmetric components of the field will impact the radial decay of the magnetic flux in a similar way to the axisymmetric components, which is the most significant driver of the location of the Alfvén radius (see discussion within FM18). MHD modeling by Garraffo et al. (2016) shows that the torque generated by pure non-axisymmetric geometries are comparable with their axisymmetric counterparts, which supports our assumption here. However, they do not disentangle the effect of mass loss rate and magnetic field geometry/strength on their angular momentum loss rates. It therefore remains to be shown if, or how, non-axisymmetric modes change the fit parameters  $K$  and  $m$  in Equation (3) from FM18.

The torque calculated in Section 4.1 is controlled largely by the combined dipole field strength, which appears to be out of phase with solar activity, displayed in the top left panel of Figure 1 (note the use of absolute magnitude field strengths). During each sunspot cycle, the torque is maximized at the start of the sunspot that clearly shows the largest angular momentum loss rate at the sunspot maxima, when the equatorial dipole component is strongest.

In order to assess the impact of including the non-axisymmetric components with Equation (8), we performed the torque analysis using both, only the axisymmetric components, and the combined strength approach of Equation (8). We find marginally differing results for both approaches, most notably, using only the axisymmetric component leads to a deeper minimum field strength during the dipole polarity reversal than in the combined approach and a far lower value for the torque during this time. This is the picture presented in Réville et al. (2015a). In these simulations the equatorial dipole component is ignored, however this component does not vanish at maximum and should impact the angular momentum loss rate.

It is certain that the non-axisymmetric field components will contribute to the open flux in some way, and perhaps it is their relation to the torque that will resolve the discrepancy in how the torque varies over the cycle between the surface field and open flux methods. To first order, we believe our method produces more realistic results than simply taking the axisymmetric components alone. But the impact on wind acceleration and the effectiveness of the magnetic braking from these components is not completely understood.

### 5.2. The Impact of Model Wind Parameters

The FM18 model uses a particular set of fit parameters in Equation (3) that are taken from simulations using a single polytropic wind temperature. Here we assume this to be an average of the slow and fast solar wind flows. However, work by Pantolmos & Matt (2017) indicates that this assumption



produces a form of uncertainty since we do not know the best fitting temperature for the Sun (and especially not for other stars). It is likely that the correct average polytropic wind temperature is also slightly variable during the solar cycle, with a differing ratio of fast and slow wind present. In general, variability in the wind temperature over the cycle will affect both torque formulas from FM18 and so represents an uncertainty in our results, i.e., for a fixed  $\dot{M}$ , a faster wind will open more flux with a weaker resulting torque.

Differences in the observed variability of the solar wind torque between FM18 methods, i.e., the open flux method being smoothly varying and the surface field method being heavily dependent on the input dipole field strength, may be explained by the 3D and multi-speed nature of the solar wind. Here we have assumed for the surface field method that the non-axisymmetric components will contribute to the torque though a quadrature addition of their strengths with the axisymmetric field, see Equation (8). However, their relationship may be more subtle and interconnected with the wind acceleration, in effect smoothing the variability of the torque over the cycle. Models of the solar wind which recover the bimodality of wind properties (Alvarado-Gómez et al. 2016), such as those produced for space weather prediction (e.g., Usmanov et al. 2000; Tóth et al. 2005), as of yet have not been used to formulate a useable scaling relation for how the solar wind angular momentum loss rate scales with various parameters, such as mass loss rate or magnetic field strength.

### 5.3. The Open Flux Problem

Synoptic magnetograms are produced from a wide range of observatories, both in space and on the ground, for which line of sight magnetic field measurements are processed, using different methods, into coherent pictures of the whole solar surface. These magnetic maps agree qualitatively, with the same morphology of active regions and distributed surface flux. However, they often disagree quantitatively, requiring saturation/correction factors to be brought into agreement with one another (Wang & Sheeley 1995; Liu et al. 2012; Riley et al. 2014).

Commonly Potential Field Source Surface (PFSS) models are used with these magnetogram observations as an input boundary condition, which allows for a quick and qualitative view of the coronal magnetic field. However, these PFSS models either underestimate the solar open flux with a source surface around  $2.5 R_*$ , but match the observed coronal hole morphology and area, or require much smaller source surface radii  $< 2 R_*$  to match the observed solar wind open flux at the cost of overpredicting the coronal hole area (Riley et al. 2006; Lee et al. 2011; Arden et al. 2014; Réville et al. 2015b; Linker et al. 2017; Réville & Brun 2017).

The surface flux and open flux methods from FM18 disagree in their prediction of the average torque over the last 22 years. The value derived based on the observed open flux in the solar wind is  $\sim 7$  times larger than the value produced using the magnetogram observations. The main disagreement between these two approaches centers on the amount of open flux produced from the magnetograms. Equating Equations (3) and (6), and solving for  $\phi_{\text{open}}$ , we can produce a relation for the open flux predicted by the FM18 models, given a surface field

strength,

$$\phi_{\text{open}} = \left[ \left( \frac{\langle R_A \rangle}{R_*} \Big|_{\text{Eq. 3}} \frac{1}{K_o} \right)^{1/m_o} R_*^2 \dot{M} v_{\text{esc}} \right]^{1/2} \quad (14)$$

where  $\langle R_A \rangle / R_* |_{\text{Eq. 3}}$  is our predicted Alfvén radii given by Equation (3). This corresponds to an average open flux of  $2.21 \times 10^{22}$  Mx from the magnetograms, a factor of 3.61 lower than is observed by ACE. This is shown through the full data set with a solid black line in the open flux panel of Figure 1. We also produce an estimate of the open flux using a PFSS model (Altschuler & Newkirk 1969) with a constant source surface radius of  $2.5 R_\odot$ , shown with a solid red line. The PFSS produces a similar magnitude of open flux to FM18 with some differences, both systematically underpredicting the observed open flux. Differences between these models are undoubtedly linked to the FM18 models predicting the coronal magnetic field becoming radial/open at much larger distances, than the fixed PFSS source surface of  $2.5 R_\odot$ , during that time.

The discrepancy when extrapolating the solar open flux from magnetogram observations has been a persistent issue in the solar community (Zhao & Hoeksema 1994; Wang et al. 2000; Lockwood et al. 2004; Stevens et al. 2012). For example, the Space Weather Modeling framework (Tóth et al. 2005) requires the input magnetograms to be scaled by a factor of 2–4 to improve comparison with observations (Cohen et al. 2006; Oran et al. 2013; Pognan et al. 2018). It has been suggested that the addition of shear and twisting of magnetic field lines can allow more open flux, but again this impacts the coronal hole area predicted from the models (Edwards et al. 2015). It is therefore generally accepted that magnetograms require multiplication by an uncertain factor or the inclusion of additional magnetic flux (typically CMEs or small scale surface fields) in order to bring observations in line with the extrapolated field strength at 1 au (Wang 1993; Zhao & Hoeksema 1995; Cohen et al. 2006; Riley 2007; Riley et al. 2014).

Authors such as Lowder et al. (2017) using the OMNI database, and Owens et al. (2008) using historical heliospheric spacecraft, obtain values in agreement with our ACE 27 day averages. However, another source of disagreement in the open flux may come from these observed values. Lockwood et al. (2009a) suggest that using the IMF measurements to infer the solar open flux may lead to overestimation. This is due to longitudinal structures in the solar wind where the IMF twists back on itself and therefore increases the observed flux passing over the spacecraft (Crooker et al. 2004). The actual impact of this effect and others on our measured open flux value is uncertain. In order to take advantage of the open flux torque formulation from FM18 and other previous works, accurate observations of the solar open flux are required, which will likely occur with the launch of both the Parker Probe (Fox et al. 2016) and Solar Orbiter missions (Mueller et al. 2013). Previous estimates of the solar Alfvén surface height, based on observed solar wind properties, place the minimum average Alfvén radius around 10–15  $R_*$  (Zhao & Hoeksema 2010; DeForest et al. 2014). These values appear most consistent with our calculation using the open flux, presented in Section 4.2. Because there also appears to be fewer uncertainties, we assume the open flux torque is the most reliable result, however more work is needed.

#### 5.4. Torque Variability over Magnetic Cycles

Section 4 discussed the average value of the solar torque. However, our interest in using this data set is primarily motivated by the variability of the angular momentum loss rate with solar cycle phase. Here we focus on this variation and the differences in the torque between sunspot cycles 23 and 24.

The angular momentum loss rate predicted from the magnetograms with Equations (1) and (3) is heavily dependent on the dipolar component of the global magnetic field. The same is not observed for the open flux formulation, which smoothly varies over the cycle but is in general positively correlated with the dipole component. The open flux torque becomes largest around periods of sunspot maximum, at which point the equatorial dipole field strength and open flux are known to be maximized (Wang & Sheeley 2002); this is why previously we included the non-axisymmetric components in our torque calculation. Despite our inclusion of the non-axisymmetric field strengths with Equation (8), the surface field method does not produce a smoothly varying angular momentum loss rate with the solar cycle. Further work is required to resolve this, potentially by employing better thermodynamics in the wind and a treatment for the non-axisymmetric components.

The angular momentum loss rates and average Alfvén radii determined from both methods are binned into 27 day (carrington rotation) averages, and presented in histograms in Figure 2. The discrepant average torque values are evident between the surface field and open flux methods. Further, data is colored by a sunspot cycle, as done in Figure 3, with cycles 23 and 24 in green and blue, respectively. Our data set spans the entirety of cycle 23 and the majority of cycle 24. Each cycle is observed to broadly follow a log-normal distribution. Both methods concur that cycle 24 has a lower average torque and Alfvén radius than cycle 23, (see vertical dashed lines for averages). The averages of the Alfvén radii predicted from the open flux method are nearly constant between cycles, but as cycle 24 is currently moving into a minimum the average is expected to move lower as it becomes complete. Viewing the *Ulysses* fast passes, the average Alfvén radii for the minimum of cycle 24 (3rd pass) is smaller than that of the minimum of cycle 23 (1st pass), supporting this hypothesis.

Despite the discrepancy in magnitude between both methods for determining the torque, the variation between cycles shows a similar trend. This implies that the surface flux formulation can be brought into rough agreement with the open flux technique using a multiplicative scaling factor, which has been done previously to match observed spin evolution distributions (Gallet & Bouvier 2015; Amard et al. 2016; Sadeghi Ardestani et al. 2017; See et al. 2018).

#### 5.5. Long-term Torque Variability

The torque from both the surface field and open flux methods are shown to be variable with magnetic cycle, and appear to be decreasing from cycles 23 to 24. This work investigates the angular momentum loss rate over decadal timescales, but the process of rotational evolution is known to occur over billions of years. In which case, it is hard to tell if the current solar wind torque is typical of the long-time average value.

The torque in the solar cycle here varies by a factor of 5–10, and the average is a factor of 2.7–18 below the inferred torque from Section 4.3, depending on the method used

(open-surface). Perhaps one way to reconcile them is if the solar wind torque varies with a much larger amplitude on a timescale much longer than 20 years, as probed here, but less than the timescales probed by observations of stellar spin rates of  $\sim 100$  Myr; i.e., it is possible that the solar wind torque is currently in some kind of “low state” relative to the long-time average. For example, if our present-day torque is a factor of about 4 smaller than the long-time average, to recover the average this implies that the Sun should either spend substantially longer in a slightly higher activity/torque state than the current low state, or spend an equivalent amount of time as the current low state with a torque seven times bigger than present. In this extreme case, it requires a dipole field strength about eight times bigger or mass loss rate 30 times bigger (or some combination of the two). If this is true, we should see Sun-like stars with the same rotation rate as the Sun, but with on average more magnetic activity than the Sun (the Sun should be below average for its Rossby number).

Using activity proxies, magnetic variability is recovered on timescales of centuries (Lockwood et al. 2007, 2009b). Models of the solar open flux from Vieira & Solanki (2010) show that the Sun is at a low in open flux, but the current value is not exceptional. With the open flux scaling almost linearly with the torque predicted from FM18, averaging the torque on longer  $\sim 100$  years timescales could increase the predicted value towards agreement with the inferred torque from Section 4.3.

Additionally, van Saders et al. (2016) suggests a transition around the solar age to a weakened form of magnetic braking. They suggest the braking torque becomes weak enough to be insignificant for subsequent main sequence evolution of rotation, requiring a very sharp reduction in the braking torque. The smaller value of torque found in other sections could be interpreted as agreement with the van Saders et al. (2016) hypothesis, although it seems unlikely that we live in a time immediately following such a transition. The discrepancies presented here from our predicted long-time average can seemingly be explained by many other factors, such as our chosen wind temperature or long-time variability, so this appears coincidental.

#### 5.6. Application to Other Sun-like Stars

Our position on Earth is unique for observing the solar wind. We are embedded in the expanding solar atmosphere, and as such we can access both in situ observations of the basic solar wind properties, and take advantage of remote sensing to build an accurate picture of solar magnetism using a variety of telescopes. This work utilizes this wealth of data available for our local star, which we have an almost complete coverage with a monthly cadence for 22 years.

For other stars this is not possible as the tenuous emission of their stellar winds is undetectable. In order to gain information about the mass loss rate and wind properties of these distant stars, we rely on proxies such as the strength of Ly $\alpha$  absorption at their astropauses (Wood 2004), and more recently the observed erosion of exoplanet atmospheres (Vidotto et al. 2011; Vidotto & Bourrier 2017). The magnetic field topology and strength of Sun-like stars are sampled using techniques such as Zeeman broadening and Zeeman Doppler Imaging, which at best, produce a measurement of the stellar magnetic field on yearly timescales (Morgenthaler et al. 2012; Jeffers et al. 2014; Saikia et al. 2016). This leads to the question, how

does our ability to measure the mass loss rate and magnetic field impact the predictions of their stellar wind torques?

While performing this analysis on the Sun, we have gained some insight into these effects:

1. Torques derived using stellar magnetic field observations and Equation (3) may be lower than in actuality, due to the FM18 model producing a smaller value of unsigned open flux than measured in the solar wind. It remains to be shown if this can be corrected for by the application of a common scaling factor (this work indicates  $\sim 15$ ).
2. Magnetic variability can lead to estimates of the angular momentum loss which are, in the solar case, up to a factor of  $\sim 10$  different from one observation to another. Observations of other Sun-like stars will therefore suffer from considerable uncertainty in their derived angular momentum loss rates based on a single or small number of observations.
3. Long-time variability may also play a role, and with the difficulty of ascertaining the true magnetic behavior of other Sun-stars, i.e., if they are cyclic or stochastic, the corresponding estimate of their angular momentum loss rate may be discrepant from rotation evolution model predictions.

Paper II, and also V. See et al. (2018, in preparation), focus on applying the formulations of FM18 onto Sun-like stars for which we have information on their magnetic topology and variability. Again, these results are compared to predictions from spin evolution modeling (Matt et al. 2015) using the information gained here from the Sun to interpret the results.

## 6. Conclusion

In this work we have utilized the wealth of current solar observations and the semi-analytic results from FM18 to produce an estimate of the current solar wind torque. This is compared with spin evolution calculations and shown to be a factor of 2–3 smaller than expected.

Two angular momentum loss prescriptions from FM18 are implemented using observed surface field strengths from the *SOHO* and *SDO* spacecraft, along with mass loss rates and open flux measurements from the *Ulysses* and *ACE* spacecraft. The methods are found to produce average torques that either differ due to the amount of unsigned open flux the FM18 model produces from a given surface field observation, or the potential overprediction of the open flux from spacecraft measurements. Assuming that the open flux measurements from the in situ spacecraft are valid, we predict that the solar wind torque has a present-day value of  $2.3 \times 10^{30}$  erg, averaged over the last 22 years.

The observation that the spin rates of Sun-like stars converge toward a single track that depends on age also allows us to derive Equation (12), describing how this spin-down depends on the torque and stellar properties. Then, using the solar parameters in Equation (13), we predict that the long-time averaged torque should be  $6.2 \times 10^{30}$  erg. Comparing this estimate of the torque from the observed spin evolution to the present-day torques predicted by the dynamical models gives additional insights. Differences in the average present-day torques to the spin evolution torques could be due to, (a) variability on a longer timescale than that probed by the present-day variability presented here (but less than spin-down time), (b) errors in using the dynamical models inferring

present-day torque, or (c) that stars spin down significantly different to Skumanich at ages of a few to several Gyr. We need additional information to discriminate between these possibilities. The required variability of (a) suggests that we should observe stars like the Sun that are on average significantly more active (i.e., they have larger torques) such that the average is correct. From the dynamical models, (b), uncertainties remain in the wind acceleration and effects of non-axisymmetric field components that both require further study to disentangle. Observationally, (c) requires more period-mass-ages for old stars to confirm or refute the van Saders et al. (2016) hypothesis.

For other Sun-like stars, measurements of their unsigned open flux and mass loss rates are not readily available. Instead we rely on surface magnetic field measurements that are gained through Zeeman Doppler Imaging and Doppler Broadening techniques. Using the FM18 formula, predictions of the angular momentum loss rates for these stars based on their surface measurements may be smaller than in reality. Future models should be refined to better match the wealth of solar data available, such models should be able to open the correct amount of flux from a given surface magnetic field observation and continue to remain general for application to other Sun-like and low-mass stars.

We would like to thank Mark DeRosa, Todd Hoeksema, and Aline Vidotto for helpful discussions and technical advice. We thank Victor Réville for supplying the addition data from his MHD simulations. This project has received funding from the European Research Council (ERC) under the European Unions Horizon 2020 research and innovation programme (grant agreement No. 682393 AWESoMeStars). The sunspot numbers used in this work are from WDC-SILSO, Royal Observatory of Belgium, Brussels. Data supplied courtesy of the *SDO*/HMI and *SDO*/AIA consortia. *SDO* is the first mission to be launched for NASA's Living With a Star (LWS) Program. Data provided by the *SOHO*/MDI consortium. *SOHO* is a project of international cooperation between ESA and NASA. We thank the *ACE* MAG and SWEPAM instrument teams and the *ACE* Science Center for providing the *ACE* data. We thank the *Ulysses* FGM/VHM and SWOOPS instrument teams and the ESAC Science Data Center for providing the *Ulysses* data. We thank the developers of SHTOOLS, M. A. Wicczorek, M. Meschede, I. Oshchepkov, E. Sales de Andrade, and heroxbd (2016). SHTOOLS: Version 4.0. figures within this work are produced using the python package matplotlib (Hunter 2007).

*Software:* matplotlib (Hunter 2007), SHTOOLS (Wicczorek 2011).

## Appendix A Spherical Harmonic Decomposition

For the synoptic magnetograms used in this work, we used the pySHTOOLS code (Wicczorek 2011) to deconstruct the observed surface magnetic field into its constituent spherical harmonic components, described by Equation (7). This produces coefficients  $B_m^l$  that weight each spherical harmonic mode  $Y_m^l$  given a magnetic order,  $l > 0$ , and degree,  $-l \leq m \leq l$ . Figure 4 displays the full spherical harmonic decomposition of both *SOHO*/MDI (1996–2010) and *SDO*/HMI (2010–2018) synoptic magnetograms. The strength of the axisymmetric dipole, quadrupole, and octupole are given by  $B_0^1$ ,  $B_0^2$ , and  $B_0^3$ , respectively. The absolute magnitude of the non-axisymmetric

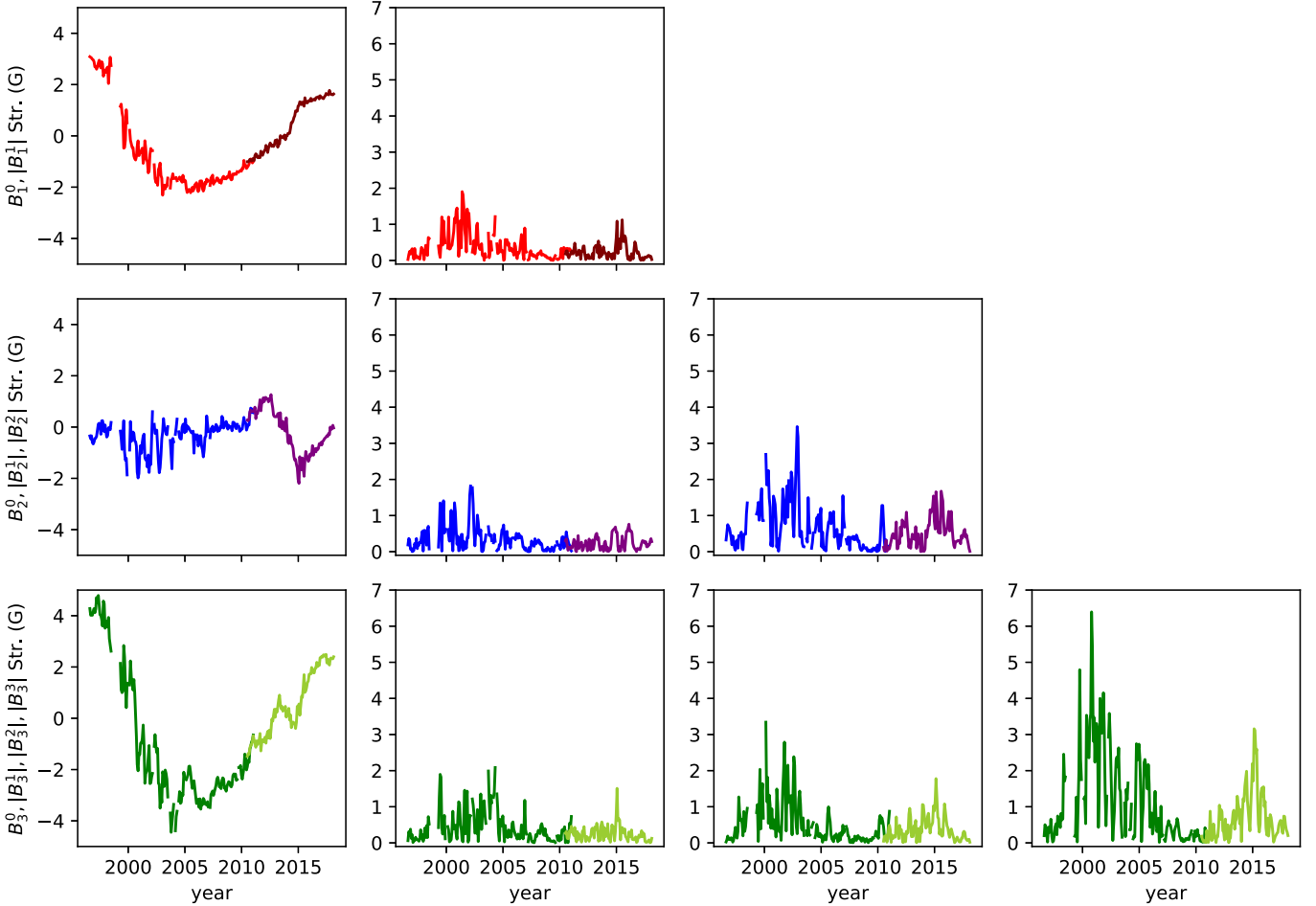


**Figure 4.** Evolution of the lowest order ( $l \leq 3$ ) spherical harmonic coefficients from *SOHO*/MDI and *SDO*/HMI. The rows display different spherical harmonic order  $l$ , increasing towards the bottom, and the columns show increasing spherical harmonic degree  $m$ , increasing from left to right. The components for each  $l$  are combined in quadrature to produce a single value for each spherical harmonic, dipole, quadrupole, and octupole, shown in the top left panels of Figure 1. If only the axisymmetric components are used in our torque calculation, the predicted torque from Equation (1) will have artificially small minima during polarity reversals.

components are given, e.g.,  $|B_1^1|$ , which incorporates both  $m = 1$  and  $m = -1$  harmonic degrees. A deeper analysis of the variation in spherical harmonic components with time is available in DeRosa et al. (2012).

### Appendix B Validity of the Torque Predicted from Observed Stellar Rotation Rates

The prediction of Equation (13) is completely independent of any knowledge of solar magnetism or wind properties, or indeed even of the angular momentum loss mechanism itself, beyond the assumption of Equation (11). Because this is a robust and independent estimate of the solar torque, it is worth discussing the uncertainties that are inherent in this calculation.

First, the functional form of Equation (11) should be taken as approximate. However, it is predicted by the stellar wind torque Equations (1)–(3), if the stellar field strengths and mass loss rates depend on rotation rate as a power law. This form is the usual assumption made in spin evolution models (e.g., Kawaler 1988; Gallet & Bouvier 2013; Matt et al. 2015; Amard et al. 2016).

Second, Equation (12) is an asymptotic solution for the converged spin rates. A more precise calculation depends on the initial spin rate (which is unknown for the Sun), but the

calculation can still be done by using the observed range of spin rates of young clusters. For example, Gallet & Bouvier (2015) showed (using observations of Agüeros et al. 2011 and Delorme et al. 2011) that, in the nearly 600 Myr old clusters Praesepe and Hyades, 25% of solar-mass stars rotate faster than  $2.4\Omega_{\odot}$  and 90% rotate slower than  $2.9\Omega_{\odot}$ . This range of rotation rates at that age predicts a present-day solar torque in the range  $(5.9\text{--}6.3) \times 10^{30}$  erg. Even extending further into the tails of the distributions of spin rates in those clusters implies a possible spin rate from 2 to 10 times  $\Omega_{\odot}$ , which gives a range of the present-day torque of  $(5.3\text{--}7.0) \times 10^{30}$  erg.

Third, the analysis assumes a constant moment of inertia and solid-body rotation. The assumption of constant moment of inertia is correct to better than 2% for solar-mass stars in the age range from 600 Myr to that of the Sun (Baraffe et al. 2015). The Sun and Sun-like stars are known to possess surface latitudinal differential rotation with an amplitude of approximately 20% (Messina & Guinan 2003; Barnes et al. 2005; Croll et al. 2006; Matt et al. 2011). The effects of latitudinal differential rotation should thus have a comparably small effect on the observed (single-value) surface rotation rates as being representative of the whole surface of the stars. Helioseismic observations constrain the internal differential rotation profile also to an amplitude of approximately 20% (Schou et al. 1998;

Charbonneau et al. 1999). There is some evidence that the inner-most regions (10% of the radius) of the Sun may rotate substantially faster than the surface (García et al. 2007; Fossat et al. 2017), but this would only affect the total angular momentum by a small amount, compared to that inferred by assuming a solid-body rotation at the surface rate. We have much less information about the internal rotation profile of Sun-like and younger stars. It is possible that young stars' inner radiative zones rotate much more rapidly than the surfaces. Rotational evolution models of Gallet & Bouvier (2015) predict that this differential rotation can be substantial at ages of  $\sim 100$  Myr but decrease rapidly with time and has an amplitude of approximately 20% by an age of 1 Gyr. Thus, it seems unlikely that differential rotation would affect the torque prediction by more than a few percent. However, given the uncertainty in internal rotation and angular momentum transport, it is worth noting that even in the most extreme case where the convective envelope is completely decoupled from the radiation zone a lower limit of  $7.0 \times 10^{29}$  erg is implied (calculated by putting the moment of inertia of the convective zone from Baraffe et al. 2015 into Equation (13)).

Fourth, the average value of  $p$  is fairly tightly constrained by the behavior of the observed spin rates over long timescales (Skumanich 1972; Karoff et al. 2013; Barnes et al. 2016a; Metcalfe et al. 2016). However, it is possible that the spin-down in time does not follow a single power law at all times (e.g., Lanzafame & Spada 2015), and there are relatively few observational constraints for stars with known ages between about a Gyr and solar age (Meibom et al. 2011, 2015; Barnes et al. 2016a, 2016b). For example, the stellar wind torque model of Gallet & Bouvier (2013, 2015) had an asymptotic (i.e., late-time) value of  $p \approx 3.2$ , and they were able to fit the available data. van Saders et al. (2016) suggested that stars become abruptly less efficient at spinning down at around the solar age, which within the present formalism could imply larger values of  $p$  (or generally speaking that the current torque could be significantly lower than predicted by Equation (13)). It is not possible with the present analysis to rule out that the solar torque has undergone a recent transition, which would invalidate this calculation of the torque based on observed rotation rates of younger stars.

Despite the caveats listed above, Equation (13) remains a robust estimate of the solar angular momentum loss rate, derived empirically from the observed rotation rates of other Sun-like stars.

### ORCID iDs

Adam J. Finley  <https://orcid.org/0000-0002-3020-9409>

Sean P. Matt  <https://orcid.org/0000-0001-9590-2274>

### References

Aarmio, A. N., Matt, S. P., & Stassun, K. G. 2012, *ApJ*, 760, 9  
 Agüeros, M. A. 2017, *RMxAC*, 49, 80  
 Agüeros, M. A., Covey, K. R., Lemonias, J. J., et al. 2011, *ApJ*, 740, 110  
 Altschuler, M. D., & Newkirk, G. 1969, *SoPh*, 9, 131  
 Alvarado-Gómez, J., Hussain, G., Cohen, O., et al. 2016, *A&A*, 594, A95  
 Amard, L., Palacios, A., Charbonnel, C., Gallet, F., & Bouvier, J. 2016, *A&A*, 587, A105  
 Arden, W., Norton, A., & Sun, X. 2014, *JGRA*, 119, 1476  
 Azizi, F., & Mirtorabi, M. T. 2018, *MNRAS*, 475, 2253  
 Babcock, H. 1961, *ApJ*, 133, 572  
 Baliunas, S., Donahue, R., Soon, W., et al. 1995, *ApJ*, 438, 269  
 Baraffe, I., Homeier, D., Allard, F., & Chabrier, G. 2015, *A&A*, 577, A42

Barnes, J. R., Cameron, A. C., Donati, J.-F., et al. 2005, *MNRAS*, 357, L1  
 Barnes, S., Spada, F., & Weingrill, J. 2016a, *AN*, 337, 810  
 Barnes, S. A. 2003, *ApJ*, 586, 464  
 Barnes, S. A. 2010, *ApJ*, 722, 222  
 Barnes, S. A., Weingrill, J., Fritzewski, D., Strassmeier, K. G., & Platais, I. 2016b, *ApJ*, 823, 16  
 Bouvier, J., Matt, S. P., Mohanty, S., et al. 2014, in *Protostars and Planets VI*, ed. H. Beuther et al. (Tucson, AZ: Univ. Arizona Press), 433  
 Brown, S., Donati, J.-F., Rees, D., & Semel, M. 1991, *A&A*, 250, 463  
 Browning, M. K. 2008, *ApJ*, 676, 1262  
 Brun, A. S., & Browning, M. K. 2017, *LRSP*, 14, 4  
 Cane, H., & Richardson, I. 2003, *JGRA*, 108, 1156  
 Charbonneau, P., Dikpati, M., & Gilman, P. A. 1999, *ApJ*, 526, 523  
 Cohen, O. 2011, *MNRAS*, 417, 2592  
 Cohen, O., Sokolov, I., Roussev, I., et al. 2006, *ApJL*, 654, L163  
 Covey, K. R., Agüeros, M. A., Law, N. M., et al. 2016, *ApJ*, 822, 81  
 Cranmer, S. 2008, in *ASP Conf. Ser.* 384, 14th Cambridge Workshop on Cool Stars, Stellar Systems, and the Sun, ed. G. van Belle (San Francisco, CA: ASP), 317  
 Cranmer, S. R., Gibson, S. E., & Riley, P. 2017, *SSRv*, 212, 1345  
 Cranmer, S. R., Van Ballegoijen, A. A., & Edgar, R. J. 2007, *ApJS*, 171, 520  
 Croll, B., Walker, G. A., Kuschnig, R., et al. 2006, *ApJ*, 648, 607  
 Crooker, N., Kahler, S., Larson, D., & Lin, R. 2004, *JGRA*, 109, A03108  
 DeForest, C., Howard, T., & McComas, D. 2014, *ApJ*, 787, 124  
 Delorme, P., Cameron, A. C., Hebb, L., et al. 2011, *MNRAS*, 413, 2218  
 DeRosa, M., Brun, A., & Hoeksema, J. 2012, *ApJ*, 757, 96  
 Donati, J.-F., & Brown, S. 1997, *A&A*, 326, 1135  
 Donati, J.-F., Forveille, T., Cameron, A. C., et al. 2006, *Sci*, 311, 633  
 Donati, J.-F., Moutou, C., Fares, R., et al. 2008, *MNRAS*, 385, 1179  
 Donati, J.-F., Semel, M., & Praderie, F. 1989, *A&A*, 225, 467  
 Douglas, S. T., Agüeros, M. A., Covey, K. R., & Kraus, A. 2017, *ApJ*, 842, 83  
 Durney, B. 1985, *ApJ*, 297, 787  
 Ebert, R., McComas, D., Elliott, H., Forsyth, R., & Gosling, J. 2009, *JGRA*, 114, A01109  
 Edwards, S. J., Yeates, A. R., Bocquet, F.-X., & Mackay, D. H. 2015, *SoPh*, 290, 2791  
 Egeland, R., Soon, W., Baliunas, S., et al. 2017, *ApJ*, 835, 25  
 Finley, A. J., & Matt, S. P. 2017, *ApJ*, 845, 46  
 Finley, A. J., & Matt, S. P. 2018, *ApJ*, 854, 78  
 Folsom, C., Bouvier, J., Petit, P., et al. 2017, *MNRAS*, 474, 4956  
 Folsom, C. P., Petit, P., Bouvier, J., et al. 2016, *MNRAS*, 457, 580  
 Fossat, E., Boumier, P., Corbard, T., et al. 2017, *A&A*, 604, A40  
 Fox, N., Velli, M., Bale, S., et al. 2016, *SSRv*, 204, 7  
 Gallet, F., & Bouvier, J. 2013, *A&A*, 556, A36  
 Gallet, F., & Bouvier, J. 2015, *A&A*, 577, A98  
 García, R. A., Turck-Chièze, S., Jiménez-Reyes, S. J., et al. 2007, *Sci*, 316, 1591  
 Garraffo, C., Drake, J. J., & Cohen, O. 2015, *ApJ*, 813, 40  
 Garraffo, C., Drake, J. J., & Cohen, O. 2016, *A&A*, 595, A110  
 Gregory, S., Donati, J.-F., Morin, J., et al. 2012, *ApJ*, 755, 97  
 Güdel, M. 2007, *LRSP*, 4, 3  
 Guedel, M., Guinan, E. F., & Skinner, S. L. 1997, *ApJ*, 483, 947  
 Guenther, D. 1989, *ApJ*, 339, 1156  
 Hempelmann, A., Schmitt, J., & Stepien, K. 1996, *A&A*, 305, 284  
 Hunter, J. D. 2007, *CSE*, 9, 90  
 Irwin, J., & Bouvier, J. 2009, in *IAU Symp.* 258, *The Ages of Stars* (Cambridge: Cambridge Univ. Press), 363  
 Jeffers, S., Petit, P., Marsden, S., et al. 2014, *A&A*, 569, A79  
 Johnstone, C., Güdel, M., Lüftinger, T., Toth, G., & Brott, I. 2015, *A&A*, 577, A27  
 Karoff, C., Metcalfe, T. S., Chaplin, W., et al. 2013, *MNRAS*, 433, 3227  
 Kawaler, S. D. 1988, *ApJ*, 333, 236  
 Keppens, R., & Goedbloed, J. 2000, *ApJ*, 530, 1036  
 Lanzafame, A. C., & Spada, F. 2015, *A&A*, 584, A30  
 Lee, C., Luhmann, J., Hoeksema, J., et al. 2011, *SoPh*, 269, 367  
 Li, J. 1999, *MNRAS*, 302, 203  
 Linker, J., Caplan, R., Downs, C., et al. 2017, *ApJ*, 848, 70  
 Liu, Y., Hoeksema, J., Scherrer, P., et al. 2012, *SoPh*, 279, 295  
 Lockwood, G., Skiff, B., Henry, G. W., et al. 2007, *ApJS*, 171, 260  
 Lockwood, M., Forsyth, R., Balogh, A., & McComas, D. 2004, *AnGeo*, 22, 1395  
 Lockwood, M., Owens, M., & Rouillard, A. 2009a, *JGRA*, 114, A11104  
 Lockwood, M., Rouillard, A., & Finch, I. 2009b, *ApJ*, 700, 937  
 Lower, C., Qiu, J., & Leamon, R. 2017, *SoPh*, 292, 18  
 Marcy, G. 1984, *ApJ*, 276, 286

- Matt, S. P., Brun, A. S., Baraffe, I., Bouvier, J., & Chabrier, G. 2015, *ApJL*, 799, L23
- Matt, S. P., Do Cao, O., Brown, B. P., & Brun, A. S. 2011, *AN*, 332, 897
- Matt, S. P., MacGregor, K. B., Pinsonneault, M. H., & Greene, T. P. 2012, *ApJL*, 754, L26
- McComas, D., Angold, N., Elliott, H., et al. 2013, *ApJ*, 779, 2
- McComas, D., Barraclough, B., Funsten, H., et al. 2000, *JGRA*, 105, 10419
- McQuillan, A., Aigrain, S., & Mazeh, T. 2013, *MNRAS*, 432, 1203
- Meibom, S., Barnes, S. A., Latham, D. W., et al. 2011, *ApJL*, 733, L9
- Meibom, S., Barnes, S. A., Platais, I., et al. 2015, *Natur*, 517, 589
- Messina, S., & Guinan, E. 2003, *A&A*, 409, 1017
- Mestel, L. 1968, *MNRAS*, 138, 359
- Metcalf, T. S., Egeland, R., & van Saders, J. 2016, *ApJL*, 826, L2
- Mignone, A. 2009, *MSAIS*, 13, 67
- Mignone, A., Bodo, G., Massaglia, S., et al. 2007, *ApJS*, 170, 228
- Morgenthaler, A., Petit, P., Morin, J., et al. 2011, *AN*, 332, 866
- Morgenthaler, A., Petit, P., Saar, S., et al. 2012, *A&A*, 540, A138
- Morin, J., Donati, J.-F., Forveille, T., et al. 2008, *MNRAS*, 384, 77
- Mueller, D., Marsden, R. G., Cyr, O. S., Gilbert, H. R., et al. 2013, *SoPh*, 285, 25
- Núñez, A., Agüeros, M. A., Covey, K. R., et al. 2015, *ApJ*, 809, 161
- Oran, R., van der Holst, B., Landi, E., et al. 2013, *ApJ*, 778, 176
- Owens, M., Lockwood, M., Riley, P., & Linker, J. 2017, *JGRA*, 122, 10980
- Owens, M. J., Arge, C., Crooker, N., Schwadron, N., & Horbury, T. 2008, *JGRA*, 113, A12103
- Owens, M. J., Crooker, N., & Lockwood, M. 2011, *JGRA*, 116, A04111
- Pantolmos, G., & Matt, S. P. 2017, *ApJ*, 849, 83
- Petit, P., Dintrans, B., Solanki, S., et al. 2008, *MNRAS*, 388, 80
- Pinto, R., Brun, A., & Rouillard, A. 2016, *A&A*, 592, A65
- Pinto, R. F., Brun, A. S., Jouve, L., & Grappin, R. 2011, *ApJ*, 737, 72
- Pinto, R. F., & Rouillard, A. P. 2017, *ApJ*, 838, 89
- Pizzo, V., Schwenn, R., Marsch, E., et al. 1983, *ApJ*, 271, 335
- Pognan, Q., Garraffo, C., Cohen, O., & Drake, J. J. 2018, *ApJ*, 856, 53
- Rebull, L., Stauffer, J., Bouvier, J., et al. 2016, *AJ*, 152, 113
- Reiners, A. 2012, *LRSP*, 9, 1
- Reiners, A., & Basri, G. 2010, *ApJ*, 710, 924
- Reiners, A., Basri, G., & Browning, M. 2009, *ApJ*, 692, 538
- Réville, V., & Brun, A. S. 2017, *ApJ*, 850, 45
- Réville, V., Brun, A. S., Matt, S. P., Strugarek, A., & Pinto, R. F. 2015a, *ApJ*, 798, 116
- Réville, V., Brun, A. S., Strugarek, A., et al. 2015b, *ApJ*, 814, 99
- Réville, V., Folsom, C. P., Strugarek, A., & Brun, A. S. 2016, *ApJ*, 832, 145
- Riley, P. 2007, *ApJL*, 667, L97
- Riley, P., Ben-Nun, M., Linker, J., et al. 2014, *SoPh*, 289, 769
- Riley, P., Linker, J., & Mikić, Z. 2001, *JGRA*, 106, 15889
- Riley, P., Linker, J., Mikić, Z., et al. 2006, *ApJ*, 653, 1510
- Sadeghi Ardestani, L., Guillot, T., & Morel, P. 2017, *MNRAS*, 472, 2590
- Saikia, S. B., Jeffers, S., Morin, J., et al. 2016, *A&A*, 594, A29
- Schatzman, E. 1962, *AnAp*, 25, 18
- Scherrer, P. H., Wilcox, J. M., Svalgaard, L., et al. 1977, *SoPh*, 54, 353
- Schou, J., Antia, H., Basu, S., et al. 1998, *ApJ*, 505, 390
- Schrijver, C. J., & Liu, Y. 2008, *SoPh*, 252, 19
- See, V., Jardine, M., Vidotto, A., et al. 2015, *MNRAS*, 453, 4301
- See, V., Jardine, M., Vidotto, A., et al. 2018, *MNRAS*, 474, 536
- Semel, M. 1989, *A&A*, 225, 456
- Shulyak, D., Reiners, A., Engeln, A., et al. 2017, *NatAs*, 1, 0184
- Skumanich, A. 1972, *ApJ*, 171, 565
- Smith, E. J., & Balogh, A. 1995, *GeoRL*, 22, 3317
- Snodgrass, H. B., & Ulrich, R. K. 1990, *ApJ*, 351, 309
- Soderblom, D. 1983, *ApJS*, 53, 1
- Stevens, M. L., Linker, J. A., Riley, P., & Hughes, W. J. 2012, *JASTP*, 83, 22
- Sun, X. 2018, arXiv:1801.04265
- Sun, X., Liu, Y., Hoeksema, J., Hayashi, K., & Zhao, X. 2011, *SoPh*, 270, 9
- Tokumaru, M., Kojima, M., & Fujiki, K. 2010, *JGRA*, 115, A04102
- Tóth, G., Sokolov, I. V., Gombosi, T. I., et al. 2005, *JGRA*, 110, A12226
- Usmanov, A. V., Goldstein, M. L., Besser, B. P., & Fritzer, J. M. 2000, *JGRA*, 105, 12675
- van Saders, J. L., Ceillier, T., Metcalfe, T. S., et al. 2016, *Natur*, 529, 181
- Van Saders, J. L., & Pinsonneault, M. H. 2013, *ApJ*, 776, 67
- Vidotto, A., & Bourrier, V. 2017, *MNRAS*, 470, 4026
- Vidotto, A., Gregory, S., Jardine, M., et al. 2014, *MNRAS*, 441, 2361
- Vidotto, A., Jardine, M., & Helling, C. 2011, *MNRAS*, 411, L46
- Vieira, L. E. A., & Solanki, S. K. 2010, *A&A*, 509, A100
- Wang, Y.-M. 1993, *JGRA*, 98, 3529
- Wang, Y.-M. 1998, in ASP Conf. Ser. 154, Cool Stars, Stellar Systems, and the Sun, ed. R. A. Donahue & J. A. Bookbinder (San Francisco, CA: ASP), 131
- Wang, Y.-M., Lean, J., & Sheeley, N. 2000, *GeoRL*, 27, 505
- Wang, Y.-M., & Sheeley, N. 2002, *JGRA*, 107, 1302
- Wang, Y.-M., & Sheeley, N., Jr 1995, *ApJL*, 447, L143
- Webb, D., Howard, R., Cyr, O. S., & Vourlidas, A. 2017, *ApJ*, 851, 142
- Weber, E. J., & Davis, L. 1967, *ApJ*, 148, 217
- Wieczorek, M. 2011, SHTOOLS: Tools for Working with Spherical Harmonics, Astrophysics Source Code Library, ascl:1110.004
- Wilcox, J. M., & Scherrer, P. H. 1972, *JGR*, 77, 5385
- Willson, R. C., & Hudson, H. S. 1991, *Natur*, 351, 42
- Wood, B. E. 2004, *LRSP*, 1, 1
- Zhao, X., & Hoeksema, J. 2010, *SoPh*, 266, 379
- Zhao, X., & Hoeksema, J. T. 1994, *SoPh*, 151, 91
- Zhao, X., & Hoeksema, J. T. 1995, *JGRA*, 100, 19

## 4.4 Observations of Stellar Magnetism and Winds

### 4.4.1 The Zeeman-Doppler Imaging Technique

The magnetic fields of other stars can be probed in a few ways, many of which rely on the Zeeman effect. One example is Zeeman Broadening (ZB), where the splitting of energy levels due to the presence of a magnetic field causes observed Zeeman sensitive lines to broaden (e.g. Johns-Krull and Valenti 1996; Reiners and Basri 2007). As the measured signal is a disk-averaged quantity, a broadening is measured rather than a splitting. This is because the stellar surface magnetic field is not homogenous in field strength, therefore the measured signal is a combination of many different field strengths. This technique uses unpolarised light and provides a value for the average surface magnetic field (generally expressed as a photospheric field strength and a surface filling factor). On the other hand, observations using circularly-polarised light can be used to reconstruct the large-scale magnetic field of a star through the Zeeman-Doppler imaging (ZDI) technique (see review by Donati and Landstreet 2009). Stars which we have both ZB and ZDI measurements are compared in See et al. (2019b), where it is shown that ZDI recovers around 10 – 20% of the magnetic field strength from ZB (see also Reiners and Basri 2009; Morin et al. 2010).

ZDI is a tomographic technique which requires a time-series of high resolution circularly-polarised stellar spectra (containing Zeeman sensitive lines), that span at least one stellar rotation (Semel 1989; Brown et al. 1991; Donati and Brown 1997; Donati et al. 2006). As the magnetic features responsible for the circularly-polarised light move across the visible portion of the stellar surface, the integrated flux/signal varies. The Doppler shift of the polarised light is crucial for spatially separating different magnetic features. Different polarity regions produce opposite polarisations, and so ZDI suffers from flux cancellation when features (with opposite polarities) cannot be resolved by the Doppler shift. Therefore, stars with high  $v_{eq} \sin i$  are favoured, i.e. high equatorial rotation speeds  $v_{eq}$ , and a rotation axis inclined to the line of sight (note that at the largest inclinations i.e.  $i = 90^\circ$ , the ZDI technique is unable to distinguish if features are in the northern or southern hemisphere). The magnetic fields of rapidly rotating stars are subsequently better recovered. The modulation of the circularly-polarised flux as a function of rota-

tional phase is then used to reconstruct the surface magnetic field configuration (typically in terms of spherical harmonics). Note, this process is highly degenerate, and so choices must be made to constrain the solution (e.g. the minimisation of energy).

The reconstructed magnetic fields, or magnetic “maps”, contain information about the large-scale radial ( $r$ ), azimuthal ( $\phi$ ) and meridional ( $\theta$ ) magnetic field components. In terms of spherical harmonics, these are given in the form of the  $\alpha_{lm}$ ,  $\beta_{lm}$ , and  $\gamma_{lm}$  coefficients (see Appendix A). The poloidal magnetic field is given by the  $\alpha_{lm}$  and  $\beta_{lm}$  coefficients, whereas the toroidal magnetic field is given by the  $\gamma_{lm}$  coefficients. The poloidal component describes field lines which wrap around the surface of a torus (doughnut) structure. The toroidal component represents magnetic field lines which point in a ring around the torus, i.e. around the star. Note the poloidal component can point in all three directions ( $r, \theta, \phi$ ), whereas the toroidal component is limited to the  $\theta$  and  $\phi$  directions. Recently, vector solar magnetograms have been compared to pseudo ZDI reconstructions (see Vidotto 2016; Vidotto et al. 2018), by restricting the spherical harmonic order of the solar magnetograms to  $l_{max} = 5$  (or similar). In this context, the Sun’s magnetic field appears poloidal dominated throughout the solar activity cycle, with the fraction of non-axisymmetric magnetic field increasing during solar maximum (compared with the relatively axisymmetric solar minima configuration).

Over the last two decades, the ZDI technique has been applied to over 100 stars, some of which have had their magnetic fields mapped multiple times (Petit et al. 2009; Morgenthaler et al. 2012; Jeffers et al. 2014; Saikia et al. 2016; Jeffers et al. 2017, 2018; Saikia et al. 2018a). These observations are often discussed in terms of their field strength, poloidal/toroidal fraction and degree of axisymmetry (see Figure 4.5). When the magnetic properties of these stars are plotted with stellar mass versus rotation rate, some interesting trends appear. Most obvious is the effect of stellar mass, which fundamentally controls its internal structure on the main sequence (e.g. Baraffe et al. 2015), and governs the size of a star’s convective envelope. Given that low-mass stars generate magnetic field through the interplay of rotation and convection (dynamo action), it can be seen in Figure 4.5 that stars with larger convective envelopes (and faster rotation rates) have stronger magnetic fields (this is also observed in x-rays, see Wright et al. 2011). As stars age on the main sequence,



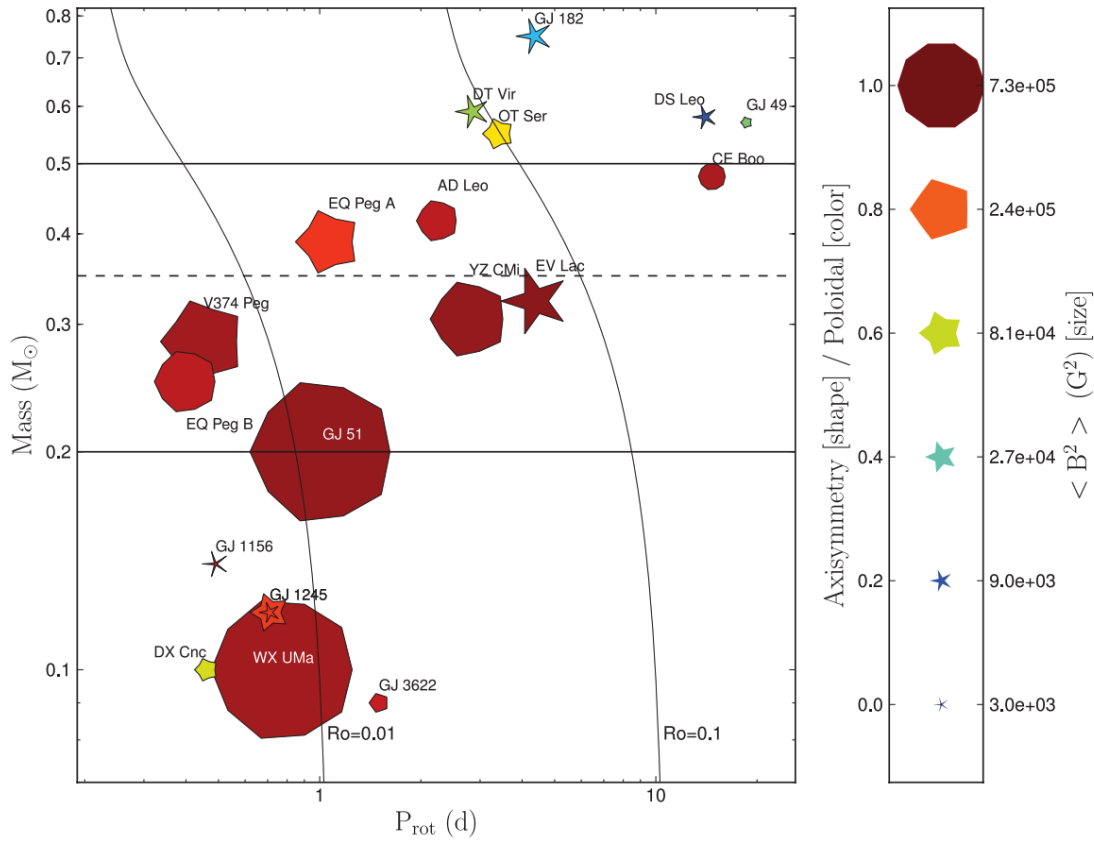


**Figure 4.5:** Magnetic topologies from Zeeman-Doppler imaging observations plotted in the stellar mass versus rotation period plane. Symbols follow the colloquially known “Confusogram” system: symbol size corresponds to magnetic field strength, symbol colour is poloidal fraction (dark blue is purely toroidal field), symbol shape is the level of axisymmetry (note this is not the same as complexity!). Solid lines represent constant Rossby number. The horizontal dashed line indicates the fully convective limit ( $M_* \approx 0.35M_\odot$ ). Taken from Morin et al. (2010).

stellar winds remove angular momentum slowing their rotation rates and weakening the magnetic dynamo (Skumanich 1972), which is shown by the decreased symbol size for slower rotators (the large-scale magnetic field also becomes less axisymmetric). However, there are some exceptions to this referred to as the “bistable” M-dwarfs (Morin et al. 2010). In Figure 4.5, these stars can be seen at low-masses and high rotation rates with bimodal properties. The mechanism responsible for this is unknown, though some dynamo models point towards a Rossby number regime change in fully-convective stars (Gastine et al. 2013).

A few stars have had multiple ZDI maps produced during the last decade, which has allowed for the magnetic variability of stars other than our Sun to be assessed. These stars are the focus of the following published paper. One very clear example is the K dwarf star 61 Cyg A (Saikia et al. 2016, 2018a), for which its magnetic field from ZDI is shown in

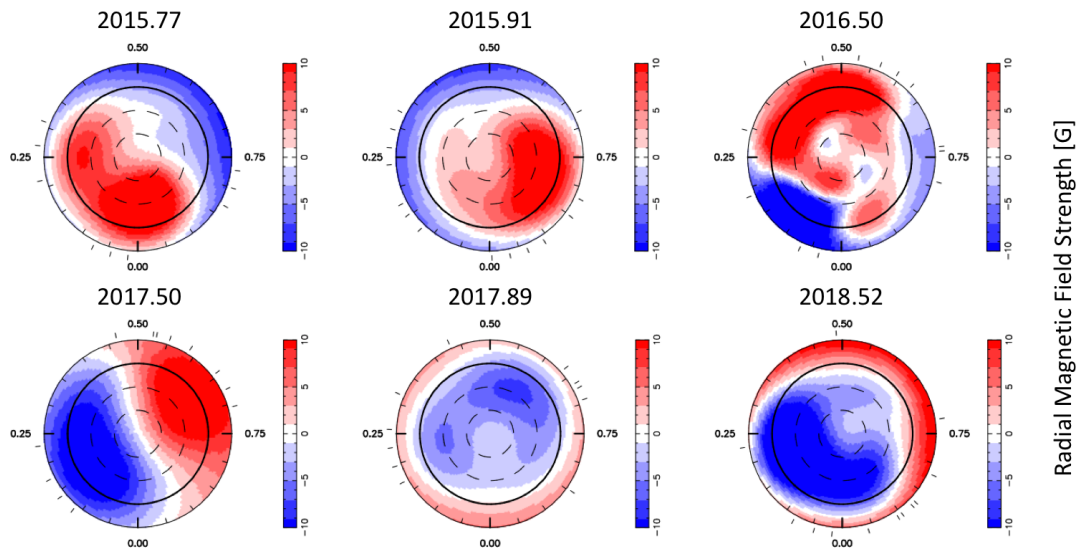


**Figure 4.6:** Reconstructions of the radial magnetic field strength for 61 Cyg A. For the maps in this representation, the north pole is in the centre of each circle, the south pole surrounds the outer edge. The polarity of the large-scale magnetic field is shown to reverse, as is observed during the solar cycle. Taken from Saikia et al. (2018a).

Figure 4.6 (as shown in Saikia et al. 2018a). 61 Cyg A is estimated to have a mass of  $0.66M_{\odot}$ , and its magnetic field undergoes polarity reversals following its activity cycle period of around 7 years. Out of all the stars currently imaged with ZDI, 61 Cyg A has magnetic variability which is the most similar to the Sun’s i.e., clear polarity reversals which are in phase with its chromospheric activity. The magnetic variability of other stars imaged with ZDI is not generally as clear as this, often displaying more stochastic behaviours which are unlike what is observed for the Sun (Petit et al. 2009; Morgenthaler et al. 2012).

#### 4.4.2 Mass-loss Rates from Astrospheric Lym- $\alpha$ Absorption

In order to apply the braking law from Chapter 3, along with the large-scale magnetic field geometry retrieved with ZDI, the mass-loss rate in the stellar wind needs to be constrained. The mass-loss rate is important in establishing what area of the parameter space each star occupies, with the angular momentum-loss rates from stars with higher mass-loss rates likely being influenced by the higher order magnetic field components (quadrupole, octupole, etc). The mass-loss rate dependence of the braking law from Chapter 3 has been studied thoroughly by See et al. (2019a). Due to the tenuous optically thin nature of stellar wind plasma, assessing the mass-loss rates of stars (including the Sun) is very difficult.

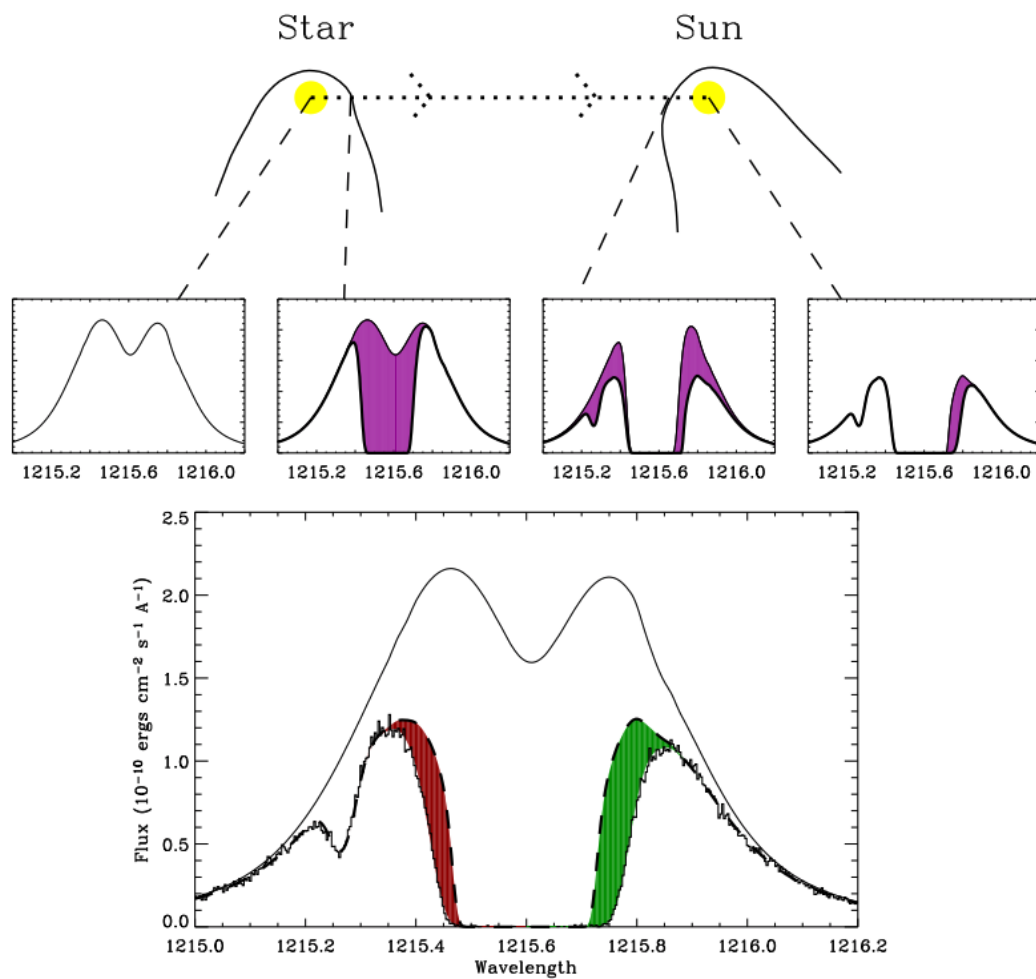


**Figure 4.7:** Schematic representation of measuring mass-loss rates using Ly $\alpha$  absorption from the hydrogen wall of an astrosphere (carved out by the stellar wind of another star) embedded in the Interstellar Medium (ISM). The Ly $\alpha$  emission from the star passes through the hydrogen wall of the astrosphere, undergoing an absorption with a strength that is a diagnostic for the stellar wind ram pressure. Green shaded area is absorption from the Sun’s heliopause, red shaded area corresponds to the astrospheric absorption. This can be modelled and a mass-loss rate can be reconstructed based on the geometry of the astrosphere and its relative motion through the ISM. Taken from Wood (2004).



One of the most successful techniques is that of astrospheric Ly $\alpha$  absorption (see the review of Wood 2004).

Ly $\alpha$  (at 1216Å) is emitted from the chromospheres of low-mass stars, however this emission line is heavily contaminated by the Interstellar Medium (ISM). The ISM contains neutral Hydrogen and Deuterium which both absorb parts of the broad Ly $\alpha$  emission (the Deuterium absorption feature is shifted relative to the Hydrogen absorption by -0.33Å). There is an additional component of absorption which comes from the neutral Hydrogen wall surrounding the star, formed by the interaction of the star’s stellar wind and the ISM. If the ratio of Deuterium to Hydrogen is known along the line of sight to

the distant astrosphere, then this absorption can be removed given the strength of the Deuterium absorption, leaving the astrospheric Hydrogen absorption. The astrospheric absorption contains two components, one from the observed star, and the other from the Sun's heliopause. Wind models are produced in order to reproduce the observed Ly $\alpha$  absorption, which in turn provide an estimate for the mass-loss rate of the star. Note, the model results are mainly sensitive to the ram pressure of the wind  $P_w = 4\pi r^2 \rho v_r^2$ , not the mass-loss rate  $\dot{M} = 4\pi r^2 \rho v_r$  (where quantities are evaluated at the astrosphere), and so assumptions must be made which limit the accuracy of these estimates (there is likely at least a factor of two uncertainty on a given  $\dot{M}$  from this method). This technique can only be used on stars in the local neighbourhood to the Sun, as the ISM absorption obscures the astrospheric feature for stars at distances larger than  $\sim 20$ pc.



# The Effect of Magnetic Variability on Stellar Angular Momentum Loss. II. The Sun, 61 Cygni A, $\epsilon$ Eridani, $\xi$ Bootis A, and $\tau$ Bootis A

Adam J. Finley , Victor See, and Sean P. Matt 

University of Exeter, Exeter, Devon, EX4 4QL, UK; \*af472@exeter.ac.uk

Received 2019 January 14; revised 2019 March 22; accepted 2019 March 23; published 2019 May 1

## Abstract

The magnetic fields of low-mass stars are observed to be variable on decadal timescales, ranging in behavior from cyclic to stochastic. The changing strength and geometry of the magnetic field should modify the efficiency of angular momentum loss by stellar winds, but this has not been well quantified. In Finley et al. (2018), we investigated the variability of the Sun and calculated the time-varying angular momentum-loss rate in the solar wind. In this work, we focus on four low-mass stars that have all had their surface magnetic fields mapped for multiple epochs. Using mass-loss rates determined from astrospheric Ly $\alpha$  absorption, in conjunction with scaling relations from the MHD simulations of Finley & Matt (2018), we calculate the torque applied to each star by their magnetized stellar winds. The variability of the braking torque can be significant. For example, the largest torque for  $\epsilon$  Eri is twice its decadal averaged value. This variation is comparable to that observed in the solar wind, when sparsely sampled. On average, the torques in our sample range from 0.5 to 1.5 times their average value. We compare these results to the torques of Matt et al. (2015), who use observed stellar rotation rates to infer the long-time-averaged torque on stars. We find that our stellar wind torques are systematically lower than the long-time-averaged values, by a factor of  $\sim 3$ –30. Stellar wind variability appears unable to resolve this discrepancy, implying that there remain some problems with observed wind parameters, stellar wind models, or the long-term evolution models, which have yet to be understood.

*Key words:* evolution – magnetohydrodynamics (MHD) – stars: low-mass – stars: winds, outflows – stars: magnetic field – stars: rotation

## 1. Introduction

For low-mass stars like the Sun ( $M_* \lesssim 1.3 M_\odot$ ), magnetic activity is observed to decline with stellar age (Hartmann & Noyes 1987; Mamajek & Hillenbrand 2008). This is a consequence of the dynamo mechanism, which is responsible for sustaining the stellar magnetic field, and its dependence on rotation and convection (Brun & Browning 2017). During the main sequence, angular momentum is removed by magnetized stellar winds. This wind braking increases the observed rotation periods of stars with age (Skumanich 1972; Bouvier et al. 2014). The connections between stellar rotation, magnetic activity, and wind braking converge the rotation and activity indices of low-mass stars during the main sequence, such that these quantities appear to follow a mass-dependent relationship with age (Noyes et al. 1984; Gilliland 1986; Wolff & Simon 1997; Stelzer & Neuhäuser 2001; Pizzolato et al. 2003; Barnes 2010; Meibom et al. 2015). This connection with age is useful in a number of ways. For example, empirical relations can be derived in order to determine the ages of some stars from their rotation or magnetic activity (Barnes 2003; Mamajek & Hillenbrand 2008; Meibom et al. 2009; Delorme et al. 2011; Van Saders & Pinsonneault 2013; Vidotto et al. 2014).

The observed evolution of rotation also provides a constraint on the torque applied to stars, independent of our understanding of stellar winds. Models for computing the rotational evolution of stars give us an indication of how stellar wind torques evolve on secular (up to several gigayear) timescales (e.g., Gallet & Bouvier 2013, 2015). These torques can then be compared to calculations that are based on observed wind and magnetic properties, in order to test our understanding of stellar magnetism and winds (Amard et al. 2016; Réville et al. 2016). One caveat, however, is that the torques derived from rotational evolution

models are only sensitive to the angular momentum losses of stars averaged over some fraction of the spin-down timescale. For Sun-like main sequence stars, the rotational evolution torques thus represent a value averaged over  $\sim 10$ –100 Myr. Clearly, any variability of wind and magnetic properties on timescales shorter than this will inhibit a comparison between the long-time torque from rotational evolution models and those calculated based on observed present-day magnetic and wind properties.

Variability in the magnetic activity of low-mass stars is commonly observed at short timescales, ranging from days to years (Baliunas et al. 1995; Hall et al. 2007; Egeland et al. 2017). The magnetic fields are driven by the stellar dynamo, whose variability can take many forms—be it in exhibiting a cyclic magnetic field like that of the Sun (Boro Saikia et al. 2016; Jeffers et al. 2018), magnetic fields with multiple cycles (Jeffers et al. 2014), or magnetism with apparently stochastic behaviors (Petit et al. 2009; Morgenthaler et al. 2012). Such variability appears to occur throughout the main sequence lifetime of low-mass stars. It is therefore interesting to characterize the impact this has on the stellar wind torques.

In order to quantify the impact of magnetic variability on stellar wind braking, we first studied the solar wind in Finley et al. (2018, hereafter Paper I), for which we have both in situ observations of the wind plasma and remote observations of the photospheric magnetic field. In Paper I, available data allowed us to study the variability on timescales from one solar rotation ( $\sim 27$  days) up to a few decades. We quantified how the torque varies on all timescales, and found that the decadal-averaged value was smaller than the rotational evolution torque by a factor of  $\sim 15$ . Although the reason for the discrepancy is still not clear, it could be due to gaps in our understanding of the solar magnetism and wind, variability in the solar torque on

timescales much longer than a decade, issues with the rotational-evolution torques, or a combination thereof.

In the present paper, we examine the influence of observed magnetic variability on the wind braking of four Sun-like stars, using semi-analytic relations derived from MHD wind simulations, and we compare these values to the long-time-averaged torques derived from modeling the rotational evolution of low-mass stars. In Section 2, we first describe the semi-analytic wind braking formula from Finley & Matt (2017, 2018, hereafter FM18), and the rotational evolution torque prescription from Matt et al. (2015, hereafter M15). In Section 3, we gather stellar properties and magnetic field observations for our four sample stars: 61 Cyg A,  $\epsilon$  Eri,  $\xi$  Boo A, and  $\tau$  Boo A. Each star has repeat observations using the Zeeman–Doppler imaging (ZDI) technique, and three of them also have observed mass-loss rates estimated from astrospheric Ly $\alpha$  absorption. We also re-examine the Sun, limiting the available data to observations  $\sim 2$  yr apart, which is more comparable to the cadence of observations for the other stars. In Section 4, we calculate the angular momentum-loss rates using both torque formulas. We discuss our results in Section 5.

## 2. Angular Momentum-loss Prescriptions

### 2.1. Stellar Wind Torques from Finley & Matt (2018)

As in Paper I, we will make use of the semi-analytic formula derived from the MHD simulations of FM18. Such formulations are intended to characterize the braking torques on stars that host convective outer envelopes. In Paper I, we used a formulation based on the open magnetic flux in the solar wind. Such formulae are independent of the magnetic geometry at the stellar surface (Réville et al. 2015), but the open magnetic flux cannot be measured for stars other than the Sun. For this work, we instead use a formula based on the observed surface magnetic field. Previous formulae of this kind have only been valid for single magnetic geometries (Matt & Pudritz 2008; Matt et al. 2012; Réville et al. 2015; Pantolmos & Matt 2017), but the magnetic fields of low-mass stars are observed to contain mixed magnetic geometries that vary from star to star (e.g., See et al. 2016), as well as in time, with geometries evolving in strength with respect to one another (e.g., DeRosa et al. 2012, for the Sun).

The FM18 formulation is simplified, but is capable of approximating the observed behavior of full MHD simulations without the computational expense. The MHD simulations are performed using axisymmetric magnetic geometries combined with polytropic Parker-like wind solutions (Parker 1958; Pneuman & Kopp 1971; Keppens & Goedbloed 1999), which are relaxed to a steady state. The application of results derived from such simulations to a time-varying problem emulates a sequence of independent steady-state solutions. Given that the characteristic timescales for disturbances caused by the reorganization of the coronal magnetic field to propagate through the solution are short with respect to the evolution of the system, this is a valid approximation.

The torque due to a stellar wind is prescribed in terms of the average Alfvén radius,  $\langle R_A \rangle$ , which acts as an efficiency factor for the stellar wind in extracting angular momentum (Weber & Davis 1967; Mestel 1968). The torque,  $\tau$ , is given by

$$\tau = \dot{M} \Omega_* R_*^2 \left( \frac{\langle R_A \rangle}{R_*} \right)^2, \quad (1)$$

where  $\dot{M}$  is the mass-loss rate of the stellar wind,  $\Omega_*$  is the stellar rotation rate (approximated as solid body rotation at the surface), and  $R_*$  is the stellar radius. In FM18,  $\langle R_A \rangle$  is parameterized in terms of the wind magnetization,

$$\Upsilon = \frac{B_*^2 R_*^2}{M v_{\text{esc}}}, \quad (2)$$

where the total field strength is evaluated from the first three spherical harmonic components  $B_* = |B_{\text{dip}}| + |B_{\text{quad}}| + |B_{\text{oct}}|$ , the escape velocity is given by  $v_{\text{esc}} = \sqrt{2GM_*/R_*}$ , and  $M_*$  is the stellar mass. Previous works have shown the reduced efficiency of magnetic braking with increasingly complex magnetic fields (Réville et al. 2015; Garraffo et al. 2016). Furthermore, FM18 examined the behavior of mixed magnetic geometries. They were able to show that higher-order modes (e.g., octupole) play a diminishing role in braking stellar rotation, when modeled in conjunction with lower-order modes (e.g., dipole, quadrupole). For mixed geometries, FM18 showed that the average simulated Alfvén radius behaves approximately as a broken power law of the form

$$\frac{\langle R_A \rangle}{R_*} = \max \begin{cases} K_{\text{dip}} [\mathcal{R}_{\text{dip}}^2 \Upsilon]^{m_{\text{dip}}}, \\ K_{\text{quad}} [(\mathcal{R}_{\text{dip}} + \mathcal{R}_{\text{quad}})^2 \Upsilon]^{m_{\text{quad}}}, \\ K_{\text{oct}} [(\mathcal{R}_{\text{dip}} + \mathcal{R}_{\text{quad}} + \mathcal{R}_{\text{oct}})^2 \Upsilon]^{m_{\text{oct}}}. \end{cases} \quad (3)$$

This approximates the stellar wind solutions from Finley & Matt (2018), for their fit parameters  $K_{\text{dip}} = 1.53$ ,  $K_{\text{quad}} = 1.70$ ,  $K_{\text{oct}} = 1.80$ ,  $m_{\text{dip}} = 0.229$ ,  $m_{\text{quad}} = 0.134$ , and  $m_{\text{oct}} = 0.087$ . The magnetic field geometry is input using  $\mathcal{R}_{\text{dip}}$ ,  $\mathcal{R}_{\text{quad}}$ , and  $\mathcal{R}_{\text{oct}}$ , defined as the ratios of the polar strengths for each component over the total field strength, i.e.,  $\mathcal{R}_{\text{dip}} = |B_{\text{dip}}|/B_*$ , etc. We neglect modes of higher order than the octupole, as they do not significantly contribute to the torque on the star.

### 2.2. Rotation Evolution Torques from Matt et al. (2015)

In this work, we will compare our results to the rotation evolution model of M15, which uses the observed distribution of mass versus rotation, at given ages, to find empirical torques that reproduce these observations. To date, no single model (including M15) precisely reproduces the observed mass-rotation distributions, but M15 reproduces the broad dependences of rotation rates on mass and age. The torque in this model has two regimes: either unsaturated, where the stellar Rossby number (defined as  $Ro = 2\pi/(\Omega_* t_{\text{cz}})$ , where  $t_{\text{cz}}$  is the convective turnover time) is greater than the saturation value,  $Ro_{\text{sat}} = 0.1 R_{o,\odot}$ ; or saturated, where the Rossby number is smaller. All the stars in this paper are in the unsaturated regime. The M15 torque is given by

$$\tau = \tau_0 \left( \frac{t_{\text{cz}}}{t_{\text{cz},\odot}} \right)^p \left( \frac{\Omega_*}{\Omega_\odot} \right)^{p+1} \quad (Ro_* > Ro_{\text{sat}}), \quad (4)$$

$$\tau = \tau_0 (10)^p \left( \frac{\Omega_*}{\Omega_\odot} \right) \quad (Ro_* \leq Ro_{\text{sat}}), \quad (5)$$

where  $p$  is constrained by observations to  $\sim 2$  (Skumanich 1972), and  $\tau_0$  provides the normalization to the torque based on

**Table 1**  
Stellar Parameters

Star Name	Mass ( $M_{\odot}$ )	Radius ( $R_{\odot}$ )	Teff (K)	$t_{cz}$ (days)	Rot. Period (days)	Rossby Number	Cyc. Period (yr)	$\dot{M}$ ( $M_{\odot}$ )
Sun	1.00	1.00	5780	12.7	28	2.20	11	1
61 Cyg A	0.66	0.67	4310	34.5	35.5	1.03	7.3	0.5
$\epsilon$ Eri	0.86	0.74	4990	24.0	11.7	0.49	3.0	30
$\xi$ Boo A	0.93	0.86	5410	18.3	6.4	0.35	7.5 <sup>a</sup>	5
$\tau$ Boo A	1.34	1.42	6460	1.88	3.0	1.60	0.3	$\sim 150$ <sup>b</sup>

**Notes.**

<sup>a</sup> Fit from this work.

<sup>b</sup> Average mass-loss rate from the MHD simulations of Nicholson et al. (2016).

the stellar mass and radius,

$$\tau_0 = 6.3 \times 10^{30} \text{erg} \left( \frac{R_*}{R_{\odot}} \right)^{3.1} \left( \frac{M_*}{M_{\odot}} \right)^{0.5}, \quad (6)$$

which is fit empirically from the observed rotation rates of Sun-like stars.

For determining the convective turnover timescales, as in M15, we adopt the fit of Cranmer & Saar (2011) to the stellar models of Gunn et al. (1998),

$$t_{cz} = 314.24 \exp \left[ - \left( \frac{T_{\text{eff}}}{1952.5 \text{ K}} \right) - \left( \frac{T_{\text{eff}}}{6250 \text{ K}} \right)^{18} \right] + 0.002, \quad (7)$$

where the effective temperature,  $T_{\text{eff}}$ , is the only variable determining  $t_{cz}$ . Cranmer & Saar (2011) showed this to be a reasonable approximation that is valid for the temperature range  $3300 \leq T_{\text{eff}} \leq 7000$  K. Such a monotonic function of  $t_{cz}(T_{\text{eff}})$  is also supported by other works (Barnes & Kim 2010; Landin et al. 2010).

### 3. Observed Stellar Properties

We select a sample from all stars that have been monitored with ZDI, requiring that each have six or more ZDI observations that clearly show magnetic variability. This criterion selects four stars, as most stars that have been observed with ZDI have only one or two epochs. Along with our sample stars, we also consider the Sun. This section contains information on each star, including results from ZDI, studies of their astrospheric Ly $\alpha$  absorption, and proxies of their magnetic activity. Both solar and stellar parameters can be found in Table 1.

#### 3.1. The Sun

The study of the Sun's magnetism has afforded the astrophysics community a great wealth of information on the apparent behavior of the magnetic dynamo process (Brun et al. 2015). We observe the Sun to have a cyclic pattern in its magnetic activity, with a sunspot cycle of around 11 yr and a magnetic cycle lasting approximately 22 yr (Babcock 1961; Schrijver & Liu 2008; DeRosa et al. 2012). At the minimum of magnetic activity, the wind dynamics on large scales are dominated by the axisymmetric dipole component and the solar wind is, in general, fast and diffuse, emerging on open polar field lines (Wang & Sheeley 1990; Schwenn 2006). As the cycle progresses, the solar magnetic field becomes increasingly

complex toward maximum, with the appearance of sunspots as buoyant magnetic flux tubes rise through the photosphere (Parker 1955; Spruit 1981; Caligari et al. 1995; Fan 2008). Due to the increased complexity, more of the solar wind emerges in the slow, dense component, and transient magnetic phenomena are more frequent (Webb & Howard 1994; Neugebauer et al. 2002; McComas et al. 2003). The average surface magnetic field is stronger at maximum, and so too are magnetic activity indicators and the solar irradiance (Lean et al. 1998; Wenzler et al. 2006). Following the decline of magnetic activity into the next minimum, the polarity of the field is reversed (Babcock 1959; Sun et al. 2015). Numerous mechanisms have been proposed to explain this phenomenon (e.g., Fisher et al. 2000; Ossendrijver 2003). The solar magnetic field returns to its original polarity after one further sunspot cycle, completing the magnetic cycle.

As was done for the Sun in Paper I, we use synoptic magnetograms taken by the Michelson Doppler Imager on board the *Solar and Heliospheric Observatory* (SOHO/MDI) and the Helioseismic and Magnetic Imager on board the *Solar Dynamic Observatory* (SDO/HMI). We calculate the average surface magnetic field strength  $B_{\text{mean}}$ , the combined polar dipole, quadrupole and octupole field strength  $B_*$ , and the field fractions  $\mathcal{R}_{\text{dip}}$ ,  $\mathcal{R}_{\text{quad}}$ , and  $\mathcal{R}_{\text{oct}}$ . Unlike Paper I, in order to better compare the solar case with other stars, and to illustrate the effect of sparse time sampling, we take only 13 Carrington rotations, equally spaced over the  $\sim 20$  yr of data. This information is plotted in the top two panels of Figure 1 and tabulated in Appendix A.

The first panel of Figure 1 compares the average surface magnetic field,  $B_{\text{mean}}$ , which is often used when discussing results from ZDI, to the combined polar field strength of the lowest three spherical harmonic components,  $B_*$ , which is required by the FM18 torque formulation. Typically,  $B_*$  is larger than  $B_{\text{mean}}$ , because it sums the absolute magnitude of the polar field strengths, whereas  $B_{\text{mean}}$  allows for opposing field polarities to cancel and is averaged over the stellar surface.

Sparsely sampling the solar magnetograms has made the well-known cyclic behavior of the large-scale magnetic field less obvious, especially when considering  $B_*$ . However, the cycle is more clear in the second panel, where we plot the fraction of  $B_*$  in the dipole, quadrupole, and octupole components. We illustratively recover the magnetic behavior of the Sun by fitting sinusoids of  $B_*$ ,  $\mathcal{R}_{\text{dip}}$ ,  $\mathcal{R}_{\text{quad}}$ , and  $\mathcal{R}_{\text{oct}}$  with a fixed 11 yr period, and allowing the phase and amplitude of each fit to vary. These illustrations are shown in Figure 1, and will be repeated for the ZDI sample in Section 3.3 to produce feasible distributions of magnetic properties for each star,

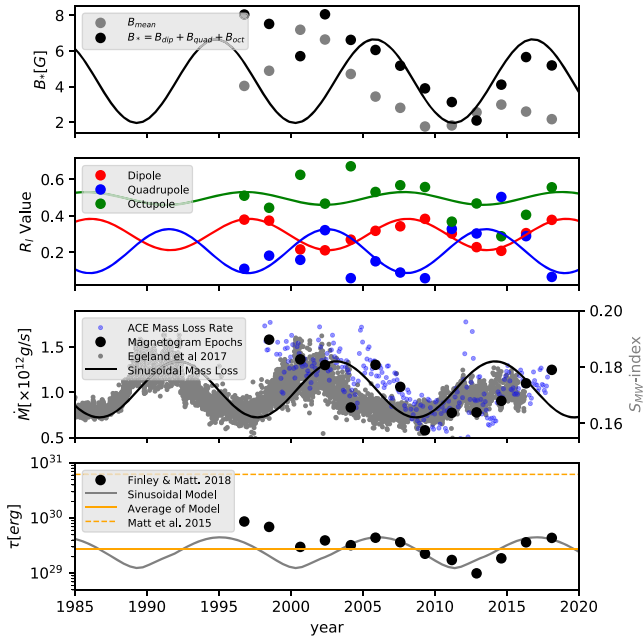


**Figure 1.** Angular momentum-loss calculation for the solar wind (the Sun-as-a-star approach). The top two panels show the magnetic field properties of the Sun using synoptic magnetograms from *SOHO*/MDI and *SDO*/HMI. Dots represent sparsely sampled epochs of observation. The first panel shows the evolution of the magnetic field strength at the surface of the Sun. The second panel shows the ratio of dipole, quadrupole, and octupole components to the combined (dipole, quadrupole, and octupole) magnetic field strength. The third panel displays the mass-loss rate measurements derived from the *ACE* spacecraft (see Paper I) in blue, with the selected epochs shown with black dots (left scale), along with the evolution of solar  $S$ -index from Egeland et al. (2017) indicated by gray dots (right scale). We fit sinusoids to the magnetic and mass-loss rate variables with a fixed 11 yr period, which roughly represents the solar chromospheric activity cycle. Black dots in the fourth panel indicate the calculated torques for each magnetogram epoch using FM18. The torque using our continuous sinusoidal fits is plotted as a solid gray line, and its average is highlighted by a solid orange horizontal line. The torque calculated using M15 is indicated by a dashed orange horizontal line.

allowing us to further examine the role of magnetic variability on stellar wind torques.

### 3.2. Other Stars

Four stars observed with ZDI meet our criteria for selection: 61 Cyg A,  $\epsilon$  Eri,  $\xi$  Boo A, and  $\tau$  Boo A. Their basic properties are compiled in Table 1. Masses are determined using the stellar evolution model of Takeda et al. (2007). If available, radii are evaluated with interferometry by Kervella et al. (2008), Baines & Armstrong (2011), or Boyajian et al. (2013); otherwise, they are evaluated spectroscopically by Borsa et al. (2015). Effective temperatures are taken from Boeche & Grebel (2016), and then used in conjunction with Equation (7) to produce convective turnover timescales. Rotation periods for each star are determined by Boro Saikia et al. (2016), Rüedi et al. (1997), Toner & Gray (1988), Donahue et al. (1996), Donati et al. (2008), and Fares et al. (2009), respectively. These are then used to calculate the Rossby number  $R_o = P_{\text{rot}}/t_{\text{cz}}$  for each object. Further details for each star are listed below.

61 Cyg A (HD 201091) is a K5V star, located 3.5 pc away (Brown et al. 2016) in the constellation of Cygnus as a visual binary with 61 Cyg B, a K7V star. Age estimations for 61 Cyg A range from 1.3 to 6.0 Gyr, with the majority of estimates at the younger end of this range: 2 Gyr (Barnes 2007), 3.6 Gyr

(Mamajek & Hillenbrand 2008), 6 Gyr (Kervella et al. 2008), and 1.3 Gyr (Marsden et al. 2014). Cyclic chromospheric/coronal activity is detected in many forms, including X-ray emission (Robrade et al. 2012), with a period in phase with its magnetic activity cycle (Baliunas et al. 1995; Boro Saikia et al. 2016, 2018).

$\epsilon$  Eri (HD 22049) is a K2V star in the constellation of Eridanus, at a distance of 3.2 pc (Brown et al. 2016).  $\epsilon$  Eri is a young star with multiple age estimations (e.g., Song et al. 2000; Fuhrmann 2004). From gyrochronology, Barnes (2007) arrives at an age of 400 Myr, which is thought to be the most reliable (see discussion in Janson et al. (2008)). Chromospheric activity has been recorded for  $\epsilon$  Eri by Metcalfe et al. (2013). It displays an activity cycle length of  $\sim 3$  yr, as well as a longer one of  $\sim 13$  yr that vanished after a 7 yr minimum in activity around 1995.

$\xi$  Boo A (HD 131156A), a spectral-type G7V, lies in the constellation of Boötes, 6.7 pc away (Brown et al. 2016), in a visual binary with  $\xi$  Boo B of spectral type K5V. The age of  $\xi$  Boo A is determined from gyrochronology by Barnes (2007) as 200 Myr. Variations in  $\xi$  Boo A’s chromospheric activity have been noted by multiple authors (Hartmann et al. 1979; Gray et al. 1996; Morgenthaler et al. 2012), but no clear cycle has been detected.

$\tau$  Boo A (HD 120136) is a very well-studied planet-hosting F7V star, sitting at a distance of 15.7 pc (Brown et al. 2016) in a multiple star system with  $\tau$  Boo B, a faint M2V companion.  $\tau$  Boo A has an age of around 1 Gyr (Borsa et al. 2015), and has an observed chromospheric activity cycle (Mengel et al. 2016; Mittag et al. 2017) that is in phase with the reversals of its global magnetic field (Jeffers et al. 2018). This is also the case for the Sun and 61 Cyg A. As  $\tau$  Boo A has a close-in planetary companion, Walker et al. (2008) searched for star–planet interactions and found that the planet is likely inducing an active region on the stellar surface, causing further variability in the star’s chromospheric emission.

### 3.3. Zeeman–Doppler Imaged Fields

61 Cyg A (Boro Saikia et al. 2016),  $\epsilon$  Eri (Jeffers et al. 2014, 2017),  $\xi$  Boo A (Morgenthaler et al. 2012), and  $\tau$  Boo A (Fares et al. 2009; Mengel et al. 2016; Jeffers et al. 2018) have all been monitored with ZDI. This is a tomographic technique that is capable of reconstructing their large-scale photospheric magnetic fields (Donati et al. 1989; Semel 1989; Brown et al. 1991; Donati & Brown 1997; Donati & Landstreet 2009). Magnetic fields cause spectral lines to split and become polarized due to the Zeeman effect (Zeeman 1897). By monitoring this splitting over multiple phases, taking advantage of the Doppler shifts due to rotation, and combining multiple line profiles together using a Least Squares Deconvolution (LSD) technique (Donati et al. 1997), the large-scale stellar magnetic field topology can be reconstructed.

Papers reporting ZDI results typically tabulate the fraction of the total magnetic field energy that is poloidal ( $E_{\text{pol}}$ ) and the fraction of this poloidal field energy that is dipolar, quadrupolar, or octupolar ( $E_{\text{dip}}$ ,  $E_{\text{quad}}$ , and  $E_{\text{oct}}$ ), as well as the average surface field ( $B_{\text{mean}}$ ). For the maps of Fares et al. (2009) and Mengel et al. (2016), we compute the values using data supplied by the authors; these values are not tabulated in the original papers. Using MHD stellar wind models, Jardine et al. (2013) were able to show that large-scale wind dynamics are largely unaffected by toroidal magnetic field structures



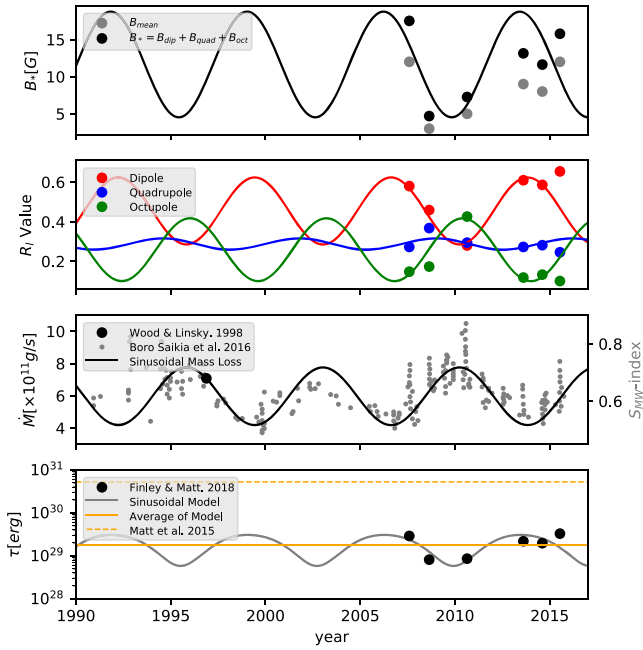


**Figure 2.** Angular momentum-loss calculation for 61 Cyg A. The top two panels show the magnetic field properties taken from the ZDI measurements of Boro Saikia et al. (2016). The first panel shows the evolution of the average unsigned magnetic field strength and the combined (dipole, quadrupole, and octupole) magnetic field strength, at the surface of the star. The second panel shows the ratios of dipole, quadrupole, and octupole components of the magnetic field to the combined magnetic field strength. We fit sinusoids to these properties with a fixed period of 7.3 yr, matching the chromospheric activity cycle. The third panel displays the mass-loss rate measurement of Wood & Linsky (1998) as a black dot, along with the  $S$ -index evolution of the chromospheric activity as gray dots (Boro Saikia et al. 2016). A sinusoidal mass-loss rate with a solar-like amplitude, as well as phase and period matching the observed chromospheric activity, is shown as a solid black line. Black dots in the fourth panel display the calculated torques for each ZDI epoch using FM18. A solid gray line plots the torque using our continuous sinusoidal fits; its average is highlighted by a solid orange horizontal line. The torque calculated using M15 is indicated with a dashed orange horizontal line.

embedded in the photosphere. Therefore, we assume the toroidal component does not impact our torque calculations. We convert the percentage energies into the poloidal dipole, quadrupole, and octupole field fractions, as well as combined field strength,

$$f_{\text{dip}} = \sqrt{E_{\text{pol}} E_{\text{dip}}}, \quad (8)$$

$$f_{\text{quad}} = \sqrt{E_{\text{pol}} E_{\text{quad}}}, \quad (9)$$

$$f_{\text{oct}} = \sqrt{E_{\text{pol}} E_{\text{oct}}}, \quad (10)$$

$$B_* = B_{\text{mean}}(f_{\text{dip}} + f_{\text{quad}} + f_{\text{oct}}). \quad (11)$$

Here, care has been taken in transforming fractional energy into fractional field strengths for each magnetic component. Subsequently, the field fractions,  $f_{\text{dip}}$ ,  $f_{\text{quad}}$ , and  $f_{\text{oct}}$  are converted into the ratios of each magnetic component to the combined field strength,  $\mathcal{R}_l$ ,

$$\mathcal{R}_{\text{dip}} = \frac{B_{\text{dip}}}{B_*} \equiv \frac{f_{\text{dip}}}{f_{\text{dip}} + f_{\text{quad}} + f_{\text{oct}}}, \quad (12)$$

$$\mathcal{R}_{\text{quad}} = \frac{B_{\text{quad}}}{B_*} \equiv \frac{f_{\text{quad}}}{f_{\text{dip}} + f_{\text{quad}} + f_{\text{oct}}}, \quad (13)$$

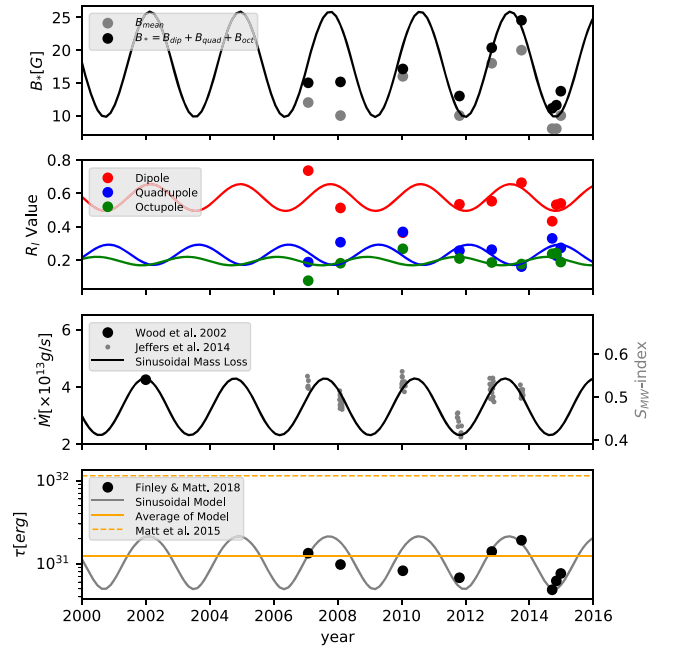


**Figure 3.** Same as Figure 2, but for  $\epsilon$  Eri.

$$\mathcal{R}_{\text{oct}} = \frac{B_{\text{oct}}}{B_*} \equiv \frac{f_{\text{oct}}}{f_{\text{dip}} + f_{\text{quad}} + f_{\text{oct}}}. \quad (14)$$

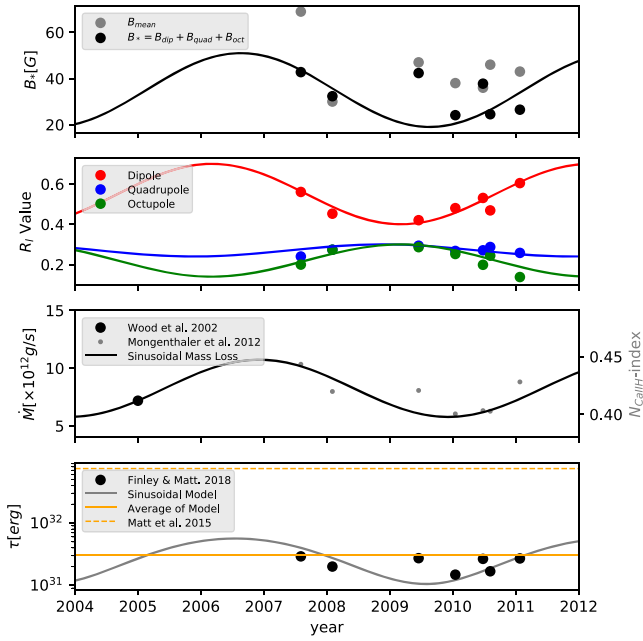
These results are shown in the top two panels in each of Figures 2–5, and tabulated in Table 2 for each ZDI epoch. Calculating the ratios of each field component using this method, rather than recomputing the field strengths of each component from the original ZDI maps, introduces some errors that will be discussed in Section 5.1.

In each of Figures 2–5, the first panel displays the recorded mean magnetic field from the ZDI reconstructions,  $B_{\text{mean}}$ , with gray dots. The black dots represent the combined polar field strength of the dipole, quadrupole, and octupole components,  $B_*$ . Typically, the  $B_*$  value is larger than  $B_{\text{mean}}$ , unless a significant fraction of the magnetic energy is stored in the toroidal or high-order ( $l > 3$ ) components. The second panels show the varying field fractions,  $\mathcal{R}_{\text{dip}}$ ,  $\mathcal{R}_{\text{quad}}$ , and  $\mathcal{R}_{\text{oct}}$ .

Although multiple magnetic maps exist for each of our ZDI stars, they are still sampled relatively sparsely, compared to the Sun. To examine their variability further, we fit sinusoidal functions to  $B_*$ ,  $\mathcal{R}_{\text{dip}}$ ,  $\mathcal{R}_{\text{quad}}$ , and  $\mathcal{R}_{\text{oct}}$ , as we did for the Sun, using chromospheric activity periods taken from the literature for each star (see Table 1). We allow the phase and amplitude of each fit to vary, but we constrain the fits of  $\mathcal{R}_{\text{dip}}$ ,  $\mathcal{R}_{\text{quad}}$ , and  $\mathcal{R}_{\text{oct}}$  to sum to  $\sim 1$ . In some cases, there is no strong evidence for periodicity—and even if so, a sinusoidal behavior is a gross simplification. We do this simply to illustratively construct continuous predictions for feasible cyclic behaviors, from which we can make more general comments about the impact of stellar cycles on stellar wind torques.

### 3.4. Inferred Mass-loss Rates and Activity Proxies

The solar mass-loss rate is observed to be variable in time (Hick & Jackson 1994; Webb & Howard 1994; McComas et al. 2000, 2013). In the third panel of Figure 1, we use blue dots to plot the solar mass-loss rate calculated in Paper I, based on data


 Figure 4. Same as Figure 2, but for  $\xi$  Boo A.

from the *Advanced Composition Explorer*<sup>1</sup>, and we highlight our selected magnetogram epochs with black dots. During the solar cycle, the mass-loss rate from Paper I is found to vary around the mean by about  $\pm 30\%$ .<sup>2</sup> We fit the function,

$$\dot{M}(t) = \langle \dot{M} \rangle \left[ 0.3 \sin\left(\frac{2\pi t}{P} + \phi\right) + 1 \right], \quad (15)$$

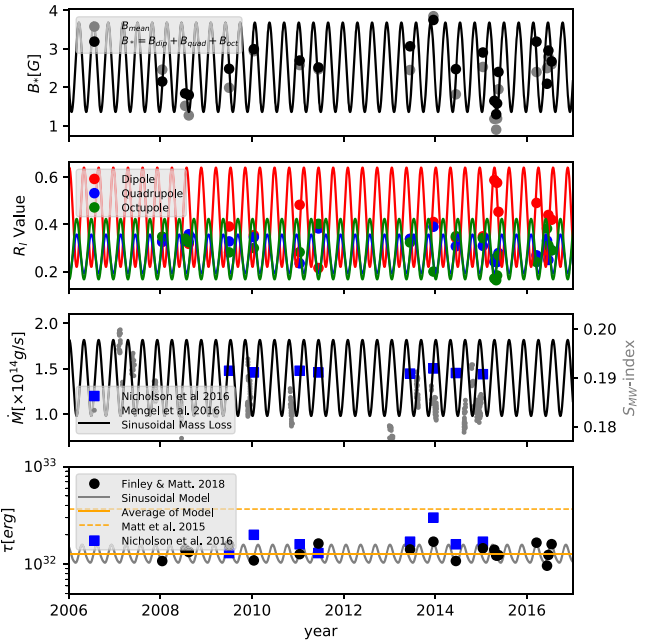
to the 13 selected magnetogram epochs. Here,  $t$  is the decimal year (1985–2020 are plotted), the mass-loss rate variation is constrained to  $\Delta \dot{M} = 0.6 \langle \dot{M} \rangle$ , and the period is fixed as that of the chromospheric activity period,  $P = 11$  yr. The fit values of the phase,  $\phi$ , and the average mass-loss rate,  $\langle \dot{M} \rangle$ , are  $\sim \pi/6$  and  $1.03 \times 10^{12} \text{ g s}^{-1}$ , respectively. This fit is displayed as a solid black line in the third panel.

For nearby stars, Ly $\alpha$  observations can reveal information about their stellar winds (Wood 2004). Absorption in this line occurs at the edge of the star’s astrosphere, as well as at the Sun’s heliosphere. At these locations, the solar and stellar winds collide with the ISM and become shocked, reaching temperatures and densities much greater than the average ISM. Based on their models of this absorption, estimated mass-loss rates are available from Wood & Linsky (1998) and Wood et al. (2002, 2005) for 61 Cyg A,  $\epsilon$  Eri, and  $\xi$  Boo A. There are no measurements of the mass-loss rate for  $\tau$  Boo A, so instead we use the results of MHD simulations from Nicholson et al. (2016). The mass-loss rate used for each star is shown in Table 1.

For the ZDI stars, the mass-loss rates gathered from Ly $\alpha$  observations are taken at a single epoch. These are plotted as black dots in the third panel of Figures 2–4. However, we might expect the mass-loss rates of these stars to vary with their magnetic activity, similarly to the Sun. Currently, there are no observations in the literature capable of quantifying this variability, so we must draw comparisons with the Sun.

<sup>1</sup> <http://srl.caltech.edu/ACE/ASC/level2/>

<sup>2</sup> In calculating this variation, we ignore extreme values that are seen in time averages shorter than a few months.


 Figure 5. Same as Figure 2, but for  $\tau$  Boo A. Mass-loss rate and torque panels (3 and 4) include values (blue squares) from the MHD simulations of  $\tau$  Boo A from Nicholson et al. (2016). A phase-folded version of this plot is available in Appendix B.

Increased emission in Ca II H&K is thought to correlate directly with the deposition of magnetic energy into the stellar chromosphere (Eberhard & Schwarzschild 1913; Noyes et al. 1984; Testa et al. 2015). This is observed for the Sun (Schrijver et al. 1989) and can be correlated with the mass-loss rate of the solar wind. Overplotted with the mass-loss rates in Figure 1, we show the solar  $S$ -index values from Egeland et al. (2017). The  $S$ -index evaluates the flux in the H and K lines and normalizes it to the nearby continuum (Wilson 1978). Both the solar mass-loss rate and the sinusoidal fit to our selected epochs appear roughly in phase with this measure of chromospheric activity. The slight lag between mass-loss rate and magnetic activity is not surprising, as a similar lag is observed in the rate of coronal mass ejections (Ramesh 2010; Webb & Howard 2012) and open magnetic flux in the solar wind (Wang et al. 2000; Owens et al. 2011). The Ca II H&K lines are now regularly monitored for hundreds of stars (Wilson 1978; Baliunas et al. 1995; Hall et al. 2007; Egeland et al. 2017). Using gray dots, we plot the available  $S$ -index measurements for each star in the third panel of Figures 2–5. The temporal coverage differs from star to star, with  $\xi$  Boo A having only the Ca II H band index,<sup>3</sup> taken concurrently with the ZDI observations (Morgenthaler et al. 2012).

Similarly to the Sun, we represent the mass-loss variation for each star using a sinusoidal function,

$$\dot{M}(t) = 0.3 \langle \dot{M} \rangle \left[ \sin\left(\frac{2\pi t}{P} + \phi\right) - \sin\left(\frac{2\pi t_{\text{obs}}}{P} + \phi\right) \right] + \dot{M}_{\text{obs}}, \quad (16)$$

with the phase,  $\phi$ , and period,  $P$ , matching the variation of their Ca II H&K emission. We use chromospheric activity periods from

<sup>3</sup> As both the H and K lines scale together, only information about one is required.

**Table 2**  
Magnetic Properties from ZDI and Angular Momentum-loss Results

Star Name	ZDI Obs Epoch	$B_*$ (G)	$\mathcal{R}_{\text{dip}} \equiv B_{\text{dip}}/B_*$	$\mathcal{R}_{\text{quad}} \equiv B_{\text{quad}}/B_*$	$\mathcal{R}_{\text{oct}} \equiv B_{\text{oct}}/B_*$	$\langle R_A \rangle / R_*$	$\tau_{\text{FM18}} (\times 10^{30} \text{ erg})$	$\tau_{\text{spinev}} (\times 10^{30} \text{ erg})$	$\tau_{\text{spinev}} / \langle \tau_{\text{FM18}} \rangle$	Reference (ZDI Data)
61 Cyg A	2007.59	17.5	0.58	0.27	0.15	11.8	0.29	5.25	26.25	1
	2008.64	4.7	0.46	0.37	0.17	5.5	0.08	...	...	1
	2010.55	7.3	0.28	0.29	0.43	5.1	0.09	...	...	1
	2013.61	13.1	0.61	0.27	0.12	10.9	0.22	...	...	1
	2014.61	11.6	0.59	0.28	0.13	9.9	0.20	...	...	1
	2015.54	15.6	0.65	0.25	0.10	11.4	0.32	...	...	1
eEri	2007.08	15.0	0.74	0.19	0.08	4.7	13.4	114	11.41	2
	2007.09	15.1	0.51	0.31	0.18	4.0	9.8	...	...	2
	2010.04	17.1	0.36	0.37	0.27	3.5	8.2	...	...	2
	2011.81	13.0	0.53	0.26	0.21	4.2	6.8	...	...	2
	2012.82	20.3	0.55	0.26	0.19	4.7	14.0	...	...	2
	2013.75	24.6	0.66	0.16	0.18	5.6	19.1	...	...	2
	2014.71	11.1	0.43	0.33	0.24	3.6	4.8	...	...	3
	2014.84	11.6	0.53	0.23	0.24	4.0	6.2	...	...	3
	2014.98	13.7	0.54	0.27	0.19	4.2	7.6	...	...	3
	$\xi$ Boo A	2007.56	42.8	0.56	0.24	0.20	11.0	29.1	748	32.4
2008.09		32.3	0.45	0.27	0.27	8.5	20.0	...	...	4
2009.46		42.4	0.42	0.29	0.29	8.8	27.3	...	...	4
2010.04		24.1	0.48	0.27	0.25	7.9	14.8	...	...	4
2010.48		37.8	0.53	0.27	0.20	9.8	26.6	...	...	4
2010.59		24.5	0.47	0.29	0.24	7.4	16.8	...	...	4
2011.07		26.5	0.60	0.26	0.14	8.1	27.0	...	...	4
$\tau$ Boo A	2008.04	2.2	0.33	0.33	0.35	2.1	108	367	2.72	5
	2008.54	1.8	0.33	0.33	0.34	2.0	141	...	...	5
	2008.62	1.8	0.32	0.36	0.32	2.0	133	...	...	5
	2009.5	2.5	0.39	0.33	0.28	2.1	156	...	...	5
	2010.04	3.0	0.35	0.35	0.30	2.2	109	...	...	6
	2011.04	2.7	0.48	0.23	0.28	2.1	127	...	...	6
	2011.45	2.5	0.22	0.38	0.40	2.1	163	...	...	6
	2013.45	3.1	0.34	0.34	0.32	2.2	142	...	...	6
	2013.96	3.8	0.41	0.39	0.20	2.2	170	...	...	6
	2014.45	2.5	0.34	0.31	0.35	2.1	108	...	...	6
	2015.04	2.9	0.35	0.31	0.34	2.2	146	...	...	6
	2015.29	1.6	0.59	0.24	0.17	1.9	141	...	...	6
	2015.33	1.3	0.58	0.26	0.16	1.8	123	...	...	6
	2015.35	1.6	0.58	0.24	0.18	1.9	123	...	...	6
	2015.38	2.4	0.45	0.28	0.27	2.1	124	...	...	6
	2016.21	3.2	0.49	0.27	0.24	2.2	166	...	...	7
	2016.44	2.1	0.29	0.33	0.38	2.1	97	...	...	7
	2016.47	3.0	0.44	0.25	0.31	2.2	124	...	...	7
	2016.54	2.7	0.42	0.29	0.29	2.1	160	...	...	7

**References.** (1) Boro Saikia et al. (2016); (2) Jeffers et al. (2014); (3) Jeffers et al. (2017); (4) Morgenthaler et al. (2012); (5) Fares et al. (2009); (6) Mengel et al. (2016); (7) Jeffers et al. (2018).

the existing literature (see Table 1), and show the available Ca II H&K indices in Figures 2–4. Although a correlation between mass-loss rate and Ca II H&K emission seems to exist for the Sun (visible in Figure 1), the correlation is complex; it is not obvious whether a similar relationship exists for other stars. If we were to use the correlation for the Sun to estimate the mass-loss rate variation of our sample stars, given their variability in Ca II H&K emission, i.e.,  $\Delta \dot{M} \propto \Delta S_{\text{index}}$ , we would find a range of amplitudes around  $\Delta \dot{M} = 0.01\text{--}1.5 \langle \dot{M} \rangle$ . Given the uncertainties, we simply adopt the same amplitude for the mass-loss rate as was determined for the Sun ( $\Delta \dot{M} = 0.6 \langle \dot{M} \rangle$ ), and require the function to reproduce the astropheric Ly $\alpha$  observations (i.e.,  $\dot{M}(t_{\text{obs}}) = \dot{M}_{\text{obs}}$ ). The solid black line in each figure represents this projected

variability. Note that, because the torque is a relatively weak function of mass-loss rate (see Equations (1)–(3)), our assumption about the amplitude of variability in mass-loss rate has a similarly weak effect on the amplitude of variability in the torque.

#### 4. Angular Momentum-loss Rates

Here, we apply the FM18 braking law to our sample stars to calculate their stellar wind torques. We also calculate the rotational evolution torques from M15.

##### 4.1. Predicted Alfvén Radii

Through the application of FM18 to our sample stars, we are able to examine their individual locations in our MHD

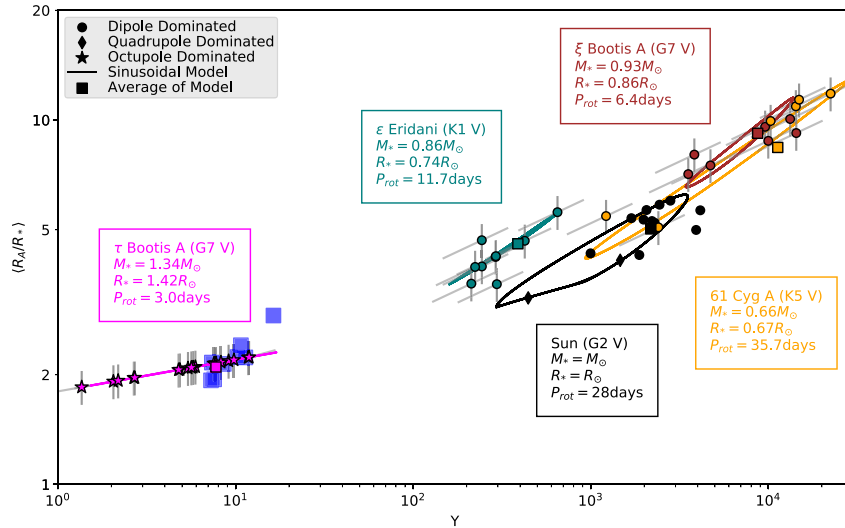


**Figure 6.** Average Alfvén radius vs. wind magnetization,  $\Upsilon$ . Results for the Sun are shown in black. The ZDI epochs for 61 Cyg A (orange),  $\epsilon$  Eri (teal),  $\xi$  Boo A (brown), and  $\tau$  Boo A (magenta) are displayed with their uncertainties, in gray. The shape of each point signifies the magnetic geometry governing the angular momentum-loss rate according to Equation (3): dipolar-dominated with circles, quadrupolar-dominated with diamonds, and octupolar-dominated with stars. The sinusoidal models are shown with a corresponding colored line. Colored squares mark the average of both quantities for each star. The majority of ZDI epochs and solar magnetograms are dominated by the dipolar component—with the exception of  $\tau$  Boo A, which hosts a weakly magnetized wind (according to the predictions of  $\dot{M}$  of Nicholson et al. 2016) and so is dominated by the octupolar term in Equation (3). Results from the 3D MHD simulations of  $\tau$  Boo A from Nicholson et al. (2016) are displayed using blue squares, in good agreement with this work.

parameter space. Figure 6 displays the location of each ZDI epoch and sinusoidal model in  $\langle R_A \rangle - \Upsilon$  space. Uncertainties in the recovered field strengths from ZDI are difficult to quantify. Typically, errors quoted in ZDI papers are obtained by varying the input parameters to reconstruct additional ZDI maps, from which the variation in field strengths are quoted as error (see the discussion in Petit et al. (2008)). We propagate typical uncertainties for the magnetic field strength ( $\pm 30\%$ ) and the mass-loss rates ( $\pm 50\%$ ), respectively, using standard error analysis. The resulting uncertainty in wind magnetization,  $\Upsilon$ , and the average Alfvén radius,  $\langle R_A \rangle$ , are correlated, as we show with diagonal gray lines in Figure 6. Vertical lines represent a  $\pm 10\%$  uncertainty on our prediction of  $\langle R_A \rangle$ , which considers the approximations made in fitting Equation (3). This is discussed further in FM18 (see their Figure 10).

The wind magnetization parameterizes the effectiveness of the wind braking, or more physically, the size of the torque-averaged Alfvén radius. However, Equation (3) also encodes information about the magnetic geometry of the field, approximating this effect as a twice-broken power law. Depending on the strength of the three magnetic geometries considered here, the dipolar, quadrupolar, or octupolar (top, middle, or bottom) formula in Equation (3) will be used to calculate  $\langle R_A \rangle$ . To identify when each formula is used, different symbols are plotted in Figure 6.

The average Alfvén radii of our sample stars range from  $\sim 2$  to  $11R_*$ ; most are typically dipole-dominated, with the exception of  $\tau$  Boo A. The predicted  $\langle R_A \rangle$  values for  $\tau$  Boo A follow a shallower slope than the other dipolar-dominated stars, due to the weaker dependence of the octupolar geometry (as compared to the dipole or quadrupole geometries) on wind magnetization in Equation (3). The MHD model results of Nicholson et al. (2016) for the  $\langle R_A \rangle$  of  $\tau$  Boo A are also plotted with light blue squares in Figure 6. Their values for  $\langle R_A \rangle$  are shown to be in good agreement with results from the FM18 braking law.

The Sun appears typical when compared with the three dipole-dominated stars; some have larger  $\langle R_A \rangle$  and others have smaller. However, the Sun shows some quadrupolar-dominated behavior around solar maximum, which is not observed in the other dipole-dominated stars. Each sinusoidal model roughly represents the observed epochs from ZDI, and they are able to show how subsampling may skew our perception of where each star lies in this parameter space. A similar representation of the solar cycle in this parameter space was explored in the work of Pinto et al. (2011) (see Figure 11 within). We find (though we do not depict it here) that the sinusoidal prediction for the location of the Sun in this parameter space is representative of using the full data set examined in Paper I.

## 4.2. Torques

### 4.2.1. The Sun as a Star

In Paper I, we produced an estimate for the solar angular momentum-loss rate using the wealth of observations available for our closest star. Here, we instead treat the Sun as a star by reducing the number of observations to intervals of approximately 2 yr, thus illustrating the effect of sparse time sampling. Details on the selected magnetogram epochs are tabulated in Appendix A.

Figure 1 shows the result of our angular momentum-loss calculation. For the Sun, the dipole and octupole geometries are shown to cycle in phase, with the quadrupole out of phase, as previously discussed in DeRosa et al. (2012). The  $S$ -index values from Egeland et al. (2017) appear in phase with the quadrupolar geometry and the mass-loss rates taken from Paper I. The torques for each epoch using FM18 are plotted with black dots in the bottom panel. A gray line indicates the torque using the sinusoidal fits of the magnetic field and mass-loss rate.

From Figure 1, it is clear that simple sinusoids with fixed amplitude and phase are a poor fit to the data. This is primarily due to variation from cycle to cycle, i.e., the length of the Sun's magnetic cycle is known to vary, along with the strength of each

cycle (e.g., Solanki et al. 2002). However, the poor fit is also representative of the effects of sparse sampling on a system that contains variability on much shorter timescales than considered. Therefore, when considering the magnetic behavior of other stars, we expect not to see clear cyclical behaviors, even if the stars are truly cyclical, like we know the Sun to be.

We calculate the average torque for the solar magnetogram epochs to be  $0.37 \times 10^{30}$  erg, which is in close agreement with the estimate produced in Paper I. The sinusoidal fits produce an average torque of  $0.30 \times 10^{30}$  erg. The model torque has a different phase, with respect to the solar magnetic cycle, than using the full data set in Paper I, which is a consequence of fitting to sparsely sampled data. The torque given by M15 is  $6.2 \times 10^{30}$  erg. The discrepancy between these torques is discussed in Section 4.3.

#### 4.2.2. 61 Cygni A

61 Cyg A was observed with ZDI by Boro Saikia et al. (2016) from 2007.59 to 2015.54, with an average of 1.19 yr between observations. They find the star to be very much like the Sun in its magnetic behavior: both the poloidal and toroidal field components reverse polarity in phase with its chromospheric activity, and it displays a weak, solar-like differential rotation profile. Like the Sun's, this global field is strongly dipolar: the dipole component strengthens at activity minimum, but weakens at activity maximum in favor of more multipolar field geometries.

Figures 2 and 6 display the full results of our angular momentum-loss calculation. Block dots in the bottom panel of Figure 2 plot the values of the torque calculated for the individual ZDI epochs using the projected mass-loss rates. The sinusoidal model torque is plotted with a solid gray line. The dipole component is strong, with activity minima in 2007 and 2014, so we predict a large average Alfvén radius ( $\sim 10R_*$ ; see Figure 6). At the activity maximum around 2010, the field is at its most complex. However, the magnetic braking is still dominated by the dipolar component, due to the relative strengths of the other modes. This produces the smallest average Alfvén radius ( $\sim 5R_*$ ).

The average torque for the ZDI epochs of 61 Cyg A, using FM18, is  $0.20 \times 10^{30}$  erg. The average of the sinusoidal model has a similar value of  $0.18 \times 10^{30}$  erg. The torque from M15 is calculated to be  $5.25 \times 10^{30}$  erg.

#### 4.2.3. $\epsilon$ Eridani

$\epsilon$  Eri was observed with ZDI by Jeffers et al. (2014) from 2007.08 to 2014.98. Jeffers et al. (2014) originally monitored  $\epsilon$  Eri with an average of 1.11 yr between observations until 2013.75. Jeffers et al. (2017) followed up these observations taking three observations in quick succession (approximately once a month) during its activity minimum. The magnetic geometry of  $\epsilon$  Eri at minimum activity is more complicated than the axisymmetric dipolar structure seen from the Sun and 61 Cyg A. The dipole component instead strengthens at activity maxima, producing the largest Alfvén radii when the chromospheric activity is highest. Figure 3 details the angular momentum-loss calculation for  $\epsilon$  Eri, and the average Alfvén radii are displayed in Figure 6.

The ZDI epochs of  $\epsilon$  Eri, using FM18, have an average torque of  $1.00 \times 10^{31}$  erg. With the sinusoidal fits, we find a larger average value of  $1.24 \times 10^{31}$  erg. The sinusoidal model suggests that the ZDI epochs have preferentially sampled

minima of activity, and therefore average to a lower torque. We calculate the torque using M15 and find a value of  $1.14 \times 10^{32}$  erg.

#### 4.2.4. $\xi$ Bootis A

The magnetic variability of  $\xi$  Boo A is unlike both 61 Cyg A and  $\epsilon$  Eri. It was observed with ZDI by Morgenthaler et al. (2012) from 2007.59 to 2011.07, with an average time between observations of half a year. The star hosts a persistent toroidal component with fixed polarity through all observations. This field contains a large fraction of the magnetic energy, shown by the mean field strength (gray dots) in the top panel of Figure 4 being much larger than the combined magnetic field strength (black dots). The total magnetic field appears to have short time variability. However, the second panel in Figure 4 appears to show a coherent pattern. With the limited data available, and no cyclic variability detected in other activity indicators, we fit a sinusoid to this slowly varying magnetic geometry.

Note that the data are best-represented with maxima occurring where there are no data. The existence and amplitude of the fit maxima are poorly constrained by the available data, and the sinusoidal fit is merely speculative. This leads the torque for the cycle, shown with a solid gray line in the bottom panel of Figure 4, to be much larger than the ZDI epochs, shown with black dots.

The average torque calculated for the ZDI epochs of  $\xi$  Boo A, using FM18, is  $2.31 \times 10^{31}$  erg. Averaging the sinusoidal model instead, we produce a torque of  $3.10 \times 10^{31}$  erg. The rotational evolution torque from M15 gives a value of  $7.48 \times 10^{32}$  erg.

#### 4.2.5. $\tau$ Bootis A

$\tau$  Boo A is currently the star most extensively monitored with ZDI (Donati et al. 2008; Fares et al. 2009; Mengel et al. 2016; Jeffers et al. 2018). From these studies, authors have found  $\tau$  Boo A to have a magnetic cycle with polarity reversals in phase with its chromospheric activity cycle of 120 day, as observed for the Sun and 61 Cyg A. Its mass-loss rate is not observationally constrained, but MHD simulations of the stellar wind surrounding  $\tau$  Boo A have been produced by Nicholson et al. (2016), using maps from some of the ZDI epochs considered here. We include these results in Figure 5, using blue squares to indicate their derived mass-loss rates and angular momentum-loss rates. We calculate the torque-averaged Alfvén radii associated with these simulated values using Equation (1), and display them in Figure 6 as light blue squares. For clarity, we also show a phase-folded version of Figure 5 in Appendix B (Figure 8).

Equation (3) predicts the efficiency of angular momentum loss to be low and dominated by the octupolar scaling. Both this work and the simulations of Nicholson et al. (2016) predict a torque-averaged lever arm of  $\sim 2R_*$ , which is much lower than the other stars in the sample (see Figure 6). We calculate the average torque from the ZDI epochs of  $\tau$  Boo A, using FM18, to be  $1.23 \times 10^{32}$  erg. The sinusoidal model has an average torque of  $1.32 \times 10^{32}$  erg. The torque from M15 is calculated to be  $3.67 \times 10^{32}$  erg.

### 4.3. Comparison of Torques

In Figure 7, the predictions of M15 for each star are shown with a range of Rossby numbers, using solid lines. We indicate the torque for each star in this model, at its respective Rossby

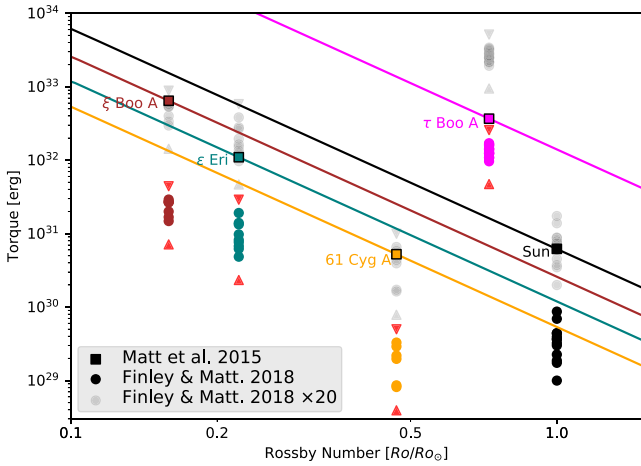


**Figure 7.** Angular momentum-loss rate vs. Rossby number. Solid lines represent the **M15** models for each star in our sample, over a range of Rossby numbers. Colored squares indicate the predicted value, given our calculated Rossby numbers in Table 1. The torques computed from ZDI epochs and the **FM18** braking law are shown with colored circles. The range of observational uncertainty in the prediction of **FM18** is shown with red limiting triangles. In all cases, the modeled torques using **FM18** are lower when compared to those from **M15**. Multiplication of the **FM18** torques by a factor of 20, shown in gray, brings the models toward rough agreement.

number from Table 1, with a colored square. The torques using **FM18** and the multiple ZDI epochs are shown with corresponding colored circles. As with Figure 6, typical uncertainties in observed rotation rates ( $\pm 10\%$ ), mass-loss rates ( $\pm 10\%$ ), and field strengths ( $\pm 1\text{G}$ ) of each star lead to errors in the predictions of Equations (1)–(3). The range of possible torques for each star, given these uncertainties, is indicated with red limits. While these uncertainties are significant, they are not large enough to affect any of our conclusions. For the dipole-dominated stars, the **FM18** torques appear systematically lower than those expected from **M15**, by a factor of roughly 10–30. Gray points show the result of multiplying all the **FM18** torques by a factor of 20, which brings all of the dipole-dominated stars into agreement.

However,  $\tau$  Boo A requires a much smaller factor of  $\sim 3$  to bring the two torques into agreement. Why the torques for  $\tau$  Boo A are in better agreement than the other stars’ is unknown. However, it is worth noting that the mass-loss rate for this star has not been measured. Instead, we used the average mass-loss rate from Nicholson et al. (2016), which is directly dependent on their choice of base wind density and temperature. Given that these quantities are not constrained well by observations, the mass-loss rates obtained from these simulations are effectively (although indirectly) assumed a priori. The same is true for all such models. If the true mass-loss rate is smaller than the value used here, the difference between torques may increase such that we may find a truly systematic value between the two methods for all of the sample stars. If the mass-loss rate of  $\tau$  Boo A were smaller, its torque might also become dipole-dominated like the rest of the sample.

## 5. Discussion

### 5.1. Systematic Differences between the **FM18** and **M15** Torques

For all the stars in our sample, the torques from **FM18** systematically predict lower angular momentum-loss rates when

compared to the rotational evolution torques from **M15**. This was also the case in Paper I, wherein we suggested a possible solution: the Sun may be in a low torque state at present. Given that all five stars here are low, and it seems unlikely that they would all be in a low state, a different explanation should be explored.

A systematic difference between the **FM18** and **M15** torques suggests there should be sources of underestimation in either the MHD modeling, the rotation-evolution models, or the observed properties of these stars. Paper I showed that, for the Sun, using the surface field strength leads to a torque estimate lower than those based on the open magnetic flux, by a factor of  $\sim 7$ . It remains unclear why this is so. It may be due to underestimation of field strengths in magnetograms, or to the coronal magnetic field becoming open much closer to the solar surface. Underprediction of the open magnetic flux will artificially reduce the braking torque, given the strong correlation shown by Réville et al. (2015).

There are likely also systematics in the magnetic field strengths obtained from ZDI. It is well-known that ZDI does not reconstruct all of the photospheric magnetic field due to flux cancellation effects (Reiners & Basri 2009; Lehmann et al. 2018; V. See et al. 2019a, in preparation). Recently, Lehmann et al. (2019) showed that ZDI sometimes underestimates the field strengths of the large-scale field components, i.e., the dipole, quadrupole, and octupole, by a factor of a few. Consequently, the spin-down torques will also be underestimated (see also the discussion by V. See et al. (2019b), in preparation). Additionally, the method used to calculate  $\mathcal{R}_{\text{dip}}$ ,  $\mathcal{R}_{\text{quad}}$ , and  $\mathcal{R}_{\text{oct}}$  from the results of ZDI may lead to underestimation of the strength of the magnetic field. Given the inherent non-axisymmetry of the ZDI fields, the values we calculate simply approximate the relative strengths of each component. Typically, the polar field values required for the Equation (3) will be larger than the global average field strength used in this work, but the effect this has is not large enough to modify our conclusions.

To increase the **FM18** torques by a factor of 20, for example, would require  $\sim 4\times$  greater average Alfvén radii (or  $\sim 26\times$  stronger dipole field strengths) than observed. Based on this, it is not clear whether this discrepancy can be explained with our current knowledge. Perhaps a combination of wind energetics (as discussed in Paper I for the open flux problem) and the systematics of ZDI might be able to explain the underprediction of the **FM18** torques versus those of **M15**.

### 5.2. The Impact of Magnetic Variability on Dynamical Torque Estimates

During each sequence of ZDI observations, our sample stars experience variability in their global magnetic field strength and topology. In Figure 6, the predicted average Alfvén radii for each ZDI epoch are plotted with a symbol that represents the governing topology in Equation (3). In the majority of cases, despite strengthening of the multipolar components, the dipole component governs the location of the torque-averaged Alfvén radius.

Similarly, V. See et al. (2019b, in preparation) show, for a large range of stars observed with ZDI, that Equation (3) predicts angular momentum-loss rates to be dominated by the dipolar component. However, for sufficiently high mass-loss rates and weak dipolar fields, as seen in this work with  $\tau$  Boo A, some stars can have multipolar-dominated wind braking. These stars possess low wind magnetizations and therefore have small average Alfvén radii. Note that, if the field strengths are underestimated, as discussed in Section 5.1, even  $\tau$  Boo A could then be dipole-dominated.

In general, the extrema of the torques from our ZDI stars are 0.5–1.9 times the average torque,  $\langle\tau_{\text{FM18}}\rangle$ . Using the subsampled solar epochs, we find the maximum torque to be  $2.3\langle\tau_{\text{FM18}}\rangle$ . If we instead consider the complete data set from Paper I, we find the maximum torque to be  $2.5\langle\tau_{\text{FM18}}\rangle$ , slightly larger than the subsampled value. Similarly, for other stars, we expect that the true amplitude of variability could be larger than represented by the sparse sampling. The next-largest amplitude of variation is found for  $\epsilon$  Eri, where the maximum torque is  $1.9\langle\tau_{\text{FM18}}\rangle$  in the ZDI epoch of 2013.75. The smallest amplitude of torque variability belongs to  $\tau$  Boo A, which has a minimum torque of  $0.7\langle\tau_{\text{FM18}}\rangle$ , and a maximum torque of  $1.3\langle\tau_{\text{FM18}}\rangle$ .

We find results gained by subsampling the solar data set produce average torques that are dependent on the selected magnetogram epochs. For example, by changing the length of the available data set and selecting a different set of 13 epochs, we can find average torques of  $0.3\text{--}0.4 \times 10^{30}$  erg, due to preferentially selecting epochs from cycle 24 or 23, respectively (with 23 being stronger than 24). Equally, reducing the number of epochs used in the data set from 13 to 6 can change the average torque to a similar degree, but also generally decreases the maximum torque to values comparable to those of the ZDI stars ( $\sim 2\langle\tau_{\text{FM18}}\rangle$ ). Reducing the number of epochs further can lead to extreme values in the average torques from  $0.1$  to  $0.8 \times 10^{30}$  erg, due to short-term variability in the data set.

Estimates like this for the Sun hint at how a restricted data set may bias the time-varying torque estimates for other stars. Based on the results from this work, it appears that stellar wind variability has a much smaller effect than is required to remedy the discrepancy between stellar wind torques and their long-time rotation evolution counterparts. However, variability can confuse the issue and should be accounted for in future works.

### 5.3. Establishing the Timescales of Variability

In this work, we are able to calculate the time-varying torque for four stars with a cadence of  $\sim 1\text{--}2$  yr, over a period of nearly a decade. The torque’s variation due to magnetic variability can be thought of as an uncertainty in estimating the current average torque for a given star based on a single observation. In Paper I, the variability of the solar wind was examined on a much shorter ( $\sim 27$  day) cadence over two decades, so we were able to estimate the torque more continuously. Even so, variability in the solar wind is observed on still-shorter timescales. These day-to-day and hour-to-hour variations in the solar wind are averaged in our calculations in Paper I, in order to better represent the global wind when using observations from a single in situ location. The impact such fluctuations have on the 27 day torque averages remains an open question.

On timescales of centuries to millennia (still shorter than the braking timescale), there is also evidence for further magnetic variability. For the Sun, indirect methods of detecting this variability, such as examining the concentration of cosmogenic radionuclides ( $^{14}\text{C}$ ,  $^{10}\text{Be}$ , etc.) in tree trunks or polar ice cores, have been successful at recovering changes in the magnetic field over the last millennium (Wu et al. 2018). For other stars, we are unable to examine the evolution of their magnetism for longer than current observations allow. However, the observed spread of magnetic activity indicators (e.g., X-rays;

Wright et al. 2011) around their secular trends could be caused by variability (as opposed to true differences in stars’ average properties). It is still not clear how such long-term variability may skew our current evaluation of stellar braking torques.

## 6. Conclusion

In this paper, we have quantified the effect of observed magnetic variability on the predicted angular momentum-loss rates for four Sun-like stars. Our sample stars have all been repeatedly observed with ZDI, which provides information on the topology of the magnetic field. This information is then combined with estimates of their mass-loss rates from studies of astrospheric Ly $\alpha$ , as well as a relationship for the stellar wind braking given by FM18. We compare these time-varying estimates of the angular momentum-loss rate to the long-time-averaged value predicted by M15, a rotational evolution model.

We find that, similarly to what was found for the Sun in Paper I, the angular momentum-loss rates predicted vary significantly (roughly 0.5–1.5 times their average values), such that torques calculated using single observational epochs can differ from the decadal average torque on the star. This represents an uncertainty when calculating torques for stars with single epochs of observation.

Our calculated angular momentum-loss rates based on FM18 are found to be systematically lower than the long-time-averaged torques required by M15. We do not know the origin of this discrepancy, but it could be due (at least in part) to several factors: the open flux problem, whereby wind models currently underpredict the observed open magnetic flux for the Sun; problems with observed parameters, such as the potential systematic effects from the ZDI technique in recovering the correct field strengths (Lehmann et al. 2019); problems with rotation-evolution models; or longer-term variability in the torque. Such longer-term variability has the potential to affect our predictions for the long-time ( $\sim 10\text{--}100$  Myr) average torque required by rotation evolution models.

The authors thank the anonymous referee for a constructive report that helped to improve this work. We are also thankful for the ongoing efforts of the ZDI community for making work like this possible. In particular, we thank Rim Fares and Matthew Mengel for providing the data required to compute the magnetic properties of  $\tau$  Boo A. We thank the SDO/HMI and SOHO/MDI consortia for providing magnetograms of the Sun. We thank the ACE/MAG and ACE/SWEPAM instrument teams, along with the ACE Science Center, for providing in situ plasma and magnetic field measurements of the solar wind. This project has received funding from the European Research Council (ERC) under the European Unions Horizon 2020 Research and Innovation Programme (grant agreement No. 682393 AWESoMeStars). Figures within this work are produced using the Python package matplotlib (Hunter 2007).

## Appendix A Sun-as-a-star Data

Table 3 displays the selected magnetogram observations from SOHO/MDI and SDO/HMI used in Figure 1, along with the results of the angular momentum-loss calculation using

**Table 3**  
Solar Magnetic Properties and Angular Momentum-loss Results

Star Name	Magnetogram Epoch (Instrument)	$B_*$ (G)	$\mathcal{R}_{\text{dip}} \equiv B_{\text{dip}}/B_*$	$\mathcal{R}_{\text{quad}} \equiv B_{\text{quad}}/B_*$	$\mathcal{R}_{\text{oct}} \equiv B_{\text{oct}}/B_*$	$\langle R_A \rangle / R_*$	$\tau_{\text{FM18}} (\times 10^{30} \text{ erg})$	$\tau_{\text{M15}} (\times 10^{30} \text{ erg})$	$\tau_{\text{M15}} \langle \tau_{\text{FM18}} \rangle$
Sun	1996.76(MDI)	8.0	0.38	0.11	0.51	5.9	0.87	6.20	16.55
	1998.49(MDI)	7.5	0.37	0.18	0.45	6.0	0.69	...	...
	2000.65(MDI)	5.7	0.22	0.16	0.62	4.3	0.30	...	...
	2002.37(MDI)	8.1	0.21	0.32	0.47	5.0	0.39	...	...
	2004.16(MDI)	6.6	0.27	0.06	0.67	5.7	0.32	...	...
	2005.88(MDI)	6.1	0.32	0.15	0.53	5.3	0.44	...	...
	2007.59(MDI)	5.2	0.34	0.09	0.57	5.3	0.37	...	...
	2009.31(MDI)	3.9	0.38	0.06	0.56	5.7	0.23	...	...
	2011.18(HMI)	3.1	0.30	0.33	0.37	4.3	0.17	...	...
	2012.89(HMI)	2.1	0.23	0.30	0.47	3.2	0.10	...	...
	2014.61(HMI)	4.1	0.21	0.50	0.29	4.1	0.19	...	...
	2016.33(HMI)	5.7	0.31	0.29	0.40	5.2	0.36	...	...
	2018.12(HMI)	5.2	0.38	0.07	0.55	5.4	0.44	...	...

both the formulae from FM18 and M15, where symbols have the same meaning as in Table 2.

### Appendix B Alternative View of $\tau$ Bootis A Data

Here, we show the result of phase-folding the data from Figure 5 (Figure 8).  $\tau$  Boo A is estimated to have a short

magnetic cycle period of around 240 days, which is in-phase with its 120 day chromospheric activity cycle. We phase-fold the data for  $\tau$  Boo A on the timescale of its chromospheric cycle, rather than its magnetic cycle, as our predictions do not consider the polarity of the magnetic field. Given cycle-to-cycle variation in length and strength, fitting a simple sinusoid does not fit all of the magnetic variation well.



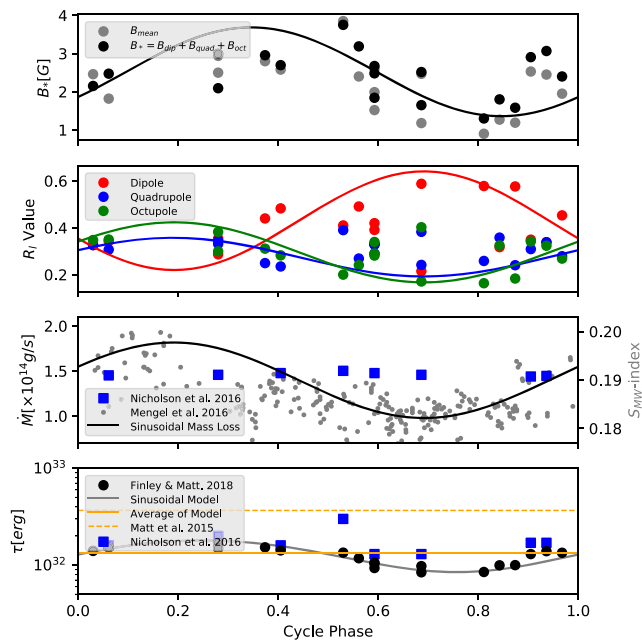


**Figure 8.** Same as Figure 5, with the data phase folded into the 120 day chromospheric cycle.

### ORCID iDs

Adam J. Finley <https://orcid.org/0000-0002-3020-9409>

Sean P. Matt <https://orcid.org/0000-0001-9590-2274>

### References

- Amard, L., Palacios, A., Charbonnel, C., Gallet, F., & Bouvier, J. 2016, *A&A*, **587**, A105
- Babcock, H. 1961, *ApJ*, **133**, 572
- Babcock, H. D. 1959, *ApJ*, **130**, 364
- Baines, E. K., & Armstrong, J. T. 2011, *ApJ*, **744**, 138
- Baliunas, S., Donahue, R., Soon, W., et al. 1995, *ApJ*, **438**, 269
- Barnes, S. A. 2003, *ApJ*, **586**, 464
- Barnes, S. A. 2007, *ApJ*, **669**, 1167
- Barnes, S. A. 2010, *ApJ*, **722**, 222
- Barnes, S. A., & Kim, Y.-C. 2010, *ApJ*, **721**, 675
- Boeche, C., & Grebel, E. 2016, *A&A*, **587**, A2
- Boro Saikia, S., Jeffers, S., Morin, J., et al. 2016, *A&A*, **594**, A29
- Boro Saikia, S., Lueftinger, T., Jeffers, S., et al. 2018, *A&A*, **620**, L11
- Borsa, F., Scandariato, G., Rainer, M., et al. 2015, *A&A*, **578**, A64
- Bouvier, J., Matt, S. P., Mohanty, S., et al. 2014, in *Protostars and Planets VI*, ed. H. Beuther et al. (Tucson, AZ: Univ. Arizona Press), 433
- Boyajian, T. S., von Braun, K., van Belle, G., et al. 2013, *ApJ*, **771**, 40
- Brown, A. G., Vallenari, A., Prusti, T., et al. 2016, *A&A*, **595**, A2
- Brown, S., Donati, J.-F., Rees, D., & Semel, M. 1991, *A&A*, **250**, 463
- Brun, A., Browning, M., Dikpati, M., Hotta, H., & Strugarek, A. 2015, *SSRv*, **196**, 101
- Brun, A. S., & Browning, M. K. 2017, *LRSP*, **14**, 4
- Caligari, P., Moreno-Insertis, F., & Schussler, M. 1995, *ApJ*, **441**, 886
- Cranmer, S. R., & Saar, S. H. 2011, *ApJ*, **741**, 54
- Delorme, P., Cameron, A. C., Hebb, L., et al. 2011, *MNRAS*, **413**, 2218
- DeRosa, M., Brun, A., & Hoeksema, J. 2012, *ApJ*, **757**, 96
- Donahue, R. A., Saar, S. H., & Baliunas, S. L. 1996, *ApJ*, **466**, 384
- Donati, J.-F., & Brown, S. 1997, *A&A*, **326**, 1135
- Donati, J.-F., & Landstreet, J. 2009, *ARA&A*, **47**, 333
- Donati, J.-F., Moutou, C., Fares, R., et al. 2008, *MNRAS*, **385**, 1179
- Donati, J.-F., Semel, M., Carter, B. D., Rees, D., & Cameron, A. C. 1997, *MNRAS*, **291**, 658
- Donati, J.-F., Semel, M., & Praderie, F. 1989, *A&A*, **225**, 467
- Eberhard, G., & Schwarzschild, K. 1913, *ApJ*, **38**, 292
- Egeland, R., Soon, W., Baliunas, S., et al. 2017, *ApJ*, **835**, 25
- Fan, Y. 2008, *ApJ*, **676**, 680
- Fares, R., Donati, J.-F., Moutou, C., et al. 2009, *MNRAS*, **398**, 1383
- Finley, A. J., & Matt, S. P. 2017, *ApJ*, **845**, 46
- Finley, A. J., & Matt, S. P. 2018, *ApJ*, **854**, 78
- Finley, A. J., Matt, S. P., & See, V. 2018, *ApJ*, **864**, 125
- Fisher, G., Fan, Y., Longcope, D., Linton, M., & Pevtsov, A. 2000, *SoPh*, **192**, 119
- Fuhrmann, K. 2004, *AN*, **325**, 3
- Gallet, F., & Bouvier, J. 2013, *A&A*, **556**, A36
- Gallet, F., & Bouvier, J. 2015, *A&A*, **577**, A98
- Garraffo, C., Drake, J. J., & Cohen, O. 2016, *A&A*, **595**, A110
- Gilliland, R. 1986, *ApJ*, **300**, 339
- Gray, D. F., Baliunas, S. L., Lockwood, G., & Skiff, B. A. 1996, *ApJ*, **465**, 945
- Gunn, A., Mitrou, C., & Doyle, J. 1998, *MNRAS*, **296**, 150
- Hall, J. C., Lockwood, G., & Skiff, B. A. 2007, *AJ*, **133**, 862
- Hartmann, L., Schmidtke, P., Davis, R., et al. 1979, *ApJL*, **233**, L69
- Hartmann, L. W., & Noyes, R. W. 1987, *ARA&A*, **25**, 271
- Hick, P., & Jackson, B. 1994, *AdSpR*, **14**, 135
- Hunter, J. D. 2007, *CSE*, **9**, 90
- Janson, M., Reffert, S., Brandner, W., et al. 2008, *A&A*, **488**, 771
- Jardine, M., Vidotto, A., van Ballegoijen, A., et al. 2013, *MNRAS*, **431**, 528
- Jeffers, S., Boro Saikia, S., Barnes, J., et al. 2017, *MNRAS*, **471**, L96
- Jeffers, S., Mengel, M., Moutou, C., et al. 2018, *MNRAS*, **479**, 5266
- Jeffers, S., Petit, P., Marsden, S., et al. 2014, *A&A*, **569**, A79
- Keppens, R., & Goedbloed, J. 1999, *A&A*, **343**, 251
- Kervella, P., Mérand, A., Pichon, B., et al. 2008, *A&A*, **488**, 667
- Landin, N., Mendes, L., & Vaz, L. 2010, *A&A*, **510**, A46
- Lean, J., Cook, J., Marquette, W., & Johansson, A. 1998, *ApJ*, **492**, 390
- Lehmann, L. T., Hussain, G. A. J., Jardine, M. M., Mackay, D. H., & Vidotto, A. A. 2019, *MNRAS*, **483**, 5246
- Lehmann, L. T., Jardine, M. M., Mackay, D. H., & Vidotto, A. A. 2018, *MNRAS*, **478**, 4390
- Mamajek, E. E., & Hillenbrand, L. A. 2008, *ApJ*, **687**, 1264
- Marsden, S., Petit, P., Jeffers, S., et al. 2014, *MNRAS*, **444**, 3517
- Matt, S., & Pudritz, R. E. 2008, *ApJ*, **678**, 1109
- Matt, S. P., Brun, A. S., Baraffe, I., Bouvier, J., & Chabrier, G. 2015, *ApJL*, **799**, L23
- Matt, S. P., MacGregor, K. B., Pinsonneault, M. H., & Greene, T. P. 2012, *ApJL*, **754**, L26
- McComas, D., Angold, N., Elliott, H., et al. 2013, *ApJ*, **779**, 2
- McComas, D., Barraclough, B., Funsten, H., et al. 2000, *JGRA*, **105**, 10419
- McComas, D., Elliott, H., Schwadron, N., et al. 2003, *GeoRL*, **30**, 1517
- Meibom, S., Barnes, S. A., Platais, I., et al. 2015, *Natur*, **517**, 589
- Meibom, S., Mathieu, R. D., & Stassun, K. G. 2009, *ApJ*, **695**, 679
- Mengel, M., Fares, R., Marsden, S., et al. 2016, *MNRAS*, **459**, 4325
- Mestel, L. 1968, *MNRAS*, **138**, 359
- Metcalfe, T., Buccino, A. P., Brown, B., et al. 2013, *ApJL*, **763**, L26
- Mittag, M., Robrade, J., Schmitt, J., et al. 2017, *A&A*, **600**, A119
- Morgenthaler, A., Petit, P., Saar, S., et al. 2012, *A&A*, **540**, A138
- Neugebauer, M., Liewer, P., Smith, E., Skoug, R., & Zurbuchen, T. 2002, *JGRA*, **107**, 1488
- Nicholson, B., Vidotto, A., Mengel, M., et al. 2016, *MNRAS*, **459**, 1907
- Noyes, R., Hartmann, L., Baliunas, S., Duncan, D., & Vaughan, A. 1984, *ApJ*, **279**, 763
- Ossendrijver, M. 2003, *A&ARv*, **11**, 287
- Owens, M. J., Crooker, N., & Lockwood, M. 2011, *JGRA*, **116**, A04111
- Pantolmos, G., & Matt, S. P. 2017, *ApJ*, **849**, 83
- Parker, E. N. 1955, *ApJ*, **121**, 491
- Parker, E. N. 1958, *ApJ*, **128**, 664
- Petit, P., Dintrans, B., Morgenthaler, A., et al. 2009, *A&A*, **508**, L9
- Petit, P., Dintrans, B., Solanki, S., et al. 2008, *MNRAS*, **388**, 80
- Pinto, R. F., Brun, A. S., Jouve, L., & Grappin, R. 2011, *ApJ*, **737**, 72
- Pizzolato, N., Maggio, A., Micela, G., Sciortino, S., & Ventura, P. 2003, *A&A*, **397**, 147
- Pneuman, G., & Kopp, R. A. 1971, *SoPh*, **18**, 258
- Ramesh, K. 2010, *ApJL*, **712**, L77
- Reiners, A., & Basri, G. 2009, *A&A*, **496**, 787
- Réville, V., Brun, A. S., Matt, S. P., Strugarek, A., & Pinto, R. F. 2015, *ApJ*, **798**, 116
- Réville, V., Folsom, C. P., Strugarek, A., & Brun, A. S. 2016, *ApJ*, **832**, 145
- Robrade, J., Schmitt, J., & Favata, F. 2012, *A&A*, **543**, A84
- Rüdi, I., Solanki, S., Mathys, G., & Saar, S. 1997, *A&A*, **318**, 429
- Schrijver, C., Cote, J., Zwaan, C., & Saar, S. 1989, *ApJ*, **337**, 964
- Schrijver, C. J., & Liu, Y. 2008, *SoPh*, **252**, 19
- Schwenn, R. 2006, *SSRv*, **124**, 51
- See, V., Jardine, M., Vidotto, A., et al. 2016, *MNRAS*, **462**, 4442

- Semel, M. 1989, *A&A*, **225**, 456
- Skumanich, A. 1972, *ApJ*, **171**, 565
- Solanki, S., Krivova, N., Schüssler, M., & Fligge, M. 2002, *A&A*, **396**, 1029
- Song, I., Caillault, J.-P., y Navascués, D. B., Stauffer, J. R., & Randich, S. 2000, *ApJL*, **533**, L41
- Spruit, H. C. 1981, *A&A*, **98**, 155
- Stelzer, B., & Neuhäuser, R. 2001, *A&A*, **377**, 538
- Sun, X., Hoeksema, J. T., Liu, Y., & Zhao, J. 2015, *ApJ*, **798**, 114
- Takeda, G., Ford, E. B., Sills, A., et al. 2007, *ApJS*, **168**, 297
- Testa, P., Saar, S. H., & Drake, J. J. 2015, *RSPTA*, **373**, 20140259
- Toner, C., & Gray, D. F. 1988, *ApJ*, **334**, 1008
- Van Saders, J. L., & Pinsonneault, M. H. 2013, *ApJ*, **776**, 67
- Vidotto, A., Gregory, S., Jardine, M., et al. 2014, *MNRAS*, **441**, 2361
- Walker, G. A., Croll, B., Matthews, J. M., et al. 2008, *A&A*, **482**, 691
- Wang, Y.-M., Lean, J., & Sheeley, N. 2000, *GeoRL*, **27**, 505
- Wang, Y.-M., & Sheeley, N. 1990, *ApJ*, **355**, 726
- Webb, D. F., & Howard, R. A. 1994, *JGRA*, **99**, 4201
- Webb, D. F., & Howard, T. A. 2012, *LRSP*, **9**, 3
- Weber, E. J., & Davis, L. 1967, *ApJ*, **148**, 217
- Wenzler, T., Solanki, S., Krivova, N., & Fröhlich, C. 2006, *A&A*, **460**, 583
- Wilson, O. 1978, *ApJ*, **226**, 379
- Wolff, S., & Simon, T. 1997, *PASP*, **109**, 759
- Wood, B. E. 2004, *LRSP*, **1**, 1
- Wood, B. E., & Linsky, J. L. 1998, *ApJ*, **492**, 788
- Wood, B. E., Müller, H.-R., Zank, G. P., & Linsky, J. L. 2002, *ApJ*, **574**, 412
- Wood, B. E., Müller, H.-R., Zank, G. P., Linsky, J. L., & Redfield, S. 2005, *ApJL*, **628**, L143
- Wright, N. J., Drake, J. J., Mamajek, E. E., & Henry, G. W. 2011, *ApJ*, **743**, 48
- Wu, C. J., Usoskin, I., Krivova, N., et al. 2018, *A&A*, **615**, A93
- Zeeman, P. 1897, *Natur*, **55**, 347

## 4.6 Additional Information

Here I would like to propose an adjustment to the braking laws based on my work on the Sun. Additionally, I provide some thoughts/discussion on the angular momentum-loss due to CMEs, and how the braking laws can be applied to rotation-evolution calculations.

### 4.6.1 Empirical Correction to the Surface Field Formulation

One solution to the significant differences between the two semi-analytic formulae when applied to the Sun, is that some physical effect is causing the coronal magnetic field to open much closer to the Sun than the MHD models predict. Thus leading to an increase in open magnetic flux in the heliosphere. In Figure 4.8, I compare the source surface radius  $R_{ss}$  from the Potential Field Source Surface (PFSS) model (see Appendix A), the opening radius  $R_o$  as defined in Sections 3.3 and 3.4, and the Alfvén radius  $R_A$ . For simplicity I assume a dipolar magnetic field (as the solar wind in Section 4.3 is generally dipole-dominated), then  $R_o$  is given by,

$$\frac{R_o}{R_*} = \frac{\phi_*}{\phi_{open}}, \quad (4.3)$$

where  $\phi_*$  is the magnetic flux at the stellar surface and  $\phi_{open}$  is the open magnetic flux in the wind. In Figure 4.8, the magnetic flux is shown in log-log space, which for the dipole decays as  $1/r$  (shown with a dashed line). The decay of the potential dipole intersects the value of  $\phi_{open}$  at  $R_o$ . Note in the simulations, the magnetic flux transitions between these regimes in a smooth manner, and  $R_o$  is simply a useful mathematical construct. The relation between  $R_o$  and  $R_A$  is governed by the energetics in the simulations, typically I find  $R_o/R_A \sim 0.3$ .

$R_{ss}$  and  $R_o$  are distinctly different but related quantities, which can be related algebraically (for a dipole) by,

$$R_o = \frac{2R_{ss}^3 + 1}{3R_{ss}^2}. \quad (4.4)$$

Therefore,  $R_o/R_{ss} \sim 2/3$  (see the Appendix of See et al. 2018). Using this relation,  $R_o$  can be approximated by considering the size of  $R_{ss}$  needed to reproduce the observed

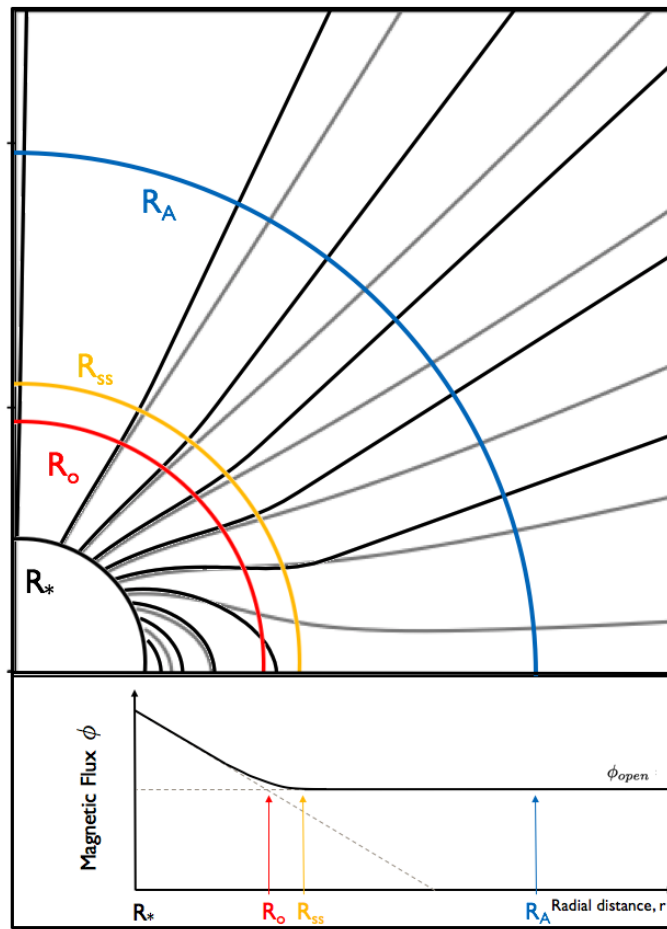


**Figure 4.8:** Schematic depiction of the radii of interest (not to scale). Field lines from an MHD simulation and a PFSS model are shown in grey and black, respectively. The opening radius  $R_o$  is given by the radius at which the potential field flux matches the open flux of the MHD model. The source surface radius  $R_{ss}$  is the distance whereby the coronal field is completely radial in the PFSS model. Generally,  $R_{ss}$  is larger than  $R_o$ , and for a dipole typically  $R_{ss}/R_o \sim 3/2$ . In the MHD simulations the Alfvén radius  $R_A$  is always larger than both of these radii, and located in the “open” magnetic field. Note that in the 2.5D MHD simulations the  $R_A$  is non spherical. However for this schematic  $R_A$  is drawn in-line with the one-dimensional scaling relations (i.e. representing an average value).

$\phi_{open}$  from in-situ measurements, given the surface field measurements and a PFSS model. Knowing that  $R_A$  from the open flux formulation is around  $10 - 15R_\odot$ , the value of  $R_o/R_A$  needs to be  $\sim 0.1$  to get a better agreement between the semi-analytic formulae, i.e. the surface magnetic field must open around  $R_{ss} = 1.5 - 1.9R_\odot$ , which is very close to the stellar surface (below the classical  $R_{ss} = 2.5R_\odot$ ). This introduces some issues, as a decreased  $R_o$  will increase the importance of the higher order magnetic geometries which I have ignored in this analysis.

To investigate the discrepancy further, I recall the result from Pantolmos and Matt

(2017),

$$\left(\frac{R_A}{R_*}\right)^{2l+1} \left(\frac{R_o}{R_A}\right)^{2l} = \Upsilon \frac{v_{esc}}{v(R_A)}, \quad (4.5)$$

which typically is simplified with  $v_{esc}/v(R_A) = K_q(R_A/R_*)^q$  and  $R_o/R_A = \text{const}$ , from which the  $R_A$  scaling with  $\Upsilon$  is derived (see Section 2.5.4). Instead if I keep these factors,

$$\frac{R_A}{R_*} = \left( \Upsilon \frac{v_{esc}}{v(R_A)} \left(\frac{R_A}{R_o}\right)^{2l} \right)^{\frac{1}{2l+2}}, \quad (4.6)$$

the differences in our  $K_s$  and  $m_s$  from simulations and those required to match observations can be explained by the behaviour of the wind acceleration and relationship between  $R_A$  and  $R_o$ . I explored many different avenues to correct for these terms, primarily through producing an updated relationship for  $R_A/R_o \propto \Upsilon$ , however I believe this quantity is connected to the wind acceleration, and so a fundamental correction is at present unavailable. I instead show a rudimentary correction factor which simply accounts for the difference between the two semi-analytic formulae as a function of  $\Upsilon$ ,

$$\frac{R_{A,open}}{R_{A,surf}} = K_{corr} \Upsilon^{m_{corr}}. \quad (4.7)$$

This fit is shown in Figure 4.9, which produces  $K_{corr} = 5.6$  and  $m_{corr} = -0.155$ . Notice that there is structure in this diagram that is not explained by a power law fit in  $\Upsilon$ . Regardless, the empirically “corrected” semi-analytic formula is then,

$$\frac{R_{A,new}}{R_*} = K_s K_{corr} \Upsilon^{m_s + m_{corr}}, \quad (4.8)$$

and I have plotted the updated solar wind prediction (based on the surface magnetic field and mass-loss rate) in Figure 4.10 with a purple line. This new relation is able to reproduce some, but not all, of the solar cycle variation. It remains to be understood how this correction factor fits together in the framework of the 1D semi-analytic wind theory.

## 4.6.2 Transient Mechanisms of Angular Momentum-Loss

For the work in Section 4.3, I included the ICMEs in the in-situ observations primarily because the role they play in removing angular momentum is unknown. Only a few works

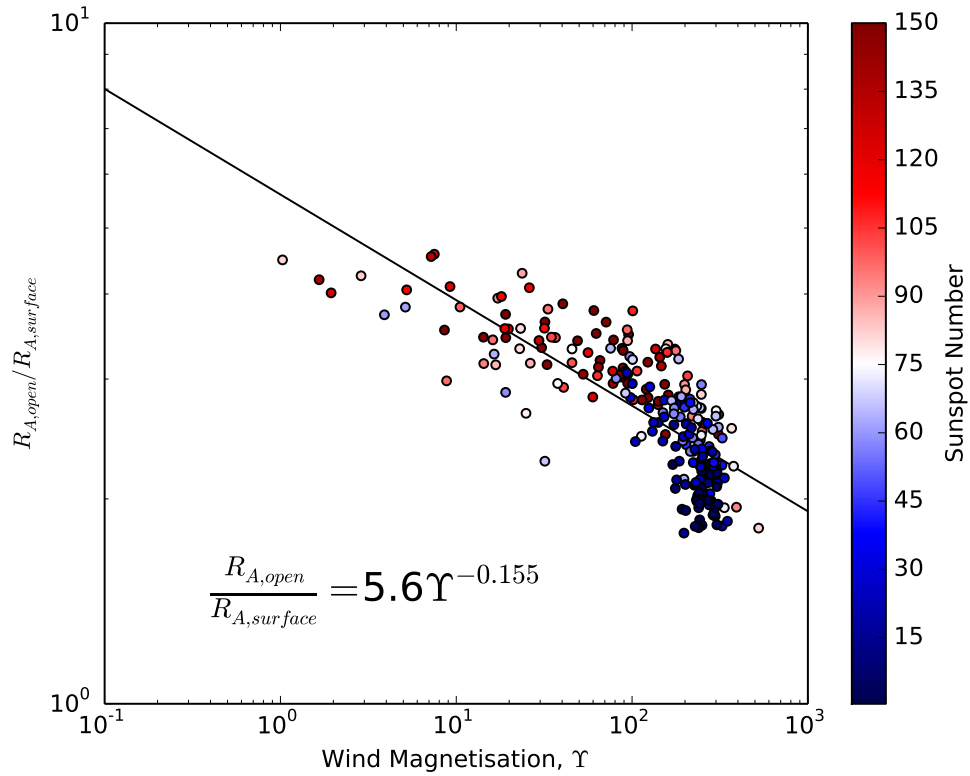


**Figure 4.9:** Correction factor, which is a proxy for the differences in opening radii (and wind acceleration) scaling between observation and simulation, versus wind magnetisation  $\Upsilon$ . Data points are coloured by sunspot number, which is a proxy for magnetic activity.

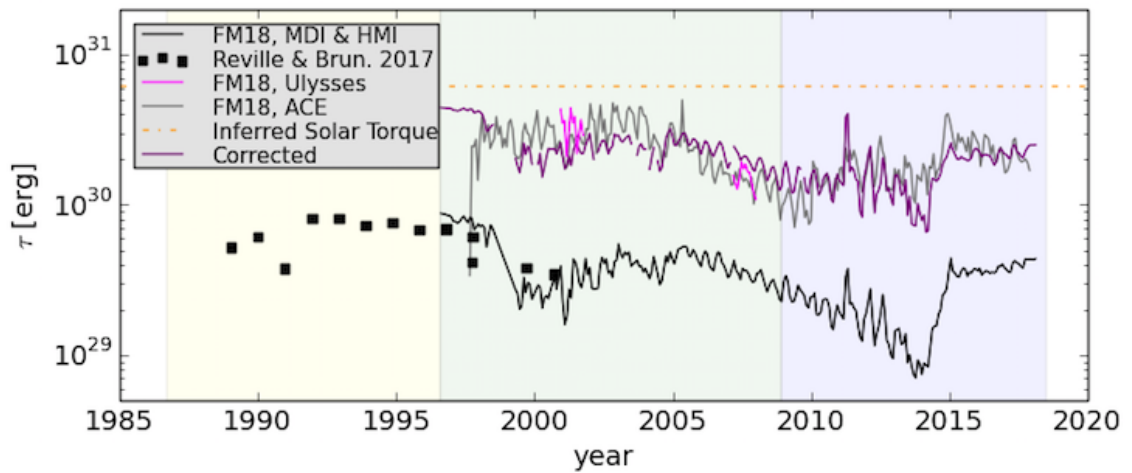


**Figure 4.10:** Solar wind torque predictions from Figure 1 in Section 4.3, now with an updated surface torque formulation shown in purple.

have attempted to study the properties of CMEs in removing angular momentum (e.g. Aarnio et al. 2012; Cranmer et al. 2017). The main difficulty in studying this process is the uncertainty surrounding the triggering of CMEs, meaning that MHD simulations have

to make immediate assumptions that dramatically affect the outcome. In terms of the 1D semi-analytic wind theory, CMEs could be thought of as a steady wind when averaged over long enough timescales, such a wind would have a high wind acceleration which from previous works is understood to reduce the effectiveness of the angular momentum-loss process. Following this logic, it is therefore likely that CMEs contribute little to angular momentum-loss rate, even if they contribute strongly to the global mass-loss rate for younger stars. The caveat being, that if the material in CMEs can maintain a strong magnetic connection to the Sun, as they travel into interplanetary space, then they carry a significant amount of mass for angular momentum to be exchanged with.

A slightly different perspective may be to consider the second order effects of CMEs. When a CME is released from the low corona, it likely forces open closed regions of magnetic field that once were above/near it. Solar wind could now travel along these previous closed field lines and increase the angular momentum-loss rate through the additional mass and open flux, though this would likely be on a short timescale. As this is a time-dependent effect, it is not captured by current steady-state wind models. Future works could address this with time-dependent MHD simulations, however there first needs to be better observational constraints on the initial conditions.

### 4.6.3 Application to Rotation Period Evolution

Consider the rotation period evolution of a one solar mass star, whose structural evolution is given by the models of Baraffe et al. (2015). Then the stellar wind angular momentum-loss rate can be predicted by the braking law from Sections 3.3 and 3.4 when supplied with the mass-loss rate and surface magnetic fields strengths of the dipole, quadrupole, and octupole components. From the work of See et al. (2019a), using many stars with magnetic field imaged by the ZDI technique, their are fit relations for how the strength of large-scale field components vary versus Rossby number (rotation period). These are as follows:

$$B_{dip} = \begin{cases} 137\text{G}, & \text{for } P < 0.64 \text{ days,} \\ 137\text{G} \left( \frac{P}{0.64 \text{ days}} \right)^{-1.31}, & \text{for } P \geq 0.64 \text{ days,} \end{cases} \quad (4.9)$$

$$B_{quad} = \begin{cases} 73G, & \text{for } P < 0.64 \text{ days,} \\ 73G \left( \frac{P}{0.64 \text{ days}} \right)^{-1.25}, & \text{for } P \geq 0.64 \text{ days,} \end{cases} \quad (4.10)$$

$$B_{oct} = \begin{cases} 65G, & \text{for } P < 0.64 \text{ days,} \\ 65G \left( \frac{P}{0.64 \text{ days}} \right)^{-1.37}, & \text{for } P \geq 0.64 \text{ days,} \end{cases} \quad (4.11)$$

where I have converted their Rossby number scaling to a period scaling for the solar convective turnover timescale of 12.7 days. Additionally, from the work of Ó Fionnagáin and Vidotto (2018), the mass-loss rates for solar mass stars are predicted to follow,

$$\dot{M} = \begin{cases} 1.0 \times 10^{15} \text{ g/s,} & \text{for } P < 2.8 \text{ days,} \\ 1.0 \times 10^{15} \text{ g/s} \left( \frac{P}{2.8 \text{ days}} \right)^{-1.4}, & \text{for } 2.8 \text{ days} < P < 20 \text{ days,} \\ 6.4 \times 10^{13} \text{ g/s} \left( \frac{P}{20 \text{ days}} \right)^{-7.7}, & \text{for } P \geq 20 \text{ days,} \end{cases} \quad (4.12)$$

where I have added the condition for  $P < 2.8$  days, as this was unconstrained in their work. By combining all of these ingredients, including the correction to my braking law from Section 4.6.1, I produce a rotation period evolution model in Figure 4.11. This shows the evolution of rotation for an initially fast, medium, and slow rotator, and the corresponding angular momentum-loss rates (wind torque) from the model. The tracks are coloured by the component of the magnetic field which is governing the angular momentum-loss rate, according to my braking law. It can be seen that the angular momentum-loss rate is stronger than Skumanich for a larger period of the main sequence, and so to reach the same rotation rate at the age of the Sun, the angular momentum-loss rate must decrease to the MHD model value (using open flux). The mass-loss rate relation from Ó Fionnagáin and Vidotto (2018) plays a vital role in creating this feature, with the “break” in slope occurring at a period of 20 days, as found in equation (4.12). Note, this is just an explorative example of what can be done in future with a higher degree of rigour.



## 4.7 Summary

In this Chapter, I applied the braking laws from Chapter 3 to the Sun and four other Sun-like stars in order to examine the effect of magnetic variability on their angular momentum-loss rates. I found that the formula using  $\Upsilon$  (surface field strength) significantly under-predicts their angular momentum-loss rates, when compared with rotation-evolution models, by a factor of around 20. For the Sun, there is an additional discrepancy when calculating the angular momentum-loss rate from the open magnetic flux (instead of using the surface field strength), where the  $\Upsilon_{open}$  formula predicts a value that is a factor of  $\sim 7$  larger than using the  $\Upsilon$  formula. Therefore, there is only a factor of  $\sim 3$  difference between the  $\Upsilon_{open}$  formula and the value found using rotation evolution models. The reason for the general under-prediction of angular momentum-loss rates could be a combination of factors, from the under-estimation of mass-loss rates, magnetic field strengths, or the amount of surface flux that is being opened to form the stellar wind.

Unlike the other stars, my calculations for the Sun are over-constrained and so it is interesting that none of the three methods agree on a value. Using the in-situ open magnetic flux in the solar wind ( $\Upsilon_{open}$  formula) removes many of the uncertainties in how the magnetic field is opened (compared with using  $\Upsilon$ ), and yet the value I calculate is significantly lower than the rotation evolution models. It is interesting to entertain the possibility that the  $\Upsilon_{open}$  value is correct, and it is in fact the rotation evolution models that need to be updated. There is some observational support for a weakened angular momentum-loss rate for older main sequence stars (see van-Saders et al. 2016; Metcalfe et al. 2016), though this Chapter has only constrained the solar angular momentum-loss rate for  $\sim 20$  years and the timescale for the Sun's rotation evolution is around 10-100 million years.

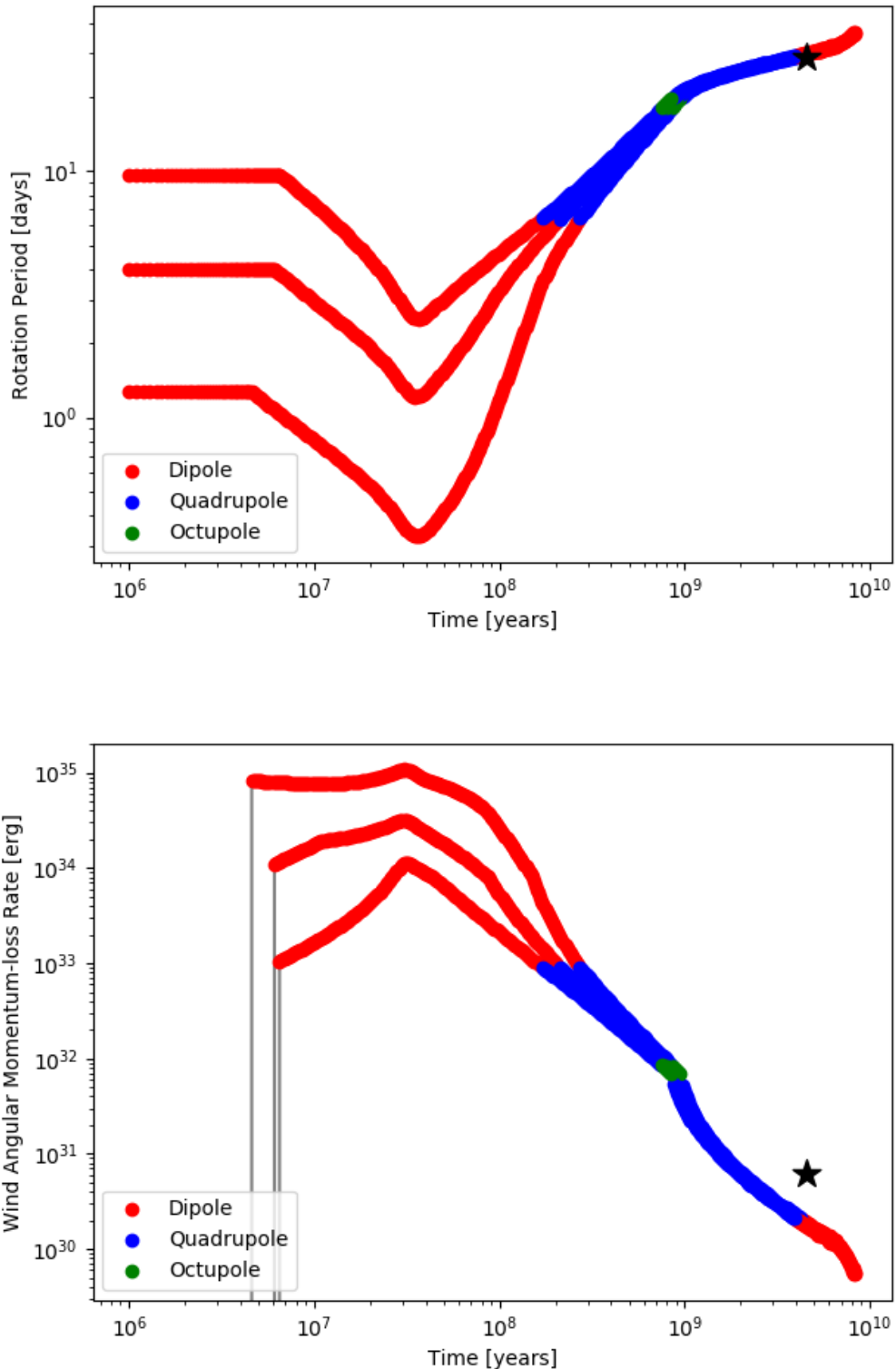


**Figure 4.11:** Top: Rotation period evolution of an initially fast (0.1 day), medium (4 days), and slow (10 days) rotator, using the corrected braking law from Section 4.6.1, mass loss rates from Ó Fionnagáin and Vidotto (2018), and magnetic field strengths from See et al. (2019a). Each track is coloured by the geometry in the braking law that is governing the spin-evolution, dipole (red), quadrupole (blue), and octupole (green). The Sun is marked with a black star. Bottom: Angular momentum-loss rates from the stellar wind in the top panel. The predicted value of the Sun’s current angular momentum-loss rate, given a Skumanich spin-down ( $6.2 \times 10^{30}$  erg), is marked with a black star. In this model, stars have a stronger than Skumanich spin-down initially, which allows for the stars at the age of the Sun to have a weaker angular momentum-loss rate (than purely Skumanich) and still match the rotation period of the Sun.

## Chapter 5

# Solar Angular Momentum-Loss Over the Past Several Millennia

### 5.1 Introduction

Following from Chapter 4, in which I used semi-analytic formulae and in-situ measurements of the solar wind to estimate the angular momentum-loss rate of the Sun, I found the current solar angular momentum loss rate to be  $2.3 \times 10^{30}$  erg (based on the open magnetic flux and mass-loss rate). Surprisingly, this is smaller than the value predicted by a Skumanich (1972) spin-down for the Sun, which produces a value of  $6.2 \times 10^{30}$  erg. A smaller value is also favoured by a few other MHD wind models (e.g. Usmanov et al. 2018), and “direct” measurements of the solar wind angular momentum flux (e.g. Pizzo et al. 1983). Before asserting that the Sun’s rotation evolution differs from Skumanich, it is important to realise that these values are compatible. Rotation period evolution models for stars around the age of the Sun are sensitive to timescales of around 10-100 million years, and the previous Chapter only used data from  $\sim 20$  years, therefore further temporal variability in the solar wind could explain this value (provided the Sun is currently in a “low-torque” state).

To investigate this hypothesis, I collect observations/reconstruction of the Sun’s ac-

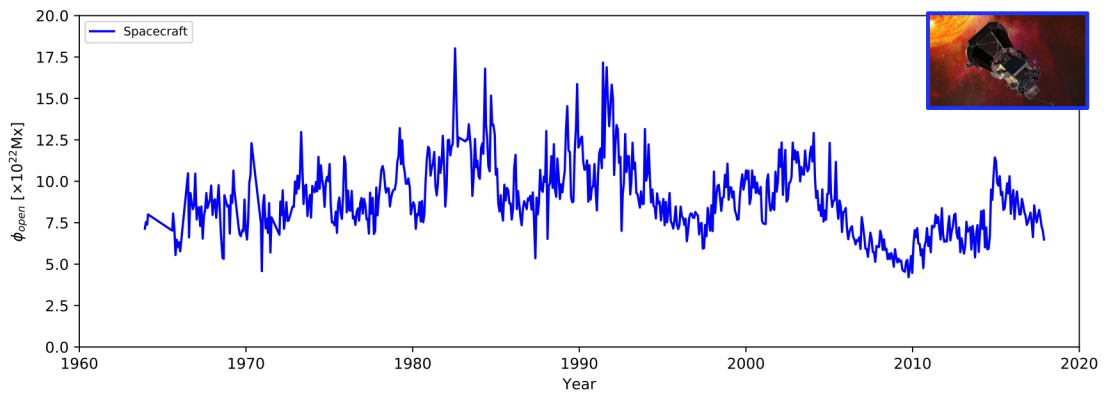


**Figure 5.1:** Open magnetic flux in the heliosphere during the space-age. Data for this plot is taken from the OMNI database, which incorporates many different spacecraft into a continuous dataset of near-Earth solar wind properties. Radial magnetic field measurements are averaged on hourly timescales as  $(B_r)_{1hr}$  and then averaged over 27 days as  $|B_r|_{1hr}$ , to evaluate the average unsigned magnetic field. The distribution of magnetic flux is then assumed to be isotropic (see Owens et al. 2008), and this value multiplied by  $4\pi r^2$ . The solar magnetic cycle appears as a clear feature.

tivity which I use to infer how the solar wind angular momentum-loss rate has varied over the last 9000 years. Starting with in-situ observations from the space-age, moving through the centuries of sunspot recordings, and finally examining the millennial variation found in cosmogenic radionuclide records. The interpretation of these, in terms of an angular momentum-loss rate, appear as it was published in *The Astrophysical Journal*. I then present some additional discussion surrounding the mass-loss rate of the Sun, that was left out of the paper, and finish the Chapter with a summary of the results.

## 5.2 Observations of the Solar Wind During the Space-age

Since the mid-1960s, spacecraft carrying magnetometers and particle detectors have patrolled near-Earth space making valuable measurements of the solar wind (a more detailed discussion is available in Chapter 6). The OMNIWeb service<sup>1</sup> has collated these measurements to form a continuous estimate of near-Earth solar wind properties, such as magnetic field strength, proton density, flow speed, etc. From these measurements, as done in Chapter 4, the proton mass-flux and average unsigned magnetic field can be evaluated. Again, though these observations have an adequate temporal cadence, they are generally limited to one observing location in the heliosphere. I therefore average in-situ

1. <https://omniweb.gsfc.nasa.gov/>

observations over the Sun's rotation period (27 days) to remove longitudinal variations, and then assume the heliospheric magnetic flux and mass flux to be isotropic in latitude (see the methods in Sections 4.3, and 5.4).

Using the OMNI data for the interplanetary magnetic field strength, I estimate the open magnetic flux  $\phi_{open}$  in the heliosphere, shown in Figure 5.1 for the entire space-age. Measurements of the magnetic field in the solar wind become more regular and accurate as time progresses (note that error bars are not shown). The solar activity cycle is clearly visible in Figure 5.1, with solar maxima generally having a larger amount of open magnetic flux than solar minima. This is interesting, as the dipole component of the Sun's surface magnetic field is generally weaker during solar maxima. So given that the dipolar component is thought to be the main contributor to the open magnetic flux (Jardine et al. 2017), it could be expected that the open magnetic flux should be weaker during solar maxima. This was also found in Section 4.3. One solution to this is that the coronal magnetic field becomes "open" closer to the Sun's surface at maxima (see Section 4.6.1 for a schematic of the magnetic field "opening"). When modelling the Sun's coronal magnetic field with a PFSS model (see Appendix A), there is evidence that a smaller source surface radius is required to reproduce the open magnetic flux in the solar wind (see Lee et al. 2011; Badman et al. 2020), and that a time-varying source surface radius is needed to reproduce its solar cycle dependence (e.g. Arden et al. 2014).

Additionally, in Figure 5.1 there is a clear cycle to cycle difference in the amount of open magnetic flux in the heliosphere. For example, sunspot cycle 22 has more open magnetic flux than either of cycle 23 and 24. Therefore if the study from Section 4.3 were performed with data from cycle 22, the predicted angular momentum-loss rate would inevitably be higher. Given the variation between cycles observed during the space-age, it is logical to assume there may exist further variation on timescales that the rotation-evolution models are insensitive to (i.e. shorter than 10-100 million years).

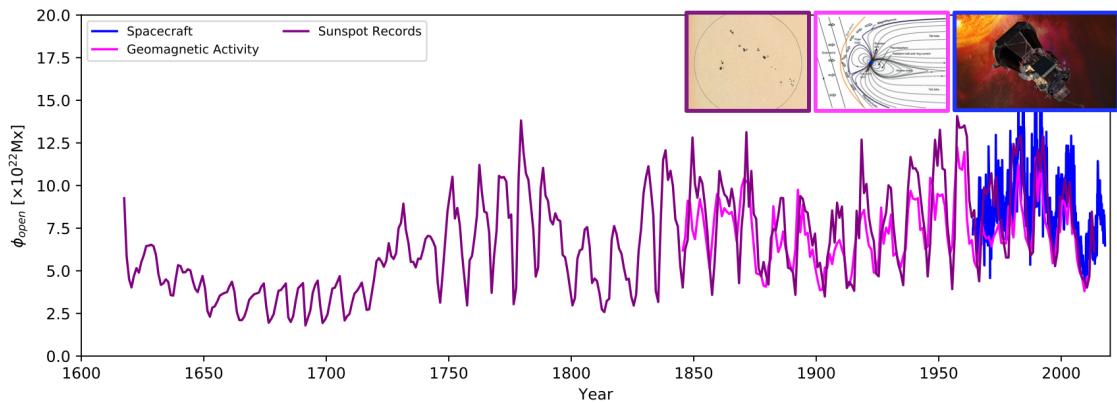


**Figure 5.2:** Open magnetic flux in the heliosphere during the last four centuries. Data for this plot is taken from Lockwood et al. (2014a) (geomagnetic) and Owens and Lockwood (2012) (sunspots), shown in magenta and purple respectively. The space-age open flux from Figure 5.1 is shown in blue. As with Figure 5.1 the sunspot cycle is a clear feature, but now there exists further centennial variation which includes the Maunder minimum from 1640 to 1720, and the current grand maximum.

## 5.3 Reconstructions of Solar Activity from Centuries to Millennia

All information surrounding the solar wind before the space-age is derived from indirect measurements. These include records of geomagnetic disturbances (e.g Lockwood et al. 2014b), sunspot number records (e.g. Owens and Lockwood 2012), and cosmogenic radionuclide records (e.g. Wu et al. 2018a). These proxies indicate how the solar wind has changed on a range of timescales, but each require careful interpretation and calibration. In this Section, I provide some background information on each proxy to better prepare the reader for the following published paper.

### 5.3.1 Geomagnetic Indices

Geomagnetic indices of various forms are routinely derived from ground-based magnetometer observations (see Cliver and Ling 2002). Mayaud (1972) first derived the *aa*-index which combined observations from England and Australia to form a long-term record of the Earth's geomagnetic activity. The disturbances measured in the geomagnetic field are linked to the Earth's dynamo, changes in the ionosphere/magnetosphere, and disturbances to the near-Earth solar wind environment (Stamper et al. 1999). Over the solar

activity cycle, changes in the coupling of the solar wind and the Earth's magnetosphere, through the varying interplanetary field strength or location of the heliospheric current sheet, significantly impact the value of the *aa*-index. Thus, by understanding the response of the Earth's geomagnetic field to geomagnetic disturbances, the *aa*-index provides information about the interplanetary magnetic field strength (or open magnetic flux). The *aa*-index showed a strong increase during the twentieth century, which authors connected to variability in the Sun's magnetic field (Russell 1975), and the solar wind (Feynman and Crooker 1978). The long-term variation of the *aa*-index was later interpreted by Lockwood et al. (1999), as results from a strengthening of the Sun's open magnetic flux. From there on, the *aa*-index has been frequently used to infer historical changes in the Sun's magnetic field and the solar wind (Rouillard et al. 2007; Svalgaard and Cliver 2010; Lockwood 2013). The open magnetic flux inferred from the *aa*-index in Lockwood et al. (2014a) is plotted in Figure 5.2 with a magenta line. This reconstruction starts around 1850, and reproduces (by construction) the space-age variability. Interestingly the open flux from the *aa*-index indicates a maximum of solar activity during the space-age, with the early twentieth century having a weaker strength than the present day.

### 5.3.2 Sunspot Number Records

As a visible indication of the Sun's magnetic activity, sunspots appear in the solar photosphere due to the suppression of convection by kG enhancements in the Sun's surface magnetic field. Sunspots have been nearly continuously recorded for the last four centuries (see review of Clette et al. 2014), dating back to the time of Galileo (Galilei 1957). Observers tracked the size, shape and number of sunspots, including hand drawn depictions (e.g. Arlt 2008; Arlt and Vaquero 2020). Commonly used as a proxy for solar activity is the sunspot number, for which various measures exist (Wolf number; Wolf 1851, Group number; Hoyt and Schatten 1998, etc). As historical records span many different observers, differences in their techniques, instruments and eye-sight affect how different dataset are connected together (with some deemed more reliable than others, etc). Sunspots are well correlated with the magnetic activity of the Sun, with a high sunspot number corresponding to a time of substantial flux emergence and magnetic energy release. For this reason,

sunspot number also roughly tracks with the frequency of transient features, such as flares and CMEs. From the sunspot number alone, it is clear the Sun has a substantial centennial variation, for which we are just leaving a grand maximum in activity (Chapman et al. 2014). The opposite feature to this, a grand minimum of activity was last observed from 1640 to 1720, the so called Maunder minimum (Sporer 1887; Eddy 1976).

By definition, the sunspot number is an indicator of the amount of flux emergence. The emerging magnetic field joins the coronal magnetic field and is responsible for the solar wind, along with maintaining the dynamo at the heart of the solar cycle (Babcock 1959). By using flux transport simulations, driven by sunspot number, previous authors have been able to reconstruct the evolution of the Sun's magnetic field over the course of the last four centuries (Solanki et al. 2002; Vieira and Solanki 2010; Owens and Lockwood 2012). The equations describing these models are illustrative and so I have included them below. Consider the Sun's magnetic field to have three main components: 1) active region flux  $\phi_{activ}$ , 2) ephemeral/distributed surface flux  $\phi_{surf}$ , and 3) open magnetic flux  $\phi_{open}$ . Both 1) and 2) are driven by the emergence of sunspots, with source terms  $S_{activ}(t)$  and  $S_{surf}(t)$  (that can be derived from sunspot number records), and decay timescales given by  $\tau_{activ}$  and  $\tau_{surf}$ . Then the open flux  $\phi_{open}$  is formed from the transfer of emerging flux from active region flux and surface flux on timescales of  $\tau_{a \rightarrow o}$  and  $\tau_{s \rightarrow o}$  respectively, and then lost on its decay timescale  $\tau_{open}$ . The time evolution of these three fluxes is thus given by,

$$\frac{d\phi_{activ}}{dt} = S_{activ}(t) - \frac{\phi_{activ}}{\tau_{activ}} - \frac{\phi_{activ}}{\tau_{a \rightarrow o}}, \quad (5.1)$$

$$\frac{d\phi_{surf}}{dt} = S_{surf}(t) - \frac{\phi_{surf}}{\tau_{surf}} - \frac{\phi_{surf}}{\tau_{s \rightarrow o}}, \quad (5.2)$$

$$\frac{d\phi_{open}}{dt} = \frac{\phi_{activ}}{\tau_{a \rightarrow o}} + \frac{\phi_{surf}}{\tau_{s \rightarrow o}} - \frac{\phi_{open}}{\tau_{open}}, \quad (5.3)$$

where the decay and transfer timescales are tuned to match observations, e.g. from Solanki et al. (2002),  $\tau_{activ} \approx 0.22$  years,  $\tau_{surf} \approx 14$  hours,  $\tau_{a \rightarrow o} \approx 10$  years, etc. Note, different models parameterise the flux evolution differently, but all treat it as a balance of source and decay terms. These flux transport models are empirical in nature, with timescales and



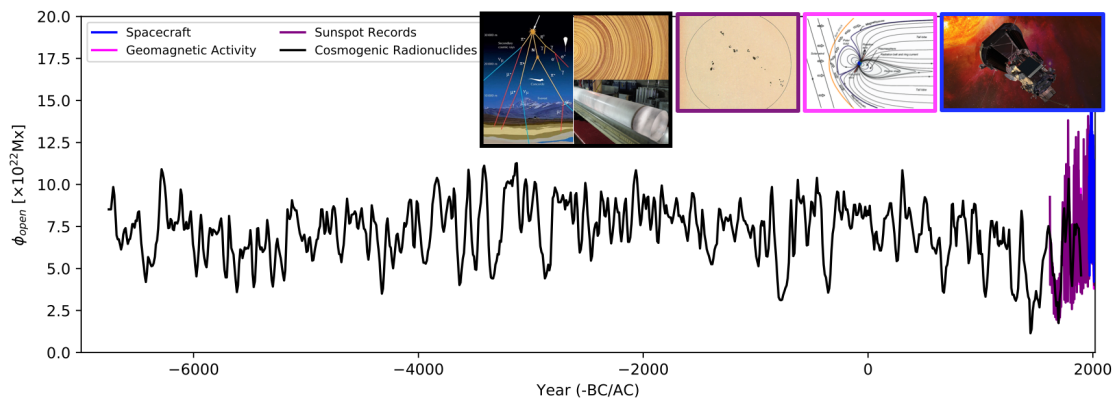


**Figure 5.3:** Open magnetic flux in the heliosphere during the last several millennia. Data for this plot is taken from Wu et al. (2018b) (cosmogenic radionuclides), shown with a black line. The space-age open flux from Figure 5.1 is shown in blue. The centennial reconstructions from Figure 5.2 are shown in magenta and purple. No longer is the sunspot cycle a clear feature, instead this reconstruction is only sensitive to changes on 20-40 year timescales. The modern era appears as a grand maximum in this reconstruction. Note that the absolute values from the space-age are higher because they are not effectively-averaged in the same way as the cosmogenic radionuclide data.

rates that have been evaluated from modern-day observations. Given these constraints, flux transport simulations are allowed to evolve from an initial flux. Though it takes time to remove any unphysical dependence on this initial condition. Once the evolution of the modelled flux is only dependent on the driving sunspot number record (rather than the initial condition), the reconstructed open magnetic flux can be recorded.

The reconstructed open magnetic flux from Owens and Lockwood (2012) is plotted in Figure 5.2 with a purple line. This reconstruction begins in the early seventeenth century, and covers the Maunder minimum along with the modern maximum. The location of the space-age in this reconstruction is clear, with a higher open magnetic flux than anytime previously. From both the geomagnetic and sunspot reconstructions, the average open magnetic flux is similar (if not a little smaller) than the average from Section 4.3, meaning the predicted angular momentum-loss rates are similar.

### 5.3.3 Cosmogenic Radionuclides

It is clear that the Sun's magnetic field contains variability on longer timescales than just the sunspot cycle. Reliably documented observations of the Sun's activity, such as those from magnetometers and eye-witness sunspot records, do not extend much further into

the past than  $\sim 400$  years. However, there does exist evidence for further variability in Sun's magnetic activity (open flux) which can be found in terrestrial archives (formed by natural processes). This comes in the form of cosmogenic radionuclides, which are produced when Galactic Cosmic Rays (GCRs) collide with the Earth's upper atmosphere (see review of Beer et al. 2012). The production of radionuclides from Solar Energetic Particles (SEPs), is generally deemed to be sporadic and negligible to the effect of GCRs. The frequency of GCRs arriving at Earth, and subsequently producing Beryllium-10, Carbon-14, etc, is modulated by the varying magnetic shielding provided by the Sun, in the heliosphere (Lal and Peters 1967). This means that during times of increased solar activity, when the heliosphere is filled with more open flux, CMEs, interacting wind-streams, etc, there is a reduced GCR count at Earth, and so the abundance of cosmogenic radionuclides in Earth's atmosphere decreases. However, the abundance of cosmogenic radionuclide stored in, for example, the polar ice sheets also depends on 1) the geomagnetic field (additional shielding), 2) transport in the atmosphere, 3) deposition and storage. For example Carbon-14 is taken into the carbon-cycle, and so the signal of this radionuclide, in tree rings, is smeared out.

Despite the complications of modelling the many processes involved, quantitative reconstructions of solar activity, generally referred to as the solar modulation potential (e.g. Bard et al. 2000; Muscheler et al. 2007; Steinhilber et al. 2012), have been produced by many authors. Some of the better reconstructions attempt to use multiple radionuclide sources, in order to produce a more accurate result (Wu et al. 2018a). The open flux reconstruction from Wu et al. (2018b) is plotted in Figure 5.3 with a solid black line. No longer can the sunspot cycle be resolved, as the timescales for transport and deposition are of a similar order to it. Additionally, the amplitudes are not as extreme as the space-age because of the effective-averaging/smoothing timescale. Note that reconstructions such as this are limited by the last ice-age, as before this the ice cores/tree rings cannot be reliably dated. Over the last several millennia it is clear that the Sun has additional variability, though it is not obvious if the Sun has varied enough to change the result from Section 4.3.



# Solar Angular Momentum Loss over the Past Several Millennia

Adam J. Finley<sup>1</sup> , Siddhant Deshmukh<sup>1</sup>, Sean P. Matt<sup>1</sup> , Mathew Owens<sup>2</sup> , and Chi-Ju Wu<sup>3</sup>

<sup>1</sup>University of Exeter, Exeter, Devon, EX4 4QL, UK; [af472@exeter.ac.uk](mailto:af472@exeter.ac.uk)

<sup>2</sup>University of Reading, Reading, Berkshire, RG6 6BB, UK

<sup>3</sup>Max-Planck-Institut für Sonnensystemforschung, Justus-von-Liebig-Weg 3, Göttingen, Germany

Received 2019 April 8; revised 2019 July 22; accepted 2019 July 29; published 2019 September 20

## Abstract

The Sun and Sun-like stars lose angular momentum to their magnetized stellar winds. This braking torque is coupled to the stellar magnetic field, such that changes in the strength and/or geometry of the field modifies the efficiency of this process. Since the space age, we have been able to directly measure solar wind properties using in situ spacecraft. Furthermore, indirect proxies such as sunspot number, geomagnetic indices, and cosmogenic radionuclides, constrain the variation of solar wind properties on centennial and millennial timescales. We use near-Earth measurements of the solar wind plasma and magnetic field to calculate the torque on the Sun throughout the space age. Then, reconstructions of the solar open magnetic flux are used to estimate the time-varying braking torque during the last nine millennia. We assume a relationship for the solar mass-loss rate based on observations during the space age which, due to the weak dependence of the torque on mass-loss rate, does not strongly affect our predicted torque. The average torque during the last nine millennia is found to be  $2.2 \times 10^{30}$  erg, which is comparable to the average value from the last two decades. Our data set includes grand minima (such as the Maunder Minimum), and maxima in solar activity, where the torque varies from  $\sim 1$  to  $5 \times 10^{30}$  erg (averaged on decadal timescales), respectively. We find no evidence for any secular variation of the torque on timescales of less than 9000 yr.

*Key words:* magnetohydrodynamics (MHD) – solar wind – Sun: evolution – Sun: rotation

## 1. Introduction

The observed rotation periods of most low-mass stars ( $M_* \lesssim 1.3M_\odot$ ) on the main sequence can be explained by their magnetized stellar winds. These winds efficiently remove angular momentum causing stars to spin-down with age (Skumanich 1972; Soderblom 1983; Barnes 2003, 2010; Delorme et al. 2011; Van Saders & Pinsonneault 2013; Bouvier et al. 2014). Throughout this process, their magnetic field generation (due to the dynamo mechanism) is strongly linked with rotation (Brun & Browning 2017), and the strength of the magnetic field is found to influence the efficiency of angular momentum transfer through the stellar wind (Weber & Davis 1967; Mestel 1968; Kawaler 1988; Matt et al. 2012; Garraffo et al. 2015). The resulting strong dependence of torque on rotation rate leads to a convergence of rotation periods with age, as initially fast rotating stars generate strong magnetic fields and experience a larger braking torque than the initially slowly rotating stars. This spin-down is also observed to be a function of stellar mass (Agüeros et al. 2011; McQuillan et al. 2013; Núñez et al. 2015; Covey et al. 2016; Rebull et al. 2016; Agüeros 2017; Douglas et al. 2017).

Many models now exist to study the rotation period evolution of low-mass stars (Gallet & Bouvier 2013; Brown 2014; Gallet & Bouvier 2015; Johnstone et al. 2015; Matt et al. 2015; Amard et al. 2016; Blackman & Owen 2016; Sadeghi Ardestani et al. 2017; Garraffo et al. 2018; See et al. 2018). Such models provide insight on how stellar wind torques evolve on secular timescales ( $\sim$ Gyr), independently from our understanding of the braking mechanism. For Sun-like stars, the torques prescribed by these models are averaged over fractions of the braking timescale ( $\sim 10$ – $100$  Myr). However, we observe variability in the magnetic field of the Sun on a range of much shorter timescales (DeRosa et al. 2012; Vidotto et al. 2018), which is expected to influence the angular

momentum loss rate in the solar wind (Pinto et al. 2011; Réville & Brun 2017; Finley et al. 2018; Perri et al. 2018).

In Finley et al. (2018), the short timescale variability (from  $\sim 27$  days up to a few decades) of the solar wind was examined using in situ observations of the solar wind plasma and magnetic field. By applying a braking law derived from magnetohydrodynamic (MHD) simulations by Finley & Matt (2018), they calculated the time-varying torque on the Sun due to the solar wind. When averaged over the last  $\sim 20$  yr they found a solar wind torque of  $2.3 \times 10^{30}$  erg. This value is in agreement with previous in situ and data driven calculations (Pizzo et al. 1983; Li 1999), and also recent simulation results (Alvarado-Gómez et al. 2016; Réville & Brun 2017; Ó Fionnagáin et al. 2018; Usmanov et al. 2018).

When compared to the torques required by rotation–evolution models (e.g., Matt et al. 2015), current estimates of the solar wind torque are smaller by a factor of  $\sim 3$  (this discrepancy was noted already by Soderblom 1983). One possible explanation for the discrepancy is that the solar wind torque is variable, and that the torque is currently in a “low state,” or that the torque has recently, but permanently weakened (e.g., as suggested by van Saders et al. 2016; Garraffo et al. 2018; Ó Fionnagáin & Vidotto 2018). For this to be true, the variations in the torque must have happened on timescales much longer than the space age (decades), but shorter than the timescales on which the rotation–evolution models are sensitive to ( $\sim 10^8$  yr, for solar-aged stars).

In this work, we employ reconstructions of solar wind properties from the literature, in order to estimate the solar wind torque further back in time than has been probed so far (more than two orders of magnitude). Although we still cannot probe the timescales of rotational evolution, this helps to elucidate the types of variability that may occur in the solar wind torque. We first describe the Finley & Matt (2018)

braking law, hereafter **FM18**, in Section 2. Then we estimate the angular momentum loss rate, due to the solar wind, through the space age using in situ data in Section 3. Finally, in Section 4, we use reconstructions of the Sun's open magnetic flux (which are based on sunspot number, geomagnetic indices, and cosmogenic radionuclide records), to estimate the angular momentum loss rate on centennial and millennial timescales.

## 2. Angular Momentum Loss Formulation

Generally, the torque on a star due its magnetized wind can be written as

$$\tau = \dot{M} \Omega_* R_*^2 \left( \frac{\langle R_A \rangle}{R_*} \right)^2, \quad (1)$$

where  $\dot{M}$  is the mass-loss rate,  $\Omega_*$  is the stellar rotation rate,  $R_*$  is the stellar radius, and  $\langle R_A \rangle / R_*$  can be thought of as an efficiency factor for the angular momentum loss rate which, under the assumption of ideal steady-state MHD, scales as the average Alfvén radius (Weber & Davis 1967; Mestel 1968).

We use a semi-analytic formula for  $\langle R_A \rangle$ , which depends on the open magnetic flux,  $\phi_{\text{open}}$ , and mass-loss rate,  $\dot{M}$ , in the wind (Strugarek et al. 2014; Réville et al. 2015a, 2015b, 2016; Finley & Matt 2017; Pantolmos & Matt 2017; **FM18**). We define the open magnetic flux as the total unsigned flux that permeates the stellar wind,

$$\phi_{\text{open}} = \oint_A |\mathbf{B} \cdot d\mathbf{A}|, \quad (2)$$

where  $\mathbf{B}$  is the magnetic field strength in the wind, and  $A$  is a closed surface that is located outside the last closed magnetic field line. In a steady state, the last closed magnetic field line resides within the Alfvén radius,  $R_A$ , which is defined as the location where the wind speed becomes equal to the Alfvén speed,  $v(R_A) = v_A = B_A / \sqrt{4\pi\rho_A}$ , where the subscript  $A$  denotes values taken at  $R_A$ . Considering a steady MHD flow, along a one-dimensional magnetic flux tube, mass and magnetic flux are conserved. Therefore, in a steady-state stellar wind, where the flow is spherically symmetric, the magnetic field strength at  $R_A$  is specified by flux conservation as  $B_A = \phi_{\text{open}} / (4\pi R_A^2)$ . The Alfvén speed is then,

$$v_A^2 = \frac{\phi_{\text{open}}^2 / (4\pi)^2 R_A^4}{4\pi\rho_A}, \quad (3)$$

which by rearranging, and then substituting for  $\dot{M}$ , produces a relation for  $R_A$ ,

$$R_A^2 = \frac{\phi_{\text{open}}^2}{(4\pi)^2 v_A (4\pi\rho_A v_A R_A^2)} = \frac{\phi_{\text{open}}^2}{(4\pi)^2 v_A \dot{M}}. \quad (4)$$

Since real stellar winds are multi-dimensional in nature, several authors (e.g., Matt & Pudritz 2008; Pinto et al. 2011; Matt et al. 2012; Cohen & Drake 2014; Réville et al. 2015a, 2015b; Garraffo et al. 2016; Finley & Matt 2017; Pantolmos & Matt 2017; **FM18**) have employed MHD numerical simulations to derive semi-analytic scalings for the wind torques. A few of these studies have derived a relationship similar to

Equation (4), which has the form

$$\frac{\langle R_A \rangle}{R_*} = K \left[ \frac{\phi_{\text{open}}^2 / R_*^2}{\dot{M} v_{\text{esc}}} \right]^m, \quad (5)$$

where  $\langle R_A \rangle / R_*$  is calculated from the simulations by inverting Equation (1), and  $K$  and  $m$  are fit constants. In Equation (5), compared to Equation (4),  $v_A$  has been replaced by the surface escape speed,  $v_{\text{esc}} = \sqrt{2GM_\odot / R_\odot}$ , and any dependence  $v_A$  has on  $\phi_{\text{open}}$  and  $\dot{M}$  is absorbed into the fit constants. These fit constants also account for the multiplicative factor of  $(4\pi)^2$ , and any effects introduced by the flow being multi-dimensional in nature. The formulation of Equation (5) for  $\langle R_A \rangle$ , using  $\phi_{\text{open}}$ , is insensitive to how the coronal magnetic field is structured (i.e., insensitive to the geometry of the magnetic field; Réville et al. 2015a), but the fit constants can be affected by differing wind acceleration profiles (Pantolmos & Matt 2017), and 3D structure in the mass flux.

We adopt the fit parameters from **FM18**. For the Sun, Equation (5) then reduces to,

$$\langle R_A \rangle = (12.9 R_\odot) \left( \frac{\dot{M}}{1.1 \times 10^{12} \text{ g s}^{-1}} \right)^{-0.37} \times \left( \frac{\phi_{\text{open}}}{8.0 \times 10^{22} \text{ Mx}} \right)^{0.74}, \quad (6)$$

using values of the solar mass,  $M_\odot = 1.99 \times 10^{33} \text{ g}$ , and radius,  $R_\odot = 6.96 \times 10^{10} \text{ cm}$ . For the solar wind torque, Equation (1) becomes,

$$\tau = (2.3 \times 10^{30} \text{ (erg)}) \left( \frac{\dot{M}}{1.1 \times 10^{12} \text{ g s}^{-1}} \right)^{0.26} \times \left( \frac{\phi_{\text{open}}}{8.0 \times 10^{22} \text{ Mx}} \right)^{1.48}, \quad (7)$$

using the solar rotation rate  $\Omega_\odot = 2.6 \times 10^{-6} \text{ rad s}^{-1}$ . The torque depends only on  $\phi_{\text{open}}$  and  $\dot{M}$ , given the choice of polytropic base wind temperature used in **FM18**. By comparing feasible base wind temperatures, Pantolmos & Matt (2017) showed there is at most a factor of  $\sim 2$  difference in the prediction of Equation (7) between the coldest and hottest polytropic winds (1.3–4.2 MK for the Sun). The simulations of **FM18**, from which we derived Equations (6) and (7), correspond to a base wind temperature of  $\sim 1.7 \text{ MK}$ , which sits at the lower edge of this temperature range (where the torques are strongest).

## 3. Solar Wind Torque During the Space Age

### 3.1. Observed Solar Wind Properties

Hourly near-Earth solar wind plasma and magnetic field measurements are available from the OMNIWeb service.<sup>4</sup> The OMNI data set is compiled from the in situ observations of

<sup>4</sup> <https://omniweb.gsfc.nasa.gov/> (Accessed in 2018 July).

several spacecraft, from 1963 to present. We use measurements of the solar wind to estimate the open magnetic flux using

$$\phi_{\text{open}} = 4\pi \langle R^2 |B_R(R)| \rangle_{1 \text{ hr} / 27 \text{ days}}, \quad (8)$$

where we average the radial magnetic field  $B_R$ , (taken from a single observing location) at a distance  $R$  from the Sun, over a full solar rotation (27 days), and assume that the solar wind is roughly isotropic on our averaging timescale, in order to estimate the open magnetic flux. Smith & Balogh (1995) were able to show that  $R^2|B_R(R)|$  is approximately independent of heliographic latitude, as the solar wind is thought to redistribute significant variations in magnetic flux due to latitudinal magnetic pressure gradients caused by non-isotropy (Wang & Sheeley 1995; Lockwood et al. 2004; Pinto & Rouillard 2017). Subsequently, the use of a single point measurement to infer the global open magnetic flux has been shown to be a reasonable approximation at distances less than  $\sim 2$  au by Owens et al. (2008).

The open magnetic flux calculated using Equation (8), during the space age, is plotted in the top panel of Figure 1. The 27 day averages are shown with circles that are colored according to the different sunspot cycles in our data set. The average of this data set is indicated with a gray horizontal line. The open magnetic flux roughly declines in time over the past three cycles, with the current sunspot cycle hosting some of the weakest values recorded in the OMNI data set. Due to kinematic effects that occur between the Alfvén surface and the measurements taken at 1 au, our estimate of the open magnetic flux is likely an upper limit (Owens et al. 2017a).

Similarly to Equation (8) for the open magnetic flux, the solar mass-loss rate is estimated from in situ measurements using

$$\dot{M} = 4\pi \langle R^2 v_R(R) \rho(R) \rangle_{27 \text{ days}}, \quad (9)$$

which is plotted in the middle panel of Figure 1. Equation (9) assumes the mass flux evaluated at a single observing location in the solar wind is representative of all latitudes when averaged over 27 days. Using data from the fast latitude scans of the *Ulysses* spacecraft, Finley et al. (2018) showed that the calculation of  $\dot{M}$  from Equation (9) varies by a few 10's of percent when the spacecraft was immersed in slow, versus fast, solar wind streams (see also Phillips et al. 1995). Thus, the errors due to latitudinal variability are comparable to, but appear somewhat smaller than, the time variability (see, e.g., McComas et al. 2013). The cyclical variations of  $\dot{M}$  are less clear than for the open flux, but they show a similar decreasing trend over the past three cycles.

### 3.2. Coronal Mass Ejections

Equations (8) and (9) do not take into account the effects of coronal mass ejections (CMEs) in the data. These appear as impulsive changes (generally increases) in the observed solar wind properties, and clearly violate the assumed isotropy of wind conditions in Equations (8) and (9). CMEs occur once every few days at solar minimum, however their occurrence rate tracks solar activity, and at solar maximum they are observed on average five times a day (Webb et al. 2017; Mishra et al. 2019). Previous authors have removed these events through the use of CME catalogs (Cane & Richardson 2003) or clipping anomalous spikes (Cohen 2011). CMEs carry only a

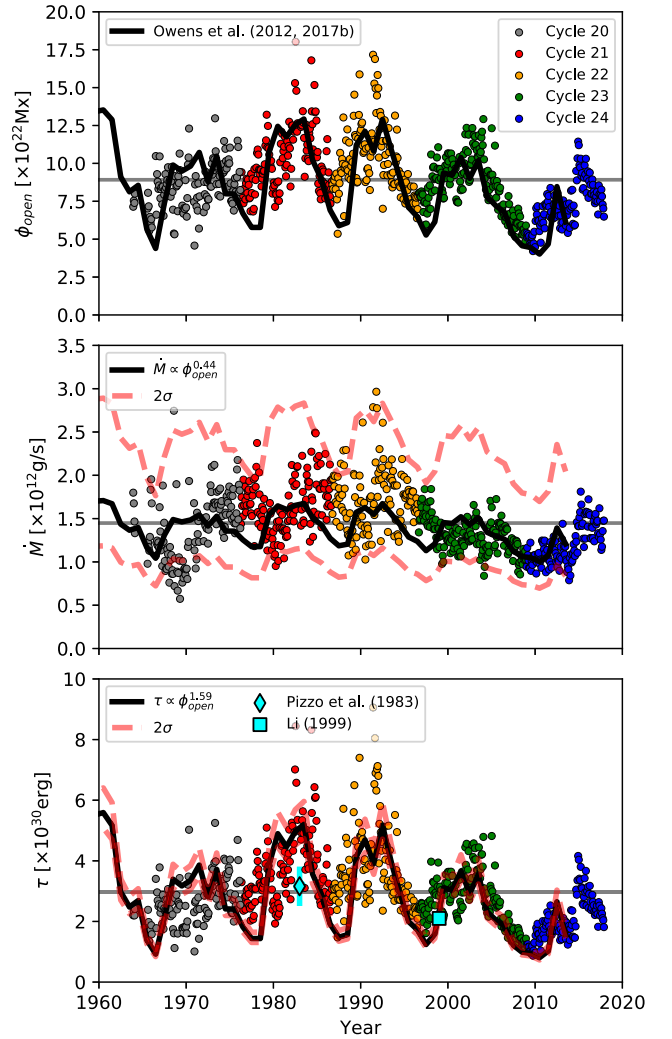


**Figure 1.** Several decades of open magnetic flux,  $\phi_{\text{open}}$ , and mass-loss rate,  $\dot{M}$ , estimated from the OMNI data set (near-Earth measurements), are shown with circles (color-coded by sunspot cycle number, 20–24) in the top two panels. The predicted solar wind torque,  $\tau$ , using Equation (7) is then shown in the bottom panel. Averages of these three quantities are shown with gray horizontal lines. Over-plotted in each panel are the  $\phi_{\text{open}}$  reconstruction from Owens et al. (2017b), the  $\dot{M}$  predicted by Equation ((10)), and the  $\tau$  from Equation (11), with solid black lines. The  $2\sigma$  bounds for the predicted  $\dot{M}$  and  $\tau$ , are indicated with dashed red lines.

few percent of the total solar mass-loss rate (Cranmer et al. 2017), however, at solar maximum they can provide a significant fraction of the average mass flux in the equatorial solar wind (Webb & Howard 1994).

Finley et al. (2018) examined the effect of removing periods of high wind density ( $>10 \text{ cm}^3$ ) and high magnetic field strength ( $>10 \text{ nT}$ ), thought to correspond to the CMEs. They determined that the average open magnetic flux and mass-loss rate, over their  $\sim 20$  yr of data, decreased by  $\sim 4\%$  after these cuts were applied. As the role of CMEs in removing angular momentum is still in question (see, e.g., Aarnio et al. 2012), and their inclusion here is limited to a few percent, we present our results using the full unclipped data set.

### 3.3. Decades of Solar Wind Torque

We use the open magnetic flux and mass-loss rate estimates from Section 3.1 to compute the angular momentum loss rate in

the solar wind using Equation (7). The results from this calculation are shown in the bottom panel of Figure 1. We calculate the average torque on the Sun during the space age to be  $2.97 \times 10^{30}$  erg, which is larger than the value obtained by Finley et al. (2018) of  $2.3 \times 10^{30}$  erg, due to the fact that Finley et al. (2018) only examined the past  $\sim 20$  yr. Averaging over each individual sunspot cycle, we find values of  $2.67 \times 10^{30}$  erg,  $3.66 \times 10^{30}$  erg,  $3.70 \times 10^{30}$  erg,  $2.69 \times 10^{30}$  erg, and  $2.06 \times 10^{30}$  erg, for cycles 20–24, respectively. Using Equation (6),  $\langle R_A \rangle$  is calculated to have its largest value in cycle 21 of  $20.4R_\odot$ , and minimum value of  $7.7R_\odot$  in cycle 22. The value of  $\langle R_A \rangle$  during the current sunspot cycle ranges from  $\sim 8$  to  $16R_\odot$ .

The time-varying torque computed here is in agreement with previous calculations of the solar wind torque. From the in situ measurements of Pizzo et al. (1983) using the *Helios* spacecraft, to the recalculation of Li (1999) based on data from the *Ulysses* spacecraft. Both of these estimates agree within the scatter of the 27 day averages computed in this work.

#### 4. Solar Wind Torque on Centennial and Millennial Timescales

Up until now, we have examined only direct measurements of the solar wind. These observations have been facilitated by the exploration of near-Earth space, which began a few decades ago. For the centuries and millennia before this, only indirect measurements are available, such as sunspot observations (Clette et al. 2014), measurements of geomagnetic activity (Echer et al. 2004), and studies of cosmogenic radionuclides found in tree rings or polar ice cores (Usoskin 2017). These indirect measurements are used to estimate longer time variability of the Sun’s open magnetic flux (Lockwood et al. 2004; Vieira & Solanki 2010; Owens et al. 2011; Wu et al. 2018b). However, these indirect measurements have limitations. Significantly for this work, they do not produce estimates for how the mass-loss rate of the Sun has varied.

In this section we produce a relation for the mass-loss rate of the Sun, in terms of the open magnetic flux, which is constructed using the range of observed values from Section 3.1. We then use this prescription for the mass-loss rate, and Equation (7), to evaluate the torque on the Sun due to the solar wind based on indirect reconstructions of the open magnetic flux.

##### 4.1. Estimating the Mass-loss Rate, and Wind Torque with the Open Magnetic Flux

Predicting the mass-loss rates for low-mass stars, such as the Sun, is a difficult challenge, which has been attempted by previous authors to varying success (Reimers 1975, 1977; Mullan 1978; Schröder & Cuntz 2005; Cranmer & Saar 2011; Cranmer et al. 2017). The mass-loss rates from Section 3.1 are plotted against their respective open magnetic flux values in the top panel of Figure 2, colored by sunspot cycle. A weak trend of increasing mass-loss rate with increasing open magnetic flux is observed. We fit a power-law relation for the mass-loss rate in terms of the open magnetic flux,

$$\dot{M}_{\text{fit}} = (1.26 \times 10^{12} \text{ g s}^{-1}) \left( \frac{\phi_{\text{open}}}{8.0 \times 10^{22} (\text{Mx})} \right)^{0.44}, \quad (10)$$

which is plotted as a solid black line.

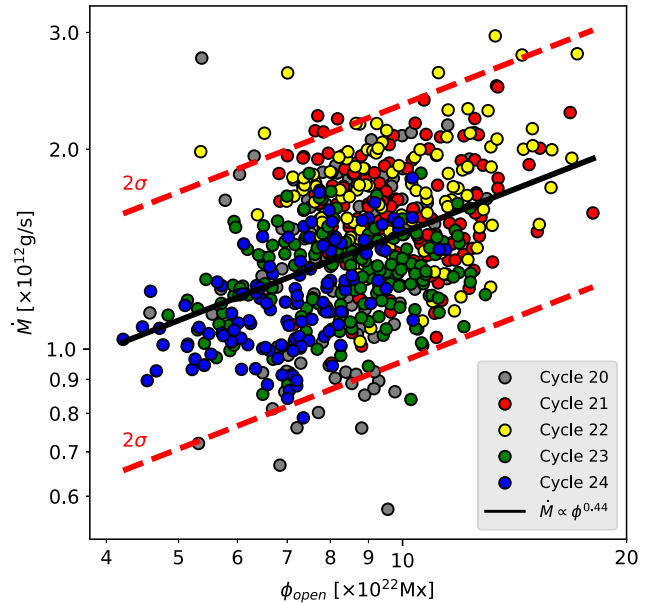


**Figure 2.** Mass-loss rate,  $\dot{M}$ , vs. open magnetic flux,  $\phi_{\text{open}}$ , derived in the in situ observations of the OMNI data set. Values are color-coded by sunspot cycle, 20–24. The black line corresponds to the power-law fit of Equation (10). The dashed red lines indicate the  $2\sigma$  bounds given by a log-Gaussian centered on the fit line.

There is a large scatter around the fit of Equation (10), which we wish to propagate through our calculation. We show the  $2\sigma$  limits of a log-Gaussian function, centered on the fit, with red dashed lines. These lines are given by  $\dot{M}_{\text{fit}}^- = 0.64\dot{M}_{\text{fit}}$ , and  $\dot{M}_{\text{fit}}^+ = 1.57\dot{M}_{\text{fit}}$ . When we estimate the mass-loss rate for the historical estimates of the open magnetic flux in Sections 4.3, we will use both Equation (10) and the  $2\sigma$  bounds.

With the mass-loss rate prescribed in terms of the open magnetic flux, we simplify Equation (7) further to

$$\tau = (2.4 \times 10^{30} \text{ erg}) \left( \frac{\phi_{\text{open}}}{8.0 \times 10^{22} \text{ Mx}} \right)^{1.59}, \quad (11)$$

where the solar wind torque is now given solely as a function of open magnetic flux. Similarly, the  $2\sigma$  bound of Equation (10) is propagated through Equation (7) to give,  $\tau^- = 0.89\tau(\phi_{\text{open}})$ , and  $\tau^+ = 1.12\tau(\phi_{\text{open}})$ . This allows us to predict the torque on the Sun due to the solar wind solely from the value of the open magnetic flux. Note that large ( $\sim 50\%$ ) uncertainties in  $\dot{M}$  translates to only a  $\sim 10\%$  uncertainty in torque, due to the weak dependence of  $\tau$  on  $\dot{M}$  in Equation (7).

##### 4.2. Reconstructions of the Solar Open Magnetic Flux

For the centuries and millennia pre-dating the space age, estimates of the open magnetic flux have been produced using a number of different indirect methods. To compare them with indirect methods and over a wide range of timescales, we plot the spacecraft data from Figure 1 also in Figure 3, which displays the solar wind parameters versus (inverse) logarithmic look-back time since 2019.

###### 4.2.1. Centennial Variability

Geomagnetic disturbances, caused by the interaction of the solar wind and the Earth’s magnetosphere, have been found to

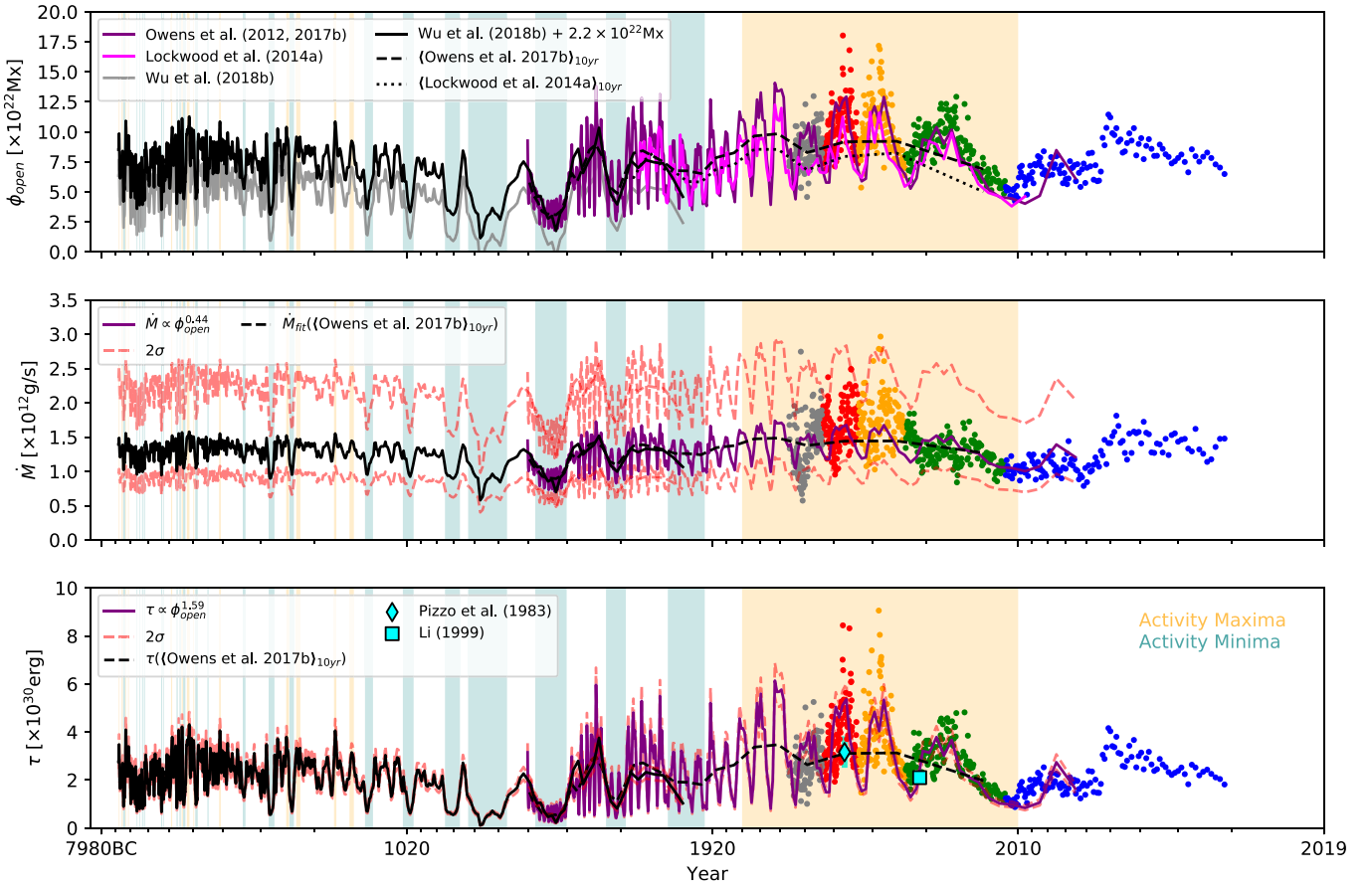


**Figure 3.** 9000 yr of solar open flux,  $\phi_{\text{open}}$ , mass-loss rate,  $\dot{M}$ , and our predicted solar wind torque,  $\tau$ , vs. inverse logarithmic look-back time from 2019. The results derived from the OMNI data set are plotted as they appeared in Figure 1. The  $\phi_{\text{open}}$  reconstructed by Owens et al. (2017b; group sunspot number) and Lockwood et al. (2014a; geomagnetic,  $aa$ -index) are plotted in the top panel with purple and magenta lines, respectively. We calibrate the long-time  $\phi_{\text{open}}$  reconstruction from Wu et al. (2018b; cosmogenic radionuclides), plotted in the top panel in gray, by first averaging the Owens et al. (2017b) and Lockwood et al. (2014a) reconstructions on the same decadal timescale, shown with dashed and dotted black lines, respectively, then we shifted the Wu et al. (2018b)  $\phi_{\text{open}}$  to match by adding a constant value. This reconstruction is shown with a solid black line, in good agreement with the smoothed values in the overlapping time period of  $\sim 1600$ –1900. Using the  $\phi_{\text{open}}$  from Owens et al. (2017b) and Wu et al. (2018b), the  $\dot{M}$  predicted using Equation (10) is plotted in the middle panel with solid purple and black lines, respectively. The  $\tau$  predicted by Equation (11), for each reconstruction is then plotted with solid purple and black lines in the bottom panel. For both predicted  $\dot{M}$  and  $\tau$ , the  $2\sigma$  bound is indicated with dashed red lines. Maxima and minima in solar activity are shaded with color.

correlate well with solar activity, and thus the amount of open magnetic flux in the heliosphere (Stamper et al. 1999; Rouillard et al. 2007; Svalgaard & Cliver 2010; Lockwood 2013; Lockwood et al. 2014b). We plot the open magnetic flux reconstructed by Lockwood et al. (2014a) using geomagnetic indices in the top panel of Figure 3 with a solid magenta line. Additionally, the amount of open magnetic flux can be estimated from records of the observed sunspot number, which date back further than the records of the geomagnetic field (Solanki et al. 2002; Krivova et al. 2007; Vieira & Solanki 2010; Owens & Lockwood 2012). We plot one such reconstruction from Owens & Lockwood (2012), which is also used in Owens et al. (2017b), with a solid purple line in the top panel of Figure 3.

The two reconstructions (using geomagnetic and sunspot records), agree with each other and, during the space age, with the open magnetic flux from Section 3.1 as they were tuned by the authors to do so. These reconstructions reveal the behavior of solar activity on a longer timescale than the 11 yr sunspot cycle. It has been noted that during the last century the open magnetic flux has been at a sustained high with respect to the longer data set (Lockwood et al. 2009). Inspecting the past four

centuries, there are also times when the open magnetic flux is shown to weaken for several magnetic cycles (Usoskin et al. 2015). We will examine the impact these different periods have on the solar wind torque in Section 4.3.

To examine the validity of our approach, we over-plot the reconstructed open magnetic flux (during the space age) from Owens et al. (2017b), the mass-loss rate it predicts using Equation (10), and the torque it predicts from Equation (11) in Figure 1 with solid black lines. Some temporal lag appears between the open magnetic flux and the observed mass-loss rate, which is not captured in our prediction for the mass-loss rate.<sup>5</sup> Despite this, the  $2\sigma$  bounds of Equation (10) roughly encompass the observed variation of the mass-loss rate (as constructed). The predicted torque, from Equation (11), is found to be in good agreement with the torques calculated in Section 3.1. The  $2\sigma$  bound from the torque prediction, shown by red dashed lines, indicates a weak dependence of solar wind torque on the assumed mass-loss rate. Therefore, provided the

<sup>5</sup> We attempted to fit many different functions for  $\dot{M}$ , some of which considered a time-lag between  $\dot{M}$  variations and the  $\phi_{\text{open}}$ . However, the additional complications did not statistically improve our  $\dot{M}$  predictions. Therefore, we present a simple function of  $\dot{M}(\phi_{\text{open}})$ .

mass-loss rate of the Sun has not changed significantly over each reconstructed timescale considered in this work, the open magnetic flux alone is capable of providing a good estimate of the solar wind torque.

#### 4.2.2. Millennial Variability

To go back further the open magnetic flux can only be reconstructed using cosmogenic radionuclides. Cosmogenic radionuclides, such as  $^{14}\text{C}$  and  $^{10}\text{Be}$ , are produced as a byproduct of the interaction of galactic cosmic rays and the Earth’s atmosphere. This rate is modulated by the geomagnetic field, but also by features in the heliosphere, such as the interplanetary magnetic field and solar wind (Stuiver 1961; Stuiver & Quay 1980). Therefore, the concentration of cosmogenic radionuclides can be used as a proxy for solar variability (see review by Beer et al. 2012).

Wu et al. (2018b) reconstructed the first solar modulation potential using multiple cosmogenic radionuclide records (e.g., from tree rings for  $^{14}\text{C}$ , and ice cores for  $^{10}\text{Be}$ ), from which the solar open magnetic flux was calculated with a physics-based model (Wu et al. 2018a). We plot the open magnetic flux from Wu et al. (2018b) in the top panel of Figure 3 with a solid gray line. However, the values of the open magnetic flux appear too low where they overlap with the centennial reconstructions, and they sometimes contain negative values. This occurs as the generation of open magnetic flux is dependent on the reconstructed sunspot number, such that times when the modulation potential recovers zero sunspot number, they predict anomalously low values for the open magnetic flux. It is difficult to correctly account for this, so we will simply adjust this reconstruction to match the centennials reconstructions. To adjust the reconstructions of Wu et al. (2018b), we create a comparison data set by averaging the open magnetic flux values from Lockwood et al. (2014a) and Owens et al. (2017b) on decadal timescales, to match the cadence recovered by the millennial reconstruction. These smoothed values are plotted with dotted and dashed lines, respectively, in the top panel of Figure 3. We then rescale the reconstruction of Wu et al. (2018b) by adding a constant offset of  $2.2 \times 10^{22}$  Mx, shown with a solid black line, which brings the smoothed and millennial reconstructions into agreement. It is worth noting that we have no physical justification for applying this linear shift to the reconstruction, which could introduce some (unknown) systematic error.

Examining all the values of open magnetic flux collected in Figure 3, the variability of the solar magnetic field appears to have a similar behavior across a range of timescales. During the last several millennia, there appear to be times similar to the modern grand maxima, and the grand minima which are observed in the centennial reconstructions. We find no clear evidence for times of solar open magnetic flux significantly greater than present in any of these records.

#### 4.3. Centuries and Millennia of Solar Wind Torque

To evaluate the solar wind torque during the last four centuries we use the open magnetic flux from Owens et al. (2017b). In Figure 3, we plot the mass-loss rate using Equation (10) and the resulting torque using Equation (11) with solid purple lines, and the  $2\sigma$  bounds with dashed red lines. The average solar wind torque during this “centennial”-scale reconstruction is calculated to be  $2.01 \times 10^{30}$  erg. Similarly, in Figure 3 we plot

the mass-loss rate and torque using the “millennial”-scale open flux reconstruction from Wu et al. (2018b) with solid black lines, along with the  $2\sigma$  bound in dashed red. We calculate the average torque for this data set to be  $2.16 \times 10^{30}$  erg. To better understand these results, we highlight historical maxima and minima of solar activity in Figure 3, and evaluate the average torque for each of these time periods, where available. The dates for these are taken from the review of Usoskin (2017) and are listed in Table 1, along with their average torques.

Using the centennial reconstruction, the *modern maximum* (which spans the majority of the 20th century), has a larger average torque of  $3.14 \times 10^{30}$  erg than considering the full centennial reconstruction. This is because the last four centuries also include multiple minima in solar activity, which host lower than average torques. Perhaps the most notable is the *Maunder minimum* (which spans the years 1640–1720), which has an average torque of  $0.67 \times 10^{30}$  erg. Using the millennial reconstruction, we find the torque calculated during the *Maunder minimum* is similar in strength to the many other named activity minima from the last 9000 yr, such as the *Spörer*, *Wolf* and *Oort* Minima. Reconstructions of solar activity appear to suggest the Sun spends around a sixth of its time in such a low torque state (see Usoskin et al. 2007), consistent with the Wu et al. (2018b) reconstruction. We find the solar wind torque during these activity minima have average values that span  $0.62$ – $1.73 \times 10^{30}$  erg, in contrast to the activity maxima that have much larger average values ranging from  $2.44$  to  $3.87 \times 10^{30}$  erg.

Reconstructions of the solar open magnetic flux (or sunspot number), based on proxies of solar activity, allow for the detection of periodicities in the Sun’s magnetic activity, on longer timescales than can be directly observed (Steinhilber et al. 2012; Usoskin et al. 2016; Wu et al. 2018b). Currently, there is little evidence for further variation, periodic or otherwise, in solar activity on longer timescales than the Hallstatt cycle which has a period of  $\sim 2400$  yr (Sonett et al. 1991). Since the solar wind torque derived in this work is directly linked to solar activity, a similar conclusion can be made about the secular variation of the solar angular momentum loss rate.

## 5. Discussion

We have now calculated the solar wind torque on a variety of timescales. In this section, we explore potential caveats to our results, and then compare our torques to those prescribed by models of the rotation period evolution of Sun-like stars.

### 5.1. Reliability of Open Flux Proxies and Our Predicted Mass-loss Rates

Indirect reconstructions of the solar open magnetic flux are by no means certain, and require careful examination and calibration. Geomagnetic indices (such as the *aa*-index) are often compiled from multiple ground-based monitoring stations, at differing latitudes in order to produce the most reliable value possible (e.g., Clilverd et al. 2005). The interpretation of geomagnetic records as a proxy for open magnetic flux appears robust, at least for times where direct measurements are available for comparison (see Figure 2 of Lockwood et al. 2004). Sunspot number records, from which our centennial torque is ultimately generated, often suffer from historical periods that are incomplete or uncertain due to a lack of reliable observers (Vaquero et al. 2011; Vaquero & Trigo 2014; Muñoz-Jaramillo & Vaquero 2018), or the modern



interpretation of their recordings being under debate (e.g., Usoskin et al. 2015). Models that recover the open magnetic flux based on sunspot number are shown to match concurrent geomagnetic and in situ measurements where available (Solanki et al. 2002; Vieira & Solanki 2010; Owens & Lockwood 2012). Our millennial torque is based on the changing concentration of cosmogenic radionuclides found in a range of terrestrial archives. This requires knowledge of the physical mechanisms which produce, transport, and deposit each radioisotope (e.g., Reimer et al. 2009; Heikkilä et al. 2013). These processes typically smooth variability on decadal timescales, such that the familiar 11 yr sunspot cycle is not observed. Furthermore, linking these results to the open magnetic flux requires careful calibration (e.g., Usoskin et al. 2003; Solanki et al. 2004).

The fact that the various proxies agree with each other where they overlap is because they were calibrated to do so. Typically, the amplitude of variation in each reconstruction is a free parameter, but the waveform is fixed by the data. The implicit assumption made is that the relationship between each proxy and the open magnetic flux is the same in the past as it is now, though it is difficult to know whether these relationships may have changed during the timescale of each reconstruction. Despite the potential limitations of each reconstruction, we have taken each reconstruction at “face value” to characterize long-term variability, so our calculated torques carry all their associated uncertainties.

To reconstruct the mass-loss rate of the Sun, we chose to fit Equation (10) to the available data, and represented the apparent spread of values around this fit using a  $2\sigma$  bound. The solar mass-loss rate is not observed to vary substantially (extremes of  $0.7\text{--}3.0 \times 10^{12} \text{ g s}^{-1}$ , see also Cohen 2011), and the torques calculated using Equation (7) are weakly dependent on our choice of mass-loss rate (when compared to the open magnetic flux). For example, to double the solar wind torque by only modifying the mass-loss rate would require the mass-loss rate to increase by a factor of  $\sim 14$ ; therefore, unless the solar wind mass flux was very different in the past, uncertainties in the functional form of Equation (2) do not significantly influence our results.

### 5.2. Impacts of Magnetic Variability on Short Timescales

Reconstructions of solar activity based on the concentrations of cosmogenic radionuclides incur smoothing effects from the transport and deposition timescales of each radionuclide. Therefore, such records struggle to recover short timescales variability, such as the 11 yr sunspot cycle. Typically, this can be thought of as averaging the activity of the Sun over decadal timescales. Additionally, the centennial reconstruction is averaged on annual timescales and our in situ measurements are averaged to 27 days. Due to the nonlinear dependence of Equation (11) on the open magnetic flux in the solar wind, short-term variability in the open magnetic flux, even around a fixed average value, will increase the long-term average torques. So, our millennial averaged torque using Wu et al. (2018b) is most likely slightly smaller than the true value.

The significance of this effect over the complete nine millennia can be probed in a few ways. The standard deviation of the torque for each reconstruction about its average value is found to decrease as the averaging timescale grows. Consequently, each reconstruction is only sensitive to variability on timescales larger than the cadence of the data set. By comparing the average torques from the smoothed reconstructions of Lockwood et al. (2014a) and Owens et al. (2017b) to their original data sets, we find the original data sets have a

larger torque by  $\sim 4\%$  than their smoothed counterparts; a result of the nonlinearity of the torque on open magnetic flux. For timescales shorter than 27 day, we have no measure of how variability affects our average values compared to the true value, but observed variations on shorter timescales may be ever more dominated by spatial variations in the wind, rather than variations in the global, integrated wind properties.

### 5.3. Comparison to Rotation–evolution Torques

One motivation for the present work was the finding of Finley et al. (2018), that the solar wind torque is less than that predicted by a Skumanich (1972) relation (a value of  $6.2 \times 10^{30} \text{ erg}$ ). One possible solution to this is that the torque varies on a longer timescale than the  $\sim 20 \text{ yr}$  examined in that work. Here we rule out that variability on timescales of up to 9000 yr can be the cause of this difference. The average torque from the last nine millennia appears consistent with present-day torque calculations for the Sun (Pizzo et al. 1983; Li 1999; Alvarado-Gómez et al. 2016; Réville & Brun 2017; Ó Fionnagáin et al. 2018; Usmanov et al. 2018). In order to reconcile the solar wind torque with that predicted by the Skumanich relation, the average open magnetic flux, for example, would need to be  $\sim 14 \times 10^{22} \text{ Mx}$ , which is well above most measurements shown in the top panel of Figure 3.

However, we cannot rule out that the torque varies on longer timescales. Any cyclical variations in the torque on timescales shorter than  $\sim 10^7\text{--}10^8 \text{ yr}$  would not noticeably change the observed spin distributions of stars with ages  $\gtrsim 1 \text{ Gyr}$ . Thus, the solar torque could still be reconciled with the Skumanich torque, if it varies on much longer timescales than probed here, and if the Sun is currently in a “low torque state.” Alternatively, if the estimates of the present-day solar wind torque are correct, they may be consistent with the suggestion of van Saders et al. (2016), that Sun-like stars transition to a state of permanently weakened torque at approximately the solar age. If that is the case, our results mean that this transition either occurred more than  $\sim 10^4 \text{ yr}$  ago for the Sun, or that any continuing transition is so gradual as to not be measurable on that timescale.

If the solar wind torque does indeed vary significantly on longer timescales than probed here, it suggests that the present-day wind torques of other stars should scatter (by at least a factor of  $\sim 3$ ) around the torque predicted by rotation–evolution models. Recently, Finley et al. (2019) estimated the torques of four stars that had surface magnetic field measurements and some information about their mass-loss rates (see also See et al. 2019, submitted). In all cases, the estimated torques were a factor of several times smaller than inferred from rotation–evolution models. They only studied four stars, and the systematic uncertainties are large, but this is evidence against significant long-term cyclical variability causing the discrepancy.

If long-term variability in the angular momentum loss rate of Sun-like stars does not resolve this discrepancy, then it could indicate systematic errors in the wind models, or the observed wind parameters, although the origins of such errors are unclear. On the shortest timescales, there also exist a range of transient phenomena in the corona (Cane & Richardson 2003; Rod’kin et al. 2016; Sanchez-Diaz et al. 2017), along with short timescale variations in the solar wind (King & Papitashvili 2005; Thatcher & Müller 2011), which are not incorporated into steady-state solutions of the wind. The impact these have on our semi-analytic formulae for the torque (i.e., Equation (7)) are poorly constrained (Aarnio et al. 2012).

## 6. Conclusion

In this paper we have investigated the angular momentum loss rate of the Sun on a longer timescale than previously attempted. To do this, we use the semi-analytic braking law of FM18 to calculate the torque on the Sun due to the solar wind. We first expand the calculation of Finley et al. (2018) throughout the entire space age by using in situ spacecraft measurements, taken from the OMNI data set. We then utilize reconstructions of the solar open magnetic flux, based on geomagnetic indices (Lockwood et al. 2014a), sunspot number records (Owens & Lockwood 2012), and concentrations of cosmogenic radionuclides (Wu et al. 2018b), to estimate the braking torque over the last four centuries, and then the last nine millennia.

The Sun undergoes significant variation in its magnetic activity on centennial and millennial timescales, which include times of grand maxima and minima of activity. The average torque during grand maxima ranges from  $2.4$  to  $3.9 \times 10^{30}$  erg, with peaks of  $\sim 5 \times 10^{30}$  erg. To contrast this, grand minima (such as the *Maunder*, *Spörer*, *Wolf*, and *Oort* minimum) produce some of the lowest values from  $0.6$  to  $1.7 \times 10^{30}$  erg. Overall, we find the average angular momentum loss rate of the Sun during the last nine millennia to be  $2.2 \times 10^{30}$  erg, which is equal to the average value during the last two decades.

The values calculated in this work remain contrary to those required by current rotation–evolution models of Sun-like stars. Such models predict a braking torque of  $6.2 \times 10^{30}$  erg (Matt et al. 2015; Finley et al. 2018), which we do not recover by using data spanning from present to 6755BC, roughly 9000 yr. This discrepancy could be due to the simplicity of the current MHD wind models, or to much longer timescale variation in the solar torque, or to uncertainties in measuring solar wind parameters (and inferring them in the past), or to significant deviations in the spin-down torque of low-mass stars from the Skumanich (1972) relation around the age of the Sun. Further exploration of this discrepancy is required, and with Parker Solar Probe making in situ measurements of the solar wind closer to the Sun than previously attempted (Fox et al. 2016), a direct measurement of the angular momentum loss rate would help to validate, or discredit, our calculations.

We thank the many instrument teams whose data contributed to the OMNI data set, and the NASA/GSFC’s Space Physics Data Facility’s OMNIWeb service for providing this data. A.J.F., S.D., and S.P.M. acknowledge funding from the European Research Council (ERC) under the European Unions Horizon 2020 research and innovation programme (grant agreement No. 682393 AWESoMeStars). M.O. is funded by Science and Technology Facilities Council (STFC) grant Nos. ST/M000885/1 and ST/R000921/1. Figures in this work are produced using the python package matplotlib (Hunter 2007).

## Appendix

### Grand Maxima and Minima Solar Wind Torques

For the solar angular momentum loss rate generated using Equation (11) and the open magnetic flux reconstructions of Owens & Lockwood (2012) and Wu et al. (2018b), centennial and millennial-scale reconstructions, respectively, we list in Table 1 the average values during historical grand maxima and minima in solar activity. The dates for which are taken from the review of Usoskin (2017).

**Table 1**  
Average Solar Wind Torques for Historical Activity Maxima and Minima

Activity	Period Name	Duration		$\langle \tau \rangle$	
		Year (–BC/AC)		$(\times 10^{30} \text{ erg})$	
		Start	End	Centennial	Millennial
Activity Maxima	Modern	1940	2010	3.14	...
	...	480	530	...	2.91
	...	290	330	...	3.67
	...	–280	–210	...	2.93
	...	–460	–410	...	3.26
	...	–2090	–2040	...	3.68
	...	–2970	–2940	...	3.47
	...	–3220	–3120	...	3.80
	...	–3430	–3380	...	3.72
	...	–3885	–3835	...	3.23
	...	–6140	–6100	...	2.95
	...	–6300	–6260	...	3.87
	...	–6550	–6480	...	2.44
...	–6730	–6690	...	3.09	
Activity Minima	Glassberg	1880	1914	2.22	...
	Dalton	1797	1828	1.22	1.11
	Maunder	1640	1720	0.67	0.67
	Spörer	1390	1550	...	0.62
	Wolf	1270	1350	...	0.74
	Oort	990	1070	...	1.20
	...	650	730	...	1.12
	...	–400	–320	...	1.04
	...	–810	–690	...	0.89
	...	–1400	–1350	...	1.46
	...	–2470	–2430	...	1.73
	...	–2900	–2810	...	1.30
	...	–3370	–3280	...	1.21
	...	–3520	–3470	...	1.39
	...	–3645	–3595	...	1.18
	...	–4235	–4205	...	1.42
	...	–4340	–4290	...	1.05
...	–5220	–5170	...	1.25	
...	–5325	–5275	...	1.20	
...	–5480	–5440	...	1.03	
...	–5630	–5590	...	0.93	
...	–6450	–6320	...	1.33	

## ORCID iDs

Adam J. Finley  <https://orcid.org/0000-0002-3020-9409>  
 Sean P. Matt  <https://orcid.org/0000-0001-9590-2274>  
 Mathew Owens  <https://orcid.org/0000-0003-2061-2453>  
 Chi-Ju Wu  <https://orcid.org/0000-0002-9998-4657>

## References

- Aarnio, A. N., Matt, S. P., & Stassun, K. G. 2012, *ApJ*, 760, 9  
 Agüeros, M. A. 2017, *RMxAA*, 49, 80  
 Agüeros, M. A., Covey, K. R., Lemosias, J. J., et al. 2011, *ApJ*, 740, 110  
 Alvarado-Gómez, J., Hussain, G., Cohen, O., et al. 2016, *A&A*, 594, A95  
 Amard, L., Palacios, A., Charbonnel, C., Gallet, F., & Bouvier, J. 2016, *A&A*, 587, A105  
 Barnes, S. A. 2003, *ApJ*, 586, 464  
 Barnes, S. A. 2010, *ApJ*, 722, 222  
 Beer, J., McCracken, K., & Steiger, R. 2012, *Cosmogenic Radionuclides: Theory and Applications in the Terrestrial and Space Environments* (Berlin: Springer)  
 Blackman, E. G., & Owen, J. E. 2016, *MNRAS*, 458, 1548

- Bouvier, J., Matt, S. P., Mohanty, S., et al. 2014, *Protostars and Planets VI*, 914 (Tucson, AZ: Univ. Arizona Press), 433
- Brown, T. M. 2014, *ApJ*, 789, 101
- Brun, A. S., & Browning, M. K. 2017, *LRSP*, 14, 4
- Cane, H., & Richardson, I. 2003, *JGRA*, 108
- Clette, F., Svalgaard, L., Vaquero, J. M., & Cliver, E. W. 2014, *SSRv*, 186, 35
- Ciliverd, M. A., Clarke, E., Ulich, T., Linthe, J., & Rishbeth, H. 2005, *JGRA*, 110
- Cohen, O. 2011, *MNRAS*, 417, 2592
- Cohen, O., & Drake, J. J. 2014, *ApJ*, 783, 55
- Covey, K. R., Agüeros, M. A., Law, N. M., et al. 2016, *ApJ*, 822, 81
- Cranmer, S. R., Gibson, S. E., & Riley, P. 2017, *SSRv*, 1
- Cranmer, S. R., & Saar, S. H. 2011, *ApJ*, 741, 54
- Delorme, P., Cameron, A. C., Hebb, L., et al. 2011, *MNRAS*, 413, 2218
- DeRosa, M., Brun, A., & Hoeksema, J. 2012, *ApJ*, 757, 96
- Douglas, S. T., Agüeros, M. A., Covey, K. R., & Kraus, A. 2017, *ApJ*, 842, 83
- Echer, E., Gonzalez, W., Gonzalez, A., et al. 2004, *JASTP*, 66, 1019
- Finley, A. J., & Matt, S. P. 2017, *ApJ*, 845, 46
- Finley, A. J., & Matt, S. P. 2018, *ApJ*, 854, 78
- Finley, A. J., Matt, S. P., & See, V. 2018, *ApJ*, 864, 125
- Finley, A. J., See, V., & Matt, S. P. 2019, *ApJ*, 876, 44
- Fox, N., Velli, M., Bale, S., et al. 2016, *SSRv*, 204, 7
- Gallet, F., & Bouvier, J. 2013, *A&A*, 556, A36
- Gallet, F., & Bouvier, J. 2015, *A&A*, 577, A98
- Garraffo, C., Drake, J., Dotter, A., et al. 2018, *ApJ*, 862, 90
- Garraffo, C., Drake, J. J., & Cohen, O. 2015, *ApJ*, 813, 40
- Garraffo, C., Drake, J. J., & Cohen, O. 2016, *A&A*, 595, A110
- Heikkilä, U., Beer, J., Abreu, J., & Steinhilber, F. 2013, *SSRv*, 176, 321
- Hunter, J. D. 2007, *CSE*, 9, 90
- Johnstone, C., Güdel, M., Lüftinger, T., Toth, G., & Brott, I. 2015, *A&A*, 577, A27
- Kawaler, S. D. 1988, *ApJ*, 333, 236
- King, J., & Papatashvili, N. 2005, *JGRA*, 110
- Krivova, N., Balmaceda, L., & Solanki, S. 2007, *A&A*, 467, 335
- Li, J. 1999, *MNRAS*, 302, 203
- Lockwood, M. 2013, *LRSP*, 10, 4
- Lockwood, M., Forsyth, R., Balogh, A., & McComas, D. 2004, *AnGeo*, 22, 1395
- Lockwood, M., Nevanlinna, H., Barnard, L., et al. 2014a, *Copernicus Publications for the European Geosciences Union*, 383
- Lockwood, M., Owens, M., & Barnard, L. 2014b, *JGRA*, 119, 5172
- Lockwood, M., Rouillard, A., & Finch, I. 2009, *ApJ*, 700, 937
- Matt, S., & Pudritz, R. E. 2008, *ApJ*, 678, 1109
- Matt, S. P., Brun, A. S., Baraffe, I., Bouvier, J., & Chabrier, G. 2015, *ApJL*, 799, L23
- Matt, S. P., MacGregor, K. B., Pinsonneault, M. H., & Greene, T. P. 2012, *ApJL*, 754, L26
- McComas, D., Angold, N., Elliott, H., et al. 2013, *ApJ*, 779, 2
- McQuillan, A., Aigrain, S., & Mazeh, T. 2013, *MNRAS*, 432, 1203
- Mestel, L. 1968, *MNRAS*, 138, 359
- Mishra, W., Srivastava, N., Wang, Y., et al. 2019, *MNRAS*, 486, 4671
- Mullan, D. 1978, *ApJ*, 226, 151
- Muñoz-Jaramillo, A., & Vaquero, J. M. 2018, *NatAs*, 1
- Núñez, A., Agüeros, M. A., Covey, K. R., et al. 2015, *ApJ*, 809, 161
- Ó Fionnagáin, D., & Vidotto, A. 2018, *MNRAS*, 476, 2465
- Ó Fionnagáin, D., Vidotto, A., Petit, P., et al. 2018, *MNRAS*, 483, 873
- Owens, M., & Lockwood, M. 2012, *JGRA*, 117
- Owens, M., Lockwood, M., Riley, P., & Linker, J. 2017a, *JGRA*, 122
- Owens, M. J., Arge, C., Crooker, N., Schwadron, N., & Horbury, T. 2008, *JGRA*, 113
- Owens, M. J., Crooker, N., & Lockwood, M. 2011, *JGRA*, 116
- Owens, M. J., Lockwood, M., & Riley, P. 2017b, *NatSR*, 7, 41548
- Pantolmos, G., & Matt, S. P. 2017, *ApJ*, 849, 83
- Perri, B., Brun, A. S., Réville, V., & Strugarek, A. 2018, *JPhI*, 84
- Phillips, J., Bame, S., Barnes, A., et al. 1995, *GeoRL*, 22, 3301
- Pinto, R. F., Brun, A. S., Jouve, L., & Grappin, R. 2011, *ApJ*, 737, 72
- Pinto, R. F., & Rouillard, A. P. 2017, *ApJ*, 838, 89
- Pizzo, V., Schwenn, R., Marsch, E., et al. 1983, *ApJ*, 271, 335
- Rebull, L., Stauffer, J., Bouvier, J., et al. 2016, *AJ*, 152, 113
- Reimer, P. J., Baillic, M. G., Bard, E., et al. 2009, *Radiocarbon*, 51, 1111
- Reimers, D. 1975, *Problems in Stellar Atmospheres and Envelopes* (Berlin: Springer), 229
- Reimers, D. 1977, *A&A*, 61, 217
- Réville, V., & Brun, A. S. 2017, *ApJ*, 850, 45
- Réville, V., Brun, A. S., Matt, S. P., Strugarek, A., & Pinto, R. F. 2015a, *ApJ*, 798, 116
- Réville, V., Brun, A. S., Strugarek, A., et al. 2015b, *ApJ*, 814, 99
- Réville, V., Folsom, C. P., Strugarek, A., & Brun, A. S. 2016, *ApJ*, 832, 145
- Rod'kin, D., Shugay, Y. S., Slemzin, V., & Veselovskii, I. 2016, *SoSyR*, 50, 44
- Rouillard, A., Lockwood, M., & Finch, I. 2007, *JGRA*, 112
- Sadeghi Ardestani, L., Guillot, T., & Morel, P. 2017, *MNRAS*, 472, 2590
- Sanchez-Diaz, E., Rouillard, A. P., Davies, J. A., et al. 2017, *ApJ*, 851, 32
- Schröder, K.-P., & Cuntz, M. 2005, *ApJL*, 630, L73
- See, V., Jardine, M., Vidotto, A., et al. 2018, *MNRAS*, 474, 536
- See, V., et al. 2019, *ApJ*, submitted
- Skumanich, A. 1972, *ApJ*, 171, 565
- Smith, E. J., & Balogh, A. 1995, *GeoRL*, 22, 3317
- Soderblom, D. 1983, *ApJS*, 53, 1
- Solanki, S., Schüssler, M., & Fligge, M. 2002, *A&A*, 383, 706
- Solanki, S. K., Usoskin, I. G., Kromer, B., Schüssler, M., & Beer, J. 2004, *Natur*, 431, 1084
- Sonett, C. P., Giampapa, M. S., & Matthews, M. S. 1991, *The Sun in Time* (Tucson, AZ: Univ. Arizona Press)
- Stamper, R., Lockwood, M., Wild, M., & Clark, T. 1999, *JGRA*, 104, 28325
- Steinhilber, F., Abreu, J. A., Beer, J., et al. 2012, *PNAS*, 109, 5967
- Strugarek, A., Brun, A., Matt, S., et al. 2014, in *SF2A-2014: Proc. Annual Meeting of the French Society of Astronomy and Astrophysics*, ed. J. Ballet et al., 279
- Stuiver, M. 1961, *JGR*, 66, 273
- Stuiver, M., & Quay, P. D. 1980, *Sci*, 207, 11
- Svalgaard, L., & Cliver, E. W. 2010, *JGRA*, 115
- Thatcher, L., & Müller, H.-R. 2011, *JGRA*, 116
- Usmanov, A. V., Matthaues, W. H., Goldstein, M. L., & Chhiber, R. 2018, *ApJ*, 865, 25
- Usoskin, I., Gallet, Y., Lopes, F., Kovaltsov, G., & Hulot, G. 2016, *A&A*, 587, A150
- Usoskin, I. G. 2017, *LRSP*, 14, 3
- Usoskin, I. G., Arlt, R., Asvestari, E., et al. 2015, *A&A*, 581, A95
- Usoskin, I. G., Solanki, S. K., & Kovaltsov, G. A. 2007, *A&A*, 471, 301
- Usoskin, I. G., Solanki, S. K., Schüssler, M., Mursula, K., & Alanko, K. 2003, *PhRvL*, 91, 211101
- van Saders, J. L., Ceillier, T., Metcalfe, T. S., et al. 2016, *Natur*, 529, 181
- Van Saders, J. L., & Pinsonneault, M. H. 2013, *ApJ*, 776, 67
- Vaquero, J. M., Gallego, M., Usoskin, I. G., & Kovaltsov, G. A. 2011, *ApJL*, 731, L24
- Vaquero, J. M., & Trigo, R. 2014, *SoPh*, 289, 803
- Vidotto, A., Lehmann, L., Jardine, M., & Pevtsov, A. 2018, *MNRAS*, 480, 477
- Vieira, L. E. A., & Solanki, S. K. 2010, *A&A*, 509, A100
- Wang, Y.-M., & Sheeley, N., Jr 1995, *ApJL*, 447, L143
- Webb, D., Howard, R., Cyr, O. S., & Vourlidas, A. 2017, *ApJ*, 851, 142
- Webb, D. F., & Howard, R. A. 1994, *JGRA*, 99, 4201
- Weber, E. J., & Davis, L. 1967, *ApJ*, 148, 217
- Wu, C.-J., Krivova, N., Solanki, S. K., & Usoskin, I. G. 2018a, *A&A*, 620, A120
- Wu, C. J., Usoskin, I., Krivova, N., et al. 2018b, *A&A*, 615, 93

## 5.5 Additional Information

The published paper (Section 5.4) benefitted from the work of Siddhant Deshmukh, who tirelessly searched for a way to connect the Sun's mass-loss rate to any of the activity proxies/reconstructions, during his summer project in 2018. In the paper, a simple power law fit between mass-loss and open flux was used for simplicity, so here I provide some additional findings.

### 5.5.1 Improving the Solar Mass-loss Rate Prediction

When plotted as a time-series, the mass-loss rate calculated from in-situ data (by assuming isotropy etc), appears to be proportional to the open magnetic flux for large parts of the space-age. This is why the log-log fit was a reasonable enough scaling, however the mass-loss rate also appears to lag slightly behind the variation in the open magnetic flux. With this in mind, it was hoped that a relationship could be derived empirically that could be used for the entirety of the open flux reconstructions. This proved to be a difficult challenge, with many different relationships being explored, from parameterising the fraction of fast/slow wind using the model of Owens et al. (2017a), to applying a basic neural network. Figure 5.4 shows one attempt at improving on the simple power law fit used in the previous paper. The bottom panel shows mass-loss rate versus open magnetic flux which is now coloured by decimal year. It can be easily seen that different power law slopes  $m$ , are needed to fit different time periods. The top panel shows the sunspot number during the same time period, over which I have plotted the value of the fit slopes, as found in the bottom panel. Though there is structure, it does not follow any proxy for solar activity and so it cannot be easily applied to the reconstructed open flux.

## 5.6 Summary

In this Chapter the  $\Upsilon_{open}$  braking law is applied to open flux reconstructions spanning several millennia. Previously the  $\Upsilon_{open}$  braking law produced a solar angular momentum-

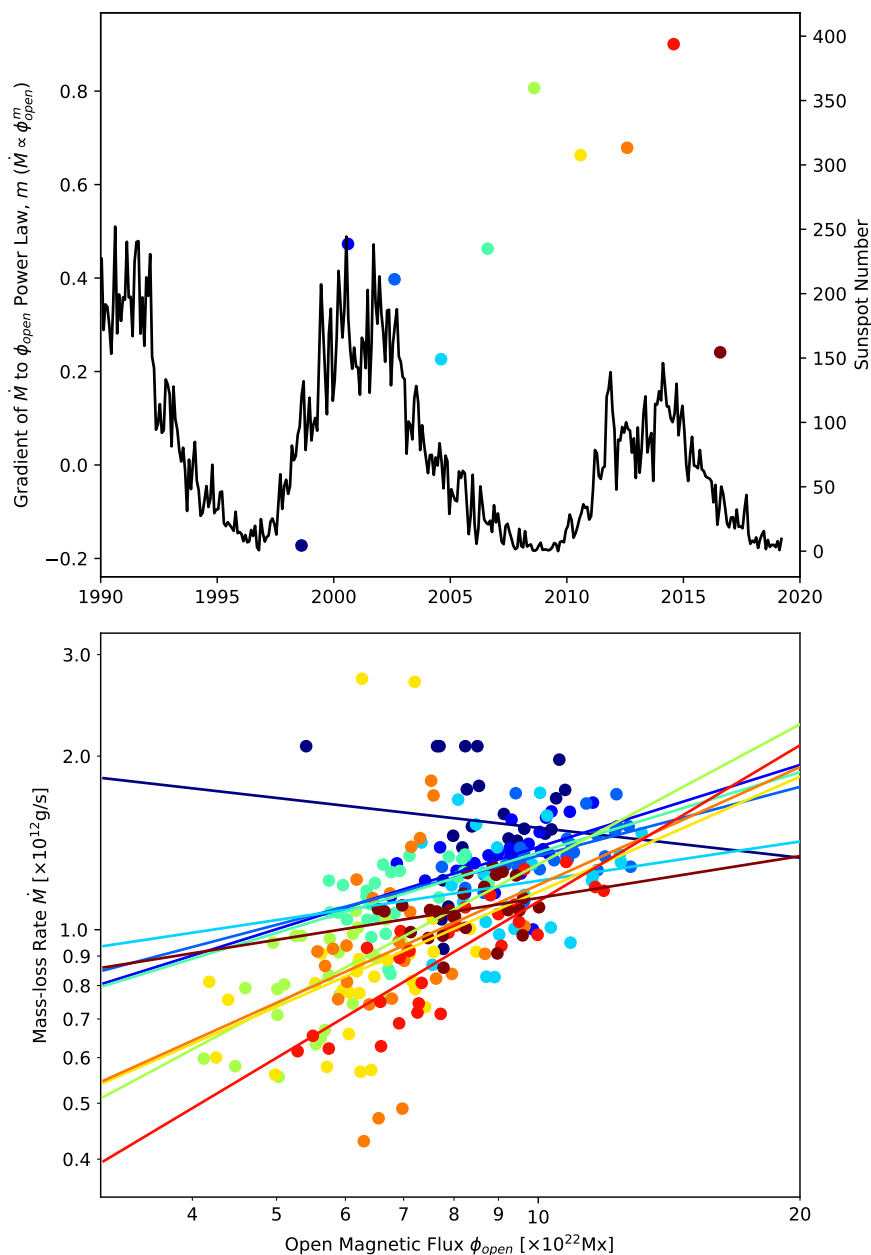


**Figure 5.4:** Experiment in improving the mass-loss rate versus open magnetic flux relation used in Section 4.3. Top: Sunspot number shown in black. The power law index  $m$  found by considering different 2 year periods in the data are coloured and plotted versus time. Bottom: The fits and data from in-situ observations of the solar wind, coloured by time.

loss rate that was around a factor of three smaller than the value required for a Skumanich spin-down at the age of the Sun. By using a longer dataset, I looked to see if this discrepancy is explained by further temporal variability in the Sun's magnetic activity. In order to apply the braking law, I connect the mass-loss rate of the Sun to the open flux using a power law relationship, as the mass-loss rate is an unknown quantity. I show that during the last several millennia, the variation of the open magnetic flux is not enough

---

to reconcile the braking law result with the rotation-evolution result. However, it must be strongly emphasised that the characteristic timescale for the rotation period evolution of the Sun is 10-100 million years which far exceeds the temporal coverage of this work. Therefore I cannot rule out further magnetic variability as being the reason for the angular momentum-loss rate discrepancy.

## Chapter 6

# Attempts to Directly Measure the Solar Angular Momentum-Loss Rate

### 6.1 Introduction

The results from Chapters 4 and 5 clearly show that the MHD model-driven estimates of the solar angular momentum-loss rate are around a factor of 3 smaller than the value produced by most rotation-evolution models. It is unclear if the wind models presented in this thesis are under-predicting the angular momentum-loss rate, or if the current angular momentum-loss rate in the solar wind is actually less than predicted by a Skumanich rotation-evolution. To investigate this further, in this Chapter I attempt to directly measure the angular momentum flux in the solar wind using in-situ spacecraft. This is a difficult measurement to make as the tangential flow speed of the solar wind at 1au (where most in-situ observations are made) is of the same order as instrumental noise and the error produced by a 1-2 degree pointing error in spacecraft attitude control. I first perform a review of current in-situ spacecraft and the instruments used to measure the solar wind plasma and magnetic field properties. Then I assess the angular momentum flux in the solar wind using the *Wind* spacecraft, which appears as it was published in *The Astrophysical Journal Letters*. Following this, I present some preliminary work using data from the Parker Solar Probe and discuss potential future observations with the recently launched

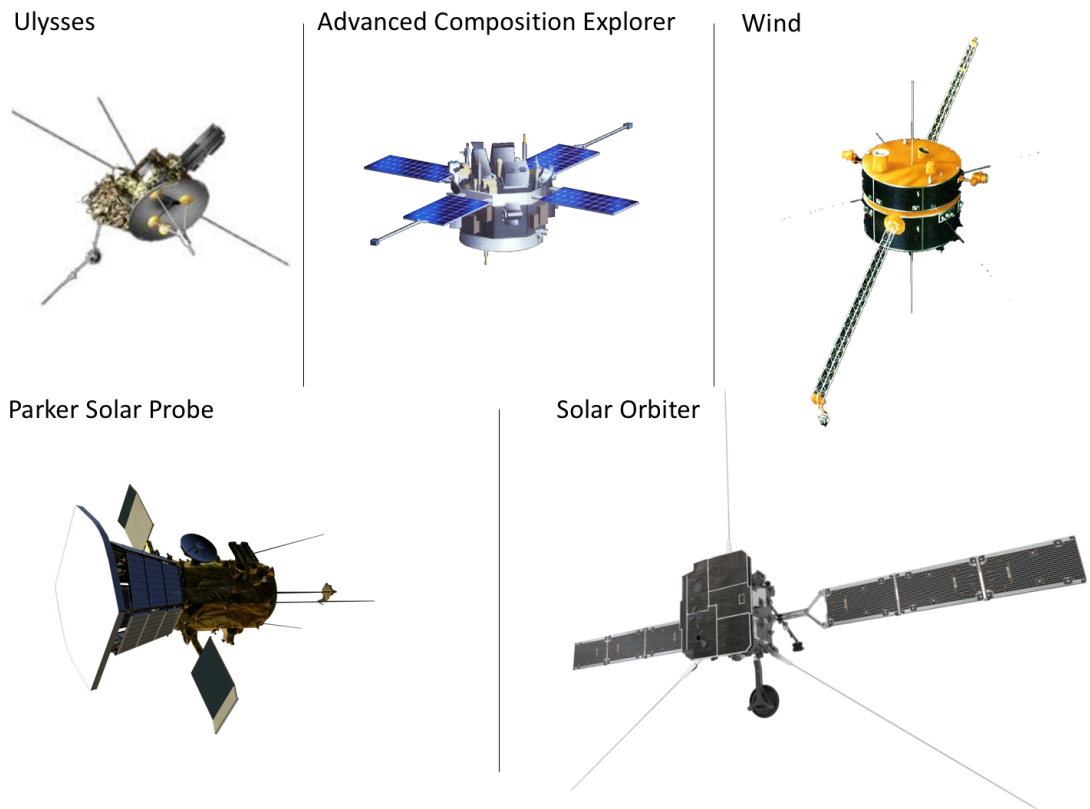


**Figure 6.1:** Examples of spacecraft which have been (or are still) immersed in the solar wind. Ulysses explored the polar wind of the Sun. The Advanced Composition Explorer (ACE) spacecraft monitors the solar wind arriving at Earth, stationed at L1. The *Wind* spacecraft explored the Earth's magnetosphere before joining ACE at L1. Parker Solar Probe (PSP) is currently studying the solar wind closer to the surface of the Sun than any man-made object previously. Solar Orbiter (SolO) has just been launched and will take remote sensing and in-situ data from inside Venus's orbit, at progressively higher latitudes. Images not to scale, taken from NASA/ESA sources.

Solar Orbiter spacecraft. I finish this Chapter with a summary of the results in the context of the overall thesis.

## 6.2 Review of In-situ Spacecraft Capabilities

There exist a variety of spacecraft that have travelled through the solar wind, measuring the properties of the plasma and magnetic field. Generally each spacecraft has a unique purpose, or area of study to which it aims to provide valuable observations. This could be magnetospheric physics, space weather, or fundamental plasma physics. A few examples of spacecraft which have studied (or will study) the solar wind specifically are depicted in Figure 6.1, most have been mentioned in the text previously. One of the key differences



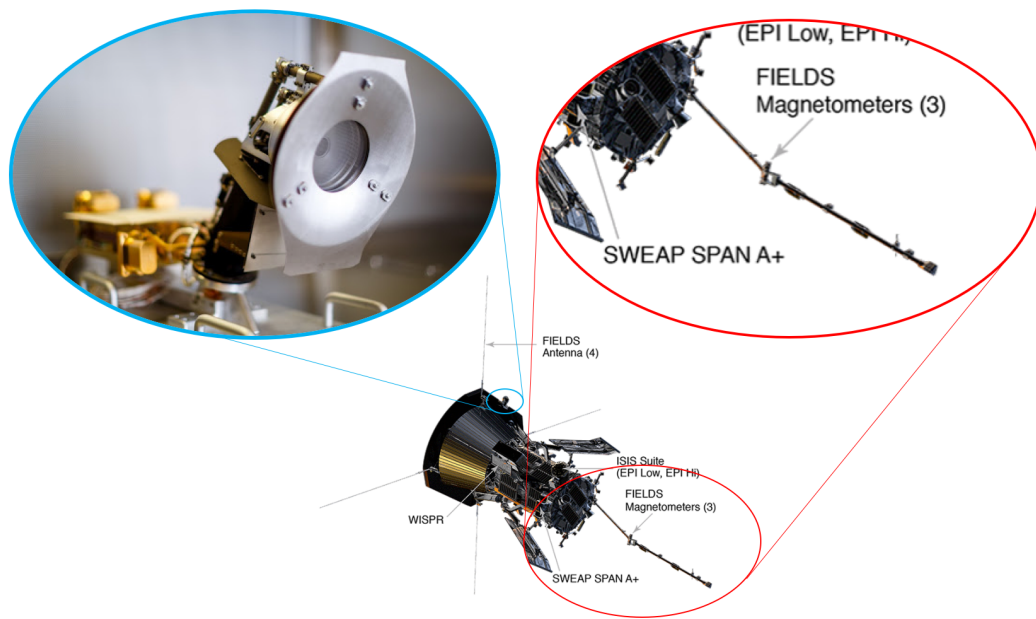


**Figure 6.2:** Example of two common instruments, a faraday cup (in blue), and a boom magnetometer (in red), using the Parker Solar Probe as an example. The faraday cup sits outside the heat-shield measuring the solar wind directly. The magnetometer instruments sit on a boom in the shadow of the spacecraft. The boom removes the influence of the spacecraft from measurements of the solar wind magnetic field. Images taken from NASA.

between the spacecraft in Figure 6.1 is the configuration of their orbits. Both the Advanced Composition Explorer (ACE) and *Wind* have spent a large amount of time at the L1 Lagrangian point between the Sun and Earth, whereas Ulysses and Solar Orbiter (SolO) are polar orbiters and so have sampled (will sample) the solar wind out of the ecliptic plane. Parker Solar Probe (PSP) is on a mission to “touch the Sun”, by which they mean to get closer than any spacecraft has ever been to the Sun before ( $< 10R_{\odot}$ ). As each mission is different, the spacecraft have different designs. Both PSP and SolO have heat shields to protect them from the increased temperatures close to the Sun. Ulysses, ACE, and *Wind* are all spin-stabilised spacecraft, which is an easy way to ensure the spacecraft point in a certain direction (this method was used mainly by earlier spacecraft).

### 6.2.1 Instrumentation Overview

Irrespective of their purpose, there are many commonalities between instrumentation due to the preferential selection of reliable and well-tested designs. One such example is the

faraday cup, which is an instrument designed to measure the kinematics of the solar wind plasma. The faraday cup has been a recurring design from the Voyager spacecraft to the recent PSP mission, from which the Solar Probe Cup is shown in Figure 6.2. Generally faraday cups work by collecting the charge from incoming ions which strike the detector. The flow of particles into the detector is modulated by an initial electrostatic field. The detector plate is then discharged and a current measured, from which the incoming particle distribution is reconstructed. The velocity of the particles can be recovered by comparing the relative fluxes measured on the different detector plates within the instrument. Another common instrument is the flux-gate magnetometer, which is used to detect the magnetic field vector in the solar wind. A fluxgate magnetometer is generally comprised of a magnetically susceptible core material wrapped in two coils of wire. An alternating current is passed through one coil, which drives the core material through a cycle of magnetic saturation (i.e. magnetised, unmagnetised, inversely magnetised, unmagnetised, magnetised, etc). The changing field induces a current in the second coil, which is measured by a detector. In zero magnetic field, the input and output currents are the same. However, when the core material experiences an external magnetic field, it is more easily saturated when aligned with the field and less easily when in opposition. This physical effect is used to measure the solar wind magnetic field in three directions by combining multiple perpendicular flux-gates. To avoid measuring the magnetic field of the spacecraft, magnetometer instruments are held away from the spacecraft by a boom structure, see Figure 6.2 as an example from PSP.

Each of these instruments have different limitations and uncertainties, which are compounded by the launch of the spacecraft. Instruments must generally be calibrated after launch, dealing with errors from issues with spacecraft attitude to instrumentation faults caused by the violent nature of rocket launches. Generally, the radial wind speed, density, and magnetic field vector are all reliably measured by in-situ detectors, however the non-radial wind speed of the solar wind is often ill-constrained. This is mainly a result of the comparatively small tangential wind speeds ( $v_T \sim 1 - 5\text{km/s}$  at 1au), which are easily washed out by errors in the spacecraft pointing (which allows some of the radial wind to contaminate the tangential).

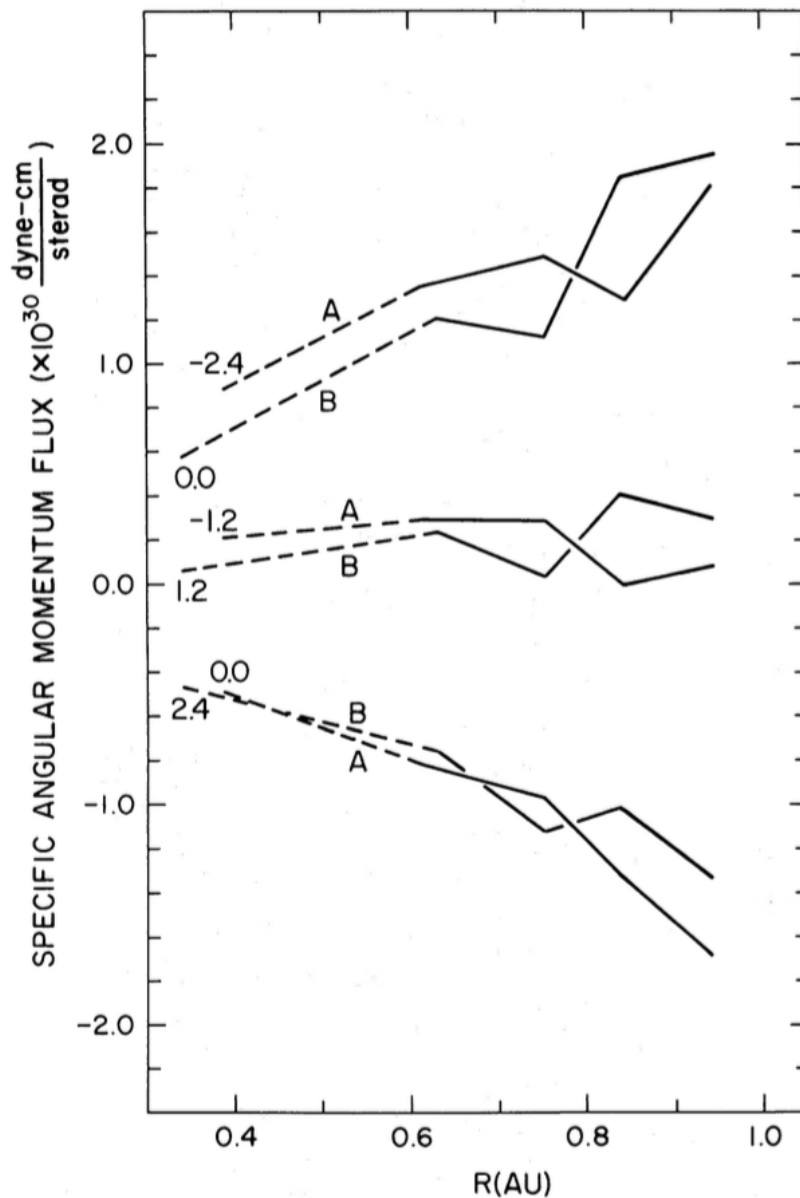


**Figure 6.3:** Measured angular momentum flux from the two Helios spacecraft (A and B). The unadjusted values are shown with 0.0, then the data is manipulated to remove an equal and opposite pointing error in spacecraft attitude. There appears to be a combined pointing error of 2.4 degrees between each spacecraft, and so assuming an equal and opposite error of 1.2 degrees the angular momentum flux are made to match. Note the error doesn't have to be equal and opposite, this is just the simplest (and easiest to correct for) possibility. Taken from Pizzo et al. (1983).

## 6.2.2 Examples of Past and Present Spacecraft Observations

A few examples of attempts to measure the tangential wind speed (or mechanical angular momentum flux) are detailed in this Section. Up until the work of this Chapter, the best previous measurement of the angular momentum flux in the solar wind was performed using the twin Helios spacecraft (Pizzo et al. 1983; Marsch and Richter 1984b).

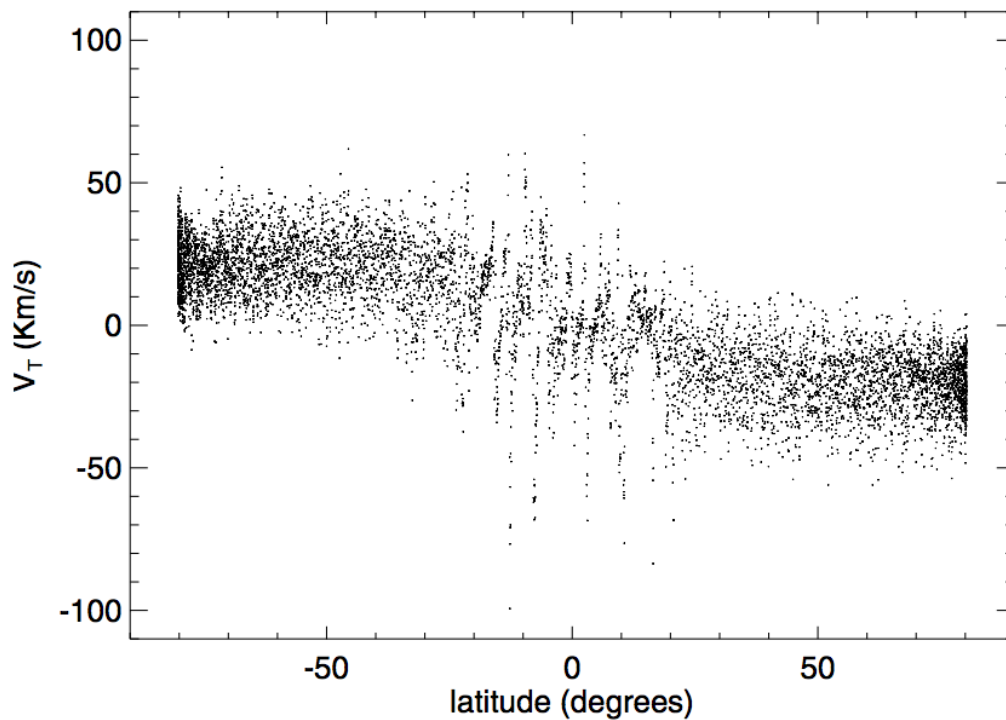


**Figure 6.4:** Tangential solar wind speed measured by Ulysses versus heliographic latitude. The solar wind is expected to have positive values at all latitudes, rather than rotating prograde in one hemisphere and retrograde in the other. This is an example of a pointing error, and so Ulysses (like many other spacecraft) cannot be used to measure angular momentum flux directly. Taken from Sauty et al. (2005).

During their lifetime, the Helios spacecraft approached closer to the Sun than any spacecraft before them ( $\approx 0.3\text{au}$ ). They measured the magnetic field stresses and mechanical angular momentum flux in the protons and alpha particles, however they discovered that the spacecraft suffered from a few degrees of pointing error, which skewed the results based on which spacecraft was used (this is shown in Figure 6.3). To resolve this, the instrument teams looked at a period of time when the spacecraft both measured the “same” solar wind, and used this to calibrate a correction to spacecraft pointing. The original angular momentum flux and the result from calibration is shown in Figure 6.3, where the Helios A and B spacecraft begin to agree with a correction of 2.4 degrees split equally between them. Despite the uncertainties produced by this correction, the measurement from Pizzo et al. (1983) remains one of the only direct measurements of the solar wind angular momentum flux.

I experimented with using other spacecraft to recreate this kind of direct measurement of angular momentum flux, for example using Ulysses as this would also be able

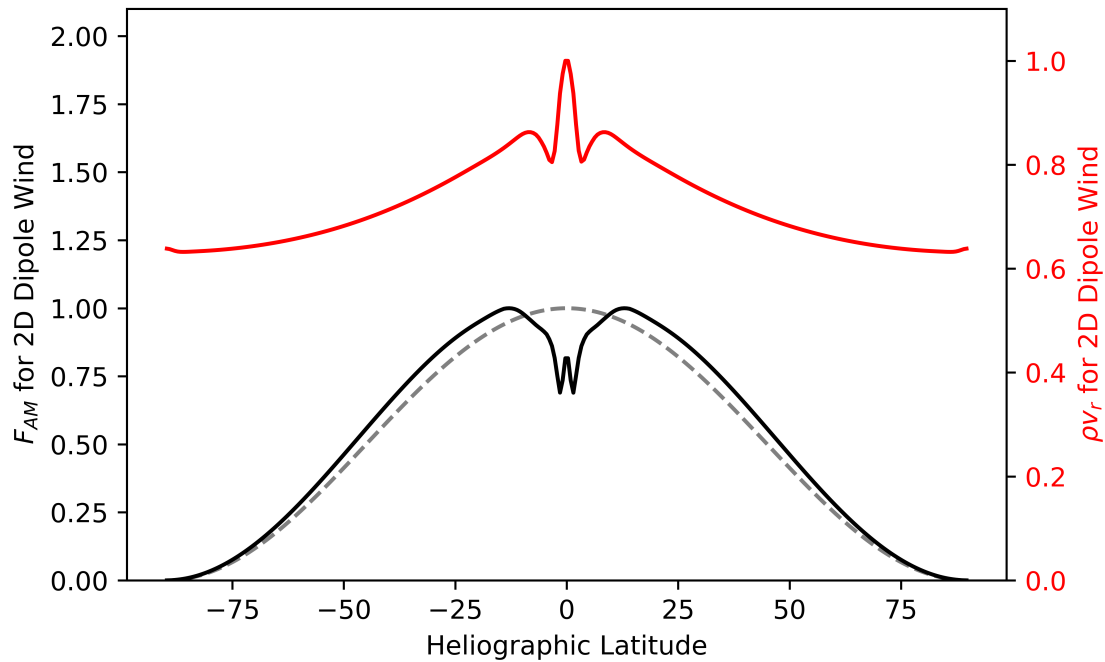


**Figure 6.5:** Latitudinal distribution of mass flux (red) and angular momentum flux  $F_{AM}$  (black) for one of the 2.5D dipole wind solution, computed with PLUTO in Chapter 3. Fluxes are normalised to their respective maximum values. A  $(\sin \theta)^2$  function is plotted with a dashed line, in comparison to the simulated angular momentum flux distribution. The simulated angular momentum flux, for the most part, is similar in shape to the  $(\sin \theta)^2$  function.

to track the latitudinal distribution. However, the Ulysses non-radial wind speeds contain strong pointing errors which contaminate the actual tangential wind speed signal. This is exemplified in a figure from Sauty et al. (2005), which I have reproduced in Figure 6.4. The tangential wind speeds recovered by Ulysses are far too large and are counter rotating in the Sun's northern and southern hemispheres. Similar errors appear across many spacecraft, which is why the Pizzo et al. (1983) measurement has not be surpassed. However, it was noticed by Mathew Owens (Private Communication) that the *Wind* spacecraft appeared to have tangential wind speeds which were not so heavily contaminated by spacecraft pointing errors, which motivated the published paper in this Chapter.

### 6.3 Latitudinal Distribution of Mass and Angular Momentum Flux from Simulations

In-situ observations from the *Wind* spacecraft, which are used in the following published paper, are limited to the equatorial solar wind. Therefore, there is uncertainty when transforming a given measurement of the angular momentum flux into a global loss rate. In order to guide my interpretation of the equatorial angular momentum flux, in Figure 6.5 I have plotted the latitudinal dependence of the mass flux and angular momentum flux from a typical dipole wind simulation in Chapter 3. The mass flux is observed to be roughly isotropic, with a variation of around 10 – 20% in the open stellar wind. The streamer wind above the closed dipolar magnetic field shows a large variation in both mass flux and angular momentum flux, some of which is likely numerical. The *Wind* spacecraft is not simply located in the heliospheric current sheet, instead it observes a variety of structures including solar wind emerging from equatorial coronal holes. Thus, the equatorial structure shown in Figure 6.5 is likely smoothed out by the typical 27-day averaging timescale.

In comparison to the angular momentum flux, I plot a  $(\sin \theta)^2$  function which appears to match well (except for the streamer structure). This function is motivated by two factors; 1) the angular momentum flux varies with cylindrical radius ( $r \sin \theta$ ), meaning it vanishes over the rotation poles, and 2) as the Sun roughly rotates as a solid body, from conservation of angular momentum, the tangential wind speeds would be expected to depend on latitude i.e.  $v_T \approx \Omega_{\odot} r \sin \theta$ . This introduces two  $\sin \theta$  dependencies which roughly explain the observed latitudinal distribution. Thus, from an estimation of the equatorial angular momentum flux, I can incorporate the likely flux versus latitude distribution by integrating over the  $(\sin \theta)^2$  function to find the global angular momentum-loss rate. Note that there are a few assumptions here, such as the MHD models being representative of the real solar wind, and the streamer belt structures being averaged out on 27-day timescales.



# Direct Detection of Solar Angular Momentum Loss with the *Wind* Spacecraft

Adam J. Finley<sup>1</sup> , Amy L. Hewitt<sup>1</sup>, Sean P. Matt<sup>1</sup> , Mathew Owens<sup>2</sup> , Rui F. Pinto<sup>3</sup> , and Victor Réville<sup>3</sup> 

<sup>1</sup>University of Exeter, Exeter, Devon, EX4 4QL, UK; [af472@exeter.ac.uk](mailto:af472@exeter.ac.uk)

<sup>2</sup>University of Reading, Reading, Berkshire, RG6 6BB, UK

<sup>3</sup>IRAP, Université Toulouse III—Paul Sabatier, CNRS, CNES, Toulouse, France

Received 2019 October 2; revised 2019 October 16; accepted 2019 October 22; published 2019 November 6

## Abstract

The rate at which the solar wind extracts angular momentum (AM) from the Sun has been predicted by theoretical models for many decades, and yet we lack a conclusive measurement from in situ observations. In this Letter we present a new estimate of the time-varying AM flux in the equatorial solar wind, as observed by the *Wind* spacecraft from 1994 to 2019. We separate the AM flux into contributions from the protons, alpha particles, and magnetic stresses, showing that the mechanical flux in the protons is  $\sim 3$  times larger than the magnetic field stresses. We observe the tendency for the AM flux of fast wind streams to be oppositely signed to the slow wind streams, as noted by previous authors. From the average total flux, we estimate the global AM loss rate of the Sun to be  $3.3 \times 10^{30}$  erg, which lies within the range of various magnetohydrodynamic wind models in the literature. This AM loss rate is a factor of  $\sim 2$  weaker than required for a Skumanich-like rotation period evolution ( $\Omega_* \propto \text{stellar age}^{-1/2}$ ), which should be considered in studies of the rotation period evolution of Sun-like stars.

*Unified Astronomy Thesaurus concepts:* Solar wind (1534); Solar rotation (1524); Solar evolution (1492); Stellar evolution (1599); Stellar rotation (1629); Magnetohydrodynamics (1964)

## 1. Introduction

During the last  $\sim 4$  billion years, the Sun's rotation period is thought to have changed significantly due to the solar wind (Gallet & Bouvier 2013, 2015; Brown 2014; Johnstone et al. 2015; Matt et al. 2015; Amard et al. 2016, 2019; Blackman & Owen 2016; Sadeghi Ardestani et al. 2017; Garraffo et al. 2018; See et al. 2018). This process, broadly referred to as wind braking, appears to explain the observed rotation periods of many low-mass (i.e.,  $\leq 1.3M_{\odot}$ ), main-sequence stars (Skumanich 1972; Soderblom 1983; Barnes 2003, 2010; Delorme et al. 2011; Van Saders & Pinsonneault 2013; Bouvier et al. 2014). Due to the interaction of the large-scale magnetic field on the outflowing plasma, this process is very efficient at removing angular momentum (AM), despite only a small fraction of a star's mass being lost to the stellar wind, during the main sequence (Weber & Davis 1967; Mestel 1968; Kawaler 1988).

Generally, the stellar magnetic field is thought of as providing a lever arm for the wind, which many authors have attempted to quantify using results from magnetohydrodynamic (MHD) simulations (Matt et al. 2012; Garraffo et al. 2015; Réville et al. 2015; Finley & Matt 2017, 2018; Pantolmos & Matt 2017). However, the AM loss rates from these MHD models have thus far been difficult to reconcile with the rates required by models of rotation period evolution for low-mass stars (Finley et al. 2018, 2019b; See et al. 2019). Since many solar quantities are known to high precision (such as mass, radius, rotation rate, and age), the Sun is often used to calibrate these rotation period evolution models. However, there are relatively few works that have attempted to model the current AM loss rate of the Sun (e.g., Alvarado-Gómez et al. 2016; Réville & Brun 2017; Finley et al. 2018; Usmanov et al. 2018; Ó Fionnagáin et al. 2019) and only a few studies that used in situ measurements of the solar wind plasma and magnetic field (Lazarus & Goldstein 1971; Pizzo et al. 1983; Marsch & Richter 1984a; Li 1999). Consequently, the value of the solar

AM loss rate remains uncertain, and the discrepancy between these two approaches remains in the literature.

The most direct, previous measurement of solar AM loss was performed using data from the two *Helios* spacecraft by Pizzo et al. (1983) and Marsch & Richter (1984a). Despite requiring significant corrections to account for errors in spacecraft pointing, and using less than one year's worth of data, these authors were able to separate the individual contributions of the protons, alpha particles, and magnetic field stresses. Interestingly, they showed that the alpha particles in the solar wind had an oppositely signed AM flux to the proton and magnetic components. Moreover, fast-slow stream-interactions appeared to transfer AM away from the fast component of the wind (causing the fast wind to often carry negative AM flux, like the alpha particles), which had also been noted by Lazarus & Goldstein (1971). When compared, the contribution of the protons ( $F_{AM,p}$ ) and magnetic field stresses ( $F_{AM,B}$ ) were found on average to be comparable in strength ( $F_{AM,p}/F_{AM,B} \sim 1$ ), although the AM flux in the protons was one of the most poorly determined components of the total flux. This result differs from previous work by Lazarus & Goldstein (1971) using the *Mariner 5* spacecraft, who found the AM flux of the protons to dominate over the magnetic field stresses ( $F_{AM,p}/F_{AM,B} \sim 4.3$ ). Marsch & Richter (1984a) showed that the ratio of AM flux in the particles and magnetic field stresses varies considerably with heliocentric distance and different solar wind conditions.

More recently, Finley et al. (2018) combined observations of the solar wind (spanning  $\sim 20$  yr) with a semi-analytic relation for the AM loss rate, derived from MHD simulations. Theirs was a semi-indirect method, requiring in situ measurements of only the mass flux and magnetic flux. They found a global AM loss rate that varied in phase with the solar activity cycle, and had an average value of  $2.3 \times 10^{30}$  erg, compatible with the results from Pizzo et al. (1983) and Li (1999) ( $\sim 3 \times 10^{30}$  erg and  $2.1 \times 10^{30}$  erg respectively). By examining proxies of solar activity which span centuries and millennia into the Sun's past, Finley et al. (2019a) showed this value to be

representative of the average over the last  $\sim 9000$  yr. However, this value is lower than the AM loss rate of  $\sim 6 \times 10^{30}$  erg used in models that reproduce the rotational history of the Sun (and Sun-like stars) (Gallet & Bouvier 2013, 2015; Matt et al. 2015; Finley et al. 2018; Amard et al. 2019). Deviation from the rotational evolution value has significant implications for our understanding of stellar rotation rates (van Saders et al. 2016; Garraffo et al. 2018), as well as for the technique of gyrochronology (e.g., Barnes 2003; Metcalfe & Egeland 2019), in which stellar ages are derived from rotation rates.

In this Letter, we provide a new direct measurement of the solar AM loss, which follows that of Pizzo et al. (1983) and Marsch & Richter (1984a) but uses data from the *Wind* spacecraft. These data span a period of  $\sim 25$  yr and appear not to require the pointing corrections that were applied to the *Helios* data. This Letter is organized as follows: in Section 2 we describe the data available from the *Wind* spacecraft and calculate the time-varying mass flux and AM flux observed in the equatorial solar wind. Then in Section 3, we estimate the global AM loss rate and discuss the possible implications for the rotation period evolution of Sun-like stars.

## 2. Observed Properties of the Solar Wind

### 2.1. Spacecraft Selection

The measurements required to accurately constrain the AM content in the solar wind particles are challenging to make (see the discussion in Section 3a of Pizzo et al. 1983). Not only are the fluctuations in the AM flux comparable to the average value, but from an instrument standpoint, small errors in determining the wind velocity translate to large errors in the AM flux (because the radial wind speed is 2–3 orders of magnitude larger than the typical tangential speed of  $1\text{--}10 \text{ km s}^{-1}$  at 1 au). The latter problem appears to be the main reason why data from most spacecraft have not been used to measure AM (see Figure 6 of Sauty et al. 2005, which shows data from the *Ulysses* spacecraft; there is an approximately 1 yr periodicity in the observations that is likely due to spacecraft pointing). The magnetic field direction is generally more accurately determined because it is not as radial as the flow, and the instruments used are less sensitive to spacecraft pointing than the particle detectors (which get different exposures as the spacecraft pointing changes). Therefore, the magnetic stress component of the AM flux is typically better constrained.

While the *Advanced Composition Explorer* spacecraft’s nonradial solar wind speed measurements show the expected behaviors during periods of high variability (Owens & Cargill 2004), they appear to suffer from the same spacecraft-pointing-related issues as *Ulysses* over longer time averages, in this case showing a strong  $\sim 6$  month periodicity. The *Wind* and *Interplanetary Monitoring Platform 8 (IMP8)* spacecraft do not obviously show such features. Furthermore, during the period of overlap between *Wind* and *IMP8*, there is good agreement in tangential wind speed, both in terms of the distributions and time series (linear regression of  $r = 0.81$  at the hourly timescale), suggesting limited instrumental effects.

In this work we focus on the high time cadence *Wind* observations. *Wind* was designed to be a comprehensive solar wind laboratory for long-term solar wind measurements, and has certainly stood the test of time; currently approaching its 25th yr since launch (1994 November 1st). During its mission

lifetime the *Wind* spacecraft completed multiple orbits of the Earth–Moon system, before relocating to a halo orbit about the  $L_1$  Lagrangian point (on the Sun–Earth line) in 2004 May. All the while collecting plasma and magnetic field measurements of the solar wind and Earth’s magnetosphere with the Solar Wind Experiment (Ogilvie et al. 1995; Kasper et al. 2006) and Magnetic Field Investigation instruments (Lepping et al. 1995).

### 2.2. In Situ Measurements from the Wind Spacecraft

We analyze data recorded by the *Wind* spacecraft<sup>4</sup> from 1994 November to 2019 June. Using data taken when the spacecraft was immersed in the solar wind, i.e., outside the Earth’s magnetosphere. Additionally, we remove times when the spacecraft encountered interplanetary coronal mass ejections (ICMEs) using the catalogs<sup>5</sup> of Cane & Richardson (2003) and Richardson & Cane (2010) because ICMEs can produce large, nonradial, local flows that are not likely representative of global AM loss (Owens & Cargill 2004). For times not covered by the ICME catalog (1994 November–1996 June), we remove data with properties that are indicative of ICMEs, specifically data with a proton density greater than  $70 \text{ cm}^{-3}$  or field strengths greater than 30nT (a similar method was used by Cohen 2011 on *Ulysses* data).

Measurements of the solar wind magnetic field vector, proton density, and velocity are available throughout the entire *Wind* mission at  $\sim 2$  minute cadence. These parameters have a small number of entries flagged by the instrument team as containing unusable data, which we simply remove. Similarly, measurements of the alpha particle density and velocity are available; however, the number of unusable data entries (where the proton and alpha particle populations cannot be deconvolved by the detector) is far greater. Therefore, when the alpha particles are flagged as unusable, we assume that the alpha particle density is 4% of the proton density (a representative value taken from Borrini et al. 1983) and that the alphas’ velocities are identical to the protons’. We transform the vector quantities of velocity and magnetic field from GSE coordinates to RTN coordinates, where R points from the Sun to the spacecraft, T points perpendicular to the Sun’s rotation axis in the direction of rotation, and N completes the right-handed triad (further details are available in Fränz & Harper 2002).

For each quantity derived using *Wind* data in this work, we calculate values at the smallest available cadence ( $\sim 2$  minutes) and then average them over each Carrington rotation (CR,  $\sim 27$  days) in our data set. This helps to remove longitudinal variability caused by the rotation of features on the solar surface and smooths local fluctuations that occur on a range of shorter timescales. Finally, we require that each CR-average has more than 50% of the data from that time period (after our cuts have been made). Otherwise, that CR is removed. In the top panel of Figure 1, we plot the tangential wind speed of the protons and alpha particles as observed by *Wind*. For the tangential speeds shown in Figure 1, we have weighted the CR averages by density, in order to reduce the obscuring effect of wind stream-interactions (see the discussion in Section 3.3). Figure 1 shows typical tangential flow speeds of a few  $\text{km s}^{-1}$ , with variability that appears genuine and not to suffer from the

<sup>4</sup> <https://wind.nasa.gov/data.php>—Data accessed in 2019 June.

<sup>5</sup> <http://www.srl.caltech.edu/ACE/ASC/DATA/level3/icmetable2.htm>—Data accessed in 2019 September.



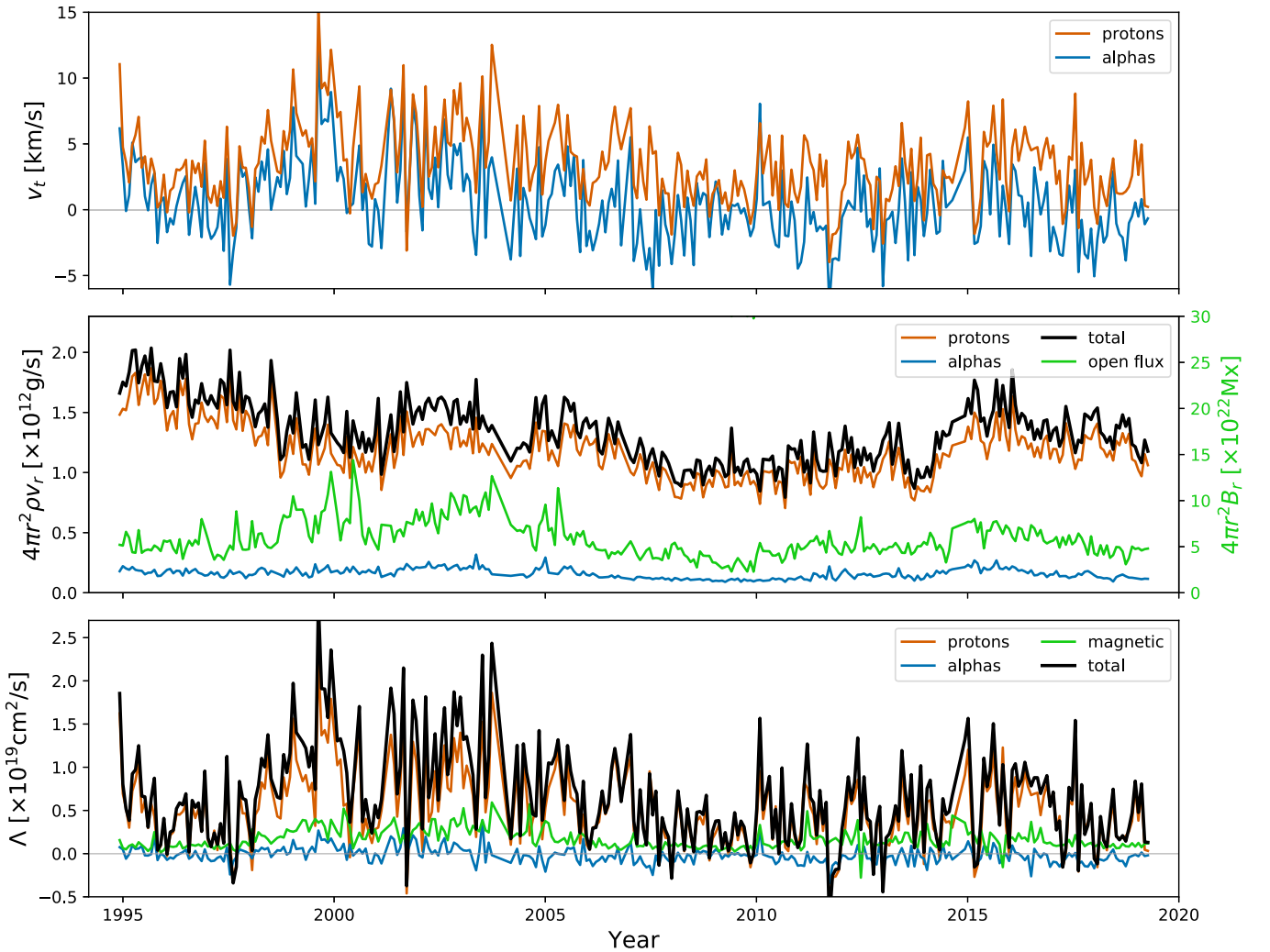


**Figure 1.** Top: CR averages of the density-weighted, tangential speed of the protons and alpha particles in the solar wind vs. time, plotted in orange and blue respectively. Middle: CR averages of mass flux in the protons, alpha particles, and their total (orange, blue, and black lines), each multiplied by  $4\pi r^2$ , vs. time. The prediction of Equation (5) for the open magnetic flux during the same time period is overplotted using a green line, y-axis on the right (see Section 3.1). Bottom: CR averages of specific AM (defined as the AM flux per proton mass flux; density-weighted velocities are used here, see Section 3.3) in the protons, alpha particles, and magnetic field stresses (orange, blue, and green lines) vs. time. The total specific AM is plotted with a black line.

errors present in data from other spacecraft (as discussed in Section 2.1).

### 2.3. Proton and Alpha Particle Properties

The solar wind removes AM from the Sun at a rate proportional to the mass flux ( $\rho v_r$ ) multiplied by the specific AM per unit mass ( $\Lambda$ ). Using data from the *Wind* spacecraft, we plot the mass flux in the protons, alpha particles, and their total in the middle panel of Figure 1. We multiply each by  $4\pi r^2$  for an estimate of the global mass-loss rate,

$$\dot{M} \approx \langle 4\pi r^2 (\rho_p v_{r,p} + \rho_\alpha v_{r,\alpha}) \rangle_{\text{CR}}, \quad (1)$$

where the spacecraft's radial distance from the Sun is  $r$ , the radial wind speed is  $v_r$ , the solar wind density is  $\rho$ , the subscripts  $p$  and  $\alpha$  denote the proton and alpha particle components, and  $\langle \rangle_{\text{CR}}$  denotes an average over a ( $\sim 27$  day) CR. The total mass flux is dominated by the proton component of the wind and varies in a way that does not precisely correlate with the Sun's activity cycle (see also Phillips et al. 1995;

McComas et al. 2000; Finley et al. 2018; Mishra et al. 2019). By contrast, the alpha particle mass flux appears to be more strongly correlated with solar activity throughout the *Wind* data set (which is not surprising as the relative abundance of helium in the equatorial solar wind is strongly correlated with solar activity, see Kasper et al. 2007).

We define the specific AM as the AM flux divided by the proton mass flux (i.e., the specific AM per proton in the solar wind), which is given by,

$$\Lambda = \left\langle r \sin \theta \left( v_{t,p} + v_{t,\alpha} \frac{\rho_\alpha v_{r,\alpha}}{\rho_p v_{r,p}} - \frac{B_t B_r}{4\pi \rho_p v_{r,p}} \right) \right\rangle_{\text{CR}}, \quad (2)$$

where  $\theta$  is the heliographic latitude of the spacecraft,  $v_t$  is the tangential wind velocity,  $B_r$  is the radial magnetic field strength and  $B_t$  is the tangential magnetic field strength. The first term in Equation (2) is the mechanical AM carried by the protons, the second term relates to the relative contribution of the alpha particles, and the final term describes the AM content of the

magnetic field stresses. Equation (2) does not include the correction factor for the magnetic stresses which accounts for thermal pressure anisotropies, as it is expected to be negligible (see Marsch & Richter 1984b). In the bottom panel of Figure 1, we plot the total specific AM along with the individual proton, alpha particle, and magnetic field components. We use density-weighted tangential velocities, as in the top panel of Figure 1, to reduce the effect of wind stream-interactions (see the discussion in Section 3.3). Figure 1 shows the protons to dominate the specific AM of the solar wind, with the magnetic field stresses and alpha particles carrying much less specific AM (per proton).

#### 2.4. AM Flux Detection

The total AM flux in the protons, alpha particles, and magnetic field stresses is given by multiplying the specific AM by the proton mass flux,

$$F_{AM} = \langle \rho_p v_{r,p} \Lambda \rangle_{CR} = \left\langle r \sin \theta \left( \rho_p v_{r,p} v_{t,p} + \rho_\alpha v_{r,\alpha} v_{t,\alpha} - \frac{B_t B_r}{4\pi} \right) \right\rangle_{CR}. \quad (3)$$

We plot the AM fluxes (multiplied by radial distance squared) in the protons, alphas, magnetic field, and their total in the top panel of Figure 2. There is a large scatter/variability in the AM flux, despite averaging over whole CRs. The variability is mainly due to the varying specific AM (i.e., in the tangential wind speed), rather than changes in the mass flux (see Figure 1), and which is likely affected by local fluctuations in the solar wind, caused by transients (Roberts et al. 1987; Tokumaru et al. 2012). The solid black line in Figure 2 shows a 13-CR (i.e.,  $\sim 1$  yr) moving average on the total AM flux, which more clearly describes the longer-term variability of the AM flux. Our data set contains sunspot cycles 23 and 24 (left and right halves of the figures, respectively), which have notable differences in their AM fluxes. Generally, during times of increased solar activity the specific AM of the protons and magnetic field stresses increase together, such that  $F_{AM,p}/F_{AM,B}$  does not vary with solar activity. We find cycle 24, which is currently in its declining phase, has a much lower average AM flux than cycle 23 ( $\sim 40\%$  of cycle 23).

The average value for the AM flux, and that of each constituent, is listed and compared to previous estimates in Table 1. The *Wind* total is primarily composed of the proton and magnetic field components, with the alpha particles contributing a small and mostly negative AM flux contribution. In comparison with the work of Pizzo et al. (1983) and Marsch & Richter (1984a), the *Wind* data show a much stronger AM flux in the protons and a large reduction (in amplitude) to the AM flux carried by the alpha particles. These differences could be related to long-term change in the solar wind. For example, the solar wind appears denser in the last decade compared to the *Helios* era (see McComas et al. 2013). Or alternatively, due to the exchange of momentum between protons and alphas as the wind propagates into the heliosphere (for which there is some evidence in Sanchez-Diaz et al. 2016).

The AM flux in the magnetic field stress in the *Wind* data is similar to that determined by Pizzo et al. (1983) and Marsch & Richter (1984a) but is smaller than that determined by

Lazarus & Goldstein (1971). Interestingly, the dominant contribution to the *Wind*-measured AM flux comes from the protons, with the magnetic field of secondary importance. In simplified MHD simulations of the solar wind (such as those of Finley & Matt 2017), the ratio  $F_{AM,p}/F_{AM,B}$  depends on parameters such that the larger the Alfvén radius ( $R_A$ ) the larger the contribution of the magnetic field. The average ratio measured by *Wind* is  $F_{AM,p}/F_{AM,B} = 2.6$ , which is significantly different from the ratio of  $\sim 1$  found by Pizzo et al. (1983). Marsch & Richter (1984a) showed that *Helios* data from smaller heliocentric distances gives larger ratios, which might account for the difference. The proton-dominated regime shown by the *Wind* data is consistent with MHD simulations that have cylindrically averaged  $R_A$  smaller than  $15R_\odot$ .

### 3. Discussion

Using data from the *Wind* spacecraft, we have evaluated the flux of AM in the equatorial solar wind. In this section, we estimate the global AM loss rate of the Sun and compare with an MHD model and rotational evolution models. Additionally, we discuss the effect of ICMEs and interacting wind streams on our data set.

#### 3.1. Comparison to Theory

To show our result in the context of current theoretical predictions, we compare to the AM loss rate of Finley et al. (2018), which was derived using MHD simulations. In their work, the AM loss rate is given by,

$$J_{FM18} = (2.3 \times 10^{30} [\text{erg}]) \left( \frac{\dot{M}}{1.1 \times 10^{12} [\text{g s}^{-1}]} \right)^{0.26} \times \left( \frac{\phi_{\text{open}}}{8.0 \times 10^{22} [\text{Mx}]} \right)^{1.48}, \quad (4)$$

where the AM loss rate of the Sun is parameterized in terms of the mass-loss rate,  $\dot{M}$ , and the open magnetic flux,  $\phi_{\text{open}}$ . The open magnetic flux in the solar wind is estimated by,

$$\phi_{\text{open}} = \langle 4\pi r^2 |B_r|_{1 \text{ hr}} \rangle_{CR}, \quad (5)$$

where the average value of the radial magnetic field is assumed to be representative of the global open magnetic flux in the solar wind. This assumption has been discussed by many previous authors (Wang & Sheeley 1995; Lockwood et al. 2004; Pinto & Rouillard 2017) and has observational support (Smith & Balogh 1995; Owens et al. 2008). Using Equation (5) we plot the open magnetic flux using data from the *Wind* spacecraft in the middle panel of Figure 1 with a solid green line.

Using Equation (4) we calculate the predicted AM loss rate of the solar wind, where the mass-loss rate and open magnetic flux (Equations (1) and (5)) are calculated using data from the *Wind* spacecraft. We then relate the AM loss rate and AM flux using,

$$J = \oint_A \mathbf{F}_{AM} \cdot d\mathbf{A} = F_{AM,eq} \int_0^{2\pi} \int_0^\pi r^2 (\sin \theta)^3 d\theta d\phi, \quad (6)$$

where  $A$  represents a closed surface in the heliosphere (we adopt a sphere of radius  $r$ ),  $\phi$  is heliographic longitude, and  $F_{AM,eq}$  is the AM flux in the solar equatorial plane, assumed to

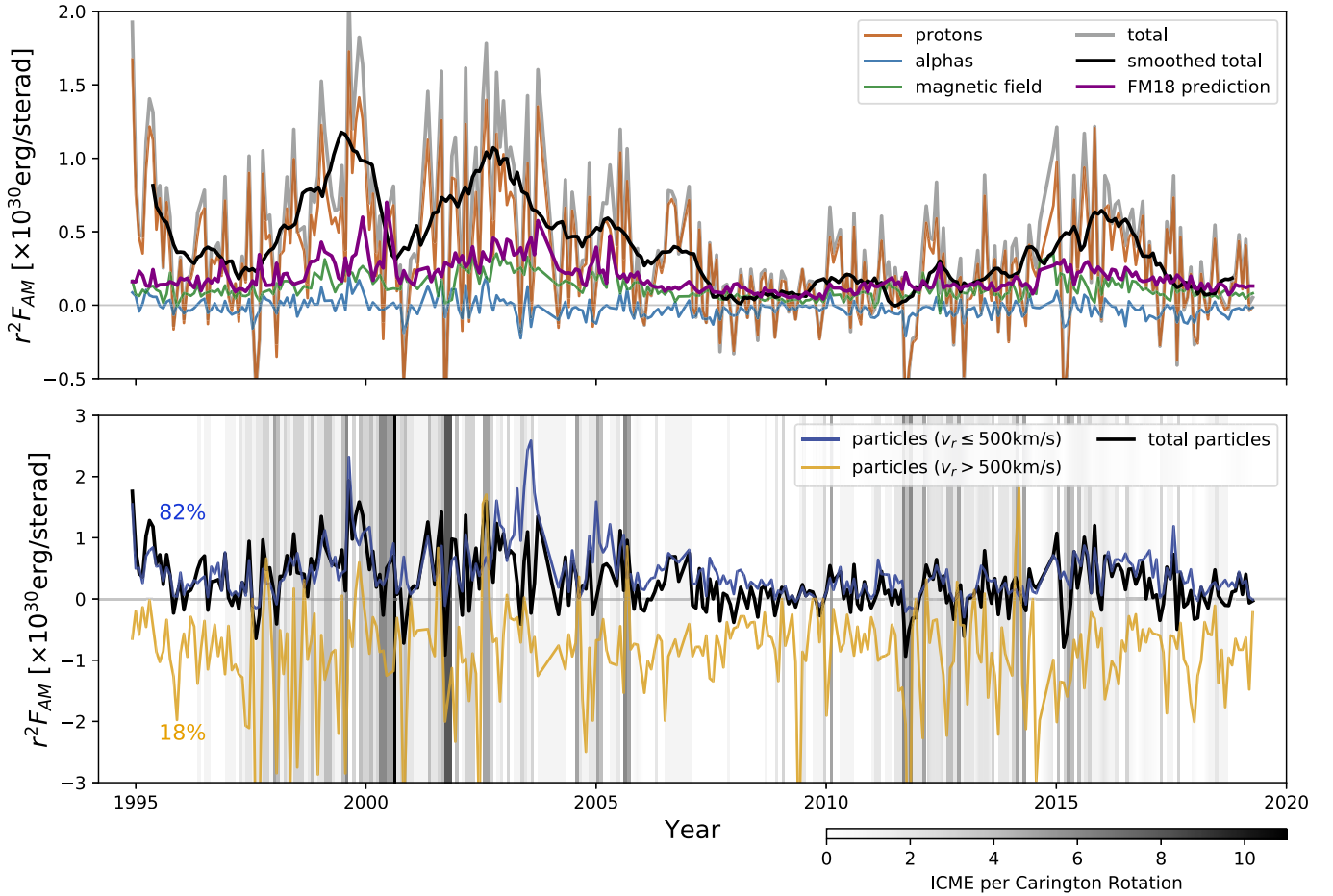


**Figure 2.** Top: CR averages of AM flux multiplied by radial distance squared vs. time. The proton, alpha particle, and magnetic components are shown with orange, blue, and green lines respectively. The total of these is indicated with a gray line. A 13 CR moving average is shown with a thick black line. The prediction of the AM loss rate prescription of Finley et al. (2018) (from Equations (4) and (7)) is shown with a purple line. Bottom: similar plot as above, now only showing the particle component (protons plus alphas). We plot the average AM flux for particles with a radial speed less than, and greater than,  $500 \text{ km s}^{-1}$ , in blue and yellow respectively. On average the *Wind* spacecraft encountered the slower wind 82% of the time. The number of near-Earth ICMEs per CR is shown with a color gradient in the background (following the colorbar at bottom right).

**Table 1**  
Mean of the CR-averaged Solar Angular Momentum Fluxes

Component	$\langle r^2 F_{AM} \rangle$ ( $\times 10^{30}$ erg/ster)	Source	Citation
Protons	0.29	<i>Wind</i>	This work
	0.17	<i>Helios</i>	Pizzo et al. (1983)
	$\sim 1$	<i>Mariner 5</i>	Lazarus & Goldstein (1971)
Alpha Particles	-0.02	<i>Wind</i>	This work
	-0.13	<i>Helios</i>	Pizzo et al. (1983)
Magnetic Field	0.12	<i>Wind</i>	This work
	0.15	<i>Helios</i>	Pizzo et al. (1983)
	0.23	<i>Mariner 5</i>	Lazarus & Goldstein (1971)
Total	0.39	<i>Wind</i>	This work
	0.20	<i>Helios</i>	Pizzo et al. (1983)
	0.26	Theory	This work, Equations (4) and (7)

be equivalent to that measured by CR averages of data taken in the ecliptic. As the AM flux in the solar wind is expected to vary with latitude, we have assumed a physically motivated

functional form,<sup>6</sup>  $F_{AM}(\theta) \approx F_{AM,eq}(\sin \theta)^2 \hat{r}$ . By rearranging Equation (6) we produce a relation for the equatorial AM flux,

$$F_{AM,eq} = \frac{j}{2\pi r^2 \int (\sin \theta)^3 d\theta} \approx \frac{j}{2.7\pi r^2}. \quad (7)$$

The AM flux from Equation (7), using the AM loss rate from Equation (4), is plotted with a solid purple line in the top panel of Figure 2. Strikingly, this result matches well during solar minimum wind conditions. However, it consistently underestimates the AM flux during solar maxima. The Finley et al. (2018) AM loss rates were derived from simulations with only one wind acceleration profile, but differing wind acceleration profiles have been shown to affect the predicted AM loss rates (Pantolmos & Matt 2017). Therefore changes in the balance of fast and slow wind in the heliosphere are not taken into account by this model. It is known that the proportion of slow wind

<sup>6</sup> If the wind is spherically symmetric, the latitude dependence can be understood by considering the proton term in Equation (3), where a geometric factor of  $\sin \theta$  appears at the start of the equation to compute the cylindrical radius. Another geometric factor of  $\sin \theta$  appears from the approximation of solid body rotation (i.e.,  $v_t \propto \sin \theta$ ).

changes significantly from solar minimum to maximum, while the ecliptic remains essentially dominated by the slow wind the whole time (*Wind* encountered slow wind streams, with  $v_r < 500 \text{ km s}^{-1}$ , 82% of the time). Importantly, this implies that the *Wind* observations may be more representative of global conditions at solar maximum than solar minimum. Uncertainties in our assumed latitudinal distribution of AM flux prevent us from producing a more conclusive estimate of the global AM loss rate. For us to better constrain this, there is a need for simultaneous observations at higher latitude (e.g., combined measurements with both the *Wind* spacecraft and the upcoming *Solar Orbiter*) but at present, the current approach is the best we can do without introducing further uncertainty.

### 3.2. Implications for the Rotation Evolution of Sun-like Stars

Rearranging Equation (7) produces an estimate of the global AM loss rate based on the average AM flux detected by the *Wind* spacecraft,  $\dot{J}_{\text{Wind}} = 2.7\pi \langle r^2 F_{\text{AM}} \rangle = 3.3 \times 10^{30} \text{ erg}$ . This AM loss rate is approximately half that required by the empirical Skumanich relationship, where rotation period evolves proportional to the square root of stellar age (Skumanich 1972). Specifically, for the Sun's rotation to follow the Skumanich relationship, the present-day AM loss rate must be  $\approx 6.2 \times 10^{30} \text{ erg}$  (Finley et al. 2018). The torque-averaged Alfvén radius,  $R_A = \sqrt{\dot{J}/(M\Omega)}$ , implied by the *Wind* result is  $R_A \approx 15R_\odot$ , in contrast to  $R_A \approx 20R_\odot$  using the AM loss rate required for Skumanich-like rotation. We note the value of  $R_A$  from *Wind* is in better agreement with MHD simulations that reproduce the observed ratio of  $F_{\text{AM},p}/F_{\text{AM},B}$  (see Section 2.4).

The (unknown) systematic uncertainties in our result could be large enough to resolve this discrepancy. However, taken at face value, and assuming the Sun is not special, our result could be evidence that stars deviate significantly from the Skumanich relationship at around the solar age (or Rossby number, for example, as suggested by van Saders et al. 2016). Alternatively, our result could mean that the present-day solar wind is in some kind of “low state,” such that the AM loss rate averaged over timescales of  $\gg 25 \text{ yr}$  is significantly larger (see Finley et al. 2018, 2019a for a discussion and other caveats).

### 3.3. Coronal Mass Ejections and Fast–Slow Stream-interactions

Detecting the AM flux is complicated by the myriad of transients and fluctuations in the solar wind. With sufficient spatial averaging of the heliosphere (or sufficient temporal averaging at a fixed location), the contribution of transients to the AM flux is likely to be small. However, with the available observations, large transient structures can bias estimates of the AM flux. In this work we have attempted to remove times when ICMEs interacted with the *Wind* spacecraft. We show the number of near-Earth ICMEs per CR as a color gradient in the bottom panel of Figure 2, which is well correlated with solar activity. The plasma properties of ICMEs are often very different to the ambient wind, typically having stronger magnetic fields and increased mass fluxes. Surprisingly, if we include these events in our calculation, the computed equatorial AM flux decreases by 4%. Although we have been careful to remove such events, ICME catalogs are not perfect, and therefore errors due to ICMEs are more likely to be introduced

in times of high solar activity, or times where no ICME catalogs are available (i.e., 1994 November–1996 June).

Additionally, as noted by previous authors (Lazarus & Goldstein 1971; Pizzo et al. 1983; Marsch & Richter 1984a), our results contain evidence for fast–slow wind interactions. The net effect of these interactions is expected to be zero, given sufficient averaging. We plot the average AM flux in the solar wind particles with radial wind speeds greater and less than  $500 \text{ km s}^{-1}$  separately in the lower panel of Figure 2. The slower component of the wind, when compared with the total particle AM flux plotted in black, is shown to carry the bulk of the AM flux in the particles. The faster component is shown to have a mostly small or negative AM flux. However, this component does not strongly contribute to the total AM flux during each CR because of the small fraction (on average 18%) of the time *Wind* encountered this flow, but also because fast wind streams tend to carry smaller mass flux, further reducing their contribution to the total AM flux.

This dichotomy between faster and slower wind streams occurs because of interactions within the solar wind as it propagates into interplanetary space. When fast and slow wind streams “collide,” the slow wind undergoes an acceleration in the direction of corotation and the fast component is deflected oppositely (see Figure 1 in Pizzo 1978). Though most of this acceleration occurs in the radial direction, some is directed tangentially. The impact this has on our fluxes is far more pronounced in the faster component because it is typically less dense than the slower component. This effect makes the tenuous AM flux signal harder to distinguish when simply looking at the raw tangential wind speeds, and has been shown to become increasingly important with increasing heliocentric distances (see Figure 2 in Marsch & Richter 1984a). Since *Wind* data are taken at  $\sim 1 \text{ au}$ , and in the equatorial plane (where stream-interactions are expected to be more pronounced), we chose to present the tangential wind speeds and specific AM in Section 2 weighted by density. Doing so produces values that are more representative of their contribution to the AM flux.

## 4. Conclusion

In this Letter we have attempted to measure the current AM loss rate of the Sun, using data from the *Wind* spacecraft to directly evaluate the equatorial AM flux in the solar wind. Our findings are summarized as follows:

1. The strongest contribution to the AM flux at  $\sim 1 \text{ au}$  comes from the protons, which carry on average  $\sim 75\%$  of the total flux. Our result is similar to that of Lazarus & Goldstein (1971) using the *Mariner 5* spacecraft ( $\sim 80\%$ ), and some of the measurements from the *Helios* spacecraft at smaller heliocentric distances of  $\sim 0.3 \text{ au}$  (Marsch & Richter 1984a).
2. Both the alpha particles and fast ( $v_r > 500 \text{ km s}^{-1}$ ) wind components contribute a negative source of AM flux (at  $\sim 1 \text{ au}$ ), most likely resulting from dynamical processes in the solar wind. We find the alpha particles carrying a much smaller AM flux than Pizzo et al. (1983) found in the *Helios* data.
3. The average equatorial AM flux is  $0.39 \times 10^{30} \text{ erg/sterad}$ , which lies within the predictions of various current theoretical works. The equatorial AM flux varies with solar cycle and during solar maxima is observed to be

significantly larger than the predictions of Finley et al. (2018).

- We estimate the global AM loss rate of the Sun to be  $3.3 \times 10^{30}$  erg, which is a factor of  $\sim 2$  smaller than is expected from a Skumanich-like rotation period evolution of a Sun-like star. It is difficult to conclude whether this discrepancy indicates a weakened braking (e.g., as inferred by van Saders et al. 2016), or is due to differences in the latitudinal distribution of AM flux from our assumed profile, or is perhaps indicative of long-time variability in the AM loss rate of the Sun (see Finley et al. 2019a).

We are hopeful that missions such as *Parker Solar Probe* (Fox et al. 2016) and *Solar Orbiter* (Mueller et al. 2013) will begin to provide valuable data toward addressing the AM loss rate of the Sun. Specifically, *Parker Solar Probe* is sampling the solar wind at distances where stream-interactions are expected to be weaker (or not formed yet), and the signal to noise should be enhanced.

We thank the instrument teams who contributed to the *Wind* spacecraft, and the NASA/GSFC's Space Physics Data Facility for providing this data. A.J.F., A.L.H., and S.P.M. acknowledge funding from the European Research Council (ERC) under the European Unions Horizon 2020 research and innovation programme (grant agreement No. 682393 AWE-SoMeStars). M.O. is funded by Science and Technology Facilities Council (STFC) grant Nos. ST/M000885/1 and ST/R000921/1. R.F.P. acknowledges support from the French space agency (Centre National des Etudes 624 Spatiales; CNES; <https://cnes.fr/fr>). V.R. acknowledges funding by the ERC SLOW\_SOURCE project (SLOW\_SOURCE—DLV-819189). Figures in this work are produced using the python package matplotlib (Hunter 2007).

### ORCID iDs

Adam J. Finley  <https://orcid.org/0000-0002-3020-9409>  
 Sean P. Matt  <https://orcid.org/0000-0001-9590-2274>  
 Mathew Owens  <https://orcid.org/0000-0003-2061-2453>  
 Rui F. Pinto  <https://orcid.org/0000-0001-8247-7168>  
 Victor Réville  <https://orcid.org/0000-0002-2916-3837>

### References

Alvarado-Gómez, J., Hussain, G., Cohen, O., et al. 2016, *A&A*, 594, A95  
 Amard, L., Palacios, A., Charbonnel, C., et al. 2019, *A&A*, 631, A77  
 Amard, L., Palacios, A., Charbonnel, C., Gallet, F., & Bouvier, J. 2016, *A&A*, 587, A105  
 Barnes, S. A. 2003, *ApJ*, 586, 464  
 Barnes, S. A. 2010, *ApJ*, 722, 222  
 Blackman, E. G., & Owen, J. E. 2016, *MNRAS*, 458, 1548  
 Borrini, G., Gosling, J., Bame, S., & Feldman, W. 1983, *SoPh*, 83, 367  
 Bouvier, J., Matt, S. P., Mohanty, S., et al. 2014, in *Protostars and Planets VI*, ed. H. Beuther et al. (Tucson, AZ: Univ. Arizona Press), 433  
 Brown, T. M. 2014, *ApJ*, 789, 101  
 Cane, H., & Richardson, I. 2003, *JGRA*, 108, 1156  
 Cohen, O. 2011, *MNRAS*, 417, 2592  
 Delorme, P., Cameron, A. C., Hebb, L., et al. 2011, *MNRAS*, 413, 2218

Finley, A. J., Deshmukh, S., Matt, S. P., Owens, M., & Wu, C.-J. 2019a, *ApJ*, 883, 67  
 Finley, A. J., & Matt, S. P. 2017, *ApJ*, 845, 46  
 Finley, A. J., & Matt, S. P. 2018, *ApJ*, 854, 78  
 Finley, A. J., Matt, S. P., & See, V. 2018, *ApJ*, 864, 125  
 Finley, A. J., See, V., & Matt, S. P. 2019b, *ApJ*, 876, 44  
 Fox, N., Velli, M., Bale, S., et al. 2016, *SSRv*, 204, 7  
 Fränz, M., & Harper, D. 2002, *P&SS*, 50, 217  
 Gallet, F., & Bouvier, J. 2013, *A&A*, 556, A36  
 Gallet, F., & Bouvier, J. 2015, *A&A*, 577, A98  
 Garraffo, C., Drake, J., Dotter, A., et al. 2018, *ApJ*, 862, 90  
 Garraffo, C., Drake, J. J., & Cohen, O. 2015, *ApJ*, 813, 40  
 Hunter, J. D. 2007, *CSE*, 9, 90  
 Johnstone, C., Güdel, M., Lüftinger, T., Toth, G., & Brott, I. 2015, *A&A*, 577, A27  
 Kasper, J., Lazarus, A., Steinberg, J., Ogilvie, K., & Szabo, A. 2006, *JGRA*, 111, A03105  
 Kasper, J. C., Stevens, M. L., Lazarus, A. J., Steinberg, J. T., & Ogilvie, K. W. 2007, *ApJ*, 660, 901  
 Kawaler, S. D. 1988, *ApJ*, 333, 236  
 Lazarus, A. J., & Goldstein, B. E. 1971, *ApJ*, 168, 571  
 Lepping, R., Acuña, M., Burlaga, L., et al. 1995, *SSRv*, 71, 207  
 Li, J. 1999, *MNRAS*, 302, 203  
 Lockwood, M., Forsyth, R., Balogh, A., & McComas, D. 2004, *AnGeo*, 22, 1395  
 Marsch, E., & Richter, A. 1984a, *JGR*, 89, 5386  
 Marsch, E., & Richter, A. 1984b, *JGR*, 89, 6599  
 Matt, S. P., Brun, A. S., Baraffe, I., Bouvier, J., & Chabrier, G. 2015, *ApJL*, 799, L23  
 Matt, S. P., MacGregor, K. B., Pinsonneault, M. H., & Greene, T. P. 2012, *ApJL*, 754, L26  
 McComas, D., Angold, N., Elliott, H., et al. 2013, *ApJ*, 779, 2  
 McComas, D., Barraclough, B., Funsten, H., et al. 2000, *JGR*, 105, 10419  
 Mestel, L. 1968, *MNRAS*, 138, 359  
 Metcalfe, T. S., & Egeland, R. 2019, *ApJ*, 871, 39  
 Mishra, W., Srivastava, N., Wang, Y., et al. 2019, *MNRAS*, 486, 4671  
 Mueller, D., Marsden, R. G., Cyr, O. S., Gilbert, H. R., et al. 2013, *SoPh*, 285, 25  
 Ó Fionnagáin, D., Vidotto, A. A., Petit, P., et al. 2019, *MNRAS*, 483, 873  
 Ogilvie, K., Chornay, D., Fritzenreiter, R., et al. 1995, *SSRv*, 71, 55  
 Owens, M., & Cargill, P. 2004, *AnGeo*, 22, 4397  
 Owens, M. J., Arge, C., Crooker, N., Schwadron, N., & Horbury, T. 2008, *JGRA*, 113, A12103  
 Pantolmos, G., & Matt, S. P. 2017, *ApJ*, 849, 83  
 Phillips, J., Bame, S., Barnes, A., et al. 1995, *GeoRL*, 22, 3301  
 Pinto, R. F., & Rouillard, A. P. 2017, *ApJ*, 838, 89  
 Pizzo, V. 1978, *JGR*, 83, 5563  
 Pizzo, V., Schwenn, R., Marsch, E., et al. 1983, *ApJ*, 271, 335  
 Réville, V., & Brun, A. S. 2017, *ApJ*, 850, 45  
 Réville, V., Brun, A. S., Matt, S. P., Strugarek, A., & Pinto, R. F. 2015, *ApJ*, 798, 116  
 Richardson, I., & Cane, H. 2010, *SoPh*, 264, 189  
 Roberts, D., Goldstein, M., Klein, L., & Matthaeus, W. 1987, *JGR*, 92, 12023  
 Sadeghi Ardestani, L., Guillot, T., & Morel, P. 2017, *MNRAS*, 472, 2590  
 Sanchez-Diaz, E., Rouillard, A. P., Lavraud, B., et al. 2016, *JGRA*, 121, 2830  
 Sauty, C., Lima, J., Iro, N., & Tsinganos, K. 2005, *A&A*, 432, 687  
 See, V., Jardine, M., Vidotto, A., et al. 2018, *MNRAS*, 474, 536  
 See, V., Matt, S. P., Finley, A. J., et al. 2019, *ApJ*, in press  
 Skumanich, A. 1972, *ApJ*, 171, 565  
 Smith, E. J., & Balogh, A. 1995, *GeoRL*, 22, 3317  
 Soderblom, D. 1983, *ApJS*, 53, 1  
 Tokumaru, M., Kojima, M., & Fujiki, K. 2012, *JGRA*, 117, A06108  
 Usmanov, A. V., Matthaeus, W. H., Goldstein, M. L., & Chhiber, R. 2018, *ApJ*, 865, 25  
 van Saders, J. L., Ceillier, T., Metcalfe, T. S., et al. 2016, *Natur*, 529, 181  
 Van Saders, J. L., & Pinsonneault, M. H. 2013, *ApJ*, 776, 67  
 Wang, Y.-M., & Sheeley, N., Jr 1995, *ApJL*, 447, L143  
 Weber, E. J., & Davis, L. 1967, *ApJ*, 148, 217

## 6.5 Additional Information

After publication of the previous paper, I discussed the result with members of the *Wind* instrument team, who pointed out that the error in the tangential wind speeds measured by *Wind* is of the same order as the averaged speeds I used for the angular momentum-loss calculation. It remains to be understood if by averaging the data over such long times in the paper, these effects were negated/removed. In any case, there continues to be ambiguity around the value of the solar angular momentum-loss rate. Currently Parker Solar Probe and Solar Orbiter have both started their missions to obtain in-situ observations and remote-sensing data from as close to the Sun as currently possible. These missions provide another dataset to carry out the analysis from this Chapter. In this Section I will discuss first some evidence towards my assumed latitudinal angular momentum flux distribution (from Ulysses observations), then the work I am doing with Parker Solar Probe data, and finally some future work that I would like to do with Solar Orbiter.

### 6.5.1 Latitudinal Angular Momentum Flux Distribution with Ulysses

As discussed previously, the Ulysses spacecraft made observations of the solar wind at varying latitudes. Although the tangential wind speed measurements (mechanical angular momentum flux in the particles) have been shown to be plagued by pointing error (see Section 6.2.2), the measurements of the solar wind magnetic field appear to be relatively robust. In Figure 6.6 I have plotted the magnetic stress term of the angular momentum flux, averaged on 27 day intervals, versus heliographic latitude. This is compared with the value of the magnetic stress term measured by *Wind* in the previous paper, and a  $(\sin \theta)^2$  function (as reasoned in the previous paper) with a dashed line. Ulysses made three fast-latitude scans, which are coloured differently. Generally, the measured magnetic stresses are in line with the functional form I suggested in the previous paper. However there is a sharper decrease in the magnetic stresses moving towards the rotation poles than given by the  $(\sin \theta)^2$  function. In future, this could be looked at more carefully and compared with MHD model results, but for now this appears to show the functional form used in the previous paper is adequate.

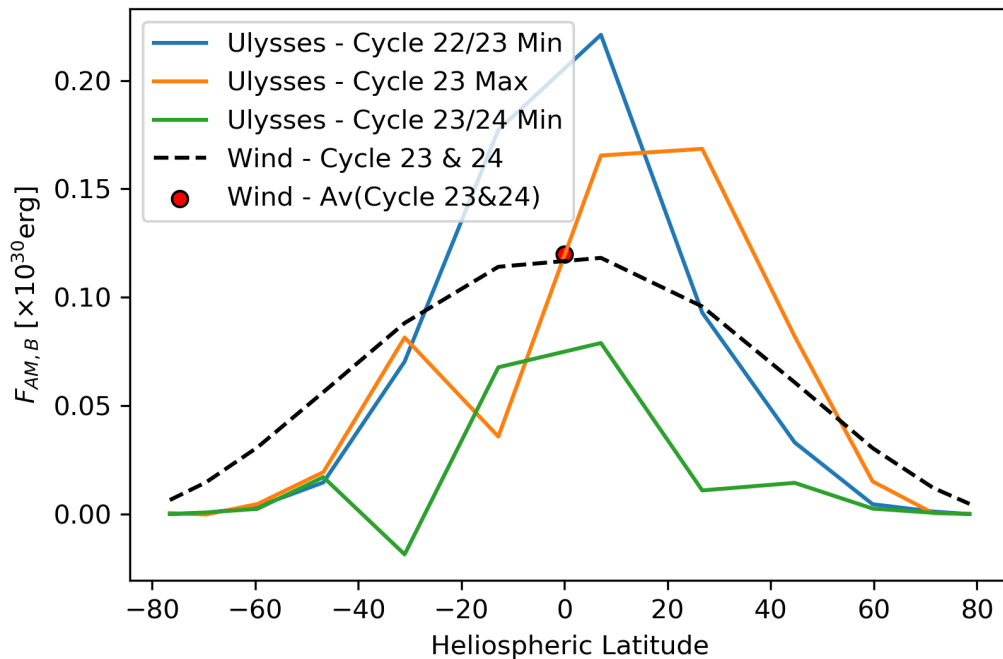


**Figure 6.6:** Comparison of the magnetic stress term of angular momentum flux, measured by the Ulysses spacecraft, and the  $(\sin \theta)^2$  function from Figure 6.5 with a maximum value from the average *Wind* magnetic stress term. Values from Ulysses are averaged over 27 days to remove any longitudinal dependencies.

## 6.5.2 Results from the Parker Solar Probe

Recently I have begun working with the PSP instrument teams to examine the angular momentum flux measured by the SWEAP (protons and alpha particles mechanical flux) and FIELDS (magnetic stresses) instrument suites. During each perihelion pass, the magnetic field vector is measured at a continuous cadence by a fluxgate magnetometer, whereas particle properties are measured by the Solar Probe Cup (a faraday cup) at a variable rate throughout the encounter. I interpolate the one minute cadence magnetometer data onto the sporadic proton data, as the magnetic field is less variable (in terms of magnetic stresses) than the proton fluxes. In Figure 6.7 I show the result of calculating the combined angular momentum flux in the protons and magnetic stresses throughout the first and second encounters with solid coloured circles, each circle represents data averaged over a 2.5 hour interval. The data is shown in the rotating frame of the Sun, and so PSP appears to co-rotate during its perihelion. In the background I use the full one minute cadence magnetometer data, averaged into 2.5 hour bins, to show the polarity of the solar

wind magnetic field as measured by PSP. This polarity is traced along the interplanetary field from PSP using a simple Parker spiral model, where the longitude of a field line is given by,

$$\phi(r) = \phi_0 - \frac{\Omega_{\odot}}{v_r}(r - r_0), \quad (6.1)$$

where  $\phi_0$  and  $r_0$  are the longitude and radial distance of PSP when the measurement of  $v_r$  is made. This model effectively shows the connectivity of the spacecraft to the Sun, and the structure of the solar wind magnetic field. It can be seen that during both perihelia the measured angular momentum flux is much higher than expected, this comes from an increase in the mechanical flux of the protons (with  $v_T \approx 50\text{km/s}$ ). Taken at face value these observations predict a much larger value of the angular momentum-loss rate (see Kasper et al. 2019), however examining the entire dataset there are locations where the angular momentum flux is negative. Upon averaging the equatorial angular momentum flux equally in longitude, I return to a value of  $2.6 \times 10^{30}\text{erg}$  for the angular momentum-loss rate, which is in line with previous calculations. I therefore propose that there is a high degree of structure in the angular momentum flux of the solar wind which needs to be accounted for. Looking at the interplanetary magnetic field, the structure in the angular momentum flux appears to share some similarities with the location of current sheet crossing, etc, hinting that there may be a causal link between the angular momentum distribution and the large-scale magnetic field. Further observations are needed to confirm these findings, as well as a rigorous analysis of the Solar Probe Cup's ability to detect the solar wind flow angle further away from the Sun.

### 6.5.3 Future work with Solar Orbiter

Given my findings with PSP, if there is structure in the angular momentum flux SolO will also be able to examine it in-situ. Along with achieving a close proximity to the Sun ( $\sim 0.3\text{au}$ ), SolO will also begin to gain an inclined orbit, out of the ecliptic. This means SolO can measure the variation of the angular momentum flux in latitude, as well as longitude (as with PSP). Figure 6.8 shows a comparison of the current perihelion passes by PSP and a few example perihelia from SolO. SolO also has an imaging suite and so it



will be able to locate the source regions for the in-situ measured solar wind and provide information about the mechanisms that create the angular momentum flux distribution. SolO launched successfully in February 2020 and is beginning its two year “cruise phase” during which it will collect in-situ observations (but not remote sensing images).

## 6.6 Summary

In this Chapter I attempted to resolve the discrepancy between MHD model results for the solar angular momentum-loss rate and the value produced by rotation-evolution models. To do this I analysed the flux of angular momentum measured by the *Wind* spacecraft at 1au, and found the value to be more variable than the MHD result, but to still be less than the rotation-evolution value on average. I found a large amount of the angular momentum flux is being carried in the protons with a reduced fraction in the alpha particles and magnetic field stresses, when compared to previous works. However, there exist instrumental uncertainty in this result which requires further investigation before this value can be used as evidence of a weaker than Skumanich rotation-evolution. I continue to work with current spacecraft to find a more reliable value for the angular momentum-loss rate in the solar wind.

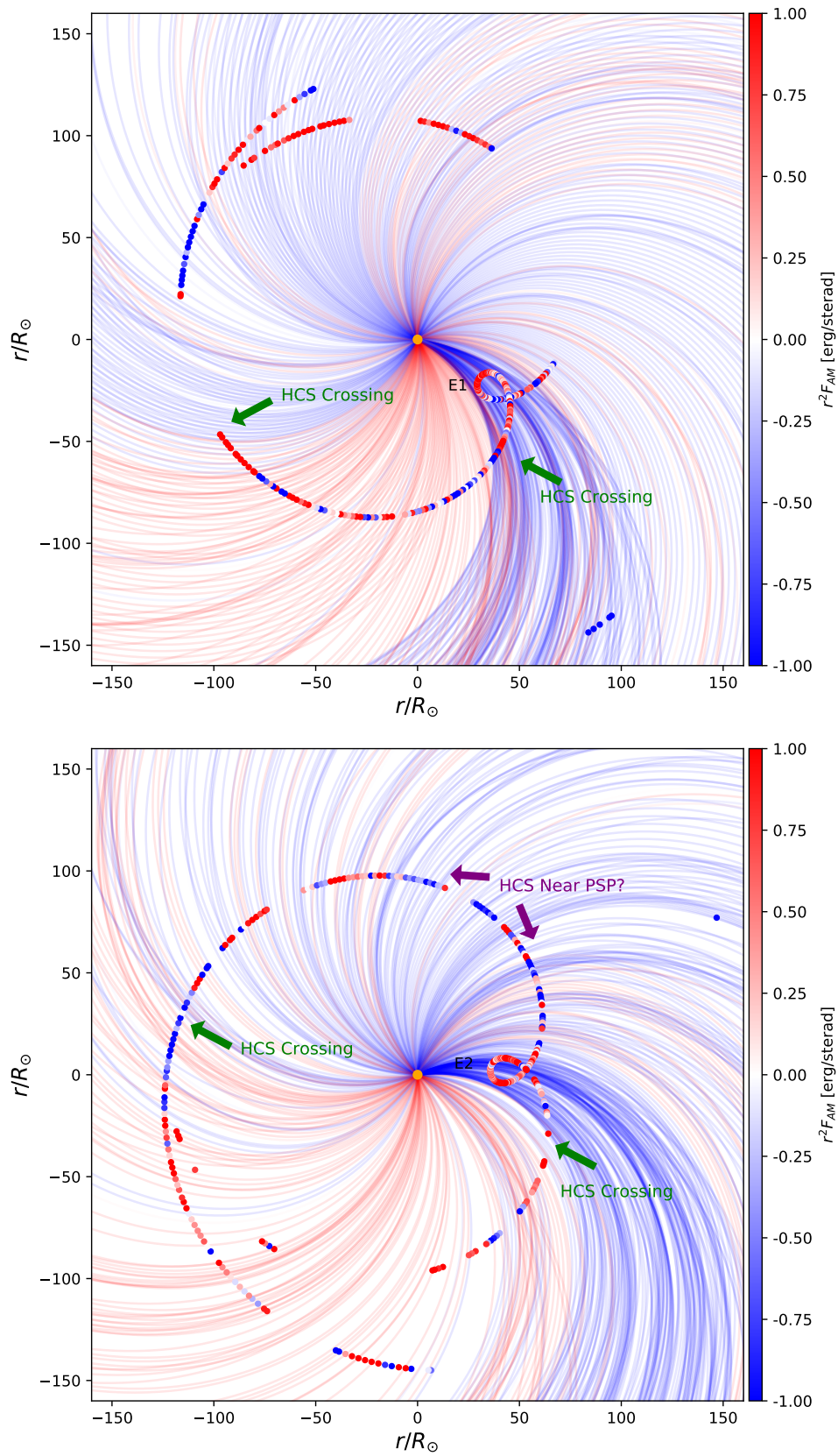


**Figure 6.7:** Data from the Parker Solar Probe during the first orbit (E1; top panel) and the second orbit (E2; bottom panel) in the rotating frame of the Sun. Coloured lines in the background indicate the polarity of the solar wind magnetic field as measured by the *FIELDS* instrument suite, projected onto a Parker spiral using the radial wind speed from the Solar Probe Cup instrument (where available, otherwise 350km/s is assumed). 2.5 hour averages of the angular momentum flux (proton plus magnetic terms) are plotted where available, and features of interest are highlighted with coloured arrows.

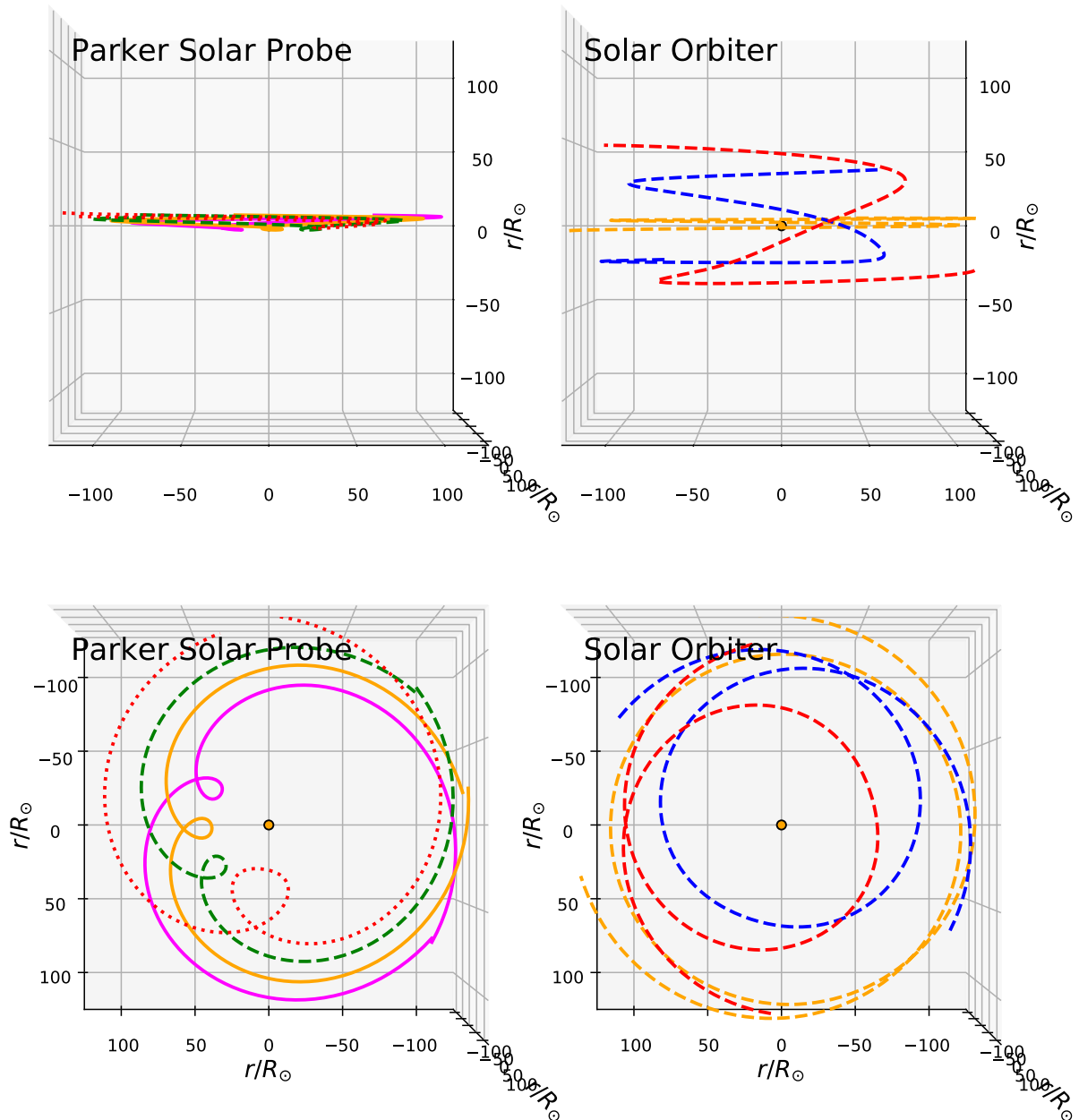


**Figure 6.8:** Comparison of Parker Solar Probe (PSP) and Solar Orbiter (SolO) trajectories. For PSP the colours represent the 1st, 2nd, 3rd, and 4th (after the 1st Venus gravity assist) perihelion passes, magenta, orange, dashed green, and dotted red, respectively. For SolO the colours represent orbits from a range of perihelia during the mission, an example cruise phase perihelion is shown in dashed orange, then future orbits with increased latitudinal extent (due to gravity assists from Venus) are shown with blue and red dashed lines. PSP is confined to the ecliptic, whereas SolO samples many different latitudes over its lifetime.

## Chapter 7

# Modelling Non-axisymmetric Stellar Winds

### 7.1 Introduction

In this final research Chapter, I would like to address the effect of non-axisymmetric magnetic field geometries on the braking laws from Chapter 3. Throughout this work, the braking laws (derived from axisymmetric wind simulations) have been applied under the assumption that non-axisymmetric fields behave in a similar way to the axisymmetric fields. In this Chapter I perform a set of 3D MHD wind simulations with the PLUTO code (see Section 3.2), in which a dipole magnetic field is inclined at different angles to the rotation axis. The results from this study appear as an unpublished manuscript. Following the manuscript, I summarise the results and discuss the impact this work has on the previous Chapters.

## The Influence of Magnetic Field Inclination on Angular Momentum Loss from Thermally Driven Winds

ADAM J. FINLEY,<sup>1</sup> SEAN P. MATT,<sup>1</sup> AND CLAUDIO ZANNI<sup>2</sup>

<sup>1</sup>*University of Exeter, Exeter, Devon, EX4 4QL, UK*

<sup>2</sup>*Università di Torino, 10124 Turino, Italy*

(Received –; Revised –; Accepted –)

### ABSTRACT

The observed rotation period evolution of low-mass stars on the main sequence is explained by the presence of magnetised stellar winds. Through numerical simulation, previous authors have quantified how the angular momentum-loss rates of thermally-driven winds are affected by the temperature of the corona, the structure of the coronal magnetic field, and the rotation rate of the star. However most of these results were derived using axisymmetric magnetic fields. Therefore the effect that non-axisymmetric magnetic fields have on the angular momentum-loss rate has yet to be systematically studied. Here we use the magnetohydrodynamic (MHD) code PLUTO to compute 3D steady-state wind solutions for a range of inclined dipolar magnetic fields ( $0^\circ$ ,  $30^\circ$ ,  $60^\circ$ , and  $90^\circ$  to the rotation axis), each with three different field strengths, in the slowly rotating regime. We find that the angular momentum-loss rate from each inclined case can be inferred by considering a geometric transformation of the Alfvén surface from the corresponding axisymmetric case. This is generalised to previous 2.5D MHD wind simulations with axisymmetric dipole, quadrupole and octupole magnetic geometries. Depending on their field strength, we find that fully-inclined dipolar magnetic fields can have angular momentum-loss rates up to  $\sim 20\%$  stronger than their axisymmetric counterparts. For higher order magnetic geometries, the effect of non-axisymmetry is reduced as their Alfvén surfaces are increasingly spherically symmetric. These results are finally discussed in the context of the solar angular momentum-loss rate.

*Keywords:* Stellar Wind; Rotational Evolution

### 1. INTRODUCTION

Stellar winds are thought to explain the rotation periods of low-mass stars ( $M_* \leq 1.3M_\odot$ ) during the main sequence (Agüeros et al. 2011; McQuillan et al. 2013; Núñez et al. 2015; Covey et al. 2016; Rebull et al. 2016; Agüeros 2017; Douglas et al. 2017). These winds are driven by high temperature coronae (Parker 1958), though the exact mechanism(s) for heating and accelerating the coronal plasma remains an open question (see reviews of Klimchuk 2006; Parnell & De Moortel 2012; Priest 2014). Low-mass stars enter the main sequence with a broad range of rotation rates which begin to converge as they age in a mass-dependent way (Matt et al. 2015; Garraffo et al. 2018). This convergence is largely due to the generation of magnetic fields

in low-mass stars, as the amount of angular momentum removed through stellar winds is a function of magnetic field strength (Weber & Davis 1967; Mestel 1968; Kawaler 1988; Sakurai 1990; Matt et al. 2012; Garraffo et al. 2015). The magnetic fields of low-mass stars are generated through the interplay of convection and rotation in their outermost layers (see review by Brun & Browning 2017). Observations of their magnetic activity clearly show the strength of magnetic fields generated by this dynamo-action generally increases with rotation (Wright et al. 2011; Wright & Drake 2016).

Stellar winds have been studied numerically using magnetohydrodynamic (MHD) models with varying physical prescriptions for the heating and acceleration of coronal plasma (e.g. Parker 1965; Weber & Davis 1967; Keppens & Goedbloed 2000; Matt et al. 2012; Vidotto et al. 2013; Cohen & Drake 2014; Alvarado-Gómez et al. 2016; Réville et al. 2016). In order to produce useful scaling relations for the stellar wind an-

Corresponding author: Adam J. Finley  
\*af472@exeter.ac.uk

gular momentum-loss rate (i.e. that depend on known properties like stellar mass, radius, rotation rate, and magnetic field strength), thermally-driven winds have been used to explore a large parameter space with a reduced number of input parameters. Previous studies using thermally-driven winds have shown that the angular momentum-loss rate is strongly influenced by the acceleration of the wind out to the Alfvén surface (Pantolmos & Matt 2017), and the geometry of the coronal magnetic field (Matt et al. 2012; Réville et al. 2015; Garraffo et al. 2016; Finley & Matt 2017; Finley et al. 2018; Perri et al. 2018). However, these studies require further input to determine which areas of their parameter space correspond to real stars (mass-loss rates and magnetic field strengths), and which wind acceleration profiles (driving temperature and polytropic index) approximate the effect of realistic wind heating/acceleration physics. Recently, Shoda et al. (Submitted) acknowledged this and showed that these scaling relations, derived from thermally-driven winds, are compatible with the relations derived from their more sophisticated 1D Alfvén wave-driven model.

Despite many works studying angular momentum-loss, little has been done to quantify how non-axisymmetric magnetic field geometries modify the relationships from studies that used axisymmetric fields (i.e. Réville et al. 2015; Finley & Matt 2017; Finley et al. 2018). These scaling relations have been applied in a variety of ways, from studying the magnetic cycle dependence of angular momentum-loss (Finley et al. 2018, 2019b), to ascertaining whether the multipolar components of observed stellar magnetic fields influence their angular momentum-loss rates (See et al. 2019), and studying how systematic errors in the magnetic field strengths recovered from Zeeman-Doppler imaging may impact simulations of their angular momentum-loss rates (See et al. 2020).

In this paper, we quantify how non-axisymmetric magnetic fields impact the previously existing scaling relations for angular momentum-loss, that were derived from axisymmetric MHD simulations. The paper is structured as follows: Section 2 describes the model setup, parameter space and key quantities, Section 3 contains our simulation results and their application to previous axisymmetric simulations, and finally Section 4 contains discussion pertinent to the limitations of this work, and its application to the solar angular momentum-loss rate.

## 2. SIMULATION METHOD AND DERIVED QUANTITIES

### 2.1. Stellar Wind Setup

In this work we use the PLUTO code (Mignone et al. 2007; Mignone 2009) to solve the time-dependent MHD equations in a 3D spherical geometry ( $r, \theta, \phi$ ), using a finite-volume Godunov scheme and a linearised Roe Riemann solver (Roe 1981). The magnetic field solenoidality condition ( $\nabla \cdot \mathbf{B} = 0$ ) is maintained using the Hyperbolic Divergence Cleaning method<sup>1</sup> (Dedner et al. 2002). We solve the MHD equations in a rotating frame of reference, which follows the stellar surface rotation rate  $\boldsymbol{\Omega} = \Omega_*(\cos\theta\hat{\mathbf{r}} - \sin\theta\hat{\boldsymbol{\theta}})$ , assumed to be solid body. In this case, the MHD equations are written (in conservative form) as,

$$\frac{\partial \rho}{\partial t} + \nabla \cdot \rho \mathbf{v} = 0, \quad (1)$$

$$\frac{\partial \rho \mathbf{v}}{\partial t} + \nabla \cdot (\rho \mathbf{v} \mathbf{v} - \mathbf{B} \mathbf{B} + \mathbf{I} p_T) = \rho [\mathbf{g} - \boldsymbol{\Omega} \times (\boldsymbol{\Omega} \times \mathbf{r}) - 2\boldsymbol{\Omega} \times \mathbf{v}], \quad (2)$$

$$\frac{\partial E}{\partial t} + \nabla \cdot [(E + p_T)\mathbf{v} - \mathbf{B}(\mathbf{v} \cdot \mathbf{B})] = \rho \mathbf{v} \cdot [\mathbf{g} - \boldsymbol{\Omega} \times (\boldsymbol{\Omega} \times \mathbf{r})], \quad (3)$$

$$\frac{\partial \mathbf{B}}{\partial t} + \nabla \cdot (\mathbf{v} \mathbf{B} - \mathbf{B} \mathbf{v}) = 0, \quad (4)$$

where  $\rho$  is the mass density,  $\mathbf{v}$  is the velocity field,  $\mathbf{g}$  is the gravitational acceleration,  $\mathbf{B}$  is the magnetic field<sup>2</sup>,  $p_T = p + B^2/2$  is the combined thermal and magnetic pressure,  $\mathbf{I}$  is the identity matrix, and  $E = \rho\epsilon + \rho\mathbf{v}^2/2 + \mathbf{B}^2/2$  is the total energy density, with  $\epsilon$  representing the internal energy per unit mass of the fluid. The closing equation of state takes the form  $\rho\epsilon = p/(\gamma - 1)$ , where  $\gamma$  represents the ratio of specific heats. In this study we artificially lower  $\gamma$  from 5/3 to 1.05 such that the wind is heated as it expands without needing an explicit heating term in equation (3) (further discussion of this ‘‘polytropic approximation’’ is available in Finley & Matt 2018, and references therein).

The computational domain extends from the stellar surface ( $1R_*$ ) to  $50.8R_*$  in  $r$  (radial distance), 0 to  $\pi$  in  $\theta$  (latitude), and 0 to  $2\pi$  in  $\phi$  (longitude). The domain is discretised such that there are 160 grid cells in the radial direction which grow logarithmically from an initial spacing of  $0.025R_*$  to  $1.2R_*$  at the outer boundary. Each latitude-longitude plane is further comprised of  $128 \times 256$  uniformly spaced grid cells. Our initial conditions consist of an isotropic polytropic Parker wind

<sup>1</sup> The Constrained Transport method is more accurate (see Tóth et al. 2005), however its current implementation in the PLUTO code is incompatible with our choice of spherical domain.

<sup>2</sup> The PLUTO code operates with a factor of  $1/\sqrt{4\pi}$  absorbed into the normalisation of  $\mathbf{B}$ . Tabulated parameters are given in cgs units with this factor incorporated.

velocity profile  $(v_r, 0, 0)$ , which depends on the ratio of the sound speed at the coronal base  $c_s = \sqrt{\gamma p_*/\rho_*}$ , to the surface escape velocity  $v_{esc} = \sqrt{2GM_*/R_*}$ , where  $G$  is the gravitational constant,  $M_*$  is the mass of the star, and fluid quantities denoted with ‘\*’ are evaluated at the stellar surface (see Appendix A and Parker 1965; Keppens & Goedbloed 1999). Superimposed on this is a potential dipole magnetic field  $(B_r, B_\theta, B_\phi)$  with a polar strength of  $B_{pole}$ , and a magnetic axis inclined to the rotation axis by an angle of  $\Theta$ . This magnetic field is described by,

$$B_r = \frac{B_{pole}R_*^3}{r^3}(\cos\Theta \cos\theta + \sin\Theta \cos\phi \sin\theta), \quad (5)$$

$$B_\theta = \frac{B_{pole}R_*^3}{2r^3}(\cos\Theta \sin\theta - \sin\Theta \cos\phi \cos\theta), \quad (6)$$

$$B_\phi = \frac{B_{pole}R_*^3}{2r^3}(\sin\Theta \sin\phi). \quad (7)$$

From these initial conditions, we use the PLUTO code to solve the MHD equations until a steady-state wind is established. The stellar wind solutions are strongly influenced by choices in boundary conditions, especially those set at the stellar surface. During the simulation runtime, density, pressure, and the radial magnetic field strength are fixed at the stellar surface. However, we allow the wind velocity and non-radial magnetic field components to influence each other, provided the flow remains parallel to the magnetic field. All quantities at the outer radial boundary have vanishing derivatives (e.g.  $dv_r/dr = 0$ ), which allow an outward transfer of mass, momenta and magnetic field from the simulation domain. For the coordinate singularities; the  $\phi = 0$  or  $2\pi$  boundary is periodic, and the  $\theta = 0$  and  $\theta = \pi$  boundaries are  $\pi$ -periodic whereby the fluid variables are translated from  $\phi$  to  $\phi + \pi$ , effectively jumping across the coordinate singularities at the poles (see e.g. van der Holst & Keppens 2007).

To best exploit our computational setup, we use normalised simulation units and dimensionless input parameters,  $c_s/v_{esc}$ ,  $v_A/v_{esc}$  ( $v_A = B_{pole}/\sqrt{4\pi\rho_*}$ , the Alfvén speed at the magnetic pole), and  $\Omega_*R_*/v_{kep}$  ( $v_{kep} = \sqrt{GM_*/R_*}$ , the Keplerian rotation speed at the stellar surface). Each simulation therefore represents a family of solutions with different gravities. For all of our simulations we adopt  $c_s/v_{esc} = 0.25$  (for solar parameters this is a coronal temperature of  $\sim 1.7$  MK), and  $\Omega_*R_*/v_{kep} = 0.0039$  (which corresponds to a solar rotation rate of  $\Omega_* = 2.6 \times 10^{-6}$  rad/s). Our simulations reside in the slowly rotating regime (i.e.  $\Omega_*R_*/v_{kep} < 0.03$ , see Matt et al. 2012), where the effects of rotation can be generally neglected. In this work we explore a range of different magnetic field strengths

( $v_A/v_{esc} = 0.71, 2.1$  and  $4.2$ ) and inclination angles ( $\Theta = 0^\circ, 30^\circ, 60^\circ$  and  $90^\circ$ ) which, for solar parameters, span polar magnetic field strengths of 1.4G to 8.5G. Our input parameters are tabulated for all our simulations in Table 1.

## 2.2. Wind Fluxes and Conserved Quantities

The simulations produce steady-state solutions for the flow variables  $(\rho, p, \mathbf{v}$  and  $\mathbf{B})$  which adhere to the ideal MHD equations, therefore key quantities are expected to be conserved along magnetic field lines (Lovelace et al. 1986; Ustyugova et al. 1999; Keppens & Goedbloed 2000; Bogovalov 1999). These include:

- the mass flux per magnetic flux,

$$\kappa = \frac{\rho \mathbf{v}_p \cdot \mathbf{B}_p}{|\mathbf{B}_p|^2}, \quad (8)$$

where the subscript ‘p’ indicates the poloidal components. The conservation of this quantity is used at the inner boundary when evolving the poloidal velocity.

- the specific angular momentum flux,

$$\Lambda = \omega \left( v_\phi - \frac{B_\phi}{\kappa} \right), \quad (9)$$

where  $\omega = r \sin\theta$  is the cylindrical radius, and the subscript ‘ $\phi$ ’ indicates the azimuthal component of a vector quantity. The specific angular momentum is given analytically by  $\Lambda = \Omega_* R_A^2$ , with the cylindrical Alfvén radius  $R_A$  governing how efficiently angular momentum is transferred to the wind from the star (Weber & Davis 1967).

- the effective rotation rate of magnetic field lines,

$$\Omega_{eff} = \frac{1}{\omega} \left( v_\phi - B_\phi \frac{\kappa}{\rho} \right), \quad (10)$$

which should match the rotation rate of the field footpoint at the stellar surface. Given that we use solid body rotation in our simulations,  $\Omega_{eff}$  should equal  $\Omega_*$  everywhere in our computational domain. In practise this is numerically challenging, see Section 4.1 (and the Appendices of Réville et al. 2015 and Pantolmos & Matt 2017 for more details). This quantity is used at the inner boundary when setting the azimuthal velocity.

## 2.3. Global Wind Properties

Following the methodology of previous works, we find the global mass-loss rate in our simulations by evaluating,

$$\dot{M} = \int_{\mathbf{A}} \rho \mathbf{v} \cdot d\mathbf{A}, \quad (11)$$

where we integrate over a spherical shell of area  $A$ , which is located in the open wind i.e. outside of closed magnetic field regions. This mass flux carries away angular momentum which applies a torque on the star given by,

$$\tau = \int_{\mathbf{A}} \Lambda \rho \mathbf{v} \cdot d\mathbf{A}. \quad (12)$$

Given the analytic expression for  $\Lambda$  given by [Weber & Davis \(1967\)](#), the torque can also be written as,

$$\tau = \dot{M} \Omega_* R_*^2 \left( \frac{\langle R_A \rangle}{R_*} \right)^2, \quad (13)$$

with the ratio of the Alfvén radius to the stellar radius squared acting as a dimensionless efficiency factor for removal of angular momentum. Given our wind solutions are multidimensional,  $\langle R_A \rangle$  is an average value which contains information about the shape of the Alfvén radius and the mass flux through it. In this work we evaluate  $\langle R_A \rangle$  in two different ways. Firstly we use the mass-loss rate and angular momentum-loss rate found using equations (11) and (12) to calculate a torque-averaged Alfvén radius,

$$\langle R_A \rangle_{\tau} = \sqrt{\frac{\tau}{\dot{M} \Omega_*}}, \quad (14)$$

which was the primary method used in many previous studies (given its simplicity). Secondly, we evaluate a mass-loss weighted cylindrical Alfvén radius,

$$\langle R_A \rangle_{\dot{M}} = \sqrt{\frac{\int_{\mathbf{S}_A} \omega^2 \rho \mathbf{v} \cdot d\mathbf{S}_A}{\int_{\mathbf{S}_A} \rho \mathbf{v} \cdot d\mathbf{S}_A}}, \quad (15)$$

where each integral is evaluated over the Alfvén surface  $\mathbf{S}_A$  ([Mestel & Spruit 1987](#); [Washimi & Shibata 1993](#)). In ideal MHD, these two methods for evaluating  $\langle R_A \rangle$  are equivalent (see Appendix of [Vidotto et al. 2013](#)). Though given the limitations of our numerics, we find some differences (see Section 4.1).

Ultimately, we wish to find semi-analytic relations for  $\langle R_A \rangle$  in term of dimensionless parameters which relate to stellar quantities. In this work we will consider the wind magnetisation,

$$\Upsilon = \frac{B_{pole}^2 R_*^2}{\dot{M} v_{esc}}, \quad (16)$$

and the open flux wind magnetisation,

$$\Upsilon_{open} = \frac{\Phi_{open}^2 / R_*^2}{\dot{M} v_{esc}}, \quad (17)$$

where  $\Phi_{open}$  is the unsigned magnetic flux outside of any closed field regions, given by,

$$\Phi_{open} = \int_{\mathbf{A}} |\mathbf{B} \cdot d\mathbf{A}|. \quad (18)$$

**Table 1.** Summary of Simulation Input Parameters and Results

$\Theta$	$v_A/v_{esc}$	$\Upsilon$	$\Upsilon_{open}$	$\langle R_A \rangle_{\tau}/R_*$	$\langle R_A \rangle_{\dot{M}}/R_*$
0°	0.71	430	2028	5.7	5.7
0°	2.1	5600	11363	10.5	10.9
0°	4.2	31177	33386	16.1	17.1
30°	0.71	428	2036	5.8	5.9
30°	2.1	5537	11488	10.9	11.1
30°	4.2	30764	33897	16.8	17.5
60°	0.71	427	2045	6.1	6.1
60°	2.1	5471	11615	11.3	11.6
60°	4.2	30403	34348	17.5	18.2
90°	0.71	427	2051	6.2	6.2
90°	2.1	5481	11619	11.5	11.7
90°	4.2	30404	34318	17.8	18.3

All simulations use  $c_s/v_{esc} = 0.25$ ,  $\gamma = 1.05$ , and  $\Omega_* R_* / v_{kep} = 3.9 \times 10^{-3}$ .

Importantly, by including the mass-loss rate in these parameters we remove any dependence of our result on the mass-loss rates from our simulations, which are not physically motivated. A relationship between  $\langle R_A \rangle$  and both  $\Upsilon$  and  $\Upsilon_{open}$  can be derived analytically when considering spherically symmetric steady-state winds (see Section 2 of [Finley et al. 2019a](#), for a summary). As done by previous authors ([Matt & Pudritz 2008](#); [Matt et al. 2012](#); [Réville et al. 2015](#); [Pantolmos & Matt 2017](#); [Finley & Matt 2017, 2018](#)), we generalise those results to multidimensional flows and produce semi-analytic scalings for  $\langle R_A \rangle / R_*$  in the following Section.

### 3. SIMULATION RESULTS

#### 3.1. 3D Inclined Dipolar Winds

We find wind solutions for each inclination angle and dipole field strength in our parameter space. The results for  $v_A/v_{esc} = 2.1$  are displayed in Figure 1. From Figure 1 it is clear that the three different non-axisymmetric winds have the same overall morphology as the axisymmetric case, simply rotated away from the rotation axis. Given the imperfect boundary conditions over the rotation poles, artefacts appear in some of our wind solutions, though they do not change our conclusions (see Section 4.1).

To quantify the effect inclination has on the angular momentum-loss rate, we plot  $\langle R_A \rangle_{\tau}$  versus both  $\Upsilon$  and  $\Upsilon_{open}$  for all our 3D simulations with coloured circles in Figure 2. For comparison, the relations found by [Finley & Matt \(2018\)](#) for dipolar magnetic fields are plotted



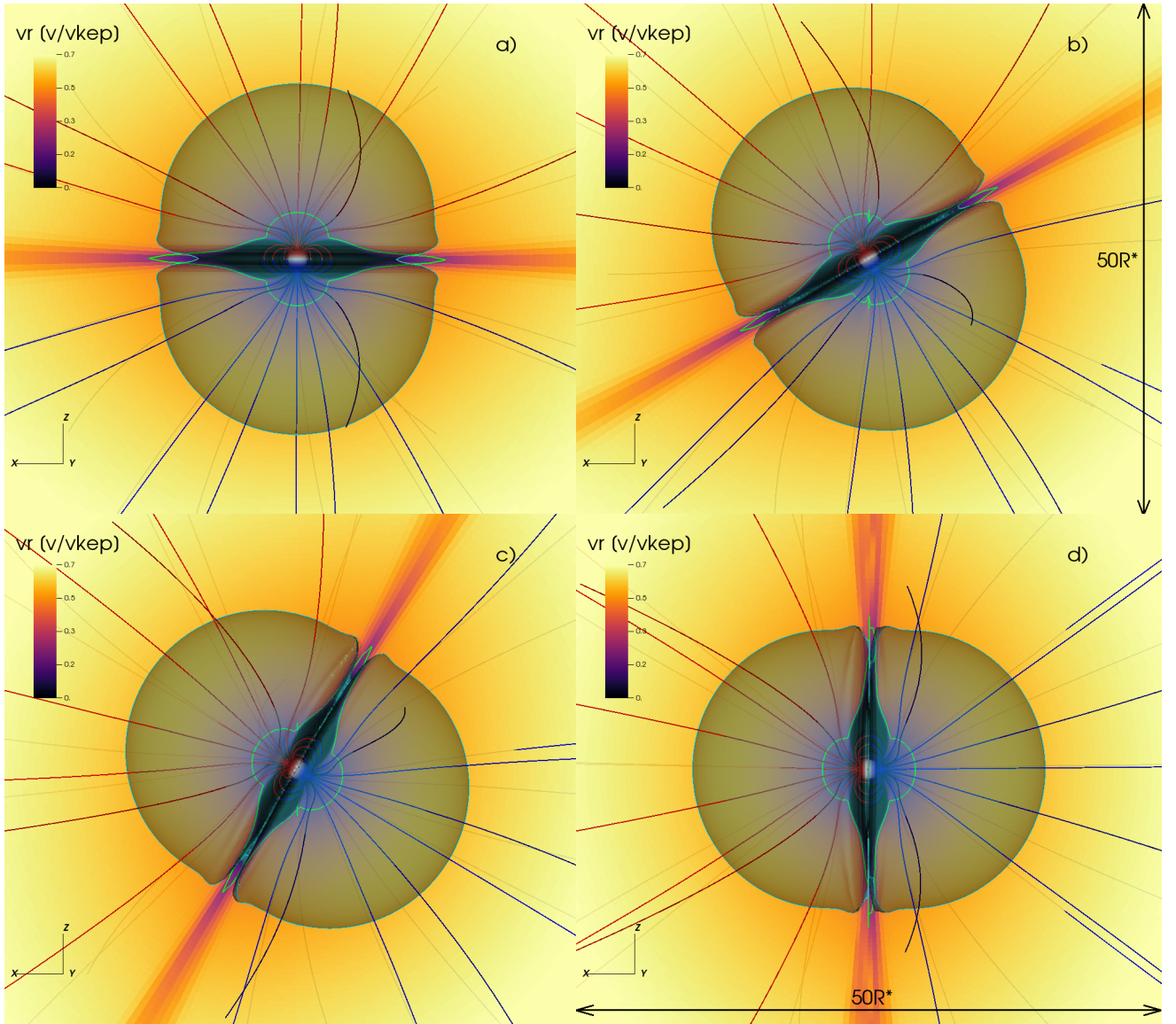


**Figure 1.** 3D simulation results for the  $v_A/v_{esc} = 2.1$  cases with different dipolar magnetic field inclination angles to the rotation axis (along the  $z$ -axis); a)  $\Theta = 0^\circ$ , b)  $\Theta = 30^\circ$ , c)  $\Theta = 60^\circ$  and d)  $\Theta = 90^\circ$ . The background colour scale shows the radial wind velocity  $v_r$  in units of  $v_{kep}$ , in the  $y = 0$  plane. Magnetically closed regions restrict the flow, and magnetically open regions facilitate the stellar wind. Magnetic field lines are coloured by their polarity, red and blue for positive and negative  $B_r$  respectively. Similarly the stellar surface is coloured by  $B_r$ . The 3D Alfvén surface for each case is identified with a semi-transparent cyan surface. The location of the Alfvén surface and sonic surface in the  $y = 0$  plane are shown with cyan and green lines respectively.

with a black dashed lines. These are given by,

$$\frac{\langle R_A \rangle_\tau}{R_*} = 1.53 \Upsilon^{0.229}, \quad (19)$$

and

$$\frac{\langle R_A \rangle_\tau}{R_*} = 0.33 \Upsilon_{open}^{0.371}, \quad (20)$$

where the constants were fit to their 2.5D wind simulations which have the same thermal driving ( $c_s/v_{esc}$  and  $\gamma$ ) as this work.

For a given  $\Upsilon$  or  $\Upsilon_{open}$ , we show the inclined dipolar magnetic fields (red, yellow and cyan) produce a larger angular momentum-loss rate or  $\langle R_A \rangle_\tau$ , than the axisymmetric cases (shown in purple). Given that  $B_{pole}$  is fixed (through  $v_A/v_{esc}$ ) for each set of inclination angles, the

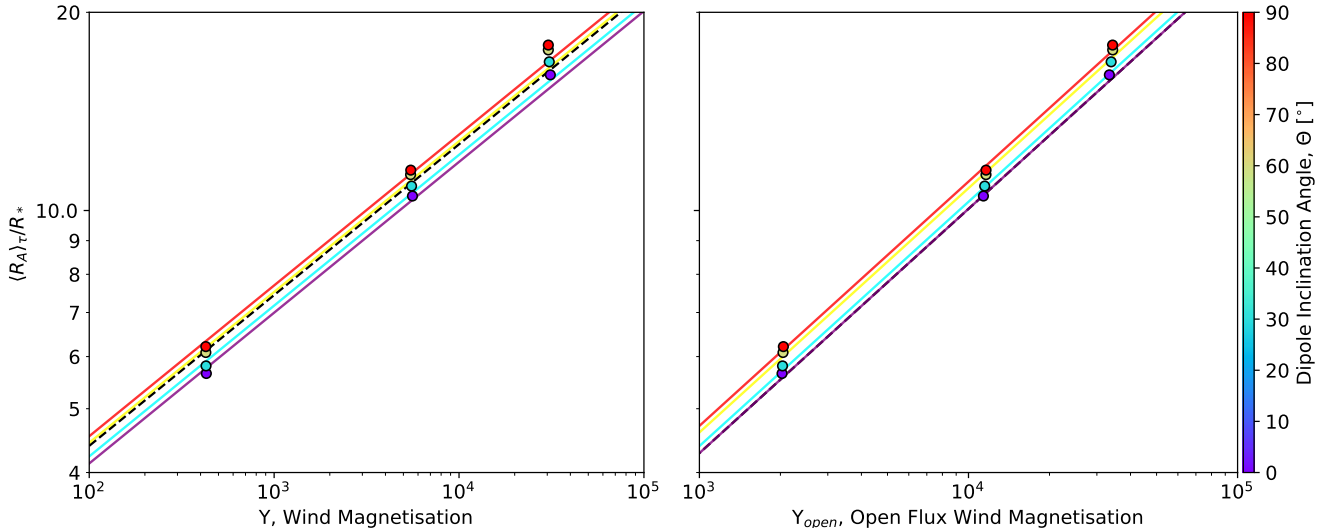


**Figure 2.** Left: Torque-averaged Alfvén radius versus wind magnetisation  $\Upsilon$ . Right: Torque-averaged Alfvén radius versus open-flux wind magnetisation  $\Upsilon_{open}$ . Our 12 3D dipole simulations are plotted with circles coloured by their inclination angle  $\Theta$ . In both plots, the scaling relations from Finley & Matt (2018) (equations (19) and (20)) are shown with dashed black lines. There is good agreement between the  $\Upsilon_{open}$  scaling and our 3D axisymmetric simulations, however the  $\Upsilon$  scaling is offset (likely due to a reduced fraction of the surface flux opening into the wind). We multiply equation (19) by 0.94 to better fit the axisymmetric cases, shown with a purple solid line in the left panel. We then multiply both axisymmetric scalings (purples lines) by equation (21), using  $\delta\langle R_A \rangle / \langle R_A \rangle(0^\circ) = 0.1$ , for each inclination angle (ignoring any dependence on field strength). These lines are coloured to match the inclination angle of the circles, and show the rough scaling of  $\langle R_A \rangle_\tau$  with differing inclination angles.

similarity of their  $\Upsilon$  values indicates their mass-loss rates are mostly independent of inclination angle. Additionally, the differences in  $\Upsilon_{open}$  show that the more inclined cases produce a slightly larger amount of unsigned magnetic flux. We note that our 3D axisymmetric cases agree with the dashed line from Finley & Matt (2018) in  $\Upsilon_{open} - \langle R_A \rangle_\tau$  space, but produce smaller values than expected in  $\Upsilon - \langle R_A \rangle_\tau$  space ( $\sim 6\%$  smaller). This is likely a result of our lower resolution, which modifies how much magnetic field is opened versus closed for a given thermal driving.

Interestingly, previous works using  $\Upsilon_{open}$  have found it characterises  $\langle R_A \rangle_\tau$  very well, often collapsing simulations with different magnetic geometries onto a single power law relation (e.g. Réville et al. 2015). However we do not find this for our inclined dipole cases. Further works using  $\Upsilon_{open}$  have shown that, in order to fully describe  $\langle R_A \rangle_\tau$ , information about how the wind accelerates is also required<sup>3</sup> (Pantolmos & Matt 2017; Finley & Matt 2017). The different scalings of  $\Upsilon_{open} - \langle R_A \rangle_\tau$  imply that by changing the inclination angle, we are

<sup>3</sup> The use of  $\Upsilon_{open}$  to characterise  $\langle R_A \rangle_\tau$  is independent of how the field is opened and in most cases the topology of the field, so long as the wind acceleration is unaffected.

modifying the average speed of the wind at locations on the Alfvén surface that facilitate the most angular momentum-loss i.e, over the equator and mid-latitudes.

### 3.2. Prediction of Inclined $R_A$ from the Axisymmetric Cases

In Figure 3, we plot the difference in  $\langle R_A \rangle_\tau$  from the axisymmetric cases versus inclination angle  $\Theta$  with coloured diamonds, and similarly the difference in the mass-loss weighted  $\langle R_A \rangle_{\dot{M}}$  (using equation (15)) with coloured squares. These values do not always agree, especially for the strongest field cases where  $\langle R_A \rangle_\tau$  can differ from  $\langle R_A \rangle_{\dot{M}}$  by up to 6%. This is likely due to numerical errors in our simulations for the higher field strengths, which are more likely to influence our value of  $\langle R_A \rangle_\tau$ . By using  $\langle R_A \rangle_{\dot{M}}$ , we are instead comparing the geometric shape of each Alfvén surface, which should be less influenced by numerical errors.

Given the morphological similarities between our 3D wind solutions, we find it is possible to make predictions (to within a few percent) for  $\langle R_A \rangle_{\dot{M}}$  by considering a geometric transformation of the axisymmetric Alfvén surface about the rotation axis. We calculate a continuous prediction for  $\langle R_A \rangle_{\dot{M}}$  by taking each of the 3D axisymmetric cases and rotating the simulation domain with respect to the rotation axis from  $0^\circ$  to  $90^\circ$ . We calcu-

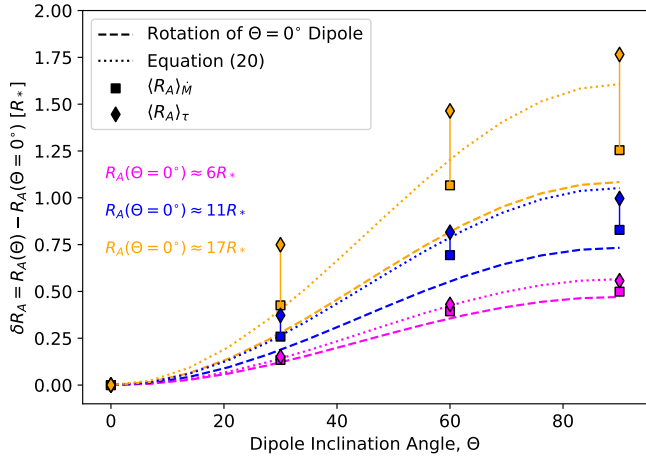


**Figure 3.** Change in Alfvén radius from the axisymmetric case versus dipole inclination angle  $\Theta$ . Symbols and lines are coloured by  $v_A/v_{esc} = 0.71, 2.1$  and  $4.2$  (magenta, blue and orange respectively). Coloured diamonds and squares correspond to  $\langle R_A \rangle_{\dot{M}}$  and  $\langle R_A \rangle_{\tau}$  respectively. Coloured dashed lines correspond to values from equation (15) when using the axisymmetric Alfvén surface for each  $v_A/v_{esc}$ , which we rotate with respect to the rotation axis through  $0^\circ$  to  $90^\circ$  (see Section 3.2). Coloured dotted lines show the value of equation (21) with  $\delta\langle R_A \rangle/\langle R_A \rangle(0^\circ) = 0.1$ , which is used in Figure 2.

late  $\langle R_A \rangle_{\dot{M}}$  at various inclination angles for each field strength, these are shown with coloured dashed lines in Figure 3. As  $\langle R_A \rangle_{\dot{M}}$  is calculated using a mass-loss weighted averaging, the slight differences between our prediction and the simulation values are likely due to differences in the distribution of mass flux through each Alfvén surface. Note, we must use  $\langle R_A \rangle_{\dot{M}}$  to make these predictions, as it does not require information about the azimuthal flow speed and magnetic field direction, unlike  $\langle R_A \rangle_{\tau}$  (which require the 3D simulations to compute).

The variation of  $\langle R_A \rangle_{\dot{M}}$  (and  $\langle R_A \rangle_{\tau}$ ) follows a sinusoidal behaviour which we characterise using,

$$\langle R_A \rangle(\Theta) = \langle R_A \rangle(0^\circ) + \frac{\delta\langle R_A \rangle}{2} \left[ 1 - \cos\left(\frac{\Theta}{90^\circ}\right) \right], \quad (21)$$

where  $\delta\langle R_A \rangle = \langle R_A \rangle(90^\circ) - \langle R_A \rangle(0^\circ)$  is the difference between the fully inclined case and the axisymmetric case. This equation is plotted in Figure 3 with coloured lines for the three different polar field strengths using  $\delta\langle R_A \rangle/\langle R_A \rangle(0^\circ) = 0.1$ . This is the same value used in Figure 2, and broadly reproduces the observed trends in both  $\langle R_A \rangle_{\dot{M}}$  and  $\langle R_A \rangle_{\tau}$ . A more detailed analysis reveals the value of  $\delta\langle R_A \rangle/\langle R_A \rangle(0^\circ)$  decreases with polar field strength. This is shown in Figure 4, where we compare normalised  $\langle R_A \rangle_{\dot{M}}$  for the 3D simulations (coloured

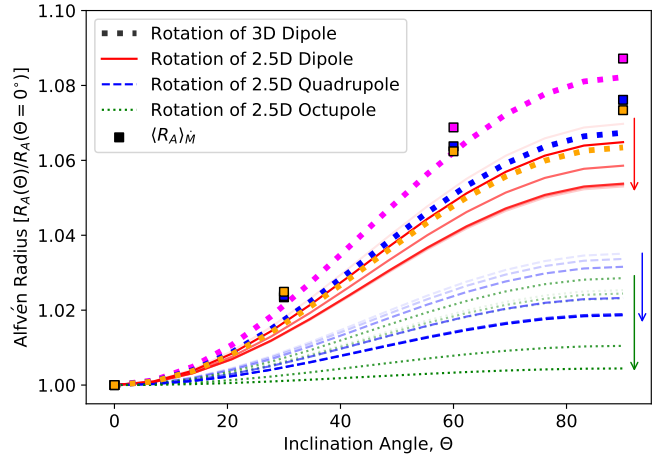


**Figure 4.** Normalised Alfvén radius versus inclination angle  $\Theta$ . Values of  $\langle R_A \rangle_{\dot{M}}$  from the 3D simulations are shown with coloured squares (matching Figure 3). The dashed lines from Figure 3 are now shown with thick dotted lines. Thin lines correspond to values from equation (15) when using the 2.5D axisymmetric dipole (solid red), quadrupole (dashed blue) and octupole (dotted green) simulations of Finley & Matt (2018) which we revolve into 3D and then rotate with respect to the rotation axis through  $0^\circ$  to  $90^\circ$  (see Section 3.3). Arrows indicate the overall trend with increasing polar field strengths.

squares), and the rotations of the 3D axisymmetric cases (thick coloured dotted lines).

### 3.3. Generalisation to Other Magnetic Geometries

The use of  $\langle R_A \rangle_{\dot{M}}$  simply requires the shape of the Alfvén surface and the mass flux through it, both of which we can acquire from axisymmetric simulations (which in future, could include different thermal driving, etc). To exemplify this we take the dipole, quadrupole and octupole cases from Finley & Matt (2018), which were run at  $256 \times 512$  in  $(r, \theta)$ , and revolve them to make 3D results with a pseudo resolution of  $256 \times 512 \times 1024$  in  $(r, \theta, \phi)$ . Then we rotate these, now 3D, Alfvén surfaces about the rotation axis from  $0^\circ$  to  $90^\circ$ . Calculating  $\langle R_A \rangle_{\dot{M}}$  using equation (15) at various inclination angles. The results from this are displayed in Figure 4, where dipolar fields are shown with solid red lines, quadrupolar fields are shown with dashed blue lines and octupolar fields are shown with dotted green lines. The strength of the line colour indicates the strength of the polar magnetic field in each case. Coloured arrows help to show the trend with increasing polar field strength. The 3D dipole rotations from Figure 3 are also shown with thick dotted lines.

For the 2.5D dipolar simulations we observe the same behaviour as the 3D simulations, where the value of

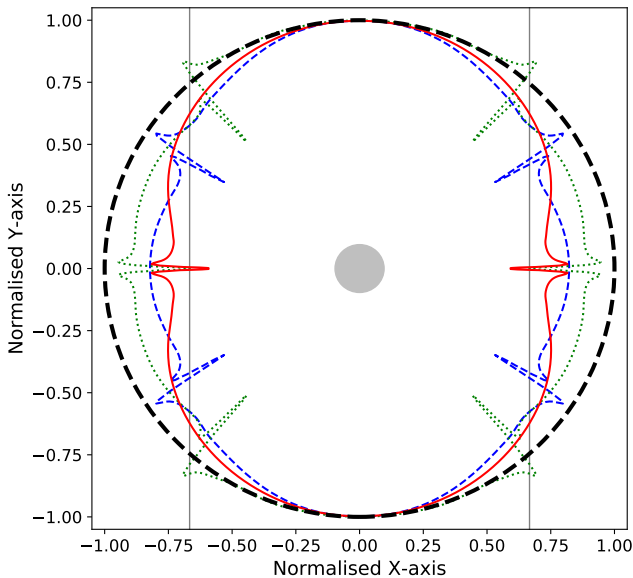


**Figure 5.** Comparison of 2.5D dipolar, quadrupolar and octupolar Alfvén surfaces, shown with solid red, dashed blue, and dotted green lines respectively. Each simulation has a similar polar magnetic field strength, and has been scaled such that their y-axis extent is unity (coincidentally the value of  $\langle R_A \rangle_\tau$  for each scaled surface is approximately the same, indicated by the grey vertical lines). The higher order magnetic geometries are more spherically-symmetric than the dipole, which is reflected in the reduced influence of inclination in Figure 4. Note, that the exact shape of each Alfvén surface can vary depending on their polar magnetic field strength.

$\delta\langle R_A \rangle / \langle R_A \rangle(0^\circ)$  generally decreases with field strength. This occurs due to the changing shape of the Alfvén surface with increasing field strength, i.e. the strongest field strength simulations have Alfvén surfaces that are more spherically symmetric than weaker field simulations (whose Alfvén surfaces are more pill-shaped). Due to the differences in resolution between the 2.5D and 3D simulations, it is hard to directly compare their results, though they do show the same trends and approximate values.

The quadrupolar and octupolar cases show the same trend as the dipole cases, but with a weaker dependence on inclination. This is understood as the quadrupolar and octupolar Alfvén surfaces being nearer to spherical symmetry than those of the dipolar cases. This is exemplified in Figure 5, where we have compared the shape of typical Alfvén surfaces for each magnetic geometry. The higher order magnetic fields are clearly nearer to spherical symmetry (indicated by the dashed circle),

thus when they are revolved into 3D their  $\langle R_A \rangle_{\dot{M}}$  is less affected by inclination to the rotation axis. As  $\langle R_A \rangle_{\dot{M}}$  depends on the distribution of mass flux through the Alfvén surface, this also has an effect, but in general the observed trends are controlled primarily by the shape of the Alfvén surface.

It is important to remember that the rotations of the axisymmetric quadrupole and octupole correspond to a specific subset of the  $l = 2$  and  $3$  spherical harmonics. Therefore our result is not exhaustive with regards to these multipoles, unlike the dipole case (for which the  $m > 0$  harmonics correspond to inclined dipolar fields). However, it is thought unlikely that the other spherical harmonic combinations ( $m > 0$ ) produce Alfvén radii with sufficient variation in shape and/or mass flux distribution that would change the overall result. Though proof of this is left for further work.

## 4. DISCUSSION

### 4.1. Numerical Challenges

For a given simulation in Table 1, the value of  $\langle R_A \rangle_\tau$  is on average a few percent smaller than  $\langle R_A \rangle_{\dot{M}}$ , and the size of this effect varies with polar field strength. For the lowest polar field strength cases, their values agree to within one or two decimal places. This is unlike the highest field strength cases, which can disagree by up to  $1R_*$ . Additionally this difference is dependent on the inclination of the dipole magnetic field, and it is this dependence that leads to the stark discrepancies in Figure 3. For example, the strongest field strength cases (shown in orange) have a relative difference in  $\langle R_A \rangle_\tau$  between the axisymmetric and fully-inclined cases that is much greater than when using  $\langle R_A \rangle_{\dot{M}}$ . This occurs because of the varying error in  $\langle R_A \rangle_\tau$ , i.e. for the axisymmetric case  $\langle R_A \rangle_\tau$  is lower than  $\langle R_A \rangle_{\dot{M}}$  by  $1R_*$  whereas for the full-inclined case it is lower by only  $0.5R_*$ . Therefore the relative difference appears larger, but it is instead the result of varying numerical error.

The source of the numerical error in our 3D simulations is likely our relatively low grid resolution, which is exacerbated by flow crossing the coordinate singularities. Compared to previous 2.5D axisymmetric simulations, our 3D simulations have a much lower resolution which is due to two main factors. Firstly, the inclusion of the third spacial dimension increases the computational expense, particularly as we needed to perform a systematic study. Secondly, our choice of resolution is constrained by the size of the grid cells over the poles which, in spherical geometry, have an increasing aspect ratio with increasing resolution.

As done in previous works (see both Réville et al. 2015; Pantolmos & Matt 2017), we consider the effec-

tive rotation rate of magnetic field lines (equation (10)) as our measure of numerical error, i.e.  $\Omega_{eff}$  should be equal to  $\Omega_*$  everywhere in our computational domain. We find our numerics produce steady state solutions, which have significant deviations from the conservation of  $\Omega_{eff}$ . These departures from ideal MHD are larger for the stronger field cases than the weaker field cases, and are more significant when the closed-open magnetic field boundary threads the coordinate singularities over the rotation poles. Thus errors due to the coordinate singularities become larger when the dipole field is highly inclined. Generally, the low resolution of our simulation domain (and more diffusive  $\nabla \cdot \mathbf{B}$  scheme) allows the magnetic field to “slip” with respect to the ideal MHD equations. The overall effect of this is to produce smaller values of  $\langle R_A \rangle_\tau$ , than simulations which better conserve the ideal MHD quantities.

The main results from this work are dependent on the values of  $\langle R_A \rangle_M$ , which are derived from the shape of the Alfvén surfaces. Though numerical errors can also deform the Alfvén surfaces in our simulations, these deformations are small, as can be seen in Figure 1. Therefore our results are less sensitive to the numerical errors discussed above, and are supported by the results of manipulating the 2.5D simulations in Section 3.3.

#### 4.2. Application to the Solar Wind Torque

The Sun’s magnetic field is observed to vary on a 11-year timescale where it evolves from being highly axisymmetric and dipolar, to non-axisymmetric and multipolar, then back to axisymmetric and dipolar with a reversed polarity (see DeRosa et al. 2012, Vidotto et al. 2018, the Appendix of Finley et al. 2018, and Obridko et al. 2020). Previous works that studied the solar angular momentum-loss rate have generally used axisymmetric models or scaling relations (e.g. Pinto et al. 2011; Finley et al. 2018; Perri et al. 2018). Finley et al. (2018) found the dipole component of the Sun’s magnetic field generally governed the solar angular momentum-loss rate, however at activity maximum the dipole field is often non-axisymmetric. This is not captured in the scaling relations of Finley & Matt (2018) which were used in that study.

Given the results of this paper, in Figure 6 we show the inclination angle of the solar dipole (calculated using the spherical harmonic decomposition from Finley et al. (2018) using SOHO/MDI and SDO/HMI magnetograms) and calculate the “error” on their axisymmetric calculation as a function of solar cycle. It is clear that for a significant fraction of the solar cycle the solar wind torque is under-predicted by axisymmetric calculations. However the “error” is no larger than  $\sim 20\%$ .

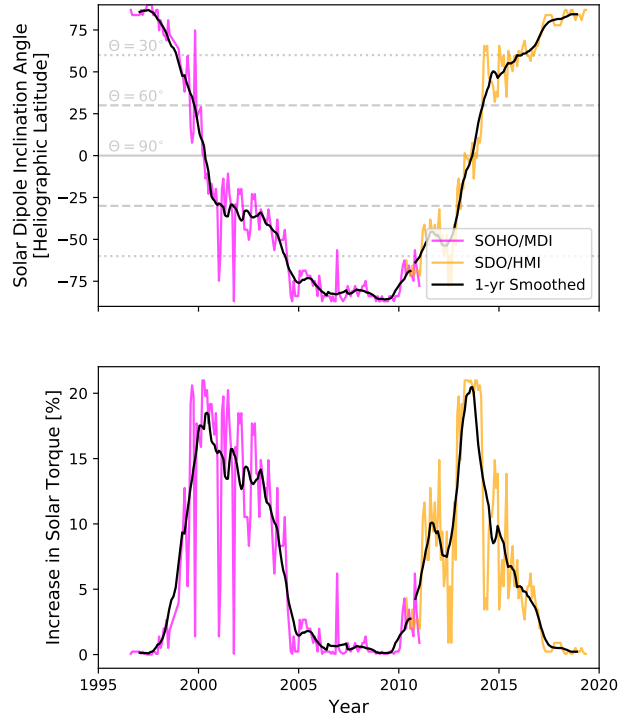


**Figure 6.** Top: Inclination of the solar dipole magnetic field from 1996-2019. The dipole field is retrieved by decomposing the polar field corrected synoptic magnetograms from SOHO/MDI and SDO/HMI, coloured magenta and orange respectively, into spherical harmonics. Bottom: Increase in the predicted angular momentum-loss rate from axisymmetric calculations, for example Finley et al. (2018), using  $\delta \langle R_A \rangle / \langle R_A \rangle(0^\circ) = 0.1$ . During solar maximum the dipole axis becomes inclined to the rotation axis, however the dipole field is relatively weak and so the predicted solar angular momentum-loss rate is less affected than this figure suggests.

Given that the angular momentum-loss rate during solar maximum is less than solar minimum (using the surface magnetic field formulation), the absolute change to the angular momentum-loss rate (or wind torque) when averaged over the solar cycle is far less than suggested by Figure 6. Though, the effect of dipole inclination does help to resolve some of the differences in the solar cycle dependence of the  $\Upsilon$  (surface field) and  $\Upsilon_{open}$  (open magnetic field) formulations, found in Finley et al. (2018). Though there still remains a significant offset between the two predictions, which appears not to be explained by dipole inclination.

#### 4.3. In the Case of Rapid Rotation

Rotation has been shown to collimate the stellar wind outflow along the rotation axis, wrapping the magnetic field and increasing the wind density (see Washimi & Shibata 1993). For rapidly rotating stars, the effect

of magneto-centrifugal forces cause the Alfvén surface to shrink in the equator and expand over the rotation poles (Matt et al. 2012; Réville et al. 2015). Therefore, when comparing rapidly rotating dipolar winds with different inclinations, it is expected that changes to the Alfvén surface caused by inclination are no longer represented by rotations of the axisymmetric case. Instead, the influence of inclination on the value of  $\langle R_A \rangle$  is likely significantly reduced, with the Alfvén surfaces of different dipole inclinations appearing similar to one another, due to the collimating effect of the magneto-centrifugal force. However, for intermediate rotation rates it is less-obvious how non-axisymmetric geometries affect the shape of the Alfvén surface, and subsequently the value of  $\langle R_A \rangle$ . Though it is clear that rotations of the axisymmetric Alfvén surface would be ineffective in predicting  $\langle R_A \rangle$ .

## 5. CONCLUSION

We have conducted a systematic study of stellar winds with a variety of inclined dipolar magnetic fields using the PLUTO MHD code. These simulations compliment previous 2.5D studies, using a similar thermal driving and Sun-like rotation rate. We find that our inclined dipole winds are morphologically similar to the axisymmetric cases. We take advantage of this and propose that the average Alfvén radius  $\langle R_A \rangle$  can be predicted for the inclined cases by considering a geometric transformation of the corresponding axisymmetric case. Changing the inclination of the magnetic field, with respect to the rotation axis, is shown to weakly influence the angular momentum-loss rate. At most, inclination increases the size of  $\langle R_A \rangle$  (or increases the angular momentum-

loss rate) by  $\sim 10\%$  (or  $\sim 20\%$ ), i.e. when the magnetic axis is inclined by  $90^\circ$  to the rotation axis.

We generalise our results to previous 2.5D MHD simulations from Finley & Matt (2018), which are less computationally challenging and costly. The trend observed by rotating the 2.5D dipolar magnetic fields agrees well with our conclusions based on the 3D simulations. Additionally, the angular momentum-loss rates of quadrupolar and octupolar magnetic fields are shown to be less affected by inclination. Though for the quadrupolar and octupolar geometries, the rotation of their axisymmetric ( $m = 0$ ) field corresponds to a specific subset of spherical harmonics, such that those results are not exhaustive. Finally, we apply our results to the solar angular momentum-loss rate, and show that the previous calculation from Finley et al. (2018) likely under-predicted the angular momentum-loss rate during solar maxima based on the axisymmetric simulations of Finley & Matt (2018).

Thanks for helpful discussions and technical advice from Georgios Pantolmos, Victor Réville, and Simon Daley-Yates. We thank Andrea Mignone and others for the development and maintenance of the PLUTO code. AJF and SPM acknowledge funding from the European Research Council (ERC) under the European Unions Horizon 2020 research and innovation programme (grant agreement No 682393 AWESoMeStars). CZ is funded by ? Data supplied courtesy of the SDO/HMI and SDO/AIA consortia. SDO is the first mission to be launched for NASAs Living With a Star (LWS) Program. Data provided by the SOHO/MDI consortium. SOHO is a project of international cooperation between ESA and NASA. We thank the developers of SHTOOLS, M. A. Wicczorek, M. Meschede, I. Oshchepkov, E. Sales de Andrade, and heroxbd (2016). Figures in this work are produced using the python package matplotlib (Hunter 2007).

## APPENDIX

### A. POLYTROPIC PARKER WIND SETUP

In this work our initial velocity, density and pressure distributions are spherically symmetric and follow a polytropic Parker wind solution. The velocity profile is found by solving the following set of transcendental equations,

$$\left(\frac{v_r}{v_c}\right)^{\gamma+1} - \left(\frac{v_r}{v_c}\right)^{\gamma-1} \left[ \frac{4r_c}{r} + \left(\frac{5-3\gamma}{\gamma-1}\right) \right] + \frac{2}{\gamma-1} \left(\frac{r}{r_c}\right)^{2-2\gamma} = 0, \quad (\text{A1})$$

$$v_c = \sqrt{\frac{GM_*}{2r_c}}, \quad (\text{A2})$$

$$\frac{R_*}{r_c} - \frac{\gamma-1}{5-3\gamma} \left(\frac{v_{esc}}{2c_s}\right)^{\frac{4}{\gamma-1}} \left(\frac{R_*}{r_c}\right)^{\frac{5-3\gamma}{\gamma-1}} - \frac{2}{5-3\gamma} \left(\frac{2c_s}{v_{esc}}\right)^2 + 4\frac{\gamma-1}{5-3\gamma} = 0, \quad (\text{A3})$$

where equation (A1) describes a radial velocity  $v_r$  which is driven by thermal pressure from subsonic to supersonic speeds, passing through the critical point  $r_c$ . The wind speed at  $r_c$  is  $v_c$ , as given by equation (A2). Due to the

polytropic nature of our flow ( $p \propto \rho^\gamma$  with  $\gamma = 1.05$ ) the location of  $r_c$  must be solved for using equation (A3), which depends on the ratio of the sound speed at the coronal base  $c_s = \sqrt{\gamma p_*/\rho_*}$ , to the surface escape velocity  $v_{esc} = \sqrt{2GM_*/R_*}$ , where  $G$  is the gravitational constant and  $M_*$  is the mass of the star. The wind density is initialised by considering mass conservation  $\rho(r) = \rho_* v_r(R_*) R_*^2 / v_r(r) r^2$ , given a coronal base density  $\rho_* = \rho(R_*)$  and wind speed  $v_r(R_*)$ . The wind pressure is then related to the density through the polytropic approximation by  $p(r) = c_s^2 \rho_*^{1-\gamma} \rho(r)^\gamma / \gamma$ .

## REFERENCES

- Agüeros, M. A. 2017, *Revista Mexicana de Astronomía y Astrofísica*, 49, 80
- Agüeros, M. A., Covey, K. R., Lemonias, J. J., et al. 2011, *The Astrophysical Journal*, 740, 110
- Alvarado-Gómez, J., Hussain, G., Cohen, O., et al. 2016, *Astronomy & Astrophysics*, 594, A95
- Bogovalov, S. V. 1999, *A&A*, 349, 1017
- Brun, A. S., & Browning, M. K. 2017, *Living Reviews in Solar Physics*, 14, 4
- Cohen, O., & Drake, J. J. 2014, *The Astrophysical Journal*, 783, 55
- Covey, K. R., Agüeros, M. A., Law, N. M., et al. 2016, *The Astrophysical Journal*, 822, 81
- Dedner, A., Kemm, F., Kröner, D., et al. 2002, *Journal of Computational Physics*, 175, 645
- DeRosa, M., Brun, A., & Hoeksema, J. 2012, *The Astrophysical Journal*, 757, 96
- Douglas, S. T., Agüeros, M. A., Covey, K. R., & Kraus, A. 2017, *The Astrophysical Journal*, 842, 83
- Finley, A. J., Deshmukh, S., Matt, S. P., Owens, M., & Wu, C.-J. 2019a, *The Astrophysical Journal*, 883, 67
- Finley, A. J., & Matt, S. P. 2017, *The Astrophysical Journal*, 845, 46
- . 2018, *The Astrophysical Journal*, 854, 78
- Finley, A. J., Matt, S. P., & See, V. 2018, *The Astrophysical Journal*, 864, 125
- Finley, A. J., See, V., & Matt, S. P. 2019b, *The Astrophysical Journal*, 876, 44
- Garraffo, C., Drake, J. J., & Cohen, O. 2015, *The Astrophysical Journal*, 813, 40
- . 2016, *Astronomy & Astrophysics*, 595, A110
- Garraffo, C., Drake, J., Dotter, A., et al. 2018, *The Astrophysical Journal*, 862, 90
- Hunter, J. D. 2007, *Computing In Science & Engineering*, 9, 90
- Kawaler, S. D. 1988, *The Astrophysical Journal*, 333, 236
- Keppens, R., & Goedbloed, J. 1999, *Astron. Astrophys.*, 343, 251
- . 2000, *The Astrophysical Journal*, 530, 1036
- Klimchuk, J. A. 2006, *Solar Physics*, 234, 41
- Lovelace, R., Mehanian, C., Mobarry, C., & Sulkanen, M. 1986, *The Astrophysical Journal Supplement Series*, 62, 1
- Matt, S., & Pudritz, R. E. 2008, *The Astrophysical Journal*, 678, 1109
- Matt, S. P., Brun, A. S., Baraffe, I., Bouvier, J., & Chabrier, G. 2015, *The Astrophysical Journal Letters*, 799, L23
- Matt, S. P., MacGregor, K. B., Pinsonneault, M. H., & Greene, T. P. 2012, *The Astrophysical Journal Letters*, 754, L26
- McQuillan, A., Aigrain, S., & Mazeh, T. 2013, *Monthly Notices of the Royal Astronomical Society*, 432, 1203
- Mestel, L. 1968, *Monthly Notices of the Royal Astronomical Society*, 138, 359
- Mestel, L., & Spruit, H. 1987, *Monthly Notices of the Royal Astronomical Society*, 226, 57
- Mignone, A. 2009, *Memorie della Societa Astronomica Italiana Supplementi*, 13, 67
- Mignone, A., Bodo, G., Massaglia, S., et al. 2007, *The Astrophysical Journal Supplement Series*, 170, 228
- Núñez, A., Agüeros, M. A., Covey, K. R., et al. 2015, *The Astrophysical Journal*, 809, 161
- Obridko, V., Sokoloff, D., Shelting, B., Shibalova, A., & Livshits, I. 2020, arXiv preprint arXiv:2001.05433
- Pantolmos, G., & Matt, S. P. 2017, *The Astrophysical Journal*, 849, 83
- Parker, E. 1965, *Space Science Reviews*, 4, 666
- Parker, E. N. 1958, *The Astrophysical Journal*, 128, 664
- Parnell, C. E., & De Moortel, I. 2012, *Philosophical Transactions of the Royal Society A: Mathematical, Physical and Engineering Sciences*, 370, 3217
- Perri, B., Brun, A. S., Réville, V., & Strugarek, A. 2018, *Journal of Plasma Physics*, 84
- Pinto, R. F., Brun, A. S., Jouve, L., & Grappin, R. 2011, *The Astrophysical Journal*, 737, 72
- Priest, E. 2014, *Magnetohydrodynamics of the Sun* (Cambridge University Press)
- Rebull, L., Stauffer, J., Bouvier, J., et al. 2016, *The Astronomical Journal*, 152, 113
- Réville, V., Brun, A. S., Matt, S. P., Strugarek, A., & Pinto, R. F. 2015, *The Astrophysical Journal*, 798, 116

- Réville, V., Folsom, C. P., Strugarek, A., & Brun, A. S. 2016, *The Astrophysical Journal*, 832, 145
- Roe, P. L. 1981, *Journal of computational physics*, 43, 357
- Sakurai, T. 1990, *Computer Physics Reports*, 12, 247
- See, V., Lehmann, L., Matt, S. P., & Finley, A. J. 2020, arXiv preprint arXiv:2002.11774
- See, V., Matt, S. P., Finley, A. J., et al. 2019, *The Astrophysical Journal*, 886, 120
- Tóth, G., Sokolov, I. V., Gombosi, T. I., et al. 2005, *Journal of Geophysical Research: Space Physics*, 110
- Ustyugova, G., Koldoba, A., Romanova, M., Chechetkin, V., & Lovelace, R. 1999, *The Astrophysical Journal*, 516, 221
- van der Holst, B., & Keppens, R. 2007, *Journal of computational physics*, 226, 925
- Vidotto, A., Jardine, M., Morin, J., et al. 2013, *Monthly Notices of the Royal Astronomical Society*, 438, 1162
- Vidotto, A., Lehmann, L., Jardine, M., & Pevtsov, A. 2018, *Monthly Notices of the Royal Astronomical Society*, 480, 477
- Washimi, H., & Shibata, S. 1993, *Monthly Notices of the Royal Astronomical Society*, 262, 936
- Weber, E. J., & Davis, L. 1967, *The Astrophysical Journal*, 148, 217
- Wright, N., & Drake, J. 2016, *Nature*, 535, 526
- Wright, N. J., Drake, J. J., Mamajek, E. E., & Henry, G. W. 2011, *The Astrophysical Journal*, 743, 48



### 7.3 Summary

In the slow-rotating regime, the effect of non-axisymmetry magnetic fields when predicting the Alfvén radius from axisymmetric wind simulations, is shown to be generally small. The inclined dipolar magnetic fields produced a larger angular momentum-loss rate by up to  $\sim 20\%$  of the axisymmetric case. Furthermore, given the morphological similarities in the geometry of the Alfvén surface between inclined and axisymmetric winds, it is shown that the influence of inclination can be assessed by calculating the mass-loss weighted average of the Alfvén radius from the axisymmetric case when rotated from the axis of rotation. This “trick” allows for the angular momentum-loss rates of previous 2.5D (axisymmetric) wind models to be evaluated at different inclinations to the rotation axis. For example, using this technique it is shown that the effect of non-axisymmetry is lessened for the quadrupole and octupole geometries (compared with dipolar winds), as their Alfvén radii are closer to spherical-symmetry.

The effect of non-axisymmetry is parameterised and applied to the solar wind torque from Section 4.3. The Sun’s dipole magnetic field is known to be relatively axisymmetric (within  $\sim 10^\circ$  of the rotation axis) during times of low solar activity (minima). However, during solar maxima, the axisymmetric dipole component weakens and energy in the non-axisymmetric component grows. In the calculation of Section 4.3, the strength of the non-axisymmetric component was simply added to the axisymmetric component when using the braking law, though this Chapter shows the inclined field would be more effective at removing angular momentum from the Sun. The effect this has is examined and it is shown that the solar wind torque is under-predicted by the axisymmetric braking law during many years of the solar cycle. During these times, however, the solar wind torque is generally weaker than the rest of the solar cycle, and so a  $\sim 20\%$  increase doesn’t make that much difference when averaged over the solar cycle.

Due to the computational set-up, the results presented in this Chapter are not perfect, and neither are they exhaustive. It is important that future works continue to build upon this, and examine the effects of non-axisymmetric magnetic geometries with more realistic wind driving, and differing rotation rates.

## Chapter 8

# The Conclusion

*“There’s nothing quite as frightening as someone who knows they are right.”*

— *Michael Faraday*

### 8.1 Concluding Remarks

In this thesis I have worked to constrain the angular momentum-loss rate of the Sun, and other Sun-like stars, using a variety of methods including; MHD simulations, in-situ measurements, and rotation-evolution modelling. The main results are summarised as follows:

- Differences arise between estimations of the angular momentum-loss rate in the solar wind when either the observed surface magnetic field strength, or open magnetic flux, is used as an input parameter to “braking laws” derived from MHD simulations (for thermally-driven winds).
- Assuming the estimation based on open magnetic flux is more reliable, as it is insensitive to how the surface magnetic field is opened (see Réville et al. [2015a](#)), the solar angular momentum-loss rate varies throughout the solar cycle and has an average value of  $2 - 3 \times 10^{30}$  erg. The solar angular momentum-loss rate is typically larger during solar maxima than minima, as there is a larger amount of open magnetic flux

in the heliosphere.

- The solar angular momentum-loss rate predicted by a Skumanich (1972) ( $\Omega_* \propto t^{-1/2}$ ) rotation period evolution is  $6.2 \times 10^{30}$ erg, which is a factor of  $\sim 3$  larger than the value from MHD simulations that reproduce the observed open magnetic flux.
- Using Zeeman-Doppler imaging observations, and mass-loss rates derived from astrophysical Ly $\alpha$  absorption, the angular momentum-loss rates of other Sun-like stars are calculated using the  $\Upsilon$  braking law. These stars are also predicted to have angular momentum-loss rates much lower than what the rotation period evolution models suggest (Matt et al. 2015). However surface magnetic field strengths must be used as an input to the braking law, which has already been shown to under-predict the solar angular momentum-loss rate. Therefore it is difficult to untangle the systematic under-prediction of the braking law, the error in field strengths derived from Zeeman-Doppler imaging, unknowns in the mass-loss rate, etc, from any physical deviation from the expected rotation evolution value.
- In an attempt to resolve the discrepancy in the solar angular momentum-loss rates between MHD simulation results and those derived from rotation period evolution, I extend the period of time for which the solar angular momentum-loss rate is estimated from two decades to nine millennia. Despite the large increase in temporal coverage, for which I use cosmogenic radionuclide records along with sunspot records and geomagnetic indices, the average solar angular momentum-loss rate remains similar to the decadal average, at  $2.2 \times 10^{30}$ erg. Additionally, 9000 years is still much smaller than the 10-100 million years over which the rotation evolution models are sensitive, and so the MHD prediction may still satisfy the rotation-evolution value provided the Sun is in a “low-torque” state presently.
- More directly, I calculate the angular momentum flux in the solar wind from observations by the *Wind* spacecraft. I calculate an average value over the last  $\sim 25$  years of  $0.39 \times 10^{30}$ erg/steradian. Assuming a distribution of angular momentum flux that is similar to the MHD simulations, this leads to a solar angular momentum-loss rate of  $3.3 \times 10^{30}$ erg. This result appears to support the MHD value over the Skumanich

angular momentum-loss rate. However, given uncertainties in the tangential wind speeds from *Wind*, this cannot be taken as direct evidence. Though ongoing work with the Parker Solar Probe also appears to support a lower value ( $2.6 \times 10^{30}$  erg).

- The MHD models, from which the braking laws are fit, are axisymmetric. The effect non-axisymmetric magnetic fields have on these scaling relations is explored through the use of 3D dipolar MHD winds. From these simulations it is shown that the angular momentum-loss rate can increase by up to 20% when the dipole field is inclined to the rotation axis. This is shown to have little effect on the previous results for solar angular momentum-loss rate, though I provide a parameterisation of the effect so it can be easily accounted for in future works.

To arrive at these conclusions, I first expanded pre-existing semi-analytic wind theory to incorporate the effect of more realistic surface magnetic fields in Chapter 3. I computed hundreds of MHD wind simulations which contained a varying fraction of axisymmetric dipole, quadrupole and octupole geometries. These simulations showed that depending on where the magnetic field becomes “open”, different magnetic geometries affect the scaling of the angular momentum-loss rate. E.g., for a given magnetic field configuration, increasing the mass-loss rate of the wind under the same thermal driving (i.e. forcing the wind to open closer to the star) will increase the importance of the higher order magnetic field components. This effect is parameterised in the form of a twice-broken power law, which approximates the behaviour of the wind simulations from Chapter 3. Not only is this “braking law” applied throughout this thesis, it has also been used in other works (See et al. 2019a, 2020), and compared to results from Alfvén wave-driven models (Shoda et al. Submitted).

## 8.2 Further Work

Given that a definitive value of the solar angular momentum-loss rate was not reached during the course of this thesis, I hope that measurements from the Parker Solar Probe (Fox et al. 2016; Kasper et al. 2019) and the Solar Orbiter (Mueller et al. 2013) will finally

distinguish the MHD results from the rotation-evolution predictions. In the case that the solar angular momentum-loss rate is truly lower than Skumanich (1972) predicts, this provides evidence towards the van-Saders et al. (2016) hypothesis where stars at the age, or older than, the Sun experience a weakened angular momentum-loss rate. Such a connection between the solar physics and astrophysics would truly be very unique.

More generally, the angular momentum-loss rates of other Sun-like stars will remain difficult to constrain. Advances in stellar wind modelling that draw from, but are not limited to, solar physics such as the inclusion of Alfvén wave driving and more realistic physical prescriptions for their associated input Poynting flux, are needed. There is also a separation between models of the stellar interior (i.e. dynamos) and the observational signatures of magnetic fields at the stellar surface (which are used to drive stellar wind models). This is a direct result of the difficulty in modelling the range of scales between the top of the convection zone and the solar atmosphere. Perhaps future models that are able to capture the connection between these regions will also be able to shed light on the angular momentum-loss rates of other Sun-like stars. With the wealth of rotation period observations and interest in stellar magnetic fields (in part due to the search for exoplanets), there is a plethora of data to compare future simulation results with.

**THE**  
**APPENDICES**

## Appendix A

# Stellar Magnetic Field Modelling

This appendix contains a summary of commonly used magnetic field models, for which I have drawn inspiration from the works of See (2016) and Vidotto (2016).

### A.1 Potential Magnetic Fields

Consider a magnetic field  $\mathbf{B}(r, \theta, \phi)$ , in the absence of currents ( $\mathbf{j} = 0$ ), such that Ampere's law is written as,

$$\nabla \times \mathbf{B} = 0, \quad (\text{A.1})$$

therefore there exists a potential field  $\psi(r, \theta, \phi)$  which describes  $\mathbf{B}(r, \theta, \phi)$ , as  $\nabla \times \nabla\psi = 0$ , i.e.,

$$\mathbf{B} = -\nabla\psi. \quad (\text{A.2})$$

This potential field must also satisfy zero-divergence of the magnetic field vector,

$$\nabla \cdot \mathbf{B} = \nabla \cdot (-\nabla\psi) = -\nabla^2\psi = 0, \quad (\text{A.3})$$

which produces Laplace's equation. The solutions for which are well known, and their derivation can be found in many undergraduate textbooks. I simply state the general solution to Laplace's equation in spherical geometry, summing over all spherical harmonics

(described by their order  $l$ , and degree  $m$ ),

$$\psi(r, \theta, \phi) = R(r)\Theta(\theta)\Phi(\phi) = \sum_{l=0}^{\infty} \sum_{m=-l}^l \left( \Phi_{lm}^a r^l + \Phi_{lm}^b r^{-(l+1)} \right) P_{lm}(\cos \theta) e^{im\phi}, \quad (\text{A.4})$$

where  $\Phi^a$  and  $\Phi^b$  are constants, and  $P_{lm}(\cos \theta)$  represents the Legendre polynomials. From the potential field, the magnetic field can be found as follows,

$$B_r(r, \theta, \phi) = -\frac{\partial \psi}{\partial r} = -\sum_{l=0}^{\infty} \sum_{m=-l}^l \left( \Phi_{lm}^a l r^{l-1} - \Phi_{lm}^b (l+1) r^{-(l+2)} \right) P_{lm}(\cos \theta) e^{im\phi}, \quad (\text{A.5})$$

$$B_\theta(r, \theta, \phi) = -\frac{1}{r} \frac{\partial \psi}{\partial \theta} = -\sum_{l=0}^{\infty} \sum_{m=-l}^l \left( \Phi_{lm}^a r^{l-1} + \Phi_{lm}^b r^{-(l+2)} \right) \frac{dP_{lm}(\cos \theta)}{d\theta} e^{im\phi}, \quad (\text{A.6})$$

$$B_\phi(r, \theta, \phi) = -\frac{1}{r \sin \theta} \frac{\partial \psi}{\partial \phi} = -\sum_{l=0}^{\infty} \sum_{m=-l}^l \left( \Phi_{lm}^a r^{l-1} + \Phi_{lm}^b r^{-(l+2)} \right) P_{lm}(\cos \theta) \frac{im}{\sin \theta} e^{im\phi}. \quad (\text{A.7})$$

As magnetic fields must satisfy  $\nabla \cdot \mathbf{B} = 0$ , the  $l = 0$  mode can be ignored as it represents a monopole. Additionally, consider the magnetic field at larger radii  $r \rightarrow \infty$ , it is expected that  $\mathbf{B} \rightarrow 0$ , and so  $\Phi_{lm}^a$  must vanish to prevent the  $r^{l-1}$  term from blowing up.

From here, many choices can be made in how these equations are presented for example the  $-m$  harmonics orders are equal in amplitude to the  $m$  orders and so the summation can instead proceed over only the positive  $m$  values with a factor of two absorbed into each non-zero harmonic order. For simplicity, here I keep summing over all  $-l < m < l$ . The magnetic field at the stellar surface is now written,

$$B_r(\theta, \phi) = \sum_{l=1}^{\infty} \sum_{m=-l}^l R_*^{-(l+2)} \Phi_{lm}^b (l+1) P_{lm}(\cos \theta) e^{im\phi} \quad (\text{A.8})$$

$$= \sum_{l=1}^{\infty} \sum_{m=-l}^l \alpha_{lm} c_{lm} P_{lm}(\cos \theta) e^{im\phi} = \sum_{l=1}^{\infty} \sum_{m=-l}^l \alpha_{lm} Y_{lm}(\theta, \phi), \quad (\text{A.9})$$



$$B_\theta(\theta, \phi) = - \sum_{l=1}^{\infty} \sum_{m=-l}^l R_*^{-(l+2)} \Phi_{lm}^b \frac{dP_{lm}(\cos \theta)}{d\theta} e^{im\phi} \quad (\text{A.10})$$

$$= - \sum_{l=1}^{\infty} \sum_{m=-l}^l \alpha_{lm} \frac{c_{lm}}{(l+1)} \frac{dP_{lm}(\cos \theta)}{d\theta} e^{im\phi} = - \sum_{l=1}^{\infty} \sum_{m=-l}^l \alpha_{lm} Z_{lm}(\theta, \phi), \quad (\text{A.11})$$

$$B_\phi(\theta, \phi) = - \sum_{l=1}^{\infty} \sum_{m=-l}^l R_*^{-(l+2)} \Phi_{lm}^b P_{lm}(\cos \theta) \frac{im}{\sin \theta} e^{im\phi} \quad (\text{A.12})$$

$$= - \sum_{l=1}^{\infty} \sum_{m=-l}^l \alpha_{lm} \frac{c_{lm}}{(l+1)} P_{lm}(\cos \theta) \frac{im}{\sin \theta} e^{im\phi} = - \sum_{l=1}^{\infty} \sum_{m=-l}^l \alpha_{lm} X_{lm}(\theta, \phi), \quad (\text{A.13})$$

where  $\alpha_{lm} c_{lm} = R_*^{-(l+2)} \Phi_{lm}^b (l+1)$ , such that  $\alpha_{lm}$  is the strength of each spherical harmonic when normalised by the constant  $c_{lm}$ , and the symbols  $Y_{lm}$ ,  $X_{lm}$ , and  $Z_{lm}$  are common notation for spherical harmonics. Note: the magnetic fields described here decay radially as  $r^{-(l+2)}$ , which is the standard result for potential magnetic fields. The value of  $c_{lm}$  can be evaluated by considering the orthogonality of the spherical harmonics, and is simply given here as,

$$c_{lm} = \sqrt{\frac{2l+1(l-m)!}{4\pi(l+m)!}} \quad (\text{A.14})$$

Typically potential magnetic fields are then described as a summation of spherical harmonics with a weighting for each mode,

$$B_r(r, \theta, \phi) = \sum_{l=1}^{\infty} \sum_{m=-l}^l \alpha_{lm} Y_{lm}(\theta, \phi) \left(\frac{r}{R_*}\right)^{l+2}, \quad (\text{A.15})$$

$$B_\theta(r, \theta, \phi) = \sum_{l=1}^{\infty} \sum_{m=-l}^l \beta_{lm} Z_{lm}(\theta, \phi) \left(\frac{r}{R_*}\right)^{l+2}, \quad (\text{A.16})$$

$$B_\phi(r, \theta, \phi) = \sum_{l=1}^{\infty} \sum_{m=-l}^l \beta_{lm} X_{lm}(\theta, \phi) \left(\frac{r}{R_*}\right)^{l+2}, \quad (\text{A.17})$$

with the condition that  $\alpha_{lm} = -\beta_{lm}$ .

The  $\alpha_{lm}$  coefficients can be retrieved from a given radial surface magnetic field

$B_r(\theta, \phi)$  by using the orthogonal properties of the spherical harmonics,

$$\int B_r(\theta, \phi) Y_{l'm'}^* \sin \theta d\theta d\phi = \int \sum_{l=1}^{\infty} \sum_{m=-l}^l \alpha_{lm} Y_{lm} Y_{l'm'}^* \sin \theta d\theta d\phi \quad (\text{A.18})$$

$$= \sum_{l=1}^{\infty} \sum_{m=-l}^l \alpha_{lm} c_{lm} \delta_{l'l} \delta_{m'm} = \alpha_{lm} c_{lm}, \quad (\text{A.19})$$

such that the observed field mapped onto each spherical harmonic retrieves the weighting of that harmonic. As the spherical harmonics contain imaginary components, so do the  $\alpha_{lm}$  coefficients. Given that  $Y_{l'm'}^* = P_{l'm'}(\cos \theta)[\cos(m'\phi) - i \sin(m'\phi)]$ , it is possible to write the real and imaginary components of  $\alpha_{lm}$  as,

$$\Re(\alpha_{lm}) = \frac{1}{c_{lm}} \int B_r(\theta, \phi) P_{lm}(\cos \theta) \cos(m\phi) \sin \theta d\theta d\phi, \quad (\text{A.20})$$

and,

$$\Im(\alpha_{lm}) = -\frac{1}{c_{lm}} \int B_r(\theta, \phi) P_{lm}(\cos \theta) \sin(m\phi) \sin \theta d\theta d\phi. \quad (\text{A.21})$$

## A.2 Non-potential Magnetic Fields

More generally, surface magnetic fields can contain non-potential components which are written as,

$$B_r(\theta, \phi) = \sum_{l=1}^{\infty} \sum_{m=-l}^l \alpha_{lm} Y_{lm}(\theta, \phi), \quad (\text{A.22})$$

$$B_\theta(\theta, \phi) = \sum_{l=1}^{\infty} \sum_{m=-l}^l \beta_{lm} Z_{lm}(\theta, \phi) - \gamma_{lm} X_{lm}(\theta, \phi), \quad (\text{A.23})$$

$$B_\phi(\theta, \phi) = \sum_{l=1}^{\infty} \sum_{m=-l}^l \beta_{lm} X_{lm}(\theta, \phi) + \gamma_{lm} Z_{lm}(\theta, \phi), \quad (\text{A.24})$$

where  $\alpha_{lm}$ ,  $\beta_{lm}$ , and  $\gamma_{lm}$  are coefficients that weight the spherical harmonics. These coefficients can be evaluated, as done for the potential field  $\alpha_{lm}$ , using,

$$\Re(\beta_{lm}) = \frac{1}{c_{lm}l} \int \left[ B_{\theta}(\theta, \phi) \cos(m\phi) \frac{dP_{lm}}{d\theta} + B_{\phi}(\theta, \phi) \frac{m \sin(m\phi)}{\sin \theta} P_{lm} \right] \sin \theta d\theta d\phi, \quad (\text{A.25})$$

$$\Im(\beta_{lm}) = \frac{-1}{c_{lm}l} \int \left[ B_{\theta}(\theta, \phi) \sin(m\phi) \frac{dP_{lm}}{d\theta} - B_{\phi}(\theta, \phi) \frac{m \cos(m\phi)}{\sin \theta} P_{lm} \right] \sin \theta d\theta d\phi, \quad (\text{A.26})$$

and,

$$\Re(\gamma_{lm}) = \frac{-1}{c_{lm}l} \int \left[ B_{\theta}(\theta, \phi) \frac{m \sin(m\phi)}{\sin \theta} P_{lm} - B_{\phi}(\theta, \phi) \cos(m\phi) \frac{dP_{lm}}{d\theta} \right] \sin \theta d\theta d\phi, \quad (\text{A.27})$$

$$\Im(\gamma_{lm}) = \frac{-1}{c_{lm}l} \int \left[ B_{\theta}(\theta, \phi) \frac{m \cos(m\phi)}{\sin \theta} P_{lm} + B_{\phi}(\theta, \phi) \sin(m\phi) \frac{dP_{lm}}{d\theta} \right] \sin \theta d\theta d\phi. \quad (\text{A.28})$$

In order to evaluate these coefficients for an observed magnetic field with a discretised array of latitude vs longitude points, these equations must be further manipulated into a discrete form (see Appendix B of Vidotto 2016).

There exist many different non-potential magnetic field models that are applicable to stellar magnetic fields, one example is Non-linear Force Free Fields (NLFFF). When applied to the Sun, NLFFF models remain close to potential, with the main differences surrounding active regions (see Wiegmann et al. 2017). This model is given by,

$$\mathbf{j} \times \mathbf{B} = (\nabla \times \mathbf{B}) \times \mathbf{B} = \mathbf{0}, \quad (\text{A.29})$$

and  $\nabla \cdot \mathbf{B} = \mathbf{0}$ , which is equivalent to,

$$\nabla \times \mathbf{B} = \xi \mathbf{B}, \quad (\text{A.30})$$

and,

$$\mathbf{B} \cdot \nabla \xi = \mathbf{0}, \quad (\text{A.31})$$

where  $\xi$  is a force-free function that remains constant along magnetic field lines. Typically these equations are solved numerically, driven by a vector magnetogram, starting with

a current-free potential field (using only the radial magnetic field component) to which currents are added.

### A.3 Potential Field Source Surface (PFSS) Model

One of the simplest (and quite useful) magnetic field models is the potential field source surface model which assumes the stellar magnetic field to be potential ( $\nabla \times \mathbf{B} = 0$ ), and that at some radius  $R_{ss}$  the magnetic field becomes purely radial. This allows for Laplace's equation to be solved again, now with a boundary condition on the non radial magnetic field components at  $R_{ss}$  which emulates the coronal magnetic field being opened by the outflow of a stellar wind. Due to its simplicity, the PFSS model is still used for solar and stellar coronal magnetic field extrapolations. Here I derive the  $\alpha_{lm}$  and  $\beta_{lm}$  coefficients for the PFSS model, which now contain a radial dependence that describes the entire coronal magnetic field. Consider the previous solution of Laplace's equation in equations (A.5), (A.6), and (A.7), then at the stellar surface ( $R_*$ ) the radial magnetic field is known which gives,

$$\Phi_{lm}^a l R_*^{l-1} - \Phi_{lm}^b (l+1) R_*^{-(l+2)} = \alpha_{lm}, \quad (\text{A.32})$$

and the non-radial magnetic field components are zero on the source surface ( $R_{ss}$ ) so,

$$\Phi_{lm}^a R_{ss}^{l-1} + \Phi_{lm}^b R_{ss}^{-(l+2)} = 0. \quad (\text{A.33})$$

These conditions produce,

$$\Phi_{lm}^a = -\Phi_{lm}^b R_{ss}^{(2l+1)}, \quad (\text{A.34})$$

and,

$$\Phi_{lm}^b = \frac{\alpha_{lm}}{R_{ss}^{(2l+1)} l R_*^{l-1} - (l+1) R_*^{-(l+2)}}, \quad (\text{A.35})$$

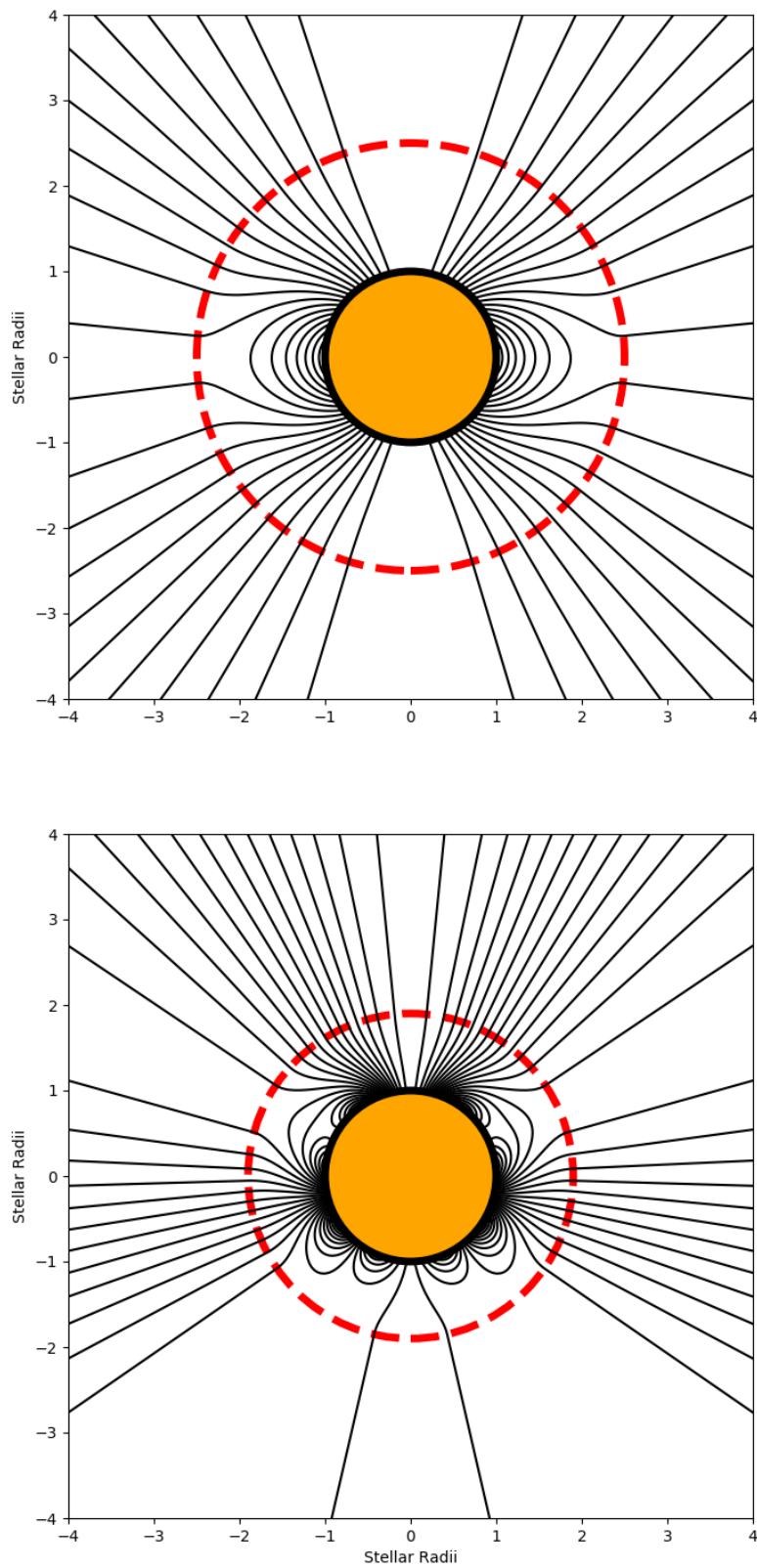


**Figure A.1:** Potential Field Source Surface Models. Top: Dipolar magnetic field with  $R_{ss} = 2.5R_*$ . Bottom: Solar Magnetogram from SDO/HMI for CR2120 using spherical harmonics up to  $l_{max} = 5$  and  $R_{ss} = 1.9R_*$  (note,  $m = 0$  due to axisymmetry). Field lines are shown in black, and the location of the source surface is indicated by a dashed red line.

which ultimately provide values for the PFSS using the decomposition of equations (A.22), (A.23), and (A.24),

$$\alpha_{lm}^{PFSS} = \alpha_{lm} \frac{l(R_*/R_{ss})^{2l+1}(r/R_*)^{l-1} + (l+1)(r/R_*)^{-(l+2)}}{l(R_*/R_{ss})^{2l+1} + (l+1)}, \quad (\text{A.36})$$

$$\beta_{lm}^{PFSS} = (l+1)\alpha_{lm} \frac{(R_*/R_{ss})^{2l+1}(r/R_*)^{l-1} - (r/R_*)^{-(l+2)}}{l(R_*/R_{ss})^{2l+1} + (l+1)}, \quad (\text{A.37})$$

$$\gamma_{lm}^{PFSS} = 0, \quad (\text{A.38})$$

which are driven by the radial component of the surface magnetic field, written in terms of  $\alpha_{lm}$  coefficients. An example of the PFSS model for an axisymmetric dipole magnetic field, and an axisymmetric multipolar field is shown in Figure A.1.

## A.4 Visualising Magnetic Field Lines

Magnetic field lines are drawn as tangents to magnetic field vector  $\mathbf{B}$ . This can be thought of as following the needle of a (non-perturbative) compass through a magnetic field, with the field line being the path the compass takes through the magnetic field. As field lines are always tangential, the condition,

$$\frac{dr}{B_r} = \frac{rd\theta}{B_\theta} = \frac{r \sin \theta d\phi}{B_\phi}, \quad (\text{A.39})$$

can be used to describe them (in spherical coordinates). Typically, a location is given from which a field line is computed (in the context of this thesis, this is generally the stellar surface). The magnetic field direction is assessed and a step along the magnetic field is taken  $\Delta l$ , this process is then repeated until the magnetic field line is complete, i.e. it returns to the stellar surface or exits the simulation domain. This process can be sped-up through the use of higher order computational methods, such as the Runge-Kutta method.

### A.4.1 Contours of the Magnetic Stream Function $\Psi$

In order to visualise the magnetic field in the stellar wind simulations of Chapter 3, I calculate the stream function  $\Psi$  which satisfies,

$$\nabla\Psi \cdot \mathbf{B} = 0, \quad (\text{A.40})$$

such that in the case of axisymmetry ( $d/d\phi = 0$ ), leads to,

$$B_r \frac{\partial\Psi}{\partial r} + \frac{B_\theta}{r} \frac{\partial\Psi}{\partial\theta} = 0. \quad (\text{A.41})$$

This equation indicates that the gradient of  $\Psi$  is perpendicular to the magnetic field vector, making the contours of  $\Psi$  equivalent to magnetic field lines. These contours can be plotted quickly and easily, once the stream function  $\Psi$  is known. To calculate  $\Psi$ , I write the magnetic field  $\mathbf{B}$  in the form of a vector potential  $\mathbf{A}$ ,

$$\nabla \times \mathbf{A} = \mathbf{B}. \quad (\text{A.42})$$

For an axisymmetric magnetic field, the vector potential can be written as  $\mathbf{A} = (0, 0, A_\phi)$  in spherical coordinates. Therefore,

$$\nabla \times \mathbf{A} = \frac{\hat{r}}{r \sin\theta} \left[ \frac{\partial}{\partial\theta}(\sin\theta A_\phi) \right] + \frac{\hat{\theta}}{r} \left[ - \frac{\partial}{\partial r}(r A_\phi) \right], \quad (\text{A.43})$$

such that the terms on the right represent  $B_r$  and  $B_\theta$  respectively.

Substituting this representation of the magnetic field vector into equation (A.41), I find,

$$\frac{1}{r \sin\theta} \left[ \frac{\partial}{\partial\theta}(\sin\theta A_\phi) \right] \frac{\partial\Psi}{\partial r} + \frac{1}{r} \left[ - \frac{\partial}{\partial r}(r A_\phi) \right] \frac{1}{r} \frac{\partial\Psi}{\partial\theta} = 0. \quad (\text{A.44})$$

Where rearranged this gives,

$$\left[ \frac{\partial}{\partial\theta}(r \sin\theta A_\phi) \right] \frac{\partial\Psi}{\partial r} = \left[ \frac{\partial}{\partial r}(r \sin\theta A_\phi) \right] \frac{\partial\Psi}{\partial\theta}, \quad (\text{A.45})$$

from which is it easy to deduce,

$$\Psi = r \sin \theta A_\phi. \quad (\text{A.46})$$

Now the stream function  $\Psi$  is described by the vector potential  $\mathbf{A} = A_\phi \hat{\phi}$ , that can be related to simulation variables. Ergo, by calculating  $A_\phi$ , a simple scaling can return the stream function  $\Psi$ . The vector potential is related to the magnetic field by,

$$B_r = \frac{1}{r \sin \theta} \left[ \frac{\partial}{\partial \theta} (\sin \theta A_\phi) \right], \quad (\text{A.47})$$

and,

$$B_\theta = \frac{1}{r} \left[ - \frac{\partial}{\partial r} (r A_\phi) \right]. \quad (\text{A.48})$$

The absolute value of  $A_\phi$  is not important, the magnetic field  $\mathbf{B}$  is derived from the gradients of  $A_\phi$ , therefore the positive magnetic pole in the simulation is given the value of  $A_\phi(R_*, 0^\circ) = 0$ . The PLUTO simulations, from Chapter 3, return an array of grid cells in the  $r - \theta$  plane. I adopt the indexing  $i$  for  $r$ -direction and  $j$  for  $\theta$ -direction when stepping through the grid cell array. Therefore the initial value at the pole is written  $A_\phi[0, 0] = 0$ . Then the vector potential is found throughout the simulation domain by discretising the equations (A.47) and (A.48) using a forward difference scheme gives,

$$B_r[i, j] = \frac{1}{r[i, j] \sin \theta[i, j]} \left( \frac{(\sin \theta[i, j + 1] A_\phi[i, j + 1]) - (\sin \theta[i, j] A_\phi[i, j])}{\theta[j + 1] - \theta[i, j]} \right), \quad (\text{A.49})$$

and,

$$B_\theta[i, j] = \frac{1}{r[i, j]} \left( - \frac{(r[i + 1, j] A_\phi[i + 1, j]) - (r[i, j] A_\phi[i, j])}{r[i + 1, j] - r[i, j]} \right). \quad (\text{A.50})$$

These can be rearranged to produce an equation for  $A_\phi$  given the previous cell's value:

$$A_\phi[i, j + 1] = \frac{B_r[i, j] r[i, j] \sin \theta[i, j] (\theta[i, j + 1] - \theta[i, j])}{\sin \theta[i, j + 1]} + \frac{\sin \theta[i, j] A_\phi[i, j]}{\sin \theta[i, j + 1]}, \quad (\text{A.51})$$

and,

$$A_\phi[i + 1, j] = \frac{-r[i, j] B_\theta[i, j] (r[i + 1, j] - r[i, j])}{r[i + 1, j]} + \frac{r[i, j] A_\phi[i, j]}{r[i + 1, j]}. \quad (\text{A.52})$$



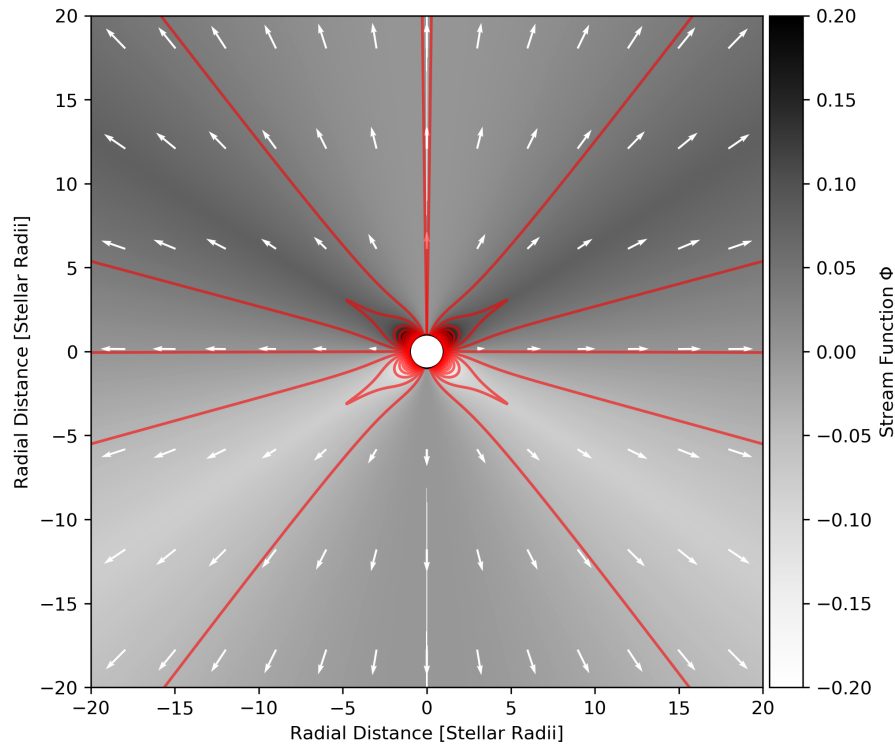


**Figure A.2:** Example of a PLUTO wind simulation. The magnetic field lines, shown in red, are described using contours of the stream function (background colour gradient).

From the initial condition,  $A_\phi[0, 0] = 0$ , the  $[i, 0]$  row ( $r$ -direction) can be calculated using equation (A.52). Then these values allow for the  $[:, j]$  columns ( $\theta$ -direction) to be calculated with equation (A.51). Once the vector potential  $\mathbf{A} = A_\phi \hat{\phi}$  has been calculated, it can be transformed into the stream function  $\Psi$  by,

$$\Psi[i, j] = r[i, j] \sin\theta[i, j] A_\phi[i, j]. \quad (\text{A.53})$$

Contours of this function can then be used to show magnetic field lines throughout the simulation domain. An example is shown in Figure A.2.

## Appendix B

# Derivation of Conserved Quantities

This appendix contains a derivation of the conserved quantities along magnetic field lines in idealised steady-state MHD flows. These derivations are adapted from Réville (2016).

Consider a steady-state MHD flow which is described by the velocity,

$$\mathbf{v} = v_r(r, \theta)\hat{r} + v_\theta(r, \theta)\hat{\theta} + v_\phi(r, \theta)\hat{\phi} = \mathbf{v}_p + v_\phi(r, \theta)\hat{\phi}, \quad (\text{B.1})$$

and magnetic field vector,

$$\begin{aligned} \mathbf{B} &= B_r(r, \theta)\hat{r} + B_\theta(r, \theta)\hat{\theta} + B_\phi(r, \theta)\hat{\phi} = \mathbf{B}_p + B_\phi(r, \theta)\hat{\phi} \\ &= \frac{\nabla\Psi \times \hat{\phi}}{r \sin\theta} + B_\phi(r, \theta)\hat{\phi}, \end{aligned} \quad (\text{B.2})$$

where  $\Psi$  represents the magnetic stream function (see Appendix A). The azimuthal electric field  $E_\phi$  must be zero therefore,

$$\mathbf{v}_p \times \mathbf{B}_p = 0, \quad (\text{B.3})$$

i.e.  $\mathbf{v}_p$  is aligned with  $\mathbf{B}_p$  and,

$$\rho\mathbf{v}_p = \kappa\mathbf{B}_p. \quad (\text{B.4})$$

Given the conservation of mass, and that the magnetic field is divergence free, it is possible

to show,

$$\nabla \cdot (\rho \mathbf{v}_p) = \nabla \cdot (\kappa \mathbf{B}_p) = \mathbf{B}_p \cdot \nabla \kappa = 0. \quad (\text{B.5})$$

This describes the scalar quantity  $\kappa$  as a constant along magnetic field lines. Similarly, for a steady-state solution,

$$(\nabla \times \mathbf{E})_\phi = (\nabla \times (\mathbf{v} \times \mathbf{B}))_\phi = 0, \quad (\text{B.6})$$

where,

$$\begin{aligned} \mathbf{v} \times \mathbf{B} &= (\mathbf{v}_p + v_\phi(r, \theta) \hat{\phi}) \times \left( \frac{\nabla \Psi \times \hat{\phi}}{r \sin \theta} + B_\phi(r, \theta) \hat{\phi} \right), \\ &= \mathbf{v}_p \times B_\phi \hat{\phi} + v_\phi \hat{\phi} \times \left( \frac{\nabla \Psi \times \hat{\phi}}{r \sin \theta} \right), \\ &= -\hat{\phi} \times \frac{\mathbf{B}_p \kappa B_\phi}{\rho} + v_\phi \hat{\phi} \times \left( \frac{\nabla \Psi \times \hat{\phi}}{r \sin \theta} \right), \\ &= -\frac{B_\phi v_p}{B_p} \hat{\phi} \times \left( \frac{\nabla \Psi \times \hat{\phi}}{r \sin \theta} \right) + v_\phi \hat{\phi} \times \left( \frac{\nabla \Psi \times \hat{\phi}}{r \sin \theta} \right), \\ &= \frac{1}{r \sin \theta} \left( v_\phi - B_\phi \frac{v_p}{B_p} \right) \hat{\phi} \times (\nabla \Psi \times \hat{\phi}), \\ &= \Omega_{eff} \left( \nabla \Psi (\hat{\phi} \cdot \hat{\phi}) - (\hat{\phi} \cdot \nabla \Psi) \hat{\phi} \right), \\ &= \Omega_{eff} \nabla \Psi. \end{aligned} \quad (\text{B.7})$$

This leads to,

$$\begin{aligned} (\nabla \times \mathbf{E})_\phi &= (\nabla \times (\Omega_{eff} \nabla \Psi))_\phi, \\ &= \left( \frac{\nabla \Psi \times \hat{\phi}}{r \sin \theta} \right) \cdot \nabla \Omega_{eff} = \mathbf{B}_p \cdot \nabla \Omega_{eff} = 0. \end{aligned} \quad (\text{B.8})$$

So  $\Omega_{eff}$  is another conserved quantity, which ensure that the rotation of the magnetic field lines is such that they remain anchored into the stellar surface.

Next, examining the azimuthal component of the momentum equation gives,

$$\rho(\mathbf{v} \cdot \nabla)\mathbf{v} \cdot \hat{\phi} = \frac{1}{c}(\mathbf{j} \times \mathbf{B}) \cdot \hat{\phi}, \quad (\text{B.9})$$

$$\rho \mathbf{v}_{\mathbf{p}} \frac{1}{r \sin \theta} \cdot \nabla(r \sin \theta v_{\phi}) = \frac{1}{4\pi r \sin \theta} \mathbf{B}_{\mathbf{p}} \cdot \nabla(r \sin \theta B_{\phi}), \quad (\text{B.10})$$

$$\kappa \mathbf{B}_{\mathbf{p}} \cdot \nabla(r \sin \theta v_{\phi}) = \frac{1}{4\pi} \mathbf{B}_{\mathbf{p}} \cdot \nabla(r \sin \theta B_{\phi}), \quad (\text{B.11})$$

$$\mathbf{B}_{\mathbf{p}} \cdot \nabla \left( r \sin \theta v_{\phi} - r \sin \theta \frac{B_{\phi}}{4\pi \kappa} \right) = 0, \quad (\text{B.12})$$

$$\mathbf{B}_{\mathbf{p}} \cdot \nabla \Lambda = 0, \quad (\text{B.13})$$

so  $\Lambda$  the specific angular momentum flux is conserved along magnetic field lines.

Finally, consider the radial momentum equation multiplied by the poloidal velocity,

$$\mathbf{v}_{\mathbf{p}} \cdot \nabla \left( \frac{v^2}{2} + \frac{\gamma}{\gamma-1} p + \frac{GM_*}{r} \right) - \mathbf{v}_{\mathbf{p}} \cdot \frac{\mathbf{j} \times \mathbf{B}}{\rho c} = 0. \quad (\text{B.14})$$

The magnetic terms can be rearranged for,

$$\mathbf{v}_{\mathbf{p}} \cdot \frac{\mathbf{j} \times \mathbf{B}}{\rho c} = \frac{\mathbf{B}_{\mathbf{p}} \cdot \nabla(r \sin \theta \Omega_{eff} B_{\phi})}{\rho}, \quad (\text{B.15})$$

and so using equation (B.4),

$$\mathbf{v}_{\mathbf{p}} \cdot \nabla \left( \frac{v^2}{2} + \frac{\gamma}{\gamma-1} p + \frac{GM_*}{r} \right) - \frac{\rho \mathbf{v}_{\mathbf{p}}}{\kappa} \cdot \nabla(r \sin \theta \Omega_{eff} B_{\phi}) = 0, \quad (\text{B.16})$$

$$\mathbf{v}_{\mathbf{p}} \cdot \nabla \left( \frac{v^2}{2} + \frac{\gamma}{\gamma-1} p + \frac{GM_*}{r} - \frac{\rho}{\kappa} r \sin \theta \Omega_{eff} B_{\phi} \right) = 0, \quad (\text{B.17})$$

$$\frac{\kappa \mathbf{B}_{\mathbf{p}}}{\rho} \cdot \nabla \left( \frac{v^2}{2} + \frac{\gamma}{\gamma-1} p + \frac{GM_*}{r} - r \sin \theta \Omega_{eff} \frac{\rho B_{\phi}}{\kappa} \right) = 0, \quad (\text{B.18})$$

$$\mathbf{B}_{\mathbf{p}} \cdot \nabla E_T = 0, \quad (\text{B.19})$$

$E_T$  can also be shown to be conserved along magnetic field lines.

TEX root=./thesis.tex

## Appendix C

# Numerical Methods

This appendix contains discussion of numerical techniques, for completeness, which are not essential in understanding the work in this thesis.

### C.1 Newton-Raphson Solver

When solutions cannot be approached analytically, numerical methods can be utilised, one such example is the Newton-Raphson method. Named after Isaac Newton and Joseph Raphson, this method is a root-finding algorithm for a single valued function  $f(x)$  which produces better and better approximations to the value of  $x$  when  $f(x) = 0$ . Each progressive prediction of  $x_{n+1}$  is based on the previous guess  $x_n$ , and the value of the function and its derivative, i.e.,

$$x_{n+1} = x_n - \frac{f(x_n)}{f'(x_n)}, \quad (\text{C.1})$$

where  $f' = df/dx$ . This process is repeated until a satisfactory accuracy is obtained. In this thesis, Parker wind solutions are used as initial conditions in the MHD simulations. These Parker wind solutions are found using the Newton-Raphson method, the equations for which are as follows.

### C.1.1 Application to Isothermal Parker Wind

The isothermal Parker wind velocity  $v_r$  is found at a given radius  $r$  by solving,

$$f(x) = x^2 - \frac{4r_c}{r} - 4 \ln\left(\frac{r}{r_c}\right) - 2 \ln(x) + 3 = 0, \quad (\text{C.2})$$

where  $x$  is the wind velocity normalised by the isothermal sound speed  $v_r/c_s$ . Using the Newton-Raphson method required the derivative of this function,

$$f'(x) = 2x - \frac{1}{x}, \quad (\text{C.3})$$

which are then combined,

$$x_{n+1} = x_n - \frac{x_n^2 - \frac{4r_c}{r} - 4 \ln\left(\frac{r}{r_c}\right) - 2 \ln(x_n) + 3}{2x_n - \frac{1}{x_n}}. \quad (\text{C.4})$$

The value of the critical point  $r_c$  is given by  $GM_*/(2c_s^2)$ , where  $c_s$  is the isothermal sound speed, as discussed in Chapter 2.

### C.1.2 Application to Polytropic Parker Wind

Similarly, for the polytropic wind velocity requires the solution of,

$$f(x) = x^{\gamma+1} - x^{\gamma-1} \left[ \frac{4r_c}{r} + \left( \frac{5-3\gamma}{\gamma-1} \right) \right] + \frac{2}{\gamma-1} \left( \frac{r}{r_c} \right)^{2-2\gamma} = 0, \quad (\text{C.5})$$

where  $x = v_r/v_c$  is the wind velocity normalised by the sound speed at the critical point, which has a derivative,

$$f'(x) = (\gamma+1)x^\gamma - (\gamma-1)x^{\gamma-2} \left[ \frac{4r_c}{r} + \left( \frac{5-3\gamma}{\gamma-1} \right) \right]. \quad (\text{C.6})$$

However, the value of the critical point  $r_c$  is no longer know, as the sound speed varies with distance. Therefore  $r_c$  must be solved for numerically as well. The function that must be solved is,

$$f(x) = \frac{1}{x} - \frac{\gamma - 1}{5 - 3\gamma} \left( \frac{v_{esc}}{2c_{s,*}} \right)^{\frac{4}{\gamma - 1}} \left( \frac{1}{x} \right)^{\frac{5 - 3\gamma}{\gamma - 1}} - \frac{2}{5 - 3\gamma} \left( \frac{2c_{s,*}}{v_{esc}} \right)^2 + 4 \frac{\gamma - 1}{5 - 3\gamma} = 0, \quad (C.7)$$

where  $x = r_c/R_*$  is the critical radius normalised by the stellar radius, and  $c_{s,*}/v_{esc}$  is the ratio of the sound speed at the stellar surface to the surface escape speed. The derivative of  $f(x)$  in this case is,

$$f'(x) = 1 - \left( \frac{v_{esc}}{2c_{s,*}} \right)^{\frac{4}{\gamma - 1}} \left( \frac{1}{x} \right)^{\frac{6 - 4\gamma}{\gamma - 1}}. \quad (C.8)$$

The polytropic wind velocity can be solved for by first using a Newton-Raphson for the normalised radius  $z = r/r_c$  and then another for the normalised velocity profile  $x = v_r/v_c$ , as follows,

$$z_{n+1} = z_n - \frac{\frac{1}{z_n} - \frac{\gamma - 1}{5 - 3\gamma} \left( \frac{v_{esc}}{2c_{s,*}} \right)^{\frac{4}{\gamma - 1}} \left( \frac{1}{z_n} \right)^{\frac{5 - 3\gamma}{\gamma - 1}} - \frac{2}{5 - 3\gamma} \left( \frac{2c_{s,*}}{v_{esc}} \right)^2 + 4 \frac{\gamma - 1}{5 - 3\gamma}}{1 - \left( \frac{v_{esc}}{2c_{s,*}} \right)^{\frac{4}{\gamma - 1}} \left( \frac{1}{z_n} \right)^{\frac{6 - 4\gamma}{\gamma - 1}}}. \quad (C.9)$$

and,

$$x_{n+1} = x_n - \frac{x_n^{\gamma+1} - x_n^{\gamma-1} \left[ \frac{4}{z} + \left( \frac{5 - 3\gamma}{\gamma - 1} \right) \right] + \frac{2}{\gamma - 1} z^{2-2\gamma}}{(\gamma + 1)x_n^\gamma - (\gamma - 1)x_n^{\gamma-2} \left[ \frac{4}{z} + \left( \frac{5 - 3\gamma}{\gamma - 1} \right) \right]}. \quad (C.10)$$

The critical speed  $v_c$  is connected to the critical radius  $r_c$  via,

$$v_c = \sqrt{\frac{GM_*}{2r_c}}. \quad (C.11)$$



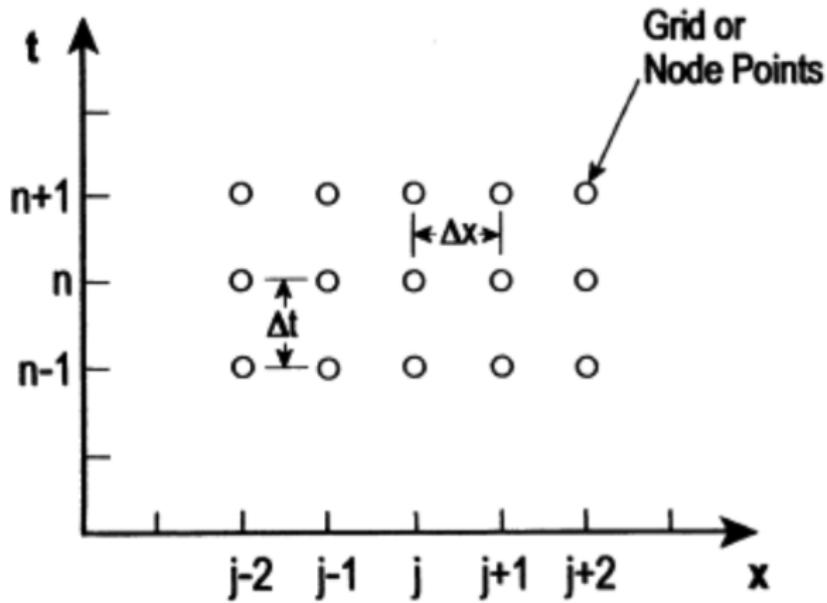


Figure C.1: An example of 1D discretisation in  $x$  and  $t$ . Taken from Lomax et al. (2002).

## C.2 Basics of Computational Fluid Dynamics

In order to implement the hydrodynamic (HD) or magnetohydrodynamic (MHD) equations, when the solutions cannot be reached analytically, numerical methods are required. Coupled partial differential equations (PDEs) must therefore be solved at every location in the system. Exact solutions to such problems are hard to find, so approximations are made along with discretisation of the spatial and temporal system. Computers are programmed to implement simplified equations which they solve at every point in a grid (or array of mesh points). A time-stepping scheme is then used to find solutions at a future time, typically this is an iterative method. The process of solving the HD or MHD equations numerically is broadly referred to as Computational Fluid Dynamics (CFD), a term which encompasses many different numerical techniques.

Here I will illustrate this with a simple PDE, consider a scalar field  $u(x, t)$  which evolves following,

$$\frac{\partial u}{\partial t} + c \frac{\partial u}{\partial x} = 0, \quad (\text{C.12})$$

with a constant flow speed of  $c$ . The first step is to discretise the equation, the computer

cannot interpret the differential operator and so it must be linearised in terms of the primitive variables available in the array of computation. The simplest way to do this is by employing a Taylor expansion, for simplicity in this example we use a 1D grid which is discretised into linear steps of  $\Delta x$  in space and  $\Delta t$  in time, shown in Figure C.1. The scalar field has a value at every grid point in the domain  $u(j + k\Delta x, n + m\Delta t)$ , which I write in the form of  $u_{j+k}^{n+m}$  for simplicity of notation. Expanding this in the spacial dimension using a Taylor expansion (up to Nth degree) gives,

$$u_{j+k} = u_j + k\Delta x \left( \frac{\partial u}{\partial x} \right)_j + \frac{1}{2}(k\Delta x)^2 \left( \frac{\partial^2 u}{\partial x^2} \right)_j + \dots + \frac{1}{N!}(k\Delta x)^N \left( \frac{\partial^N u}{\partial x^N} \right)_j, \quad (\text{C.13})$$

where all values are taken at  $t = n$  and so the superscript has been dropped. This can be rearranged to provide an approximation for the differential,

$$\left( \frac{\partial u}{\partial x} \right)_j = \frac{u_{j+k} - u_j}{k\Delta x} - \frac{1}{2}(k\Delta x) \left( \frac{\partial^2 u}{\partial x^2} \right)_j - \dots - \frac{1}{N!}(k\Delta x)^{N-1} \left( \frac{\partial^N u}{\partial x^N} \right)_j. \quad (\text{C.14})$$

In this case I truncate the approximation at the order of  $\Delta x$  and write,

$$\left( \frac{\partial u}{\partial x} \right)_j = \frac{u_{j+k} - u_j}{k\Delta x} - \vartheta(\Delta x), \quad (\text{C.15})$$

where  $\vartheta()$  indicates the degree of the truncation error. This is referred to as the forward difference approximation (a Euler stepping method) and, when combined with a discretisation for the temporal domain, allows for the initial PDE to be numerically evaluated. This is not the only method, other simple methods include central difference, backward difference, and more complex methods that involve multiple steps (e.g. predictor and corrector steps) which are said to be “higher order” methods. For equation (C.12), if  $u(x, t_0)$  is given at an initial start time  $t_0$ , what is the best direction to discretise the spatial derivative, i.e. forward, central, or backward?. Equation (C.15) is referred to as a downwind scheme (for  $c > 0$ ), as the information required to compute the derivative is taken at  $x_{j+k} > x_j$  which is downstream of the flow direction. By definition, information should flow downstream (i.e., information from above  $x_j$  should not be able to influence the flow below it)

and so an upwind scheme is favoured for numerical stability, e.g.,

$$\left(\frac{\partial u}{\partial x}\right)_j = \frac{u_j - u_{j-k}}{k\Delta x} - \vartheta(\Delta x), \quad (\text{C.16})$$

which incorporates values from the direction of the flows origin.

The examples above are termed explicit methods, as they use only information which is available from the current time step ( $n$ ), however there also exist implicit methods which require values from adjacent grid points at the same future time step ( $n + m$ ), so all grid points are interconnected with the solution for each step. This complexity tends to require the use of tridiagonal matrices to store the arrays, and compute the values simultaneously across each time step (rather than using the previous steps to calculate the next step). An example of this for equation (C.12) is,

$$\frac{u_j^{n+1} - u_j^n}{\Delta t} + \frac{c(u_{j+1}^{n+1} - u_{j-1}^{n+1})}{2\Delta x} = 0. \quad (\text{C.17})$$

which uses a forward difference in time and central difference in space. This clearly requires neighbouring values to  $u_j^{n+1}$  at  $t = n + 1$  in order to evaluate the derivatives. The main advantage of an implicit method, over an explicit method, is the larger step size  $\Delta t$  that the implicit methods can perform whilst remaining numerically stable. This comes at the cost of the implicit methods being much more complex to program, and with each individual step requiring more computational effort than an explicit one.

Here I will examine the natural limits of an explicit method (implicit methods are outside the scope of this work), consider a 1st order upwind scheme (forward difference in time, with backward difference in space) for equation (C.12),

$$\frac{u_j^{n+1} - u_j^n}{\Delta t} + \frac{c(u_j^n - u_{j-1}^n)}{\Delta x} = 0. \quad (\text{C.18})$$

It is now possible to advance through the 1D grid of Figure C.1 using,

$$u_j^{n+1} = u_j^n - \frac{c\Delta t}{\Delta x}(u_j^n - u_{j-1}^n), \quad (\text{C.19})$$

to evaluate  $u$  at the next time step for each spatial grid point. This produces an interesting quantity  $c\Delta t/\Delta x = \sigma_{\text{CFL}}$  which is referred to as the CFL number (Courant et al. 1928), whose importance is quickly recognised by considering the difference between the exact solution of the discretised equation (C.18), and the original equation (C.12), for which it can be written,

$$\begin{aligned} & \frac{u_j^{n+1} - u_j^n}{\Delta t} + \frac{c(u_j^n - u_{j-1}^n)}{\Delta x} - \left(\frac{\partial u}{\partial t}\right)_j^n - c\left(\frac{\partial u}{\partial x}\right)_j^n = \\ & \frac{u_j^{n+1} - u_j^n}{\Delta t} + \frac{c(u_j^n - u_{j-1}^n)}{\Delta x} - \left[ \frac{u_j^n - u_j^{n-1}}{\Delta t} - \frac{1}{2}(\Delta t)\left(\frac{\partial^2 u}{\partial t^2}\right)_j^n + \vartheta(\Delta t^2) \right] \\ & - c\left[ \frac{u_j^n - u_{j-1}^n}{\Delta x} - \frac{1}{2}(\Delta x)\left(\frac{\partial^2 u}{\partial x^2}\right)_j^n + \vartheta(\Delta x^2) \right], \end{aligned}$$

where now  $u$  corresponds to the exact solution of equation (C.18). This is simplified to,

$$-\left(\frac{\partial u}{\partial t}\right)_j^n - c\left(\frac{\partial u}{\partial x}\right)_j^n = -\frac{1}{2}(\Delta t)\left(\frac{\partial^2 u}{\partial t^2}\right)_j^n - \frac{c}{2}(\Delta x)\left(\frac{\partial^2 u}{\partial x^2}\right)_j^n + \frac{u_j^{n+1} - 2u_j^n + u_j^{n-1}}{\Delta t} - \vartheta(\Delta x^2) - \vartheta(\Delta t^2), \quad (\text{C.20})$$

as equation (C.18) is exactly solved by  $u$  (LHS), and the backward differences (in space) cancel (RHS). The third term on the RHS of this equation is actually the central difference method mentioned previously, and so this equation becomes,

$$\left(\frac{\partial u}{\partial t}\right)_j^n + c\left(\frac{\partial u}{\partial x}\right)_j^n = \frac{1}{2}(\Delta t)\left(\frac{\partial^2 u}{\partial t^2}\right)_j^n + \frac{c}{2}(\Delta x)\left(\frac{\partial^2 u}{\partial x^2}\right)_j^n - (\Delta t)\left(\frac{\partial^2 u}{\partial t^2}\right)_j^n + \vartheta(\Delta x^2) + \vartheta(\Delta t^2), \quad (\text{C.21})$$

and simplifies to,

$$\left(\frac{\partial u}{\partial t}\right)_j^n + c\left(\frac{\partial u}{\partial x}\right)_j^n = -\frac{1}{2}(\Delta t)\left(\frac{\partial^2 u}{\partial t^2}\right)_j^n + \frac{c}{2}(\Delta x)\left(\frac{\partial^2 u}{\partial x^2}\right)_j^n + \vartheta(\Delta x^2) + \vartheta(\Delta t^2). \quad (\text{C.22})$$

Here to first order,

$$\left(\frac{\partial^2 u}{\partial t^2}\right)_j^n = c^2\left(\frac{\partial^2 u}{\partial x^2}\right)_j^n + \vartheta(\Delta x^2) + \vartheta(\Delta t^2), \quad (\text{C.23})$$

and so with some rearranging, it is possible to show,

$$\left(\frac{\partial u}{\partial t}\right)_j^n + c\left(\frac{\partial u}{\partial x}\right)_j^n = \frac{c\Delta x}{2}\left(1 - \frac{c\Delta t}{\Delta x}\right)\left(\frac{\partial^2 u}{\partial x^2}\right)_j^n + \vartheta(\Delta x^2) + \vartheta(\Delta t^2). \quad (\text{C.24})$$

This is the modified differential equation and shows by using equation C.18 the PDE for advection has been replaced with an advection-diffusion equation. A negative diffusion term corresponds to an explosive solution, and so the right hand side must remain positive for the numerical scheme to be stable. This leads quickly to a condition on the CFL number,

$$\frac{c\Delta x}{2}\left(1 - \frac{c\Delta t}{\Delta x}\right) > 0, \quad (\text{C.25})$$

$$1 > \frac{c\Delta t}{\Delta x} = \sigma_{\text{CFL}}. \quad (\text{C.26})$$

When looking deeper into these numerical methods and their solutions a few terms become required to distinguish the results of a model to the analytic solution. These are numerical dispersion and numerical dissipation. A system with large dissipation will tend to have a solution that progressed slower than the analytic, requiring more time to reach the same point. A system with a large dispersion will tend to develop oscillations/artefacts as differing wavenumber solutions separate. The combination of these two effects lead to the wider term, numerical diffusion. There are many ways to quantify the stability and diffusion of different numerical schemes, most notably Von-Neumann analysis where Fourier modes are used to probe the system on a range of scales (temporal or spatial) to find stability. Some systems may be unconditionally stable but have high numerical diffusion, others may only be conditionally stable but with low diffusion around a particular wavenumber. Further details are left to the reader, as this topic is a research field of its own.

## Appendix D

### Other Publications

**Title:** Estimating Magnetic Filling Factors from Zeeman–Doppler Magnetograms

**Authors:** Victor See, Sean P. Matt, Colin P. Folsom, Sudeshna Boro Saikia, Jean-Francois Donati, Rim Fares, Adam J. Finley, Élodie M. Hébrard, Moira M. Jardine, Sandra V. Jeffers, Lisa T. Lehmann, Stephen C. Marsden, Matthew W. Mengel, Julien Morin, Pascal Petit, Aline A. Vidotto, Ian A. Waite, and The BCool Collaboration

**DOI:** <https://doi.org/10.3847/1538-4357/ab1096>

**Summary:** The Zeeman effect can be used in multiple ways to understand the magnetic fields of stars like Sun, whose outer convective envelopes are host to magnetism with a wide range of length scales and strengths. Zeeman-Doppler imaging (ZDI) uses circularly polarised light to extract information about the large scale magnetic field topology (i.e. the dipole, quadrupole, octupole, components), however is insensitive to small-scale features. Small-scale features which have opposing polarities, like star spots, if unresolved by the doppler shifting of spectral lines will have opposing signals that cancel each other. Zeeman Broadening (ZB) instead uses the linear intensity and is sensitive to the strongest field strengths on the stellar surface, which broaden the spectral lines the most due to the Zeeman effect. In this work the authors compare the field strengths recovered by ZDI and ZB in an effort to understanding how much magnetic field is missing from ZDI due to flux cancellation. The authors estimate that ZDI recovers around a few to 20% of the

photospheric magnetic flux implied by ZB observations.

**Contribution:** For this work, I had verbal discussions with the author and provided comments on the manuscript before publication.

**Title:** Do Non-dipolar Magnetic Fields Contribute to Spin-down Torques?

**Authors:** Victor See, Sean P. Matt, Adam J. Finley, Colin P. Folsom, Sudeshna Boro Saikia, Jean-Francois Donati, Rim Fares, Élodie M. Hébrard, Moira M. Jardine, Sandra V. Jeffers, Stephen C. Marsden, Matthew W. Mengel, Julien Morin, Pascal Petit, Aline A. Vidotto, Ian A. Waite, and the BCool Collaboration

**DOI:** <https://doi.org/10.3847/1538-4357/ab46b2>

**Summary:** The authors combine results from Zeeman-Doppler imaging and the braking laws derived from my MHD simulations in Chapter 3 in order to investigate the role of magnetic geometry in angular momentum-loss from stellar winds. Given that the mass-loss rates of the sample stars cannot (in general) be detected, the authors set about establishing a critical mass-loss rate, for which larger mass-loss rates mean the higher order magnetic geometries become influential in calculating the angular momentum-loss rate. These critical values are compared with mass-loss rates derived from the model of Cranmer and Saar (2011) and those inferred by the rotation period evolution of low-mass stars (e.g. Matt et al. 2015). The authors are able to show that most of the stars in their sample had predicted mass-loss rates lower than the critical value, so their angular momentum-loss rates were nearly all governed by the dipolar component of their magnetic fields.

**Contribution:** This work relies heavily on the braking law developed in Chapter 3, therefore I provided technical advice on its use, and comments for the manuscript.

**Title:** How Much do Underestimated Field Strengths from Zeeman–Doppler Imaging Affect Spin-down Torque Estimates?

**Authors:** Victor See, Lisa Lehmann, Sean P. Matt, and Adam J. Finley

**DOI:** <https://arxiv.org/abs/2002.11774>

---

**Summary:** The authors attempt to estimate how using field strengths from Zeeman-Doppler imaging (ZDI), which are known to generally be underestimated, affect the angular momentum-loss rates predicted by my braking law from Chapter 3. This is done using the work of Lehmann et al. (2019), who produced synthetic ZDI reconstructions of flux transport simulations. The authors find that the underestimation of field strengths is lessened for stronger magnetic fields, and that the angular momentum-loss rates calculated using ZDI field strengths can be underestimated by up to a factor of 10. This work reinforces conclusions made in "Do Non-dipolar Magnetic Fields Contribute to Spin-down Torques?", by showing the dipole magnetic field is still the most significant component in determining the angular momentum-loss rate.

**Contribution:** For this work, I had verbal discussions with the author and provided comments on the manuscript, which uses the braking law developed in Chapter 3.

**Title:** Alfvén-wave Driven Magnetic Rotator Winds from Low-mass Stars I: Rotation Dependences of Magnetic Braking and Mass-loss Rate

**Authors:** Munehito Shoda, Takeru K. Suzuki, Sean P. Matt, Steven R. Cranmer, Aline A. Vidotto, Antoine Strugarek, Victor See, Victor Réville, Adam J. Finley, and Allan Sacha Brun

**DOI:** TBC

**Summary:** The authors simulate the stellar winds of Sun-like stars using a one-dimensional Alfvén-wave driven solar wind model. This model incorporates the effect of rotation through the magneto-centrifugal force. The model is used to study the angular momentum-loss rates and mass-loss rates of stars with different rotation periods, for which they must specify how the open-flux filling factor of the magnetic varies with rotation. Their Alfvén-wave drive model is able to reproduce the Skumanich spin-down relation, along with predicting the same angular momentum-loss rate for the Sun as is found in the MHD models of Chapters 4 and 5. They are able to show that this is due to the similarity in wind acceleration between their Alfvén-wave driving and the thermally-driven winds used in this thesis. This implies that thermally-driven winds are applicable for predicting the angular momentum-loss rates of Sun-like stars, despite their rudimentary thermodynamics.



**Contribution:** This work benefits from discussions held during a meeting "The Solar and Stellar Wind Connection: Heating processes and angular momentum-loss", supported by the International Space Science Institute (ISSI), of which I was in attendance. Subsequently I provided comments on the manuscript which uses one of the braking laws from Chapter 3. Before submission, I also provided assistance with grammar and sentence structure as the author is not a native english speaker.

---

# Bibliography

The Bibliography contains an entry for every reference in this thesis, including those from the published papers:

Aarnio, AN, SP Matt, and KG Stassun. 2012. 'Mass loss in pre-main-sequence stars via coronal mass ejections and implications for angular momentum loss.' *The Astrophysical Journal* 760 (1): 9.

Agüeros, MA. 2017. 'Setting stellar chronometers: the PTF (+) open cluster survey.' *Revista Mexicana de Astronomía y Astrofísica* 49:80.

Agüeros, MA, KR Covey, JJ Lemonias, et al. 2011. 'The factory and the beehive. I. rotation periods for low-mass stars in Praesepe.' *The Astrophysical Journal* 740 (2): 110.

Altschuler, MD, and G Newkirk. 1969. 'Magnetic fields and the structure of the solar corona.' *Solar Physics* 9 (1): 131–149.

Alvarado-Gómez, JD, JJ Drake, O Cohen, SP Moschou, and C Garraffo. 2018. 'Suppression of coronal mass ejections in active stars by an overlying large-scale magnetic field: a numerical study.' *The Astrophysical Journal* 862 (2): 93.

Alvarado-Gómez, JD, C Garraffo, JJ Drake, et al. 2019. 'Breezing through the space environment of Barnard's Star b.' *The Astrophysical Journal Letters* 875 (2): L12.

Alvarado-Gómez, JD, GAJ Hussain, O Cohen, et al. 2016. 'Simulating the environment around planet-hosting stars-II. stellar winds and inner astrospheres.' *Astronomy & Astrophysics* 594:A95.

- Amard, L, A Palacios, C Charbonnel, F Gallet, and J Bouvier. 2016. 'Rotating models of young solar-type stars: exploring braking laws and angular momentum transport processes.' *Astronomy & Astrophysics* 587:A105.
- Amard, L, A Palacios, C Charbonnel, et al. 2019. 'First grids of low-mass stellar models and isochrones with self-consistent treatment of rotation: from 0.2 to 1.5  $M_{\odot}$  at seven metallicities from PMS to TAMS.' *Astronomy & Astrophysics* 631:A77.
- Amari, T, JF Luciani, Z Mikic, and J Linker. 1999. 'A twisted flux rope model for coronal mass ejections and two-ribbon flares.' *The Astrophysical Journal Letters* 529 (1): L49.
- Arden, WM, AA Norton, and X Sun. 2014. 'A "breathing" source surface for cycles 23 and 24.' *Journal of Geophysical Research: Space Physics* 119 (3): 1476–1485.
- Arlt, R. 2008. 'Digitization of sunspot drawings by Staudacher in 1749–1796.' *Solar Physics* 247 (2): 399–410.
- Arlt, R, and JM Vaquero. 2020. 'Historical sunspot records.' *Living Reviews in Solar Physics* 17 (1): 1.
- Aschwanden, M. 2006. 'Physics of the solar corona: an introduction with problems and solutions.'
- Azizi, F, and MT Mirtorabi. 2017. 'A Survey of TiO  $\lambda$ 567nm absorption in solar-type stars.' *Monthly Notices of the Royal Astronomical Society*.
- Babcock, HD. 1959. 'The Sun's polar magnetic field.' *The Astrophysical Journal* 130:364.
- Babcock, HW. 1961. 'The topology of the Sun's magnetic field and the 22-year cycle.' *The Astrophysical Journal* 133:572.
- Babusiaux, C, F van-Leeuwen, MA Barstow, et al. 2018. 'Gaia data release 2: observational Hertzsprung-Russell diagrams.' *Astronomy & astrophysics* 616:A10.
- Badman, ST, SD Bale, JCM Oliveros, et al. 2020. 'Magnetic connectivity of the ecliptic plane within 0.5 au: potential field source surface modeling of the first Parker Solar Probe encounter.' *The Astrophysical Journal Supplement Series* 246 (2): 23.

- Badman, SV, G Branduardi-Raymont, M Galand, et al. 2015. 'Auroral processes at the giant planets: energy deposition, emission mechanisms, morphology and spectra.' *Space Science Reviews* 187 (1-4): 99–179.
- Badman, SV, and SWH Cowley. 2007. 'Significance of Dungey-cycle flows in Jupiter's and Saturn's magnetospheres, and their identification on closed equatorial field lines.'
- Bahcall, JN, MC Gonzalez-Garcia, and C Pena-Garay. 2003. 'Does the Sun shine by p-p or CNO fusion reactions?' *Physical review letters* 90 (13): 131301.
- Baines, EK, and JT Armstrong. 2011. 'Confirming fundamental properties of the exoplanet host star  $\epsilon$  Eridani using the Navy Optical Interferometer.' *The Astrophysical Journal* 744 (2): 138.
- Baliunas, SL, RA Donahue, WH Soon, et al. 1995. 'Chromospheric variations in main-sequence stars.' *The Astrophysical Journal* 438:269–287.
- Baraffe, I, D Homeier, F Allard, and G Chabrier. 2015. 'New evolutionary models for pre-main sequence and main sequence low-mass stars down to the Hydrogen-burning limit.' *Astronomy & Astrophysics* 577:A42.
- Bard, E, G Raisbeck, F Yiou, and J Jouzel. 2000. 'Solar irradiance during the last 1200 years based on cosmogenic nuclides.' *Tellus B* 52 (3): 985–992.
- Barnes, JR, A Collier Cameron, JF Donati, et al. 2005. 'The dependence of differential rotation on temperature and rotation.' *Monthly Notices of the Royal Astronomical Society: Letters* 357 (1): L1–L5.
- Barnes, SA. 2003. 'On the rotational evolution of solar and late-type stars, its magnetic origins, and the possibility of stellar gyrochronology.' *The Astrophysical Journal* 586 (1): 464.
- . 2007. 'Ages for illustrative field stars using gyrochronology: viability, limitations, and errors.' *The Astrophysical Journal* 669 (2): 1167.
- . 2010. 'A simple nonlinear model for the rotation of main-sequence cool stars. I. introduction, implications for gyrochronology, and color-period diagrams.' *The Astrophysical Journal* 722 (1): 222.

- Barnes, SA, and YC Kim. 2010. 'Angular momentum loss from cool stars: an empirical expression and connection to stellar activity.' *The Astrophysical Journal* 721 (1): 675.
- Barnes, SA, F Spada, and J Weingrill. 2016a. 'Some aspects of cool main sequence star ages derived from stellar rotation (gyrochronology).' *Astronomische Nachrichten* 337 (8-9): 810–814.
- Barnes, SA, J Weingrill, D Fritzewski, KG Strassmeier, and I Platais. 2016b. 'Rotation periods for cool star in the 4 Gyr old open cluster M67, the solar-stellar connection, and the applicability of gyrochronology to at least solar age.' *The Astrophysical Journal* 823 (1): 16.
- Bavassano, B, E Pietropaolo, and R Bruno. 2000. 'On the evolution of outward and inward Alfvénic fluctuations in the polar wind.' *Journal of Geophysical Research: Space Physics* 105 (A7): 15959–15964.
- Beckers, JM. 1968. 'Principles of operation of solar magnetographs.' *Solar Physics* 5 (1): 15–28.
- Beer, J, K McCracken, and R Steiger. 2012. 'Cosmogenic radionuclides: theory and applications in the terrestrial and space environments.'
- Bethe, HA. 1939. 'Energy production in stars.' *Physical Review* 55 (5): 434.
- Biermann, L. 1951. 'Kometenschweife und Solare korpuskularstrahlung.' *Zeitschrift für Astrophysik* 29:274.
- Birkeland, K. 1908. 'The Norwegian Aurora Polaris expedition 1902-1903.' 1.
- Blackman, EG, and JE Owen. 2016. 'Minimalist coupled evolution model for stellar x-ray activity, rotation, mass loss, and magnetic field.' *Monthly Notices of the Royal Astronomical Society* 458 (2): 1548–1558.
- Boeche, C, and EK Grebel. 2016. 'SP\_Ace: a new code to derive stellar parameters and elemental abundances.' *Astronomy & Astrophysics* 587:A2.
- Bogovalov, SV. 1999. 'On the physics of cold MHD winds from oblique rotators.' *A&A* 349 (September): 1017–1026.

- Böhm-Vitense, E. 2007. 'Chromospheric activity in G and K main-sequence stars, and what it tells us about stellar dynamos.' *The Astrophysical Journal* 657 (1): 486.
- Borovsky, JE, M Hesse, J Birn, and MH Kuznetsova. 2008. 'What determines the reconnection rate at the dayside magnetosphere?' *Journal of Geophysical Research: Space Physics* 113 (A7).
- Borrini, G, JT Gosling, SJ Bame, and WC Feldman. 1983. 'Helium abundance variations in the solar wind.' *Solar Physics* 83 (2): 367–378.
- Borsa, F, G Scandariato, M Rainer, et al. 2015. 'The GAPS programme with HARPS-N at TNG-VII. putting exoplanets in the stellar context: magnetic activity and asteroseismology of  $\tau$  Bootis A.' *Astronomy & Astrophysics* 578:A64.
- Bouvier, J, M Forestini, and S Allain. 1997. 'The angular momentum evolution of low-mass stars.' *Astronomy and Astrophysics* 326:1023–1043.
- Bouvier, J, SP Matt, S Mohanty, et al. 2014. 'Angular momentum evolution of young low-mass stars and brown dwarfs: observations and theory.' *Protostars and Planets VI*: 433–450.
- Boyajian, TS, K von Braun, G van Belle, et al. 2013. 'Stellar diameters and temperatures. III. main-sequence A, F, G, and K stars: additional high-precision measurements and empirical relations.' *The Astrophysical Journal* 771 (1): 40.
- Brandenburg, A, SH Saar, and CR Turpin. 1998. 'Time evolution of the magnetic activity cycle period.' *The Astrophysical Journal Letters* 498 (1): L51.
- Brown, AGA, A Vallenari, T Prusti, et al. 2016. 'Gaia data release 1 - summary of the astrometric, photometric, and survey properties.' *Astronomy & Astrophysics* 595:A2.
- Brown, SF, JF Donati, DE Rees, and M Semel. 1991. 'Zeeman-Doppler imaging of solar-type and AP stars. IV - maximum entropy reconstruction of 2D magnetic topologies.' *Astronomy and Astrophysics* 250:463–474.
- Brown, TM. 2014. 'The metastable dynamo model of stellar rotational evolution.' *The Astrophysical Journal* 789 (2): 101.

- Browning, MK. 2008. 'Simulations of dynamo action in fully convective stars.' *The Astrophysical Journal* 676 (2): 1262.
- Brun, AS, MK Browning, M Dikpati, H Hotta, and A Strugarek. 2015. 'Recent advances on solar global magnetism and variability.' *Space Science Reviews* 196 (1-4): 101–136.
- Brun, SA, and MK Browning. 2017. 'Magnetism, dynamo action and the solar-stellar connection.' *Living Reviews in Solar Physics* 14 (1): 4.
- Brun, SA, P Petit, M Jardine, and Hendrik C Spruit. 2013. 'Rotation and magnetism of solar-like stars: from scaling laws to spot-dynamos.' *International Astronomical Union. Proceedings of the International Astronomical Union* 9 (S302): 114.
- Burlaga, LF, and NF Ness. 2012. 'Heliosheath magnetic fields between 104 and 113 AU in a region of declining speeds and a stagnation region.' *The Astrophysical Journal* 749 (1): 13.
- . 2014. 'Interstellar magnetic fields observed by Voyager 1 beyond the heliopause.' *The Astrophysical Journal Letters* 795 (1): L19.
- Caligari, P, F Moreno-Insertis, and M Schussler. 1995. 'Emerging flux tubes in the solar convection zone. 1: asymmetry, tilt, and emergence latitude.' *The Astrophysical Journal* 441:886–902.
- Cane, HV, and IG Richardson. 2003. 'Interplanetary coronal mass ejections in the near-Earth solar wind during 1996–2002.' *Journal of Geophysical Research: Space Physics* 108 (A4).
- Carrington, RC. 1859. 'Description of a singular appearance seen in the Sun on September 1, 1859.' *Monthly Notices of the Royal Astronomical Society* 20:13–15.
- Castor, JI, David C Abbott, and R I Klein. 1975. 'Radiation-driven winds in Of stars.' *The Astrophysical Journal* 195:157–174.
- Chané, E, J Saur, R Keppens, and S Poedts. 2017. 'How is the Jovian main auroral emission affected by the solar wind?' *Journal of Geophysical Research: Space Physics* 122 (2): 1960–1978.

- Chapman, GA, G de Toma, and AM Cookson. 2014. 'An observed decline in the amplitude of recent solar-cycle peaks.' *Solar Physics* 289 (10): 3961–3967.
- Chapman, S. 1929. 'Solar streams of corpuscles: their geometry, absorption of light, and penetration.' *Monthly Notices of the Royal Astronomical Society* 89:456.
- Chapman, S, and H Zirin. 1957. 'Notes on the solar corona and the terrestrial ionosphere.' *Smithsonian Contributions to Astrophysics*.
- Charbonneau, P. 2010. 'Dynamo models of the solar cycle.' *Living Reviews in Solar Physics* 7 (1): 3.
- Charbonneau, P, M Dikpati, and PA Gilman. 1999. 'Stability of the solar latitudinal differential rotation inferred from helioseismic data.' *The Astrophysical Journal* 526 (1): 523.
- Clarke, C, B Carswell, RF Carswell, et al. 2007. 'Principles of astrophysical fluid dynamics.'
- Clette, F, L Svalgaard, JM Vaquero, and EW Cliver. 2014. 'Revisiting the sunspot number.' *Space Science Reviews* 186 (1-4): 35–103.
- Clilverd, MA, E Clarke, T Ulich, J Linthe, and H Rishbeth. 2005. 'Reconstructing the long-term aa index.' *Journal of Geophysical Research: Space Physics* 110 (A7).
- Cliver, EW, and AG Ling. 2002. 'Secular change in geomagnetic indices and the solar open magnetic flux during the first half of the twentieth century.' *Journal of Geophysical Research: Space Physics* 107 (A10): SSH-11.
- Cohen, O. 2011. 'The independency of stellar mass-loss rates on stellar x-ray luminosity and activity level based on solar x-ray flux and solar wind observations.' *Monthly Notices of the Royal Astronomical Society* 417 (4): 2592–2600.
- Cohen, O, and JJ Drake. 2014. 'A grid of MHD models for stellar mass loss and spin-down rates of solar analogs.' *The Astrophysical Journal* 783 (1): 55.
- Cohen, O, JJ Drake, A Glocer, et al. 2014. 'Magnetospheric structure and atmospheric joule heating of habitable planets orbiting M-dwarf stars.' *The Astrophysical Journal* 790 (1): 57.



- Cohen, O, JJ Drake, VL Kashyap, and TI Gombosi. 2009. 'The effect of magnetic spots on stellar winds and angular momentum loss.' *The Astrophysical Journal* 699 (2): 1501.
- Cohen, O, JJ Drake, VL Kashyap, GAJ Hussain, and TI Gombosi. 2010. 'The coronal structure of AB Doradus.' *The Astrophysical Journal* 721 (1): 80.
- Cohen, O, VL Kashyap, JJ Drake, et al. 2011. 'The dynamics of stellar coronae harboring Hot Jupiters. I. a time-dependent magnetohydrodynamic simulation of the interplanetary environment in the HD 189733 planetary system.' *The Astrophysical Journal* 733 (1): 67.
- Cohen, O, IV Sokolov, II Roussev, et al. 2006. 'A semiempirical magnetohydrodynamical model of the solar wind.' *The Astrophysical Journal Letters* 654 (2): L163.
- Coleman, PJ, L Davis, EJ Smith, and CP Sonett. 1962. 'Interplanetary magnetic fields.' *Science* 138 (3545): 1099–1100.
- Collier Cameron, A. 1999. 'Stellar prominences.' In *Solar and Stellar Activity: Similarities and Differences*, 158:146.
- Collier Cameron, A, and RD Robinson. 1989a. 'Fast H $\alpha$  variations on a rapidly rotating cool main sequence star: Pt. 1.' *Monthly Notices of the Royal Astronomical Society* 236 (1): 57–87.
- . 1989b. 'Fast H $\alpha$  variations on a rapidly rotating, cool main-sequence star—II. cloud formation and ejection.' *Monthly Notices of the Royal Astronomical Society* 238 (2): 657–674.
- Courant, R, K Friedrichs, and H Lewy. 1928. 'Über die partiellen differenzgleichungen der mathematischen Physik.' *Mathematische annalen* 100 (1): 32–74.
- Covey, KR, MA Agüeros, NM Law, et al. 2016. 'Why are rapidly rotating M dwarfs in the Pleiades so (infra) red? new period measurements confirm rotation-dependent color offsets from the cluster sequence.' *The Astrophysical Journal* 822 (2): 81.
- Cranmer, SR. 2008. 'Winds of main-sequence stars: observational limits and a path to theoretical prediction.' In *14th Cambridge Workshop on Cool Stars, Stellar Systems, and the Sun*, 384:317.

- Cranmer, SR, SE Gibson, and P Riley. 2017. 'Origins of the Ambient Solar Wind: implications for Space Weather.' *Space Science Reviews*: 1–40.
- Cranmer, SR, and SH Saar. 2011. 'Testing a predictive theoretical model for the mass loss rates of cool stars.' *The Astrophysical Journal* 741 (1): 54.
- Cranmer, SR, and AA Van Ballegoijen. 2005. 'On the generation, propagation, and reflection of Alfvén waves from the solar photosphere to the distant heliosphere.' *The Astrophysical Journal Supplement Series* 156 (2): 265.
- Cranmer, SR, AA Van Ballegoijen, and RJ Edgar. 2007. 'Self-consistent coronal heating and solar wind acceleration from anisotropic magnetohydrodynamic turbulence.' *The Astrophysical Journal Supplement Series* 171 (2): 520.
- Croll, B, GAH Walker, R Kuschnig, et al. 2006. 'Differential rotation of  $\epsilon$  Eridani detected by MOST.' *The Astrophysical Journal* 648 (1): 607.
- Crooker, NU, SW Kahler, DE Larson, and RP Lin. 2004. 'Large-scale magnetic field inversions at sector boundaries.' *Journal of Geophysical Research: Space Physics* 109 (A3).
- Crosley, MK, and RA Osten. 2018. 'Constraining stellar coronal mass ejections through multi-wavelength analysis of the active M Dwarf EQ Peg.' *The Astrophysical Journal* 856 (1): 39.
- Curtis, JL, MA Agüeros, ST Douglas, and S Meibom. 2019. 'A temporary epoch of stalled spin-down for low-mass stars: insights from NGC 6811 with Gaia and Kepler.' *The Astrophysical Journal* 879 (1): 49.
- D'Amicis, R, and R Bruno. 2015. 'On the origin of highly Alfvénic slow solar wind.' *The Astrophysical Journal* 805 (1): 84.
- Davenport, JRA. 2016. 'The Kepler catalog of stellar flares.' *The Astrophysical Journal* 829 (1): 23.
- . 2017. 'Rotating stars from Kepler observed with Gaia DR1.' *The Astrophysical Journal* 835 (1): 16.
- Davenport, JRA, and KR Covey. 2018. 'Rotating stars from Kepler observed with Gaia DR2.' *The Astrophysical Journal* 868 (2): 151.

- De Laval, G, and EEF Fagerstroem. 1911. *Turbine*. US Patent 986,472, March.
- De Pater, I. 1990. 'Radio images of the planets.' *Annual review of astronomy and astrophysics* 28 (1): 347–399.
- Dedner, A, F Kemm, D Kröner, et al. 2002. 'Hyperbolic divergence cleaning for the MHD equations.' *Journal of Computational Physics* 175 (2): 645–673.
- DeForest, CE, TA Howard, and DJ McComas. 2014. 'Inbound waves in the solar corona: a direct indicator of Alfvén surface location.' *The Astrophysical Journal* 787 (2): 124.
- Delamere, PA. 2015. 'Solar wind interaction with giant magnetospheres and Earth's magnetosphere.' In *Magnetotails in the Solar System*, 207:217–233. John Wiley & Sons Hoboken, NJ.
- Delorme, P, A Collier Cameron, L Hebb, et al. 2011. 'Stellar rotation in the Hyades and Praesepe: gyrochronology and braking time-scale.' *Monthly Notices of the Royal Astronomical Society* 413 (3): 2218–2234.
- DeRosa, ML, AS Brun, and JT Hoeksema. 2012. 'Solar magnetic field reversals and the role of dynamo families.' *The Astrophysical Journal* 757 (1): 96.
- Donahue, RA, SH Saar, and SL Baliunas. 1996. 'A relationship between mean rotation period in lower main-sequence stars and its observed range.' *The Astrophysical Journal* 466:384.
- Donati, JF, and SF Brown. 1997. 'Zeeman-Doppler imaging of active stars. V. sensitivity of maximum entropy magnetic maps to field orientation.' *Astronomy and Astrophysics* 326:1135–1142.
- Donati, JF, T Forveille, A Collier Cameron, et al. 2006. 'The large-scale axisymmetric magnetic topology of a very-low-mass fully convective star.' *Science* 311 (5761): 633–635.
- Donati, JF, and JD Landstreet. 2009. 'Magnetic fields of nondegenerate stars.' *Annual Review of Astronomy and Astrophysics* 47:333–370.
- Donati, JF, C Moutou, R Fares, et al. 2008. 'Magnetic cycles of the planet-hosting star  $\tau$  Bootis.' *Monthly Notices of the Royal Astronomical Society* 385 (3): 1179–1185.

- Donati, JF, M Semel, BD Carter, DE Rees, and A Collier Cameron. 1997. 'Spectropolarimetric observations of active stars.' *Monthly Notices of the Royal Astronomical Society* 291 (4): 658–682.
- Donati, JF, M Semel, and F Praderie. 1989. 'Zeeman-Doppler imaging of active stars. II - numerical simulation and first observational results.' *Astronomy and Astrophysics* 225:467–478.
- Dotter, A, and B Paxton. 2009. 'Evolutionary implications of the new triple- $\alpha$  nuclear reaction rate for low-mass stars.' *Astronomy & Astrophysics* 507 (3): 1617–1619.
- Douglas, ST, MA Agüeros, KR Covey, and A K. 2017. 'Poking the beehive from space: K2 rotation periods for Praesepe.' *The Astrophysical Journal* 842 (2): 83.
- Ud-Doula, A, SP Owocki, and RHD Townsend. 2009. 'Dynamical simulations of magnetically channelled line-driven stellar winds—III. angular momentum loss and rotational spin-down.' *Monthly Notices of the Royal Astronomical Society* 392 (3): 1022–1033.
- Dungey, JW. 1965. 'The length of the magnetospheric tail.' *Journal of Geophysical Research* 70 (7): 1753–1753.
- Dunstone, NJ, GAJ Hussain, A Collier Cameron, et al. 2008. 'The first magnetic maps of a pre-main-sequence binary star system—HD 155555.' *Monthly Notices of the Royal Astronomical Society* 387 (2): 481–496.
- Durney, BR. 1985. 'On theories of rotating convection zones.' *The Astrophysical Journal* 297:787–798.
- Eberhard, G, and K Schwarzschild. 1913. 'On the reversal of the calcium lines H and K in stellar spectra.' *The Astrophysical Journal* 38.
- Ebert, RW, DJ McComas, HA Elliott, RJ Forsyth, and JT Gosling. 2009. 'Bulk properties of the slow and fast solar wind and interplanetary coronal mass ejections measured by Ulysses: three polar orbits of observations.' *Journal of Geophysical Research: Space Physics* 114 (A1).

- Echer, E, WD Gonzalez, ALC Gonzalez, et al. 2004. 'Long-term correlation between solar and geomagnetic activity.' *Journal of Atmospheric and Solar-Terrestrial Physics* 66 (12): 1019–1025.
- Eddy, JA. 1976. 'The maunder minimum.' *Science* 192 (4245): 1189–1202.
- Edwards, SJ, AR Yeates, FX Bocquet, and DH Mackay. 2015. 'Influence of non-potential coronal magnetic topology on solar-wind models.' *Solar Physics* 290 (10): 2791–2808.
- Egeland, R. 2018. 'sunstardb: a database for the study of stellar magnetism and the solar-stellar connection.' *The Astrophysical Journal Supplement Series* 236 (1): 19.
- Egeland, R, W Soon, S Baliunas, et al. 2017. 'The Mount Wilson Observatory s-index of the Sun.' *The Astrophysical Journal* 835 (1): 25.
- Einfeldt, B. 1988. 'On Godunov-type methods for gas dynamics.' *SIAM Journal on Numerical Analysis* 25 (2): 294–318.
- Fan, Y. 2008. 'The three-dimensional evolution of buoyant magnetic flux tubes in a model solar convective envelope.' *The Astrophysical Journal* 676 (1): 680.
- Fares, R, JF Donati, C Moutou, et al. 2009. 'Magnetic cycles of the planet-hosting star  $\tau$  Bootis–II. a second magnetic polarity reversal.' *Monthly Notices of the Royal Astronomical Society* 398 (3): 1383–1391.
- Fares, R, JF Donati, C Moutou, et al. 2010. 'Searching for star–planet interactions within the magnetosphere of HD 189733.' *Monthly Notices of the Royal Astronomical Society* 406 (1): 409–419.
- Feldman, U, E Landi, and NA Schwadron. 2005. 'On the sources of fast and slow solar wind.' *Journal of Geophysical Research: Space Physics* 110 (A7).
- Feynman, J, and NU Crooker. 1978. 'The solar wind at the turn of the century.' *Nature* 275 (5681): 626–627.
- Filippone, BW. 1986. 'Nuclear reactions in stars.' *Annual Review of Nuclear and Particle Science* 36 (1): 717–743.

- Finley, AJ, S Deshmukh, SP Matt, M Owens, and CJ Wu. 2019a. 'Solar angular momentum loss over the past several millennia.' *The Astrophysical Journal* 883 (1): 67.
- Finley, AJ, and SP. Matt. 2017. 'The effect of combined magnetic geometries on thermally driven winds. I. interaction of dipolar and quadrupolar fields.' *The Astrophysical Journal* 845 (1): 46.
- Finley, AJ, and SP Matt. 2018. 'The effect of combined magnetic geometries on thermally driven winds. II. dipolar, quadrupolar, and octupolar topologies.' *The Astrophysical Journal* 854 (2): 78.
- Finley, AJ, SP Matt, and V See. 2018. 'The effect of magnetic variability on stellar angular momentum loss. I. the solar wind torque during sunspot cycles 23 and 24.' *The Astrophysical Journal* 864 (2): 125.
- Finley, AJ, V See, and SP Matt. 2019b. 'The effect of magnetic variability on stellar angular momentum loss. II. the Sun, 61 Cygni A,  $\epsilon$  Eridani,  $\xi$  Bootis A, and  $\tau$  Bootis A.' *The Astrophysical Journal* 876 (1): 44.
- Fisher, GH, Y Fan, Dana W Longcope, MG Linton, and AA Pevtsov. 2000. 'The solar dynamo and emerging flux (invited review).' In *Helioseismic Diagnostics of Solar Convection and Activity*, 119–139. Springer.
- Fisher, GH, DW Longcope, TR Metcalf, and AA Pevtsov. 1998. 'Coronal heating in active regions as a function of global magnetic variables.' *The Astrophysical Journal* 508 (2): 885.
- Fisk, LA, NA Schwadron, and TH Zurbuchen. 1998. 'On the slow solar wind.' *Space Science Reviews* 86 (1): 51–60.
- Folsom, CP, J Bouvier, P Petit, et al. 2017. 'The evolution of surface magnetic fields in young solar-type stars II: the early main sequence (250–650 Myr).' *Monthly Notices of the Royal Astronomical Society* 474 (4): 4956–4987.
- Folsom, CP, P Petit, J Bouvier, et al. 2016. 'The evolution of surface magnetic fields in young solar-type stars—I. the first 250 Myr.' *Monthly Notices of the Royal Astronomical Society* 457 (1): 580–607.

- Fossat, E, P Boumier, T Corbard, et al. 2017. 'Asymptotic g modes: evidence for a rapid rotation of the solar core.' *Astronomy & Astrophysics* 604:A40.
- Foukal, P, and J Lean. 1986. 'The influence of faculae on total solar irradiance and luminosity.' *The Astrophysical Journal* 302:826–835.
- Fox, NJ, MC Velli, SD Bale, et al. 2016. 'The Solar Probe Plus mission: humanity's first visit to our star.' *Space Science Reviews* 204 (1-4): 7–48.
- Fränz, M, and D Harper. 2002. 'Heliospheric coordinate systems.' *Planetary and Space Science* 50 (2): 217–233.
- Fuhrmann, K. 2004. 'Nearby stars of the Galactic disk and halo. III.' *Astronomische Nachrichten* 325 (1): 3–80.
- Galilei, G. 1957. 'Discoveries and opinions of Galileo: including The starry messenger (1610), Letter to the Grand Duchess Christina (1615), and excerpts from Letters on sunspots (1613), The assayer (1623).' 94.
- Gallet, F, and J Bouvier. 2013. 'Improved angular momentum evolution model for solar-like stars.' *Astronomy & Astrophysics* 556:A36.
- . 2015. 'Improved angular momentum evolution model for solar-like stars-II. exploring the mass dependence.' *Astronomy & Astrophysics* 577:A98.
- Gallet, F, C Zanni, and L Amard. 2019. 'Rotational evolution of solar-type protostars during the star-disk interaction phase.' *Astronomy & Astrophysics* 632:A6.
- García, RA, S Turck-Chièze, SJ Jiménez-Reyes, et al. 2007. 'Tracking solar gravity modes: the dynamics of the solar core.' *Science* 316 (5831): 1591–1593.
- Garraffo, C, O Cohen, JJ Drake, and C Downs. 2013. 'The effect of limited spatial resolution of stellar surface magnetic field maps on magnetohydrodynamic wind and coronal x-ray emission models.' *The Astrophysical Journal* 764 (1): 32.
- Garraffo, C, JJ Drake, and O Cohen. 2015. 'The dependence of stellar mass and angular momentum losses on latitude and the interaction of active region and dipolar magnetic fields.' *The Astrophysical Journal* 813 (1): 40.

- . 2016a. 'The missing magnetic morphology term in stellar rotation evolution.' *Astronomy & Astrophysics* 595:A110.
- . 2016b. 'The space weather of Proxima Centauri b.' *The Astrophysical Journal Letters* 833 (1): L4.
- Garraffo, C, JJ Drake, O Cohen, JD Alvarado-Gómez, and Sofia P Moschou. 2017. 'The threatening magnetic and plasma environment of the TRAPPIST-1 planets.' *The Astrophysical Journal Letters* 843 (2): L33.
- Garraffo, C, JJ Drake, A Dotter, et al. 2018. 'The revolution revolution: magnetic morphology driven spin-down.' *The Astrophysical Journal* 862 (1): 90.
- Gastine, T, J Morin, L Duarte, et al. 2013. 'What controls the magnetic geometry of M dwarfs?' *Astronomy & Astrophysics* 549:L5.
- Georgoulis, MK, A Nindos, and H Zhang. 2019. 'The source and engine of coronal mass ejections.' *Philosophical Transactions of the Royal Society A* 377 (2148): 20180094.
- Gilliland, RL. 1986. 'Relation of chromospheric activity to convection, rotation, and pre-main-sequence evolution.' *The Astrophysical Journal* 300:339–347.
- Goedbloed, Hans, Rony Keppens, and Stefaan Poedts. 2019. *Magnetohydrodynamics: Of Laboratory and Astrophysical Plasmas*. Cambridge University Press.
- Goldstein, ML, DA Roberts, and WH Matthaeus. 1995. 'Magnetohydrodynamic turbulence in the solar wind.' *Annual review of astronomy and astrophysics* 33 (1): 283–325.
- Gosain, S, AA Pevtsov, GV Rudenko, and SA Anfinogentov. 2013. 'First synoptic maps of photospheric vector magnetic field from SOLIS/VSM: non-radial magnetic fields and hemispheric pattern of helicity.' *The Astrophysical Journal* 772 (1): 52.
- Gosling, JT, and V Pizzo. 1999. 'Formation and evolution of corotating interaction regions and their three dimensional structure.' In *Corotating interaction regions*, 21–52. Springer.
- Grappin, R, J Leorat, and A Pouquet. 1983. 'Dependence of MHD turbulence spectra on the velocity field-magnetic field correlation.' *Astronomy and Astrophysics* 126:51–58.



- Gray, DF. 1984. 'Measurements of Zeeman broadening in F, G, and K dwarfs.' *The Astrophysical Journal* 277:640–647.
- Gray, DF, SL Baliunas, GW Lockwood, and BA Skiff. 1996. 'Magnetic, photometric, temperature, and granulation variations of  $\xi$  Bootis A 1984–1993.' *The Astrophysical Journal* 465:945.
- Gregory, SG, and JF Donati. 2011. 'Analytic and numerical models of the 3D multipolar magnetospheres of pre-main sequence stars.' *Astronomische Nachrichten* 332 (9-10): 1027–1044.
- Gregory, SG, JF Donati, and GAJ Hussain. 2016. 'The multipolar magnetic fields of accreting pre-main-sequence stars: B at the inner disk, B along the accretion flow, and B at the accretion shock.' *arXiv preprint arXiv:1609.00273*.
- Gregory, SG, JF Donati, J Morin, et al. 2012. 'Can we predict the global magnetic topology of a pre-main-sequence star from its position in the Hertzsprung–Russell diagram?' *The Astrophysical Journal* 755 (2): 97.
- Gregory, SG, M Jardine, CG Gray, and JF Donati. 2010. 'The magnetic fields of forming solar-like stars.' *Reports on Progress in Physics* 73 (12): 126901.
- Güdel, M. 2007. 'The Sun in time: activity and environment.' *Living Reviews in Solar Physics* 4 (1): 3.
- Guedel, M, EF Guinan, and SL Skinner. 1997. 'The X-ray Sun in time: a study of the long-term evolution of coronae of solar-type stars.' *The Astrophysical Journal* 483 (2): 947.
- Guenther, DB. 1989. 'Age of the sun.' *The Astrophysical Journal* 339:1156–1159.
- Guerrero, G, PK Smolarkiewicz, EM de Gouveia Dal Pino, AG Kosovichev, and NN Mansour. 2016. 'On the role of tachoclines in solar and stellar dynamos.' *The Astrophysical Journal* 819 (2): 104.
- Gunn, AG, CK Mitrou, and JG Doyle. 1998. 'On the rotation-activity correlation for active binary stars.' *Monthly Notices of the Royal Astronomical Society* 296:150–164.
- Hale, GE. 1908. 'On the probable existence of a magnetic field in sun-spots.' *The astrophysical journal* 28:315.

- Hale, GE, and SB Nicholson. 1925. 'The law of sun-spot polarity.' *The Astrophysical Journal* 62:270.
- Hall, JC, GW Lockwood, and BA Skiff. 2007. 'The activity and variability of the sun and sun-like stars. I. synoptic Ca II H and K observations.' *The Astronomical Journal* 133 (3): 862.
- Hansen, CJ, SD Kawaler, and V Trimble. 2012. 'Stellar interiors: physical principles, structure, and evolution.'
- Hartmann, L, PC Schmidtke, R Davis, et al. 1979. 'Chromospheres of the active dwarf binaries EQ Pegasi and XI Bootis.' *The Astrophysical Journal* 233:L69–L72.
- Hartmann, LMKB, and KB MacGregor. 1982. 'Protostellar mass and angular momentum loss.' *The Astrophysical Journal* 259:180–192.
- Hathaway, DH. 2015. 'The solar cycle.' *Living Reviews in Solar Physics* 12 (1): 4.
- Hathaway, DH, RM Wilson, and EJ Reichmann. 1994. 'The shape of the sunspot cycle.' *Solar Physics* 151 (1): 177–190.
- Hébrard, E, JF Donati, X Delfosse, et al. 2016. 'Modelling the RV jitter of early-M dwarfs using tomographic imaging.' *Monthly Notices of the Royal Astronomical Society* 461 (2): 1465–1497.
- Heikkilä, U, J Beer, JA Abreu, and F Steinhilber. 2013. 'On the atmospheric transport and deposition of the cosmogenic radionuclides ( $^{10}\text{Be}$ ): a review.' *Space Science Reviews* 176 (1-4): 321–332.
- Hempelmann, A. 2003. 'Wavelet analysis of stellar differential rotation-III. the Sun in white light.' *Astronomy & Astrophysics* 399 (2): 717–721.
- Hempelmann, A, JHMM Schmitt, and K Stepien. 1996. 'Coronal x-ray emission of cool stars in relation to chromospheric activity and magnetic cycles.' *Astronomy and Astrophysics* 305:284.
- Hick, P, and BV Jackson. 1994. 'Solar wind mass and momentum flux variations at 0.3 AU.' *Advances in Space Research* 14 (4): 135–138.

- Hickmann, KS, HC Godinez, CJ Henney, and CN Arge. 2015. 'Data assimilation in the ADAPT photospheric flux transport model.' *Solar Physics* 290 (4): 1105–1118.
- Hollweg, JV. 1986. 'Transition region, corona, and solar wind in coronal holes.' *Journal of Geophysical Research: Space Physics* 91 (A4): 4111–4125.
- Holst, Bart van der, and Rony Keppens. 2007. 'Hybrid block-AMR in cartesian and curvilinear coordinates: MHD applications.' *Journal of computational physics* 226 (1): 925–946.
- Holzer, TE. 1972. 'Interaction of the solar wind with the neutral component of the interstellar gas.' *Journal of Geophysical Research* 77 (28): 5407–5431.
- Holzwarth, V. 2005. 'Impact of non-uniform surface magnetic fields on stellar winds.' *Astronomy & Astrophysics* 440 (2): 411–423.
- Hoshino, M, and A Nishida. 1983. 'Numerical simulation of the dayside reconnection.' *Journal of Geophysical Research: Space Physics* 88 (A9): 6926–6936.
- Hoyt, DV, and KM Schatten. 1998. 'Group sunspot numbers: a new solar activity reconstruction.' *Solar physics* 179 (1): 189–219.
- Hudson, HS. 1991. 'Solar flares, microflares, nanoflares, and coronal heating.' *Solar Physics* 133 (2): 357–369.
- Hunter, JD. 2007. 'Matplotlib: a 2D graphics environment.' *Computing In Science & Engineering* 9 (3): 90–95.
- Hussain, GAJ, and E Alecian. 2013. 'The role of magnetic fields in pre-main sequence stars.' *Proceedings of the International Astronomical Union* 9 (S302): 25–37.
- Hussain, GAJ, AA Van Ballegooijen, M Jardine, and A Collier Cameron. 2002. 'The coronal topology of the rapidly rotating K0 dwarf AB doradus. I. using surface magnetic field maps to model the structure of the stellar corona.' *The Astrophysical Journal* 575 (2): 1078.
- Irwin, J, and J Bouvier. 2009. 'The ages of stars.' In *IAU Symp*, vol. 258.

- Janson, M, S Reffert, W Brandner, et al. 2008. 'A comprehensive examination of the  $\epsilon$  Eridani system - verification of a 4 micron narrow-band high-contrast imaging approach for planet searches.' *Astronomy & Astrophysics* 488 (2): 771–780.
- Jardine, M, JR Barnes, JF Donati, and A Collier Cameron. 1999. 'The potential magnetic field of AB Doradus: comparison with Zeeman-Doppler images.' *Monthly Notices of the Royal Astronomical Society* 305 (1): L35–L39.
- Jardine, M, and A Collier Cameron. 2019. 'Slingshot prominences: nature's wind gauges.' *Monthly Notices of the Royal Astronomical Society* 482 (3): 2853–2860.
- Jardine, M, A Collier Cameron, and JF Donati. 2002. 'The global magnetic topology of AB Doradus.' *Monthly Notices of the Royal Astronomical Society* 333 (2): 339–346.
- Jardine, M, A Collier Cameron, JF Donati, and GR Pointer. 2001. 'Prominence support in potential field configurations around rotating stars.' *Monthly Notices of the Royal Astronomical Society* 324 (1): 201–205.
- Jardine, M, AA Vidotto, and V See. 2017. 'Estimating stellar wind parameters from low-resolution magnetograms.' *Monthly Notices of the Royal Astronomical Society: Letters* 465 (1): L25–L29.
- Jardine, M, AA Vidotto, A Van Ballegooijen, et al. 2013. 'Influence of surface stressing on stellar coronae and winds.' *Monthly Notices of the Royal Astronomical Society* 431 (1): 528–538.
- Jeffers, SV, M Mengel, C Moutou, et al. 2018. 'The relation between stellar magnetic field geometry and chromospheric activity cycles—II the rapid 120-day magnetic cycle of  $\tau$  Bootis.' *Monthly Notices of the Royal Astronomical Society* 479 (4): 5266–5271.
- Jeffers, SV, P Petit, SC Marsden, et al. 2014. ' $\epsilon$  Eridani: an active K dwarf and a planet hosting star? - the variability of its large-scale magnetic field topology.' *Astronomy & Astrophysics* 569:A79.

- Jeffers, SV, SB Saikia, JR Barnes, et al. 2017. 'The relation between stellar magnetic field geometry and chromospheric activity cycles—I. the highly variable field of  $\epsilon$  Eridani at activity minimum.' *Monthly Notices of the Royal Astronomical Society: Letters* 471 (1): L96–L100.
- Johns-Krull, CM, and JA Valenti. 1996. 'Detection of strong magnetic fields on M dwarfs.' *The Astrophysical Journal Letters* 459 (2): L95.
- . 2000. 'Measurements of stellar magnetic fields.' In *Stellar clusters and associations: convection, rotation, and dynamos*, 198:371.
- Johnstone, Colin, M Jardine, and DH Mackay. 2010. 'Modelling stellar coronae from surface magnetograms: the role of missing magnetic flux.' *Monthly Notices of the Royal Astronomical Society* 404 (1): 101–109.
- Johnstone, CP, M Güdel, T Lüftinger, G Toth, and I Brott. 2015. 'Stellar winds on the main-sequence—I. wind model.' *Astronomy & Astrophysics* 577:A27.
- Jones, GH, A Balogh, and RJ Forsyth. 1998. 'Radial heliospheric magnetic fields detected by Ulysses.' *Geophysical research letters* 25 (16): 3109–3112.
- Karoff, C, TS Metcalfe, WJ Chaplin, et al. 2013. 'Sounding stellar cycles with Kepler—II. ground-based observations.' *Monthly Notices of the Royal Astronomical Society* 433 (4): 3227–3238.
- Kasper, JC, SD Bale, JW Belcher, et al. 2019. 'Alfvénic velocity spikes and rotational flows in the near-Sun solar wind.' *Nature* 576 (7786): 228–231.
- Kasper, JC, AJ Lazarus, JT Steinberg, KW Ogilvie, and A Szabo. 2006. 'Physics-based tests to identify the accuracy of solar wind ion measurements: a case study with the Wind Faraday Cups.' *Journal of Geophysical Research: Space Physics* 111 (A3).
- Kasper, JC, ML Stevens, AJ Lazarus, JT Steinberg, and KW Ogilvie. 2007. 'Solar wind helium abundance as a function of speed and heliographic latitude: variation through a solar cycle.' *The Astrophysical Journal* 660 (1): 901.

- Kavanagh, RD, AA Vidotto, D Ó. Fionnagáin, et al. 2019. 'MOVES-II. tuning in to the radio environment of HD189733b.' *Monthly Notices of the Royal Astronomical Society* 485 (4): 4529–4538.
- Kawaler, SD. 1988. 'Angular momentum loss in low-mass stars.' *The Astrophysical Journal* 333:236–247.
- Kay, C, and M Opher. 2014. 'Implications of CME deflections on the habitability of Pplanets around M Dwarfs.' In *American Astronomical Society Meeting Abstracts# 224*, vol. 224.
- Kay, C, M Opher, and RM Evans. 2013. 'Forecasting a coronal mass ejection's altered trajectory: ForeCAT.' *The Astrophysical Journal* 775 (1): 5.
- Keppens, R, and JP Goedbloed. 1999. 'Numerical simulations of stellar winds: polytropic models.' *Astron. Astrophys* 343:251–260.
- . 2000. 'Stellar winds, dead zones, and coronal mass ejections.' *The Astrophysical Journal* 530 (2): 1036.
- Keppens, R, KB MacGregor, and P Charbonneau. 1995. 'On the evolution of rotational velocity distributions for solar-type stars.' *Astronomy and Astrophysics* 294:469–487.
- Kervella, P, A Mérand, B Pichon, et al. 2008. 'The radii of the nearby K5V and K7V stars 61 Cygni A & B-CHARA/FLUOR interferometry and CESAM2k modeling.' *Astronomy & Astrophysics* 488 (2): 667–674.
- Khodachenko, ML, I Ribas, H Lammer, et al. 2007. 'Coronal mass ejection (CME) activity of low mass M stars as an important factor for the habitability of terrestrial exoplanets. I. CME impact on expected magnetospheres of Earth-like exoplanets in close-in habitable zones.' *Astrobiology* 7 (1): 167–184.
- King, JH, and NE Papitashvili. 2005. 'Solar wind spatial scales in and comparisons of hourly Wind and ACE plasma and magnetic field data.' *Journal of Geophysical Research: Space Physics* 110 (A2).
- Klimchuk, JA. 2006. 'On solving the coronal heating problem.' *Solar Physics* 234 (1): 41–77.
- Kochukhov, O, P Petit, KG Strassmeier, et al. 2017. 'Surface magnetism of cool stars.' *Astronomische Nachrichten* 338 (4): 428–441.

- Kopp, RA, and TE Holzer. 1976. 'Dynamics of coronal hole regions.' *Solar Physics* 49 (1): 43–56.
- Krivova, NA, L Balmaceda, and SK Solanki. 2007. 'Reconstruction of solar total irradiance since 1700 from the surface magnetic flux.' *Astronomy & Astrophysics* 467 (1): 335–346.
- Lal, D, and B Peters. 1967. 'Cosmic ray produced radioactivity on the Earth.' In *Kosmische Strahlung II/Cosmic Rays II*, 551–612. Springer.
- Lamers, HJGLM, and JP Cassinelli. 1999. 'Introduction to stellar winds.'
- Lamy, P, O Floyd, Z Mikić, and P Riley. 2019. 'Validation of MHD model predictions of the corona with LASCO-C2 polarized brightness images.' *Solar Physics* 294 (11): 162.
- Landin, NR, LTS Mendes, and LPR Vaz. 2010. 'Theoretical values of convective turnover times and Rossby numbers for solar-like, pre-main sequence stars.' *Astronomy & Astrophysics* 510:A46.
- Lanzafame, AC, and F Spada. 2015. 'Rotational evolution of slow-rotator sequence stars.' *Astronomy & Astrophysics* 584:A30.
- Larson, RB. 2003. 'The physics of star formation.' *Reports on Progress in Physics* 66 (10): 1651.
- Lazarus, AJ, and BE Goldstein. 1971. 'Observation of the angular-momentum flux carried by the solar wind.' *The Astrophysical Journal* 168:571.
- Lean, JL, J Cook, W Marquette, and A Johannesson. 1998. 'Magnetic sources of the solar irradiance cycle.' *The Astrophysical Journal* 492 (1): 390.
- Lee, CO, JG Luhmann, JT Hoeksema, et al. 2011. 'Coronal field opens at lower height during the solar cycles 22 and 23 minimum periods: IMF comparison suggests the source surface should be lowered.' *Solar Physics* 269 (2): 367–388.
- Lehmann, LT, GAJ Hussain, MM Jardine, DH Mackay, and AA Vidotto. 2019. 'Observing the simulations: applying ZDI to 3D non-potential magnetic field simulations.' *Monthly Notices of the Royal Astronomical Society* 483 (4): 5246–5266.

- Lehmann, LT, MM Jardine, DH Mackay, and AA Vidotto. 2018. 'Connecting the large- and the small-scale magnetic fields of solar-like stars.' *Monthly Notices of the Royal Astronomical Society* 478 (4): 4390–4409.
- Leighton, RB. 1964. 'Transport of magnetic fields on the Sun.' *The Astrophysical Journal* 140:1547.
- Lepping, RP, MH Acna, LF Burlaga, et al. 1995. 'The WIND magnetic field investigation.' *Space Science Reviews* 71 (1-4): 207–229.
- Li, Jianke. 1999. 'Magnetic braking of the present Sun.' *Monthly Notices of the Royal Astronomical Society* 302 (1): 203–208.
- Linker, JA, RM Caplan, C Downs, et al. 2017. 'The open flux problem.' *The Astrophysical Journal* 848 (1): 70.
- Liu, Y, JT Hoeksema, PH Scherrer, et al. 2012. 'Comparison of line-of-sight magnetograms taken by the solar dynamics observatory/heliioseismic and magnetic imager and solar and heliospheric observatory/Michelson Doppler imager.' *Solar Physics* 279 (1): 295–316.
- Lockwood, GW, BA Skiff, GW Henry, et al. 2007. 'Patterns of photometric and chromospheric variation among sun-like stars: a 20 year perspective.' *The Astrophysical Journal Supplement Series* 171 (1): 260.
- Lockwood, M. 2013. 'Reconstruction and prediction of variations in the open solar magnetic flux and interplanetary conditions.' *Living Reviews in Solar Physics* 10 (1): 4.
- Lockwood, M, RB Forsyth, A Balogh, and DJ McComas. 2004. 'Open solar flux estimates from near-Earth measurements of the interplanetary magnetic field: comparison of the first two perihelion passes of the Ulysses spacecraft.' In *Annales Geophysicae*, 22:1395–1405. Copernicus GmbH.
- Lockwood, M, H Nevanlinna, L Barnard, et al. 2014a. 'Reconstruction of geomagnetic activity and near-Earth interplanetary conditions over the past 167 yr-Part 4: near-Earth solar wind speed, IMF, and open solar flux.' In *Annales Geophysicae*, 32:383–399. 4. Copernicus Publications for the European Geosciences Union.



- Lockwood, M, MJ Owens, and L Barnard. 2014b. 'Centennial variations in sunspot number, open solar flux, and streamer belt width: 1. correction of the sunspot number record since 1874.' *Journal of Geophysical Research: Space Physics* 119 (7): 5172–5182.
- Lockwood, M, AP Rouillard, and ID Finch. 2009. 'The rise and fall of open solar flux during the current grand solar maximum.' *The Astrophysical Journal* 700 (2): 937.
- Lockwood, M, R Stamper, and MN Wild. 1999. 'A doubling of the Sun's coronal magnetic field during the past 100 years.' *Nature* 399 (6735): 437–439.
- Lomax, H, TH Pulliam, DW Zingg, and TA Kowalewski. 2002. 'Fundamentals of computational fluid dynamics.' *Appl. Mech. Rev.* 55 (4): B61–B61.
- Lovelace, RVE, C Mehanian, CM Mobarry, and ME Sulkanen. 1986. 'Theory of axisymmetric magnetohydrodynamic flows-disks.' *The Astrophysical Journal Supplement Series* 62:1–37.
- Lowder, C, J Qiu, and R Leamon. 2017. 'Coronal holes and open magnetic flux over cycles 23 and 24.' *Solar Physics* 292 (1): 18.
- Lowder, C, J Qiu, R Leamon, and Y Liu. 2014. 'Measurements of EUV coronal holes and open magnetic flux.' *The Astrophysical Journal* 783 (2): 142.
- Mamajek, EE, and LA Hillenbrand. 2008. 'Improved age estimation for solar-type dwarfs using activity-rotation diagnostics.' *The Astrophysical Journal* 687 (2): 1264.
- Marcy, GW. 1984. 'Observations of magnetic fields on solar-type stars.' *The Astrophysical Journal* 276:286–304.
- Marsch, E, and AK Richter. 1984a. 'Distribution of solar wind angular momentum between particles and magnetic field: inferences about the Alfvén critical point from Helios observations.' *Journal of Geophysical Research: Space Physics* 89 (A7): 5386–5394.
- . 1984b. 'Helios observational constraints on solar wind expansion.' *Journal of Geophysical Research: Space Physics* 89 (A8): 6599–6612.
- Marsden, SC, P Petit, SV Jeffers, et al. 2014. 'A Bcool magnetic snapshot survey of solar-type stars.' *Monthly Notices of the Royal Astronomical Society* 444 (4): 3517–3536.

- Martin-Torres, FJ, MP Zorzano, P Valenti n-Serrano, et al. 2015. 'Transient liquid water and water activity at Gale crater on Mars.' *Nature Geoscience* 8 (5): 357.
- Matt, SP, SA Brun, I Baraffe, J Bouvier, and G Chabrier. 2015. 'The mass-dependence of angular momentum evolution in sun-like stars.' *The Astrophysical Journal Letters* 799 (2): L23.
- Matt, SP, O Do Cao, BP Brown, and SA Brun. 2011. 'Convection and differential rotation properties of G and K stars computed with the ASH code.' *Astronomische Nachrichten* 332 (9-10): 897–906.
- Matt, SP, KB MacGregor, MH Pinsonneault, and TP Greene. 2012. 'Magnetic braking formulation for sun-like stars: dependence on dipole field strength and rotation rate.' *The Astrophysical Journal Letters* 754 (2): L26.
- Matt, SP, and RE Pudritz. 2004. 'Does disk locking solve the stellar angular momentum problem?' *The Astrophysical Journal Letters* 607 (1): L43.
- . 2008. 'Accretion-powered stellar winds. II. numerical solutions for stellar wind torques.' *The Astrophysical Journal* 678 (2): 1109.
- Mayaud, PN. 1972. 'The aa indices: a 100-year series characterizing the magnetic activity.' *Journal of Geophysical Research* 77 (34): 6870–6874.
- McComas, D, BL Barraclough, HO Funsten, et al. 2000. 'Solar wind observations over Ulysses' first full polar orbit.' *Journal of Geophysical Research: Space Physics* 105 (A5): 10419–10433.
- McComas, DJ, N Angold, HA Elliott, et al. 2013. 'Weakest solar wind of the space age and the current "mini" solar maximum.' *The Astrophysical Journal* 779 (1): 2.
- McComas, DJ, HA Elliott, NA Schwadron, et al. 2003. 'The three-dimensional solar wind around solar maximum.' *Geophysical research letters* 30 (10).
- McFadden, LA, T Johnson, and P Weissman. 2006. 'Encyclopedia of the solar system.'
- McFadden, PL, RT Merrill, MW McElhinny, and S Lee. 1991. 'Reversals of the Earth's magnetic field and temporal variations of the dynamo families.' *Journal of Geophysical Research: Solid Earth* 96 (B3): 3923–3933.

- McQuillan, A, S Aigrain, and T Mazeh. 2013. 'Measuring the rotation period distribution of field M dwarfs with Kepler.' *Monthly Notices of the Royal Astronomical Society* 432 (2): 1203–1216.
- Meibom, S, SA Barnes, DW Latham, et al. 2011a. 'The Kepler cluster study: stellar rotation in NGC 6811.' *The Astrophysical Journal Letters* 733 (1): L9.
- Meibom, S, SA Barnes, I Platais, et al. 2015. 'A spin-down clock for cool stars from observations of a 2.5-billion-year-old cluster.' *Nature* 517 (7536): 589.
- Meibom, S, RD Mathieu, and KG Stassun. 2009. 'Stellar rotation in M35: mass-period relations, spin-down rates, and gyrochronology.' *The Astrophysical Journal* 695 (1): 679.
- Meibom, S, RD Mathieu, KG Stassun, P Liebesny, and SH Saar. 2011b. 'The color-period diagram and stellar rotational evolution—new rotation period measurements in the open cluster M34.' *The Astrophysical Journal* 733 (2): 115.
- Mengel, MW, R Fares, SC Marsden, et al. 2016. 'The evolving magnetic topology of  $\tau$  Boötis.' *Monthly Notices of the Royal Astronomical Society* 459 (4): 4325–4342.
- Messina, S, and EF Guinan. 2003. 'Magnetic activity of six young solar analogues II. surface differential rotation from long-term photometry.' *Astronomy & Astrophysics* 409 (3): 1017–1030.
- Mestel, L. 1968. 'Magnetic braking by a stellar wind—I.' *Monthly Notices of the Royal Astronomical Society* 138 (3): 359–391.
- . 1984. 'Angular momentum loss during pre-main sequence contraction.' In *Cool Stars, Stellar Systems, and the Sun*, 49–59. Springer.
- Mestel, L, and HC Spruit. 1987. 'On magnetic braking of late-type stars.' *Monthly Notices of the Royal Astronomical Society* 226 (1): 57–66.
- Metcalfe, TS, AP Buccino, BP Brown, et al. 2013. 'Magnetic activity cycles in the exoplanet host star  $\epsilon$  Eridani.' *The Astrophysical Journal Letters* 763 (2): L26.
- Metcalfe, TS, and R Egeland. 2019. 'Understanding the Limitations of Gyrochronology for Old Field Stars.' *The Astrophysical Journal* 871 (1): 39.

- Metcalfe, TS, R Egeland, and J van-Saders. 2016. 'Stellar evidence that the solar dynamo may be in transition.' *The Astrophysical Journal Letters* 826 (1): L2.
- Michels, DJ, R Schwenn, RA Howard, et al. 1988. 'LASCO: A wide-field white light and spectrometric coronagraph for SOHO.' *The SOHO Mission. Scientific and Technical Aspects of the Instruments*.
- Mignone, A. 2009. 'The PLUTO code for astrophysical gasdynamics.' *Memorie della Societa Astronomica Italiana Supplementi* 13:67.
- Mignone, A, G Bodo, S Massaglia, et al. 2007. 'PLUTO: a numerical code for computational astrophysics.' *The Astrophysical Journal Supplement Series* 170 (1): 228.
- Mikić, Z, C Downs, JA Linker, et al. 2018. 'Predicting the corona for the 21 August 2017 total solar eclipse.' *Nature Astronomy* 2 (11): 913–921.
- Mishra, Wageesh, Nandita Srivastava, Yuming Wang, et al. 2019. 'Mass loss via solar wind and coronal mass ejections during solar cycles 23 and 24.' *Monthly Notices of the Royal Astronomical Society* 486 (4): 4671–4685.
- Mittag, M, J Robrade, JHMM Schmitt, et al. 2017. 'Four-month chromospheric and coronal activity cycle in  $\tau$  Boötis.' *Astronomy & Astrophysics* 600:A119.
- Moffatt, HK. 1978. 'Field generation in electrically conducting fluids.' *Cambridge University Press, Cambridge, London, New York, Melbourne* 2:5–1.
- Morgenthaler, A, P Petit, J Morin, et al. 2011. 'Direct observation of magnetic cycles in Sun-like stars.' *Astronomische Nachrichten* 332 (9-10): 866–871.
- Morgenthaler, A, P Petit, S Saar, et al. 2012. 'Long-term magnetic field monitoring of the Sun-like star  $\xi$  Bootis A.' *Astronomy & Astrophysics* 540:A138.
- Morin, J, JF Donati, T Forveille, et al. 2008a. 'The stable magnetic field of the fully convective star V374 Peg.' *Monthly Notices of the Royal Astronomical Society* 384 (1): 77–86.
- Morin, J, JF Donati, P Petit, et al. 2008b. 'Large-scale magnetic topologies of mid M dwarfs.' *Monthly Notices of the Royal Astronomical Society* 390 (2): 567–581.

- Morin, J, JF Donati, P Petit, et al. 2010. 'Large-scale magnetic topologies of late M dwarfs.' *Monthly Notices of the Royal Astronomical Society* 407 (4): 2269–2286.
- Mueller, D, RG Marsden, OC St Cyr, HR Gilbert, et al. 2013. 'Solar orbiter.' *Solar Physics* 285 (1-2): 25–70.
- Mullan, DJ. 1978. 'Supersonic stellar winds and rapid mass loss in cool stars.' *The Astrophysical Journal* 226:151–166.
- Muñoz-Jaramillo, A, and JM Vaquero. 2018. 'Visualization of the challenges and limitations of the long-term sunspot number record.' *Nature Astronomy*: 1.
- Muscheler, R, F Joos, J Beer, et al. 2007. 'Solar activity during the last 1000 yr inferred from radionuclide records.' *Quaternary Science Reviews* 26 (1-2): 82–97.
- Nascimento Jr, JD do, AA Vidotto, P Petit, et al. 2016. 'Magnetic field and wind of Kappa Ceti: toward the planetary habitability of the young sun when life arose on earth.' *The Astrophysical Journal Letters* 820 (1): L15.
- Ness, NF, and JM Wilcox. 1964. 'Solar origin of the interplanetary magnetic field.' *Physical Review Letters* 13 (15): 461.
- Neugebauer, M, PC Liewer, EJ Smith, RM Skoug, and TH Zurbuchen. 2002. 'Sources of the solar wind at solar activity maximum.' *Journal of Geophysical Research: Space Physics* 107 (A12): SSH–13.
- Nicholson, BA, AA Vidotto, M Mengel, et al. 2016. 'Temporal variability of the wind from the star  $\tau$  Boötis.' *Monthly Notices of the Royal Astronomical Society* 459 (2): 1907–1915.
- Noyes, RW, LW Hartmann, S Baliunas, DK Duncan, and AH Vaughan. 1984. 'Rotation, convection, and magnetic activity in lower main-sequence stars.' *The Astrophysical Journal* 279:763–777.
- Núñez, A, MA Agüeros, KR Covey, et al. 2015. 'Linking stellar coronal activity and rotation at 500 Myr: a deep Chandra observation of M37.' *The Astrophysical Journal* 809 (2): 161.
- Ó Fionnagáin, D, and AA Vidotto. 2018. 'The solar wind in time: a change in the behaviour of older winds?' *Monthly Notices of the Royal Astronomical Society* 476 (2): 2465–2475.

- Ó Fionnagáin, D, AA Vidotto, P Petit, et al. 2019. 'The solar wind in time–II. 3D stellar wind structure and radio emission.' *Monthly Notices of the Royal Astronomical Society* 483 (1): 873–886.
- Obridko, VN, DD Sokoloff, BD Shelting, AS Shibalova, and IM Livshits. 2020. 'Cyclic variations in the main components of the solar large-scale magnetic field.' *arXiv preprint arXiv:2001.05433*.
- Odstrcil, D, JA Linker, R Lionello, et al. 2002. '3-D MHD simulations of CMEs by coupled coronal and heliospheric models.' In *Solar Variability: From Core to Outer Frontiers*, 506:95–98.
- Ogilvie, KW, DJ Chornay, RJ Fritzenreiter, et al. 1995. 'SWE, a comprehensive plasma instrument for the Wind spacecraft.' *Space Science Reviews* 71 (1-4): 55–77.
- Oran, R, E Landi, B van-der-Holst, et al. 2015. 'A steady-state picture of solar wind acceleration and charge state composition derived from a global wave-driven MHD model.' *The Astrophysical Journal* 806 (1): 55.
- Oran, R, B van-der-Holst, E Landi, et al. 2013. 'A global wave-driven magnetohydrodynamic solar model with a unified treatment of open and closed magnetic field topologies.' *The Astrophysical Journal* 778 (2): 176.
- Ossendrijver, M. 2003. 'The solar dynamo.' *The Astronomy and Astrophysics Review* 11 (4): 287–367.
- Owens, M., and P. Cargill. 2004. 'Non-radial solar wind flows induced by the motion of interplanetary coronal mass ejections.' *Annales Geophysicae* 22 (12): 4397–4406.
- Owens, MJ, CN Arge, NU Crooker, NA Schwadron, and TS Horbury. 2008. 'Estimating total heliospheric magnetic flux from single-point in situ measurements.' *Journal of Geophysical Research: Space Physics* 113 (A12).
- Owens, MJ, NU Crooker, and M Lockwood. 2011. 'How is open solar magnetic flux lost over the solar cycle?' *Journal of Geophysical Research: Space Physics* 116 (A4).
- Owens, MJ, and RJ Forsyth. 2013. 'The heliospheric magnetic field.' *Living Reviews in Solar Physics* 10 (1): 5.

- Owens, MJ, and M Lockwood. 2012. 'Cyclic loss of open solar flux since 1868: the link to heliospheric current sheet tilt and implications for the maunder minimum.' *Journal of Geophysical Research: Space Physics* 117 (A4).
- Owens, MJ, M Lockwood, and P Riley. 2017a. 'Global solar wind variations over the last four centuries.' *Scientific reports* 7:41548.
- Owens, MJ, M Lockwood, P Riley, and J Linker. 2017b. 'Sunward strahl: a method to unambiguously determine open solar flux from in situ spacecraft measurements using suprathermal electron data.' *Journal of Geophysical Research: Space Physics* 122 (11).
- Pantolmos, G, and SP Matt. 2017. 'Magnetic braking of Sun-like and low-mass stars: dependence on coronal temperature.' *The Astrophysical Journal* 849 (2): 83.
- Parenti, S. 2014. 'Solar prominences: observations.' *Living Reviews in Solar Physics* 11 (1): 1.
- Parker, EN. 1955. 'Hydromagnetic dynamo models.' *The Astrophysical Journal* 122:293.
- . 1958. 'Dynamics of the interplanetary gas and magnetic fields.' *The Astrophysical Journal* 128:664.
- . 1965. 'Dynamical theory of the solar wind.' *Space Science Reviews* 4 (5-6): 666–708.
- Parnell, CE, and I De Moortel. 2012. 'A contemporary view of coronal heating.' *Philosophical Transactions of the Royal Society A: Mathematical, Physical and Engineering Sciences* 370 (1970): 3217–3240.
- Parsons, A, D Biesecker, D Odstroil, et al. 2011. 'Wang-Sheeley-Arge-Enlil cone model transitions to operations.' *Space Weather* 9 (3).
- Pauldrach, A, J Puls, and RP Kudritzki. 1986. 'Radiation-driven winds of hot luminous stars - improvements of the theory and first results.' *Astronomy and Astrophysics* 164:86–100.
- Perri, B, SA Brun, V Réville, and A Strugarek. 2018. 'Simulations of solar wind variations during an 11-year cycle and the influence of north–south asymmetry.' *Journal of Plasma Physics* 84 (5).

- Petit, P, B Dintrans, A Morgenthaler, et al. 2009. 'A polarity reversal in the large-scale magnetic field of the rapidly rotating sun HD 190771.' *Astronomy & Astrophysics* 508 (1): L9–L12.
- Petit, P, B Dintrans, SK Solanki, et al. 2008. 'Toroidal versus poloidal magnetic fields in Sun-like stars: a rotation threshold.' *Monthly Notices of the Royal Astronomical Society* 388 (1): 80–88.
- Phillips, JL, SJ Bame, A Barnes, et al. 1995. 'Ulysses solar wind plasma observations from pole to pole.' *Geophysical research letters* 22 (23): 3301–3304.
- Pinto, RF, AS Brun, and AP Rouillard. 2016. 'Flux-tube geometry and solar wind speed during an activity cycle.' *Astronomy & Astrophysics* 592:A65.
- Pinto, RF, SA Brun, L Jouve, and R Grappin. 2011. 'Coupling the solar dynamo and the corona: wind properties, mass, and momentum losses during an activity cycle.' *The Astrophysical Journal* 737 (2): 72.
- Pinto, RF, and AP Rouillard. 2017. 'A multiple flux-tube solar wind model.' *The Astrophysical Journal* 838 (2): 89.
- Pizzo, V, R Schwenn, E Marsch, et al. 1983. 'Determination of the solar wind angular momentum flux from the HELIOS data-an observational test of the Weber and Davis theory.' *The Astrophysical Journal* 271:335–354.
- Pizzolato, N, A Maggio, G Micela, S Sciortino, and P Ventura. 2003. 'The stellar activity-rotation relationship revisited: Dependence of saturated and non-saturated X-ray emission regimes on stellar mass for late-type dwarfs.' *Astronomy & Astrophysics* 397 (1): 147–157.
- Pneuman, GW, and RA Kopp. 1971. 'Gas-magnetic field interactions in the solar corona.' *Solar physics* 18 (2): 258–270.
- Pognan, Q, C Garraffo, O Cohen, and JJ Drake. 2018. 'The solar wind environment in time.' *The Astrophysical Journal* 856 (1): 53.
- Press, WH, and GB Rybicki. 1989. 'Fast algorithm for spectral analysis of unevenly sampled data.' *The Astrophysical Journal* 338:277–280.



- Priest, E. 2014. 'Magnetohydrodynamics of the Sun.'
- Pulkkinen, T. 2007. 'Space weather: terrestrial perspective.' *Living Reviews in Solar Physics* 4 (1): 1.
- Ramesh, KB. 2010. 'Coronal mass ejections and sunspots—solar cycle perspective.' *The Astrophysical Journal Letters* 712 (1): L77.
- Rebull, LM, JR Stauffer, J Bouvier, et al. 2016. 'Rotation in the Pleiades with K2. I. data and first results.' *The Astronomical Journal* 152 (5): 113.
- Regi, M. 2016. 'ULF power fluctuations in the solar-wind parameters and their relationship with the relativistic electron flux at the geosynchronous orbit.' *Il Nuovo Cimento* 39:285–295.
- Reimer, PJ, M GL Baillie, E Bard, et al. 2009. 'IntCal09 and Marine09 radiocarbon age calibration curves, 0–50,000 years cal BP.' *Radiocarbon* 51 (4): 1111–1150.
- Reimers, D. 1975. 'Circumstellar envelopes and mass loss of red giant stars.' In *Problems in stellar atmospheres and envelopes*, 229–256. Springer.
- . 1977. 'On the absolute scale of mass-loss in red giants. I - circumstellar absorption lines in the spectrum of the visual companion of Alpha-1 HER.' *Astronomy and Astrophysics* 61:217–224.
- Reiners, A. 2012. 'Observations of cool-star magnetic fields.' *Living Reviews in Solar Physics* 9 (1): 1.
- Reiners, A, and G Basri. 2007. 'The first direct measurements of surface magnetic fields on very low mass stars.' *The Astrophysical Journal* 656 (2): 1121.
- . 2009. 'On the magnetic topology of partially and fully convective stars.' *Astronomy & Astrophysics* 496 (3): 787–790.
- . 2010. 'A volume-limited sample of 63 M7-M9. 5 dwarfs. II. activity, magnetism, and the fade of the rotation-dominated dynamo.' *The Astrophysical Journal* 710 (2): 924.
- Reiners, A, G Basri, and M Browning. 2009. 'Evidence for magnetic flux saturation in rapidly rotating M stars.' *The Astrophysical Journal* 692 (1): 538.

- Reiners, A, and S Mohanty. 2012. 'Radius-dependent angular momentum evolution in low-mass stars. I.' *The Astrophysical Journal* 746 (1): 43.
- Reinhold, T, KJ Bell, J Kuszlewicz, S Hekker, and AI Shapiro. 2019. 'Transition from spot to faculae domination - an alternate explanation for the dearth of intermediate Kepler rotation periods.' *Astronomy & Astrophysics* 621:A21.
- Reinhold, T, Ansgar Reiners, and Gibor Basri. 2013. 'Rotation and differential rotation of active Kepler stars.' *Astronomy & Astrophysics* 560:A4.
- Réville, V. 2016. 'Vents et magnétisme des étoiles de type solaire: influence sur la rotation stellaire, la couronne et les (exo) planètes.'
- Réville, V, and SA Brun. 2017. 'Global solar magnetic field organization in the outer corona: influence on the solar wind speed and mass flux over the cycle.' *The Astrophysical Journal* 850 (1): 45.
- Réville, V, SA Brun, SP Matt, A Strugarek, and RF Pinto. 2015a. 'The effect of magnetic topology on thermally driven wind: toward a general formulation of the braking law.' *The Astrophysical Journal* 798 (2): 116.
- Réville, V, SA Brun, A Strugarek, et al. 2015b. 'From solar to stellar corona: the role of wind, rotation, and magnetism.' *The Astrophysical Journal* 814 (2): 99.
- Réville, V, CP Folsom, A Strugarek, and SA Brun. 2016. 'Age dependence of wind properties for solar-type stars: a 3D study.' *The Astrophysical Journal* 832 (2): 145.
- Réville, V, M Velli, O Panasenco, et al. 2020. 'The role of Alfvén wave dynamics on the large-scale properties of the solar wind: comparing an MHD simulation with Parker Solar Probe E1 data.' *The Astrophysical Journal Supplement Series* 246 (2): 24.
- Richardson, IG, and HV Cane. 2010. 'Near-Earth interplanetary coronal mass ejections during solar cycle 23 (1996–2009): catalog and summary of properties.' *Solar Physics* 264 (1): 189–237.
- Riley, P. 2007. 'An alternative interpretation of the relationship between the inferred open solar flux and the interplanetary magnetic field.' *The Astrophysical Journal Letters* 667 (1): L97.

- Riley, P, M Ben-Nun, JA Linker, et al. 2014. 'A multi-observatory inter-comparison of line-of-sight synoptic solar magnetograms.' *Solar Physics* 289 (3): 769–792.
- Riley, P, JA Linker, and Z Mikić. 2001. 'An empirically-driven global MHD model of the solar corona and inner heliosphere.' *Journal of Geophysical Research: Space Physics* 106 (A8): 15889–15901.
- Riley, P, JA Linker, Z Mikić, et al. 2006. 'A comparison between global solar magnetohydrodynamic and potential field source surface model results.' *The Astrophysical Journal* 653 (2): 1510.
- Riley, P, R Lionello, JA Linker, et al. 2011. 'Global MHD modeling of the solar corona and inner heliosphere for the whole heliosphere interval.' *Solar Physics* 274 (1-2): 361–377.
- Riley, P, and JG Luhmann. 2012. 'Interplanetary signatures of unipolar streamers and the origin of the slow solar wind.' *Solar Physics* 277 (2): 355–373.
- Roberts, DA, ML Goldstein, LW Klein, and WH Matthaeus. 1987. 'Origin and evolution of fluctuations in the solar wind: Helios observations and Helios-Voyager comparisons.' *Journal of Geophysical Research: Space Physics* 92 (A11): 12023–12035.
- Robinson, RD, SP Worden, and JW Harvey. 1980. 'Observations of magnetic fields on two late-type dwarf stars.' *The Astrophysical Journal* 236:L155–L158.
- Robrade, J, JHMM Schmitt, and F Favata. 2012. 'Coronal activity cycles in nearby G and K stars - XMM-Newton monitoring of 61 Cygni and  $\alpha$  Centauri.' *Astronomy & Astrophysics* 543:A84.
- Rod'kin, DG, YS Shugay, VA Slemzin, and IS Veselovskii. 2016. 'The effect of solar activity on the evolution of solar wind parameters during the rise of the 24th cycle.' *Solar System Research* 50 (1): 44–55.
- Roe, PL. 1981. 'Approximate Riemann solvers, parameter vectors, and difference schemes.' *Journal of computational physics* 43 (2): 357–372.
- Rosén, L, O Kochukhov, and Gregg A Wade. 2015. 'First Zeeman Doppler imaging of a cool star using all four Stokes parameters.' *The Astrophysical Journal* 805 (2): 169.

- Rosner, R, L Golub, and GS Vaiana. 1985. 'On stellar x-ray emission.' *Annual review of astronomy and astrophysics* 23 (1): 413–452.
- Rouillard, AP, M Lockwood, and I Finch. 2007. 'Centennial changes in the solar wind speed and in the open solar flux.' *Journal of Geophysical Research: Space Physics* 112 (A5).
- Rüedi, I, SK Solanki, G Mathys, and SH Saar. 1997. 'Magnetic field measurements on moderately active cool dwarfs.' *Astronomy and Astrophysics* 318:429–442.
- Russell, CT. 1975. 'On the possibility of deducing interplanetary and solar parameters from geomagnetic records.' *Solar Physics* 42 (1): 259–269.
- Saar, SH. 1990. 'Magnetic fields on solar-like stars: the first decade.' In *Symposium-International Astronomical Union*, 138:427–441. Cambridge University Press.
- Saar, SH, and A Brandenburg. 1999. 'Time evolution of the magnetic activity cycle period. II. results for an expanded stellar sample.' *The Astrophysical Journal* 524 (1): 295.
- Sadeghi Ardestani, L, T Guillot, and P Morel. 2017. 'A semi-empirical model for magnetic braking of solar-type stars.' *Monthly Notices of the Royal Astronomical Society* 472 (3): 2590–2607.
- Saikia, SB, SV Jeffers, J Morin, et al. 2016. 'A solar-like magnetic cycle on the mature K-dwarf 61 Cygni A (HD 201091).' *Astronomy & Astrophysics* 594:A29.
- Saikia, SB, T Lueftinger, SV Jeffers, et al. 2018a. 'Direct evidence of a full dipole flip during the magnetic cycle of a sun-like star.' *Astronomy & Astrophysics* 620:L11.
- Saikia, SB, CJ Marvin, SV Jeffers, et al. 2018b. 'Chromospheric activity catalogue of 4454 cool stars - questioning the active branch of stellar activity cycles.' *Astronomy & Astrophysics* 616:A108.
- Sakurai, T. 1990. 'Magnetohydrodynamic solar/stellar wind models.' *Computer Physics Reports* 12 (4): 247–273.
- Sanchez, S, A Fournier, and J Aubert. 2013. 'The predictability of advection-dominated flux-transport solar dynamo models.' *The Astrophysical Journal* 781 (1): 8.

- Sanchez-Diaz, E, AP Rouillard, JA Davies, E Kilpua, and I Plotnikov. 2017a. 'A catalogue of the small transients observed in STEREO HI-A and their associated in-situ measurements.' In *EGU General Assembly Conference Abstracts*, 19:4887.
- Sanchez-Diaz, E, AP Rouillard, JA Davies, et al. 2017b. 'The temporal and spatial scales of density structures released in the slow solar wind during solar activity maximum.' *The Astrophysical Journal* 851 (1): 32.
- Sanchez-Diaz, E, AP Rouillard, B Lavraud, et al. 2016. 'The very slow solar wind: properties, origin and variability.' *Journal of Geophysical Research: Space Physics* 121 (4): 2830–2841.
- Sauty, C, JJG Lima, N Iro, and K Tsinganos. 2005. 'Nonradial and nonpolytropic astrophysical outflows-VII. fitting ULYSSES solar wind data during minimum.' *Astronomy & Astrophysics* 432 (2): 687–698.
- Schatzman, E. 1962. 'A theory of the role of magnetic activity during star formation.' In *Annales d'astrophysique*, 25:18.
- Scherrer, PH, JM Wilcox, L Svalgaard, et al. 1977. 'The mean magnetic field of the Sun: observations at Stanford.' *Solar Physics* 54 (2): 353–361.
- Schou, J, HM Antia, S Basu, et al. 1998. 'Helioseismic studies of differential rotation in the solar envelope by the solar oscillations investigation using the Michelson Doppler Imager.' *The Astrophysical Journal* 505 (1): 390.
- Schrijver, CJ, J Cote, C Zwaan, and SH Saar. 1989. 'Relations between the photospheric magnetic field and the emission from the outer atmospheres of cool stars. I - the solar CA II K line core emission.' *The Astrophysical Journal* 337:964–976.
- Schrijver, CJ, ML DeRosa, et al. 2003. 'Asterospheric magnetic fields and winds of cool stars.' *The Astrophysical Journal* 590 (1): 493.
- Schrijver, CJ, and Y Liu. 2008. 'The global solar magnetic field through a full sunspot cycle: observations and model results.' *Solar Physics* 252 (1): 19–31.
- Schröder, KP, and M Cuntz. 2005. 'A new version of Reimers' law of mass loss based on a physical approach.' *The Astrophysical Journal Letters* 630 (1): L73.

- Schwenn, R. 2006. 'Space weather: the solar perspective.' *Living Reviews in Solar Physics* 3 (1): 2.
- . 2007. 'Solar wind sources and their variations over the solar cycle.' In *Solar Dynamics and Its effects on the Heliosphere and Earth*, 51–76. Springer.
- Sedlmayr, E, and C Dominik. 1995. 'Dust driven winds.' *Space Science Reviews* 73, no. 3 (August 1): 211–272.
- See, V. 2016. 'Stellar magnetism and activity: from stellar interiors to orbiting exoplanets.'
- See, V, M Jardine, AA Vidotto, et al. 2015. 'The energy budget of stellar magnetic fields.' *Monthly Notices of the Royal Astronomical Society* 453 (4): 4301–4310.
- See, V, M Jardine, AA Vidotto, et al. 2016. 'The connection between stellar activity cycles and magnetic field topology.' *Monthly Notices of the Royal Astronomical Society* 462 (4): 4442–4450.
- See, V, M Jardine, AA Vidotto, et al. 2017a. 'Studying stellar spin-down with Zeeman-Doppler magnetograms.' *Monthly Notices of the Royal Astronomical Society*: stw3094.
- See, V, M Jardine, AA Vidotto, et al. 2017b. 'Studying stellar spin-down with Zeeman-Doppler magnetograms.' *Monthly Notices of the Royal Astronomical Society* 466 (2): 1542–1554.
- See, V, M Jardine, AA Vidotto, et al. 2018. 'The open flux evolution of a solar-mass star on the main sequence.' *Monthly Notices of the Royal Astronomical Society* 474:536–546.
- See, V, L Lehmann, SP Matt, and AJ Finley. 2020. 'How much do underestimated field strengths from Zeeman-Doppler imaging affect spin-down torque estimates?' *arXiv preprint arXiv:2002.11774*.
- See, V, SP Matt, AJ Finley, et al. 2019a. 'Do non-dipolar magnetic fields contribute to spin-down torques?' *The Astrophysical Journal* 886 (2): 120.
- See, V, SP Matt, CP Folsom, et al. 2019b. 'Estimating magnetic filling factors from Zeeman-Doppler magnetograms.' *The Astrophysical Journal* 876 (2): 118.

- Semel, M. 1989. 'Zeeman-Doppler imaging of active stars. I - basic principles.' *Astronomy and Astrophysics* 225:456–466.
- Shapiro, AI, SK Solanki, NA Krivova, KL Yeo, and WK Schmutz. 2016. 'Are solar brightness variations faculae-or spot-dominated?' *Astronomy & Astrophysics* 589:A46.
- Shapiro, AI, SK Solanki, NA Krivova, et al. 2014. 'Variability of Sun-like stars: reproducing observed photometric trends.' *Astronomy & Astrophysics* 569:A38.
- Shkolnik, E, GAH Walker, and DA Bohlender. 2003. 'Evidence for planet-induced chromospheric activity on HD 179949.' *The Astrophysical Journal* 597 (2): 1092.
- Shulyak, D, A Reiners, A Engeln, et al. 2017. 'Strong dipole magnetic fields in fast rotating fully convective stars.' *Nature Astronomy* 1 (8): 0184.
- Siess, F, M Livio, and J Lattanzio. 2002. 'Structure, evolution, and nucleosynthesis of primordial stars.' *The Astrophysical Journal* 570 (1): 329.
- Skumanich, A. 1972. 'Time scales for CA II emission decay, rotational braking, and lithium depletion.' *The Astrophysical Journal* 171:565.
- Smith, EJ, and A Balogh. 1995. 'Ulysses observations of the radial magnetic field.' *Geophysical research letters* 22 (23): 3317–3320.
- Snodgrass, HB, and RK Ulrich. 1990. 'Rotation of Doppler features in the solar photosphere.' *The Astrophysical Journal* 351:309–316.
- Soderblom, DR. 1983. 'Rotational studies of late-type stars. II - ages of solar-type stars and the rotational history of the sun.' *The Astrophysical Journal Supplement Series* 53:1–15.
- Solanki, SK, S Motamen, and R Keppens. 1997. 'Polar spots and stellar spindown: is dynamo saturation needed?' *Astronomy and astrophysics* 325:1039–1044.
- Solanki, SK, M Schüssler, and M Fligge. 2002. 'Secular variation of the Sun's magnetic flux.' *Astronomy & Astrophysics* 383 (2): 706–712.
- Solanki, SK, IG Usoskin, B Kromer, M Schüssler, and J Beer. 2004. 'Unusual activity of the Sun during recent decades compared to the previous 11,000 years.' *Nature* 431 (7012): 1084.

- Sonett, CP, MS Giampapa, and MS Matthews. 1991. 'The sun in time.'
- Song, I, JP Caillault, DB y Navascués, JR Stauffer, and S Randich. 2000. 'Ages of late spectral type Vega-like stars.' *The Astrophysical Journal Letters* 533 (1): L41.
- Spiegel, EA. 1971. 'Convection in stars I. basic Boussinesq convection.' *Annual review of astronomy and astrophysics* 9 (1): 323–352.
- Sporer, FWG. 1887. 'tiber die Periodizitiit der Sonnenflecken seit dem Jahre 1618, vornehmlich in Bezug auf die heliographische Breite derselben, und Hinweis auf eine erhebliche Störung dieser Periodizitiit wiihrend eines langen Zeitraumes.' *Vjschr. Astron. Ges. Leipzig* 22: 323 329.
- Spruit, HC. 1981. 'Motion of magnetic flux tubes in the solar convection zone and chromosphere.' *Astronomy and Astrophysics* 98:155–160.
- Stahler, SW, F Palla, and EE Salpeter. 1986. 'Primordial stellar evolution - the pre-main-sequence phase.' *The Astrophysical Journal* 308:697–705.
- Stamper, R, M Lockwood, MN Wild, and TDG Clark. 1999. 'Solar causes of the long-term increase in geomagnetic activity.' *Journal of Geophysical Research: Space Physics* 104 (A12): 28325–28342.
- Stauffer, J, A collier Cameron, M Jardine, et al. 2017. 'Orbiting clouds of material at the Keplerian co-rotation radius of rapidly rotating low-mass WTTs in Upper Sco.' *The Astronomical Journal* 153 (4): 152.
- Stauffer, J, L Rebull, J Bouvier, et al. 2016. 'Rotation in the Pleiades with K2. III. speculations on origins and evolution.' *The Astronomical Journal* 152 (5): 115.
- Steinhilber, F, JA Abreu, J Beer, et al. 2012. '9,400 years of cosmic radiation and solar activity from ice cores and tree rings.' *Proceedings of the National Academy of Sciences* 109 (16): 5967–5971.
- Steinolfson, RS, and AJ Hundhausen. 1988. 'Density and white light brightness in loop-like coronal mass ejections: temporal evolution.' *Journal of Geophysical Research: Space Physics* 93 (A12): 14269–14276.



- Stelzer, B, and R Neuhäuser. 2001. 'X-ray emission from young stars in Taurus-Auriga-Perseus: luminosity functions and the rotation-activity-age-relation.' *Astronomy & Astrophysics* 377 (2): 538–556.
- Stevens, ML, JA Linker, P Riley, and WJ Hughes. 2012. 'Underestimates of magnetic flux in coupled MHD model solar wind solutions.' *Journal of Atmospheric and Solar-Terrestrial Physics* 83:22–31.
- Stone, EC, AC Cummings, FB McDonald, et al. 2008. 'An asymmetric solar wind termination shock.' *Nature* 454 (7200): 71–74.
- Strugarek, A, AS Brun, SP Matt, et al. 2014a. 'Modelling the corona of HD 189733 in 3D.' In *SF2A-2014: Proceedings of the Annual meeting of the French Society of Astronomy and Astrophysics*, 279–284.
- Strugarek, A, SA Brun, SP Matt, and V Réville. 2014b. 'On the diversity of magnetic interactions in close-in star-planet systems.' *The Astrophysical Journal* 795 (1): 86.
- . 2015. 'Magnetic games between a planet and its host star: the key role of topology.' *The Astrophysical Journal* 815 (2): 111.
- Stuiver, M. 1961. 'Variations in radiocarbon concentration and sunspot activity.' *Journal of Geophysical Research* 66 (1): 273–276.
- Stuiver, M, and PD Quay. 1980. 'Changes in atmospheric carbon-14 attributed to a variable sun.' *Science* 207 (4426): 11–19.
- Sun, X, Y Liu, JT Hoeksema, K Hayashi, and X Zhao. 2011. 'A new method for polar field interpolation.' *Solar Physics* 270 (1): 9.
- Suttner, G, and HW Yorke. 2001. 'Early dust evolution in protostellar accretion disks.' *The Astrophysical Journal* 551 (1): 461.
- Suzuki, TK. 2011. 'Self-consistent simulations of Alfvén wave driven winds from the sun and stars.' *Space science reviews* 158 (2-4): 339–363.
- Svalgaard, L, and EW Cliver. 2010. 'Heliospheric magnetic field 1835–2009.' *Journal of Geophysical Research: Space Physics* 115 (A9).

- Takeda, G, EB Ford, A Sills, et al. 2007. 'Structure and evolution of nearby stars with planets. II. physical properties of  $\sim 1000$  cool stars from the SPOCS catalog.' *The Astrophysical Journal Supplement Series* 168 (2): 297.
- Testa, P, JJ Drake, and G Peres. 2004. 'The density of coronal plasma in active stellar coronae.' *The Astrophysical Journal* 617 (1): 508.
- Testa, P, SH Saar, and JJ Drake. 2015. 'Stellar activity and coronal heating: an overview of recent results.' *Phil. Trans. R. Soc. A* 373 (2042): 20140259.
- Thatcher, LJ, and HR Müller. 2011. 'Statistical investigation of hourly OMNI solar wind data.' *Journal of Geophysical Research: Space Physics* 116 (A12).
- Tinker, J, M Pinsonneault, and D Terndrup. 2002. 'Angular momentum evolution of stars in the orion nebula cluster.' *The Astrophysical Journal* 564 (2): 877.
- Tokumaru, M, M Kojima, and K Fujiki. 2010. 'Solar cycle evolution of the solar wind speed distribution from 1985 to 2008.' *Journal of Geophysical Research: Space Physics* 115 (A4).
- . 2012. 'Long-term evolution in the global distribution of solar wind speed and density fluctuations during 1997–2009.' *Journal of Geophysical Research: Space Physics* 117 (A6).
- Toner, CG, and DF Gray. 1988. 'The starpatch on the G8 dwarf XI Bootis A.' *The Astrophysical Journal* 334:1008–1020.
- Tóth, G. 2000. 'The  $\nabla \cdot B = 0$  constraint in shock-capturing magnetohydrodynamics codes.' *Journal of Computational Physics* 161 (2): 605–652.
- Tóth, G, IV Sokolov, TI Gombosi, et al. 2005. 'Space Weather Modeling Framework: a new tool for the space science community.' *Journal of Geophysical Research: Space Physics* 110 (A12).
- Tu, CY. 1988. 'The damping of interplanetary Alfvénic fluctuations and the heating of the solar wind.' *Journal of Geophysical Research: Space Physics* 93 (A1): 7–20.
- Usmanov, AV, ML Goldstein, BP Besser, and JM Fritzer. 2000. 'A global MHD solar wind model with WKB Alfvén waves: comparison with Ulysses data.' *Journal of Geophysical Research: Space Physics* 105 (A6): 12675–12695.

- Usmanov, AV, ML Goldstein, and WH Matthaeus. 2014. 'Three-fluid, three-dimensional magnetohydrodynamic solar wind model with eddy viscosity and turbulent resistivity.' *The Astrophysical Journal* 788 (1): 43.
- Usmanov, AV, WH Matthaeus, ML Goldstein, and R Chhiber. 2018. 'The steady global corona and solar wind: a three-dimensional MHD simulation with turbulence transport and heating.' *The Astrophysical Journal* 865 (1): 25.
- Usoskin, IG. 2017. 'A history of solar activity over millennia.' *Living Reviews in Solar Physics* 14 (1): 3.
- Usoskin, IG, R Arlt, E Asvestari, et al. 2015. 'The Maunder minimum (1645–1715) was indeed a grand minimum: a reassessment of multiple datasets.' *Astronomy & Astrophysics* 581:A95.
- Usoskin, IG, SK Solanki, and GA Kovaltsov. 2007. 'Grand minima and maxima of solar activity: new observational constraints.' *Astronomy & Astrophysics* 471 (1): 301–309.
- Usoskin, IG, SK Solanki, M Schüssler, K Mursula, and K Alanko. 2003. 'Millennium-scale sunspot number reconstruction: evidence for an unusually active Sun since the 1940s.' *Physical Review Letters* 91 (21): 211101.
- Ustyugova, GV, AV Koldoba, MM Romanova, VM Chechetkin, and RVE Lovelace. 1999. 'Magnetocentrifugally driven winds: comparison of MHD simulations with theory.' *The Astrophysical Journal* 516 (1): 221.
- Ustyugova, GV, AV Koldoba, MM Romanova, and RVE Lovelace. 2006. "'Propeller" regime of disk accretion to rapidly rotating stars.' *The Astrophysical Journal* 646 (1): 304.
- van-der-Holst, B, WB Manchester IV, RA Frazin, et al. 2010. 'A data-driven, two-temperature solar wind model with Alfvén waves.' *The Astrophysical Journal* 725 (1): 1373.
- van-der-Holst, B, IV Sokolov, X Meng, et al. 2014. 'Alfvén wave solar model (AWSOM): coronal heating.' *The Astrophysical Journal* 782 (2): 81.
- van-Saders, JL, T Ceillier, TS Metcalfe, et al. 2016. 'Weakened magnetic braking as the origin of anomalously rapid rotation in old field stars.' *Nature* 529 (7585): 181.

- Van-Saders, JL, and MH Pinsonneault. 2013. 'Fast star, slow star; old star, young star: sub-giant rotation as a population and stellar physics diagnostic.' *The Astrophysical Journal* 776 (2): 67.
- Vaquero, JM, MC Gallego, IG Usoskin, and GA Kovaltsov. 2011. 'Revisited sunspot data: a new scenario for the onset of the Maunder minimum.' *The Astrophysical Journal Letters* 731 (2): L24.
- Vaquero, JM, and RM Trigo. 2014. 'Revised group sunspot number values for 1640, 1652, and 1741.' *Solar Physics* 289 (3): 803–808.
- Velli, M. 2010. 'Solar wind acceleration: mechanisms and scaling laws.' In *AIP Conference Proceedings*, 1216:14–19. AIP.
- Vidotto, AA. 2016. 'The magnetic field vector of the Sun-as-a-star.' *Monthly Notices of the Royal Astronomical Society* 459 (2): 1533–1542.
- Vidotto, AA, and V Bourrier. 2017. 'Exoplanets as probes of the winds of host stars: the case of the M dwarf GJ 436.' *Monthly Notices of the Royal Astronomical Society* 470 (4): 4026–4033.
- Vidotto, AA, N Feeney, and JH Groh. 2019. 'Can we detect aurora in exoplanets orbiting M dwarfs?' *Monthly Notices of the Royal Astronomical Society* 488 (1): 633–644.
- Vidotto, AA, SG Gregory, M Jardine, et al. 2014a. 'Stellar magnetism: empirical trends with age and rotation.' *Monthly Notices of the Royal Astronomical Society* 441 (3): 2361–2374.
- Vidotto, AA, M Jardine, and Ch Helling. 2011a. 'Prospects for detection of exoplanet magnetic fields through bow-shock observations during transits.' *Monthly Notices of the Royal Astronomical Society: Letters* 411 (1): L46–L50.
- Vidotto, AA, M Jardine, J Morin, et al. 2013. 'M-dwarf stellar winds: the effects of realistic magnetic geometry on rotational evolution and planets.' *Monthly Notices of the Royal Astronomical Society* 438 (2): 1162–1175.
- . 2014b. 'M-dwarf stellar winds: the effects of realistic magnetic geometry on rotational evolution and planets.' *Monthly Notices of the Royal Astronomical Society* 438 (2): 1162–1175.

- Vidotto, AA, M Jardine, M Opher, JF Donati, and TI Gombosi. 2011b. 'Understanding the angular momentum loss of low-mass stars: the case of V374 Peg.' In *16th Cambridge Workshop on Cool Stars, Stellar Systems, and the Sun*, 448:1293.
- Vidotto, AA, LT Lehmann, M Jardine, and AA Pevtsov. 2018. 'The magnetic field vector of the Sun-as-a-star-II. evolution of the large-scale vector field through activity cycle 24.' *Monthly Notices of the Royal Astronomical Society* 480 (1): 477–487.
- Vidotto, AA, M Opher, V Jatenco-Pereira, and TI Gombosi. 2009. 'Three-dimensional numerical simulations of magnetized winds of solar-like stars.' *The Astrophysical Journal* 699 (1): 441.
- . 2010. 'Simulations of winds of weak-lined T Tauri stars. II. the effects of a tilted magnetosphere and planetary interactions.' *The Astrophysical Journal* 720 (2): 1262.
- Vieira, LEA, and SK Solanki. 2010. 'Evolution of the solar magnetic flux on time scales of years to millenia.' *Astronomy & Astrophysics* 509:A100.
- Villarreal D'Angelo, C, M Jardine, CP Johnstone, and V See. 2019. 'Slingshot prominence evolution for a solar-like star.' *Monthly Notices of the Royal Astronomical Society* 485 (1): 1448–1453.
- Villarreal D'Angelo, C, M Jardine, and V See. 2018. 'Prominence formation and ejection in cool stars.' *Monthly Notices of the Royal Astronomical Society: Letters* 475 (1): L25–L29.
- Walker, Gordon AH, B Croll, JM Matthews, et al. 2008. 'MOST detects variability on  $\tau$  Bootis A possibly induced by its planetary companion.' *Astronomy & Astrophysics* 482 (2): 691–697.
- Wallis, MK. 1975. 'Local interstellar medium.' *Nature* 254 (5497): 202–203.
- Wang, YM. 1993. 'On the latitude and solar cycle dependence of the interplanetary magnetic field strength.' *Journal of Geophysical Research: Space Physics* 98 (A3): 3529–3537.
- . 1998. 'Cyclic magnetic variations of the Sun.' In *Cool Stars, Stellar Systems, and the Sun*, 154:131.
- Wang, YM, J Lean, and NR Sheeley. 2000. 'The long-term variation of the Sun's open magnetic flux.' *Geophysical Research Letters* 27 (4): 505–508.

- Wang, YM, and NR Sheeley Jr. 1990. 'Solar wind speed and coronal flux-tube expansion.' *The Astrophysical Journal* 355:726–732.
- . 1995. 'Solar implications of Ulysses interplanetary field measurements.' *The Astrophysical Journal Letters* 447 (2): L143.
- Wang, YM, and NR Sheeley. 2002. 'Sunspot activity and the long-term variation of the Sun's open magnetic flux.' *Journal of Geophysical Research: Space Physics* 107 (A10).
- Washimi, H, and T Sakurai. 1993. 'A simulation study of the solar wind including the solar rotation effect.' *Solar physics* 143 (1): 173–186.
- Washimi, H, and S Shibata. 1993. 'Thermo-centrifugal wind from a rotating magnetic dipole.' *Monthly Notices of the Royal Astronomical Society* 262 (4): 936–944.
- Washimi, H, T Tanaka, and GP Zank. 2017. 'Time-varying heliospheric distance to the heliopause.' *The Astrophysical Journal Letters* 846 (1): L9.
- Webb, DF, and RA Howard. 1994. 'The solar cycle variation of coronal mass ejections and the solar wind mass flux.' *Journal of Geophysical Research: Space Physics* 99 (A3): 4201–4220.
- Webb, DF, RA Howard, OC St Cyr, and A Vourlidas. 2017. 'Is There a CME Rate Floor? CME and Magnetic Flux Values for the Last Four Solar Cycle Minima.' *The Astrophysical Journal* 851 (2): 142.
- Webb, DF, and TA Howard. 2012. 'Coronal mass ejections: observations.' *Living Reviews in Solar Physics* 9 (1): 3.
- Weber, EJ, and L Davis. 1967. 'The angular momentum of the solar wind.' *The Astrophysical Journal* 148:217–227.
- Wenzler, T, SK Solanki, NA Krivova, and C Fröhlich. 2006. 'Reconstruction of solar irradiance variations in cycles 21–23 based on surface magnetic fields.' *Astronomy & Astrophysics* 460 (2): 583–595.
- Wieczorek, Mark. 2011. 'Shtools: tools for working with spherical harmonics.' *Astrophysics Source Code Library*.

- Wiegmann, T, Gordon JD Petrie, and P Riley. 2017. 'Coronal magnetic field models.' *Space Science Reviews* 210 (1-4): 249–274.
- Wilcox, JM, and PH Scherrer. 1972. 'Annual and solar-magnetic-cycle variations in the interplanetary magnetic field, 1926–1971.' *Journal of Geophysical Research* 77 (28): 5385–5388.
- Wilson, OC. 1978. 'Chromospheric variations in main-sequence stars.' *The Astrophysical Journal* 226:379–396.
- Wolf, R. 1851. 'Sonnenflecken Beobachtungen in der zweiten Hälfte des Jahres 1850.' *Mitt. Nat.forsch. Ges. Bern* 207:89.
- Wolff, S, and T Simon. 1997. 'The angular momentum of main sequence stars and its relation to stellar activity.' *Publications of the Astronomical Society of the Pacific* 109 (737): 759.
- Wolk, SJ, FR Harnden Jr, E Flaccomio, et al. 2005. 'Stellar activity on the young suns of Orion: COUP observations of K5-7 pre-main-sequence stars.' *The Astrophysical Journal Supplement Series* 160 (2): 423.
- Wood, BE. 2004. 'Astrospheres and solar-like stellar winds.' *Living Reviews in Solar Physics* 1 (1): 1–52.
- Wood, BE, and JL Linsky. 1998. 'The local ISM and its interaction with the winds of nearby late-type stars.' *The Astrophysical Journal* 492 (2): 788.
- Wood, BE, HR Müller, GP Zank, and JL Linsky. 2002. 'Measured mass-loss rates of solar-like stars as a function of age and activity.' *The Astrophysical Journal* 574 (1): 412.
- Wood, BE, HR Müller, GP Zank, JL Linsky, and S Redfield. 2005. 'New mass-loss measurements from astrospheric Ly $\alpha$  absorption.' *The Astrophysical Journal Letters* 628 (2): L143.
- Wright, NJ, and JJ Drake. 2016. 'Solar-type dynamo behaviour in fully convective stars without a tachocline.' *Nature* 535 (7613): 526–528.
- Wright, NJ, JJ Drake, EE Mamajek, and GW Henry. 2011. 'The stellar-activity-rotation relationship and the evolution of stellar dynamos.' *The Astrophysical Journal* 743 (1): 48.

- Wu, CJ, NA Krivova, SK Solanki, and IG Usoskin. 2018a. 'Solar total and spectral irradiance reconstruction over the last 9000 years.' *Astronomy & Astrophysics* 620:A120.
- Wu, CJ, I Usoskin, N Krivova, et al. 2018b. 'Solar activity over nine millennia: a consistent multi-proxy reconstruction.' *Astronomy & Astrophysics*.
- Xia, C, and R Keppens. 2016. 'Formation and plasma circulation of solar prominences.' *The Astrophysical Journal* 823 (1): 22.
- Yang, SH, J Zhang, CL Jin, LP Li, and HY Duan. 2009. 'Response of the solar atmosphere to magnetic field evolution in a coronal hole region.' *Astronomy & Astrophysics* 501 (2): 745–753.
- Zanni, C, and J Ferreira. 2009. 'MHD simulations of accretion onto a dipolar magnetosphere- I. accretion curtains and the disk-locking paradigm.' *Astronomy & Astrophysics* 508 (3): 1117–1133.
- Zarka, P. 2007. 'Plasma interactions of exoplanets with their parent star and associated radio emissions.' *Planetary and Space Science* 55 (5): 598–617.
- Zeeman, P. 1897. *The effect of magnetisation on the nature of light emitted by a substance*.
- Zendejas, J, Antígona Segura, and AC Raga. 2010. 'Atmospheric mass loss by stellar wind from planets around main sequence M stars.' *Icarus* 210 (2): 539–544.
- Zhang, J, KP Dere, RA Howard, MR Kundu, and SM White. 2001. 'On the temporal relationship between coronal mass ejections and flares.' *The Astrophysical Journal* 559 (1): 452.
- Zhao, X, and J Todd Hoeksema. 1994. 'A coronal magnetic field model with horizontal volume and sheet currents.' *Solar physics* 151 (1): 91–105.
- Zhao, X, and JT Hoeksema. 1995. 'Prediction of the interplanetary magnetic field strength.' *Journal of Geophysical Research: Space Physics* 100 (A1): 19–33.
- Zhao, XP, and JT Hoeksema. 2010. 'The magnetic field at the inner boundary of the heliosphere around solar minimum.' *Solar Physics* 266 (2): 379–390.



Zirin, H. 1988. 'Astrophysics of the Sun.' *Cambridge and New York, Cambridge University Press, 1988, 440 p.*

Zurbuchen, TH, and IG Richardson. 2006. 'In-situ solar wind and magnetic field signatures of interplanetary coronal mass ejections.' In *Coronal mass ejections*, 31–43. Springer.

# Index

The Index contains entries from the thesis text only, this does not include references from the published papers:

Ó Fionnagáin, D, [121](#), [171](#), [173](#)

Aarnio, AN, [169](#)

Agüeros, MA, [16](#)

Alvarado-Gómez, JD, [24](#), [63](#), [120](#), [121](#)

Amard, L, [4](#), [5](#), [16](#)

Amari, T, [24](#)

Arden, WM, [176](#)

Arlt, R, [178](#)

Böhm-Vitense, E, [10](#)

Babcock, HD, [179](#)

Babcock, HW, [13](#)

Babusiaux, C, [3](#)

Badman, ST, [53](#), [176](#)

Badman, SV, [21](#), [22](#)

Bahcall, JN, [5](#)

Baliunas, SL, [8](#), [9](#)

Baraffe, I, [4](#), [147](#), [170](#)

Bard, E, [181](#)

Barnes, SA, [16](#)

Basri, G, [146](#)

Bavassano, B, [19](#)

Beckers, JM, [124](#)

Beer, J, [181](#)

Bethe, HA, [5](#)

Biermann, L, [45](#)

Birkeland, K, [45](#)

Borovsky, JE, [22](#)

Bourrier, V, [22](#)

Bouvier, J, [3](#), [15–17](#)

Brandenburg, A, [10](#)

Brown, SF, [146](#)

Browning, MK, [11](#), [13](#)

Brun, SA, [11](#), [13](#), [121](#)

Bruno, R, [19](#)

Burlaga, LF, [27](#)

Cane, HV, [24](#), [131](#)

Carrington, RC, [45](#)

Cassinelli, JP, [48](#)

- Castor, JI, 2
- Chané, E, 22
- Chapman, GA, 179
- Chapman, S, 45
- Charbonneau, P, 6
- Clarke, C, 36, 38
- Clette, F, 178
- Cliver, EW, 177, 178
- Cohen, O, 49
- Coleman, PJ, 55
- Collier Cameron, A, 25, 26
- Courant, R, 255
- Covey, KR, 16, 18
- Cowley, SWH, 21
- Cranmer, SR, 64, 169, 258
- Crooker, NU, 178
- Crosley, MK, 24
- Curtis, JL, 18
- D'Amicis, R, 19
- Davenport, JRA, 18, 24
- Davis, L, 18, 55, 58, 61, 64
- De Laval, G, 46
- De Moortel, I, 51
- De Pater, I, 22
- Dedner, A, 79
- Delamere, PA, 22
- DeRosa, ML, 9, 74, 127–129
- Dominik, C, 2
- Donati, JF, 146
- Dotter, A, 5
- Douglas, ST, 16
- Drake, JJ, 11
- Dungey, JW, 22
- Eberhard, G, 8
- Ebert, RW, 19
- Eddy, JA, 179
- Egeland, R, 8, 9
- Einfeldt, B, 78
- Fagerstroem, EEF, 46
- Ferreira, J, 4
- Feynman, J, 178
- Filippone, BW, 5
- Fisher, GH, 51
- Fisk, LA, 20
- Forsyth, RJ, 20
- Foukal, P, 15
- Fox, NJ, 50, 231
- Galilei, G, 7, 178
- Gallet, F, 15–17
- Garraffo, C, 16, 63, 121
- Gastine, T, 148
- Georgoulis, MK, 24
- Goedbloed, Hans, 38, 57
- Goedbloed, JP, 49
- Goldstein, ML, 51
- Gosain, S, 127
- Gosling, JT, 20
- Guerrero, G, 14
- Hale, GE, 7
- Hall, JC, 8, 9
- Hansen, CJ, 5

- Hartmann, LMKB, 3  
Hathaway, DH, 7  
Hempelmann, A, 15  
Hickmann, KS, 127  
Hollweg, JV, 51  
Holzer, TE, 27, 49  
Hoshino, M, 22  
Hoyt, DV, 178  
Hudson, HS, 51  
  
Jardine, M, 25, 26, 176  
Jeffers, SV, 74, 75, 147  
Johns-Krull, CM, 146  
Jones, GH, 20  
  
Kasper, JC, 211, 231  
Kavanagh, RD, 22  
Keppens, R, 16, 25, 49  
Khodachenko, ML, 25  
Klimchuk, JA, 51  
Kopp, RA, 49  
  
Lal, D, 181  
Lamers, HJGLM, 48  
Lamy, P, 74  
Landstreet, JD, 146  
Larson, RB, 3  
Lean, J, 15  
Lee, CO, 176  
Lehmann, LT, 259  
Leighton, RB, 13  
Ling, AG, 177  
Linsky, JL, 124  
Lockwood, M, 177–180  
Lomax, H, 252  
Lowder, C, 19  
  
MacGregor, KB, 3  
Marsch, E, 61, 62, 198  
Martin-Torres, FJ, 21  
Matt, SP, 3, 4, 16, 49, 63, 64, 68, 70, 71,  
117, 120, 122, 123, 167, 230, 258  
Mayaud, PN, 177  
McComas, DJ, 3, 75  
McFadden, LA, 22  
McQuillan, A, 15, 16  
Mestel, L, 18  
Metcalf, TS, 10, 172  
Michels, DJ, 74  
Mignone, A, 75  
Mikić, Z, 74  
Moffatt, HK, 12  
Morgenthaler, A, 74, 147, 149  
Morin, J, 146, 148  
Mueller, D, 50, 231  
Muscheler, R, 181  
  
Núñez, A, 16  
Ness, NF, 27, 55  
Nicholson, SB, 7  
Nishida, A, 22  
Noyes, RW, 8  
  
Obridko, VN, 127  
Odstrcil, D, 63  
Osten, RA, 24

- Owens, MJ, 20, 175, 177, 179, 180, 191
- Pantolmos, G, 49, 63, 64, 68, 70, 71, 117, 120, 122, 167
- Parenti, S, 25
- Parker, EN, 13, 47, 49, 51, 53
- Parnell, CE, 51
- Parsons, A, 63
- Pauldrach, A, 3
- Paxton, B, 5
- Peters, B, 181
- Petit, P, 74, 147, 149
- Pizzo, V, 20, 174, 198–200
- Press, WH, 15
- Priest, E, 38, 51
- Pudritz, RE, 3, 4, 16
- Pulkkinen, T, 25
- Réville, V, 49, 63, 64, 67–70, 121, 229, 245
- Rebull, LM, 16
- Regi, M, 35
- Reiners, A, 6, 146
- Reinhold, T, 8, 15, 18
- Richardson, IG, 24, 25, 131
- Richter, AK, 61, 62, 198
- Riley, P, 63, 124
- Robinson, RD, 25
- Roe, PL, 119
- Rouillard, AP, 178
- Russell, CT, 178
- Rybicki, GB, 15
- Saar, SH, 10, 64, 258
- Sadeghi Ardestani, L, 16
- Saikia, SB, 9, 10, 75, 147–149
- Sakurai, T, 49
- Sanchez, S, 12
- Sanchez-Diaz, E, 20
- Sauty, C, 199, 200
- Schatten, KM, 178
- Schrijver, CJ, 9
- Schwarzschild, K, 8
- Schwenn, R, 24
- Sedlmayr, E, 2
- See, V, 16, 63, 146, 149, 166, 170, 173, 231, 234
- Semel, M, 146
- Shapiro, AI, 8
- Sheeley Jr, NR, 63
- Shibata, S, 49
- Shkolnik, E, 23
- Siess, F, 4
- Skumanich, A, 16, 148, 174, 230, 232
- Soderblom, DR, 16
- Solanki, SK, 16, 179
- Spiegel, EA, 5
- Sporer, FWG, 179
- Stahler, SW, 4
- Stamper, R, 177
- Stauffer, J, 25
- Steinhilber, F, 181
- Stone, EC, 27
- Strugarek, A, 23
- Sun, X, 127

- Suttner, G, 4
- Suzuki, TK, 52, 63
- Svalgaard, L, 178
- Tóth, G, 79
- Testa, P, 8
- Tinker, J, 3
- Tu, CY, 19
- Usmanov, AV, 63, 174
- Valenti, JA, 146
- van-der-Holst, B, 63
- van-Saders, JL, 18, 172, 232
- Vaquero, JM, 178
- Vidotto, AA, 16, 22, 49, 74, 127, 147, 171, 173, 234, 238
- Vieira, LEA, 179
- Villarreal D'Angelo, C, 25, 26
- Wallis, MK, 27
- Wang, YM, 63
- Washimi, H, 27, 49
- Webb, DF, 24
- Weber, EJ, 18, 55, 58, 61, 64
- Wiegelmann, T, 238
- Wilcox, JM, 55
- Wilson, OC, 9
- Wolf, R, 178
- Wood, BE, 27, 28, 124, 150
- Wright, NJ, 11, 147
- Wu, CJ, 177, 180, 181
- Xia, C, 25
- Yang, SH, 50
- Yorke, HW, 4
- Zanni, C, 4
- Zarka, P, 22
- Zeeman, P, 10
- Zendejas, J, 21
- Zhang, J, 24
- Zirin, H, 7, 45
- Zurbuchen, TH, 25